Journal of Experimental and Theoretical Physics, Vol. 90, No. 3, 2000, pp. 407–414.
Translated from Zhurnal Éksperimental'noĭ i Teoreticheskoĭ Fiziki, Vol. 117, No. 3, 2000, pp. 467–475.

ATOMS, SPECTRA, RADIATION

Scattering of Atoms in a Bichromatic Field of Oppositely Propagating Light Pulses

V. I. Romanenko* and L. P. Yatsenko

Institute of Physics, National Academy of Sciences of Ukraine, pr. Nauki 144, Kiev, 258650 Ukraine
**e-mail: vr@marion.iop.kiev.ua*

Received April 13, 1999

Abstract—The interaction of a two-level atom with two light pulses which have different carrier frequencies and propagate in opposite directions is studied in the adiabatic approximation. It is shown that when there is a delay between the light pulses, the momentum of the atom changes, as a result of the interaction with the laser field, by a definite amount that depends on the amplitude of the light pulses and on the difference of their carrier frequencies. It is predicted that the momentum transfer to the atom is a step function of the amplitude of the light pulses. © *2000 MAIK "Nauka/Interperiodica".*

1. INTRODUCTION

The mechanical action of light fields on atoms has been under study, theoretically and experimentally, for many years. An important example is the scattering of atoms by a standing wave [1–4], which an atom incident on a laser beam in a direction normal to the beam "sees" as two oppositely propagating light pulses with the same carrier frequency and the same amplitude, interacting simultaneously with the atom. During the period of time when the energy of the translational motion of the atom in the direction of propagation of the pulses can be neglected compared with the atom–field interaction energy (Raman–Nata approximation), the rms momentum transfer to the atom grows linearly with time, and the average momentum transfer to the atom is zero. The introduction of a time delay between the pulses causes the scattering of the atoms to become asymmetric due to the formation of a coherent superposition of the ground and excited states by the field of one of the traveling waves and subsequent scattering of atoms with simultaneous interaction with the field of the two oppositely propagating waves [5–7]. The average momentum transfer is no longer zero and is directly proportional to the interaction time. The rms deviation of the momentum transfer to the atom from the average value also increases linearly. On the other hand, the effect of the radiation spectrum on the interaction of an atom with a field has been studied for a long time for bichromatic fields [8–12]. Specifically, it has been shown that the force acting on an atom in a bichromatic field of two standing waves, which can be treated as two oppositely propagating bichromatic waves with the same amplitude, can be much greater than the force due to the light pressure acting on an atom in a single traveling wave [13–19].

In the present paper, the characteristic features of the scattering of atoms in the field of oppositely propagating light pulses with a time delay between the onset of their interaction with the atom are studied for the case where the carrier frequencies of the pulses are different. The delay together with the difference of the carrier frequencies of the pulses qualitatively change the picture of the scattering. The parameters of the laser radiation can be chosen so that for a certain interaction time of the atom interacting with a bichromatic field the average momentum transferred to the atom is essentially independent of the duration of the light pulses, and the rms deviation of the momentum transferred to the atom from the average value approaches zero. In this case, varying the parameters of the laser radiation over quite wide limits has no effect on the result of the interaction of an atom with the field.

2. BASIC EQUATIONS

We shall assume that the light pulses are so short that the spontaneous radiation during the interaction of an atom with the light can be neglected. The Schrödinger equation describing in this case the interaction of a two-level atom with an electromagnetic wave has the form

$$i\hbar\frac{\partial\Psi}{\partial t} = (H_0 - \hat{\mathbf{d}}\cdot\mathbf{E})\Psi, \tag{1}$$

where

$$H_0 = \frac{\hat{\mathbf{p}}^2}{2M} + \hbar\omega_0|e\rangle\langle e|, \tag{2}$$

$\hat{\mathbf{p}}$ is the momentum operator of the atom, $\hbar\omega_0$ is the eigenvalue of the Hamiltonian of a stationary atom in the absence of the light fields and corresponding to the excited state $|e\rangle$ of the atom (we assume the eigenvalue corresponding to the ground state $|g\rangle$ is zero), $\hat{\mathbf{d}}$ is the

dipole-moment operator, and **E** is the total intensity of the electric field due to the light pulses. For the present case of light pulses propagating in opposite directions

$$\begin{aligned}\mathbf{E} &= E_1(t)\mathbf{e}_1\cos(\omega_1 t - k_1 z + \varphi_1)\\ &+ E_2(t)\mathbf{e}_2\cos(\omega_2 t + k_2 z + \varphi_2),\end{aligned} \tag{3}$$

where $\mathbf{e}_i$ are unit vectors in the direction of the field intensities of the light pulses, $E_i(t)$ describe the time dependences of the envelopes of the intensities of the light fields of the pulses, ω_i and k_i are the carrier frequencies and wave vectors of the light pulses, and φ_i are their initial phases. Both initial phases can be reduced to zero by choosing an appropriate reference point for time and the coordinates, and in what follows we shall set $\varphi_1 = \varphi_2 = 0$.

We represent the wave function in the coordinate representation in the form

$$\Psi = c_e(z, t)\exp(-i\omega_0 t)|e\rangle + c_g(z, t)|g\rangle. \tag{4}$$

Substituting expressions (3) and (4) into equation (1), we find in the rotating-wave approximation equations for $c_g(z, t)$ and $c_e(z, t)$ which in the limit $M \longrightarrow \infty$ are identical to the equations ordinarily used for analyzing the interaction of a two-level atom with a bichromatic field [8]:

$$i\hbar\frac{\partial}{\partial t}\begin{bmatrix}c_g\\ c_e\end{bmatrix} = \frac{\hbar}{2}\begin{bmatrix}-\frac{\hbar}{M}\frac{\partial^2}{\partial z^2} & V_1\exp(i\eta_1) + V_2\exp(i\eta_2)\\ V_1\exp(-i\eta_1) + V_2\exp(-i\eta_2) & -\frac{\hbar}{M}\frac{\partial^2}{\partial z^2}\end{bmatrix}\begin{bmatrix}c_g\\ c_e\end{bmatrix}, \tag{5}$$

where M is the mass of an atom, $\eta_1 = \omega_1 t - \omega_0 t - k_1 z$, $\eta_2 = \omega_2 t - \omega_0 t - k_2 z$, and the matrix elements of the operator corresponding to the interaction of the atom with the field of each of the light pulses are determined by the relations

$$\begin{aligned}\hbar V_1 &= -\langle g|\hat{\mathbf{d}}\cdot\mathbf{e}_1|e\rangle E_1,\\ \hbar V_2 &= -\langle g|\hat{\mathbf{d}}\cdot\mathbf{e}_2|e\rangle E_2.\end{aligned} \tag{6}$$

As usual, we assume the matrix elements of the dipole moment to be real. In equation (5) and below, the arguments denoting the dependence of the quantities on the time t and on z are omitted in order to simplify the equations.

It is well known [3] that the observation of the scattering of an atomic beam cannot give information about the degree of coherence of the plane waves describing the atomic ensemble. The quantities observed in the scattering of an atomic beam can be obtained by solving the problem of scattering of a plane wave and then averaging the result obtained over the angular distribution of the plane waves. For this reason, we shall assume in what follows that the atomic beam prior to the interaction with the light is a plane wave. Without loss of generality, on the basis of the approximation employed we shall also assume that the velocity of the atoms before the interaction with light is directed perpendicular to the z axis. In addition, since $|\omega_1 - \omega_2| \ll \omega_0$, we shall neglect the difference between k_1 and k_2, and we shall set $k_1 = k_2 = k$.

We now represent c_g and c_e in the form

$$\begin{aligned}c_g &= \sum_{n=-\infty}^{\infty} b_{g,n}\exp\left(\frac{i}{2}(\Delta t - n\delta t)\right)\langle z|n\rangle,\\ c_e &= \sum_{n=-\infty}^{\infty} b_{e,n}\exp\left(-\frac{i}{2}(\Delta t + n\delta t)\right)\langle z|n\rangle,\end{aligned} \tag{7}$$

where $\langle z|n\rangle = \exp(inkz)$ is an eigenfunction in the coordinate representation of the z component of the momentum of the atom, a multiple of $n\hbar k$,

$$\delta = \omega_1 - \omega_2, \quad \Delta = \frac{1}{2}(\omega_1 + \omega_2) - \omega_0. \tag{8}$$

The time-dependent phases in equation (7), which are not important for determining the probabilities $|b_{g,n}|^2$ and $|b_{e,n}|^2$ of finding the atom in the states $|g, n\rangle = |g\rangle \otimes |n\rangle$ and $|e, n\rangle = |e\rangle \otimes |n\rangle$, are introduced so that the following equations obtained for $b_{g,n}$ and $b_{e,n}$ by substituting expressions (7) into equation (5):

$$\begin{aligned}i\frac{\partial}{\partial t}b_{g,n} &= \frac{1}{2}(2n^2\delta_{\mathrm{rec}} + \Delta - n\delta)b_{g,n}\\ &+ \frac{1}{2}(V_1 b_{e,n+1} + V_2 b_{e,n-1}),\\ i\frac{\partial}{\partial t}b_{e,n} &= \frac{1}{2}(2n^2\delta_{\mathrm{rec}} - \Delta - n\delta)b_{e,n}\\ &+ \frac{1}{2}(V_1 b_{g,n-1} + V_2 b_{g,n+1}),\end{aligned} \tag{9}$$

where $\delta_{rec} = \hbar k^2/(2M)$, would contain on the right-hand sides only coefficients that vary slowly with time.

It follows from equation (9) that $b_{g,n}$ with even values of n are coupled with $b_{e,n}$ with odd values of n and vice versa. Since the initial conditions are $b_{g,n} = \delta_{n0}$ and $b_{e,n} = 0$ (we assume that before interacting with the field the atom is in the ground state), we can see that only $b_{g,n}$ with even n and $b_{e,n}$ with odd n can be different from zero. Thus, the wave function in the momentum representation can be given by a quantity B_n, which has only one index, that is the same as $b_{g,n}$ if n is even and $b_{e,n}$ if n is odd. In this notation the Schrödinger equation (9) has the form

$$i\hbar\frac{\partial}{\partial t}B_n = \sum_m H_{n,j}B_j. \tag{10}$$

The nonzero matrix elements of the Hamiltonian H are

$$\begin{aligned} H_{n,n} &= \frac{\hbar}{2}[2n^2\delta_{rec} + s(n)\Delta - n\delta], \\ H_{n,n+s(n)} &= \frac{\hbar}{2}V_1, \\ H_{n,n-s(n)} &= \frac{\hbar}{2}V_2, \end{aligned} \tag{11}$$

where $s(n) = (-1)^n$.

In what follows, we shall consider the case $\delta \gg \delta_{rec}$ and neglect, almost everywhere, the term describing the kinetic energy in the Hamiltonian (the Raman–Nata approximation).

3. EXAMPLE OF THE NUMERICAL SOLUTION OF THE EQUATIONS

Equations (10) couple all probability amplitudes for finding an atom in the states $|g, 2j\rangle$ and $|e, (2n+1)\rangle$, where j and n are arbitrary integers, and it is natural to expect that after interacting with both light pulses the atom will be in a superposition of states with different z components of the momentum. An example of the numerical solution of these equations which is presented in Fig. 1 shows that this is not always so. The figure shows the time dependences of the average z component of the momentum of the atom

$$p = \hbar k\sum_n n|B_n|^2, \tag{12}$$

the rms deviation of the z component of the momentum of the atom from the average value,

$$\Delta p = \hbar k\sqrt{\sum_n n^2|B_n|^2 - p^2}, \tag{13}$$

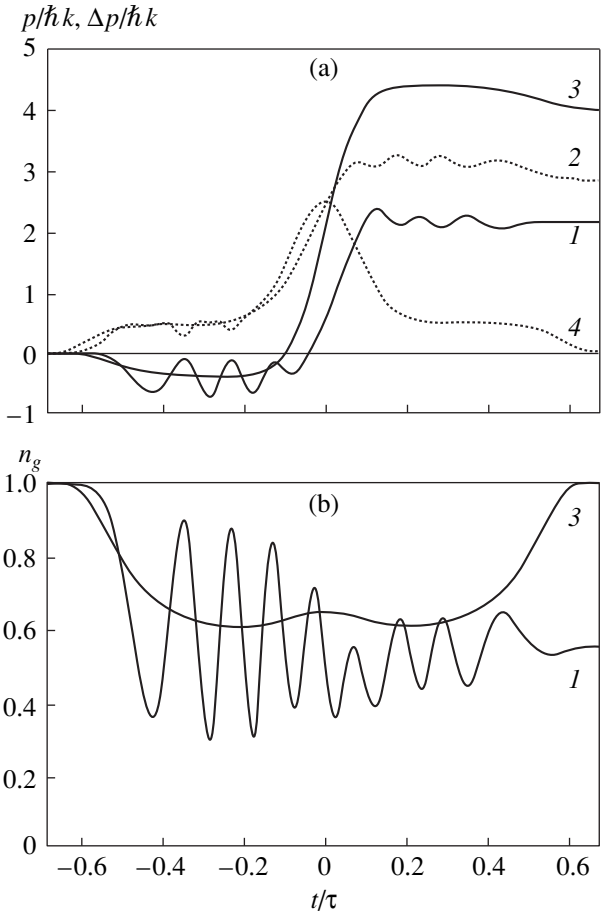

Fig. 1. Time dependences of (a) the average value of the z component of the momentum p of the atom (solid curves), the rms deviation of the momentum from the average value Δp (dotted curves) in units of $\hbar k$ and (b) the populations of the ground state n_g for the interaction of atoms with light pulses with the shape (15) for $\delta\tau = 25$ (curves *1*, *2*), $\delta\tau = 200$ (curves *3*, *4*). The delay between the pulses is $t_d = 0.35\tau$, the maximum value of the Rabi frequencies of the light pulses is $V_{01} = V_{02} = 2.4\delta$, $\Delta = 0$, $\delta_{rec} = 0$.

and the populations of the states $|g\rangle$ and $|e\rangle$,

$$n_g = \sum_{m=-\infty}^{\infty}|B_{2m}|^2, \quad n_e = \sum_{m=-\infty}^{\infty}|B_{2m+1}|^2, \tag{14}$$

for an atom interacting with oppositely propagating light pulses for short and long atom–field interaction times. The time dependences of the envelopes of the electric-field intensities of the pulses are described by the expressions

$$\begin{aligned} V_1 &= V_{01}F\left(\frac{t - t_d/2}{\tau}\right), \\ V_2 &= V_{02}F\left(\frac{t + t_d/2}{\tau}\right), \end{aligned} \tag{15}$$

where τ is the pulse duration, t_d is the delay between the pulses, and

$$F(x) = \begin{cases} \cos^2(\pi x), & -1/2 \le x \le 1/2 \\ 0, & x \le -1/2, \quad x \ge 1/2. \end{cases} \tag{16}$$

The fact that after a prolonged interaction with the field ($\delta\tau \gg 1$) the quantity Δp approaches zero indicates almost complete transfer of the population from the initial state $|g, 0\rangle$ of the atom into a state with a precisely determined z component of the momentum, in this case $|g, 4\rangle$. The time dependences of the population of the state $|g\rangle$ for various values of $\delta\tau$ also indicate that as $\delta\tau$ increases, the solutions of equations (10) approach a limit. Numerical calculations for large $\delta\tau$ give virtually the same dependences $p(t)$, $\Delta p(t)$, and $n_g(t)$ as for $\delta\tau$ = 200. This shows that the description of the atom–field interaction by means of an adiabatic basis is useful. It can be expected that for large $\delta\tau$ the atom will reside, during a substantial fraction of the time for which it interacts with the field, in a superposition of $|g, 2n\rangle$ and $|e, 2j + 1\rangle$ states (generally speaking, the integers n and j run through all values from $-\infty$ to $+\infty$).

We note that the time dependence of the populations with the interaction switched on and off adiabatically ($\delta\tau \gg 1$) is qualitatively different from the time dependence in the case when the interaction is switched on instantaneously [8], so that the populations of the levels vary periodically from 0 to 1 (for $V_1(t) = V_2(t) = \text{const}$). Evidently, the initial value $n_g = 1$ in the latter case corresponds to the atom residing in a superposition of several adiabatic states. As a result, the time dependence of the population of the lower state is determined by the interference of these states, and this results in oscillations of the populations.

4. ADIABATIC BASIS

We represent B_n in the form

$$B_n = \sum_{m=-\infty}^{\infty} C^{(m)} \exp\left(-i\int^t \varpi^{(m)}(t')dt'\right)\Phi_n^{(m)}, \tag{17}$$

where $\Phi_n^{(m)}$ and $\hbar\varpi^{(m)}$ are the components of the eigenvectors (adiabatic states) and the eigenvalues of the Hamiltonian H:

$$[H(t) - \hbar\varpi^{(m)}(t)]\Phi^{(m)} = 0. \tag{18}$$

The matrix elements of this Hamiltonian in the momentum representation are given by the expressions (11).

Substituting the expression (17) into equation (10) and keeping in mind (18) and the orthogonality of $\Phi^{(m)}$, we obtain the following equations for $C^{(m)}$:

$$\frac{d}{dt}C^{(m)} = -\sum_{j=-\infty}^{\infty}\sum_{n=-\infty}^{\infty} C^{(j)}\Phi_n^{(m)*}\frac{\partial}{\partial t}\Phi_n^{(j)} \times \exp\left(i\int^t(\varpi^{(m)}(t') - \varpi^{(j)}(t'))dt'\right). \tag{19}$$

According to equation (17), the wave function at an arbitrary time is a superposition of adiabatic states, the contribution of each of which is determined by the quantity $C^{(m)}$.

Let the atom be in the state $|g, 0\rangle$ before its interaction with the light fields. We shall enumerate the adiabatic states in a manner so that before the interaction with the field the number of the state coincides with the z component of the momentum of the atom in units of $\hbar k$. Then, initially we have $C^{(m)} = \delta_{m0}$. Correspondingly, $\varpi^{(0)}(\tau) = \Delta/2$ (this is easy to see from equation (11), since in the absence of the fields the Hamiltonian is diagonal). If

$$|\varpi^{(m)}(t) - \varpi^{(j)}(t)| \gg 1/\tau, \tag{20}$$

the terms with $j \neq m$ make virtually no contribution to the right-hand side of equation (19) because of the rapid oscillation of the exponential factors, and the term with $j = m$ leads only to a change in the phase of $C^{(m)}$. As a result, when condition (20) is satisfied, the atom is in the same adiabatic state throughout the entire time over which it interacts with the field. However, it should be noted that when the interaction with the field terminates, the energy $\hbar\varpi^{(0)}(t)$ corresponding to this state is not necessarily $\hbar\Delta/2$. From the form of the Hamiltonian (11) it can be concluded only that the energy is $\hbar[2n^2\delta_{\text{rec}} + \Delta(-1)^n - n\delta]/2$, where n is an integer. Ultimately, the atom acquires a momentum $n\hbar k$, directed along the z axis, and depending on whether n is even or odd it remains in the ground state or transfers into the excited state.

In order that a single adiabatic state couple the state of the atom with different z components of the momentum, a time shift must be present between the light pulses. Evidently, for $t_d = 0$, because of the symmetry of the problem, the internal state of the atom and the z component of the momentum of the atom before and after the interaction with the field are the same for long light pulses of the same shape. Specifically, for a symmetric offset of the carrier frequencies of the light pulses $\Delta = 0$, for pulses of the same shape and amplitude, the problem can be solved exactly, and following [8] it can be shown that in the adiabatic approximation the atom remains in the state $|g, 0\rangle$ after interacting with the field.

The changes in the state of the atom during the interaction with the field can be thought of as follows. At first, the atom is in the state $|g, 0\rangle$. For definiteness, we

assume that first the pulse $E_2(t)$ interacts with the atom (step I), then both pulses interact with the atom (step II), and at the end of the interaction the pulse $E_1(t)$ interacts with the atom (step III). Evidently, at the first step the field $E_2(t)$ gives rise to transitions between the states of the atom $|g, 0\rangle$ and $|e, -1\rangle$. In this case, p cannot exceed the value $\hbar k$, and Δp does not exceed $0.5\hbar k$ (see Fig. 1). Further, at the second step the equations (10) couple all states of the atom $|g, j\rangle$ and $|e, n\rangle$, where j are even and n are odd numbers. At this step Δp reaches its maximum value, and then it once again decreases approximately to $0.5\hbar k$. If the envelopes of the electric-field intensities change slowly enough, then at the third step of the atom–field interaction only the pair of states $|g, 2n_f\rangle$ and $|e, 2n_f + 1\rangle$, where n_f is an integer, will be populated. After the field $E_1(t)$ is switched off, the atom occupies one of these two states.

If the criterion (20) is not satisfied for a short time interval (as compared with the pulse duration τ) and the energies of the adiabatic states $\hbar\varpi^{(n)}$ and $\hbar\varpi^{(j)}$ are so close to one another that Landau–Zener transitions are possible between the corresponding adiabatic states with probability close to one, the atom after each of these transitions is in one adiabatic state. As a result, the atom is in the ground or excited state with a definite value of the z component of the momentum. However, if the Landau–Zener transition probabilities are substantially different from 1 and 0, for example, if the curves describing the time dependences of the energies of the adiabatic states touch, states with different values of the z components of the momentum could be occupied after the interaction with the field is completed.

Figure 2 illustrates the time dependence of the energies of the adiabatic states for two values of the parameters of the pulses corresponding to Fig. 1. The heavy line shows the energy of the adiabatic state occupied by the atom. It is evident that before the arrival of the first light pulse the z component of the momentum is zero, and after the interaction with both pulses it is equal to $4\hbar k$.

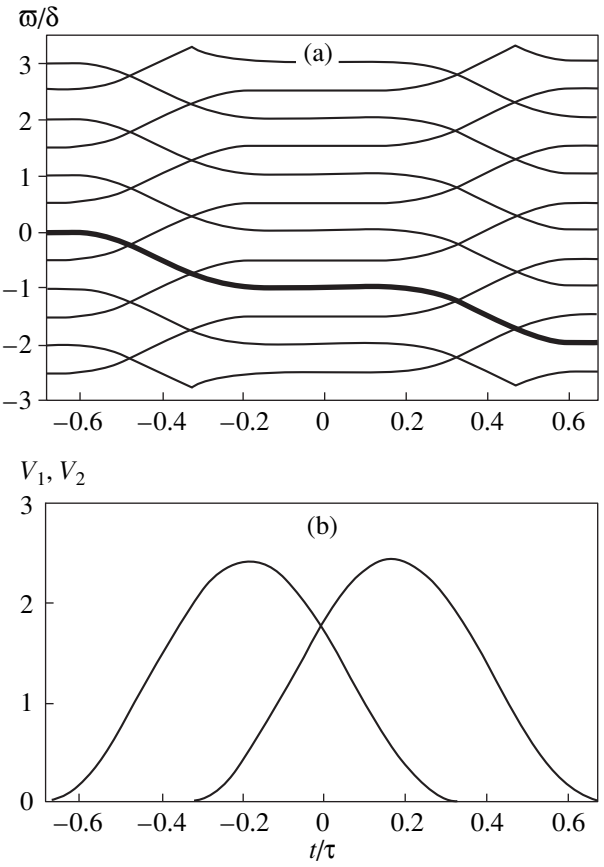

Fig. 2. Time dependences of (a) the energies of the adiabatic states $\hbar\varpi^{(m)}$ in the units $\hbar\delta$ (b) the Rabi frequencies of the light pulses. The heavy line shows the energy corresponding to a zeroth z component of the initial momentum of the atom. The pulse parameters are the same as in Fig. 1.

5. NUMERICAL RESULTS

We shall now examine the dependence of the momentum transfer to the atom on various parameters characterizing the light pulses [15]. Evidently, the result of the interaction of an atom with light should not depend on the changes in the delay between the pulses, their amplitudes, and the values of the offsets δ and Δ as long as the deformation introduced into the curves describing the time dependences of the energies of the adiabatic states by a variation of these parameters does not change qualitatively the relative arrangement of the curves. A further change in these parameters after passage through a transitional region should result in a transition of the atom into a new final state corresponding to a different value of p. On this basis, it can be expected that the dependence of the momentum transfer to the atom on the parameters describing the light pulses should be a step function.

For the case of equal amplitudes, $V_0 = V_{01} = V_{02}$, and symmetric, with respect to the frequency ω_0, offset of the carrier frequencies of the light pulses, Fig. 3 shows the quantities p and Δp and the populations of the ground and excited states as functions of V_0 obtained both in the Raman–Nata approximation and with the Hamiltonian including the kinetic energy. As a result of the interaction with the light, for values of V_0 lying in the region of the steps, the atom is in the ground state, and population transfer between the atomic states does not occur. Equalization of the populations of the states $|g\rangle$ and $|e\rangle$ is observed at the center of the transitional regions between the steps, i.e., the effect of two light pulses with different frequencies on the atom is similar to the effect of a $\pi/2$ pulse resonant with an atomic transition, the difference being that the momentum transfer can be much larger. The value of p for a given value of V_0 can be estimated from simple considerations. For $\Delta = 0$ with $|t| \ll \tau$ (at the midpoint of the

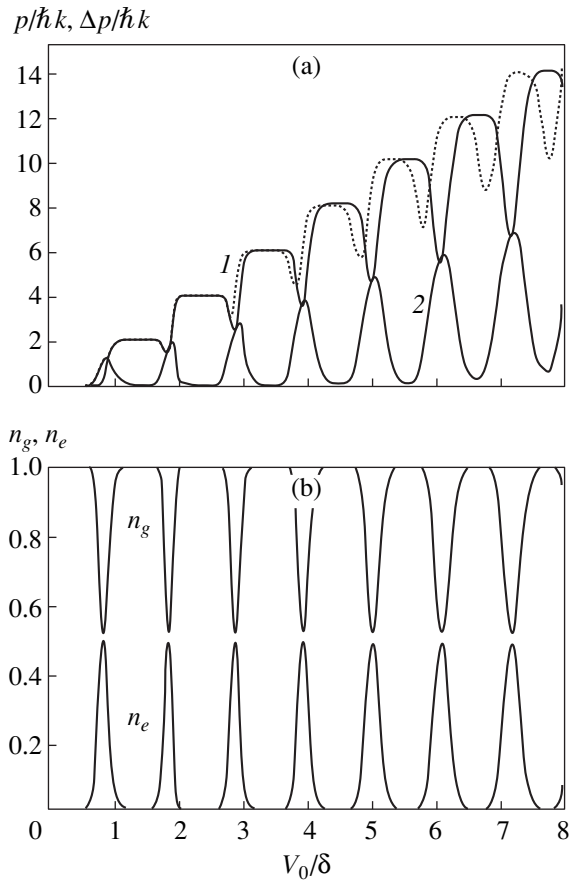

Fig. 3. (a) The average value of the z component of the momentum p of an atom (curve *1* for $\delta_{rec} = 0$, dotted curve for $\delta_{rec} = 0.002\delta$), the rms deviation of the component from the average value Δp (curve *2* for $\delta_{rec} = 0$) in units of $\hbar k$, and (b) the populations of the ground and excited states ($\delta_{rec} = 0$) as functions of V_0/δ. The pulse parameters are $\delta\tau = 200$, $\Delta = 0$, $t_d = 0.35\tau$.

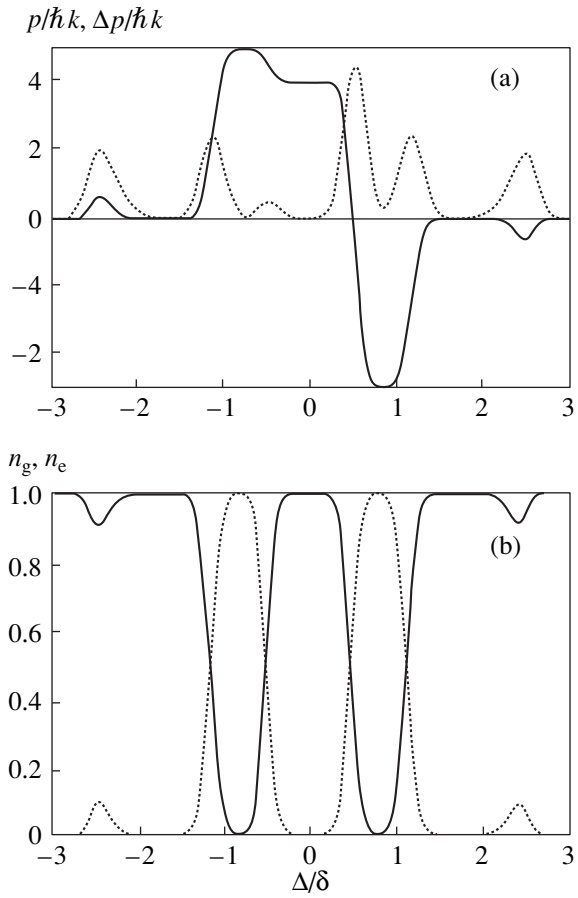

Fig. 4. (a) The average value of the z component of the momentum p of an atom (solid curve), the rms deviation of the component from the average value Δp (dotted curve) in units of $\hbar k$, and (b) the populations of the ground state n_g (solid curve) and the excited state n_e (dotted curve) as functions of Δ/δ. The pulse parameters are $V_{01} = V_{02} = 2.4\delta$, $t_d = 0.35\tau$, $\delta_{rec} = 0$.

interaction time with the field) $|\varpi^{(0)}| \sim V_0/2$. Keeping in mind the dependence $\varpi^{(0)}(t)$ (see Fig. 2), it can be assumed that when the interaction with the field terminates, $|\varpi^{(0)}| \sim V_0$. Since a change in $\varpi^{(0)}$ by δ corresponds to a change in the momentum by $2\hbar k$, we find $p \sim 2\hbar k V_0/\delta$, which agrees well with the computational results. Taking account of the kinetic energy in the Hamiltonian changes the spacing between the energies of the adiabatic states $\hbar\varpi^{(j)}$, and the position of the steps in the function $p(V_0)$ changes. Even if the kinetic energy $K = \hbar\delta_{rec}(p/\hbar k)^2$ which the atom acquires after interacting with the field is small (on the right-hand side of the plot it is less than 1/10 the atom–field interaction energy), this energy can still make a substantial contribution if it is comparable to the spacing between the eigenvalues of the Hamiltonian (11), which is $\sim\hbar\delta$ in the absence of a field (on the right-hand side of the plot it is equal to approximately 1/2 of this value, and near the third step, where the kinetic energy essentially does not change the result obtained in the Raman–Nata approximation, $K/\hbar\delta = 0.07$).

The dependences of p, Δp, n_g, and n_e on Δ for light pulses with the same amplitudes $V_0 = V_{01} = V_{02}$ and $\delta_{rec} = 0$ are shown in Fig. 4. In contrast to the case $\Delta = 0$, here population transfer between the states $|e\rangle$ and $|g\rangle$ is possible when the transfer of the momentum of the atom by an odd amount $\hbar k$ occurs, i.e., the effect of two light pulses with different frequencies and $\Delta \neq 0$ on the atom is similar to the effect of a single π pulse resonant with the atomic transition, or a pulse with slowly varying frequency ω from $\omega - \omega_0 \ll -V_0$ to $\omega - \omega_0 \gg V_0$. Choosing the ratio Δ/δ in the region between the steps, it is possible to obtain as a result a coherent superposition of $|e\rangle$ and $|g\rangle$ states of the atom. In the figure one can see that the equality $n_e = n_g$ is attained for several values of the ratio Δ/δ, specifically, for $\Delta = \pm\delta/2$. For these two values of Δ, the carrier frequency of one light pulse is in resonance with the frequency of the atomic

transition, and the eigenvalues in the absence of the field are doubly degenerate, so that from the very onset of the interaction with the field the atom is described by a superposition of two adiabatic states, one of which for $V_0 = 0$ corresponds to the atom in the ground state and the other in the excited state. It is natural to expect that after interacting with the field, the atom will be described by a superposition of two states $|g, 2j\rangle$ and $|e, (2n + 1)\rangle$, where j and n are integers. For $\Delta = +\delta/2$, the carrier frequency of the pulse $E_2(t)$, which interacts first with the atom, is in resonance with the frequency of the atomic transition. The average momentum transfer to the atom is $-0.5\hbar k$, $\Delta p = 4.5\hbar k$. From this it can be concluded (as is confirmed also by a calculation of the momentum distribution function of the atom) that after interacting with the field the atom is in a superposition of the ground state with momentum $4\hbar k$ and the excited state with momentum $-5\hbar k$, both states having the same population. For $\Delta = -\delta/2$, the carrier frequency of the pulse $E_1(t)$, which interacts last with the atom, is in resonance with the atomic transition frequency. The average momentum transfer to the atom is $4.5\hbar k$, $\Delta p = 0.5\hbar k$. It follows that after interacting with the field, the atom is in a superposition of identically populated ground state with momentum $4\hbar k$ and excited state with momentum $5\hbar k$.

Figure 5 shows p, Δp, n_g, and n_e as functions of V_{01} in the case $\Delta = -\delta/2$. For small pulse amplitudes, only the pulse $E_1(t)$, whose carrier frequency is in resonance with the frequency of the atomic transition, mainly acts on the atom, and oscillating dependences on its amplitude are observed (essentially dependences on the area of the pulse). As the pulse amplitudes increase, the populations of both atomic states after the interaction with the field become the same. This equality of the resulting populations also occurs for strong fields, when states with z component greater than $\hbar k$ are populated. In this case, the atom is described by a superposition of several, generally speaking, greater than two, states with different momenta. For example, for $V_{01}/\delta = 0.7$ and $V_{01}/\delta = 1.1$ (the values of the other parameters are indicated in the caption under Fig. 5) states with the z component of the momentum 0, $\hbar k$, $2\hbar k$, and $3\hbar k$ are equally populated.

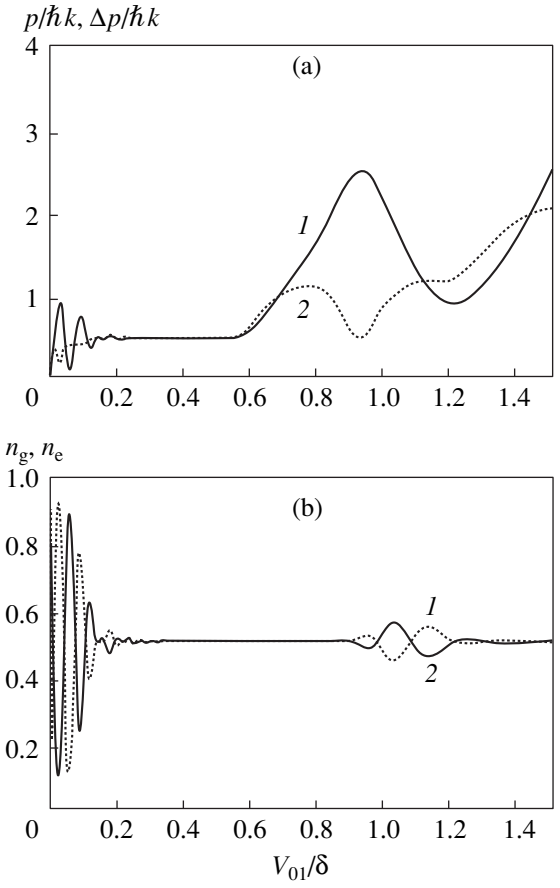

Fig. 5. (a) The average value of the z component of the momentum p of an atom (curve *1*), the rms deviation of the component from the average value Δp (curve *2*) in units of $\hbar k$, and (b) the populations of the ground state n_g (curve *1*) and excited state n_e (curve *2*) as functions of V_{01}/δ. The pulse parameters are $\delta\tau = 200$, $\Delta = -0.5\delta$, $V_{02} = 3V_{01}$, $t_d = 0.35\tau$, $\delta_{rec} = 0$.

6. CONCLUSIONS

For an adiabatic interaction of the atoms with two oppositely propagating light pulses which have different carrier frequencies ($V_0\tau \gg 1$, $\delta\tau \gg 1$) and are separated in time, the momentum of the atom changes by $n\hbar k$, where n is an integer. There exist quite wide ranges of values of the parameters of the light pulses (amplitude, offset of the carrier frequencies from the transition frequency between the ground and excited states of the atom, and time delay between the pulses) where varying the values of the parameters has virtually no effect on the final state of the atom and the momentum transfer to it. A characteristic feature is that in most cases the dispersion of the momentum transfer to the atom is small compared with the photon momentum and approaches zero as the atom–field interaction time increases. Thus, if before interacting with the field the atom is described by a plane wave, then the atom will also be described by a plane wave after interacting with the field.

The characteristic features of the scattering of an atom by a bichromatic field of oppositely propagating light pulses can be most simply observed in an experiment on the scattering of a monochromatic atomic beam by a field of two monochromatic oppositely propagating Gaussian beams, shifted in a manner so that the lighting atom “sees” first only one beam, then both beams, and at the end of the interaction only the other beam. The carrier frequencies of both beams should differ by an amount of the order of the amplitude of the fields (in frequency units). Then a single diffraction peak, whose order should vary with the amplitude

of the fields, will be observed in the scattering of the atoms. When the carrier frequencies of the fields are in resonance with the transition frequency, the time of flight of the atom through the interaction region should be much shorter than the spontaneous emission time of the atom from the upper level.

ACKNOWLEDGMENTS

We thank D. V. Surovtsev for assisting in the numerical calculations.

This work was supported by the State Foundation for Fundamental Research of the Ukrainian State Committee on questions concerning science and intellectual property (grant no. 2.4/179).

REFERENCES

1. V. G. Minogin and V. S. Letokhov, *The Pressure of Laser Radiation on Atoms* (Nauka, Moscow, 1986).
2. A. P. Kazantsev, G. I. Surdutovich, and V. P. Yakovlev, *The Mechanical Action of Light on Atoms* (Nauka, Moscow, 1991).
3. C. S. Adams, M. Siegel, and J. Mlynek, Phys. Rep. **240**, 143 (1994).
4. H. Wallis, Phys. Rep. **255**, 203 (1995).
5. V. I. Romanenko and L. P. Yatsenko, Pis'ma Zh. Éksp. Teor. Fiz. **63**, 920 (1996) [JETP Lett. **63**, 968 (1996)].
6. A. M. Ishkhanyan, Laser Phys. **7**, 1225 (1997).
7. V. I. Romanenko and L. P. Yatsenko, Zh. Éksp. Teor. Fiz. **113**, 563 (1998) [JETP **86**, 312 (1998)].
8. S. P. Goreslavskiĭ and V. P. Krainov, Zh. Éksp. Teor. Fiz. **76**, 26 (1979) [Sov. Phys. JETP **49**, 13 (1979)].
9. S. P. Goreslavskiĭ and V. P. Krainov, Zh. Éksp. Teor. Fiz. **77**, 1340 (1979) [Sov. Phys. JETP **50**, 674 (1979)].
10. A. M. Bonch-Bruevich, T. A. Vartanyan, and N. A. Chigir', Zh. Éksp. Teor. Fiz. **77**, 1899 (1979) [Sov. Phys. JETP **50**, 901 (1979)].
11. N. A. Braun and G. P. Miroshnichenko, Zh. Éksp. Teor. Fiz. **81**, 63 (1981) [Sov. Phys. JETP **54**, 27 (1981)].
12. H. Grimm, J. Söding, and Yu. B. Ovchinnikov, Opt. Lett. **19**, 658 (1994).
13. A. P. Kazantsev and I. V. Krasnov, Pis'ma Zh. Éksp. Teor. Fiz. **46**, 264 (1987) [JETP Lett. **46**, 332 (1987)].
14. V. S. Voitsekhovich, M. V. Danileĭko, A. M. Negriĭko, *et al.*, Zh. Tekh. Fiz. **58**, 1174 (1988) [Sov. Phys. Tech. Phys. **33**, 690 (1988)].
15. A. P. Kazantsev and I. Krasnov, J. Opt. Soc. Am. B **6**, 2140 (1989).
16. V. S. Voitsekhovich, M. V. Danileĭko, A. M. Negriĭko, *et al.*, Pis'ma Zh. Éksp. Teor. Fiz. **49**, 138 (1989) [JETP Lett. **49**, 161 (1989)].
17. V. S. Voitsekhovich, M. V. Danileiko, A. M. Negriiko, *et al.*, Zh. Éksp. Teor. Fiz. **99**, 393 (1991) [Sov. Phys. JETP **72**, 219 (1991)].
18. J. Söding, R. Grimm, Yu. B. Ovchinnikov, *et al.*, Phys. Rev. Lett. **78**, 1420 (1997).
19. M. R. Williams, F. Chi, M. T. Cashen, and H. Metcalf, Phys. Rev. A **60**, R1763 (1999).

Translation was provided by AIP

Journal of Experimental and Theoretical Physics, Vol. 90, No. 3, 2000, pp. 415–427.
Translated from Zhurnal Éksperimental'noĭ i Teoreticheskoĭ Fiziki, Vol. 117, No. 3, 2000, pp. 476–488.

ATOMS, SPECTRA, RADIATION

Quantum Processes in a Two-Mode Laser Field

N. B. Narozhny* and M. S. Fofanov**

Moscow State Engineering Physics Institute (Technical University), Kashirskoe sh. 31, Moscow, 115409 Russia
**e-mail: narozhny@pc1k32.mephi.ru*
***e-mail: fofanov@pc1k32.mephi.ru*

Received July 9, 1999

Abstract—The probabilities of the emission of a photon by an electron and e^+e^--pair photoproduction in a field which is a superposition of two electromagnetic plane waves with different frequencies and propagating in the same direction are obtained. The case where the frequencies of the two modes are commensurate is studied in detail. This case is interesting primarily because of the existence of effects due to the interference of amplitudes, corresponding to a different number of photons absorbed from different modes but having the same total 4-momentum. It is shown that the optimal field for observing interference effects is a field such that the ratio of the mode frequencies is 3. The probabilities of radiation and pair-photoproduction processes in the field of a monochromatic plane wave and in a two-mode field, obtained by splitting the initial wave into two waves, are compared. It is shown that the total probability of the emission of a photon by an electron in a two-mode field is lower than and the probability of pair photoproduction is higher than the probabilities of the same processes in the initial wave. The increase in the pair-photoproduction probability is explained by the fact that additional channels for reactions which are forbidden in the initial monochromatic field open up in a two-mode field.

1. INTRODUCTION

The emission of a photon by an electron and pair photoproduction in a strong unimodal laser field have been studied in detail theoretically [1] (see also [2, 3]). These effects were recently investigated experimentally by MacDonald's group at SLAC [4, 5]. In the present paper we shall examine the probabilities of the same processes in a two-mode plane-wave field.

We define a two-mode field as a superposition of two monochromatic plane waves with frequencies ω_1 and ω_2, propagating in the same direction. A two-mode field with commensurate frequencies is of special interest, since in such a field interference of the amplitudes, corresponding to a different number of photons which are absorbed from different modes but having the same total 4-momentum, can be manifested in the probabilities of quantum processes. This interference is responsible for the so-called "tunable asymmetry" in the spatial distribution of the radiation from an electron encountering a two-mode laser field consisting of a strong monochromatic component and a weak component with twice the frequency. It was first discussed by Puntajer and Leubner [6] on the basis of classical electrodynamics. Similar interference effects arising when light waves interact with a continuous medium in the presence of a resonance between multiple frequencies of the light waves and the frequencies of electromagnetic transitions of the medium were predicted theoretically in [7, 8] and subsequently observed experimentally in [9].

A quantum-electrodynamic analysis of the radiation from an electron and pair photoproduction in a two-mode field with circularly polarized components was made in [10]. Unfortunately, this work contains serious errors, a detailed analysis of which, as well as the correct answer for the probabilities of the processes examined, are contained in [11].

In the present paper we consider a two-mode field produced by two linearly polarized waves with an arbitrary angle between the polarization planes and with an arbitrary phase shift. The 4-potential of such a field can be written in the form

$$\begin{gathered} A^\mu = A_1^\mu(\varphi_1) + A_2^\mu(\varphi_2), \\ A_1^\mu = a_1^\mu \cos\varphi_1, \quad \varphi_1 = k_1 x, \\ A_2^\mu = a_2^\mu \cos(\varphi_2 + \varphi), \quad \varphi_2 = k_2 x, \quad \varphi = \text{const}, \\ k_1^2 = k_2^2 = 0, \quad k_1 a_1 = k_2 a_2 = 0. \end{gathered} \tag{1}$$

The wave 4-vectors of the modes differ by a factor of ν:

$$k_2 = \nu k_1, \tag{2}$$

which can be rational (commensurate frequencies) or irrational. We introduce the dimensionless parameters of the mode intensities[1]

$$\eta_1^2 = -\frac{e^2 a_1^2}{m^2}, \quad \eta_2^2 = -\frac{e^2 a_2^2}{m^2}, \quad \eta_2 = \zeta\eta_1. \tag{3}$$

[1] We use the system of units where $\hbar = c = 1$.

In what follows, we shall also require the quantity

$$\eta^2 = \eta_1^2 + \eta_2^2 = \eta_1^2(1+\zeta^2), \tag{4}$$

which can be called a dimensionless parameter of the intensity of the two-mode field.

In practice, a two-mode field of the form (1) can be obtained by first splitting a monochromatic laser beam into two beams and then merging the two separate beams, after passing one beam through a frequency converter. Such a scheme with $\nu = 3$ will be used in the next series of experiments at SLAC.[2] If the losses in the converter are neglected, then the intensity η_0^2 of the initial wave is related, as one can easily see, with the intensities of the modes by the relation

$$\eta_0^2 = \eta_1^2 + \nu^2\eta_2^2. \tag{5}$$

Equality (5) is important for making quantitative comparisons of the probabilities of processes in a two-mode field and in the field in an initial monochromatic wave. We note that such a scheme makes it possible to achieve a constant phase difference between the modes of the laser field.

We shall calculate the probabilities of the quantum processes in a two-mode plane-wave field using the conventional method [1] in which the interaction of charged particles with a radiation field is studied by means of perturbation theory, and their interaction with the external field is taken into account exactly (using the Furry picture). The latter is achieved by taking as the basis for calculating the transition amplitudes the exact solutions of the Dirac equation in the field of a plane wave, the so-called Volkov solutions. For a field described by the 4-potential (1), the Volkov solutions can be written in the form (compare, for example, with [12])

$$\Psi_p(x) = \left[1 + \frac{e(\gamma k_1)(\gamma a_1)}{2pk_1}\cos\varphi_1 + \frac{e(\gamma k_2)(\gamma a_2)}{2pk_2}\cos(\varphi_2+\varphi)\right] \times \frac{u_p}{\sqrt{2q_0}}\exp\{-i(qx + R_{1p} + R_{2p} + R_{3p} + R_{4p})\}, \tag{6}$$

where

$$\begin{aligned} R_{1p} &= \frac{e(a_1p)}{pk_1}\sin\varphi_1 - \frac{e^2a_1^2}{8pk_1}\sin 2\varphi_1,\\ R_{2p} &= \frac{e(a_2p)}{pk_2}\sin(\varphi_2+\varphi) - \frac{e^2a_2^2}{8pk_2}\sin 2(\varphi_2+\varphi),\\ R_{3p} &= -\frac{e^2(a_1a_2)}{2(1+\nu)pk_1}\sin(\varphi_1+\varphi_2+\varphi),\\ R_{4p} &= -\frac{e^2(a_1a_2)}{2(1-\nu)pk_1}\sin(\varphi_1-\varphi_2-\varphi). \end{aligned} \tag{7}$$

We shall call the 4-vector

$$\begin{aligned} q^\mu &= p^\mu - \frac{e^2\langle A_1^2\rangle_1}{2pk_1}k_1^\mu - \frac{e^2\langle A_2^2\rangle_2}{2pk_2}k_2^\mu\\ &= p^\mu - \frac{e^2a_1^2}{4pk_1}k_1^\mu - \frac{e^2a_2^2}{4pk_2}k_2^\mu \end{aligned} \tag{8}$$

in equation (6) the average kinetic 4-momentum of the electron. We note that the averaging for each of the squared 4-potentials A_1 and A_2 in equation (8) is performed over the period of each potential. In a periodic two-mode field with commensurate frequencies, the 4-vector q is a quasimomentum. We shall call the quantity m_* given by

$$m_*^2 = q^2 = m^2\left(1 + \frac{\eta^2}{2}\right) \tag{9}$$

the effective mass of an electron in a two-mode field irrespective of whether or not this field is periodic.

2. EMISSION OF A PHOTON BY AN ELECTRON

The S-matrix element corresponding to the emission of a photon with 4-momentum $k' = (\omega', \mathbf{k}')$ and polarization 4-vector e' is given by the formula

$$S_{fi} = -ie\int\overline{\Psi}_{p'}(\gamma e'^*)\Psi_p\frac{\sqrt{4\pi}e^{ik'x}}{\sqrt{2\omega'}}d^4x. \tag{10}$$

It is easy to see, using equations (6) and (7), that the integrand in equation (10) is a linear combination of the quantities consisting of the following factors:

$$\cos^n\varphi_1\exp\{-i(\alpha_1\sin\varphi_1 - \beta_1\sin 2\varphi_1)\}, \quad n = 0, 1, 2; \tag{11}$$

$$\cos^n(\varphi_2+\varphi)\times\exp\{-i[\alpha_2\sin(\varphi_2+\varphi) - \beta_2\sin 2(\varphi_2+\varphi)]\}, \quad n = 0, 1, 2; \tag{12}$$

$$\cos^n(\varphi_1+\varphi_2+\varphi)\exp\{iz_3\sin(\varphi_1+\varphi_2+\varphi)\}, \quad n = 0, 1; \tag{13}$$

$$\cos^n(\varphi_1-\varphi_2-\varphi)\exp\{iz_4\sin(\varphi_1-\varphi_2-\varphi)\}, \quad n = 0, 1. \tag{14}$$

Here, we have used the notation

$$\alpha_i = e\left(\frac{a_ip}{k_ip} - \frac{a_ip'}{k_ip'}\right), \quad \beta_i = \frac{e^2a_i^2}{8}\left(\frac{1}{k_ip} - \frac{1}{k_ip'}\right), \quad i = 1, 2; \tag{15}$$

[2] Private communication from professor K.T. MacDonald.

$$z_{3,4} = \frac{e^2(a_1a_2)}{2(1\pm\nu)}\left(\frac{1}{k_1p} - \frac{1}{k_1p'}\right). \tag{16}$$

Each factor in equations (11)–(14) can be expanded in a Fourier series as

$$\cos^n\varphi_1 \exp\{-i(\alpha_1\sin\varphi_1 - \beta_1\sin 2\varphi_1)\} = \sum_{s_1=-\infty}^{\infty} A_n(s_1\alpha_1\beta_1)\exp(-is_1\varphi_1), \tag{17}$$

$$\cos^n(\varphi_2+\varphi) \times \exp\{-i[\alpha_2\sin(\varphi_2+\varphi) - \beta_2\sin 2(\varphi_2+\varphi)]\} = \sum_{s_2=-\infty}^{\infty} A_n(s_2\alpha_2\beta_2)\exp[-is_2(\varphi_2+\varphi)], \tag{18}$$

$$\cos^n(\varphi_1+\varphi_2+\varphi) \times \exp\{iz_3\sin(\varphi_1+\varphi_2+\varphi)\} = \sum_{s_3=-\infty}^{\infty}\left(\frac{s_3}{z_3}\right)^n J_{s_3}(z_3)\exp[is_3(\varphi_1+\varphi_2+\varphi)], \tag{19}$$

$$\cos^n(\varphi_1-\varphi_2-\varphi) \times \exp\{iz_4\sin(\varphi_1-\varphi_2-\varphi)\} = \sum_{s_4=-\infty}^{\infty}\left(\frac{s_4}{z_4}\right)^n J_{s_4}(z_4)\exp[is_4(\varphi_1-\varphi_2-\varphi)], \tag{20}$$

where

$$A_n(s\alpha\beta) = \frac{1}{2\pi}\int_{-\pi}^{\pi} d\varphi\cos^n\varphi \times \exp(is\varphi - i\alpha\sin\varphi + i\beta\sin 2\varphi) \tag{21}$$

are functions which have been studied in detail by Nikishov and Ritus in connection with processes occurring in the field of a linearly polarized monochromatic wave [1], and $J_s(z)$ are Bessel functions. Using the relations (17)–(20), the expression (10) for the matrix element S_{fi} can be put into the form

$$S_{fi} = \sum_{s_1,s_2,s_3,s_4}\frac{M_{fi}(s_1,s_2,s_3,s_4)}{\sqrt{8q_0q_0'\omega'}}(2\pi)^4 \times \delta^{(4)}(q + (s_1-s_3-s_4)k_1 + (s_2-s_3+s_4)k_2 - q' - k'), \tag{22}$$

where

$$M_{fi}(s_1,s_2,s_3,s_4) = -ie\sqrt{4\pi}\bar{u}_{p'}O(s_1,s_2,s_3,s_4)u_p \times \exp[-i(s_2-s_3+s_4)\varphi], \tag{23}$$

$$O(s_1,s_2,s_3,s_4) = J_{s_3}(z_3)J_{s_4}(z_4) \times\left\{\left[(\gamma e'^*) - \frac{e^2(a_1a_2)}{2(k_1p)(k_1p')}(k_1e'^*)(\gamma k_1)\left(\frac{s_3}{z_3}+\frac{s_4}{z_4}\right)\right] \times A_0(s_1\alpha_1\beta_1)A_0(s_2\alpha_2\beta_2) + \left[e\left(\frac{(\gamma e'^*)(\gamma k_1)(\gamma a_1)}{2(k_1p)} + \frac{(\gamma a_1)(\gamma k_1)(\gamma e'^*)}{2(k_1p')}\right) \times A_1(s_1\alpha_1\beta_1) - \frac{e^2a_1^2(k_1e'^*)}{2(k_1p)(k_1p')}(\gamma k_1)A_2(s_1\alpha_1\beta_1)\right] \times A_0(s_2\alpha_2\beta_2) + A_0(s_1\alpha_1\beta_1) \times\left[e\left(\frac{(\gamma e'^*)(\gamma k_2)(\gamma a_2)}{2(k_2p)} + \frac{(\gamma a_2)(\gamma k_2)(\gamma e'^*)}{2(k_2p')}\right) \times A_1(s_2\alpha_2\beta_2) - \frac{e^2a_2^2(k_2e'^*)}{2(k_2p)(k_2p')}(\gamma k_2)A_2(s_2\alpha_2\beta_2)\right]\right\}. \tag{24}$$

Introducing the numbers

$$n_1 = s_1 - s_3 - s_4, \quad n_2 = s_2 - s_3 + s_4, \tag{25}$$

the expression (22) can be represented in the form

$$S_{fi} = \sum_{n_1,n_2=-\infty}^{\infty}\exp(-in_2\varphi)\frac{\tilde{M}_{fi}(n_1,n_2)}{\sqrt{8q_0q_0'\omega'}} \times (2\pi)^4\delta^{(4)}(q + n_1k_1 + n_2k_2 - q' - k'), \tag{26}$$

where

$$\exp(-in_2\varphi)\tilde{M}_{fi}(n_1,n_2) = \sum_{s_3,s_4=-\infty}^{\infty} M_{fi}(n_1+s_3+s_4, n_2+s_3-s_4, s_3, s_4). \tag{27}$$

The structure of the conservation law in equation (26) makes it possible to interpret $\tilde{M}_{fi}(n_1,n_2)$ as the partial amplitude for the emission of a photon with momentum k' as a result of the absorption of n_1 photons with momentum k_1 from the first mode and n_2 photons with momentum k_2 from the second mode of the external field. Since the dependence on the phase difference φ between the modes of the field on the right-hand side of equation (27) is completely determined by the factor $\exp(-in_2\varphi)$, the amplitude $\tilde{M}_{fi}(n_1,n_2)$ describes the emission process in a field with $\varphi = 0$.

It is easy to see that all kinematic relations for the emission of a photon by an electron in a two-mode field retain the same form as in the case of a monochromatic field (see [1]), if in the corresponding formulas the number of absorbed photons s is replaced by $n_1 + \nu n_2$,

the frequency ω_1 of the first harmonic is taken for the frequency ω, and the expression (9) is used for the effective mass m_*. Specifically, in the sum over n_1 and n_2 in equation (26) only terms for which $n_1 + \nu n_2 > 0$ are different from zero.

The squared modulus of the matrix element (26) is

$$\frac{|S_{fi}|^2}{VT} = \sum_{n_1, n_2, n_1', n_2'} \theta(n_1 + \nu n_2)\theta(n_1' + \nu n_2')$$

$$\times \frac{\tilde{M}_{fi}(n_1, n_2)\tilde{M}^*_{fi}(n_1', n_2')}{8q_0 q_0' \omega'} \exp[i(n_2' - n_2)\varphi] \tag{28}$$

$$\times \frac{(2\pi)^8}{VT}\delta^{(4)}[q + (n_1 + \nu n_2)k_1 - q' - k']$$

$$\times \delta^{(4)}[q + (n_1' + \nu n_2')k_1 - q' - k'].$$

It is obvious that the product of the delta functions on the right-hand side of the expression (28) satisfies the relation

$$\delta^{(4)}[q + (n_1 + \nu n_2)k_1 - q' - k']$$

$$\times \delta^{(4)}[q + (n_1' + \nu n_2')k_1 - q' - k'] = \frac{VT}{(2\pi)^4} \tag{29}$$

$$\times \Lambda_{n_1 n_2;\, n_1' n_2'}\delta^{(4)}[q + (n_1 + \nu n_2)k_1 - q' - k'],$$

where

$$\Lambda_{n_1 n_2;\, n_1' n_2'} = \begin{cases} \delta_{n_1 n_1'}\delta_{n_2 n_2'} & \text{for irrational } \nu, \\ \delta_{n_1 + \nu n_2,\, n_1' + \nu n_2'} & \text{for rational } \nu, \end{cases} \tag{30}$$

Using the relation (29), we obtain for the differential probability of emission per unit time, summed over polarizations of the final particles and averaged over the polarizations of the initial electron, after standard but quite cumbersome calculations,

$$dW^e = \frac{e^2 m^2}{4\pi q_0} \sum_{n_1, n_2, n_1', n_2'} \theta(n_1 + \nu n_2)\Lambda_{n_1 n_2;\, n_1' n_2'}$$

$$\times \exp[i(n_2' - n_2)\varphi] w^e(n_1, n_2; n_1', n_2') \tag{31}$$

$$\times \delta^{(4)}(q + n_1 k + n_2 k_2 - q' - k')\frac{d^3k'}{\omega'}\frac{d^3q'}{q_0'},$$

where

$$w^e(n_1, n_2; n_1', n_2')$$

$$= \sum_{s_3, s_4, s_3', s_4'} J_{s_3}(z_3)J_{s_3'}(z_3)J_{s_4}(z_4)J_{s_4'}(z_4) \tag{32}$$

$$\times v^e\begin{pmatrix} n_1 + s_3 + s_4, & n_2 + s_3 - s_4, & s_3, & s_4 \\ n_1' + s_3' + s_4', & n_2' + s_3' - s_4', & s_3', & s_4' \end{pmatrix}.$$

All summations in equations (31) and (32) extend from $-\infty$ to ∞ and

$$v^e\begin{pmatrix} s_1, & s_2, & s_3, & s_4 \\ s_1', & s_2', & s_3', & s_4' \end{pmatrix} = -\Bigg[2 + \eta_1^2\zeta\cos\phi\left(1 + \frac{u^2}{2(1+u)}\right)$$

$$\times\left(\frac{s_3 + s_3'}{z_3} + \frac{s_4 + s_4'}{z_4}\right)\Bigg]A_0(s_1)A_0(s_1')A_0(s_2)A_0(s_2')$$

$$+ \eta_1^2\left(1 + \frac{u^2}{2(1+u)}\right)\Bigg\{[2A_1(s_1)A_1(s_1') - A_0(s_1)A_2(s_1')$$

$$- A_2(s_1)A_0(s_1')]A_0(s_2)A_0(s_2') \tag{33}$$

$$+ \zeta^2 A_0(s_1)A_0(s_1')[2A_1(s_2)A_1(s_2') - A_0(s_2)A_2(s_2')$$

$$- A_2(s_2)A_0(s_2')] + 2\zeta\cos\phi[A_0(s_1)A_1(s_1')A_1(s_2)A_0(s_2')$$

$$+ A_1(s_1)A_0(s_1')A_0(s_2)A_1(s_2')]\Bigg\}.$$

The following notation is used in equation (33):

$$A_n(s_i) = A_n(s_i\alpha_i\beta_i), \quad A_n(s_i') = A_n(s_i'\alpha_i\beta_i),$$
$$u = \frac{k_1 k'}{k_1 q'}; \tag{34}$$

the angle ϕ is determined by the relation

$$e^2 a_1 a_2 = -m^2\eta_1^2\zeta\cos\phi, \tag{35}$$

and, if the gauge in which the zeroth components of the vectors a_i vanish is chosen, it is the angle between the amplitudes of the electric vectors of the two modes.

It is easy to see from equations (32) and (33) that the quantities $w^e(n_1, n_2; n_1', n_2')$ are symmetric under the permutation $(n_1, n_2) \longleftrightarrow (n_1', n_2')$:

$$w^e(n_1, n_2; n_1', n_2') = w^e(n_1', n_2'; n_1, n_2). \tag{36}$$

Carrying out the integration in equation (31) over the momenta of the final particles, just as in [1], and switching to the invariant variables u and ψ, where ψ is the angle between the $(\mathbf{k}_1, \mathbf{q}')$ and $(\mathbf{k}_1, \mathbf{a}_1)$ planes in the

coordinate system where $\mathbf{k}_1$ and $\mathbf{q}$ are oppositely directed, we obtain for the total probability of emission per unit time

$$W^e = \frac{e^2m^2}{4\pi q_0}\sum_{n_1,\,n_2;\,n_1',\,n_2'}\theta(n_1+\nu n_2)\Lambda_{n_1n_2;\,n_1'n_2'} \times \exp[i(n_2'-n_2)\varphi]\int_0^{u_s(\nu)}\frac{du}{(1+u)^2}\int_0^{2\pi}d\psi\, w^e(n_1,n_2;\,n_1',n_2'). \tag{37}$$

Here,

$$u_s(\nu) = 2s\frac{k_1q}{m_*^2},\quad s = n_1+\nu n_2, \tag{38}$$

and the parameters of the functions A_n and the arguments of the Bessel functions are expressed in terms of u and ψ as follows:

$$\alpha_1 = z_1\cos\psi,\quad \alpha_2 = z_2\cos(\psi+\phi),$$
$$z_1 = \frac{2s\eta_1}{\sqrt{1+\eta^2/2}}\sqrt{\frac{u}{u_s(\nu)}\left(1-\frac{u}{u_s(\nu)}\right)},\quad z_2 = \frac{\zeta}{\nu}z_1,$$
$$\beta_1 = \frac{s\eta_1^2}{4(1+\eta^2/2)}\frac{u}{u_s(\nu)},\quad \beta_2 = \frac{\zeta^2}{\nu}\beta_1, \tag{39}$$
$$z_3 = 4\frac{\beta_1\zeta}{1+\nu}\cos\phi,\quad z_4 = 4\frac{\beta_1\zeta}{1-\nu}\cos\phi.$$

For incommensurate frequencies, as one can see from equation (30), $n_1 = n_1'$, $n_2 = n_2'$, and expression (37) can be regarded, in complete agreement with the interpretation of amplitude (27), as the sum of partial probabilities of emission as a result of the absorption of n_1 photons from the first mode and n_2 photons from the second mode.

If the frequencies are commensurate, the partial probabilities with fixed n_1 and n_2 contain, besides the squared moduli of the corresponding amplitudes, an infinite number of terms which are due to the appearance of the interference of the amplitudes corresponding to a different number of absorbed photons n_1, n_2 and n_1', n_2' from each mode, but the same total 4-momentum

$$(n_1+\nu n_2)k_1 = (n_1'+\nu n_2')k_1.$$

We note that the dependence of the differential and total emission probabilities on the phase difference φ between the two modes is completely determined by the factor $\exp[i(n_2'-n_2)\varphi]$ in equations (31) and (37). For this reason, for incommensurate frequencies, when $n_2 = n_2'$, the dependence on φ vanishes. When the frequencies are commensurate, the emission probabilities (31) and (37) due to the presence of the interference terms depend on the phase difference between the two modes of the external field. The dependence of the total probability on the phase shift strongly distinguishes the field of linearly polarized modes from a circularly polarized two-mode field [11]. In the latter case, because there is no preferred direction in a plane perpendicular to the direction of propagation of the wave, the dependence on the angular variable ψ becomes trivial [11] and integration over it results in vanishing of the interference terms and, together with them, the dependence on the phase shift φ.

3. PHOTON EMISSION: COMMENSURATE FREQUENCIES

In this section we examine the probability of photon emission (37) for commensurate frequencies. For definiteness, we assume that ν is an integer greater than unity. If the frequencies are commensurate, then the emission processes due to the absorption of n_1 and n_2 photons from the first and second modes, respectively, with $n_1 + \nu n_2 = s = \text{const}$, i.e., with the same 4-momentum sk_1, absorbed from the field, are indistinguishable. For this reason, it is convenient to rewrite equation (37) for commensurate frequencies in the form

$$W^e = \sum_{s=1}^{\infty}W_s^e = \frac{e^2m^2}{4\pi q_0}\sum_{s=1}^{\infty}\int_0^{u_s(\nu)}\frac{du}{(1+u)^2}\int_0^{2\pi}d\psi \times \sum_{n_2,\,n_2'=-\infty}\cos[(n_2-n_2')\varphi]\,w^e(s-\nu n_2,n_2;\,s-\nu n_2',n_2'). \tag{40}$$

We used here the fact that the quantities w^e are real and the symmetry property (36).

In the weak-field limit, $\eta_1 \sim \eta_2 \ll 1$, the amplitudes $\tilde{M}_{fi}(n_1, n_2)$ and the quantities $w^e(s-\nu n_2, n_2;\, s-\nu n_2', n_2')$ can be calculated on the basis of a diagram technique [1] (see also [11], where the application of the diagram technique to the case of a two-mode field with circularly polarized components is discussed in detail). For example, the amplitude $\tilde{M}_{fi}(1, 1)$ corresponds to the diagrams shown in Fig. 1 where the dots indicate diagrams differing from the diagrams presented by all possible permutations of the vertices.

It is obvious that in the perturbation theory the amplitudes $\tilde{M}_{fi}(n_1, n_2)$ can be rewritten in the form

$$\tilde{M}_{fi}(n_1,n_2) = \sum_{m=0}^{\infty}\tilde{M}_{fi}^{(m)}(n_1,n_2),$$

where $\tilde{M}_{fi}^{(0)}$ corresponds to diagrams with absorption of n_1 photons from the first mode and n_2 photons from the second mode, and $\tilde{M}_{fi}^{(m)}$ with $m \geq 1$ describe the same diagrams with the addition of m pairs of photons from any mode, one photon from this pair being absorbed from the wave and the other being emitted into the wave. For example, the diagrams (*a*) shown in Fig. 1

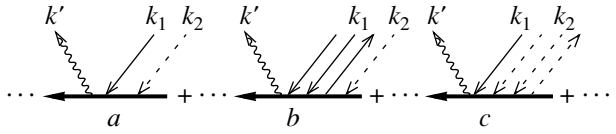

Fig. 1. Diagrams corresponding to the amplitude $\tilde{M}_{fi}(1, 1)$ of emission of a photon by an electron in a two-mode field.

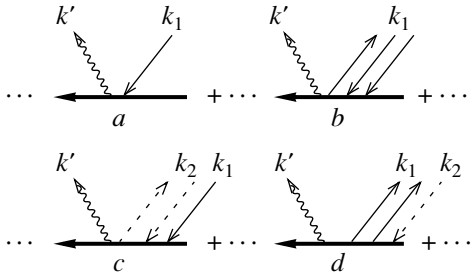

Fig. 2. Diagrams determining the partial probability W_1^e of emission of the first harmonic in a two-mode field.

correspond to the amplitude $\tilde{M}_{fi}^{(0)}(1, 1)$, and the sum of diagrams (*b*) and (*c*) in Figs. 1 describes the amplitude $\tilde{M}_{fi}^{(1)}(1, 1)$. It is obvious that for the amplitude $\tilde{M}_{fi}^{(m)}$ we have

$$\tilde{M}_{fi}^{(m)}(n_1, n_2) \sim \eta_1^{|n_1| + |n_2| + 2m},$$

and correspondingly the field dependences of the quantities $w^e(s - \nu n_2, n_2; s - \nu n_2', n_2')$ in equation (40) will be determined, on the basis of the perturbation theory, by the expression

$$w^e(s - \nu n_2, n_2; s - \nu n_2', n_2') = \sum_{m_1, m_2 = 0}^{\infty} w^e_{m_1 m_2} \eta_1^{g + 2m_1 + 2m_2}, \tag{41}$$

$$g = |s - \nu n_2| + |n_2| + |s - \nu n_2'| + |n_2'|. \tag{42}$$

The coefficients $w^e_{m_1 m_2}$ in equation (41) do not depend on the field, and the numbers m_1 and m_2 can be interpreted as the numbers of pairs of photons with zero total 4-momentum, which belong, respectively, to the first and second modes.

In the field of the monochromatic wave [1] the structure of the probability is identical to equation (40), if in the latter the double sum over n_2, n_2' is replaced by a single term with $n_2 = n_2' = 0$. The number s in this case determines the 4-momentum sk_1 absorbed by an electron from the field and the number of absorbed photons. The partial probability W_s^e in a weak field is of the order of η^{2s}, and the radiation at the first harmonic makes the maximum contribution to the total probability $W_1^e \sim \eta^2$. The situation is different in a two-mode field. The quantity W_s^e depends on the number s nonmonotonically. Here, the two partial probabilities W_1^e and W_ν^e are of the same order of magnitude η_1^2. This is very easy to understand, if it is recalled that the number s determines only the 4-momentum absorbed from the field and not the number of absorbed photons. Thus, W_ν^e is determined mainly by the diagrams with the absorption of one photon from the second mode $n_2 = 1$, $n_1 = s - \nu = 0$, while the contribution of diagrams with absorption of ν photons from the first mode $n_1 = s = \nu$, $n_2 = 0$ in accordance with equation (41) is of the order of $\eta_1^{2\nu}$ and gives a small correction of corresponding order to W_ν^e.

We determine now the minimum order in which interference effects appear in the perturbation theory. This means [see (41)] that we need to determine the minimum value of the number g (42) with $n_2 \neq n_2'$.

Let $g = 4$. Then the following equality must be satisfied:

$$4 = |s - \nu n_2| + |n_2| + |s - \nu n_2'| + |n_2'|. \tag{43}$$

It is easy to show that this equality is possible only if, in the first place, $n_2, n_2' \geq 0$ (we recall that $s \geq 1$, $\nu \geq 2$) and, in the second place, $|n_2| + |n_2'| = 1$, i.e., for $n_2 = 0$, $n_2' = 1$ or $n_2 = 1$, $n_2' = 0$. For such values of n_2 and n_2', the equality (43) becomes

$$3 = s + |s - \nu|, \tag{44}$$

which holds only for $s \leq \nu$ and only for $\nu = 3$.

Thus, the frequency multiple $\nu = 3$ is a distinguished value. In a weak field, interference effects are present even in fourth order of perturbation theory only for $\nu = 3$. For $\nu \neq 3$ they first appear, as a minimum, in sixth order, i.e., they are much weaker. In what follows, we perform all calculations for $\nu = 3$.

The first four harmonics contribute to the emission probability in a weak field, calculated up to terms of fourth order η_1^4 inclusively. For example, the first-harmonic emission probability W_1^e determined by the diagram shown in Fig. 2 is given by

$$W_1^e = \frac{e^2 m^2}{4\pi q_0} \int_0^{u_1(3)} \frac{du}{(1 + u)^2} \times \int_{-\pi}^{\pi} d\psi \{ w^e(1, 0; 1, 0) + 2\cos\varphi w^e(1, 0; -2, 1) \}, \tag{45}$$

where

$$w^e(1,0;1,0) = w_1^e(1,0;1,0) + w_2^e(1,0;1,0), \quad (46)$$

$$w_1^e(1,0;1,0) = \frac{\eta_1^2}{4}\left\{2 + \frac{u^2}{1+u} - \frac{8u}{u_1}\left(1 - \frac{u}{u_1}\right)\cos^2\psi\right.$$

$$-\frac{\eta_1^2}{4}\frac{u}{u_1}\left[2 + \frac{u^2}{1+u} + 8\left(1 - \frac{u}{u_1}\right)\left(\frac{u}{u_1} + \frac{u^2}{1+u}\right)\cos^2\psi\right.$$

$$\left.\left. - 32\frac{u}{u_1}\left(1 - \frac{u}{u_1}\right)^2\cos^4\psi\right]\right\}, \quad (47)$$

$$w_2^e(1,0;1,0) = -\frac{\eta_1^4\zeta^2}{4}\frac{u}{u_1}\left\{\frac{1}{9}\left(1 - \frac{u}{u_1}\right)\right.$$

$$\times\left[\left(4 + 2\frac{u^2}{1+u}\right)\cos^2(\psi+\phi) + \frac{18u^2}{1+u}\cos^2\psi\right.$$

$$\left. - 16\frac{u}{u_1}\left(1 - \frac{u}{u_1}\right)\cos^2\psi\cos^2(\psi+\phi)\right] \quad (48)$$

$$-\frac{1}{8}\left[\left(4 + 2\frac{u^2}{1+u}\right)\cos^2\phi\right.$$

$$\left.\left. - 16\frac{u}{u_1}\left(1 - \frac{u}{u_1}\right)\cos\phi\cos\psi\cos(\psi+\phi)\right]\right\},$$

$$w^e(1,0;-2,1) = \frac{\eta_1^4\zeta}{4}\frac{u}{u_1}\left\{\left(4 + 2\frac{u^2}{1+u}\right)\right.$$

$$\times\left[\frac{3}{4}\left(1 - \frac{u}{u_1}\right)\cos\psi\left(\cos\psi\cos\phi - \frac{\cos(\psi+\phi)}{3}\right) - \frac{\cos\phi}{16}\right]$$

$$-2\frac{u}{u_1}\left(1 - \frac{u}{u_1}\right)\cos\psi\left[\cos\psi\cos\phi + \frac{\cos(\psi+\phi)}{6}\right. \quad (49)$$

$$\left.\left.\times\left(1 + 4\left(1 - \frac{u}{u_1}\right)\cos^2\psi\right)\right]\right\}.$$

The first term on the right-hand side of equation (46) $w_1^e(1,0;1,0)$ reproduces the result obtained by Nikishov and Ritus [1] for the case of a monochromatic wave, the difference being that the quantity u_1 (38) is now determined by the electron effective mass in a two-mode field (9) and not in the field of a monochromatic wave (following [1], we determine u_1 by the exact formula (38), which is necessary in order to describe the kinematic features of the process correctly). This term is determined by the sum of diagrams (*a*) and (*b*) and one of the diagrams (*c*) in Fig. 2 that leads to "renormalization" of the effective mass. The second term $w_2^e(1,0;1,0)$ is determined by the interference of the diagrams (*a*) and (*c*) in Fig. 2 and, naturally, it is absent for a monochromatic wave. For this reason, it contains the factor ζ^2 and depends on the angle ϕ between the polarization planes of the two modes.

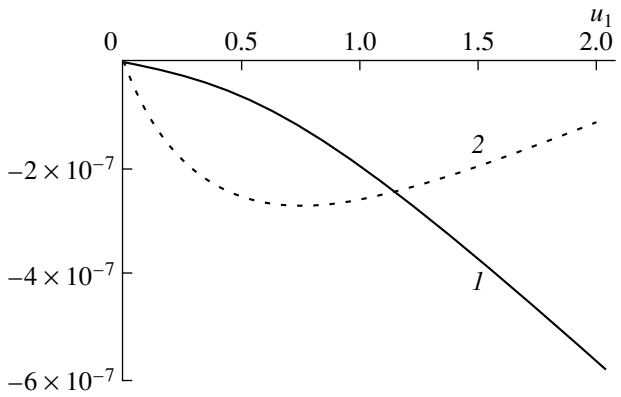

Fig. 3. Contribution of the quantities $w^{e(4)}(1,0;1,0)$ (*1*) and $2w^e(1,0;-2,1)$ (*2*) with the parameters $\eta_0 = 0.5$, $\zeta = 1.2$, and $\phi = 0$ to the total emission probability in a weak field as a function of u_1.

The interference term (49) is determined by the interference of the diagrams (*a*) and (*d*) in Fig. 2. It contains the parameter ζ to the first power, since the diagrams (*d*) in Fig. 2 contain only one line, corresponding to the absorption of a photon from the second mode, and it also depends on the angle ϕ. For $\varphi = \pi/2$, i.e., if the two modes are polarized in mutually perpendicular planes, the interference term does not contribute to the total probability. We note that this circumstance is completely unrelated with perturbation theory. Here, we have a situation similar to the case of circularly polarized modes [11].

Interference effects can strongly influence the emission probability. Plots of the u_1 dependences of the contributions of the quantity $w^{e(4)}(1,0;1,0)$, which is a term of order η_1^4 in $w^e(1,0;1,0)$ (46) and $2w^e(1,0;-2,1)$ (49), to the total probability are presented in Fig. 3. It is evident from the plots that the difference between these two quantities changes sign at a value $u_1 = u_1^*$ close to unity. This means, specifically, that for the phase difference $\varphi = \pi$ the sign of the correction of order η_1^4 to the total emission probability of the first harmonic changes, and for $u_1 = u_1^*$ this correction vanishes. We note, however, that this effect occurs not for arbitrary values of the parameter ζ, but only for $\zeta > \zeta_* \approx 0.852$. For $\zeta < \zeta_*$, the plots in Fig. 3 do not intersect and the fourth-order correction to W_1^e is always negative.

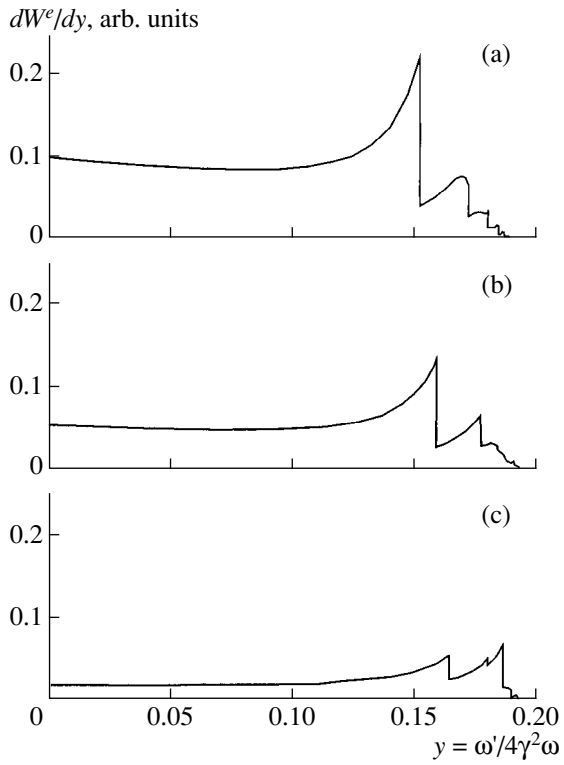

Fig. 4. Spectral distribution of the probability of emission of a photon by an electron for various ratios of the mode intensities ζ = (a) 0, (b) 0.36, and (c) 1 for the same intensity of the initial monochromatic wave $\eta_0^2 = 1$ and the parameters $m^2/k_1 p = 0.4$, $\phi = 0$, and $\varphi = 0$.

For $\eta \gtrsim 1$, i.e., in the absence of a small parameter, the representation (40) for the emission probability is no longer convenient for numerical calculations, since if it is used, the contribution of a large number of terms of the same order of magnitude in the six-fold sum for the partial probabilities must be taken into account [see (40) and (32)].

A formula for the probability that is more convenient for numerical calculations can be obtained for a field whose modes have commensurate frequencies. Then the integrand in equation (10) for the emission matrix element is a periodic function and can be expanded in a single Fourier series. Next, the same scenario as the one used in [1] gives for the probability

$$W^e = \frac{e^2 m^2}{2\pi q_0} \sum_{s=1}^{\infty} \int_0^{u_s(\nu)} \frac{du}{(1+u)^2}$$

$$\times \int_0^{2\pi} d\psi \left\{ -|A_{00}(s)|^2 + \left(1 + \frac{u^2}{2(1+u)}\right) \right.$$

$$\times [\eta_1^2 (|A_{10}(s)|^2 - \mathrm{Re}(A_{00}(s) A_{20}^*(s))) \qquad (50)$$

$$+ \eta_1^2 \zeta^2 (|A_{01}(s)|^2 - \mathrm{Re}(A_{00}(s) A_{02}^*(s)))$$

$$\left. + 2\eta_1^2 \zeta \cos\phi \, \mathrm{Re}(A_{10}(s) A_{01}^*(s) - A_{00}(s) A_{11}^*(s))\,] \right\},$$

where the functions $A_{km}(s)$ are given by the relation

$$A_{km}(s) = \frac{1}{2\pi} \int_{-\pi}^{\pi} d\varphi_1 \cos^k \varphi_1 \cos^m(\nu\varphi_1 + \varphi)$$

$$\times \exp(is\varphi_1 - i\alpha_1 \sin\varphi_1 + i\beta_1 \sin 2\varphi_1$$

$$- i\alpha_2 \sin(\nu\varphi_1 + \varphi) + i\beta_2 \sin 2(\nu\varphi_1 + \varphi) \qquad (51)$$

$$+ iz_3 \sin(\varphi_1 + \nu\varphi_1 + \varphi) + iz_4 \sin(\varphi_1 - \nu\varphi_1 - \varphi)),$$

and the definitions of all parameters are the same. In what follows, we employ the representation (50) for all numerical calculations with η_1 or $\eta_2 \sim 1$.

Figure 4 shows the curves of the spectral distribution of the radiation for various ratios of the mode intensities, i.e., for various values of the parameter $\zeta = \eta_2/\eta_1$, which correspond to the same intensity of the initial monochromatic wave. The curve in Fig. 4a corresponds to the value $\zeta = 0$, i.e., the case of the field of a monochromatic wave with frequency ω_1 and intensity η_0. It is assumed that a "head on collision" of an electron with the laser field occurs, i.e., the momentum $\mathbf{q}$ of the initial electron and the wave vector $\mathbf{k}_1$ of the field are antiparallel to one another. The radiation spectrum corresponding to the sth harmonic has a sharp boundary at the frequency $\omega_{\eta_0}^s(0)$ [2], i.e., at the frequency of a photon emitted in the direction of the momentum of the initial electron. This frequency can be easily found from the conservation laws and is determined by the expression

$$\omega_{\eta_0}^s(0) = \frac{s\omega q_-^2}{m_*^2 + 2s\omega q_-}, \qquad (52)$$

where m_* is the electron effective mass in the field of a monochromatic wave. Figures 4b and 4c show the spectral distributions of the radiation in a two-mode field for the values $\zeta = 0.36$ and 1, respectively. These curves have two important features.

In the first place, the boundaries of all harmonics in Fig. 4b and 4c are shifted rightward compared with the corresponding boundaries in the monochromatic wave. This effect has a simple explanation. Indeed, since the form of the conservation laws in the two-mode field is the same as in a monochromatic field, equation (52) for the limiting frequency remains of the same form. However, now, m_* is the effective mass (9) of an electron in a two-mode field, which, being expressed in terms of

the intensity η_0 of the initial wave [see (5)], can be written in the form

$$m_*^2 = m^2\left(1 + \frac{\eta_0^2}{2}\frac{1+\zeta^2}{1+\nu^2\zeta^2}\right). \quad (53)$$

The value of the parameter $\zeta = 0$ corresponds to the field of the initial monochromatic wave with frequency ω_1, and $\zeta = \infty$ corresponds to the case where the initial wave is completely transformed into a monochromatic wave with frequency $\omega_2 = \nu\omega_1$. It is easy to see from equation (53) that, effectively, an electron in a two-mode field ($\zeta > 0$) is lighter than an electron in the initial monochromatic wave. This is the explanation, in correspondence with equation (52), of the shift in the harmonic boundaries. Evidently, this effect can be used to make a direct measurement of the electron effective mass as a function of the intensity of the external field.

Another important feature of the curves in Fig. 4 is the change in the relative contribution of various partial probabilities W_s^e to the total probability W^e as a function of the parameter ζ. Specifically, for $\zeta = 1$ and $\eta_0 = 1$ the intensity parameters η_1 and η_2 are equal to each other, and it is evident from Fig. 4c that the partial probability W_3^e makes in this case the main contribution to the total probability. We note, however, that the redistribution of the contributions of the partial probabilities W_1^e and W_3^e to the total probability with increasing ζ occurs against the background of a decreasing total probability. This is graphically illustrated by the curves in Fig. 5 and is explained by the fact that the intensity parameter η (4) of the two-mode field is smaller than the intensity parameter η_0 (5) of the initial unsplit wave.

The spectral distributions of the radiation in a two-mode field are presented in Fig. 6 as a function of the phase shift φ between the modes. As one can see from the plots in Figs. 6a, 6b, and 6c, this dependence is strongest for the second harmonic. In the perturbation theory this is explained by the fact that the interference and noninterference terms for the second-harmonic radiation, which is determined by the diagrams shown in Fig. 7, are of the same order of magnitude. As one can see, this ratio between these terms remains even for not too small values of η_1 and η_2, when perturbation theory is no longer applicable.

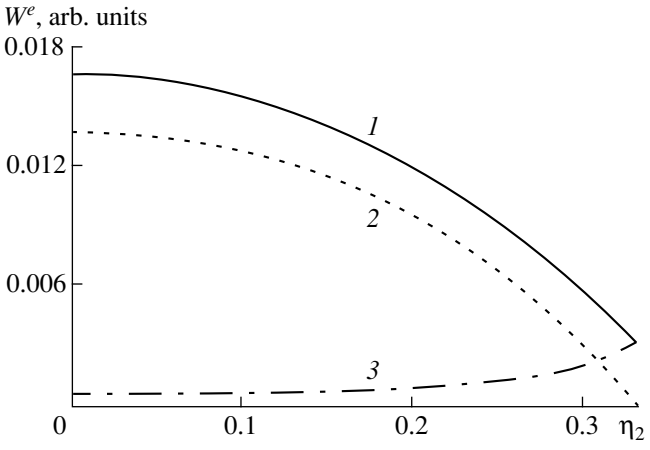

Fig. 5. Total emission probability W^e (*1*) and the contributions of the partial probabilities W_1^e (*2*) and W_3^e (*3*) to it as functions of the distribution of the intensity between the modes of the field for fixed intensity of the initial monochromatic wave $\eta_0^2 = 1$ and the parameters $m^2/k_1 p = 0.4$, $\phi = 0$, and $\varphi = 0$.

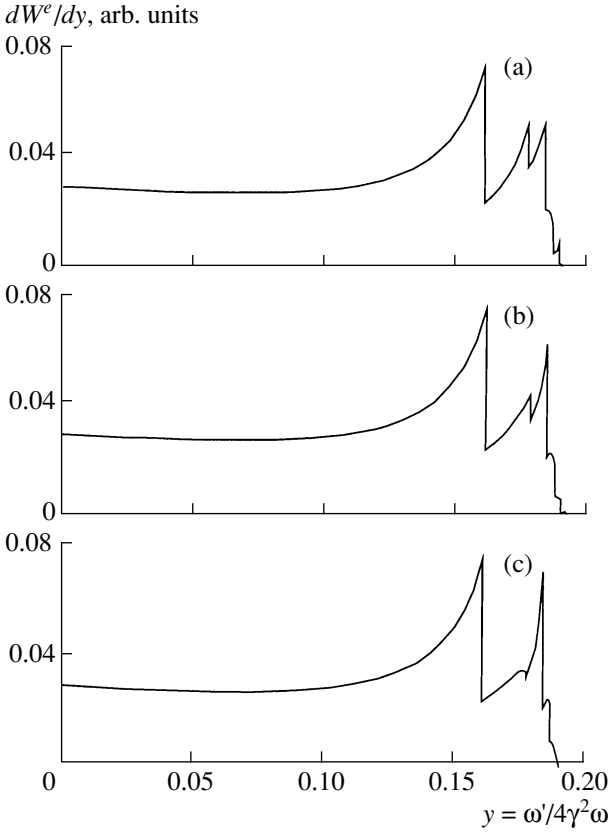

Fig. 6. Spectral distribution of the emission probability for various phase shifts φ between the modes of the field: φ = (a) 0, (b) $\pi/2$, and (c) π for the parameters $\eta_0 = 1$, $m^2/k_1 p = 0.4$, $\zeta = 0.7$, and $\phi = 0$.

4. PAIR PHOTOPRODUCTION

The differential probability of pair photoproduction by an unpolarized photon can be obtained by making in equations (31)–(33) the changes of variables $p \longrightarrow -p$, $k' \longrightarrow -k'$, and $d^3k' \longrightarrow d^3q$ and changing the overall sign of the expression (31) (compare with [1]). Inte-

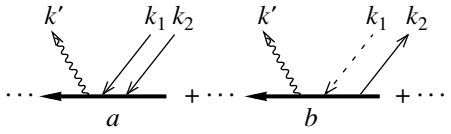

Fig. 7. Diagrams corresponding to the contribution of the second harmonic $s = 2$ to the probability of the emission of a photon by an electron in a two-mode field.

grating the expression so obtained over the momenta of the final electron and positron, just as in [1], we obtain

$$W^\gamma = \frac{e^2m^2}{8\pi\omega'}\sum_{n_1,\,n_2;\,n_1',\,n_2'}\theta(n_1-\nu n_2-s_0)\Lambda_{n_1,\,n_2;\,n_1',\,n_2'}$$
$$\times\exp[i(n_2'-n_2)\varphi]\int_1^{u_s(\nu)}\frac{du}{u\sqrt{u(u-1)}} \qquad (54)$$
$$\times\int_0^{2\pi}d\psi w^\gamma(n_1,n_2;\,n_1',n_2'),$$

where

$$u = \frac{(k_1k')^2}{4(k_1q)(k_1q')},\quad u_s(\nu) = \frac{s}{s_0},$$
$$s = n_1+\nu n_2,\quad s_0 = \frac{2m_*^2}{k_1k'}, \qquad (55)$$

and ψ is the angle between the $(\mathbf{k}_1, \mathbf{q}')$ and $(\mathbf{k}_1, \mathbf{a}_1)$ planes in a system where $\mathbf{k}$ and $\mathbf{k}_1$ are directed oppositely. An expression for $w^\gamma(n_1, n_2; n_1', n_2')$ can be obtained from $w^e(n_1, n_2; n_1', n_2')$ by making the change of variables in equations (32) and (33)

$$1+\frac{u^2}{2(1+u)}\longrightarrow 1-2u$$

and changing the overall sign. The parameters of the functions A_n and the arguments of the Bessel functions retain their form (39).

In the expressions for the corresponding pair-photoproduction probabilities, the argument of the θ function must be changed compared with equations (31) and (37). This is due to the existence of a threshold for the pair-photoproduction reaction

$$n_1+\nu n_2 = \frac{m_*^2+qq'}{k_1k'}\geq s_0.$$

We are interested in the case of commensurate frequencies, for which it makes sense to rewrite the probability (54), just as in the radiation problem, in the form [compare with (40)]

$$W^\gamma = \sum_{s=-\infty}^{\infty}\theta(s-s_0)W_s^\gamma = \frac{e^2m^2}{8\pi\omega'}\sum_{s=-\infty}^{\infty}\theta(s-s_0)$$
$$\times\int_1^{u_s(\nu)}\frac{du}{u\sqrt{u(u-1)}}\int_0^{2\pi}d\psi\sum_{n_2,\,n_2'=-\infty}^{\infty}\cos[(n_2-n_2')\varphi] \qquad (56)$$
$$\times w^\gamma(s-\nu n_2,n_2;\,s-\nu n_2',n_2').$$

For the same reasons as in the radiation problem, for numerical calculations in the case where at least one of the intensity parameters of the modes is not small compared to unity, it is convenient to represent the probability of pair photoproduction as a single sum over s. It has the form [compare with (50)]

$$W^\gamma = \frac{e^2m^2}{4\pi\omega'}\sum_{s=-\infty}^{\infty}\theta(s-s_0)\int_1^{u_s(\nu)}\frac{du}{u\sqrt{u(u-1)}}$$
$$\times\int_0^{2\pi}d\psi\Big\{|A_{00}(s)|^2+(2u-1)[\eta_1^2(|A_{10}(s)|^2 \qquad (57)$$
$$-\mathrm{Re}(A_{00}(s)A_{20}^*(s)))+\eta_1^2\zeta^2(|A_{01}(s)|^2-\mathrm{Re}(A_{00}(s)A_{02}^*(s)))$$
$$+2\eta_1^2\zeta\cos\phi\,\mathrm{Re}(A_{10}(s)A_{01}^*(s)-A_{00}(s)A_{11}^*(s))]\Big\},$$

where the functions $A_{km}(s)$ are determined by equation (51), and all parameters are determined by equations (55) and (39).

It is evident from equation (56) that pair photoproduction by a photon in a two-mode field with commensurate frequencies is characterized by the same interference effects as in the problem of emission of a photon by an electron. Since the representation (41) holds for the quantities $w^\gamma(n_1, n_2; n_1', n_2')$ when perturbation theory is applicable, we can conclude that even in this problem the frequency ratio $\nu = \omega_2/\omega_1$ equal to three, which we used in all further calculations, is optimal for observing interference effects. However, the threshold character of the pair-photoproduction reaction leads to a number of interesting features of this process.

Let us consider the dependences, shown in Figs. 8 and 9, of the total pair-photoproduction probability on the parameter η_2. The parameters for the curve shown in Fig. 8 were chosen so that the threshold value of the number s in the field of the initial monochromatic wave satisfies the condition $2 < s_0 < 3$. This means that in the field of a monochromatic wave with $\eta_0 \lesssim 1$ the partial probability W_3^γ, which is formed primarily by the process with absorption of three photons of the wave,

makes the dominant contribution to the probability. If an admixture of the second mode has appeared in the field for a fixed value of the parameter η_0 [see (5)], a channel with absorption of a single photon of the second mode starts to contribute to W_3^γ. In addition, as ζ (or η_2) increases, the contribution of this channel grows more rapidly than the contribution of the channel with the absorption of three photons of the first mode decreases. The increase in the partial probability W_4^γ as a result of the opened channel with the absorption of one photon with frequency ω_1 and one photon with frequency $\omega_2 = 3\omega_1$ from the field is also added to this.[3] As a result, in contrast to the emission problem, the total pair-photoproduction probability increases when the initial monochromatic wave is split into two components with frequencies ω_1 and $\omega_2 = 3\omega_1$.

We underscore that this increase occurs against the background of the already mentioned decrease in the intensity parameter η of the two-mode field compared with the intensity parameter η_0 of the initial monochromatic wave. The reason is that a new channel, which is forbidden by the conservation laws in the case of the monochromatic initial wave, opens up when the wave is split into two waves.

We call attention to the jump, clearly seen in Fig. 8, in the derivative of the total probability. This jump is explained by the fact that because the electron and positron effective masses decrease with increasing ζ (or η_2) another reaction channel opens up for some value $\zeta = \zeta_{02}$. The value of the parameter ζ_{02} is determined by the equation $s_0(\zeta_{02}) = 2$, and for $\zeta \geq \zeta_{02}$ the partial probability W_2^γ starts to contribute to the total probability.

Figure 9 shows the dependence of the total pair-photoproduction probability for the case where the threshold value s_0 of the number s is greater than three in the initial monochromatic field. Here, for small ζ (or η_2) we observe a completely explainable decrease of the total probability, since the decrease in the intensity parameter η as compared with η_0 is not accompanied by the opening of a new channel making a large contribution to the fundamental harmonic W_4^γ. The increase starts only at value η_2 corresponding to $\zeta = \zeta_{03}$, $s_0(\zeta_{03}) = 3$, for which a pair-photoproduction channel due to the absorption of the 4-momentum $3k_1$ from the external field opens up. Of course, for $\zeta = \zeta_{03}$ we observe a jump in the derivative of the total probability.

The spectral distributions of the probability of pair photoproduction by a photon are shown in Fig. 10 for various distributions of the intensity between the modes of the field. The intensity of the initial monochromatic wave is the same for all distributions $\eta_0^2 = 1$. Just as in the radiation spectrum, as ζ increases, the relative contribution of the harmonics with s being a multiple of three increases. However, in the radiation problem this growth occurs against the background of a decrease in the fundamental harmonic with $s = 1$, and as a result the total probability decreases. For pair photoproduction, however, because of the existence of a reaction threshold, the third harmonic is the fundamental harmonic for

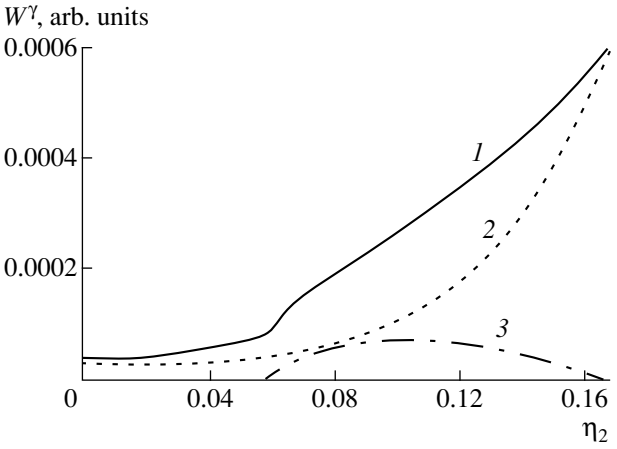

Fig. 8. Total pair-photoproduction probability W^γ (*1*) in a two-mode field as a function of the distribution of the intensity between the modes of the field for fixed intensity of the initial monochromatic wave $\eta_0 = 0.5$ with the parameters $m^2/k_1k' = 0.9$, $\varphi = 0$, and $\phi = 0$. The contribution of the partial probabilities W_3^γ (*2*) and W_2^γ (*3*) is shown.

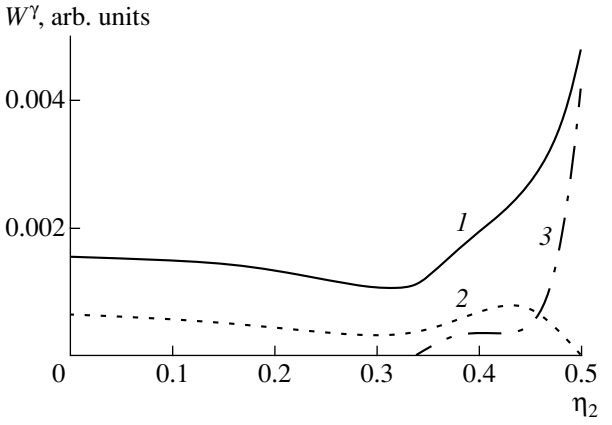

Fig. 9. Total pair-photoproduction probability W^γ (*1*) in a two-mode field and the contribution of the partial probabilities W_4^γ (*2*) and W_3^γ (*3*) to it as a function of the distribution of the intensity between the modes of the field for fixed intensity of the initial monochromatic wave $\eta_0 = 1.5$ and the parameters $m^2/k_1k' = 0.9$, $\varphi = 0$, and $\phi = 0$.

[3] The remaining harmonics make a negligibly small contribution to the total probability.

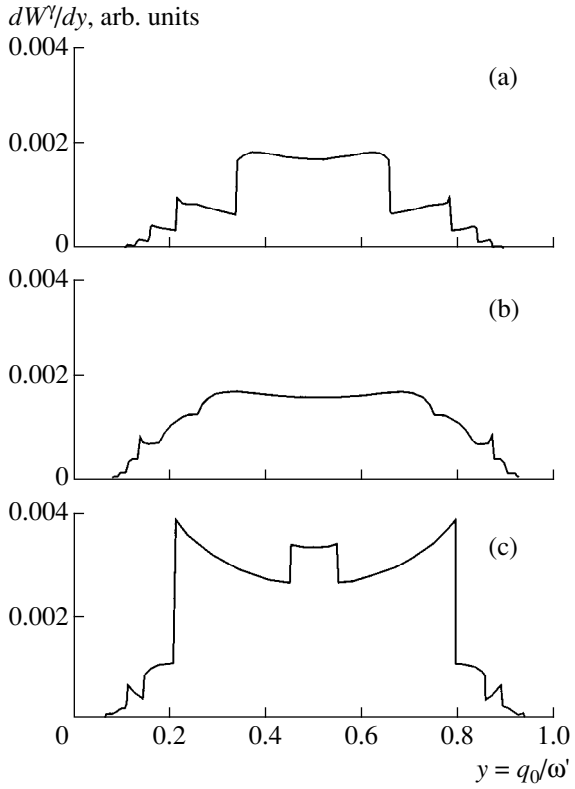

Fig. 10. Spectral distribution of the pair-photoproduction probability for various ratios between the intensities of the modes: ζ = (a) 0, (b) 0.36, and (c) 1 and the parameters $\eta_0 = 1.5$, $m^2/k_1k' = 0.9$, $\varphi = 0$, and $\phi = 0$.

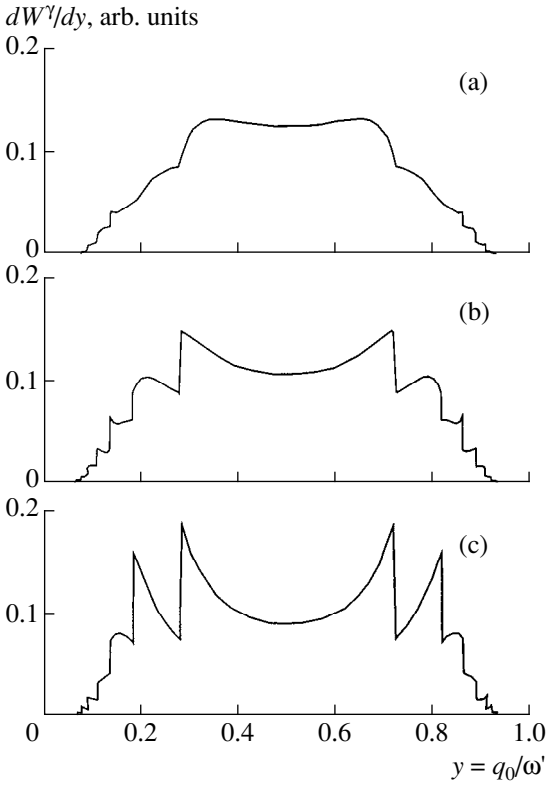

Fig. 11. Spectral distribution of the pair-photoproduction probability for various phase shifts φ between the modes of the field: φ = (a) 0, (b) $\pi/2$, and (c) π and the parameters $s_0 = 2.4$, $m^2/k_1k' = 0.9$, $\zeta = 0.25$, and $\phi = 0$.

the values chosen for the parameters, and its growth with ζ results in a higher total probability. We note that the appearance of a new local plateau in Fig. 10c is due to the opening for $\zeta > \zeta_{02}$ of a channel for pair photoproduction due to the absorption of two photons.

We note that as ζ increases, the electron and positron effective masses decrease, and s_0 decreases with them. As a result, as ζ increases, the widths of the harmonics, which are determined by the relation [3]

$$(\Delta q_0)_s = \omega'\sqrt{1-\frac{s_0}{s}}. \qquad (58)$$

increase. This effect can also be used for direct measurement of the electron effective mass in a plane-wave field as a function of the intensity of the field.

Finally, Fig. 11 illustrates the influence of interference effects on the spectral distribution of the pair-photoproduction probability, expressed as a dependence of the distribution on the phase difference φ between the modes. We note that for $\eta_1 \approx \eta_2 < 1$ the interference effects should be weak. Thus, if $\eta_0 = 1$, $2 < s_0 < 3$, the value $\zeta = 1$ is reached if $\eta_1 = \eta_2 \simeq 0.316$. Interference effects for the principal harmonic $s = 3$ are determined by the interference of channels with absorption of three photons from the mode with frequency ω_1 and one photon from the mode with frequency $\omega_2 = 3\omega_1$. The corresponding interference term is of the order of η_1^4, while the main term is of the order of $\sim\eta_1^2$. In other words, the interference term is approximately 10% of the main term. The situation changes if the mode with the tripled frequency is weak. For example, the parameters corresponding to the spectral distributions shown in Fig. 11 are such that $\eta_1 = 0.8$ and $\eta_2 = 0.2$. In this case, the channel with absorption of one photon with frequency ω_2 makes a small contribution to the total probability, since it is determined by the small factor $\eta_2^2 = 0.04$, while the contribution of the channel with the absorption of three photons from the mode with frequency ω_1 can be roughly estimated as being proportional to $\eta_1^6 = 0.26$. The interference term, however, can be estimated as $\eta_1^3\eta_2 \approx 0.1$, i.e., it is approximately 40% of the main term. We note that similar estimates can be made also for the radiation problem. However, in that problem the first harmonic W_1^e, which, for the mode intensity parameters considered here, is determining, also contributes to the total probability, and its contribution of

about η_1^2 is appreciably greater than the order of magnitude of the leading interference term. In the pair-photoproduction problem, the channel corresponding to absorption of one photon with frequency ω_1 is forbidden because of the presence of a reaction threshold, and this is what makes the interference effects noticeable, as one can see from Fig. 11.

ACKNOWLEDGMENTS

This work was supported by the Russian Foundation for Basic Research (project no. 97-02-16973) and the Ministry of Education of the Russian Federation (grant no. 97-5.2-117).

One of us (N.B.N.) is grateful to Professor K.T. MacDonald for a discussion of some questions considered in this paper.

REFERENCES

1. V. I. Ritus, Tr. Fiz. Inst. Akad. Nauk SSSR **111**, 5 (1979).
2. N. B. Narozhny and M. S. Fofanov, Zh. Éksp. Teor. Fiz. **110**, 26 (1996) [JETP **83**, 14 (1996)].
3. N. B. Narozhnyi and M. S. Fofanov, Laser Phys. **7**, 141 (1997).
4. C. Bula *et al.*, Phys. Rev. Lett. **76**, 3116 (1996).
5. D. L. Burke *et al.*, Phys. Rev. Lett. **79**, 1626 (1997).
6. A. K. Puntajer and C. Leubner, Opt. Commun. **73**, 153 (1989).
7. É. A. Manykin and A. M. Afanas'ev, Zh. Éksp. Teor. Fiz. **48**, 931 (1965) [Sov. Phys. JETP **21**, 619 (1965)].
8. É. A. Manykin and A. M. Afanas'ev, Zh. Éksp. Teor. Fiz. **52**, 1246 (1967) [Sov. Phys. JETP **25**, 828 (1967)].
9. Ce Chen, Yi-Yuan Yin, and D. S. Elliot, Phys. Rev. Lett. **64**, 507 (1990).
10. An Yu and H. Takahashi, Phys. Rev. E **57**, 2276 (1998).
11. N. B. Narozhny and M. S. Fofanov, Phys. Rev. E **60**, 3443 (1999).
12. V. B. Berestetskiĭ, E. M. Lifshitz, and L. P. Pitaevskiĭ, *Quantum Electrodynamics* (Nauka, Moscow, 1989, 3rd ed.; Pergamon Press, Oxford, 1982).

Translation was provided by AIP

Journal of Experimental and Theoretical Physics, Vol. 90, No. 3, 2000, pp. 428–433.
Translated from Zhurnal Éksperimental'noĭ i Teoreticheskoĭ Fiziki, Vol. 117, No. 3, 2000, pp. 489–495.

ATOMS, SPECTRA, RADIATION

Optical Solitons in Dense Resonant Media

A. A. Afanas'ev, R. A. Vlasov, and A. G. Cherstvyĭ*
Institute of Physics, Belarussian Academy of Sciences, Minsk, 220072 Belarus
**e-mail: lvp@dragon.bas-net.by, cherstvy@dragon.bas-net.by*
Received July 22, 1999

Abstract—Exact single-soliton solutions of the modified system of Maxwell–Bloch equations, in which the dipole–dipole interactions of the atoms of a dense resonant medium are taken into account, are obtained. Two propagation regimes are analyzed: "coherent," where the pulse duration is much shorter than both relaxation times ($T_p \ll T_1, T_2$), and "incoherent," where the pulse duration falls between the relaxation times ($T_2 \ll T_p \ll T_1$). It is predicted, for the first time, that soliton propagation of an ultrashort pulse is possible in a dense resonant absorbing medium in an incoherent interaction regime. The differences between the amplitude and phase characteristics of the solitons considered and the corresponding characteristics of the solitons for McCall–Hahn self-induced transparency are noted. © *2000 MAIK "Nauka/Interperiodica".*

1. INTRODUCTION

It is well known [1] that in dense resonant media a spectral shift appears in the absorption line as a result of the short-range dipole–dipole interaction between the atoms. The spectroscopic data confirm reliably that the short-range dipole–dipole interaction—the local field in a dense resonant medium—influence the contour of the resonance absorption line [2]. The most complete theoretical approach to the problem of the local field in a dense resonant medium has been elegantly demonstrated in [3], where a strict justification is given for the generalization of the Maxwell–Bloch equations taking account of the short-range dipole–dipole interaction. Besides purely spectroscopic effects, this qualitative modification made it possible to predict certain other effects. Specifically, internal optical bistability due to a first-order phase transition, can appear in the stationary interaction regime under certain conditions [4].

The nonstationary interaction of a light pulse with a dense resonant medium likewise can be strongly influenced by the local field. In this connection, it is interesting to study the soliton propagation of ultrashort pulses in such media. More precisely, we are talking about the possibility of the propagation of pulses of a solitary wave packet type, which, for brevity, we shall in what follows call a soliton. As far as we know, this problem has been studied only in [5, 6], which where the first works to call attention to the fact that the short-range dipole–dipole interaction affects the modulation of the envelope and phase of solitons in a dense resonant medium. However, phase modulation was neglected in [5], and an insufficiently general approach was used in [6] (see, for example, the condition (8) imposed on the frequency offset).

In the present paper , we consider two aspects of the problem touched upon. First, we consider the purely coherent process of the propagation of a light pulse. Our analysis is more general than the theory proposed in [6], since no interrelation between the Lorentzian frequency and frequency offset from resonance is assumed. This feature makes it possible to perform correctly the transition to a McCall–Hahn soliton with a constant offset from resonance.

Second, we shall give the first formulation and solution of the problem of the formation of an incoherent soliton in a dense resonant medium. This situation is interesting because an essentially incoherent interaction with the absorbing resonant medium is assumed and soliton formation is nonetheless possible under definite conditions. In both cases, the amplitude and phase characteristics of the soliton differ qualitatively from those of the solitons discovered by McCall and Hahn [7].

2. BASIC EQUATIONS

The truncated system of Maxwell–Bloch equations for the complex amplitudes of the electric field $\hat{E} = E\exp[-i(\omega T - kZ)]$ + c.c. and polarization $\hat{p} = p\exp[-i(\omega T - kZ)]$ + c.c., as well as the difference n of the populations of the resonant atom has the form

$$\frac{\partial E}{\partial Z} + \frac{1}{V}\frac{\partial E}{\partial T} = i\frac{2\pi k}{n_0^2}\mu N_0 p, \tag{1}$$

$$\frac{\partial p}{\partial T} = i\frac{\mu}{\hbar}En + i(\Omega + \Omega_L n)p - \frac{p}{T_2}, \tag{2}$$

$$\frac{\partial n}{\partial T} = i\frac{2\mu}{\hbar}(E^*p - p^*E). \tag{3}$$

Here, $V = c/n_0$ is the phase velocity of light in the medium, n_0 is the nonresonant part of the refractive

index of the medium, $k = \omega n_0/c$ is the wave number in the medium, μ is the dipole moment of the resonance transition, $\Omega = \omega - \omega_0$ is the offset of the frequency ω of the field relative to the center ω_0 of the absorption line, $\Omega_L = 4\pi\mu^2 N_0/3\hbar$ is the Lorentzian frequency, determining the frequency shift as a result of short-range dipole–dipole interactions [1], T_2 is the transverse relaxation time, and N_0 is the density of resonant atoms. The effect of the relaxation term in equation (2) is taken into account only when the incoherent interaction is studied. In equation (3) we neglected the relaxation term because of the assumption $T_p \ll T_1$, where T_p is the pulse duration and T_1 is the longitudinal relaxation time.

To simplify the equations, it is convenient to introduce the following dimensionless quantities:

$$\mathscr{E} = \frac{\mu E}{\hbar\omega_p}, \quad z = \frac{\omega_p}{V}Z, \quad t = \omega_p T,$$
$$\delta = \frac{\Omega}{\omega_p}, \quad \omega_L = \frac{\Omega_L}{\omega_p}, \quad t_2 = \omega_p T_2, \tag{4}$$
$$\omega_p^2 = \frac{2\pi N_0 \mu^2 \omega}{\hbar n_0^2}.$$

In accordance with the scaling procedure (4), the system (1)–(3) assumes a completely dimensionless form

$$\frac{\partial\mathscr{E}}{\partial z} + \frac{\partial\mathscr{E}}{\partial t} = ip, \tag{5}$$

$$\frac{\partial p}{\partial t} = i\mathscr{E}n + i(\delta + \omega_L n)p - \frac{p}{t_2}, \tag{6}$$

$$\frac{\partial n}{\partial t} = 2i(\mathscr{E}^* p - p^*\mathscr{E}). \tag{7}$$

3. COHERENT SOLITONS IN A DENSE RESONANT MEDIUM

In this section the propagation of optical pulses of duration $T_p \ll T_2$ in a dense resonant medium is studied on the basis of the system of equations (5)–(7). Under this condition, the relaxation term in equation (6) can be neglected. To solve the system of equations (5)–(7) we assume that

$$\mathscr{E} = \mathscr{E}(\tau), \quad p = p(\tau), \quad n = n(\tau), \tag{8}$$

where the autowave variable $\tau = t - z/v_0$ is introduced and $v_0 = V_0/V$ is the dimensionless velocity of the soliton.

We shall seek the analytic solution of the system of equations (5)–(7) that depends only on the variable τ under the following physical assumptions: the amplitude and first derivative of the field vanish at infinity, the derivative of the phase at infinity is a constant, and $n(\pm\infty) = 1$. We find from equations (5) and (7) that

$$n = 1 - 2\gamma|\mathscr{E}|^2, \tag{9}$$

where $\gamma = 1/v_0 - 1$. Using equations (5), (6), and (9), we obtain for $\mathscr{E}$ the resulting equation

$$\gamma\frac{d^2\mathscr{E}}{d\tau^2} - i[\delta + \omega_L(1 - 2\gamma|\mathscr{E}|^2)]\gamma\frac{d\mathscr{E}}{d\tau} = \mathscr{E}(1 - 2\gamma|\mathscr{E}|^2). \tag{10}$$

Following the standard procedure, we represent the amplitude $\mathscr{E}$ of the propagating pulse in the form

$$\mathscr{E}(\tau) = A(\tau)\exp[i\phi(\tau)]. \tag{11}$$

Substituting the expression (11) into equation (6) and using equations (5) and (9), we obtain the following equations for the envelope A and phase ϕ of the pulse:

$$\left(\frac{1}{\sqrt{\xi}}\frac{dA}{d\tau}\right)^2 = qA^2 - \frac{1}{2}A^4 - rA^6, \tag{12}$$

$$\frac{d\phi}{d\tau} = \frac{\delta + \omega_L}{2} - \frac{\omega_L\gamma}{2}A^2, \tag{13}$$

where

$$\xi = 2 - \gamma\omega_L(\delta + \omega_L),$$
$$q = \frac{4 - \gamma(\delta + \omega_L)^2}{4\gamma\xi}, \tag{14}$$
$$r = \frac{\omega_L^2\gamma^2}{4\xi}.$$

The solution of equations (12) and (13) can be represented in the form

$$A(\tau) = \frac{2\sqrt{q}}{\sqrt{1 + \sqrt{1 + 16rq}\cosh(2\sqrt{\xi q}\tau)}}, \tag{15}$$

$$\phi(\tau) = \frac{\delta + \omega_L}{2}\tau - \operatorname{arctanh}\left[\frac{\sqrt{1 + 16rq} - 1}{4\sqrt{rq}}\tanh(\sqrt{\xi q}\tau)\right]. \tag{16}$$

Next, we can introduce a parameter that represents the pulse duration $\tau_p = \omega_p T_p$:

$$\tau_p = \frac{1}{\sqrt{\xi q}}\frac{1}{\sqrt{\frac{1}{\gamma} - \left(\frac{\delta + \omega_L}{2}\right)^2}}. \tag{17}$$

Hence, it follows a relation between the soliton velocity and duration:

$$\frac{V}{V_0} - 1 = \frac{\tau_p^2}{1 + [(\delta + \omega_L)\tau_p/2]^2}. \quad (18)$$

It is easy to see that the soliton studied here differs from the McCall–Hahn soliton [7] by the Lorentzian frequency. The presence of $\omega_L \neq 0$ in equation (16) leads to the appearance of a nonlinear phase modulation, and, in addition, ω_L appears additively in the term describing the linear modulation. The soliton velocity determined by equation (18) depends parametrically on the total offset $\delta + \omega_L$. Finally, as a result of the presence of ω_L, the area of the pulse becomes less than 2π. Indeed, the area of a coherent soliton is, up to the first term in the expansion in terms of the small parameter ω_L^2,

$$S = 2\int_{-\infty}^{\infty} A(\tau)d\tau \approx 2\pi\left\{1 - \frac{3\omega_L^2}{32[1 + (\delta\tau_p/2)^2]}\right\}. \quad (19)$$

Even though varying the constant ω_L within possible limits does not greatly change the profile of a coherent soliton in a dense resonant medium, the short-range dipole–dipole interactions can have a large effect on the propagation velocity of the soliton for certain pulse durations. Moreover, for propagation of a coherent soliton in a dense resonant medium, the derivative of the phase of the soliton undergoes qualitative changes, as a result of which for $\omega_L \neq 0$ chirping of the pulse is always present, which the conclusion drawn in [6] confirms. In contrast to [6], in our case the parameters δ and ω_L are in no way related by any condition, and in the limit $\omega_L \longrightarrow 0$ the offset δ remains unchanged, which ensures the correct limit to the McCall–Hahn soliton for $\delta \neq 0$.

Here it is useful to indicate well-known analogies. In the limit $t_2 \longrightarrow \infty$ the system (5)–(7) is similar to the system that is used to describe self-induced transparency in molecular crystals in the excitonic range of the spectrum [8], where, in a certain approximation, taking account of the intermolecular interaction is equivalent to taking account of the short-range dipole–dipole interaction which we are studying. Of course, the soliton solutions obtained for different physical situations are also similar. Nonetheless, we thought it useful to examine the formation of a coherent soliton from a somewhat general standpoint, admitting the applicability of the system (5)–(7), under the indicated, assumption for describing the interaction of optical pulses not only with solid-state (ensembles of two-level impurity atoms) but also with gaseous dense resonant media. It was also important to underscore the nonthreshold character of the effect of the short-range dipole–dipole interaction on the formation of solitons, when coherence is ensured by pulse durations much shorter than the transverse relaxation time. In what follows we shall be talking about a different possible self-induced transparency regime in dense resonant media (quite unexpected compared with the one just described), where the conventionally understood coherence condition breaks down.

4. INCOHERENT SOLITONS IN A DENSE RESONANT MEDIUM

In this section we present the first investigation of the propagation of light pulses with duration T_p satisfying the condition $T_2 \ll T_p \ll T_1$ in a dense resonant medium. Such propagation is essentially "quasistationary," since under such conditions the polarization p of an atom, in contrast to the difference n of its level populations, can follow the change in the field of the propagating pulse and it can be assumed in equation (2) that $|\partial p/\partial t| \ll |p/T_2|$.

Then, for $\dot{p} = 0$, it follows from equation (6) that

$$p = i\frac{t_2 n\mathscr{E}}{1 - i(\Delta + bn)}, \quad (20)$$

where $\Delta = t_2\delta$, $b \equiv \omega_L t_2 = 4\pi\mu^2 N_0 T_2/(3\hbar)$ is the short-range dipole–dipole interaction constant of the atoms [5]. Taking into consideration equation (20) and assuming the existence of the dependences (8), we transform equation (7) to the form

$$\frac{dn}{d\tau} = -\frac{4t_2 n|\mathscr{E}|^2}{1 + (\Delta + bn)^2}. \quad (21)$$

Separating variables, equation (21) under the condition $n(\tau = -\infty) = 1$ can be integrated as

$$\ln n + \frac{2\Delta b}{1 + \Delta^2}n + \frac{b^2}{2(1 + \Delta^2)}n^2 = \frac{4b\Delta + b^2}{2(1 + \Delta^2)} - \frac{4t_2}{1 + \Delta^2}\int_{-\infty}^{\tau} |\mathscr{E}|^2 d\tau. \quad (22)$$

Next, it is assumed that the difference of the populations changes negligibly during the passage of the pulse, i.e., $n = 1 - \epsilon$, $\epsilon \ll 1$. Taking this into account, equation (22) can be reduced to the form

$$n = 1 - \epsilon = 1 - \frac{4t_2}{|\lambda|^2}\int_{-\infty}^{\tau} |\mathscr{E}(\tau')|^2 d\tau', \quad (23)$$

which corresponds to the cubic approximation. Here, $\lambda = 1 - i(\Delta + b)$. Correspondingly, the polarization amplitude (20) is now determined by the expression

$$p = \left[\chi_0 + \chi\int_{-\infty}^{\tau} |\mathscr{E}(\tau')|^2 d\tau'\right]\mathscr{E}, \quad (24)$$

where

$$\chi_0 = i\frac{t_2}{\lambda}, \quad \chi = -i\frac{4t_2^2(1-i\Delta)}{\lambda^2|\lambda|^2}. \tag{25}$$

Taking account of equations (8) and (24), equation (5) becomes

$$\frac{d\mathscr{E}}{d\tau} = -\frac{i}{\gamma}\left[\chi_0 + \chi\int_{-\infty}^{\tau}|\mathscr{E}(\tau')|^2 d\tau'\right]\mathscr{E}. \tag{26}$$

The desired solution, once again, can be put into the form (11), and substituting it into equation (26) we arrive at the following equations for the envelope and phase:

$$\frac{1}{A^2}\frac{dA^2}{d\tau} = 2\alpha_1 - 2\beta_1\int_{-\infty}^{\tau}A^2(\tau')d\tau', \tag{27}$$

$$\frac{d\phi}{d\tau} = \alpha_2 - \beta_2\int_{-\infty}^{\tau}A^2(\tau')d\tau'. \tag{28}$$

Here, we have introduced the parameters

$$\alpha = -\frac{i}{\gamma}\chi_0 \equiv \alpha_1 + i\alpha_2, \quad \beta = \frac{i}{\gamma}\chi \equiv \beta_1 + i\beta_2,$$

where α_j and β_j are real quantities. The solution of equation (27) is

$$A = A_0\,\mathrm{sech}[\tau/\tau_p], \tag{29}$$

where the soliton duration is defined as

$$\tau_p = \frac{1}{\alpha_1} = \frac{\gamma|\lambda|^2}{t_2}, \tag{30}$$

and the amplitude (the peak value) is given by the expression

$$A_0 \equiv \frac{1}{\tau_p\sqrt{\beta_1}} = \frac{|\lambda|^2}{2}\sqrt{\frac{1}{\tau_p t_2(1+\Delta^2-b^2)}}. \tag{31}$$

We find from equation (28), using equation (29),

$$\phi(\tau) = (\alpha_2 + \beta_2\tau_p A_0^2)\tau - \beta_2\tau_p^2 A_0^2\ln[\cosh(\tau/\tau_p)]. \tag{32}$$

In order for the cubic approximation introduced earlier to be valid, as follows from equations (23), (29), and (31) the inequality

$$A_0^2 \ll \frac{|\lambda|^2}{8\tau_p t_2} \tag{33}$$

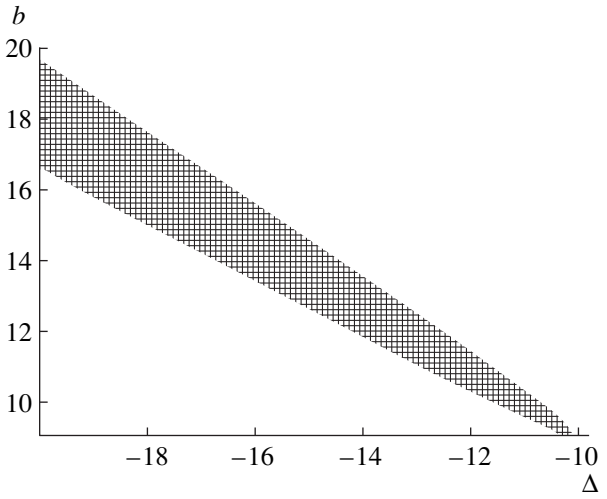

Fig. 1. The region (in the variables b and Δ) of validity of the cubic approximation (23) for studying an incoherent soliton (inside the distinguished range of parameters, the change in the population difference as a result of the passage of the pulse is less than 1/5).

must be satisfied. This condition and the requirement that the radicand in equation (31) be positive lead to the inequalities

$$u \equiv \frac{2[1+(\Delta+b)^2]}{1+\Delta^2-b^2} \ll 1, \qquad 1+\Delta^2-b^2 > 0, \tag{34}$$

to satisfy which it is possible to find an optimal ratio between the parameters b and Δ, minimizing the function u,

$$\Delta_{\mathrm{opt}} = -(b+1), \tag{35}$$

where

$$u(\Delta_{\mathrm{opt}}) = \frac{2}{1+b}. \tag{36}$$

It is remarkable that the formation of a soliton is nontrivially ensured by finite values of b and Δ, and the necessary conditions are $b \gg 1$, $|\Delta| \gg 1$, and $\Delta < 0$. These requirements reflect the unique properties of the soliton under study, which can exist only in dense resonant media for parameters determined by the inequalities (34) (see Fig. 1). Actually, they attest to the threshold character of the influence of the short-range dipole–dipole interaction on soliton formation.

The dependence of the soliton velocity on the duration of the soliton is obtained in an obvious way from equation (30):

$$1/v_0 - 1 = t_2\tau_p/|\lambda|^2. \tag{37}$$

Although this formula superficially resembles the one obtained by McCall and Hahn [7], there nonetheless

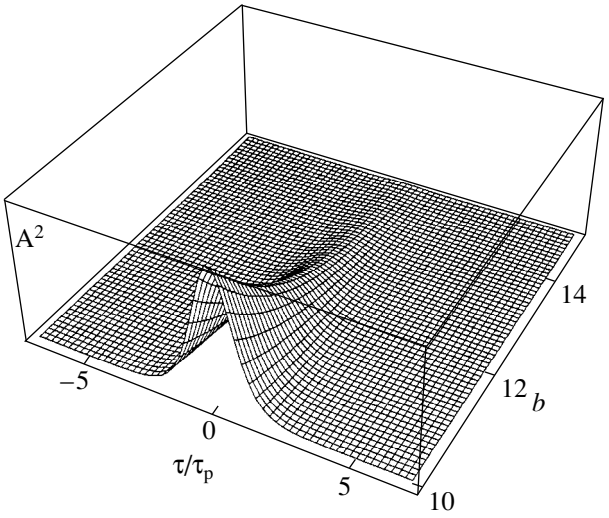

Fig. 2. The squared amplitude A^2 of an incoherent soliton versus the variables τ and short-range dipole–dipole interaction constant b for $T_2 = 10^{-11}$ s, $T_p = 10^{-10}$ s, and $\Delta = -16$.

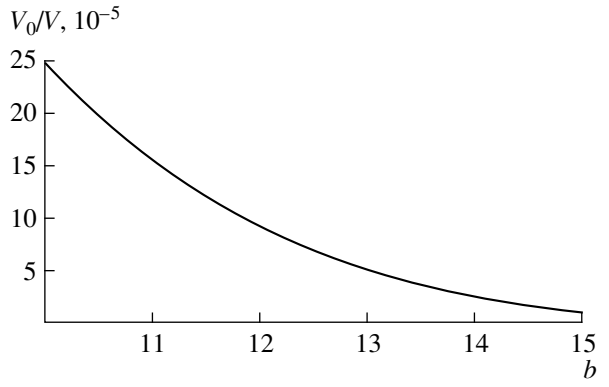

Fig. 3. The dimensionless velocity $v_0 \equiv V_0/V$ of an incoherent soliton versus the short-range dipole–dipole interaction constant b for $T_2 = 10^{-11}$ s, $T_p = 10^{-10}$ s, and $\Delta = -16$.

exists a fundamental difference, due to the decisive role of t_2 and $|\lambda|^2$ (and hence of the offset also).

The phase (32), just as in the case of a coherent soliton, contains linear and nonlinear parts. It is interesting that the area of the soliton now depends explicitly not only on the parameters b and Δ but also on the duration of the soliton τ_p:

$$S = \frac{2\pi}{\sqrt{\beta_1}} = \pi|\lambda|^2\sqrt{\frac{\tau_p}{t_2(1+\Delta^2-b^2)}}. \qquad (38)$$

Evidently, the area of the incoherent soliton can be substantially different from 2π.

Figure 2 shows the dependence of the envelope of the incoherent soliton (29) on the parameter b of the short-range dipole–dipole interactions. Figure 3 illustrates the dependence of the velocity of an incoherent soliton on the short-range dipole–dipole interaction constants.

The analytic study, performed above, of the formation of an incoherent soliton agrees well with the results of a numerical simulation.

5. CONCLUSIONS

Solitary wave packets (solitons) in dense resonant media possess very specific properties. This is due to the existence of a short-range dipole–dipole interaction between the resonant atoms, which results in a characteristic (linear and nonlinear) phase modulation (chirping). The very possibility of coherent and incoherent soliton pulse propagation regimes is a specific feature. The coherent soliton studied above is a natural generalization of a standard self-induced transparency soliton, and the difference in their properties, though small, is quite fundamental and therefore merits attention. The question of the possibility of incoherent soliton pulse propagation seems to be more fundamental. We predicted the possibility of the formation of an incoherent soliton whose amplitude–phase characteristics are qualitatively different from those of an ordinary self-induced transparency soliton. The intensity of interatomic interactions (the parameter b) and negative frequency offsets of the acting field $\Delta < 0$, which ensure the very existence of a soliton, play the decisive role here.

Undoubtedly, the search for dense resonant media with $b \gg 1$ is difficult and is, in some sense, an independent problem. Here, the prospects are, to a large degree, the same as in the long-standing search for dense resonant media for experimental realization of a first-order phase transition and the associated internal optical bistabilization (the necessary condition for observing them with respect to bistable reflection or transmission is $b > 4$ [9], and it is fundamentally unrealizable in gases). For this reason, we can focus on those considerations in this respect which have appeared in the literature in the last few years. For example, in [10] ensembles of impurity ions O_2^- in KCl crystals and bound I_2 excitons in CdF crystals were suggested in [10] as media with a large value of b. However, the authors of [11] believe that molecular crystals at low temperatures are today more promising media of this type. Their parameters do indeed favor achieving a large value of b in the excitonic range of the spectrum (for $\mu^2 \geq 10^{-36}$ CGSE and excitonic density of states $N_0 \geq 10^{18}$ cm^{-3}). As far as the formation of an incoherent soliton is concerned, such media could make it possible to obtain not only the condition $b \gg 1$, but also to choose the required intermediate duration of the injected optical pulses, since here the transverse relaxation time (due to scattering by acoustic phonons) T_2 is approximately 10^{-11}–10^{-10} s, and the longitudinal relaxation time (the excitonic lifetime) T_1

is of the order of 10^{-8}–10^{-3} s [12], i.e., the requirement $T_2 \ll T_p \ll T_1$ is easily satisfied for pulse durations in the nanosecond range.

Thus, an incoherent soliton pulse propagation regime, in principle, can be realized only in solid-state dense resonant media, for which there is a possibility of choosing suitable values of the parameters b, T_1, and T_2. The term "incoherent soliton" in this case is, as expected, somewhat arbitrary. In our opinion, such a soliton is formed as a result of competition between an incoherent dephasing process with characteristic time T_2 ($T_p \gg T_2$) and an intrinsically coherent short-range dipole–dipole interaction, which leads to a collective local-field effect. Such a qualitative explanation seems to be admissable when the interaction with the nonlinear medium is postulated to be coherent for any type of soliton.

It should be noted that the formation of an incoherent soliton has also been studied in [13], but for a combined medium consisting of amplifying resonant (without the short-range dipole–dipole interaction) and nonresonant (cubic) components, the presence of a nonresonant component being mandatory. The difference in our case is that the nonlinear medium can be a single-component absorbing resonant medium characterized by the required high density of atoms, which ensures a sufficiently strong short-range dipole–dipole interaction, a negative frequency offset of the applied field being mandatory.

ACKNOWLEDGMENTS

This work was supported by the Belarussian State Foundation for Basic Research, project F97-062.

REFERENCES

1. R. Friedberg, S. R. Hartmann, and J. T. Manassah, Phys. Rep. C **7**, 101 (1973); F. A. Hopf and C. M. Bowden, Phys. Rev. A **32**, 268 (1985).
2. J. J. Maki, M. S. Malcuit, J. E. Sipe, and R. W. Boyd, Phys. Rev. Lett. **67**, 972 (1991).
3. C. M. Bowden and J. P. Dowling, Phys. Rev. A **47**, 1247 (1993).
4. Y. Ben-Aryeh, C. M. Bowden, and J. C. Englund, Phys. Rev. A **34**, 3917 (1986).
5. C. R. Stroug, C. M. Bowden, and L. A. Allen, Opt. Commun. **67**, 387 (1988).
6. C. M. Bowden, A. Postan, and R. Inguva, J. Opt. Soc. Am. B **8**, 1081 (1991).
7. S. L. McCall and E. L. Hahn, Phys. Rev. Lett. **18**, 308 (1967); Phys. Rev. **183**, 457 (1969); Phys. Rev. A **2**, 861 (1970).
8. A. M. Agranovich and V. I. Rupasov, Fiz. Tverd. Tela (Leningrad) **18**, 801 (1976) [Sov. Phys. Solid State **18**, 459 (1976)].
9. R. Friedberg, S. R. Hartmann, and J. T. Manassah, Phys. Rev. A **39**, 3444 (1989).
10. M. E. Crenshaw, M. Scalora, and C. M. Bowden, Phys. Rev. Lett. **68**, 911 (1992).
11. V. A. Malyshev and E. Cenejero Jarque, Opt. Spektrosk. **82**, 630 (1997) [Opt. Spectrosc. **82**, 582 (1997)].
12. A. M. Agranovich, *The Theory of Excitons* (Nauka, Moscow, 1968).
13. E. V. Vanin, A. I. Korytin, A. M. Sergeev, *et al.*, Phys. Rev. A **49**, 2806 (1994).

Translation was provided by AIP

Journal of Experimental and Theoretical Physics, Vol. 90, No. 3, 2000, pp. 434–446.
Translated from Zhurnal Éksperimental'noĭ i Teoreticheskoĭ Fiziki, Vol. 117, No. 3, 2000, pp. 496–510.

ATOMS, SPECTRA, RADIATION

Classical and Quantum Theories of the Polarization Bremsstrahlung in the Local Electron Density Model

V. A. Astapenko[1, *], L. A. Bureeva[2], and V. S. Lisitsa[3]

[1] *Moscow Institute of Physics and Technology, Dolgoprudnyĭ, Moscow oblast, 141700 Russia*
[2] *Scientific Council on Spectroscopy, Russian Academy of Sciences, Moscow, 117924 Russia*
[3] *Russian Research Centre Kurchatov Institute, pl. Kurchatova 1, Moscow, 123481 Russia*
**e-mail: astval@hotmail.com*

Received September 30, 1999

Abstract—Classical and quantum theories of polarization bremsstrahlung in a statistical (Thomas–Fermi) potential of complex atoms and ions are developed. The basic assumptions of the theories correspond to the approximations employed earlier in classical and quantum calculations of ordinary bremsstrahlung in a static potential. This makes it possible to study on a unified basis the contribution of both channels in the radiation taking account of their interference. The classical model makes it possible to obtain simple universal formulas for the spectral characteristics of the radiation. The theory is applied to electrons with moderate energies, which are characteristic for plasma applications, specifically, radiation from electrons on the argon-like ion KII at frequencies close to its ionization potential. The computational results show the importance of taking account of the polarization channel of the radiation for plasma with heavy ions. © *2000 MAIK "Nauka/Interperiodica".*

1. INTRODUCTION

The process of polarization bremsstrahlung (PB) in collisions of charged particles with heavy atoms and ions has been under intensive investigation for the last ten years [1–7]. As is well known [1], the crux of this process reduces to the dynamical polarization of the atomic core by the incident charged particle (ordinarily, an electron) followed by radiation of the core and energy loss by the particle. Thus, polarization bremsstrahlung is an additional (together with the ordinary bremsstrahlung in a static potential) channel for radiation losses of a particle in collisions.

Here we are dealing, essentially, with the radiation of the compound system "atom + incident particle," the radiation being due to the total dipole moment of the system. This approach to bremsstrahlung was first formulated by M. Born (see [8]) and was subsequently applied to a number of different effects.

Many calculations of PB have been performed by quantum methods and pertain primarily to high incident-particle energies (see the review [4]). At the same time, it is relevant to pose the question of the contribution of the polarization channel to the radiation of a plasma with heavy ions. The range of electron energies in this case is of the order of the plasma temperature T and is less than (or comparable to) the ionization potential of ions. Calculations of ordinary (static) bremsstrahlung show that the methods of classical electrodynamics work well here, making it possible to obtain quite simple analytic results for the bremsstrahlung spectra (see [9]). The basis for the applicability of classical methods is the acceleration of the incident particle in the field of an atomic potential, as a result of which the electron "forgets" its initial energy, and all radiation effects depend on its kinetic energy at the point of greatest acceleration. This is why the criterion for the process to be classical is the condition that the energy of the photon $\hbar\omega$ be small compared not with the initial energy of the incident particle E ($\hbar\omega \ll E$) but rather compared with the much higher energy of the electron accelerated in the atomic potential. Thus, the classical analysis is applicable even for describing strongly inelastic processes $\hbar\omega \gg E$. This circumstance serves as a basis for the so-called Kramers electrodynamics (see [9] for a more detailed discussion).

For many plasma applications, the average spectral characteristics corresponding to the motion of an electron in an average statistical potential of the Thomas–Fermi type play the main role. Such spectra are in good agreement with the more accurate calculations performed using the Hartree–Fock method, as was shown by the calculations performed with a statistical potential [11]. For this reason, to obtain universal results it is appropriate to use statistical models for the polarization radiation also.

Thus, our objective in the present work is to calculate PB effects for the motion of an electron in a statistical atomic potential of atoms or ions. The calculations are performed for the classical and quantum motions of an electron in the same approximations which were used previously for ordinary bremsstrahlung [9–14]. The computational results make it possible to obtain simple universal formulas for the radiation in both channels, taking account of interference effects. The

1063-7761/00/9003-0434$20.00

approximations used are justified for electrons of moderate energies, characteristic for plasma systems [9].

To calculate the contribution of the polarization channel to the total cross section for collisional-radiation processes, it is necessary to know the generalized (nondipole) polarizability $\alpha(\omega, \mathbf{q})$ of the target. As is well known, the calculation of this quantity is a complicated quantum-mechanical problem, which can be solved exactly only for a hydrogen-like ion [2]. In all other cases, an exact calculation is impossible even in the dipole approximation.

For situations when one outer valence electron makes the main contribution to the process, the approximate methods of the quantum-defect and model-potential type [15], which give a solution in terms of the Coulomb wave functions with nonintegral parameters, can be used.

If, however, a multielectron subshell plays the main role, then it is found that interelectron correlation effects must also be taken into account in the radiation process. The calculation of the atomic radiative characteristics in the single-electron approximation gives a strongly distorted result. This latter circumstance is well known from the theory of the photoeffect for multielectron atoms near the photoionization threshold of *d* and *f* subshells [16], knowledge of which in the entire frequency range is sufficient for determining the dynamical (dipole) polarizability of an atom (ion).

The main characteristics of the cross section for the photoeffect and the polarizability for atoms with closed shells can be described well on the basis of the so-called random-phase approximation with exchange. The basic idea of this method consists in the fact that the interelectron correlation effects are expressed in terms of the dynamical polarizability of the atomic core.

Such calculations for the problem of calculating the cross section for polarization bremsstrahlung by an atom in a wide frequency range have been performed recently [5] for kilovolt-range electrons scattered by a krypton atom. It should be noted that such calculations present a very complicated computational problem, since the wave functions of the atomic electrons in the zeroth approximation are solutions of the Hartree–Fock integrodifferential equations.

2. BASIC RELATIONS

As already mentioned above, our objective in this paper is to develop universal semiquantitative methods for describing polarization effects in radiative processes in collisions of electrons with multielectron atoms in a wide frequency range and to analyze using these methods the general characteristics of the indicated processes on the basis of the local electron density for the polarizability of the target.

The main advantage of the approach employed is its computational simplicity, universality with respect to applicability to different targets, and physical clarity. Without pretending to give an exact quantitative description of the phenomenon, the method employed can be regarded as an approximate method for describing polarization-interference effects on multielectron systems, which is applicable in a wide range of plasma parameters.

In what follows we shall employ the so-called local approximation for the density or for the related plasma frequency, previously developed by Brandt and Lundqvist for calculating the photoionization of multielectron atoms [17] as an alternative to the single-electron approximation. In the Brandt–Lundqvist approximation an atom is regarded as a nonuniform plasma cloud with a fixed electron density distribution $n(r)$. To each point in the space inside the atom there corresponds a unique plasma frequency

$$\omega_p = \sqrt{4\pi n(r)}.$$

(Unless otherwise stated, atomic units are used everywhere.) According to the classical picture, which is used in this model, the absorption of radiation with frequency ω occurs when the resonance condition $\omega = \omega_p(r)$ is satisfied, which determines the characteristic distances $r_p(\omega)$ of the process.

The expression for the polarizability $\alpha(\omega)$ in this model has the form

$$\alpha^{BL}(\omega) = \int_0^{R_0} \frac{\omega_p^2(r) r^2 dr}{\omega_p^2(r) - \omega^2 - i\delta} = \int \beta^{BL}(r, \omega) d\mathbf{r}. \quad (1)$$

Here, R_0 is the radius of the atom (ion) and δ is an infinitesimal positive quantity.

The formula (1) gives a representation of the dynamic polarizability as an integral of a certain function $\beta(r, \omega)$, which it is natural to call the spatial density of dynamic polarizability, over the spatial coordinate. In the local approximation under study, this quantity establishes a relation between the induced polarization of an atom at frequency $\omega(P(r, \omega))$ and the intensity of the external electric field $(E(r, \omega))$ giving rise to this polarization. Both quantities are taken at the same point in space (local approximation):

$$P(r, \omega) = \beta(r, \omega) E(r, \omega). \quad (2)$$

We note that the expression (1) can be rewritten as an integral over the frequency, if the spectral density of the oscillator strength is introduced in an appropriate manner according to the following formula (here Gaussian units are employed):

$$\frac{df}{d\omega} = \frac{m\omega^2}{e^2} r_p^2(\omega) \frac{dr_p(\omega)}{d\omega}, \quad (3)$$

where the function $r_p(\omega)$ is determined by solving the equation

$$\omega = \omega_p(r). \quad (4)$$

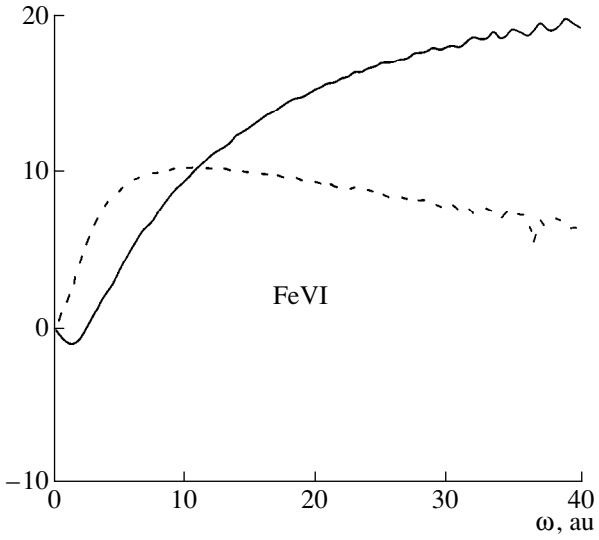

Fig. 1. Frequency dependences of the real and imaginary parts of the dynamical polarizability of an FeVI ion, obtained in a local Brandt–Lundqvist plasma model [17]: $-\omega^2\mathrm{Re}\{\alpha^{BL}(\omega)\}$ solid curve and $\omega^2\mathrm{Im}\{\alpha^{BL}(\omega)\}$ dashed curve (values given in au).

In Table 1 the static polarizabilities (in atomic units) of atoms and ions with closed electron shells, calculated by different methods on the basis of a statistical description of an atom, are compared with the experimental data ($\alpha_0^{\exp}$).

It follows from the table presented that in most cases the Brandt–Lundqvist method, being very simple, gives for the static polarizability satisfactory agreement with experiment for atoms (ions) with filled shells.

We note that the static polarizability calculated in the more general nonlocal plasma approach [20, 21] is strongly overestimated.

The frequency dependences of the quantities $-\omega^2\mathrm{Re}\{\alpha(\omega)\}$ and $\omega^2\mathrm{Im}\{\alpha(\omega)\}$ for the FeVI ion, which were calculated in the Brandt–Lundqvist approximation in a wide frequency range, are presented in Fig. 1. Comparing with analogous dependences calculated in a quantum-mechanical description of the target for a multielectron atom [5] shows that the calculation in the Brandt–Lundqvist model describes qualitatively correctly the smoothed functions $-\omega^2\mathrm{Re}\{\alpha(\omega)\}$ and $\omega^2\mathrm{Im}\{\alpha(\omega)\}$ without taking account of the characteristic features due to the shell structure of the atom (maxima and minima near the ionization thresholds of the subshells). It follows (in accordance with the physical picture) from Fig. 1, specifically, that as the frequency ω increases, the function $-\omega^2\mathrm{Re}\{\alpha(\omega)\}$ (in atomic units) approaches the total number N of electrons in the ion, and the function $\omega^2\mathrm{Im}\{\alpha(\omega)\}$ decreases rapidly to zero in the high-frequency limit.

Thus, it can be expected from an analysis of the low- and high-frequency limits that the Brandt–Lundqvist model gives, to a first approximation, a reasonable approximation for the dynamical polarizability of an atom (ion).

To calculate the cross section of polarization bremsstrahlung, we introduce the polarization potential for the interaction with an ion in a uniform external electromagnetic field $E(\omega)$ with frequency ω:

$$V_{\mathrm{pol}}(\mathbf{R}, \omega) = \int d\mathbf{r}\frac{\delta\rho(\mathbf{r}, \omega)}{|\mathbf{r}-\mathbf{R}|}. \quad (5)$$

Here, $\delta\rho(\mathbf{r}, \omega)$ is the spatial density of the perturbation of the electron charge, induced in the ion core by the external field, and R is the radius vector of the incident particle. We note that the proposed approach is also suitable for calculating spontaneous processes: in this case $E(\omega)$ is the field due to quantum fluctuations. The perturbation $\delta\rho(\mathbf{r}, \omega)$ of the electron charge is due to the polarization $\mathbf{P}(\mathbf{r}, \omega)$ induced in the ion core:

$$\delta\rho(\mathbf{r}, \omega) = \mathrm{div}\mathbf{P}(\mathbf{r}, \omega). \quad (6)$$

In the local approximation, the quantity $\mathbf{P}(\mathbf{r}, \omega)$ is given by equation (2)

In what follows, we shall assume everywhere that the electron-density distribution in an atom (ion) is spherically symmetric.

Bringing together the formulas written out, expanding the reciprocal of the distance $|\mathbf{r} - \mathbf{R}|^{-1}$ in spherical

Table 1. Static polarizabilities of atoms and ions calculated using various models (the values are given in au)

Atom (ion)	ArI	KrI	XeI	KII	PbII	CsII	SrIII	BaIII
$\alpha_0^{\exp}$	11	17	27	7.5	12	16.3	6.6	11.4
α_0^{var}	19.3	26.8	30.9	9.1	14.3	17.8	8.7	11.4
α_0^{VSh}		21.1	25.5	6.6	11.9	15.3	7.5	9.7
α_0^{BL}	22	24	27	8.6	11.6	13.5	7	8.4

Note: α_0^{var} —calculation by a variational method [18]; α_0^{VSh} —calculation in the statistical model [19]; and $\alpha_0^{\mathrm{BL}} = R_0^3/3$ —calculation in the Brandt–Lundqvist model for a Thomas–Fermi–Dirac atom (ion).

harmonics, performing simple algebraic transformations, and integrating over the angular variables, we obtain for the polarization potential in the local approximation the expression

$$V_{\rm pol}(\mathbf{R}, \omega) = \frac{\mathbf{R}\mathbf{E}(\omega)}{R^3}\int_0^R \beta(r, \omega)4\pi r^2 dr. \qquad (7)$$

It is important that this formula describes the nondipole interaction potential of an incident particle interacting with a perturbed ion core. This is expressed in the presence of the modulus R of the radius vector of this particle in the upper limit of integration. This circumstance has a simple electrostatic interpretation: the external charge interacts only with the part of the electron cloud located inside a sphere of radius R, if the process proceeds without excitation of the bound electrons in the target.

Figures 2a and 2b display the computational results for the real and imaginary parts of the polarization potential, normalized to the amplitude of the external electric field, for a KII ion. The calculation was performed in the local plasma-frequency approximation using the electron density of the ion core in the Thomas–Fermi–Dirac model [18] for two frequencies of the electromagnetic field $\omega = 0.9$ (a) and 3 au (b) using equation (7). In both cases, the real part of the polarization potential has a maximum at a distance determined by equation (4). At this distance, the local permittivity of the target vanishes and at the same time an imaginary correction appears to the polarization potential (for shorter distances it is zero).

We note that similar forms of the potential were obtained in [20] for a nonuniform plasma particle in an electromagnetic field by solving a differential equation with appropriate boundary conditions.

Using the expression for the polarization potential, a formula can be derived for the dipole moment induced in the ion core by the scattered particle. Indeed, using

$$V_{\rm pol}(\mathbf{R}, \omega) = -\mathbf{E}(\omega)\mathbf{D}_{\rm pol}(\mathbf{R}, \omega), \qquad (8)$$

we find

$$\mathbf{D}_{\rm pol}(\mathbf{R}, \omega) = -\frac{\mathbf{R}}{R^3}\int_0^R \beta(r, \omega)4\pi r^2 dr. \qquad (9)$$

The dipole moment $\mathbf{D}_{\rm pol}(\mathbf{R}, \omega)$ induced in the atomic (ion) core is a function of the frequency of the external field and the radius vector of the incident particle:

$$\mathrm{Re}\{\mathbf{D}^{\rm BL}(\omega, R)\} = \frac{\mathbf{R}}{R^3}\mathrm{V.P.}\int_0^R \frac{\omega_p^2(r)r^2 dr}{\omega_p^2(r) - \omega^2}, \qquad (9a)$$

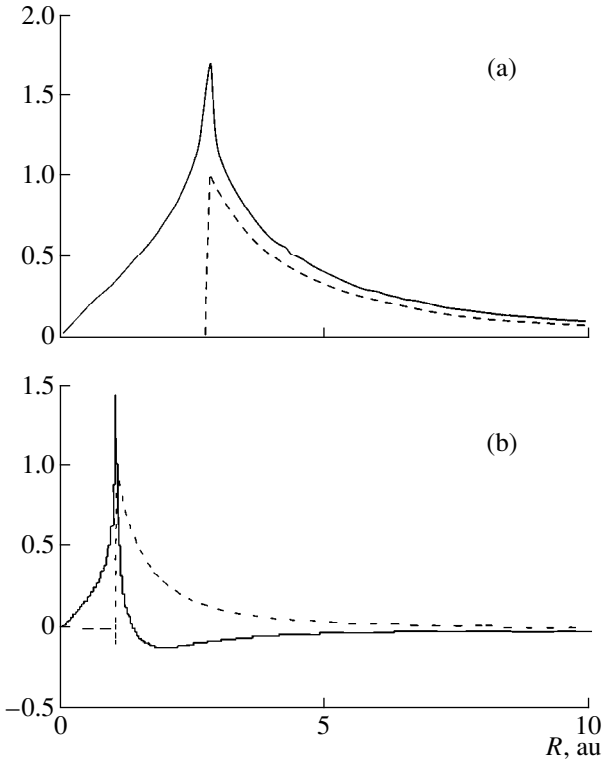

Fig. 2. Real (solid curves) and imaginary (dashed curves) parts of the polarization potential, normalized to the amplitude of the electromagnetic field, at the frequency $\omega = 0.9$ au (a) and 3 au (b) as a function of the distance from the nucleus of the KII ion. Calculation in the Brandt–Lundqvist approximation using the Thomas–Fermi–Dirac electron density.

$$\mathrm{Im}\{\mathbf{D}^{\rm BL}(\omega, R)\} = \frac{\mathbf{R}}{R^3}\frac{\pi}{2}\omega^2 \times \frac{r_p^2(\omega)}{|d\omega_p(r_p)/dr|}\theta(R - r_p(\omega)), \qquad (9b)$$

where θ is the Heaviside function. The total (including the static) radiating dipole moment of the system incident particle + atom (ion) is

$$\mathbf{D}_{\rm tot}(\mathbf{R}, \omega) = \mathbf{R} - \frac{\mathbf{R}}{R^3}\int_0^R \beta(r, \omega)4\pi r^2 dr. \qquad (10)$$

The formula (10) is the initial formula for performing calculations of polarization effects in the local approximation. It corresponds to taking account of two channels of the radiative collision process: static (first term in equation (10)) and polarization (second term). Since these terms appear in the expression for the total radiating dipole moment of the system target + incident particle, the expression (10), substituted into the standard formula for the cross section of the process or the corresponding intensity, will also describe interference effects associated with the interaction of the channels.

3. CLASSICAL THEORY OF THE POLARIZATION BREMSSTRAHLUNG OF AN ELECTRON ON A MULTIELECTRON ION

The Born parameter η, characterizing the motion of plasma electrons under the conditions of a thermodynamically equilibrium plasma, is greater than or of the order of unity:

$$\eta = \frac{Ze^2}{\hbar v} \geq 1 \tag{11}$$

(here ordinary units of measurement are used).

The inequality (11) is the inverse of the Born condition and corresponds (in the limit of a strong inequality) to the semiclassical approximation with respect to the motion of the incident particle. It is in the semiclassical approach [9, 11, 14] that V.I. Kogan *et al*. performed a detailed analysis of the static channel for bremsstrahlung, specifically, they developed the so-called rotational approximation, which makes it possible to calculate very simply the spectral cross sections for the main radiation processes, including recombination.

Comparing with the quantum-mechanical numerical calculation [10] demonstrated the high accuracy of the semiclassical approach and, specifically, the rotational approximation in the theory of static bremsstrahlung [12, 13]. For this reason, it is natural to use the semiclassical approach to investigate the polarization bremsstrahlung on a multielectron ion and to construct on the basis of this approach a generalization of the rotational approximation, including a description of the polarization channel.

As is well known [22], in the classical analysis of a radiative collision process, a quantity κ, called the effective emission,

$$\kappa = \int_0^\infty \Delta E(\rho) 2\pi\rho d\rho \tag{12}$$

is introduced. Here, $\Delta E(\rho)$ is the total emission from a single incident particle with a fixed impact parameter ρ. In what follows, we also be interested in the spectral effective emission $d\kappa(\omega)/d\omega$, the expression for which in the dipole approximation with respect to the interaction with the electromagnetic field in the emitted wave for a spontaneous process has the form

$$\frac{d\kappa(\omega)}{d\omega} = \frac{4\omega^4}{3c^3}\int_0^\infty |\mathbf{D}(\omega, \rho)|^2 \rho d\rho. \tag{13}$$

Here, $\mathbf{D}(\omega, \rho)$ is the Fourier transform of the radiating dipole moment of the system at frequency ω, calculated along the trajectory of the incident particle, characterized by the impact parameter ρ.

There is a simple relation between the quantity $d\kappa/d\omega$ and the spectral cross section for bremsstrahlung:

$$\frac{d\kappa}{d\omega} = \hbar\omega \frac{d\sigma}{d\omega}$$

(ordinary units are used).

To take account of the interference-polarization effects, in what follows we shall use for $\mathbf{D}(\omega, \rho)$ the time Fourier transform of the total dipole moment:

$$\mathbf{D}_{\text{tot}}(\omega, \rho) = \int_{-\infty}^{\infty} \mathbf{D}_{\text{tot}}(\mathbf{R}(t, \rho, v_i), \omega) e^{i\omega t} dt, \tag{14}$$

where the function $\mathbf{D}_{\text{tot}}(\mathbf{R}, \omega)$ is given by the expression (10). Thus, in the classical analysis, to calculate the spectral effective emission one must know the law of motion of the incident particle

$$\mathbf{R} = \mathbf{R}(t, \rho, v_i), \tag{15}$$

where v_i is the initial velocity of the particle.

To investigate strongly inelastic scattering processes it is convenient to express the temporal Fourier transform of the dipole moment of the incident particle (first term in equation (10)) in terms of the Fourier transform of the force exerted by the target on the particle. Then the following expression for the Fourier transform of the total radiating dipole moment of the system (equation (14)) can be obtained from equation (10):

$$\mathbf{D}_{\text{tot}}(\omega, \rho) = \frac{1}{\omega^2}\left\{\frac{\mathbf{R}}{R}\frac{dU(R)}{dR}\right\}_{\omega, \rho} - \left\{\frac{\mathbf{R}}{R^3}\int_0^R \beta(r, \omega) 4\pi r^2 dr\right\}_{\omega, \rho}. \tag{16}$$

Here, the braces denote a Fourier transform taking account of the dependence (15).

Thus, the expressions (12), (13), and (16) give a formal solution of the problem under study. It is impossible to simplify these formulas further, since the dependence (15) for the motion of the incident particle in a Thomas–Fermi potential (and its modifications) cannot be expressed in analytic form (in contrast to motion in a Coulomb field).

For numerical calculations, it is convenient to switch from the independent time variable t to an independent variable R, the distance from the incident particle to the nucleus. For this, we employ the standard representation of the trajectory time and turning angle of the radius vector of the incident particle in terms of R and the parameters ρ and v_i:

$$t(R, \rho, v_i) = \int_{r_{\min}(\rho, v_i)}^{R} \frac{dR}{v_r(R, \rho, v_i)}, \tag{17}$$

$$\varphi(R, \rho, v_i) = \rho v_i \int_{r_{\min}(\rho, v_i)}^{R} \frac{dR}{v_r(R, \rho, v_i) R^2}. \tag{18}$$

Here, $v_r(R, \rho, v_i)$ is the radial velocity

$$v_r(R, \rho, v_i) = \sqrt{v_i^2 + 2|U(R)| - v_i^2\rho^2/R^2}, \quad (19)$$

$r_{\min}(\rho, v_i)$ is the distance of closest approach of the incident particle to the center of the scattering potential and is determined by the solution of the equation

$$v_r(R, \rho, v_i) = 0. \quad (20)$$

Using equations (16)–(19), the Cartesian projections (on the focal coordinate axes) of the Fourier transform of the radiating dipole moment of the system can be calculated as

$$(\mathbf{D}_{\text{pol}})_x(\omega, \rho) = 2\int_{r_{\min}}^{\infty} \cos(\varphi(R, \rho))\cos(\omega t(R, \rho)) \times D_p(\omega, R)\frac{dR}{v_r(R, \rho)}, \quad (21)$$

where $D_p(\omega, R)$ is determined by the modulus of the vector (10). An expression for the component $(\mathbf{D}_{\text{pol}})_y$ can be obtained by replacing the cosines in equation (21) by sines.

As is well known, the statistical approximation describes well the properties of an atom in the region where most of the atomic electrons are localized. Near the nucleus and at the boundary of the ion, where single-electron effects become substantial, the accuracy of the statistical approximation decreases appreciably. Specifically, at the boundary of an ion the electron density and the local plasma frequency vanish completely in the statistical model. Here, single-electron excitations make a large contribution to the polarizability. They must be taken into account in a frequency range of the order of the ionization potential of the core, where the dimensions of the electron orbit become greater than the dimensions of the ion core in the statistical model. Actually, together with the collective plasma frequency of the oscillations of the electron density, characteristic oscillations of an electron in the field of the core appear here.[1] This effect can be approximately taken into account by shifting the frequency ω in the formula for the polarizability of the target by an amount $\Delta\omega$, so that the maximum of photoabsorption would occur on the single-electron ionization potential.

We present the computational results for the spectral effective emission for scattering of an electron by a KII ion for the following values of the parameters: $v_i = 1.4$ au and $\omega = 0.9$ au. The choice of these quantities is determined by the fact that under the conditions of a thermodynamically equilibrium plasma the emission of photons with energy close to the initial energy of the incident particle (the ionization potential of the KII ion is 1.16 au) by electrons with thermal energies (of the order of the ionization potential of an ion) is of greatest interest.

We use the polarizability density of the target in the Brandt–Lundqvist approximation (equation (1)), shifted in frequency by the amount $\Delta\omega = 0.6$ au in the direction of high frequencies, to calculate the dipole moment induced in the ion core. Then the frequency dependence of the dynamical polarizability of the ion core will correspond to its quantum-mechanical analog.

The electron density of the ion core, determining the local plasma frequency, was calculated on the basis of a numerical integration of the Thomas–Fermi–Dirac equation (with exchange and correlation corrections) using the reduced ion radius $x_0 = 8.91$ arb. units. We recall that the reduced ion radius is the ratio of the ion radius R_0 to the Thomas–Fermi radius $a_{\text{TF}} = 0.8852/Z^{1/3}$.

In this case the "local plasma radius" [see (4)] is $r_p(\omega) = 2.77$ au.

We now introduce the characteristic emission radius in the Kramers limit $r_{\text{eff}}(\omega, v_i)$ (see [9, 14]). This radius determines the revolution frequency of an electron in its orbit and is the solution of the equation

$$\frac{v_i^2}{2} + |U(r)| = \frac{\omega^2 r^2}{2}. \quad (22)$$

This quantity determines the effective emission distance with respect to the static channel. It is important that in the Kramers limit the quantity $r_{\text{eff}}(\omega, v_i)$ increases with the initial velocity.

We now consider the emission of a photon with energy 0.9 au in the case when an electron with near-threshold energy (1 au) is scattered by a KII ion. The dependences of the projections of the dipole moment induced in the ion core at the frequency of the emitted photon on the impact parameter ρ, which were obtained on the basis of the model considered, are presented in Table 2.

The calculation in a statistical Thomas–Fermi–Dirac potential shows that for impact parameters less than 1.4 au, the scattering angle is greater than 180°, which corresponds to onset of the revolution of the incident particle around the target.

On the other hand, the condition for the semiclassical picture breaks down for these impact parameters. Nonetheless, this is immaterial for calculating the polarization channel, since short distances from the nucleus make only a small contribution to it.

The computational results obtained with equations (13)–(21) for the values of the effective emission (in atomic units) for the polarization channel with subdivision into the contributions of x and y projections are presented in Table 3.

[1] We thank I. I. Sobel'man for calling our attention to this fact.

Table 2. Components of the induced dipole moment in a KII ion as a function of the impact parameter (values given in au)

ρ	1	1.5	2	2.5	3	4	5	6
r_{mix}	0.163	0.8	1.58	2.2	2.74	3.76	4.75	5.7
$\mathrm{Re}Dp_x$	−0.1	1.48	1.0	1.48	2.4	0.73	0.36	0.16
$\mathrm{Re}Dp_y$	−1.59	2.1	2.9	2.4	1.7	0.86	0.33	0.17
$\mathrm{Im}Dp_x$	−0.37	1.15	−0.03	−0.22	1.05	0.88	0.29	0.13
$\mathrm{Im}Dp_y$	−1	0.54	1.1	1.25	1.33	0.68	0.3	0.14

Table 3. Contribution of different projections of the dipole moment induced in the KII to the effective emission in the polarization channel (values presented in au)

Projections	*x* projection		*y* projection		Total
	Real	Imaginary	Real	Imaginary	
Polarization channel	5.3×10^{-6}	1.5×10^{-6}	5.4×10^{-6}	2.4×10^{-6}	1.46×10^{-5}

We now introduce the R factor characterizing the relative contribution of the polarization channel to bremsstrahlung as

$$R(\omega) = \frac{d\kappa_{pol}(\omega)}{d\kappa_{st}(\omega)}. \quad (23)$$

For obtaining a comparative assessment of the relative strength of the polarization channel, we shall use the computational result for the contribution of the static channel in the rotational approximation (see [9, 14]).

A calculation in the Thomas–Fermi–Dirac model for the effective spectral emission in the static channel gives

$$\left\{\frac{d\kappa_{st}^{rot}}{d\omega}\right\}_{TFD}(\mathrm{KII},\ \omega = 0.9\ \text{a.e.}) = 5.46\times10^{-6}\ \text{a.e.}$$

Hence, it follows that the R factor in the rotational approximation is

$$\{R\}_{clas,\,TFD}^{BL,\,rot}(\mathrm{KII},\ \omega = 0.9\ \text{a. u.}) = 2.67. \quad (24)$$

Thus, a classical estimate for the parameter values presented above gives the following lower limit for the R factor at a frequency close to the ionization potential of the KII ion for an incident particle with threshold energies (T is the energy of the incident particle):

$$R(\mathrm{KII},\ \omega \approx I_p \approx T) \geq 2, \quad (25)$$

and, therefore, the contribution of the polarization channel to the effective bremsstrahlung is much greater than that of the static channel.

4. DESCRIPTION OF POLARIZATION EFFECTS IN THE GENERALIZED ROTATIONAL APPROXIMATION

In the theory of static bremsstrahlung there exists a very effective method for calculating approximately the intensity of radiation from a semiclassical particle (the so-called rotational approximation [9, 14]) that was found to be more justified effectively than the systematic classical analysis. The physical substantiation of this approach lies in the spatial finiteness of the region responsible for the emission of quite high-frequency photons by the incident particle.

The high-frequency limit, corresponding to the so-called Kramers electrodynamics range, is understood in the sense of the inequality

$$\omega > \omega_{eff}^{Coul} = \frac{\omega Z_{eff}}{v_i^3}. \quad (26)$$

We note that quantitatively the rotational approximation also gives a reasonable result when $\omega \approx \omega_{eff}^{Coul}$.

For the bremsstrahlung cross section integrated over the impact parameter, the effective distance r_{eff} depends only on the frequency of the emitted radiation and the target potential and is determined by equation (22).

Formally, the rotational approximation corresponds to substituting into the equation for the total effective static bremsstrahlung a delta function of the difference of the frequencies ω and the rotational frequency of the incident particle at the distance r_{eff}:

$$\omega_{rot}(r) = \frac{\sqrt{v_i^2 + 2|U(r)|}}{r}. \quad (27)$$

Thus, we arrive at the following formula for the effective spectral emission in the rotational approximation [9]:

$$\left\{\frac{d\kappa_{st}(\omega)}{d\omega}\right\}_{rot} = \frac{8\pi}{3c^3 v_i}\int_0^\infty \left(\frac{dU(r)}{dr}\right)^2 \times \sqrt{1-\frac{U(r)}{v_i^2/2}}\,\delta(\omega-\omega_{rot}(r))r^2 dr. \quad (28)$$

Information about the vector character of the radiating dipole moment of the incident particle is lost in equation (28). This is because in the high-frequency approximation (26) the x component of the dipole moment of the incident particle makes the main contribution to the cross section of the process. The situation is different for the polarization channel: for the parameters presented in Table 3, the contributions of both projections are approximately the same. For this reason, to generalize the rotational approximation so as to take account of the polarization channel, the features of spatial formation of both Cartesian projections of the dipole moment of the ion core on the axis of the focal system of coordinates must be taken into consideration.

Analysis shows that the Fourier component of the y projection of the radiating dipole moment of the target core is determined by distances of the order of $r_p(\omega)$, while the x component is determined by the distances of closest approach r_{min} of the incident particle to the target.

For this reason, it is natural to make the following generalization of the rotational approximation for the polarization channel:

$$\left\{\frac{d\kappa_{pol}(\omega)}{d\omega}\right\}_{rot} = \left\{\frac{d\kappa_{pol}(\omega)}{d\omega}\right\}_x^{rot} + \left\{\frac{d\kappa_{pol}(\omega)}{d\omega}\right\}_y^{rot}, \quad (29)$$

where

$$\left\{\frac{d\kappa_{pol}(\omega)}{d\omega}\right\}_x^{rot} = \frac{8\pi}{3c^3 v_i^2}\left[\frac{\left|f_x^{pol}(\omega, R)\right|^2 v_r(R, \rho=0)}{\left|d\omega_{rot}/dR\right|}\right]_{R=r_{eff}(\omega)}, \quad (29a)$$

and

$$\left\{\frac{d\kappa_{pol}(\omega)}{d\omega}\right\}_x^{rot} = \frac{8\pi}{3c^3 v_i^2}\left[\frac{\left|f_y^{pol}(\omega, R)\right|^2 v_r(R, \rho=0)}{\left|d\omega_{rot}/dR\right|}\right]_{R=r_p(\omega)}. \quad (29b)$$

The projection of the frequency-dependent polarization force is given by

$$f_{x,y}^{pol} = \frac{\omega^2 R_{x,y}}{R^3}\int_0^R \beta(r, \omega)4\pi r^2 dr. \quad (30)$$

We note that equation (30) can be rewritten as

$$f_{x,y}^{pol} = \frac{R_{x,y}}{R^3}N_{eff}(R, \omega). \quad (30a)$$

Here,

$$N_{eff}(R, \omega) = \omega^2\int_0^R \beta(r, \omega)4\pi r^2 dr \quad (31)$$

is the effective electron charge that depends on the frequency and distance from the nucleus and determines the bremsstrahlung cross section in the polarization channel.

The formulas (29)–(31) correspond to a simple physical interpretation of the polarization bremsstrahlung in the spirit of classical electrodynamics as radiation arising as a result of the acceleration of the effective electron charge of the target under the action of the force exerted by the incident scattered particle.

In accordance with the decomposition of the effective spectral emission in the polarization channel into a sum of contributions from two projections of the induced dipole moment of the target, the spectral R factor can be written in the generalized rotational approximation as

$$R^{rot}(\omega) = \frac{1}{2}(R_x^{rot}(\omega) + R_y^{rot}(\omega)). \quad (32)$$

The numerical factor 1/2 in equation (32) arose as a result of the approximate replacement of the squared sine and cosine of the rotation angle of the incident particle by their average value.

Figure 3a shows the frequency dependences of three types of R factors appearing in equation (32) for a KII ion and the threshold energies of the incident particle. It is important that the values of the R factors become equal to one another far from the ionization threshold of the target. Near threshold (for the incident particle energies considered) the contribution of the y component prevails.

Analysis on the basis of the approximation considered shows that as the incident particle energy increases, the relative contribution of the x component increases and reaches its maximum value at the energy ($T = v_i^2/2$) determined by the equality

$$r_{eff}(T, \omega) = r_p(\omega). \quad (33)$$

The physical meaning of equation (33) is clear: the generalized rotational approximation predicts the optimal value of the initial energy of the incident particle for

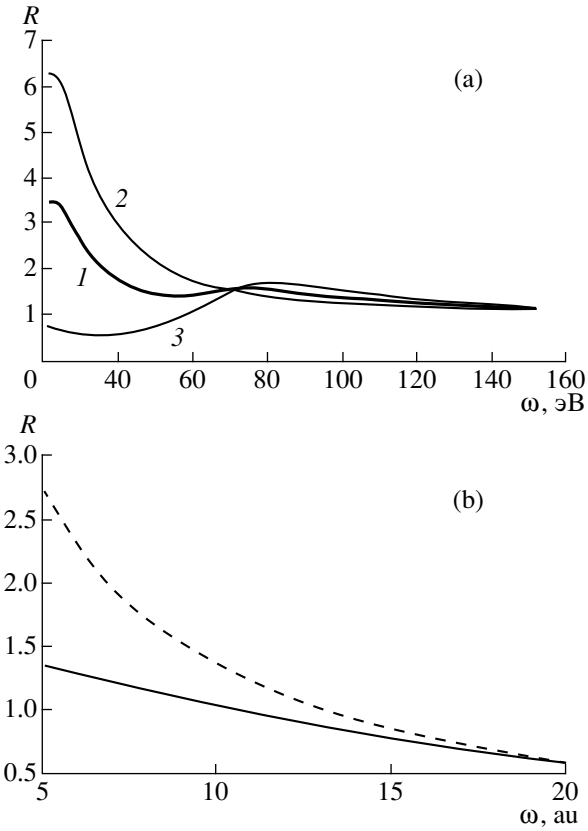

Fig. 3. (a) Frequency dependence of the *R* factor in various variants of the generalized rotational approximation, where the following are distinguished in the PB cross section: (*1*) the effective radius of the static channel, (*2*) the "plasma" radius, and (*3*) their half-sum. (b) Comparison of the *R* factor calculated in the generalized rotational approximation (solid curve) with the high-frequency *R* factor (dashed curve) for threshold energies of a particle incident on a KII ion.

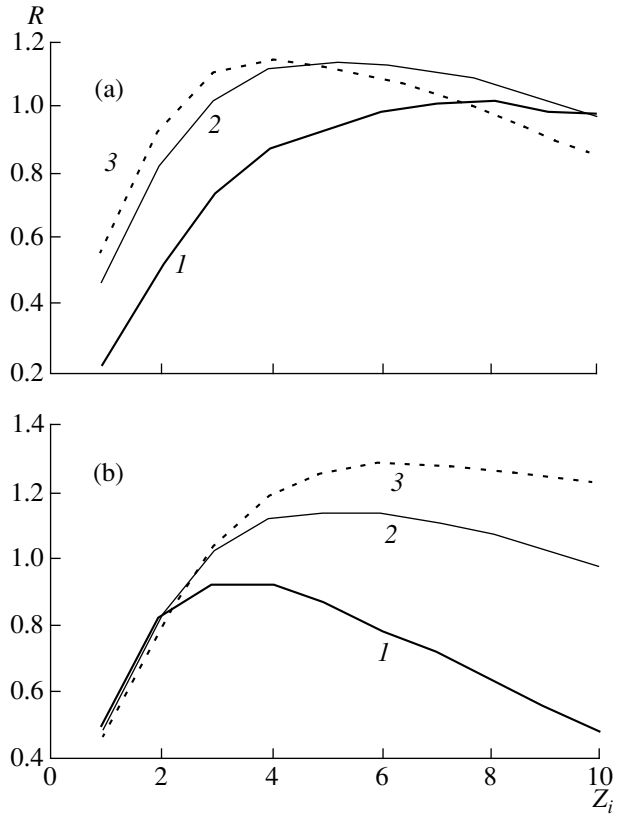

Fig. 4. Generalized-rotational-approximation calculations of the *R* factor as a function of the ion charge at a fixed frequency, which is a multiple of the ionization frequency of the target in the Thomas–Fermi model $\omega = kI_p^{\mathrm{TF}}$: (a) as a function of the ion charge at various frequencies: k = (*1*) 1, (*2*) 2, (*3*) 3; and (b) as a function of the ion charge (k = 2) for various nuclear charges: Z = (*1*) 30, (*2*) 60, (*3*) 90.

which the effective emission radius in the static channel equals the "plasma" radius, corresponding to the maximum of the spatial polarizability density of the target at the given frequency ω.

For $\hbar\omega$ = 24.5 eV the energy of the incident particle, satisfying equation (33), is T_{opt} = 75 eV for scattering by a KII ion.

This model permits answering an important question: at what frequencies does the high-frequency approximation for the polarization channel of bremsstrahlung first "work"? The computational results obtained in the generalized rotational approximation with the high-frequency spectral *R* factor are compared in Fig. 3b. It is evident from this figure that the high-frequency approximation for the scattering of an incident particle with threshold energy by a KII ion is valid for $\omega > \omega^{\mathrm{hf}}$ = 20 au. As the energy of the incident particle increases, the quantity ω^{hf} increases.

The following important consequences of calculations on the basis of the generalized rotational approximation follow from Fig. 3. The contributions of the polarization and static channels to the spectral bremsstrahlung cross section on a KII ion for electrons with threshold energies become equal to one another (R = 1) at frequency ω* = 10 au. The *R* factor reaches its maximum value for frequencies of the order of the ionization potential of the target. The generalized rotational approximation gives the following value for the *R* factor: $R_{\max}^{\mathrm{rot}} \approx 3$. We note that this value is a lower estimate, since the Brandt–Lundqvist model underestimates the polarizability. On the other hand, a quantum calculation gives a somewhat lower value of $R_{\max}$ and a much lower value of the frequency ω*.

Figure 4 displays the dependences of the spectral *R* factor on the ion charge for different bremsstrahlung frequencies (a) and nuclear charges (b), calculated for incident particles with threshold energies. This figure demonstrates the presence (on the basis of the generalized rotational approximation used here) of an optimal ion charge Z_i^{opt}, for which the *R* factor (at the frequency characteristic for this ion) has its maximum

value. It follows from Fig. 4a that the optimal charge Z_i^{opt} increases as the radiation frequency decreases, and the maximum value of the R factor decreases somewhat. As the nuclear charge of the ion increases (Fig. 4b), the quantity Z_i^{opt} shifts into the range of high values, and the R factor increases appreciably. At the same time, for low nuclear charges the R factors calculated at the corresponding (different!) characteristic frequencies do not depend on the nuclear charge.

5. QUANTUM CALCULATION OF BREMSSTRAHLUNG BY A MULTIELECTRON ATOM (ION)

We shall calculate the effective radiation in the presence of strongly inelastic scattering of an incident particle by a multielectron atom taking account of the polarization channel for the quantum motion of the incident electron.

We note that a quantum calculation of the bremsstrahlung in the static channel for a Thomas–Fermi ion was first performed in [12]. The results agreed well with the systematic quantum-mechanical calculations performed for a Hartree–Fock core of the target and, moreover, confirmed that the accuracy of the semiclassical rotational approximation is high.

The spherical symmetry of the scattering potential substantially simplifies the quantum calculation. In this case, the standard method [23] of expanding the wave function of the incident particle in spherical harmonics or in the orbital angular momentum l can be used. The wave-function component corresponding to a fixed value of l is a product of the radial and angular parts. The angular part, as is well known, is a spherical function, and the radial part $u(r, l, p)$ satisfies the Schrödinger equation with the following boundary condition at infinity:

$$u(r \longrightarrow \infty, l, p) \longrightarrow \frac{2}{r} \times \sin\left(pr + \frac{Z_i}{p}\ln(2pr) - \frac{\pi}{2}l + \delta(l, p)\right). \tag{34}$$

Here, p is the momentum of the incident particle, $\delta(l, p) = \delta^{\text{Coul}}(l, p) + \Delta\delta(l, p)$ is the total phase shift, equal to the sum of the Coulomb phase shift $\delta^{\text{Coul}}(l, p)$ and the non-Coulomb phase shift $\Delta\delta(l, p)$, which can be calculated according to the formula [24]

$$\sin(\Delta\delta(l, p)) = \frac{1}{2p}\int_0^\infty\left(\frac{Z_i}{r} - |U(r)|r\right) \times u(r, l, p)u^{\text{Coul}}(r, l, p)r^2 dr. \tag{35}$$

Here, $u^{\text{Coul}}(r, l, p)$ is the solution of the radial Schrödinger equation with the Coulomb potential of the ion.

For numerical calculations it is convenient to switch to an auxiliary radial wave function $\nu(r, l, p) = r^{-1}u(r, l, p)$ satisfying the Schrödinger equation

$$\nu'' + 2\frac{l+1}{r}\nu' + (p^2 - 2U(r))\nu = 0 \tag{36}$$

(the prime signifies differentiation with respect to the radius) with the boundary conditions

$$\nu(0) = 1 \quad \nu'(0) = -\frac{Z}{l+1}. \tag{36a}$$

Here, Z is the nuclear charge of the ion. To satisfy the asymptotic behavior (34), we introduce the normalization factor N according to the formula

$$N = \left\{r^{l+1}\sqrt{\nu^2 + [p^{-1}\nu']^2}\right\}_{r\to\infty}. \tag{37}$$

Finally, we have for the wave function

$$u(r, i, p) = \left(\frac{2}{N}\right)r^{l+1}\nu(r, l, p). \tag{38}$$

Using the functions (38), we obtain the following expression for the spectral intensity of bremsstrahlung:

$$\frac{dW}{d\omega} = \frac{2}{3c^3 p_i^3 p_f}\sum_{l=0}^{\infty}(l+1)[|M_{l,l+1}|^2 + |M_{l+1,l}|^2]. \tag{39}$$

Here, we have introduced the radial matrix elements $M_{l,l+1}$ and $M_{l+1,l}$ between the wave functions (38) of the modulus of the force acting on the incident particle and giving rise to bremsstrahlung in a definite channel.

For the static channel, the expression for the corresponding force is given by the derivative of the potential. This is the usual force determining the motion of the incident particle in the static field of the target ion. The modulus of the force leading to emission in the polarization channel can be obtained from equation (30). It is determined by the nondipole dynamical polarizability of the ion core and is given by

$$f^{\text{pol}} = -\frac{\omega^2}{R^2}\int_0^R \beta(r, \omega)4\pi r^2 dr. \tag{40}$$

Since the expression for the spatial density of the polarizability has, generally speaking, an imaginary part, the polarization force (40) and the corresponding radial matrix element $M_{l,l'}$ contains, together with a real component, an imaginary component. The radial matrix element of the static force is, naturally, purely real.

The total matrix element appearing in equation (39) is a sum of the static and polarization terms. Their real parts give the interference term in the expression for the bremsstrahlung intensity, while the imaginary part of the polarization matrix element does not contribute to the interference of the channels.

Table 4. Frequency dependences of the bremsstrahlung intensity in the static and polarization channels for a KII ion, calculated in the generalized rotational approximation and for quantum motion of the incident electron (values given in au)

ω	0.6	0.9	2	3	4	5.4	9	18	36
W_{st}	6.4(−6)	7.5(−6)	3.6(−6)	6.9(−6)	1(−5)	1.3(−5)	1.6(−5)	1.4(−5)	1(−5)
W_{st}^{rot}	3.6(−6)	5.5(−6)	8.6(−6)	9.4(−6)	9.7(−6)	9.6(−6)	9(−6)	7.4(−6)	5.4(−6)
W_p	3.7(−6)	1.1(−5)	7.9(−6)	6.5(−6)	5.8(−6)	4.4(−6)	2.6(−6)	1.6(−6)	8.2(−7)
W_p^{rot}	8.6(−6)	1.4(−5)	1.2(−5)	1(−5)	1.1(−5)	1(−5)	1(−5)	2.9(−6)	9.3(−7)

Formally, the infinite series in terms of the orbital angular momentum l in the expression for the bremsstrahlung intensity (39) converges rapidly for strongly inelastic processes, in which we are interested here. For example, for $\omega/T \approx 0.7$–0.9 (scattering of an incident particle by a KII ion) the first three or four terms of this series make the main contribution to the bremsstrahlung intensity. We note that the situation is directly opposite for weakly inelastic processes, where the series in l converges very slowly.

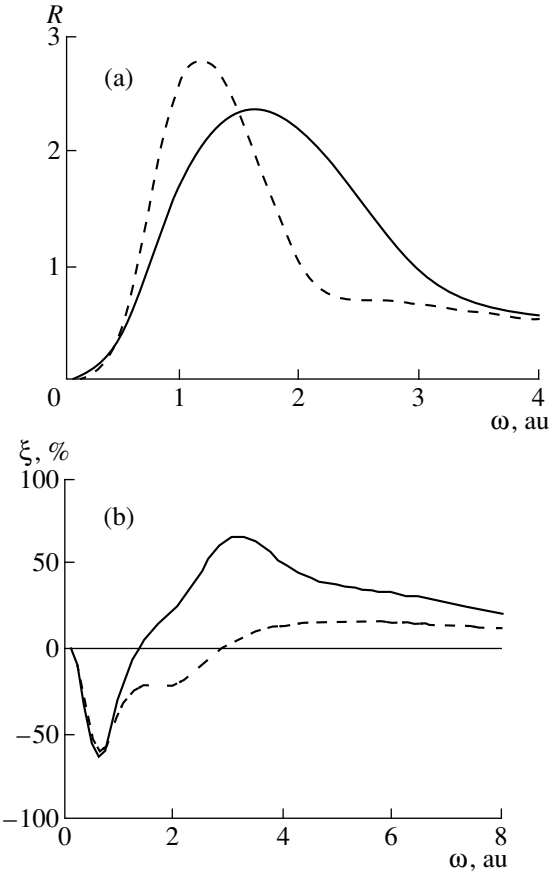

Fig. 5. Results of a quantum (with respect to the motion of the incident particle) calculation of (a) the spectral R factor and (b) contribution of interference to the intensity of bremsstrahlung for two values of the inelasticity parameter $\omega/T = 0.9$ (solid curve) and 0.6 (dashed curve) for scattering of an incident particle by a KII ion.

The computational results for the spectral intensity of bremsstrahlung obtained using equation (39) taking account of the contribution of the polarization channel with strongly inelastic scattering of the incident particle ($\omega/T = 0.9$) by a KII ion are presented in Table 4. For comparison, similar quantities calculated in the generalized rotational approximation are also given in the table. All values are given in atomic units. The exponent of the factor of 10 by which the number in front of the parentheses is multiplied is given in parentheses.

It follows from Table 4, specifically, that the best agreement between the quantum calculation and the generalized rotational approximation obtains for low frequencies near the ionization potential of the target ion. The worst agreement obtains for frequencies of the order of 9 au, where the spectral intensity of bremsstrahlung in the static channel, calculated in the quantum approach, reaches its maximum value. The calculation shows that for this frequency the imaginary part of the dipole moment induced in the core and the orbital angular momentum $l = 2$ make the main contribution to the radiation in the polarization channel. The maximum contribution of the polarization channel occurs at a frequency near the ionization potential of the target.

Analysis of the computational data shows that at low and high frequencies the real part of the dipole moment induced in the target core makes the main contribution to bremsstrahlung in the polarization channel. At "moderate" frequencies ($I_p < \omega \leq Z$), however, the imaginary part of the dipole moment of the core prevails in the polarization channel. This result also follows from calculations of PB in the random-phase approximation with exchange for the polarizability of the core [5].

The results of a quantum calculation of, respectively, the spectral R factor and the relative contribution of the interference term to the bremsstrahlung intensity for scattering of an incident particle by a KII ion are presented in Figs. 5a and 5b for two values of the ratio ω/T. It is evident that the spectral R factor has a maximum near the ionization potential of the target. The width of this maximum decreases as the degree of inelasticity of the process (the ratio ω/T) decreases, while the value of the R factor at the maximum

increases somewhat. The main difference from the results of the generalized rotational approximation is that the spectral R factor calculated for the quantum motion of the incident particle decreases more rapidly with increasing frequency in the "middle" frequency range $I_p < \omega \leq Z$.

Figure 5b demonstrates the magnitude and character of the interchannel interference as a function of the bremsstrahlung frequency. In the frequency range $\omega \leq I_p$, interference is destructive (it decreases the total intensity of the process) and substantial in magnitude. In the range $I_p < \omega \leq Z$, the interference term changes sign and increases the total intensity (constructive interference), remaining very large. The interchannel interference is negligibly small for low frequencies. At high frequencies its contribution is 10–20% and decreases as the frequency increases.

As the degree of inelasticity of the bremsstrahlung decreases, the role of interference decreases, since the overlapping of the spatial regions where the static and polarization channels are formed is smaller. This is evident from Fig. 5b, whence it also follows that for a less inelastic process, the frequency range of destructive interference is somewhat extended in the direction of high frequencies. For $\omega \leq I_p$ the character and magnitude of the interchannel interference are essentially independent of the degree of inelasticity of the process.

The main conclusion of the quantum analysis reduces to the fact that the contribution of the polarization channel to the intensity of strongly inelastic bremsstrahlung, increasing from zero at low frequencies in a power-law fashion [6], is greatest near the ionization frequency of the target ion and decreases rapidly with increasing frequency as a result of penetration of the incident particle into the target core. The width of the frequency maximum of the R factor increases with increasing inelasticity of the process.

6. CONCLUSIONS

In the present paper, a universal approach was developed for describing the polarization effects in bremsstrahlung of thermal-energy electrons on a multielectron ion in a wide spectral range using the local-density approximation for electrons for the polarizability of the target. The contribution of the polarization channel to the spectral cross section of bremsstrahlung was analyzed for semiclassical and quantum motions of the incident particle, taking account of the penetration of the particle into the target core and various degrees of inelasticity of the process. A generalized rotational approximation, making it possible to estimate easily the PB cross section on the basis of a statistical model of the target ion in the unified manner for all nuclear charges and degrees of ionization, was constructed.

It was determined that the contribution of the polarization channel to the bremsstrahlung cross section of thermal-energy electrons is maximum near the ionization frequency of the target ion. The value of the R factor (the ratio of the contribution of the channels) is approximately two. After reaching its extremal value, the spectral R factor, which increases in a power-law fashion at low frequencies, decreases rapidly as a result of the penetration of the incident particle into the target core. The width of the corresponding maximum increases with the inelasticity of the process. For characteristic frequencies of the order of the ion charge (in atomic units) the R factor is 10–15%.

Interchannel interference in the spectral dependence of the intensity of the bremsstrahlung is greatest near the ionization potential of the target, comprising at the extrema more than 60% of the total intensity of the process. For frequencies below the ionization threshold, interference is destructive, and for higher frequencies it is constructive. The role of interchannel interference decreases with decreasing inelasticity of scattering of the incident particle, since in this case the spatial regions where the bremsstrahlung channels formed are more strongly separated.

It was shown on the basis of the generalized rotational approximation developed in this paper that there exists an optimal ion charge (Z_i^{opt}) for which the magnitude of the spectral R factor at a frequency which is a multiple of the characteristic ionization frequency of a Thomas–Fermi ion is maximum. This value decreases with increasing bremsstrahlung frequency and increases with increasing ion charge.

In summary, it can be concluded that polarization and interference effects are important in bremsstrahlung by multielectron ions for characteristic plasma values of the parameters.

ACKNOWLEDGMENTS

We thank V.M. Buĭmistrov, V.I. Gervids, V.I. Kogan, A.B. Kukushkin, and I.I. Sobel'man for helpful and stimulating discussions.

This work was supported by the Russian Foundation for Basic Research (project no. 98-02-16763) and grant (no. 856-98) by the Moscow Science and Technology Center.

REFERENCES

1. *Polarized Bremsstrahlung from Particles and Atoms*, Ed. by V. N. Tsytovich and I. M. Oĭringel' (Nauka, Moscow, 1987).
2. A. Dubois and A. Maquet, Phys. Rev. A **40**, 4288 (1989).
3. V. A. Astapenko and A. B. Kukushkin, Zh. Éksp. Teor. Fiz. **111**, 419 (1997) [JETP **84**, 229 (1997)].
4. V. Korol and A. V. Solov'yov, J. Phys. B **30**, 1105 (1997).
5. A. V. Korol', A. G. Lyalin, O. I. Obolenskiĭ, *et al.*, Zh. Éksp. Teor. Fiz. **114**, 458 (1998) [JETP **87**, 251 (1998)].
6. L. Bureyeva and V. Lisitsa, J. Phys. B **31**, 1477 (1998).
7. V. A. Astapenko, Zh. Éksp. Teor. Fiz. **115**, 1619 (1999) [JETP **88**, 889 (1999)].

8. N. F. Mott and H. S. W. Massey, *The Theory of Atomic Collisions* (Clarendon Press, Oxford, 1987; Mir, Moscow, 1969).
9. V. I. Kogan, A. B. Kukushkin, and V. S. Lisitsa, Phys. Rep. **213**, 1 (1992).
10. R. H. Pratt and H. K. Tseng, Phys. Rev. A **11**, 1797 (1975).
11. V. I. Gervids and V. I. Kogan, Pis'ma Zh. Éksp. Teor. Fiz. **22**, 308 (1975) [JETP Lett. **22**, 142 (1975)].
12. V. P. Zhdanov and M. I. Chibisov, Zh. Tekh. Fiz. **47**, 1804 (1977) [Sov. Phys. Tech. Phys. **22**, 1045 (1977)].
13. V. P. Zhdanov, Fiz. Plazmy **4**, 128 (1978) [Sov. J. Plasma Phys. **4**, 71 (1978)].
14. V. I. Kogan and A. B. Kukushkin, Zh. Éksp. Teor. Fiz. **87**, 1164 (1984) [Sov. Phys. JETP **60**, 665 (1984)].
15. L. P. Rapoport, B. A. Zon, and N. L. Manakov, *The Theory of Multiphoton Processes in Atoms* (Atomizdat, Moscow, 1978).
16. M. Ya. Amus'ya, *The Photoelectric Effect in Atoms* (Nauka, Moscow, 1987).
17. W. Brandt and S. Lundqvist, Phys. Rev. **139**, A612 (1965).
18. P. Gambas, *The Statistical Theory of Atoms and Its Applications* (Die Statistische Theorie des Atoms und Ihre Anwendungen) (Springer-Verlag, Vienna, 1949; Inostrannaya Literatura, Moscow, 1951).
19. A. V. Vinogradov and V. P. Shevel'ko, Tr. Fiz. Inst. Akad. Nauk SSSR **119**, 158 (1980).
20. A. V. Vinodradov and O. I. Tolstikhin, Zh. Éksp. Teor. Fiz. **99**, 1204 (1989) [Sov. Phys. JETP **69**, 683 (1989)].
21. A. V. Vinogradov and O. I. Tolstikhin, Zh. Éksp. Teor. Fiz. **96**, 61 (1989) [Sov. Phys. JETP **69**, 32 (1989)].
22. L. D. Landau and E. M. Lifshitz, *The Classical Theory of Fields* (Nauka, Moscow 1967; Pergamon, New York, 1975, 4th ed.).
23. L. D. Landau and E. M. Lifshitz, *Quantum Mechanics: The Non-Relativistic Theory* (Nauka, Moscow, 1989; Pergamon, New York, 1977, 3rd ed.).
24. A. Messiah, *Quantum Mechanics* (Interscience, New York, 1961; Nauka, Moscow, 1978), Vol. 1.

Translation was provided by AIP

Journal of Experimental and Theoretical Physics, Vol. 90, No. 3, 2000, pp. 447–451.
Translated from Zhurnal Éksperimental'noĭ i Teoreticheskoĭ Fiziki, Vol. 117, No. 3, 2000, pp. 511–516.

ATOMS, SPECTRA, RADIATION

The Structure of Ponderomotive Forces Acting on an Electron in Relativistic Laser Fields

V. D. Taranukhin

Moscow State University, Vorob'evy gory, Moscow, 119899 Russia
e-mail: tvd@ssf.phys.msu.su

Received October 6, 1999

Abstract—An expression for the pondermotive force acting on a classical electron in a weakly nonuniform field of arbitrary intensity is derived by the method of averaging over the characteristic time of the guiding center of the electron. It is shown that in superstrong (relativistic) fields this force acquires a rotational character and depends on the polarization of the field. Fundamentally new types of systems for accelerating or confining charged particles can be developed on the basis of this effect. *© 2000 MAIK "Nauka/Interperiodica".*

1. INTRODUCTION

The problem of the interaction of free (quasifree) electrons with high-intensity laser field has become of great importance in recent years in connection with the development of laser sources with peak intensity $I \sim 10^{18}$–10^{21} W/cm^2. An electron in fields with such intensity acquires velocities comparable to the velocity of light, and relativistic effects become fundamentally important. It is also important that such fields are attained when generating ultrashort laser pulses and in hard focusing of radiation, where besides the oscillator component of the motion, drift of an electron as a result of the temporal and spatial nonuniformities of the field becomes very important. This drift is described by means of ponderomotive forces $\mathbf{F}_L$. In the present paper new features of these forces in superstrong laser fields acting on 1) free electrons (in the general case, on any charged particles) entering the laser beam from outside the beam and 2) photoelectrons which appear inside a laser beam during "multiphoton" ionization of atoms are discussed.

In relatively weak fields the average (over rapid oscillations) motion of an electron (ponderomotive drift) is described by the Gaponov–Miller force [1], which is a gradient force,

$$\mathbf{F}_L = -\nabla U_p, \tag{1}$$

where

$$U_p = \frac{e^2 E_{00}^2}{4m\omega^2}$$

is the ponderomotive potential of the field and is a scalar function which completely determines the vector $\mathbf{F}_L$ (E_{00} and ω are the amplitude and frequency of the field and e and m are the electron charge and mass). Relativistic effects in the calculation of ponderomotive forces have been taken into account in a number of works. The case of an electron entering with high (relativistic) velocity into a field was investigated in [2]. However, the field itself was assumed to be quite weak. In [3] averaging of the relativistic equations of motion over the phase

$$\eta = \omega t - \mathbf{kr}$$

(t is the time, $\mathbf{r}$ are the coordinates of the electron, and $\mathbf{k}$ is the wave vector of the radiation) was performed to calculate the ponderomotive forces in strong fields. In [4] the Lagrangian was averaged over the same parameter.

In the present work the force $\mathbf{F}_L$ was found (following the Gaponov–Miller procedure [1]) by averaging the equations of motion over the time t in the laboratory coordinate system (L system) or over the time t' in a comoving coordinate system (C system), where the electron is at rest on the average. This is the most systematic averaging procedure, making it possible to find for the first time new properties of ponderomotive forces in superstrong fields. The calculation is performed for a quite weak spatial (temporal) nonuniformity of the laser radiation without any restrictions on its intensity. It is shown that the ponderomotive force acting on an electron in the C system is not, in general, a gradient force (although, once again, it can be described by a single scalar function, the electron effective mass in the field). It is also found that this force depends on the polarization of the laser field; this is important for producing new systems for accelerating or confining charged particles in superstrong fields.

2. COMPUTATIONAL PROCEDURE

We shall assume the spatial (temporal) nonuniformity of the field to be weak, so that the following relations hold:

$$\Delta r_f \gg \lambda, \quad \Delta t_f \gg \omega^{-1}, \tag{2}$$

where λ is the wavelength, and Δr_f and Δt_f are the characteristic spatial and temporal scales of variation of the intensity of the laser radiation. Since the electron displacement δr_e over one optical cycle in any fields and for any initial velocities is less than λ, the conditions (2) make it possible to assume that the changes in the amplitude of the field (at distances $\sim\delta r_e$ or in time $\sim\omega^{-1}$) to be small compared with the changes in its phase. Using the conditions (2), we shall represent the electric component of the field in the form

$$\mathbf{E}(\mathbf{r}, t) = \mathbf{E}_0(\mathbf{r}, t)\cos[\eta + \varphi(\mathbf{r}, t)] \approx \mathbf{E}^0 + \Delta\mathbf{E}, \quad (3)$$

where $\mathbf{E}^0 = \mathbf{E}_{00}\cos\eta$ describes a plane wave and, in general, $\Delta\mathbf{E}$ takes account of the difference of the real field from $\mathbf{E}^0$ with respect to amplitude, phase, and polarization:

$$\Delta\mathbf{E} = \delta\mathbf{E}_a + \delta\mathbf{E}_\varphi + \delta\mathbf{E}_e.$$

In paraxial beams with radius r_0 the change in the polarization of the field (over distances $\sim r_0$) is

$$\left|\frac{\delta\mathbf{E}_e}{\mathbf{E}_{00}}\right|_{\max} \sim \frac{\lambda}{r_0} \ll 1$$

(see [5]). Here

$$\left|\frac{\delta\mathbf{E}_e}{\mathbf{E}_{00}}\right| \sim \left(\frac{\lambda}{r_0}\right)^2$$

for electron displacements $\delta r_e \leq \lambda$, and we shall neglect the contribution of a polarization change to $\Delta\mathbf{E}$. The magnetic field can be calculated exactly from $\mathbf{E}(\mathbf{r}, t)$ using Maxwell equations:

$$\mathbf{B} = \mathbf{B}^0 + \Delta\mathbf{B},$$

where $\mathbf{B}^0$ corresponds to a plane wave.

In accordance with the assumption made above, we shall assume that in the zeroth approximation the field is a plane wave (in any coordinate system). Then the total momentum of the electron is

$$\mathbf{p} = \mathbf{p}^0 + \Delta\mathbf{p}$$

and the following equations hold (bremsstrahlung is neglected):

$$\frac{d\mathbf{p}^0}{dt} = e\mathbf{E}^0 + e[\mathbf{v}^0 \times \mathbf{B}^0], \quad (4)$$

$$\frac{d\Delta\mathbf{p}}{dt} = e\Delta\mathbf{E} + e[\mathbf{v}^0 \times \Delta\mathbf{B}] + e[\Delta\mathbf{v} \times \mathbf{B}^0], \quad (5)$$

where $\mathbf{v} = \mathbf{v}^0 + \Delta\mathbf{v}$ is the electron velocity, $\mathbf{v}^0$ is the electron velocity in a plane wave (a system of units where the velocity of light $c = 1$ is used and the Coulomb gauge is used for the potential $\mathrm{div}\mathbf{A} = 0$). Averaging equation (5) over time in the C system (symbolically denoted by the operator $\hat{T}$) yields the expression

$$\hat{T}[d\Delta\mathbf{p}/dt] \longrightarrow \mathbf{F}_C \quad (6)$$

for the ponderomotive force. The force $\mathbf{F}_C$ can be expressed in terms of the parameters of the field in the L system, and the relation

$$\mathbf{F}_L = \frac{\mathbf{F}_C + [(\gamma - 1)/V_0^2](\mathbf{F}_C \cdot \mathbf{V}_0) \cdot \mathbf{V}_0}{\gamma}, \quad \gamma = (1 - V_0^2)^{-1/2} \quad (7)$$

establishes a relation between the ponderomotive force $\mathbf{F}_C$ in the C system (moving with velocity $\mathbf{V}_0$ relative to the L system) and the ponderomotive force $\mathbf{F}_L$ in the L system. It is assumed that the electron drift velocity $\mathbf{V}_0$ is known from the initial conditions and the solutions of the equations of motion of the guiding center of an electron (in the L system) at the preceding stage

$$\gamma m\frac{d\mathbf{V}_0}{dt} = \mathbf{F}_L - (\mathbf{V}_0\mathbf{F}_L)\mathbf{V}_0. \quad (8)$$

If the drift velocity is nonrelativistic, then $\mathbf{F}_L \approx \mathbf{F}_C$.

3. PONDEROMOTIVE FORCES IN A PLANE-WAVE PULSE

We shall examine first the action of ponderomotive forces on the leading and trailing edges of a plane-wave pulse. In this case, there exists a strict solution [6] for the evolution of an electron, its coordinates $\mathbf{r}(\eta)$ and momentum $\mathbf{p}(\eta)$, in the L system. However, this solution is implicit, and the averaging procedure leading to an explicit form for the ponderomotive force is helpful (for example, to describe new effects such as gradient stabilization of ions relative to tunneling ionization in superstrong laser fields [7]).

Differentiating the expression for the momentum $\mathbf{p}(\eta)$ [6] with respect to the "laboratory" time t, we obtain an expression for the force acting on an electron. Averaging the fast phase of this force over t gives an expression for the ponderomotive force (compare with equation (1))

$$\mathbf{F}_L = \hat{\mathbf{x}}\omega\frac{\partial U_p^*}{\partial\eta} = -\nabla U_p^*, \quad (9)$$

where U_p^* is the ponderomotive potential taking account of the electron effective mass m^* in a field and $\hat{\mathbf{x}}$ is the unit vector in the direction of the wave vector $\mathbf{k}$. The force (9) formally is of a gradient form, though only its component in the direction of $\mathbf{k}$ is different from zero.

4. PONDEROMOTIVE FORCES IN A STATIONARY LASER BEAM

We assume that the field at the location of an electron at a given moment is, in the zeroth approximation, a plane wave, specifically, in the C system, where an electron is at rest on the average, and whose velocity $\mathbf{V}_0$ relative to the L system is assumed to known from the solution of equation (8) at the preceding step. We shall examine first a linearly polarized field. We direct the unit vectors $\hat{\mathbf{y}}$ along $\mathbf{E}^0$, $\hat{\mathbf{z}}$ along $\mathbf{B}^0$, and $\hat{\mathbf{x}}$ along $\mathbf{k}$. The parametric solution of equation (4) for the coordinates of an electron in the C system is [6]

$$x = -\frac{e^2E_{00}^2}{8m^{*2}\omega^3}\sin 2\eta,$$
$$y = -\frac{eE_{00}}{m^*\omega^2}\cos\eta, \quad z = 0, \tag{10}$$

where $m^{*2} = m^2 + e^2E_{00}^2/2\omega^2$, and the relation between the time t' (the proper time of the guiding center of the electron: $dt' = dt/\gamma$) and the phase η is given by the relation

$$t' = \frac{\eta}{\omega} - \frac{e^2E_{00}^2}{8m^{*2}\omega^3}\sin 2\eta. \tag{11}$$

To find the force $\mathbf{F}_C$ (6) it is necessary to determine the increments $\Delta\mathbf{E}$, $\Delta\mathbf{B}$, and $\Delta\mathbf{v}$ (see equation (5)) due to the nonuniformity of the field. Expanding the expression (3) in a series in $\mathbf{r}$, we obtain in the first approximation

$$\Delta\mathbf{E} \approx \cos\eta(\delta\mathbf{r}_e\cdot\nabla)\mathbf{E}_0(\mathbf{r}_0) - \mathbf{E}_{00}\sin\eta(\delta\mathbf{r}_e\cdot\nabla)\varphi(\mathbf{r}_0), \tag{12}$$

$$\Delta\mathbf{v} \approx (\delta\mathbf{r}_e\cdot\nabla)\mathbf{v}^0(\mathbf{E}), \tag{13}$$

where $\delta\mathbf{r}_e$ and $\mathbf{v}^0 = \partial(\delta\mathbf{r}_e)/\partial t'$ are the displacement and velocity of the electron, calculated in the zeroth approximation (10) using equation (11); the field (3)

$$\mathbf{E}_{00} \longrightarrow \mathbf{E}_0(\mathbf{r}), \quad \eta \longrightarrow \eta + \varphi(\mathbf{r})$$

is used as the argument of $\mathbf{v}_0$; $\Delta\mathbf{B}$ is calculated from Maxwell equations.

A laser beam that is stationary in the L system is no longer stationary in the C system, and the increments (12) and (13) must also contain terms with time derivatives of the amplitude and phase of the field $\mathbf{E}$, which take into account the nonuniformity of the field on scales $\delta r_v \sim V_0/\omega$, which an electron experiences as a result of drift. If $\delta r_v < \delta r_e$ (the drift velocity is less than the velocity of the oscillations of the electron or the nonuniformity of the field in the direction $\mathbf{V}_0$ is negligible), then nonstationarity can be neglected and the expressions (12) and (13) can be used. In the opposite case, the nonstationarity of the field will make the main contribution to the ponderomotive force $\mathbf{F}_C$. We note that in real situations an electron possesses a high drift velocity, as a rule, in regions of relatively weak fields (for example, on entering or leaving a laser beam), and in the region of a strong field the velocity $\mathbf{V}_0$ is quite low (on account of retardation of the electron by ponderomotive forces after entering the beam or as a result of "zero" initial velocities of photoelectrons in multiphoton ionization of atoms (ions) in strong fields [8]). The case of relativistic velocities $\mathbf{V}_0$ and relatively weak fields is studied in [2]. Here we shall investigate the opposite case, where the nonstationarity (in the C system) does not play a fundamental role.

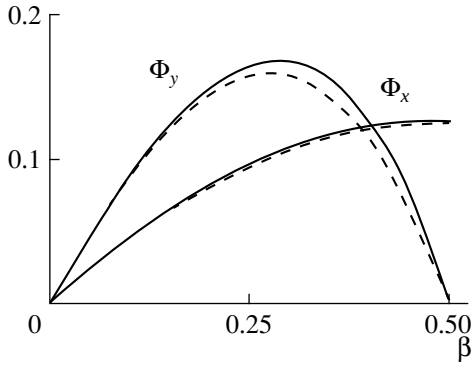

Fig. 1. The functions $\Phi_{x,y}(\beta)$, determining the dependence of the rotational part of the ponderomotive force in the C system and the intensity of the linearly polarized field. The dashed lines show the approximate dependences of $\Phi_{x,y}$ on the parameter β (see text).

Using equations (12) and (13) in equation (5) and averaging equation (6) over the time t' we obtain

$$\mathbf{F}_C = -\left(\nabla + \hat{\mathbf{y}}\Phi_y\frac{\partial}{\partial y} + \hat{\mathbf{x}}\Phi_x\frac{\partial}{\partial x}\right)m^*, \tag{14}$$

where

$$\Phi_y = \frac{2(1-2\beta)(1+\beta)(1-\beta_1)}{\beta\beta_1} \approx \beta(1+\beta)(1-2\beta),$$

$$\Phi_x = \frac{\beta^2}{2} + \frac{(1-2\beta)(1-\beta_1)}{\beta} \approx \frac{\beta(1-\beta)}{2},$$

$$\beta_1 = (1-\beta^2)^{1/2}, \quad \beta = U_p^*/m^*$$

(the functions $\Phi_{x,y}(\beta)$ are shown in Fig. 1, the dashed lines show the approximate dependences $\Phi_{x,y}(\beta)$). It is evident that the force (14) is not a gradient force in general: its rotational part contains components along the wave vector and polarization of the electric field. In the ultrarelativistic case $\Phi_x \gg \Phi_y \approx 0$. The rotational part of the force $\mathbf{F}_C$ contains all even powers of the amplitude of the vector potential of the field and approaches zero as $\mathbf{A} \longrightarrow 0$, and in addition $\Phi_{x\max} \approx 0.125$, while $\Phi_{y\max} \approx 0.168$ (we note that the possible dependence of the force $F_L \sim E_{00}^4$ has been discussed in [9]).

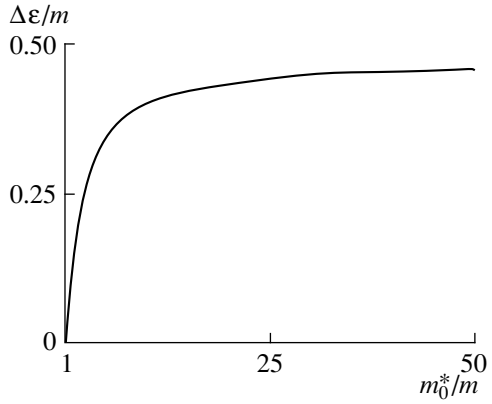

Fig. 2. The change in the drift energy of a charge for one pass of a laser beam with combined polarization of the field versus the amplitude of the field on the axis of the beam ($m_0^* = \sqrt{m^2 + e^2E_{0m}^2/2\omega^2}$).

A similar calculation for a circularly polarized field leads to the expression (14) with $\Phi_{x,y} = 0$, i.e., in this case the ponderomotive force remains a gradient force in the C system. We also note that for any polarization of the field the gradient $\nabla\varphi(\mathbf{r})$ of the phase (just as in the case of weak fields) does not contribute to the ponderomotive force. This property of ponderomotive forces breaks down for high drift velocities $\mathbf{V}_0$.

For applications, the force $\mathbf{F}_C$ (14) must be expressed in terms of the parameters of the field in the L system. Since the Lorentz transformation preserves the ratio $E_{00}/\omega \sim |\mathbf{A}|$, only the characteristic spatial scales of the field change in equation (14). These changes (corresponding to Lorentzian contraction of linear dimensions) are, in general, different along the different coordinate axes and are determined by the direction of the drift velocity $\mathbf{V}_0$. Therefore the substitutions

$$\frac{\partial}{\partial x} \longrightarrow \gamma_x\frac{\partial}{\partial x_L}, \quad \frac{\partial}{\partial y} \longrightarrow \gamma_y\frac{\partial}{\partial y_L}, \quad \frac{\partial}{\partial z} \longrightarrow \gamma_z\frac{\partial}{\partial z_L}, \tag{15}$$

where $\gamma_i = (1 - V_{0i}^2)^{-1/2}$, $i = x, y, z$, must be made in equation (14) (the index L denotes coordinates in the L system). These substitutions, generally speaking, destroy the gradient nature of the force $\mathbf{F}_C$, even for $\Phi_{x,y} = 0$. An additional breakdown of this gradient nature of the force occurs under the transformation (7). However, for sufficiently low velocities $\mathbf{V}_0$, the terms $\Phi_{x,y}$ make the main contribution to the rotational part of the force $\mathbf{F}_L$ (see equation (14)).

Thus equations (7) and (14) (or (9)) determine the ponderomotive forces in a laser field of arbitrary intensity. This makes it possible to describe the evolution of an electron in such fields using equation (8). The structure of these forces is much more complicated than in the nonrelativistic case (1), and in the general case it is determined by all even powers of the amplitude of the laser field. Combining equations (7) and (8) we obtain finally an equation for the drift velocity of an electron in a field of arbitrary intensity:

$$m\gamma^2\frac{d\mathbf{V}_0}{dt} = \mathbf{F}_C - \frac{\gamma - 1}{\gamma V_0^2}(\mathbf{V}_0 \cdot \mathbf{F}_C)\mathbf{V}_0, \tag{16}$$

where the force $\mathbf{F}_C$ (14) must be expressed in terms of the parameters of the field in the L system (see equation (15)).

The rotational character of the ponderomotive forces in strong fields means that it is possible to perform work on a charge in a closed cycle, i.e., there is a possibility of developing fundamentally new systems for accelerating or retarding (confining) charged particles. The difference found in the ponderomotive forces for linearly and circularly polarized fields makes it possible to develop such systems by combining superstrong fields with different polarization. We shall illustrate this possibility for a very simple example of an electron entering with nonrelativistic velocity $\mathbf{V}_0$ into a strong laser field which possesses a characteristic spatial nonuniformity only along a single coordinate, for example, *y*. In this case only the *y* component V_{0y} of the drift velocity of the electron will change. Then we obtain from equation (16)

$$m\frac{dV_{0y}}{dt} = -(1 + \Phi_y)\frac{\partial m^*}{\partial y}, \tag{17}$$

whence we find for the change in the kinetic energy of an electron due to its drift motion

$$\Delta\varepsilon = -\int_{y_0}^{y}(1 + \Phi_y)\frac{\partial m^*}{\partial y}dy, \tag{18}$$

where y_0 is the initial coordinate of the charge. Let the laser beam be organized so that from the periphery of the beam (whence the electron enters) to the axis of the beam the field is, for example, circularly polarized, and from the axis of the beam in the other direction the field is linearly polarized. Such beams can be produced in laser pulses with time-varying polarization [10] by combining two orthogonal fields with different frequencies. In this case, $\Phi_y = 0$ for an electron entering the beam ($y_0 < y < y_m$), where y_m is a coordinate corresponding to the axis of the beam, i.e., the maximum amplitude of the field), and on exiting the beam $\Phi_y \neq 0$:

$$\Phi_y \approx \frac{3\alpha^4 - 4\alpha^2 + 1}{4\alpha^6}, \quad \alpha = \frac{m^*}{m}. \tag{19}$$

The expression (19) corresponds to an approximate function $\Phi_y(\beta)$ (see Fig. 1). After passing through such

a beam, an electron acquires an additional kinetic energy

$$\frac{\Delta\varepsilon}{m} = \int_{m}^{m_0^*} \Phi_y(m^*)\frac{dm^*}{m} = \int_{1}^{\alpha_m} \Phi_y(\alpha)d\alpha$$
$$\approx \frac{7}{15} - \left(\frac{3}{4\alpha_m} - \frac{1}{3\alpha_m^3} + \frac{1}{20\alpha_m^5}\right), \qquad (20)$$
$$\alpha_m = \frac{m_0^*}{m}, \quad m_0^* = m^*(y_m).$$

The dependence of this energy on the effective mass m_0^* (on the amplitude E_{0m} of the field on the axis of the laser beam) is shown in Fig. 2. It is evident that even for $m_0^*/m = 10$ the increment to the energy is substantial: $\Delta\varepsilon \approx 0.4m$. The maximum increment to the kinetic energy of the charge in one pass (as $m_0^* \longrightarrow \infty$) is $\Delta\varepsilon/m = 7/15$.

In summary, a fundamentally new mechanism for accelerating charged particles (either effective "cooling" of the particles or confinement in a definite volume), based on the use of the new properties of ponderomotive forces in relativistically strong laser fields, is possible.

ACKNOWLEDGMENTS

This work was supported by the Russian Foundation for Fundamental Research, project no. 98-02-17525.

REFERENCES

1. A. V. Gaponov and M. A. Miller, Zh. Éksp. Teor. Fiz. **34**, 242 (1958) [Sov. Phys. JETP **7**, 168 (1958)].
2. D. R. Bituk and M. V. Fedorov, Zh. Éksp. Teor. Fiz. **116**, 1198 (1999) [JETP **89**, 640 (1999)].
3. S. P. Goreslavsky and N. B. Narozhny, J. Nonlinear Opt. Phys. Mater. **4**, 799 (1995).
4. D. Bauer, P. Mulser, and W.-H. Steeb, Phys. Rev. Lett. **75**, 4622 (1995).
5. H. Haus, *Waves and Fields in Optoelectronics* (Prentice-Hall, Englewood Cliffs, NJ, 1984; Mir, Moscow, 1988).
6. L. D. Landau and E. M. Lifshitz, *The Classical Theory of Fields* (Pergamon Press, Oxford, 1975, 4th ed.; Nauka, Moscow, 1988).
7. R. V. Kulyagin and V. D. Taranukhin, Laser Phys. **9**, 1026 (1999).
8. P. B. Corkum, Phys. Rev. Lett. **71**, 1994 (1993).
9. A. V. Serov, Kvantovaya Élektron. (Moscow) **25**, 197 (1998).
10. E. Constant, V. D. Taranukhin, A. Stolow, and P. B. Corkum, Phys. Rev. A **56**, 3870 (1997).

Translation was provided by AIP

Journal of Experimental and Theoretical Physics, Vol. 90, No. 3, 2000, pp. 452–459.
Translated from Zhurnal Éksperimental'noĭ i Teoreticheskoĭ Fiziki, Vol. 117, No. 3, 2000, pp. 517–525.

ATOMS, SPECTRA, RADIATION

Virtual Qubits: Multilevels Instead of Multiparticles

A. R. Kesel' and V. L. Ermakov*

Zavoĭskiĭ Physicotechnical Institute, Kazan Research Center, Russian Academy of Sciences, Kazan, 420029 Russia

**e-mail: ermakov@sci.kcn.ru*

Received October 22, 1999

Abstract—The possibility of using multilevel quantum systems with a discrete nonequidistant spectrum for the physical implementation of a universal collection of quantum gates, which is required for constructing an arbitrary algorithm for a quantum computer, is studied on the basis of the proposed virtual-spin formalism. It is shown that such a set of gates, including two-qubit gates, can be constructed on a single spin-3/2 nucleus. The assertion that three-qubit gates can also be realized on a single spin-7/2 quantum particle is substantiated. © *2000 MAIK "Nauka/Interperiodica".*

1. INTRODUCTION

One direction in the problem of developing a quantum computer, which being intensively studied now, is the search for new physical systems that are suitable for an information medium for quantum computations. Spin-1/2 nuclear magnetic resonance is one of the basic examples of physical systems of this kind [1]. The two possible stationary states of a 1/2 spin represent in a natural manner one bit of information (in the present case, a quantum bit or qubit). Thus, in the currently used model of a quantum computer a single particle corresponds to one qubit. In the present paper the possibility of using spins higher than 1/2, which have a large number of stationary states and, in general, nonequidistant corresponding energy levels, is examined. A brief exposition of these results has been published in [2]. Such a physical system gives more diverse possibilities for external action on quantum processes. Spin-3/2 nuclei will be considered as a specific example.

A spin I possesses $2I + 1$ energy levels, which can be nonequidistant, equidistant, or degenerate. Choosing in an appropriate manner the frequency, polarization, duration, and shape of the rf pulses, spins can be excited by very diverse methods, and the required evolution and form of the response can be attained. For example, in nonequidistant three-level spectra of a spin-1 nuclear quadrupole resonance it is possible to excite three resonance transitions, which is done using three mutually perpendicular rf fields with different frequencies. Even greater variety can be achieved by using pulse sequences that are constructed as combinations of diverse pulses and intervals of free evolution of the spin system.

In order to propose a new physical object as an information medium for a quantum computer, the following must be done.

1. A physical description of the object must be given, and a subset of the admissible stationary states of the system that is to be put into correspondence with one or several information bits must be singled out. For the problem examined in the present paper, this makes it necessary to show that four suitable states of a multilevel discrete spectrum can be represented as a direct product of the Hilbert spaces of two two-level systems (two qubits).

2. Methods of performing a physical action on the system that produce transitions between the stationary states of the system, thereby realizing logical operations, must be indicated. To do this it is sufficient to show that in this system it is possible to perform a one-bit rotation operation for each qubit as well as the two-qubit operation "controlled negation"—CNOT, since it is well known [9] that these two gates are sufficient to construct an algorithm of arbitrary complexity.

3. Methods for establishing the initial state $|0\rangle$, required for calculations, and reading the final state of each qubit must be given.

We shall examine systematically the realization of these requirements on a four-level spin-3/2 nucleus.

2. PHYSICAL SYSTEM

2.1 Basic Hamiltonian

The energy levels of a quadrupole spin in the gradient of the electric field of a lattice and in a constant magnetic field are determined by the Hamiltonian

$$\mathbf{H}_0 = \mathbf{H}_z + \mathbf{H}_Q, \tag{1}$$

where $\mathbf{H}_z$ is the Hamiltonian describing the interaction with the constant external magnetic field and $\mathbf{H}_Q$ is the Hamiltonian of the electric quadrupole interaction. In the specific case where the constant magnetic field is

parallel to the principal axis of the gradient of the crystal electric field, these operators have the form [1]

$$\mathbf{H}_z = -\hbar\omega_0\mathbf{I}_z,$$
$$\mathbf{H}_Q = \frac{1}{3}\hbar\omega_Q[3\mathbf{I}_z^2 - I(I+1) + \eta(\mathbf{I}_x^2 - \mathbf{I}_y^2)], \quad (2)$$

where ω_Q is the quadrupole interaction constant, ω_0 is the Zeeman frequency, and η is a dimensionless quantity ($|\eta| \le 1$) describing the deviation of the gradient of the electric field from axial symmetry. For spin 3/2 the eigenvalues of the Hamiltonian (1), (2) are

$$\hbar\varepsilon_{\pm 3/2} = \hbar\omega_Q(B_\mp \mp C),$$
$$\hbar\varepsilon_{\pm 1/2} = \hbar\omega_Q(-B_\pm \pm C), \quad (3)$$

where

$$B_\pm = \sqrt{(1 \pm 2C)^2 + \frac{\eta^2}{3}}, \quad C = \frac{\omega_0}{\omega_Q}.$$

We note that the frequency of a purely ($\omega_0 = 0$) quadrupole resonance is

$$2\omega_Q\sqrt{1 + \frac{\eta^2}{3}}.$$

The energy levels (3) correspond to the eigenfunctions

$$|\Psi_{\mp 3/2}\rangle = \cos(\alpha_\pm)|\chi_{\mp 3/2}\rangle + \sin(\alpha_\pm)|\chi_{\pm 1/2}\rangle,$$
$$|\Psi_{\pm 1/2}\rangle = \cos(\alpha_\pm)|\chi_{\pm 1/2}\rangle - \sin(\alpha_\pm)|\chi_{\mp 3/2}\rangle, \quad (4)$$

where $|\chi_m\rangle$ is the eigenfunction of the operator $\mathbf{I}_z$ corresponding to the eigenvalue m, and

$$\tan\alpha_\pm = \frac{\sqrt{3}}{\eta}[B_\pm + (1 \pm 2C)].$$

The spin energy levels and the resonance transitions required for realizing quantum logical operations are presented in Fig. 1. The formulas (1)–(4) presented above are valid for any value of the ratio $R = \omega_0/\omega_Q$. In what follows, for definiteness, we shall examine in detail the case of a magnetic resonance spectrum split by a quadrupole interaction ($\omega_0 > \omega_Q$), under the condition that ω_Q is much greater than the width of the spin levels. Then, the spin spectrum consists of four well-resolved resonance lines, where $\varepsilon_1 > \varepsilon_2 > \varepsilon_3 > \varepsilon_4$.

2.2. Hamiltonian of the Interaction with an Ac Field

Assuming the relaxational processes to be negligibly small, the complete nuclear spin Hamiltonian can be represented in the form

$$\mathbf{H} = \mathbf{H}_0 + \mathbf{H}_{rf}, \quad (5)$$

where $\mathbf{H}_{rf}$ is an operator describing the interaction with the ac field. In the case where the ac magnetic field is directed along the y axis, this operator is

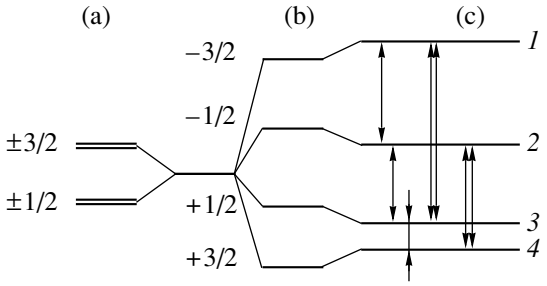

Fig. 1. Energy levels of spin 3/2 in the following cases: (a) zero external magnetic field (purely quadrupole resonance), the energy levels are doubly degenerate; (b) no quadrupole interaction (the external field determines the equidistant structure of the spectrum); (c) quadrupole interaction much weaker than the external field. The types of resonance transitions are shown: ordinary arrows—transition with $\Delta m = \pm 1$, double arrows—transitions with $\Delta m = \pm 2$. All indicated transitions can be excited by special pulse sequences.

$$\mathbf{H}_{rf}^Y(t) = 2\hbar\gamma H_{rf}\mathbf{I}_y\cos(\Omega t), \quad (6)$$

where H_{rf} and Ω are the amplitude and frequency of the ac field and γ is the gyromagnetic ratio of the nucleus.

In what follows, we shall require expressions for the operators $\mathbf{H}_{rf}(t)$ in the interaction representation:

$$\mathbf{H}_{rf}^*(t) \equiv \mathbf{D}^{-1}(t - t_0)\mathbf{H}_{rf}(t)\mathbf{D}(t - t_0),$$
$$\mathbf{D}(t - t_0) = \exp[-i\mathbf{H}_0(t - t_0)/\hbar]. \quad (7)$$

The form of the operator $\mathbf{D}$ corresponds to the case where the main Hamiltonian $\mathbf{H}_0$ of the system is independent of time.

To simply the equations and the subsequent calculations, we shall use a representation of the spin operators in terms of projection operators $\mathbf{P}_{mn}$, which are 4×4 matrices all of whose all matrix elements p_{kl} are zero except $p_{mn} = 1$. The projection operators have simple properties:

$$\mathbf{P}_{kl}\mathbf{P}_{mn} = \delta_{lm}\mathbf{P}_{kn},$$
$$\mathbf{P}_{mn} = \mathbf{P}_{nm}^+, \quad (8)$$
$$\mathbf{P}_{mn}|\Psi_k\rangle = \delta_{nk}|\Psi_m\rangle.$$

Likewise to simplify the equations, instead of indices –3/2, –1/2, +1/2, and +3/2 we shall use the indices 1, 2, 3, and 4, respectively. The spin components can be expressed as follows in terms of the projection operators:

$$\mathbf{I}_\alpha = \sum_{m,n}\langle\Psi_m|\mathbf{I}_\alpha|\Psi_n\rangle\mathbf{P}_{mn}.$$

Specifically, the main Hamiltonian in the projection-operator representation has the form

$$\mathbf{H}_0 = \sum_m \hbar\varepsilon_m\mathbf{P}_{mm}, \quad (9)$$

and the transformation into the interaction representation will be determined by the operator

$$\mathbf{D}(t-t_0) = \sum_m \mathbf{P}_{mm}\exp[-i\varepsilon_m(t-t_0)]. \quad (10)$$

When the frequency Ω of the external ac field is the same as one of the spin eigenfrequencies, for example, $\Omega_{mn} = |\varepsilon_m - \varepsilon_n|$, the interaction operator with the ac magnetic field (6) can be represented in the interaction representation in the form

$$\mathbf{H}^*_{rf}(t) = \mathbf{H}_{\mathrm{rf,\,eff}} + \sum_{kl}\mathbf{G}_{kl}\exp[i(\varepsilon_k - \varepsilon_l)t], \quad (11)$$

where $\mathbf{G}_{kl}$ and $\mathbf{H}_{\mathrm{rf,\,eff}}$ are time-independent, and

$$|\mathbf{G}_{kl}| \sim |\mathbf{H}_{\mathrm{rf,\,eff}}| \sim |\mathbf{H}_{\mathrm{rf}}|.$$

The terms which oscillate at the eigenfrequencies $\Omega_{kl} \neq \Omega_{mn}$ and have amplitudes $\sim|\mathbf{G}_{kl}|$ have a negligible effect on the evolution of the spin compared with the constant term $|\mathbf{H}_{\mathrm{rf,\,eff}}|$. This is because in NMR experiments the duration of the rf pulses is ordinarily much longer than the period $\sim\hbar/|\mathbf{H}_0|$ of the oscillations and because $\mathbf{H}_0 \gg \mathbf{H}_{\mathrm{rf}}$. Thus, the interaction (6) effectively excites resonance transitions only between the spin levels for which a resonance condition of the type $\Omega = \Omega_{mn}$ is satisfied. Therefore, in the interaction representation, the operator (6) at times greater than several periods of the characteristic oscillations ($\Omega_{kl}t \gg 1$) reduces to the effective operator

$$\mathbf{H}^y_{\mathrm{rf,\,eff}} = i\hbar\gamma H_{\mathrm{rf}}|\langle\Psi_m|\mathbf{I}_y|\Psi_n\rangle|(\mathbf{P}_{nm} - \mathbf{P}_{mn}). \quad (12a)$$

When the ac field is directed along the x axis, the effective interaction operator is

$$\mathbf{H}^x_{\mathrm{rf,\,eff}} = \hbar\gamma H_{\mathrm{rf}}|\langle\Psi_m|\mathbf{I}_x|\Psi_n\rangle|(\mathbf{P}_{nm} + \mathbf{P}_{mn}). \quad (12b)$$

Since the basis (4) of the eigenfunctions was chosen to be real, the matrix elements of the operator $\mathbf{I}_y$ are purely imaginary, and the matrix elements of the operator $\mathbf{I}_x$ are real. In addition, we note that although in the basis $|\chi\rangle$ the operators $\mathbf{I}_x$ and $\mathbf{I}_y$ possess matrix elements only with selection rules $m - n = \pm 1$, in the basis $|\Psi\rangle$ these operators have nonzero matrix elements with

$$m - n = \pm 1, \pm 2. \quad (13)$$

2.3. Evolution of the Spin System under the Influence of rf Pulses

The evolution of the state vector

$$|\Psi(t)\rangle = \mathbf{U}(t, t_0)|\Psi(t_0)\rangle \quad (14)$$

of a physical system can be determined in terms of a unitary evolution operator [3]:

$$\mathbf{U}(t, t_0) = \mathbf{D}(t-t_0)\mathbf{V}(t, t_0),$$

$$\mathbf{V}(t, t_0) = \mathbf{T}\exp\left[-\frac{i}{\hbar}\int_{t_0}^{t}\mathbf{H}^*_{\mathrm{rf}}(t')dt'\right], \quad (15)$$

$$\mathbf{H}^*_{\mathrm{rf}}(t) = \mathbf{D}^{-1}(t-t_0)\mathbf{H}_{\mathrm{rf}}(t)\mathbf{D}(t-t_0),$$

where $\mathbf{T}$ is the Dyson chronological operator, and the operator $\mathbf{V}$ is the evolution operator in the interaction representation.

Under conditions where the rapidly oscillating terms in $\mathbf{H}^*_{\mathrm{rf}}(t)$ can be neglected, the chronological exponential becomes an ordinary exponential function. Then, the operator $\mathbf{V}(t, t_0)$ reduces to

$$\mathbf{V}_x(t, t_0) \approx \exp\left[-\frac{i}{\hbar}\int_{t_0}^{t}\mathbf{H}^x_{\mathrm{rf,\,eff}}dt'\right]$$

$$= \exp\left[-i\frac{\varphi}{2}(\mathbf{P}_{nm} + \mathbf{P}_{mn})\right] \equiv \mathbf{V}_x(\Omega_{mn}, \varphi_x),$$

$$\mathbf{V}_y(t, t_0) \approx \exp\left[-\frac{i}{\hbar}\int_{t_0}^{t}\mathbf{H}^y_{\mathrm{rf,\,eff}}dt'\right]$$

$$= \exp\left[\frac{\varphi}{2}(\mathbf{P}_{nm} - \mathbf{P}_{mn})\right] \equiv \mathbf{V}_y(\Omega_{mn}, \varphi_y),$$

where

$$\varphi_\alpha = 2(t-t_0)\gamma H_{\mathrm{rf}}|\langle\Psi_n|\mathbf{I}_\alpha|\Psi_m\rangle, \quad \alpha = x, y, \quad \varepsilon_m > \varepsilon_n.$$

Expanding the exponentials in a series and using the multiplication rules (8) for projection operators, we obtain

$$\mathbf{V}_x(\Omega_{mn}, \varphi_x) = \mathbf{P}_{kk} + \mathbf{P}_{ll} + (\mathbf{P}_{nn} + \mathbf{P}_{mm})\cos\left(\frac{\varphi_x}{2}\right) - i(\mathbf{P}_{nm} + \mathbf{P}_{mn})\sin\left(\frac{\varphi_x}{2}\right), \quad (16a)$$

$$\mathbf{V}_y(\Omega_{mn}, \varphi_y) = \mathbf{P}_{kk} + \mathbf{P}_{ll} + (\mathbf{P}_{nn} + \mathbf{P}_{mm})\cos\left(\frac{\varphi_y}{2}\right) + (\mathbf{P}_{nm} - \mathbf{P}_{mn})\sin\left(\frac{\varphi_y}{2}\right). \quad (16b)$$

Here the indices $k, l \neq m, n$.

In addition, to construct quantum logical elements it is necessary to excite the spin on two transitions simultaneously. It is shown below that for this it is sufficient to excite transitions that do not have energy levels in common. Then, the evolution operator is a product of commuting evolution operators for individual transitions. Under two-frequency excitation at frequencies

Ω_{12} and Ω_{34}, direct calculations give the following expression for the evolution operator:

$$\begin{aligned}\mathbf{V}_y(\Omega_{12}, \varphi_y; \Omega_{34}, \varphi'_y) &= (\mathbf{P}_{11} + \mathbf{P}_{22})\cos\left(\frac{\varphi_y}{2}\right)\\ &+ (\mathbf{P}_{21} - \mathbf{P}_{12})\sin\left(\frac{\varphi_y}{2}\right) + (\mathbf{P}_{33} + \mathbf{P}_{44})\cos\left(\frac{\varphi'_y}{2}\right)\\ &+ (\mathbf{P}_{43} - \mathbf{P}_{34})\sin\left(\frac{\varphi'_y}{2}\right).\end{aligned} \quad (17)$$

Under two-frequency irradiation at frequencies Ω_{13} and Ω_{24} the evolution operator is

$$\begin{aligned}\mathbf{V}_y(\Omega_{13}, \varphi_y; \Omega_{24}, \varphi'_y) &= (\mathbf{P}_{22} + \mathbf{P}_{44})\cos\left(\frac{\varphi_y}{2}\right)\\ &+ (\mathbf{P}_{42} - \mathbf{P}_{24})\sin\left(\frac{\varphi_y}{2}\right) + (\mathbf{P}_{33} + \mathbf{P}_{11})\cos\left(\frac{\varphi'_y}{2}\right)\\ &+ (\mathbf{P}_{31} - \mathbf{P}_{13})\sin\left(\frac{\varphi'_y}{2}\right).\end{aligned} \quad (18)$$

3. VIRTUAL-SPIN FORMALISM

In the currently adopted NMR model of a quantum computer [4–7], two real spins $R = 1/2$ and $S = 1/2$, coupled by an exchange interaction, are being considered as a basis for constructing quantum logical elements. In the formalism of quantum mechanics, the states of such a system and the operations on them can be written in an abstract four-dimensional space, which is a direct product $\Gamma_R \otimes \Gamma_S$ of two-dimensional spaces of the eigenstates of the real spins R and S. In our case, to clarify the information aspect of the proposed logical operations, it is convenient to reverse the procedure: the four-dimensional space Γ_I corresponding to a real spin 3/2 is represented as a direct product $\Gamma_R \otimes \Gamma_S$ of two abstract two-dimensional spaces of states of the virtual spins R and S. Then, any operator $\mathbf{P}$ in the four-dimensional basis can be expressed as a linear combination of the direct products $\mathbf{R} \otimes \mathbf{S}$ of the components of the vector spin operators given in the subspaces Γ_R and Γ_S. The following isomorphic correspondence exists between the basis $|\Psi_M\rangle$ of the space Γ_I and the basis $|\xi_m\rangle \otimes |\zeta_n\rangle$ of the direct product $\Gamma_R \otimes \Gamma_S$:

$$\begin{aligned}|\Psi_1\rangle &= |\xi_1\rangle \otimes |\zeta_1\rangle \equiv |11\rangle, \quad |\Psi_3\rangle = |\xi_2\rangle \otimes |\zeta_1\rangle \equiv |01\rangle,\\ |\Psi_2\rangle &= |\xi_1\rangle \otimes |\zeta_2\rangle \equiv |10\rangle, \quad |\Psi_4\rangle = |\xi_2\rangle \otimes |\zeta_2\rangle \equiv |00\rangle,\end{aligned} \quad (19)$$

where the indices 1 and 2 are used for the indices –1/2 and +1/2, respectively, of the virtual spins. Here $|11\rangle$ and so on are the notations used in information theory to represent the states of two qubits. The following helpful relations exist between the projection operators, which will be used in the calculations, in the spaces under study:

$$\begin{aligned}\mathbf{R}_{kl} \otimes \mathbf{S}_{mn} &= \mathbf{P}_{2k-2+m,\,2l-2+n},\\ \mathbf{R}_{kl}\mathbf{R}_{mn} \otimes \mathbf{1}_S &= \delta_{lm}\mathbf{R}_{kn} \otimes \mathbf{1}_S,\\ \mathbf{R}_{kl} \otimes \mathbf{1}_S|\xi_m\rangle|\zeta_n\rangle &= \delta_{lm}|\xi_k\rangle|\zeta_n\rangle,\\ \mathbf{1}_R \otimes \mathbf{S}_{kl}\mathbf{S}_{mn} &= \delta_{lm}\mathbf{1}_R \otimes \mathbf{S}_{kn},\\ \mathbf{1}_R \otimes \mathbf{S}_{kl}|\xi_m\rangle|\zeta_n\rangle &= \delta_{ln}|\xi_m\rangle|\zeta_k\rangle,\\ (\mathbf{R}_{kl} \otimes \mathbf{S}_{ab})(\mathbf{R}_{mn} \otimes \mathbf{S}_{cd}) &= \delta_{lm}\delta_{bc}\mathbf{R}_{kn} \otimes \mathbf{S}_{ad}.\end{aligned} \quad (20)$$

Here the operators $\mathbf{R}_{mn}$ and $\mathbf{S}_{mn}$ are projection operators of the two-dimensional spaces Γ_R and Γ_S, while $\mathbf{1}_R$ and $\mathbf{1}_S$ are unit operators in the spaces. Specifically, the components $\mathbf{R}_x$, $\mathbf{R}_y$, and $\mathbf{R}_z$ and the components $\mathbf{S}_x$, $\mathbf{S}_y$, and $\mathbf{S}_z$ of the virtual spins can be expressed as follows in terms of the projection operators:

$$\mathbf{R}_x = \frac{\mathbf{R}_{12} + \mathbf{R}_{21}}{2},$$

$$\mathbf{R}_y = \frac{i(\mathbf{R}_{12} - \mathbf{R}_{21})}{2},$$

$$\mathbf{R}_z = \frac{\mathbf{R}_{11} - \mathbf{R}_{22}}{2},$$

$$\mathbf{S}_x = \frac{\mathbf{S}_{12} + \mathbf{S}_{21}}{2},$$

$$\mathbf{S}_y = \frac{i(\mathbf{S}_{12} - \mathbf{S}_{21})}{2},$$

$$\mathbf{S}_z = \frac{\mathbf{S}_{11} - \mathbf{S}_{22}}{2}.$$

It should be noted that in the four-dimensional space Γ_I two qubits can be introduced differently, in a different manner so that the top pair of levels comprises one qubit and the bottom pair comprises the second qubit. At magnetic resonance this manner of singling out two-level subsystems is widely known as the "formalism of virtual (or effective) spins 1/2." In this case, the space Γ_I is a direct sum $\Gamma_R \oplus \Gamma_S$ of the spaces of the virtual spins. In this approach the realization of one-bit rotation gates does not present any difficulties, but difficulties do arise in realizing a two-qubit CNOT gate. In addition, the virtual spins introduced above correspond well with the representations used in quantum information science.

4. PREPARATION OF THE INITIAL STATE

As is well known, the initial state for quantum algorithms implemented in an abstract quantum computer is the state $|00\rangle$.

To emulate abstract quantum computaters in real NMR experiments it is necessary to take account of at

least the following features of an NMR quantum computer. In NMR a macroscopic number of identical quantum processors are used—molecules, computations on which are performed simultaneously, and the output signal is the sum of the signals from all molecules. An adequate language for NMR experiments is the density matrix formalism. The state $|00\rangle$ is the equivalent of a density matrix of the form $\sigma_{init} = \text{const}\mathbf{P}_{44}$.

In a sample of macroscopic dimensions, a collection of identical nuclei forms an ensemble whose spin levels at equilibrium are occupied according to the Boltzmann density matrix

$$\begin{aligned} \boldsymbol{\rho}_{eq} &= Z^{-1}\exp(-\beta\mathbf{H}), \\ Z &= \mathrm{Sp}[\exp(-\beta\mathbf{H})], \\ \beta &= 1/kT. \end{aligned} \tag{21}$$

NMR experiments are conducted primarily at room temperature, where the modulus of the quantity $\beta\mathbf{H}$ in the argument of the exponential is much less than 1 ($\sim 10^{-5}$–10^{-6}). Under these conditions the initial density matrix for quantum algorithms implemented on an NMR computer is

$$\begin{aligned} \boldsymbol{\rho}_{eq} &= Z^{-1}\left[\mathbf{1}_\mathbf{I} + \sum_m \lambda_m \mathbf{P}_{mm}\right], \\ \mathbf{1}_\mathbf{I} &= \sum_m \mathbf{P}_{mm}, \\ \lambda_m &= \frac{\hbar\varepsilon_m}{kT}, \end{aligned} \tag{22}$$

where $\mathbf{1}_\mathbf{I}$ is a unit matrix in the space Γ_I.

The density matrix $\boldsymbol{\rho}_{eq}$ can be obtained directly in the form $\boldsymbol{\sigma}_{init}$ by cooling the spin system to ultralow temperatures. Besides enormous technological difficulties, this will inevitably affect the speed of the entire computational cycle. It will be shown below how the density matrix

$$\boldsymbol{\rho}_{init} = \text{const}[\mathbf{1}_\mathbf{I} + \text{const}\mathbf{P}_{44}] \tag{23}$$

can be obtained in real NMR experiments as the input for quantum algorithms. In the operator sense, the density matrix $\boldsymbol{\rho}_{init}$ differs from $\boldsymbol{\sigma}_{init}$ by a term proportional to the matrix $\mathbf{1}_\mathbf{I}$, which is not influenced by unitary transformations and does not contribute to the observed signal. For this reason, any pulse sequences, including those which implement logical operations, do not affect the matrix $\mathbf{1}_\mathbf{I}$ and, for this reason, in describing the evolution the initial density matrices $\boldsymbol{\rho}_{init}$ and $\boldsymbol{\sigma}_{init}$ give identical results.

To obtain $\boldsymbol{\rho}_{init}$ it is expedient to use the procedure of spatial [5] or temporal [6] dynamical (using additional pulsed action on the spins) reduction of the density matrix $\boldsymbol{\rho}_{eq}$ to the form $\boldsymbol{\rho}_{init}$. We shall examine the procedure for temporal reduction of the density matrix $\boldsymbol{\rho}_{eq}$ to $\boldsymbol{\rho}_{init}$ for a multiqubit spin, leaving other methods for a future study.

The following procedure, the idea for which goes back to [6], is proposed. Let the required calculation consist of performing a transformation $\mathbf{V}_{comp}$ with the initial density matrix in the form $\boldsymbol{\rho}_{init}$, while the spin system is in a state given by the equilibrium density matrix (22). We shall show that the average

$$\begin{aligned} &\frac{1}{3}[\mathbf{V}_{comp}\boldsymbol{\rho}_{eq}\mathbf{V}_{comp}^\dagger + \mathbf{V}_{comp}\mathbf{V}_1\boldsymbol{\rho}_{eq}\mathbf{V}_1^\dagger\mathbf{V}_{comp}^\dagger \\ &\qquad + \mathbf{V}_{comp}\mathbf{V}_2\boldsymbol{\rho}_{eq}\mathbf{V}_2^\dagger\mathbf{V}_{comp}^\dagger] \\ &= \frac{1}{3}\mathbf{V}_{comp}(\boldsymbol{\rho}_{eq} + \mathbf{V}_1\boldsymbol{\rho}_{eq}\mathbf{V}_1^\dagger + \mathbf{V}_2\boldsymbol{\rho}_{eq}\mathbf{V}_2^\dagger)\mathbf{V}_{comp}^\dagger \end{aligned}$$

of the results of three calculations $\mathbf{V}_{comp}$, starting with three different initial states—$\boldsymbol{\rho}_{eq}$, $\mathbf{V}_1\boldsymbol{\rho}_{eq}\mathbf{V}_1^\dagger$, and $\mathbf{V}_2\boldsymbol{\rho}_{eq}\mathbf{V}_2^\dagger$—is equivalent to the transformation $\mathbf{V}_{comp}$ of the state $\boldsymbol{\rho}_{init}$:

$$\mathbf{V}_{comp}\boldsymbol{\rho}_{init}\mathbf{V}_{comp}^\dagger. \tag{24}$$

For this, we choose the transformations $\mathbf{V}_1$ and $\mathbf{V}_2$ in the form of two successive single-frequency pulses

$$\begin{aligned} \mathbf{V}_1 &= \mathbf{V}_y(\Omega_{12}, \pi)\mathbf{V}_y(\Omega_{23}, \pi) = \mathbf{P}_{44} + \mathbf{P}_{21} + \mathbf{P}_{13} + \mathbf{P}_{32}, \\ \mathbf{V}_2 &= \mathbf{V}_y(\Omega_{23}, \pi)\mathbf{V}_y(\Omega_{12}, \pi) = \mathbf{P}_{44} - \mathbf{P}_{12} + \mathbf{P}_{31} - \mathbf{P}_{23}. \end{aligned} \tag{25}$$

Then, using the expressions (16a) and (16b) and the multiplication rules (8), we obtain

$$\begin{aligned} &\frac{\boldsymbol{\rho}_{eq} + \mathbf{V}_1\boldsymbol{\rho}_{eq}\mathbf{V}_1^\dagger + \mathbf{V}_2\boldsymbol{\rho}_{eq}\mathbf{V}_2^\dagger}{3} = Z[\alpha\mathbf{1} + \beta\mathbf{P}_{44}] \propto \boldsymbol{\rho}_{init}, \\ &\alpha = 1 + \frac{1}{3}[\lambda_1 + \lambda_2 + \lambda_3],\ \beta = \lambda_4 - \frac{1}{3}[\lambda_1 + \lambda_2 + \lambda_3]. \end{aligned} \tag{26}$$

This confirms that a logical operation on $\boldsymbol{\rho}_{init}$ can be reduced to an operation on $\boldsymbol{\rho}_{eq}$ by means of appropriate pulse sequences.

5. ONE-BIT ROTATION OPERATION

The operator $\mathbf{V}_y(\Omega_{12}, \varphi_y; \Omega_{34}, \varphi'_y)$ (17) with $\varphi_y = \varphi'_y = \varphi$ has the form

$$\begin{aligned} \mathbf{V}_y(\Omega_{12}, \varphi; \Omega_{34}, \varphi) &= (\mathbf{P}_{11} + \mathbf{P}_{22} + \mathbf{P}_{33} + \mathbf{P}_{44})\cos\left(\frac{\varphi}{2}\right) \\ &+ (\mathbf{P}_{21} - \mathbf{P}_{12} + \mathbf{P}_{43} - \mathbf{P}_{34})\sin\left(\frac{\varphi}{2}\right). \end{aligned} \tag{27}$$

Expressing by means of equations (20) the operators **P** in terms of the operators **R** and **S**, it can be shown that the operator

$$\begin{aligned}&\mathbf{V}_y(\Omega_{12}, \varphi; \Omega_{34}, \varphi)\\ &= (\mathbf{R}_{11} + \mathbf{R}_{22}) \otimes \left[(\mathbf{S}_{11} + \mathbf{S}_{22})\cos\left(\frac{\varphi}{2}\right)\right.\\ &\left. + (\mathbf{S}_{21} - \mathbf{S}_{12})\sin\left(\frac{\varphi}{2}\right)\right] = \exp\{i\varphi \mathbf{1}_R \otimes \mathbf{S}_x\}\end{aligned} \quad (28)$$

is identical to the operator (27). The latter equality on the right-hand side of the operator (28) shows that the transformation $\mathbf{V}_y(\Omega_{12}, \varphi; \Omega_{34}, \varphi)$ is a rotation by an angle φ in the space Γ_S under the condition that the space Γ_R is invariant. Using the expressions (16a) and (16b) to calculate expressions of type (17) and (27), it is possible to obtain an operator, having the same form as the operator (28), for the rotation of a virtual spin *S* around the *y* axis.

It can be shown similarly that the operator $\mathbf{V}_y(\Omega_{13}, \varphi_y; \Omega_{24}, \varphi_y')$ (18) with $\varphi_y = \varphi_y' \equiv \varphi$ is equal to the operator

$$\begin{aligned}&\mathbf{V}_y(\Omega_{13}, \varphi; \Omega_{24}, \varphi)\\ &= \left[(\mathbf{R}_{11} + \mathbf{R}_{22})\cos\left(\frac{\varphi}{2}\right)(\mathbf{R}_{21} - \mathbf{R}_{12})\sin\left(\frac{\varphi}{2}\right)\right]\\ &\otimes (\mathbf{S}_{11} + \mathbf{S}_{22}) = \exp\{i\varphi \mathbf{R}_x \otimes \mathbf{1}_S\}.\end{aligned} \quad (29)$$

The last equality on the right-hand side of the expression (29) shows that the propagator $\mathbf{V}_y(\Omega_{13}, \varphi; \Omega_{24}, \varphi)$ is a rotation by an angle φ relative to the *x* axis in the spin space Γ_R with constant Γ_S.

6. "CONTROLLED NEGATION" OPERATION, CNOT

The transformation $\mathbf{V}_x(\Omega_{12}, \varphi_x)$ (16a) on the transition $1 \longleftrightarrow 2$ with $\varphi_x = \pi$, defined as

$$\mathbf{V}_x(\Omega_{12}, \pi) = [\mathbf{P}_{33} + \mathbf{P}_{44}] - i[\mathbf{P}_{21} + \mathbf{P}_{12}], \quad (30)$$

performs the two-bit operation "controlled negation" CNOT—the NOT operation on a spin *S* if the spin *R* is in the state $|\xi_1\rangle$ and leaves the spin *S* unchanged if the spin *R* is in the state $|\xi_2\rangle$. Indeed, it is easy to check, using the definition of the projection operators, that

$$\begin{aligned}&\mathbf{V}_x(\Omega_{12}, \pi)|\Psi_1\rangle \equiv -i|\Psi_2\rangle,\ \ \mathbf{V}_x(\Omega_{12}, \pi)|\Psi_2\rangle \equiv -i|\Psi_1\rangle,\\ &\mathbf{V}_x(\Omega_{12}, \pi)|\Psi_3\rangle \equiv |\Psi_3\rangle,\ \ \mathbf{V}_x(\Omega_{12}, \pi)|\Psi_4\rangle \equiv |\Psi_4\rangle,\end{aligned}$$

or in information-theory notation

$$\begin{aligned}&\mathbf{V}_x(\Omega_{12}, \pi)|11\rangle \equiv -i|10\rangle,\ \ \mathbf{V}_x(\Omega_{12}, \pi)|10\rangle \equiv -i|11\rangle,\\ &\mathbf{V}_x(\Omega_{12}, \pi)|01\rangle \equiv |01\rangle,\ \ \mathbf{V}_x(\Omega_{12}, \pi)|00\rangle \equiv |00\rangle.\end{aligned}$$

This is (to within a phase factor $\exp(i\pi/2)$) a truth table for the CNOT operation defined above, in which the spin *R* controls the state of the spin *S*. In the projection operators of the basis $\Gamma_R \otimes \Gamma_S$, we represent the evolution operator $\mathbf{V}_x(\Omega_{12}, \pi)$ in the form

$$\mathbf{V}_x(\Omega_{12}, \pi) = -i\mathbf{R}_{11} \otimes (\mathbf{S}_{12} + \mathbf{S}_{21}) + \mathbf{R}_{22} \otimes \mathbf{1}_S. \quad (31)$$

It can be shown similarly that the transformation $\mathbf{V}_x(\Omega_{13}, \varphi_x)$ on the transition $1 \longleftrightarrow 3$ for $\varphi_x = \pi$, equal to

$$\mathbf{V}_x(\Omega_{13}, \pi) = [\mathbf{P}_{22} + \mathbf{P}_{44}] - i[\mathbf{P}_{13} + \mathbf{P}_{31}], \quad (32)$$

performs the CNOT operation in which the spin *S* controls the state of the spin *R*:

$$\begin{aligned}&\mathbf{V}_x(\Omega_{13}, \pi)|\Psi_1\rangle \equiv -i|\Psi_3\rangle,\ \ \mathbf{V}_x(\Omega_{13}, \pi)|\Psi_2\rangle \equiv |\Psi_2\rangle,\\ &\mathbf{V}_x(\Omega_{13}, \pi)|\Psi_3\rangle \equiv -i|\Psi_1\rangle,\ \ \mathbf{V}_x(\Omega_{13}, \pi)|\Psi_4\rangle \equiv |\Psi_4\rangle.\end{aligned}$$

This gives the truth table

$$\begin{aligned}&\mathbf{V}_x(\Omega_{13}, \pi)|11\rangle = i|01\rangle,\ \ \mathbf{V}_x(\Omega_{13}, \pi)|10\rangle = |10\rangle,\\ &\mathbf{V}_x(\Omega_{13}, \pi)|01\rangle = i|11\rangle,\ \ \mathbf{V}_x(\Omega_{13}, \pi)|00\rangle = |00\rangle.\end{aligned}$$

In the projection operators of the basis $\Gamma_R \otimes \Gamma_S$, we represent the evolution operator $\mathbf{V}_x(\Omega_{13}, \pi)$ in the form

$$\mathbf{V}_x(\Omega_{13}, \pi) = \mathbf{1}_R \otimes \mathbf{S}_{22} - i(\mathbf{R}_{12} + \mathbf{R}_{21}) \otimes \mathbf{S}_{11}. \quad (33)$$

Thus, pulsed excitation of spin $I = 3/2$, corresponding to the evolution operators $\mathbf{V}_x(\Omega_{12}, \pi)$ and $\mathbf{V}_x(\Omega_{13}, \pi)$, realizes the logical operation CNOT on virtual spins such that the spin *R* controls the dynamics of the spin *S* and vice versa.

7. READOUT OF THE COMPUTATIONAL RESULT

To find the computational result, it is necessary to read the state of the final density matrix $\boldsymbol{\rho}_{out}$. NMR methods make it possible to measure all elements of the density matrix by means of the tomography of states [7]. On account of the complexity of this method, for purposes of illustration we shall discuss here the readout in the case where the computational result $\boldsymbol{\rho}_{out}$ has the diagonal form:

$$\boldsymbol{\rho}_{out} = \mu_0 \mathbf{1} + \mu_1 \mathbf{P}_{11} + \mu_2 \mathbf{P}_{22} + \mu_3 \mathbf{P}_{33} + \mu_4 \mathbf{P}_{44}, \quad (34)$$

and the computational result is one of the states (19), i.e., only one of the quantities μ_i can be different from zero. It is proposed that a two-frequency electromagnetic pulse, which rotates the density matrix elements by the angle $\varphi_y = \pi/2$, be used to act on the spin 3/2 under study. As a result, a free-precession signal arises at the resonance frequencies Ω_{12} and Ω_{34}. The evolution operator (27) corresponding to such a pulse is

$$\begin{aligned}\mathbf{V}_3 &= \mathbf{V}_y(\Omega_{12}, \pi/2; \Omega_{34}, \pi/2)\\ &= (1/\sqrt{2})[\mathbf{1}_I + \mathbf{P}_{21} - \mathbf{P}_{12} + \mathbf{P}_{43} - \mathbf{P}_{34}].\end{aligned} \quad (35)$$

After the pulse (35) the density matrix (34) evolves under the action of the Hamiltonian (9) and acquires in the Schrödinger representation the form

$$\begin{aligned}\rho(t) &= \frac{1}{2}\{[\mu_1+\mu_2][\mathbf{P}_{11}+\mathbf{P}_{22}] \\ &+ [\mu_3+\mu_4][\mathbf{P}_{33}+\mathbf{P}_{44}] \\ &+ [\mu_1-\mu_2][\mathbf{P}_{21}\exp\{-it\Omega_{21}\}+\mathbf{P}_{12}\exp\{it\Omega_{12}\}] \\ &+ [\mu_3-\mu_4][\mathbf{P}_{43}\exp\{-it\Omega_{34}\}+\mathbf{P}_{34}\exp\{it\Omega_{34}\}]\},\end{aligned} \tag{36}$$

where time is measured from the end of the pulse (35). In a state described by the density matrix (36), oscillating quantum mechanical averages of the experimentally observed transverse components of the spin **I** appear:

$$\begin{aligned}\langle \mathbf{I}_+(t)\rangle &\equiv \langle \mathbf{I}_x + i\mathbf{I}_y\rangle = \langle \sqrt{3}(\mathbf{P}_{43}+\mathbf{P}_{23})+\mathbf{P}_{32}\rangle \\ &= \mathrm{Sp}\{\boldsymbol{\rho}(t)(\mathbf{I}_x+i\mathbf{I}_y)\} = \sqrt{3}[\mu_3-\mu_4]\exp\{-it\Omega_{34}\} \\ &+ \sqrt{3}[\mu_1-\mu_2]\exp\{-it\Omega_{12}\}.\end{aligned} \tag{37}$$

Thus, in the situation described above, precession of the nuclear spin, inducing in the detecting coil a periodic voltage on at two resonance frequencies with Fourier components $\sqrt{3}[\mu_3 - \mu_4]$ and $\sqrt{3}[\mu_1 - \mu_2]$, will arise in a plane perpendicular to the constant magnetic field. We note that the same pulse acting on the equilibrium density matrix (22) would lead to a similar precession but with the Fourier components $\sqrt{3}\,Z[\lambda_3 - \lambda_4]$ and $\sqrt{3}\,Z[\lambda_1 - \lambda_2]$. Measurement of the sign of the ratios

$$b_{34} \equiv \frac{\mu_3-\mu_4}{\lambda_3-\lambda_4}, \quad b_{12} \equiv \frac{\mu_1-\mu_2}{\lambda_1-\lambda_2}$$

of the corresponding Fourier components, following after and before the computational procedure, makes it possible to determine the final states of the two virtual spins:

if $b_{34} < 0$ and $b_{12} = 0$, the computational result is $|00\rangle$;

if $b_{34} > 0$ and $b_{12} = 0$, the computational result is $|01\rangle$;

if $b_{34} = 0$ and $b_{12} < 0$, the computational result is $|10\rangle$; and,

if $b_{34} = 0$ and $b_{12} > 0$, the computational result is $|11\rangle$.

If the operator $\boldsymbol{\rho}_{out}$ contains, together with-diagonal projection operators, nondiagonal projection operators $\mathbf{P}_{mn}$ ($m \neq n$) also, an rf pulse similar to one considered in this section generates not only free-precession signals but also spin-echo signals. The special role of the latter in logical quantum operations requires additional study.

8. CONCLUSIONS

For definiteness, we examined above a four-level energy spectrum of spin-3/2 nuclei in a constant magnetic field. A nuclear 3/2 spin is not a rarity; nuclei with such spin (^{7}Li, ^{7}Be, ^{21}Na, ^{35}Cl, ^{63}Cu, ^{65}Cu, ^{79}Br, ^{81}Br, …) appear in the most diverse and easily available substances. It was assumed that as a result of the interaction of the electric quadrupole moment of a nucleus with the gradient of the crystal field, the spin resonance absorption spectrum splits into several lines, the splitting between which is much greater than their widths. The scheme described pertains to quantum systems of any physical nature. In principle, large nuclear spins can be used for this purpose, choosing four appropriate energy levels, as well as EPR spectra with effective spin $S^* \geq 3/2$, optical energy levels, and so on. Only the expression for the resonance frequencies and matrix elements of the operators of physical quantities will change. Specifically, the nuclear quadrupole resonance spectrum, split by the interaction with a constant magnetic field ($\omega_0 < \omega_Q$), is completely suitable. This case differs from the case studied in this paper only by the relative arrangement of the spin energy levels, while the expressions (1)–(10) for the operators and eigenfunctions remain valid.

The use of four or more discrete energy levels gives, generally speaking, additional possibilities. In previously proposed schemes [4, 5] for quantum two-qubit gates of an NMR quantum computer, it was suggested that two 1/2 spins coupled by an exchange interaction be used. In order for them to function as a two-qubit gate, it must be possible experimentally to switch on an exchange interaction between different particles for a precisely fixed time and, which is even more difficult, to switch off this interaction for the time when the gate under consideration is not functioning. These times are determined by the magnitude of the exchange interaction in the material and could be so long that they are longer than the coherency period. In addition, in order to switch off the exchange interaction it is necessary to use complicated pulse sequences, which could increase the computational time substantially, expend additional energy on heating, and so on.

It was shown in the present paper that the above-indicated difficulties can be overcome by using spins greater than or equal to 3/2 for memory elements and logical elements of a quantum computer. This is expressed in the fact that two-qubit gates can be implemented on a single quantum particle, and for this reason there is no need to expend time on actuating the interaction between spatially separated particles. The required logical operations, including also the operations which previously required the presence of an exchange interaction, in the case at hand are achieved by using short rf pulses whose duration is determined by the amplitude of the rf field and is under the control of the experimenter. Actually, in our scheme the rf pulses assume the function of two-particle interactions.

Another advantage of implementing gates on a single particle is that analogs of three-particle interactions can be constructed using virtual spins. The problem is that a reversible computer operating on the principles

of classical physics requires the presence of a universal set of reversible gates, including three-bit gates. The study of ways to materialize the idea of a quantum computer, initially advanced by Feynman [8], has shown that physical systems with three-particle interactions are required in order to realize three-bit reversible gates. Such interactions do not occur in nature. This problem was circumvented in [9], where it was shown that specially designed two-qubit gates, constructed on two-particle physical interactions, are sufficient to realize an arbitrary quantum algorithm. At the same time, three-bit gates could be helpful in the future for producing compact algorithms or for other purposes. For this reason, it is of interest to propose an alternative way to produce information analogs of three-particle interactions, a method based on the idea of the present work—multilevels instead of multiparticles. The Hilbert space Γ_I of nuclei with spin $I = 7/2$ can be treated as a direct product of three Hilbert spaces of virtual spins 1/2. Therefore, the Hilbert space Γ_I of one such particle fits three qubits of information (spin 7/2 is encountered, for example, in the nuclei ^{43}Ca, ^{45}Sc, ^{49}Ti, ^{51}V, ^{121}Sb, ^{123}Sb, ^{133}Cs, …). Another variant of this method is to use physical systems with an exchange interaction between two spins one of which is greater than or equal to 3/2. This will also make it possible to obtain a physical system in a natural manner, which, even though it has a pair interaction, nonetheless contains three qubits. An example of such systems are crystals in which a double electron-nuclear resonance is observed, as well as molecules with a spin Hamiltonian of the form

$$\omega_{01}\mathbf{I}_{z1} + \frac{1}{3}\hbar\omega_Q[3\mathbf{I}_{z1}^2 - I_1(I_1+1) + \eta(\mathbf{I}_{x1}^2 - \mathbf{I}_{y1}^2)] + \omega_{02}\mathbf{I}_{z2} + J\mathbf{I}_{z1}\mathbf{I}_{z2},$$

where I_2 is any spin, and the spin $I_1 \geq 3/2$ and J is the exchange interaction constant. However, these questions require a separate analysis.

ACKNOWLEDGMENT

This work is supported by the Foundation for Scientific Research and Development Work of the Republic of Tatarstan, project no. 14-29.

REFERENCES

1. T. P. Das and E. L. Hahn, in *Solid State Physics* (Academic Press, New York, 1958), Supplement 1.
2. A. R. Kessel' and V. L. Ermakov, Pis'ma Zh. Éksp. Teor. Fiz. **70**, 59 (1999) [JETP Lett. **70**, 61 (1999)].
3. T. P. Das and A. K. Saha, Phys. Rev. **98**, 516 (1955).
4. N. A. Gershenfeld and I. L. Chuang, Science **275**, 350 (1997).
5. D. G. Cory, M. D. Price, and T. F. Havel, Physica D **120**, 82 (1998).
6. E. Knill, I. L. Chuang, and R. Laflamme, Phys. Rev. A **57**, 3348 (1998).
7. R. Laflamme, E. Knill, W. H. Zurek, *et al.*, Philos. Trans. R. Soc. London, Ser. A **356**, 1941 (1998).
8. R. P. Feynman, Int. J. Theor. Phys. **21**, 467 (1982).
9. A. Barenco, C. H. Bennett, R. Cleve, *et al.*, Phys. Rev. A **52**, 3457 (1995).

Translation was provided by AIP

Journal of Experimental and Theoretical Physics, Vol. 90, No. 3, 2000, pp. 460–469.
Translated from Zhurnal Éksperimental'noĭ i Teoreticheskoĭ Fiziki, Vol. 117, No. 3, 2000, pp. 526–536.

PLASMA, GASES

Diffusion of Charged Particles in Strong Large-Scale Random and Regular Magnetic Fields

Yu. P. Mel'nikov

Rybinsk State Aviation Technology Academy, Rybinsk, Yaroslavl oblast, 152934 Russia
e-mail: rgata@ryb.adm.yar.ru

Received June 3, 1999

Abstract—The nonlinear collision integral for the Green's function averaged over a random magnetic field is transformed using an iteration procedure taking account of the strong random scattering of particles on the correlation length of the random magnetic field. Under this transformation the regular magnetic field is assumed to be uniform at distances of the order of the correlation length. The single-particle Green's functions of the scattered particles in the presence of a regular magnetic field are investigated. The transport coefficients are calculated taking account of the broadening of the cyclotron and Cherenkov resonances as a result of strong random scattering. The mean-free path lengths parallel and perpendicular to the regular magnetic field are found for a power-law spectrum of the random field. The analytical results obtained are compared with the experimental data on the transport ranges of solar and galactic cosmic rays in the interplanetary magnetic field. As a result, the conditions for the propagation of cosmic rays in the interplanetary space and a more accurate idea of the structure of the interplanetary magnetic field are determined. © *2000 MAIK "Nauka/Interperiodica".*

1. INTRODUCTION

The investigation of the diffusion of high-energy charged particles with low density in a regular magnetic field and in a strong random magnetic field is a topical problem for the physics of cosmic rays in the interplanetary and interstellar medium [1–6], high-temperature laboratory plasma [7–10], and ionospheric plasma [11, 12]. The propagation of cosmic rays in the interplanetary and interstellar media for sufficiently low particle energies is usually investigated in the approximation of large-scale random scattering by MHD waves taking account of all cyclotron harmonics in a regular magnetic field [1–6, 13–15].

Large-scale scattering of cosmic rays in a magnetic field is usually described in the weak random scattering approximation, which consists in the fact that the scattering by cyclotron and Cherenkov resonances is slightly broadened by viscosity and the finite conductivity of the plasma. Broadening as a result of random scattering is either neglected or introduced phenomenologically [1–6], since it is assumed that it is quite weak.

Likewise, the strong regular magnetic field approximation [1–6, 13], where $R_0 \ll L_c$ and R_0 is the Larmor radius of a particle in a regular magnetic field and L_c is the correlation length of the random magnetic field, is used for large-scale random scattering. The momentum dependence, obtained in so doing, for the transport range $\Lambda_\parallel$ in the direction of the regular magnetic field for a power-law spectrum of the random field has a power-law character, $\Lambda_\parallel \propto \mathbf{p}^{2-\nu}$, where $\mathbf{p}$ is the momentum of the particle and ν is the spectral index of the correlation function of the random magnetic field.

The existence of a wide spectrum of magnetic irregularities, which scatter particles by large angles, in the interplanetary and interstellar media makes it necessary to take account of strong random scattering processes in the interaction of particles with the large-scale random magnetic field. In addition, to take Cherenkov resonance into account correctly its broadening due to strong random scattering must be taken into account [1, 4–6].

In [14–16] the nonlinear kinetic equations are investigated and, correspondingly, the broadening of resonances as a result of scattering of particles by a strong random magnetic field, produced by a set of Alfvén waves, is taken into account. These works employ an approximation similar to the diffusion approximation. General relations for the broadening of resonances are obtained in these works, but the final formulas for the transport ranges taking account of the spectral and other characteristics of the random magnetic field are not obtained. In [4] the diffusion coefficients of particles in the presence of a small-scale random, large-scale random, and regular magnetic fields were obtained, i.e., taking account of the broadening of the resonances, but the power-law spectrum of the random magnetic field was not taken into account.

In the present paper the kinetic equation obtained in a systematic theory of diffusion of cosmic rays that takes account of strong scattering of particles by large-scale irregularities of the random magnetic field, using a nonlinear collision integral, i.e., taking account of the broadening of cyclotron resonances [1, 6, 17–19], is

1063-7761/00/9003-0460$20.00

used. The collision integral is linearized using single-particle Green's functions in random and regular magnetic fields. The transport ranges parallel and perpendicular to the regular magnetic field are calculated for a power-law spectrum of the random field. The conditions under which the single-particle Green's function, obtained in various approximations, are used for linearizing the nonlinear collision integral are determined. The inflection in the momentum dependence of the transport ranges accompanying a transition from weak to strong random scattering is investigated. The theoretical results are compared with the experimental results on the transport ranges of cosmic rays in the interplanetary magnetic field. As a result, the characteristics of the regular and random components of the interplanetary magnetic field are determined more accurately.

2. GREEN'S FUNCTION OF THE LINEAR KINETIC EQUATION FOR A WEAK REGULAR FIELD

We shall study particles in a wide range of kinetic energies, including kinetic energies for which the Larmor radius in a regular magnetic field is somewhat greater than the size of the nonuniformity. In this case, we shall employ in the nonlinear collision integral the Green's function for the small-scale random field [1, 2, 17–19]. For this, we shall find first the Green's function in a small-scale random and weak regular magnetic fields.

For substitution into the nonlinear collision integral of the kinetic equation, we shall use for the distribution function averaged over the random magnetic field [17–19] the solution of the linear kinetic equation for the average Green's function $G_1(x, x_0)$:

$$\left\{\frac{\partial}{\partial t} + \mathbf{v}\frac{\partial}{\partial \mathbf{r}} - \mathbf{H}_0\mathbf{D}\right\}G_1(x, x_0) = \mathrm{St}G_1 + \delta(x - x_0), \quad (1)$$

where $x \equiv \mathbf{r}, \mathbf{p}, t$; $x_0 \equiv \mathbf{r}_0, \mathbf{p}_0, t_0$; $\mathbf{r}$, $\mathbf{v}$, and $\mathbf{p}$ are the particle coordinates, velocity, and momentum, respectively; t is the time; $\mathbf{H}_0(\mathbf{r}, t)$ is the intensity of the regular magnetic field; $\mathbf{u}$ is the velocity of the magnetic field; and, $\mathbf{D} = (e/c)[(\mathbf{v} - \mathbf{u}) \times \partial/\partial\mathbf{p}]$. The collision integral $\mathrm{St}G_1$ has the form [18, 19]

$$\mathrm{St}G_1 = D_\alpha \int dx_1 B_{\alpha\beta}(\mathbf{r}, t; \mathbf{r}_1, t_1) \times G_0(x, x_1) D_{1\beta} G_1(x_1, x_0), \quad (2)$$

where

$$\delta(x - x_0) = \delta(t - t_0)\delta(\mathbf{r} - \mathbf{r}_0)\delta(\mathbf{p} - \mathbf{p}_0),$$

and

$$G_0(\mathbf{r} - \mathbf{r}_0, t - t_0) = \theta(t - t_0)\delta(\mathbf{r} - \Delta\mathbf{r}(t - t_0) - \mathbf{r}_0) \times \delta(\mathbf{p} - \Delta\mathbf{p}(t - t_0) - \mathbf{p}_0) \quad (3)$$

is the Green's function of a particle moving in a regular magnetic field $\mathbf{H}_0$ in the absence of a random field, and $\Delta\mathbf{r}(t - t_0)$ and $\Delta\mathbf{p}(t - t_0)$ are, respectively, the change in the coordinates and momentum of a particle in a regular magnetic field over a time $t - t_0$. Summation over repeated tensor indices is performed.

We shall investigate the case $u \ll v$, so that we shall set $u = 0$. We shall consider the case of an isotropic random magnetic field, produced, for example, by a set of Alfvén waves with random phases and amplitudes. This field is described by the correlation tensors [1, 5, 6]

$$B_{\alpha\beta}(\mathbf{r}_1, t_1; \mathbf{r}_2, t_2) = \int d\mathbf{k} B(k)\left(\delta_{\alpha\beta} - \frac{k_\alpha k_\beta}{k^2}\right) \times \exp\{i\mathbf{k}\mathbf{x} - i\omega_a\tau\}, \quad (4)$$

where

$$B(k) = \frac{A_\nu k^2}{(k_0^2 - k^2)^{2+\nu/2}},$$

$$A_\nu = \frac{\Gamma(2 + \nu/2)k_0^{\nu-1}\langle H_1^2\rangle}{3\pi^{3/2}\Gamma((\nu - 1)/2)},$$

$\mathbf{r} = (\mathbf{r}_1 + \mathbf{r}_2)/2$, $\mathbf{x} = \mathbf{r}_1 - \mathbf{r}_2$, $\tau = t_1 - t_2$, $k_0 = L_c^{-1}$, $\mathbf{H}_1(\mathbf{r}, t)$ is the intensity of the random magnetic field, and $\Gamma(n)$ is the gamma function. In the present case, $\omega_a = \mathbf{v}_a\mathbf{k}_\parallel$, $\mathbf{k}_\parallel = \mathbf{H}_0(\mathbf{H}_0\mathbf{k})/H_0^2$, and $v_a \ll v$, where $\mathbf{v}_a$ is the velocity of Alfvén waves in the interplanetary magnetic field. In what follows, we neglect ω_a, i.e., we switch to the "frozen" turbulence approximation.

In the nonlinear collision integral $\mathrm{St}G$ [17–19], the Green's function $G(x, x_1)$ is integrated over $\mathbf{r}_1$ and t_1 with the correlation tensor $B_{\alpha\beta}(\mathbf{r}, t; \mathbf{r}_1, t_1)$, so that the Green's function for short times $t - t_0 \ll L_c/v$ will make the main contribution to this integral.

We shall determine the Green's function for high-energy particles in a weak regular magnetic field for the following values of the parameters: $R_0 > L_c$, $R_1 \gg L_c$, and $t - t_0 \ll L_c/v$, where R_1 is the Larmor radius in a random magnetic field. We shall switch to the Fourier transform of the Green's function $G_1(\mathbf{k}, t - t_0)$:

$$G_1(\mathbf{r} - \mathbf{r}_0, t - t_0) = (2\pi)^{-3} \times \int d\mathbf{k} G_1(\mathbf{k}, t - t_0)\exp\{i\mathbf{k}(\mathbf{r} - \mathbf{r}_0)\}.$$

Then, equation (1) for the Fourier transform of $G_1(\mathbf{k}, t - t_0)$ at short times in uniform regular and random magnetic fields can be written approximately in the form [18]

$$\left\{\frac{\partial}{\partial t} + i\mathbf{k}\mathbf{v} - i\Omega(\mathbf{h}_0\hat{\mathbf{L}})\right\}G_1(\mathbf{k}, t - t_0) = -\frac{1}{3}\omega_1^2(t - t_0)\hat{\mathbf{L}}^2 G_1(\mathbf{k}, t - t_0) + \delta(t - t_0)\delta(\mathbf{p} - \mathbf{p}_0), \quad (5)$$

where $\omega_1 = e\langle H_1^2\rangle^{1/2}/mc$ is the Larmor frequency in a random magnetic field,

$$\hat{\mathbf{L}} = -i\left[\mathbf{p}\times\frac{\partial}{\partial\mathbf{p}}\right], \quad \Omega = \frac{eH_0}{mc},$$

$$\mathbf{d} = \left[\mathbf{v}\times\frac{\partial}{\partial\mathbf{p}}\right], \quad \mathbf{h}_0 = \frac{\mathbf{H}_0}{H_0}.$$

Here the correlation tensor, normalized to 1, of the random field is chosen as follows:

$$b_{\alpha\beta}(\mathbf{x}) = \frac{1}{3}\left\{\psi(x)\delta_{\alpha\beta} + \psi_1(x)\frac{x_\alpha x_\beta}{x^2}\right\},$$

and the correlation function of the random magnetic field has the form [1]

$$\psi(z) = \left[2^{(\nu-1)/2}\Gamma\left(\frac{\nu-1}{2}\right)z\right]^{-1}\frac{\partial}{\partial z} \times [z^{(\nu+3)/2}K_{(\nu-1)/2}(z)], \tag{6}$$

where $K_\mu(z)$ is the Macdonald function. We introduce the function $g_1(\mathbf{k}, t-t_0)$ given by

$$g_1(\mathbf{k}, t-t_0) = \exp\{i\mathbf{k}\mathbf{v}(t-t_0) - i\Omega(t-t_0)(\mathbf{h}_0\hat{\mathbf{L}})\} \times G_1(\mathbf{k}, t-t_0). \tag{7}$$

In the equation obtained for $g_1(\mathbf{k})$ we neglect the term describing the decrease in the average velocity of the scattered particles, making the assumption that the squared average angle of random scattering at the correlation length is sufficiently small. We also neglect terms describing the correlation of the position of a particle in **r** space and the direction of the momentum **p** of the particle [17–19]. We factorize the solution obtained into factors related with scattering in the **r** and **p** spaces. As a result, we obtain

$$G_1(\mathbf{k}, t-t_0) = \exp\{-i\mathbf{k}\mathbf{v}(t-t_0) + i\Omega(t-t_0)(\mathbf{h}_0\hat{\mathbf{L}})\} \times \exp\left\{-\frac{1}{12}\omega_1^2(t-t_0)^4[\mathbf{v}\times\mathbf{k}]^2\right\} \times \exp\left\{-\frac{1}{6}\omega_1^2(t-t_0)^2\hat{\mathbf{L}}^2\right\}G_1(\mathbf{k}, t\longrightarrow t_0). \tag{8}$$

The operator

$$\exp\{-i\mathbf{k}\mathbf{v}(t-t_0) + i\Omega(t-t_0)(\mathbf{h}_0\hat{\mathbf{L}})\}$$

acting on the function $g_1(\mathbf{k}, t-t_0)$, changes the coordinates and momentum in accordance with the law of motion of a particle in a regular magnetic field $\mathbf{H}_0$ over time $t-t_0$ [20]. Thus, we obtain finally

$$G_1(\mathbf{k}, t-t_0) = \exp\{-i\mathbf{k}\Delta\mathbf{r}(t-t_0)\} \times \exp\left\{-\frac{1}{12}\omega_1^2(t-t_0)^4[(\mathbf{v}-\Delta\mathbf{v}(t-t_0))\times\mathbf{k}]^2\right\} \times \exp\{-\Delta\mathbf{p}(t-t_0)\frac{\partial}{\partial\mathbf{p}}\} \times \exp\left\{-\frac{1}{6}\omega_1^2(t-t_0)^2\hat{\mathbf{L}}^2\right\}G_1(\mathbf{k}, t\longrightarrow t_0). \tag{9}$$

We shall assume that cylindrical symmetry exists in a direction of the regular magnetic field. Then the exponential factors associated with the change in the coordinates and momentum of a particle in the **r** and **p** spaces can be averaged over the angle φ in the plane of cyclotron rotation of the particle in a regular magnetic field. After averaging over the angle φ, the Green's function assumes the form

$$G_1(\mathbf{k}, t-t_0) = \exp\{-i\mathbf{k}\Delta\mathbf{r}_\parallel(t-t_0)\} \times \exp\left\{-\frac{1}{12}\omega_1^2(t-t_0)^4\left[v_\parallel^2k_\perp^2 + v_\perp^2k_\parallel^2 + \frac{1}{2}v_\perp^2k_\perp^2\right]\right\} \times \exp\left\{-\frac{1}{6}\omega_1^2(t-t_0)^2\hat{\mathbf{L}}^2\right\} \times \exp\left\{-\Delta\mathbf{p}_\parallel(t-t_0)\frac{\partial}{\partial\mathbf{p}}\right\}G_1(\mathbf{k}, t\longrightarrow t_0), \tag{10}$$

where $\mathbf{v}_\parallel = \mathbf{h}_0(\mathbf{h}_0\mathbf{v})$, $\mathbf{v}_\perp = \mathbf{v} - \mathbf{v}_\parallel$, $\mathbf{k}_\parallel = \mathbf{h}_0(\mathbf{h}_0\mathbf{k})$, and $\mathbf{k}_\perp = \mathbf{k} - \mathbf{k}_\parallel$, and $\Delta\mathbf{r}_\parallel$ and $\Delta\mathbf{p}_\parallel$ are the functions $\Delta\mathbf{r}$ and $\Delta\mathbf{p}$ averaged over the cyclotron rotation angle φ, and the operator $\hat{\mathbf{L}}^2$ is also averaged over φ. It is clear from the Green's function obtained that under the action of a random magnetic field the momentum vector of a particle and the coordinate of a particle undergo "broadening" relative to its direction and trajectory of motion only in the regular magnetic field. The term proportional to $v_\parallel^2k_\perp^2$ in the argument of the exponential makes the main contribution to the "broadening" factor in the collision integral.

3. GREEN'S FUNCTION AT SHORT TIMES IN A STRONG REGULAR MAGNETIC FIELD

We shall now find the Green's function of a particle in strong regular and weak random magnetic fields. For this, we shall find the change in the momentum and coordinate of a particle in a weak random magnetic field in the presence of a strong regular magnetic field. We introduce the unit vector of the total magnetic field:

$$\mathbf{h}(\mathbf{r}) = \mathbf{h}_0 + \Delta\mathbf{h}(\mathbf{r}), \quad \Delta\mathbf{h} = \mathbf{H}_1/H_0, \quad |\mathbf{h}_0 + \Delta\mathbf{h}(\mathbf{r})| = 1,$$

where $\Delta\mathbf{h}(\mathbf{r})$ is the relative vector of the random magnetic field. Thus, the random component of the magnetic field is directed for small $\Delta\mathbf{h}$ almost perpendicular to $\mathbf{h}_0$. We shall assume that the random magnetic field is quite weak, and we shall find the solution of the dynamical equation taking into account only the first order in $\Delta\mathbf{h}_0/\mathbf{h}_0$. Then, the relative vector of the random magnetic field can be represented as

$$\Delta\mathbf{h} = \Delta\mathbf{h}_{\perp 1} + \Delta\mathbf{h}_{\perp 2}, \quad \Delta\mathbf{h}_{\perp 1} + \Delta\mathbf{h}_{\perp 2},$$

where $\Delta\mathbf{h}_{\perp 1}$ and $\Delta\mathbf{h}_{\perp 2}$ are independent random components of $\Delta\mathbf{h}$, which lie in a plane perpendicular to $\mathbf{h}_0$. We shall neglect the random change in the modulus of the magnetic field $\mathbf{H}$ and the random change in the momentum of a particle parallel to the regular magnetic field $\mathbf{H}_0$. In this case, the iteration solution of the equation of motion of a particle can be written in the form

$$\mathbf{p} = \mathbf{p}_1 + \Omega(t - t_0)\mathbf{p}_{0\parallel} \times \Delta\mathbf{h}, \tag{11}$$

where

$$\mathbf{p}_1 = \mathbf{p}_0 + \mathbf{p}_{0\perp}(\cos\Omega(t - t_0) - 1) + \mathbf{p}_0 \times \mathbf{h}_0 \sin\Omega(t - t_0).$$

This solution neglects particles trapped in a magnetic bottle and takes account of only the scattered transmitted particles [1, 6]. The solution (11) is found at distances of the order of R_0, at which we assume for the large-scale field $\Delta\mathbf{h}$ = const.

The coordinates of the particle change as follows:

$$\mathbf{r} - \mathbf{r}_0 = \mathbf{r}_1 + \frac{1}{2}\Omega(t - t_0)^2 \mathbf{v}_{0\parallel} \times \Delta\mathbf{h}, \tag{12}$$

where

$$\mathbf{r}_1 = \mathbf{v}_{0\parallel}(t - t_0) + \frac{\mathbf{v}_{0\perp}}{\Omega}\sin\Omega(t - t_0) \times \frac{\mathbf{v}_0 \times \mathbf{h}_0}{\Omega}(\cos\Omega(t - t_0) - 1).$$

Neglecting in the Green's function obtained the factors related with the correlation terms between the $\mathbf{r}$ and $\mathbf{p}$ spaces, we represent the Green's function of the particle in a strong regular magnetic field in the form

$$G_s(x, x_0) = \theta(t - t_0) \times \langle \delta(\mathbf{r} - \mathbf{r}_0 - \mathbf{r}_1 - (1/2)\Omega(t - t_0)^2 \mathbf{v}_{0\parallel} \times \Delta\mathbf{h}) \rangle_{\Delta\mathbf{h}} \times \langle \delta(\mathbf{p} - \mathbf{p}_1 - \Omega(t - t_0)^2 \mathbf{p}_{0\parallel} \times \Delta\mathbf{h}) \rangle_{\Delta\mathbf{h}}, \tag{13}$$

where $\langle \ldots \rangle_{\Delta\mathbf{h}}$ signifies averaging over the components of the random magnetic field $\Delta\mathbf{h}_{\perp 1}$ and $\Delta\mathbf{h}_{\perp 2}$, which are assumed to be independent.

We now switch in the coordinate space to the Fourier transform of the average Green's function in $\mathbf{k}$ space. After averaging over the direction of the relative vector $\Delta\mathbf{h}$ of the random magnetic field and performing transformations, the Green's function (13) can be written in the form

$$G_s(x, x_0) = \theta(t - t_0) G_{sr}(t - t_0) G_{sp}(t - t_0), \tag{14}$$

where

$$G_{sr}(\tau) = (2\pi)^{-3} \int d\mathbf{k} \times \exp\left\{ -\frac{1}{16}\omega_1^2 \tau^4 \mathbf{v}_{0\parallel}^2 (\mathbf{k}_{\perp 1}^2 + \mathbf{k}_{\perp 2}^2) \right\} \times \exp\left\{ i\mathbf{k}\left(\mathbf{r} - \mathbf{r}_0 - \mathbf{v}_{0\parallel}\tau - \frac{\mathbf{v}_{0\perp 1}}{\Omega}\sin\Omega\tau + \frac{\mathbf{v}_{0\perp 2}}{\Omega}(\cos\Omega\tau - 1) \right) \right\}, \tag{15}$$

$$G_{sp}(\tau) = (2\pi)^{-3} \int d\mathbf{q} \times \exp\left\{ -\frac{1}{16}\omega_1^2 \tau^4 \mathbf{p}_{0\parallel}^2 (\mathbf{q}_{\perp 1}^2 + \mathbf{q}_{\perp 2}^2) \right\} \times \exp\{ i\mathbf{q}(\mathbf{p} - \mathbf{p}_0 - \mathbf{p}_{0\perp 1}(\cos\Omega\tau - 1) - \mathbf{p}_{0\perp 2}\sin\Omega\tau) \}, \tag{16}$$

and $\mathbf{q}_{\perp 1}$, $\mathbf{q}_{\perp 2}$, and $\mathbf{k}_{\perp 1}$, $\mathbf{k}_{\perp 2}$ are the projections of the vectors $\mathbf{q}$ and $\mathbf{k}$ in the plane perpendicular to $\mathbf{h}_0$. The Green's function $G_s(x, x_0)$ (14) obtained for the case of a strong regular magnetic field is essentially identical to the Green's function $G_1(x, x_0)$ (10) for a weak regular field. Only the rate of random scattering decreases somewhat. This rate is related in the argument of the exponential with the factors

$$-\frac{1}{16}\omega_1^2 \tau^4 \mathbf{p}_{0\parallel}^2 (\mathbf{q}_{\perp 1}^2 + \mathbf{q}_{\perp 2}^2),$$

$$-\frac{1}{16}\omega_1^2 \tau^4 \mathbf{v}_{0\parallel}^2 (\mathbf{k}_{\perp 1}^2 + \mathbf{k}_{\perp 2}^2).$$

For this reason, we shall employ the formulas for the transport ranges of particles with energies for which the condition of magnetization will hold for all practical purposes.

4. TRANSPORT COEFFICIENTS TAKING ACCOUNT OF STRONG RANDOM SCATTERING

We shall now find the transport coefficients appearing in the collision integral for the large-scale random magnetic field. We employ the kinetic equation for the distribution function $F(x, x_0)$ [17–19]

$$\left\{ \frac{\partial}{\partial t} + \mathbf{v}\frac{\partial}{\partial \mathbf{r}} - \mathbf{H}_0 \mathbf{D} \right\} F(x, x_0) = \mathrm{St}F \tag{17}$$

with the nonlinear collision integral in the form

$$\mathrm{St}F = D_\alpha \int dx_1 B_{\alpha\beta}(\mathbf{r}, t; \mathbf{r}_1, t_1) G_s(x, x_1) D_{1\beta} F(x, x_0),$$

where the function (14) for a strong regular field is chosen as the Green's function in the integrand. The equation (17) takes into account small-angle random scattering microprocesses and simple strong random scattering microprocesses [18–20]:

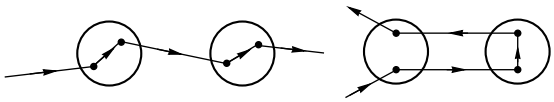

Averaging equation (17) over the Larmor rotation of particles in a regular magnetic field, taking account of the condition $H_1 \ll H_0$ [1–6], we obtain

$$\left\{\frac{\partial}{\partial t} + \nu\mu\frac{\partial}{\partial z} - \frac{1}{2}\nu \mathrm{div}\mathbf{h}_0 \sin\vartheta \frac{\partial}{\partial\vartheta}\right\}\Phi = \langle \mathrm{St}F\rangle_\varphi, \quad (18)$$

where $\Phi = \langle F\rangle_\varphi$, ϑ is the angle between the vectors $\mathbf{p}$ and $\mathbf{h}_0$, $\mu = \cos\vartheta$, φ is the azimuthal angle of the vector $\mathbf{p}$ in a plane perpendicular to $\mathbf{h}_0$, and z is the coordinate in the direction $\mathbf{h}_0$. In this equation the average collision integral is

$$\langle \mathrm{St}F\rangle_\varphi = \frac{\partial}{\partial\mu}(1-\mu^2) b(\mu) \frac{\partial}{\partial\mu}\Phi(\mathbf{r}, p, \mu, t), \quad (19)$$

where

$$b(\mu) = \int_0^\infty d\tau \int d\mathbf{k} B(k) \times \left[\cos\Omega\tau + \frac{k_\perp^2}{k^2}\sin\varphi\sin(\Omega\tau - \varphi)\right] \times \exp\left\{-\frac{1}{16}\omega_1^2\tau^4 \nu_\parallel^2 k_\perp^2\right\} \times \cos\{ik_\parallel \nu_\parallel \tau + k_\perp R_\perp[\sin(\Omega\tau - \varphi) + \sin\varphi]\},$$

and $R_\perp = \nu_\perp/\Omega$, φ is the angle between $\mathbf{k}_\perp$ and $\mathbf{v}_\perp$.

In the derivation of the formula for $b(\mu)$ it was assumed that the collision integral averaged over the Larmor rotation of particles in a regular field can be written as a product of the average scattering operator and the average distribution function. Likewise, we neglect the additional random scattering in $\mathbf{p}$ space, given by the function $G_s(x, x_1)$ in the integrand. In these approximations, the terms which are not taken into account in the final expression for the transport range (19) are of the order of $\langle H_1^2\rangle / H_0^2 \ll 1$.

In the formula for $b(\mu)$ (19) we expand the exponential with imaginary argument in a series in Bessel functions. The series of products of Bessel functions so obtained can be summed exactly using the addition formulas for Bessel functions [21, 22]:

$$J_n(\rho)\exp\left\{in\frac{\beta}{2}\right\} = \sum_{k=-\infty}^{k=+\infty} J_{n+k}(z) J_k(z) \exp\{ik\beta\}, \quad (20)$$

where $\rho = 2z\sin\{\beta/2\}$ and $J_n(\rho)$ is a Bessel function of order n. After summation, the expression for the transport coefficient $b(\mu)$ can be written in the form

$$b(\mu) = b_1(\mu) + b_2(\mu), \quad (21)$$

where

$$b_1(\mu) = \frac{\pi e^4 A_\nu}{4m^2c^2}\int_0^\infty d\tau \int_0^\infty dk_\perp \times \int_{-\infty}^\infty dk_\parallel \frac{k_\perp k^2}{(k_0^2 + k^2)^{2+\nu/2}} J_0(\rho_\perp)\exp\left\{-\frac{1}{16}\omega_1^2\tau^4\nu_\parallel^2 k_\perp^2\right\} \times [\exp\{i(k_\parallel\nu_\parallel + \Omega)\tau\} + \exp\{i(k_\parallel\nu_\parallel - \Omega)\tau\}], \quad (22)$$

$$b_2(\mu) = \frac{\pi e^4 A_\nu}{4m^2c^2}\int_0^\infty d\tau \int_0^\infty dk_\perp \times \int_{-\infty}^\infty dk_\parallel \frac{k_\perp^3}{(k_0^2 + k^2)^{2+\nu/2}} \cos\{k_\parallel\nu_\parallel\tau\} \times \exp\left\{-\frac{1}{16}\omega_1^2\tau^4\nu_\parallel^2 k_\perp^2\right\} \times [J_2(\rho_\perp)\cos 2\Omega\tau - J_0(\rho_\perp)\cos\Omega\tau], \quad (23)$$

$$\rho_\perp = 2k_\perp R_\perp \sin\left\{\frac{\Omega\tau}{2}\right\}.$$

Integrating over the inner variables, we obtain

$$b_1(\mu) = \frac{\pi^2 e^2 A_\nu |\nu_\parallel|^{\nu-1}\Gamma\left(\frac{\nu+1}{2}\right)}{4m^2c^2\Omega^\nu\Gamma\left(1+\frac{\nu}{2}\right)} \times \int_{-\infty}^\infty \frac{dz\exp[-|z|]}{\left[\left(1 + \frac{\omega_1 z}{4k_0|\nu_\parallel|}\right)^2 + k_0^2 R_\perp^2 \frac{\nu_\parallel^2}{\nu_\perp^2}\right]^{(\nu+1)/2}}. \quad (24)$$

We do not present the expression for $b_2(\mu)$, since for $\nu_\perp \gtrsim \nu_\parallel$ the function $b_2(\mu)$ is much less than $b_1(\mu)$, and

in what follows we shall neglect $b_2(\mu)$. Taking account of the expression for $b_1(\mu)$ (24) for $k_0 v_\parallel \ll \omega_1$, $k_0^2 R_\perp^2 v_\parallel^2 v_\perp^{-2} \ll 1$, and $k_0 v_\parallel \approx \omega_1$, and also for $k_0 v_\parallel \gg \omega_1$, the approximate expression for the transport coefficient $b(\mu)$ can be written finally in the form

$$b(\mu) = \frac{\pi^2 e^2 A_\nu}{m^2 c^2}\left[\frac{\Gamma\left(\frac{\nu+1}{2}\right)|\nu|^{\nu-1}}{2\Gamma\left(1+\frac{\nu}{2}\right)\Omega^\nu} + \frac{2\sqrt{\pi}}{\nu\omega_1 k_0^{\nu-1}}\exp\left\{-\frac{4R_1|\mu|}{L_c}\right\}\right]. \quad (25)$$

The expression obtained for $b(\mu)$ takes account of all cyclotron harmonics, including the zeroth harmonic corresponding to a Cherenkov resonance. It is obvious from this formula that the dependence of the coefficient $b(\vartheta)$ on the angle ϑ for $R_1 \gg L_c$ is qualitatively of the same form as the dependence $b(\vartheta)$ displayed graphically in [1]. It also follows from equation (25) that the ratio of the maximum value of $b(\vartheta)$ to its minimum value was of the order of $\Omega L_c^{\nu-1}/\omega_1 R_0^{\nu-1}$. For this reason, the Cherenkov resonance can be observed only if the random field is sufficiently weak. The width of the Cherenkov resonance is inversely proportional to R_1.

5. TRANSPORT RANGE IN THE DIRECTION OF THE REGULAR MAGNETIC FIELD

We shall use the diffusion approximation to calculate the transport range [1, 2, 5, 6]. We shall represent the distribution function $\Phi(\mathbf{r}, p, \mu, t)$ in the form

$$\Phi(\mathbf{r}, p, \mu, t) = N(\mathbf{r}, p, t)/4\pi + \delta\Phi(\mathbf{r}, p, \mu, t).$$

We substitute this expansion into the kinetic equation (17) and, taking account of the transport coefficient (25), the integration over the angle, and the symmetry properties of the terms appearing in this equation, as well as the smallness of $\delta\Phi$, we obtain the following formula for the transport range in the direction of the regular magnetic field:

$$\Lambda_\parallel = \frac{6R_1^2 L_c^{\nu-1}}{\sqrt{\pi}\left(1+\frac{\nu}{2}\right)(\nu-1)R_0^\nu}\int_0^1 d\mu(1-\mu^2) \times\left[1+\frac{2\sqrt{\pi}\left(\frac{\nu}{2}\right)R_1 L_c^{\nu-1}}{\Gamma\left(\frac{\nu+1}{2}\right)R_0^\nu}\exp\left\{-\frac{4R_1\mu}{L_c}\right\}\right]^{-1}. \quad (26)$$

It follows from this formula that for sufficiently large particle momenta and weak random magnetic fields, for which

$$\ln(R_1/R_0) + (\nu-1)\ln(L_c/R_0) \ll 3^{1/2}R_1/L_c - 1,$$

the transport range is

$$\Lambda_\parallel = 8R_1^2 L_c^{\nu-1}/\sqrt{3\pi}(\nu-1)(1+\nu/2)R_0^\nu. \quad (27)$$

Here the numerical factor is somewhat greater than the value obtained in [1]. It is clear from the expression (27) that for weak random magnetic fields and $\nu = 2$ the transport range does not depend on the particle energy and is proportional to the size L_c of the magnetic nonuniformity multiplied by the ratio $H_0^2/\langle H_1^2\rangle$.

Using the expression (26), we shall estimate the parallel transport range for cosmic rays of moderate energies with $E = 0.1$ GeV, propagating in the interplanetary space. Taking $R_0 = 3\times10^8$ m, $R_1 = 10^9$ m, $L_c = 6\times10^8$ m, and $\nu = 2$ [23, 24], we obtain $\Lambda_\parallel = 2\times10^{10}$ m. The value obtained for the transport range is essentially independent of the energy and the type of scattered particles, and it agrees with most experimental results presented in [1, 25–27] for cosmic rays with energies 0.05–0.5 GeV.

For sufficiently low particle energies, $R_1 \ll L_c$, the expression for the transport range (26) becomes

$$\Lambda_\parallel = \frac{2\Gamma((\nu-1)/2)R_1}{\pi\Gamma(\nu/2)(1+\nu/2)}. \quad (28)$$

Such or a close momentum dependence of the transport range is often observed for galactic cosmic rays with energies 2–20 GeV propagating in the interplanetary space [27–30]. The sector structure and other large-scale irregularities of the interplanetary magnetic field make the main contribution to the scattering. The values of $\Lambda_\parallel$ calculated using the expression (26) will be close to the experimentally observed values in the interplanetary space for random magnetic field intensities approximately ten times lower than the intensity of the regular magnetic field, but for large values of the correlation length, $L_c \gtrsim 10^9$ m.

6. DIFFUSION OF PARTICLES PERPENDICULAR TO A REGULAR MAGNETIC FIELD TAKING ACCOUNT OF STRONG RANDOM SCATTERING

6.1. Diffusion of Particles in a Moderate Random Magnetic Field

We shall use the method proposed in [1] to determine the transverse diffusion coefficient in a large-scale random magnetic field. Assuming the large-scale random field to be sufficiently weak and neglecting the acceler-

ation of the particles, we obtain for the transverse diffusion coefficient $\kappa_{\alpha\beta}^{\perp}$ [1]

$$\kappa_{\alpha\beta}^{\perp} = \frac{1}{H_0^2}\int dq' G_q(q, q') v_{\parallel} v_{\parallel}' \times \langle H_{\perp\alpha}(\mathbf{r}, t) H_{\perp\beta}(\mathbf{r}', t')\rangle, \tag{29}$$

where $q \equiv \mathbf{r}, \mu, t$; $q' \equiv \mathbf{r}', \mu', t'$; and, $\langle H_{\perp\alpha}(\mathbf{r}, t) H_{\perp\beta}(\mathbf{r}', t')\rangle$ is the correlation tensor of the perpendicular components of the random magnetic field $\mathbf{H}_1$, and $v_{\parallel} = v\mu$. The Green's function $G_q(q, q')$ is a solution of the equation

$$\left\{\frac{\partial}{\partial t} + v_{\parallel}\left(\mathbf{h}_0 \frac{\partial}{\partial \mathbf{r}}\right) - \hat{S}\right\} G_q(q, q') = \delta(t - t')\delta(\mathbf{r} - \mathbf{r}')\delta(\mu - \mu'), \tag{30}$$

where $\hat{S}$ is the large-scale scattering operator [1, 5, 6],

$$\hat{S} = \frac{\partial}{\partial \mu}(1 - \mu^2) b(\mu) \frac{\partial}{\partial \mu}. \tag{31}$$

The expression obtained for the transverse diffusion coefficient $\kappa_{\alpha\beta}^{\perp}$ must be averaged over the angle ϑ.

We shall first analyze the case of moderate random scattering. In this case, the Green's function with average angles of random scattering of the order of 1 and short times makes the main contribution to the integral (29). The spatial part of the Green's function makes the main contribution to the transverse diffusion coefficient. For this reason, we shall choose the Green's function in the integrand in the short-time approximation in the form (15)

$$G_q(q, q') = \theta(t - t') G_{sr}(\mathbf{r}, t; \mathbf{r}', t')\delta(\mu - \mu'). \tag{32}$$

Substituting the correlation tensor of the perpendicular components of the random magnetic field and the Green's function (32) into the integral (29), we obtain

$$\kappa_{\alpha\beta}^{\perp} = \frac{v_{\parallel}^2 \langle H_1^2\rangle}{3H_0^2}\varphi_1(\delta_{\alpha\beta} - h_{0\alpha}h_{0\beta}) + \frac{v_{\parallel}^2 \langle H_1^2\rangle}{3H_0^2}\hat{\varphi}_2\left\{\frac{x_\alpha x_\beta}{x^2} - \frac{(\mathbf{x}\mathbf{h}_0)^2}{x^2}h_{0\alpha}h_{0\beta}\right\}, \tag{33}$$

where the function φ_1 has the form

$$\varphi_1 = \int_0^{\infty} d\tau \int d\mathbf{x} \int \frac{d\mathbf{k}}{8\pi^3} \exp\{i\mathbf{k}(\mathbf{x} - \mathbf{v}_{\parallel}\tau)\} \times \exp\left\{-\frac{1}{16}\omega_1^2 \tau^4 v_{\parallel}^2 k_{\perp}^2\right\} \psi\left(\frac{x}{L_c}\right), \tag{34}$$

and the operator $\hat{\varphi}_2$ can be written in the form

$$\hat{\varphi}_2\left\{\frac{x_\alpha x_\beta}{x^2} - \frac{(\mathbf{x}\mathbf{h}_0)^2}{x^2}h_{0\alpha}h_{0\beta}\right\} = \int_0^{\infty} d\tau \int d\mathbf{x} \int \frac{d\mathbf{k}}{(2\pi)^3} \exp\{i\mathbf{k}(\mathbf{x} - \mathbf{v}_{\parallel}\tau)\} \times \exp\left\{-\frac{1}{16}\omega_1^2 \tau^4 v_{\parallel}^2 k_{\perp}^2\right\} \times \left[\frac{x_\alpha x_\beta}{x^2} - \frac{(\mathbf{x}\mathbf{h}_0)^2}{x^2}h_{0\alpha}h_{0\beta}\right] \psi\left(\frac{x}{L_c}\right). \tag{35}$$

Let us consider the function φ_1. Performing in equation (34) the integration over the inner variable and assuming perpendicular diffusion to be sufficiently weak, we represent φ_1 in the form [1, 6]

$$\varphi_1 = \begin{cases} \dfrac{\sqrt{\pi}\Gamma(\nu/2) L_c}{2\Gamma((\nu-1)/2)|v_{\parallel}|} & \text{for } |\mu| R_1 \gg L_c, \\ \dfrac{\pi}{v}\sqrt{\dfrac{R_1 L_c}{|\mu|}} & \text{for } |\mu| R_1 \lesssim L_c. \end{cases} \tag{36}$$

Using the expression obtained for φ_1, we shall calculate the first term in the perpendicular diffusion coefficient (33) and average it over the angle ϑ. Next, we shall find the second term, proportional to $\hat{\varphi}_2$, appearing in the perpendicular diffusion coefficient $\kappa_{\alpha\beta}^{\perp}$ (33). As a result, it turns out that the second term is much smaller than the first term, so that it can be neglected. The final expressions for the transverse diffusion coefficient and the transverse transport range in a moderate random magnetic field have the form

$$\kappa_{\alpha\beta}^{\perp} = \frac{\Lambda_{\perp} v}{3}(\delta_{\alpha\beta} - h_{0\alpha}h_{0\beta}),$$

$$\Lambda_{\perp} = \begin{cases} \dfrac{\sqrt{\pi}\Gamma(\nu/2)\langle H_1^2\rangle L_c}{2\Gamma((\nu-1)/2) H_0^2} & \text{for } R_1 \gg L_c, \\ \dfrac{8\pi\langle H_1^2\rangle}{5H_0^2}\sqrt{R_1 L_c} & \text{for } R_1 \lesssim L_c. \end{cases} \tag{37}$$

The expressions obtained for the diffusion coefficient and the transport range for a weak random magnetic field $R_1 \gg L_c$ are identical to the results obtained in [1, 6]. For a moderate random magnetic field and low particle energies, $R_1 \lesssim L_c$, the transport range is $\Lambda_{\perp} \propto p^{1/2}$.

We shall now compare the computational results and the experimental data. The experimental results obtained, by various methods, for the transverse diffu-

sion coefficient of cosmic rays in the interplanetary magnetic field are reviewed in [26]. As a result, it was agreed that the transverse transport length of solar cosmic rays with energy of the order of 100 MeV is about 10^9 m and essentially independent of the particle energy. Setting the particle energy equal to 100 MeV, $L_c = 0.5 \times 10^9$ m, $R_1 = 10^9$ m, and using the relation $\langle H_1^2 \rangle / H_0^2 = 0.1$, the transport range $\Lambda_\perp$, calculated from equation (37), for $R_1 \gg L_c$ is 0.5×10^8 m, and for moderate random scattering $R_1 \lesssim L_c$ it is equal to 0.3×10^9 m and essentially independent of particle energy, $\Lambda_\perp \propto p^{1/2}$. Thus, the estimates for moderate random scattering are more suitable.

The ratio of the transverse to the longitudinal transport range is also determined in the experiments [26]. We shall find this ratio using the expressions obtained for $\Lambda_\perp$ and $\Lambda_\parallel$, equations (26) and (37). As a result, we obtain

$$\frac{\Lambda_\parallel}{\Lambda_\perp} = \begin{cases} \dfrac{\pi\Gamma(\nu/2)(1+\nu/2)(\nu-1)R_0^{\nu+2}}{4\sqrt{3}\Gamma((\nu-1)/2)R_1^4 L_c^{\nu-2}} & \text{for } R_1 \gg L_c, \\ \dfrac{4\pi^{3/2}(1+\nu/2)(\nu-1)R_0^{\nu+2}}{5\sqrt{3}R_1^{7/2}L_c^{\nu-3/2}} & \text{for } R_1 \lesssim L_c. \end{cases} \quad (38)$$

The expression (27), which is applicable for R_1 somewhat less than L_c, is used for $\Lambda_\parallel$ in the second value of the ratio $\Lambda_\perp/\Lambda_\parallel$. Substituting into equation (38) $L_c = 0.5 \times 10^9$ m, $R_1 = 10^9$ m, $R_0 = 0.3 \times 10^9$ m, and $\nu = 2$ for particle energies 100 MeV we obtain $\Lambda_\perp/\Lambda_\parallel = \langle H_1^4 \rangle / 2H_0^4 = 0.005$ for $R_1 \gg L_c$ and $\Lambda_\perp/\Lambda_\parallel = 5R_0^{1/2} \langle H_1^2 \rangle / H_0^2 L_c^{1/2} = 0.14$ for $R_1 \lesssim L_c$.

According to experiments [26], the ratio $\Lambda_\perp/\Lambda_\parallel$ of the transverse to the longitudinal transport range lies in the range 0.01–0.2, and the average value is 0.1. It follows from the expression (38) that for weak random scattering the ratio $\Lambda_\perp/\Lambda_\parallel$ depends primarily on the ratio $\langle H_1^4 \rangle / H_0^4$ and is of the order of 0.01. Such a value of the ratio $\Lambda_\perp/\Lambda_\parallel$ is observed experimentally, but it is much less than the average value 0.1 adopted [26]. For moderate random scattering, the ratio $\Lambda_\perp/\Lambda_\parallel$ determined from equation (38) is close to the average value adopted.

It is also clear from equation (38) that the ratio $\Lambda_\perp/\Lambda_\parallel$ increases as the average deflection angle in a single random scattering microprocess increases.

6.2. Diffusion of Cosmic Rays in the Case of Strong Random Scattering

We shall determine the transverse diffusion coefficient in the extreme case of very strong random scattering for $R_1 \ll L_c$. In this approximation the particles are strongly scattered at the correlation length, and the diffusion approximation can be used to determine the Green's function [1, 6]:

$$\mathcal{G}(\mu) = \mathcal{G}_0 + \delta\mathcal{G}(\mu), \quad |\delta\mathcal{G}| \ll \mathcal{G}_0, \qquad \int_{-1}^{+1} d\mu \delta\mathcal{G}(\mu) = 0. \quad (39)$$

In this case the diffusion coefficient $\kappa_{\alpha\beta}^\perp$ is determined by the formula

$$\kappa_{\alpha\beta}^\perp = \frac{\kappa_\parallel}{H_0^2} \int_{-\infty}^{t} dt' \int d\mathbf{r}' \langle H_{\perp\alpha}(\mathbf{r}, t) H_{\perp\beta}(\mathbf{r}', t') \rangle \frac{\partial G_g}{\partial t}, \quad (40)$$

where

$$\kappa_\parallel = \frac{\Lambda_\parallel v}{3}, \quad \Lambda_\parallel = \frac{3}{8} v \int_{-1}^{+1} d\mu \frac{1-\mu^2}{b(\mu)},$$

and the Green's function $G_g(r, t; r', t')$ is the solution of the equation

$$\left\{ \frac{\partial}{\partial t} - k_\parallel \left(\mathbf{h}_0 \frac{\partial}{\partial \mathbf{r}} \right)^2 \right\} G_g(\mathbf{r}, t; \mathbf{r}', t') = \delta(t-t')\delta(\boldsymbol{r} - \mathbf{r}'). \quad (41)$$

Substituting $G_g(\mathbf{r}, t; \mathbf{r}', t')$ into equation (40), we obtain an expression for the transverse diffusion coefficient $\kappa_{\alpha\beta}^\perp$ and the transverse transport range $\Lambda_\perp$. The transport range $\Lambda_\perp$ in the approximation $R_1 \ll L_c$, taking account of the strong random scattering [18], can be written in the form

$$\Lambda_\perp = \frac{4\Gamma((\nu-1)/2) R_0 \langle H_1^2 \rangle^{1/2}}{3\pi\Gamma(\nu/2)(1+\nu/2) H_0}. \quad (42)$$

Thus, in the limit of very strong random scattering the transverse transport range (42) $\Lambda_\perp \approx R_0 \langle H_1^2 \rangle^{1/2} / H_0$, and its numerical value for the parameters of the interplanetary medium $\langle H_1^2 \rangle^{1/2} / H_0 = 0.3$ and $R_0 = 0.3 \times 10^9$ m is of the order of 10^8 m. This value of the transverse transport range $\Lambda_\perp$ is an order of magnitude less than the experimental average value, but it is sometimes observed in experiments [26]. The ratio $\Lambda_\perp/\Lambda_\parallel$ calculated using equations (28) and (42) is for very strong random scattering

$$\Lambda_\perp/\Lambda_\parallel = 2\langle H_1^2 \rangle / 3H_0^2 \approx 0.067, \quad (43)$$

i.e., it falls within the range of the numerical values of the experimental data [26]. This result also confirms the conclusion that as the average deflection angle in a single random scattering microprocess increases, the ratio $\Lambda_\perp/\Lambda_\parallel$ increases.

7. DISCUSSION AND CONCLUSIONS

The results obtained above and the approximations used make it possible to draw the following conclusions. The use of the nonlinear kinetic equation for describing strong random large-scale scattering makes it possible to obtain final formulas for the average collision integral and transport range parallel and perpendicular to the regular magnetic field which are close to the formulas obtained in [1–6], in the weak random field limit. In contrast to the preceding works, in the present work exact summation of all cyclotron resonances was performed, taking account of the broadening of the resonances, using a summation theorem for Bessel functions. It was also shown that the additional functional factors in the nonlinear collision integral which are related with the broadening of resonances as a result of the strong small-scale and strong large-scale random scattering are quantitatively close to one another.

The computed parallel transport range is $\Lambda_\| \approx L_c^{\nu-1} R_1^2 R_0^{-\nu}$ in the weak random scattering limit, and $\Lambda_\| \approx R_1$ in the strong random scattering limit. This result is due to the fact that as the energy of the particles decreases, the strong, random, small-scale scattering makes the main contribution [17–19]. The perpendicular transport range in the weak random scattering limit is $\Lambda_\perp \approx L_c \langle H_1^2 \rangle / H_0^2$, for moderate random scattering $\Lambda_\perp \approx L_c^{1/2} R_1^{1/2} \langle H_1^2 \rangle / H_0^2$, and for strong random scattering $\Lambda_\perp \approx R_0 \langle H_1^2 \rangle^{1/2}/H_0$. The ratio $\Lambda_\perp/\Lambda_\|$ computed in this work in the weak random scattering limit (for $\nu = 2$) is of the order of $\langle H_1^4 \rangle / H_0^4$, for moderate random scattering $\Lambda_\perp/\Lambda_\| \approx 5 R_0^{\nu-3/2} \langle H_1^2 \rangle / H_0^2 L_c^{\nu-3/2}$, and for strong random scattering $\Lambda_\perp/\Lambda_\| = 2 \langle H_1^2 \rangle / 3 H_0^2$.

The experimental results on the longitudinal transport range of solar cosmic rays with energies 0.05–1 GeV in the interplanetary space [25–30] can be described well by the results of the present work, obtained in Sec. 5, in the weak and moderate random scattering limits (26), (27). The experimental data on the transverse transport range can be described well by the results of this work in the moderate random scattering limit; see equation (37). The ratio $\Lambda_\perp/\Lambda_\|$ obtained in the present paper agrees better with the experimental results for moderate and strong random scattering; see equations (38) and (43).

In summary, the results obtained here agree with the model of a filamentary structure of the interplanetary magnetic field with transverse size of the "filaments" of the order of 10^9 m, which agrees with the experimental results [27–32]. It can be assumed on the basis of the results of this work that a particle moving along a "filament" undergoes weak random scattering associated with the entanglement of the "filaments," and when a particle transfers from one "filament" to another in the process of transverse drift, it undergoes moderate random scattering, associated with the difference of the magnetic fields in neighboring "filaments."

The experimental results on the longitudinal transport range of cosmic rays with energies 2–20 GeV can be described by the results of the present work in the strong random scattering limit (see equation (28)), for random magnetic field intensity less than the intensity of the regular magnetic field, but for large values of the correlation length.

ACKNOWLEDGMENTS

In conclusion, I thank A.Z. Dolginov, I.N. Toptygin, and V.N. Fedorenko for a discussion of certain aspects of this work.

REFERENCES

1. I. N. Toptygin, *Cosmic Rays in Interplanetary Magnetic Fields* (Nauka, Moscow, 1983).
2. L. I. Dorman, *The Experimental and Theoretical Principles of the Astrophysics of Cosmic Rays* (Nauka, Moscow, 1975).
3. V. S. Berezinskiĭ, S. V. Bulanov, V. L. Ginzburg, *et al.*, *The Astrophysics of Cosmic Rays*, Ed. by V. L. Ginzburg (Nauka, Moscow, 1984).
4. L. G. Chuvilgin and V. S. Ptuskin, Astron. Astrophys. **279**, 278 (1993).
5. B. A. Gal'perin, I. N. Toptygin, and A. A. Fradkin, Zh. Éksp. Teor. Fiz. **60**, 972 (1971) [Sov. Phys. JETP **33**, 526 (1971)].
6. I. N. Toptygin, Astrophys. Space Sci. **20**, 329 (1973).
7. M. N. Rosenbluth, R. Z. Sagdeev, J. B. Teylor, *et al.*, Nucl. Fusion **6**, 297 (1966).
8. V. V. Kadomtsev and O. P. Pogutse, in *Proceedings of the 7th International Conference on Plasma Physics and Controlled Nuclear Fusion Research* (IAEA, Vienna, 1978), Vol. 1, p. 649.
9. J. A. Krommes, C. Oberman, and R. G. Kleva, J. Plasma Phys. **30**, 11 (1983).
10. A. V. Nedospasov and M. Z. Tokar', in *Reviews of Plasma Physics*, Ed. by V. V . Kadomtsev (Énergoizdat, Moscow, 1990; Consultants Bureau, New York, 1990), Vol. 18.
11. A. Hasegawa, *Plasma Instabilities and Nonlinear Effects* (Springer-Verlag, Berlin, 1975).
12. A. V. Gurevich and A. B. Shvartsburg, *The Nonlinear Theory of the Propagation of Radio Waves in the Ionosphere* (Nauka, Moscow, 1973).
13. V. N. Fedorenko, Preprint No. 995 (Ioffe Physicotechnical Institute, Russian Academy of Sciences, Leningrad, 1986).
14. A. Achterberg, Astron. Astrophys. **98**, 161 (1981).
15. H. J. Völk, Astrophys. Space Sci. **25**, 471 (1973).
16. M. L. Goldstein, A. J. Klimas, and G. Sandri, Astrophys. J. **195**, 787 (1975).
17. Yu. P. Mel'nikov, Geomagn. Aéron. **33** (6), 18 (1993).
18. Yu. P. Mel'nikov, Zh. Éksp. Teor. Fiz. **109**, 1599 (1996) [JETP **82**, 860 (1996)].

19. Yu. P. Mel'nikov, Candidate's Dissertation in Physics and Mathematics (Leningrad Polytechnical Institute, Leningrad, 1989).
20. A. Z. Dolginov and I. N. Toptygin, Zh. Éksp. Teor. Fiz. **51**, 1771 (1966).
21. *Handbook of Mathematical Functions*, Ed. by M. Abramowitz and I. A. Stegun (Dover, New York, 1965; Nauka, Moscow, 1979).
22. D. S. Kuznetsov, *Special Functions* (Vysshaya Shkola, Moscow, 1965).
23. J. W. Sari and N. F. Ness, Solar Phys. **8**, 155 (1969).
24. H. J. Völk, Space Sci. Rev. **17**, 255 (1975).
25. J. W. Bieber, W. H. Matthaeus, C. W. Smith, *et al.*, Astrophys. J. **420**, 294 (1994).
26. I. D. Palmer, Rev. Geophys. Space Phys. **20** (2), 335 (1982).
27. L. I. Dorman and L. I. Miroshnichenko, *Solar Cosmic Rays* (Nauka, Moscow, 1968).
28. I. V. Dorman, L. I. Dorman, V. M. Dvornikov, *et al.*, Izv. Akad. Nauk, Ser. Fiz. **38**, 1946 (1974).
29. S. N. Vernov, L. I. Dorman, and B. A. Tverskoĭ, Izv. Akad. Nauk, Ser. Fiz. **32**, 1835 (1968).
30. W. C. Bartley, R. P. Bukata, K. G. McCracken, *et al.*, J. Geophys. Res. **71**, 3297 (1966).
31. K. G. Ivanov, Geomagn. Aéron. **36** (2), 19 (1996).
32. K. G. Ivanov, Geomagn. Aéron. **38** (5), 1 (1998).

Translation was provided by AIP

Journal of Experimental and Theoretical Physics, Vol. 90, No. 3, 2000, pp. 470–473.
Translated from Zhurnal Éksperimental'noĭ i Teoreticheskoĭ Fiziki, Vol. 117, No. 3, 2000, pp. 537–541.

PLASMA, GASES

Diffraction of Optical Radiation on Spatially Ordered Structures of Macroparticles in a Strongly Nonideal Thermal Plasma

O. S. Vaulina*, A. P. Nefedov, A. A. Samaryan, O. F. Petrov, and A. V. Chernyshev
Research Center for Thermal Physics of Pulsed Actions, Russian Academy of Sciences, Moscow, 127412 Russia
**e-mail: ipdustpe@redline.ru*
Received October 21, 1999

Abstract—The first observation of the diffraction of optical radiation on ordered structures of macroparticles in a low-temperature thermal plasma was reported. The experiments were conducted in an air thermal plasma at atmospheric pressure with CeO_2 particles at temperatures 1800–2200 K. The parameters of the plasma medium were determined using probe and optical diagnostics methods. The binary correlation function of the system of macroparticles was reconstructed from measurements of the structure factor. Simulation of nonideal plasma with the parameters corresponding to experiment was performed by the molecular dynamic method. The computed and experimental correlation functions were compared, and it was noted that they are in good agreement with one another. © *2000 MAIK "Nauka/Interperiodica".*

The recently observed ordered structures of macroscopic charged (dust) particles in various types of plasma [1–8] possess a variety of unique properties which make it possible to use them for studying phase transitions in a strongly nonideal plasma and as model systems for studying the properties of solids. It should be noted that the characteristic distances in plasma–dust structures are of the order of fractions of a millimeter, which makes it possible to use such a structure as a natural three-dimensional diffraction grating in the visible range and to study the diffraction of optical radiation. In the optical wavelength range, diffraction by natural three-dimensional structures was previously observed only for cholesteric and colloidal liquid crystals [9, 10].

In the present work we investigated the diffraction of optical radiation by ordered structures of macroparticles in a low-temperature thermal plasma. We present here the method used for determining the binary correlation function of the system of particles from measurements of the structure factor, analogous to the methods of X-ray crystallographic analysis for investigating the atomic structure of matter.

The kinematic approximation is used to describe the diffraction of radiation by amorphous and liquid structures. The correctness of this approximation for determining the binary correlation function $g(r)$ from measurements of the diffraction of optical radiation has been checked in [11], using model masks simulating the structure of macroparticles in a thermal dust plasma. The radiation intensity $I_s(\theta)$ scattered at the angle θ with respect to the direction of the incident radiation is given by the expression [9]

$$I_s(\theta) = I_0(\theta)[1 + 4\pi n_p \int (g(r) - 1) r \sin(rQ) dr/Q], \quad (1)$$

where $Q = 4\pi m_0 \sin(\theta/2)\lambda$, m_0 is the refractive index of the medium, n_p is the particle density, λ is the wavelength, and $I_0(\theta)$ is the intensity of the radiation scattered by a disordered cluster of particles. The structure factor is introduced as the intensity ratio $S(\theta) = I_s(\theta)/I_0(\theta)$. Measurements of the angular dependence of the structure factor make it possible to find the correlation function $g(r)$ as the inverse Fourier transform of the function $S(Q)$ [12].

For observing a diffraction pattern the spatial dispersion $V = \lambda/\langle r \rangle$ is determined by the condition for the existence of diffraction peaks of nonzero order and should not exceed 1 ($V < 1$) [12]. The lower limit ($V > \sin\theta_l$) is fixed by the finite dimensions of the probe beam and the parameters of the optical detector, which do not make it possible to detect the scattered radiation at angles less than θ_l. The limiting particle densities for observing a diffraction pattern can be estimated taking into account the limits on the value of $V \sim 0.005$–1.0. Thus, for the wavelength of the Ar^+-laser radiation ($\lambda = 0.489$ μm), the admissible particle density lies in the range 5×10^5–4×10^{12} cm^{-3}.

The experiments were performed in a thermal air plasma at atmospheric pressure in temperature range 1800–2200 K on the automated experimental stand described in detail in [13]. A two-flame propane–air Mekker burner was used as the plasma generator. Cerium oxide CeO_2 particles were introduced into the inner flame of the burner. The diagnostics complex made it possible to perform measurements of the diffraction of the optical radiation and to determine simultaneously the plasma parameters, such as, the temperature of the gas phase T_g, the density of alkali-metal atoms n_a, the electron density n_e, the average Sauter

diameter D_{32}, the particle density n_p, and the particle temperature T_p.

In the experiment the sizes of the particles investigated were in the range $D_{32} = 1$–1.5 μm, and the average distance between the particles was $\langle r\rangle = (4\pi n_p/3)^{-1/3} =$ 20–60 μm, which corresponds to the density $n_p = (1–30) \times 10^6$ cm^{-3}. The particle temperature was close to the gas temperature $T_g = 1700$–2200 K, the charge and screening length of the particles were determined from the density of the electronic component $n_e = 10^9$–10^{10} cm^{-3}, and they were in the range $Z_p = (0.5–1) \times 10^3$ and $r_D = (0.3–1)\langle r\rangle$, respectively.

Using the results of diagnostics measurements as a basis, we shall examine the possibility of the formation of an ordered structure of CeO_2 particles in a thermal plasma. In the single component plasma approximation, the state of the system of charged particles is determined by the nonideality parameter $\gamma = Z_p^2 e^2/\langle r\rangle kT_p$. The value $\gamma \simeq 170$ is taken as the condition for crystallization (gas–liquid phase transition) [14]. The screening of the charges of the macroparticles by plasma electrons and ions is taken into account in the Yukawa model. The effect of the screening is determined by the ratio $\kappa = \langle r\rangle/r_D$, and the parameter $\Gamma = \gamma\exp(-\langle r\rangle/r_D)$ is also used. Short-range order is established in such a system for $\Gamma > 1$ [15]. Figure 1 shows the dependence of Γ on the particle temperature T_p, calculated from measurements of the parameters of a plasma with CeO_2 particles. The nonmonotonic behavior of the function $\Gamma(T_p)$ is determined by two competing processes: charging of particles by thermionic emission and screening of particles by the electronic component formed by the ionization of alkali-metal atoms, usually present in the form of a natural impurity in the particle material. It is evident from the plot presented that in the temperature range 1700–2100 K, ordered structures of the liquid type can form in a thermal plasma. Such structures have been observed previously in an experimental study of a thermal plasma with CeO_2 particles [13]. The particle density was ~10^7 cm^{-3}, and the plasma temperature was about 1700 K.

The arrangement used to measure scattering (I_s and I_0) by CeO_2 particles is shown in Fig. 2a. The argon-ion laser radiation ($\lambda = 0.489$ μm) scattered by the macroparticles was collected by an objective in the range of angles $0.3° < \theta < 3.5°$ and directed onto a CCD array consisting of 700×1000 elements each with the dimensions 10×10 μm^2. Since the dynamic range of the array is comparatively small (8 digits), the transmitted laser beam was extracted outside the limits of the light-sensitive field of the array (see Fig. 2b). An inference filter placed in front of the objective was used to select the scattered radiation. A portion of the diffraction pattern was screened for measurements of the structure factor on the CCD array (see Fig. 2b). A video image of the scattering pattern was recorded with a video tape recorder and digitized using a computer program. The data array $I(n_{ij})$ obtained, where I is the signal amplitude and n_{ij} is the pixel number, was used to construct the angular dependence $I(\theta)$ of the scattered radiation.

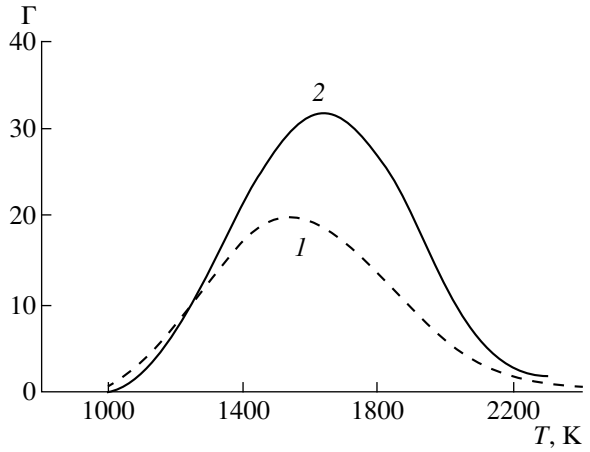

Fig. 1. Temperature dependence of the parameter Γ: (*1*) $n_p = 10^6$ cm^{-3}, (*2*) $n_p = 10^7$ cm^{-3}.

Figure 3 shows the characteristic angular dependences of the scattered radiation for an experiment with particles at temperatures 2200 and 1800 K. According to the analysis presented above, at $T = 1800$ K a liquid-type structure should be formed in the system of particles. A peak corresponding to the first diffraction ring is clearly seen in the angular dependence measured at $T = 1800$ K (curve *1*, Fig. 3). Subsequent peaks are less pronounced because of the absence of long-range order in the system. As temperature increases to 2200 K, the parameter Γ decreases to 0.5 (Fig. 1), the system of particles becomes weakly interacting, and the angular dependence of the scattered radiation is determined by the characteristics (size and refractive index) of individual particles (curve *2* in Fig. 3).

The structure factor of the system can be found by measuring the angular dependence of the scattered radiation. Figure 4 shows the dependence of the structure factor $S(\theta)$ for an experiment with CeO_2 at 1800 K. The time-averaged angular dependences of the scattered radiation for a system of particles at temperature 1800 K, $I_s(\theta)$, was used to calculate $S(\theta)$. We used for $I_0(\theta)$ the dependence measured at $T = 2200$ K for the same particle density ($n_p = 7.5 \times 10^6$ cm^{-3}).

The correlation function $g(r)$ was reconstructed from the obtained dependence $S(\theta)$, using the inverse Fourier transform. Since the effect of the characteristic laser radiation on the detection of scattering makes it difficult to determine $S(\theta)$ accurately at small angles, the quantity $S(\theta)$ for $\theta < 0.4°$was set equal to 0, which could distort the initial form of $g(r)$. The reconstructed function $g(x)$, where $x = r/\langle r\rangle$, is shown in Fig. 5 (curve *1*). The model correlation functions calculate by the molecu-

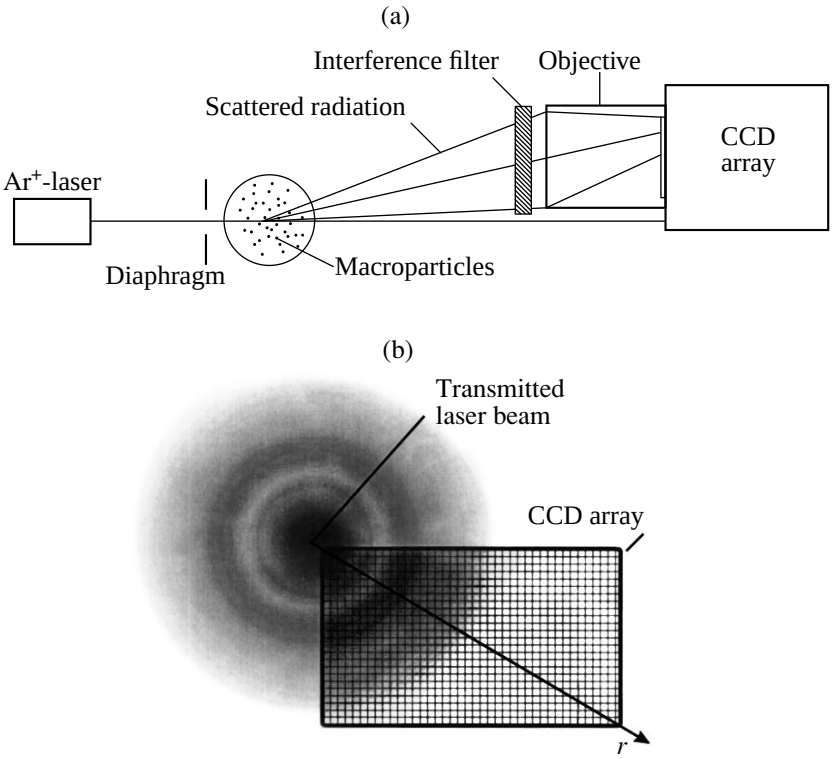

Fig. 2. Diagram of the optical measurements of the diffraction of radiation: (a) overall view, (b) combined arrangement of the photosensitive area and the diffraction pattern.

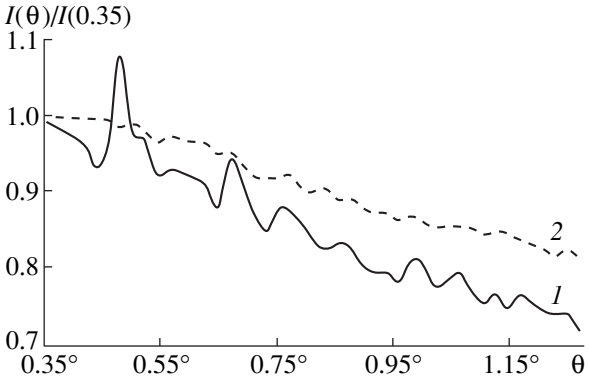

Fig. 3. Measurements of the intensity $I(\theta)$ of the radiation scattered by a system of CeO_2 particles: $T = (1)$ 1800, (*2*) 2200 K.

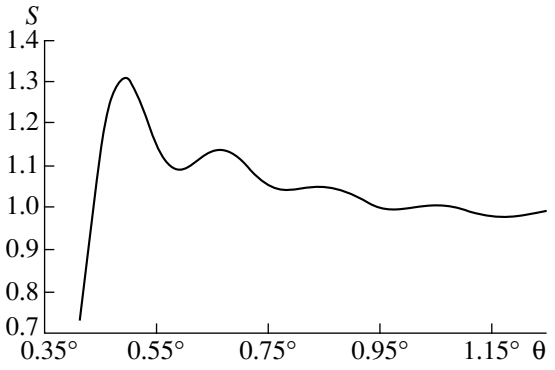

Fig. 4. Angular dependence of the structure factor S for a plasma with CeO_2 particles at $T = 1800$ K, $n_p = 7.5 \times 10^6$ cm^{-3}.

lar dynamic method for various formation times of the structure are also presented there.

The following data obtained from measurements of a plasma with CeO_2 particles were used for a numerical simulation of a dust system: $D_{32} = 2R_p = 1$ μm, $r_D/\langle r\rangle = 1.3$, $n_p = 7.5 \times 10^6$ cm^{-3}, $\nu_{fr} = 4 \times 10^4$ s^{-1}, $T = 1800$ K, $\gamma \simeq 73$, and $\Gamma \simeq 30$. The calculation was performed by the molecular-dynamic method for 512 particles using periodic boundary conditions along the *x*, *y*, and *z* axes. A three-dimensional equation of motion, in which the interparticle interaction F_{int}, friction due to the neutral component, and random Brownian force F_{br}, arising as a result of the impacts due to molecules of the surrounding gas, was solved for each macroparticle:

$$m_p \frac{d^2\mathbf{r}_k}{dt^2} = \sum_j F_{\text{int}}(r)\big|_{r=|\mathbf{r}_k-\mathbf{r}_j|} \frac{\mathbf{r}_k-\mathbf{r}_j}{|\mathbf{r}_k-\mathbf{r}_j|} - m_p \nu_{fr} \frac{d\mathbf{r}_k}{dt} + F_{br}, \tag{2}$$

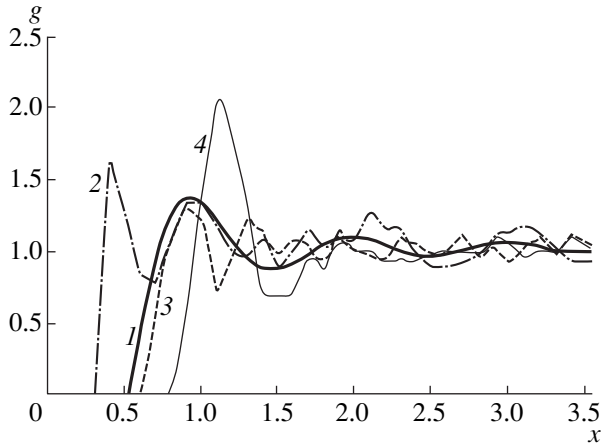

Fig. 5. Pair correlation functions obtained from measurements of the structure factor (*1*) and computed with D_{32} = 1 μm, $r_D/\langle r\rangle = 1.3$, $n_p = 7.5 \times 10^6$ cm^{-3}, $\nu_{fr} = 4 \times 10^4$ s^{-1}, T = 1800 K, $\gamma \simeq 73$, and $\Gamma \simeq 30$ for the times t = (*2*) 5 ms, (*3*) 35 ms, (*4*) 3.5 s.

where m_p is the particle mass, ν_{fr} is the friction frequency, and $F_{\text{int}}(r)$ was determined assuming a Debye interaction between the macroparticles:

$$F_{\text{int}}(r) = \frac{Z_p^2 e^2}{r^2}\left[1 + \frac{r}{r_D}\right]\exp\left(-\frac{r}{r_D}\right). \qquad (3)$$

The quantity ν_{fr} was calculated in the free-molecular regime approximation [16]

$$\nu_{fr} = \frac{8PR_p^2}{3m_p}\sqrt{\frac{2\pi m_g}{T_g}}$$

and for our conditions $\nu_{fr} = 4 \times 10^4$ s^{-1}. Here m_g is the mass of the neutral component and P is the gas pressure.

The temporal evolution of the function $g(r)$, illustrating the dynamics of the formation of a plasma–dust structure from a disordered cluster of particles, is shown in Fig. 5 for the times t = 5 ms, 35 ms, and 3.5 s. The calculations showed that the system reaches equilibrium in $t \sim 1$ s, when the binary correlation function no longer depends on the time. For this reason, for $t < 1$ s a correct comparison of the experimental and computed functions can be made only at the corresponding moments in time. In our experiment the measurements were performed at a height of 40 mm with flow velocity 1.2 m/s, which corresponds to a formation time of the structure t = 33 ms. Comparing the measured and computed at t = 35 ms correlation functions (Fig. 5) shows that they are in good agreement with one another.

In summary, in the present work the diffraction of optical radiation on ordered plasma–dust structures was observed for the first time. The binary correlation function, which agrees well with the correlation function calculated for this system by the molecular-dynamic method, was obtained from measurements of the structure factor.

ACKNOWLEDGMENT

This work was supported by the Russian Foundation for Fundamental Research, projects nos. 98-02-16825 and 98-02-16828.

REFERENCES

1. J. Chu and I. Lin, Phys. Rev. Lett. **72**, 4009 (1994).
2. H. Thomas, G. E. Morfill, V. Demmel, *et al.*, Phys. Rev. Lett. **73**, 652 (1994).
3. A. Barkan and R. L. Merlino, Phys. Plasmas **2**, 3261 (1995).
4. V. E. Fortov, A. P. Nefedov, O. F. Petrov, *et al.*, Pis'ma Zh. Éksp. Teor. Fiz. **63**, 176 (1996) [JETP Lett. **63**, 187 (1996)].
5. V. E. Fortov, A. P. Nefedov, V. M. Torchinskiĭ, *et al.*, Pis'ma Zh. Éksp. Teor. Fiz. **64**, 86 (1996) [JETP Lett. **64**, 92 (1996)].
6. V. E. Fortov, A. P. Nefedov, and O. S. Vaulina, Zh. Éksp. Teor. Fiz. **114**, 2004 (1998) [JETP **87**, 1087 (1998)].
7. Yu. N. Gerasimov, A. P. Nefedov, V. A. Sinel'shchikov, *et al.*, Pis'ma Zh. Tekh. Fiz. **24** (19), 62 (1998) [Tech. Phys. Lett. **24**, 774 (1998)].
8. V. E. Fortov, V. I. Vladimirov, L. V. Deputatova, *et al.*, Dokl. Akad. Nauk **366**, 184 (1999) [Phys. Dokl. **44**, 279 (1999)].
9. A. K. Sood, Solid State Phys. **45**, 1 (1991).
10. J. C. Knight, D. Ball, and G. N. Robertson, Appl. Opt. **30**, 4795 (1991).
11. O. S. Vaulina, O. F. Petrov, and M. V. Taranin, Fiz. Plazmy **25**, 311 (1999) [Plasma Phys. Rep. **25**, 281 (1999)].
12. M. A. Krivoglaz, *Diffraction of X-rays and Neutrons in Nonideal Crystals* (Naukova Dumka, Kiev, 1983).
13. V. E. Fortov, A. P. Nefedov, O. F. Petrov, *et al.*, Zh. Éksp. Teor. Fiz. **111**, 467 (1997) [JETP **84**, 256 (1997)].
14. S. Ichimaru, Rev. Mod. Phys. **54**, 1017 (1982).
15. H. Ikezi, Phys. Fluids **29**, 1764 (1986).
16. A. P. Nefedov, O. F. Petrov, S. A. Khrapak, *et al.*, Teplofiz. Vys. Temp. **36**, 141 (1998).

Translation was provided by AIP

Journal of Experimental and Theoretical Physics, Vol. 90, No. 3, 2000, pp. 474–478.
Translated from Zhurnal Éksperimental'noĭ i Teoreticheskoĭ Fiziki, Vol. 117, No. 3, 2000, pp. 542–547.

SOLIDS
Structure

New Low-Frequency Magnetic Excitations in $LaMnO_3$ Single Crystals

A. M. Balbashov[1], M. K. Gubkin[2], V. V. Kireev[2], O. K. Mel'nikov[2], T. M. Perekalina[2], S. V. Pushko[2], L. E. Svistov[2,*], and A. Ya. Shapiro[2]

[1]*Moscow Power Institute, Moscow, 111250 Russia*

[2]*Shubnikov Institute of Crystallography, Russian Academy of Sciences, Moscow, 117333 Russia*

**e-mail: svistov@kapitza.ras.ru*

Received August 5, 1999

Abstract—Microwave magnetic resonance of close to stoichiometric antiferromagnetic $LaMnO_{3-\delta}$ was investigated. $LaMnO_{3-\delta}$ single crystals were grown and a series of samples with a small oxygen excess and deficiency was prepared. Residual magnetization was observed for all samples in the series. The maximum value of the residual magnetic moment in the series of samples obtained was 2.5% of the maximum possible value ($4_{\mu B}$ for each Mn ion). An absorption line, whose angular and frequency dependences cannot be explained on the basis of a previously proposed [S. Mitsudo, *et al.*, J. Magn. Magn. Mater. **177–181**, 877 (1998)] model of two-sublattice antiferromagnet with "easy axis" magnetic anisotropy (|| *b*) and canting of the magnetic sublattices due to the Dzyaloshinskiĭ–Moriya interaction, was observed in the experiments performed on all samples in a series as well as on specially prepared ceramic samples with the same composition. It was inferred that the low-frequency excitations in a system of ferromagnetic drops observed in [M. Hennion, *et al.*, Phys. Rev. Lett. **81**, 1957 (1998)] are observed in the experiment. © *2000 MAIK "Nauka/Interperiodica".*

1. INTRODUCTION

One of the rapidly developing areas of solid-state physics is the investigation of the properties of materials containing ions with variable valence. The great interest in these objects is due primarily to the discovery of high-temperature superconductivity and the phenomenon of giant magnetoresistance in them. One such compound is $LaMnO_3$, whose magnetic and conducting properties depend strongly on the presence of quadrivalent manganese ions in it. The presence of a quadrivalent manganese ion is usually achieved either by substituting divalent ions, for example, Ca or Sr, for lanthanum or by means of excess oxygen. There are many publications on magnetic systems based on $LaMnO_3$ (see, for example, [2, 3, 5]).

In the present work the magnetic properties of $LaMnO_3$ were investigated by the magnetic resonance method. A manganese ion in an $LaMnO_3$ matrix possesses a $3d^4$ configuration, in which the three electrons occupy the bottom t_{2g} orbitals and one occupies the upper e_g orbital. On account of the half-filled outer orbital, $LaMnO_3$ is a Mott-type antiferromagnetic insulator.

According to neutron-diffraction data [11], the crystal structure of $LaMnO_3$ is orthorhombic with *Pbnm* symmetry. Below the antiferromagnetic transition temperature $T_N \approx 140$ K the compound $LaMnO_3$ becomes antiferromagnetic with a type-*A* layered structure: the ferromagnetic *ab* planes become ordered antiferromagnetically. In the absence of a magnetic field the antiferromagnetic vector is directed along the *b* axis. $LaMnO_3$ crystals consist of twins, and all six types of twins possible for the given structure are realized in the growth process [11].

The magnetic properties of $LaMnO_{3-\delta}$ are strongly associated with the deviation from oxygen stoichiometry or, in other words, with the number of Mn^{4+}ions. According to the first works, whose results entered in [6], stoichiometric $LaMnO_3$ ($\delta = 0$) is an antiferromagnet. Away from stoichiometry a weak ferromagnetic moment, which is usually associated with the canting of the magnetic sublattices, appears. The appearance of a magnetic moment is ordinarily explained by the interaction of magnetic sublattices and charge carriers. This explanation was proposed by Zener [4] and de Gennes [3].

In the last few years the validity of this model for $LaMnO_{3-\delta}$ with a small deviation from oxygen stoichiometry has been questioned. In the first place, according to [9] a weak ferromagnetic moment also remains in samples with $\delta = 0$. In the second place, several theoretical works have appeared [7, 8] in which it has been shown that for a small value of δ a uniform canting of the sublattices should not occur, and a stratification of the sample into regions with different values of the ferromagnetic moment is energetically preferable.

Magnetic stratification has been reported in the experimental works [12, 13]. According to neutron-scattering experiments [12], the diameter of the region

with a large magnetic moment is ≈18 Å, and the difference of the magnetic moment inside these regions and in the bulk of the crystal is $0.6\mu_B$.

In the present work we investigated electron spin resonance in $LaMnO_{3-\delta}$ with a small deviation from a stoichiometric composition in the microwave range at temperatures below T_N.

2. SAMPLES AND PROCEDURE

In the present work $LaMnO_{3-\delta}$ samples grown by zone melting were investigated. The initial polycrystalline rods were prepared using the standard solid-phase method and La_2O_3 and Mn_2O_3 reagents. Taking account of the tendency of La_2O_3 to absorb water and carbon dioxide from air, the initial material was heated at 900°C. The mass losses (4.25%) were monitored by a thermogravimetric method. The initial substances, taken in the required proportion, were pulverized and mixed in a ball mill. The charge was annealed at 1200°C for 10 h. The cake formed was pulverized in an agate mortar and then molded into 12-mm rods. Polyvinyl alcohol in amounts of three or four drops per 100 g of material was added as a binder. The rods were annealed at 1400°C for 20 h. A 3000-W xenon lamp, whose rays were focused by two ellipsoidal mirrors, was used as a heater for zone melting. The growth rate was 8 mm/h. The 0.5 cm in diameter and 2 cm long samples obtained by such a method were investigated by powder X-ray diffraction analysis and X-ray topography. Figure 1 shows a characteristic topogram of a section of a sample. Many twinning boundaries can be seen in the topogram. Using the neutron diffraction data from [11], we infer that all six types of twins which are possible for the structure of $LaMnO_{3-\delta}$ are present in the crystal. The characteristic size of a twin is $\delta \approx 0.01$ mm.

The data obtained show that the volume of the twins, whose *b* axes are collinear, in the samples investigated is approximately an order of magnitude greater than the volume of twins with other orientations. In what follows we shall indicate the orientation of the static magnetic field relative to the *b* axis of the twins with the predominant orientation in the sample.

In the present work we endeavored to investigate compositions as close as possible to stoichiometry. The data from [14], where the dependence of the lattice parameters on the stoichiometric composition was investigated, were used to estimate the oxygen content. This method makes it possible to determine δ to within ± 0.03. We note that the samples obtained in the growth process were stoichiometric to within the indicated accuracy. The crystals were cut into ≈1 mm thick plates and annealed in oxygen (1300°C, 250 h) and nitrogen (700°C, 48 h). By varying the annealing conditions we obtained a series of five samples with almost identical lattice parameters ($a = 5.535$ nm, $b = 5.736$ nm, and $c = 7.707 \pm 0.003$nm). The change in oxygen composition as a result of annealing could be judged according to the change in the residual magnetic moment of the sample. The magnetic moment of the sample was measured with a vibrating coil magnetometer at liquid-nitrogen temperature. The residual magnetic moment increased with saturation and with depletion of oxygen in the $LaMnO_3$ sample. We classified the samples with the minimum residual magnetic moment as being closest to stoichiometry. The minimum residual magnetic moment in the series of samples obtained was 2.5% of the maximum possible value ($4\mu_B$ for each Mn ion). The magnetization curves in weak fields showed hysteresis. The presence of a residual magnetic moment for all samples in the series agrees with [9], where ceramic samples were studied.

Fig. 1. X-ray topogram of a $LaMnO_3$ crystal plate, cut perpendicular to the growth axis corresponding to the [101] direction.

Electron spin resonance was investigated on a pass-through microwave spectrometer. A $1 \times 1 \times 0.5$ mm^3 sample was placed in a rectangular resonator, where different modes were excited in the frequency range 18–78 GHz. The construction made it possible to rotate the sample in the course of the experiment. A magnetic field from 0 to 40 kOe was produced with a superconducting solenoid. The measuring cell was placed into a vacuum jacket, which made it possible to perform measurements in the temperature range 1.2–200 K.

3. EXPERIMENTAL RESULTS

Figure 2 shows a trace of the microwave power at 36 GHz which has passed through the resonator as a function of the magnetic field for different values of the

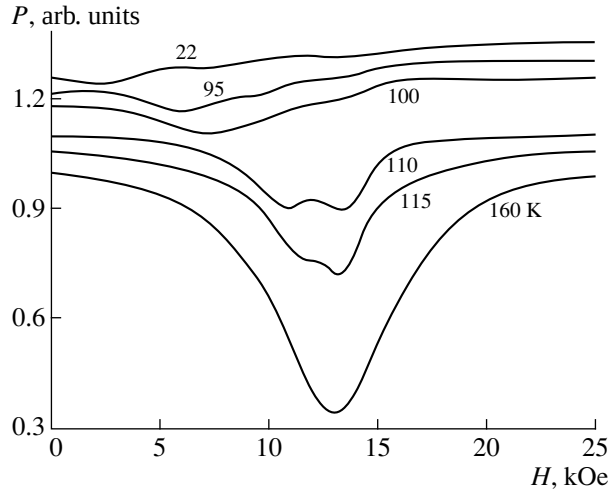

Fig. 2. Characteristic traces of the microwave power at 36 GHz passing through the resonator as a function of the magnetic field for various values of the temperature for samples closest to stoichiometry. At temperatures close to T_N the intensity of the line decreases sharply and the line splits first into two and then, at even lower temperatures, into three lines. At low temperatures the absorption is observed in a wide range of fields, less than the EPR field. The static field H lies in a plane perpendicular to the predominant direction of the b axis.

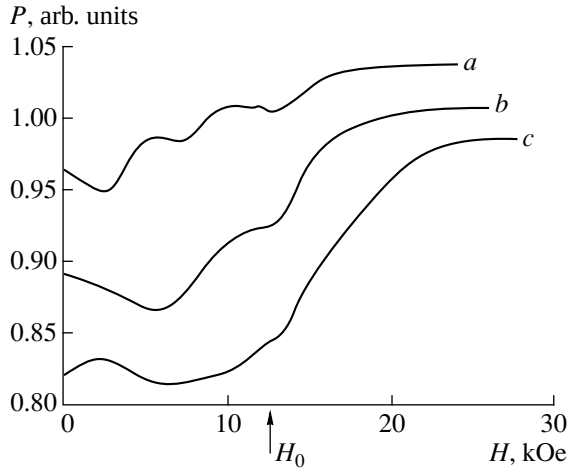

Fig. 3. Traces of absorption lines for three samples with different composition at $T = 4.2$ K, $\nu = 36$ GHz, $H \perp b$; H_0 is the EPR field measured at $T > T_N$. (*a*) Trace corresponding to a sample closest to stoichiometry. Its residual magnetic moment was 2.5% of the maximum possible value; (*b*) the trace corresponding to the sample whose residual magnetic moment was ≈5%; (*c*) the trace corresponding to $LaMnO_{3+0.04}$. The composition was determined according to the parameters of the crystal lattice and the data from [14].

temperature. At temperatures close to T_N the intensity of the electron paramagnetic resonance (EPR) line decreases and splits first into two and then three lines as temperature decreases. The resonance field of each line decreases with temperature. At low temperatures absorption is observed in a wide range of fields, less than the EPR field (H_0). At temperatures below 15 K (the measurements were performed down to 1.7 K) the intensity and form of the trace of the transmitted microwave power remained unchanged. The data presented in Fig. 2 were obtained on the samples closest to stoichiometry. The static field H is directed in a plane perpendicular to the b axis. The traces obtained at other frequencies were similar to the traces presented in the figure. We note that at all frequencies investigated, just as in Fig. 2, in the temperature range below 15 K absorption of microwave power is observed in the entire range of fields $0 < H < H_0$.

Figure 3 shows traces of the absorption lines for three samples with different composition at $T = 4.2$ K, $\nu = 36$ GHz, and $H \perp b$. The first sample (*a*) is closest to stoichiometry. The residual magnetic moment of the second sample was ≈5%. The composition of the third sample $LaMnO_{3+0.04}$ (Fig. 3, curve *c*) deviated strongly from stoichiometry, and for this reason it could be determined by measuring the lattice parameters. It is evident that for samples with an appreciable deviation from oxygen stoichiometry a shift of the absorption line into the region of weaker fields at temperatures $T < T_N$ was also observed, while the splitting of the lines disappeared, possibly as a result of their being broadened.

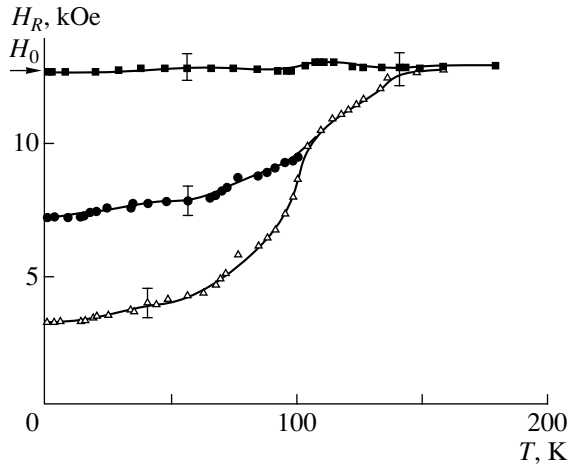

Fig. 4. Temperature dependences of the resonance fields for samples closest to stoichiometry. $\nu = 36$ GHz, $H \perp b$, H_0 is EPR field measured at $T > T_N$.

Figure 4 shows the temperature dependences of the resonance fields. The smooth decrease of the resonance fields, occurring in a wide temperature range $T < T_N$, is interesting. Besides the temperature-dependent absorption lines, there is present an absorption line whose position is almost temperature-independent and which corresponds to the position of the electron paramagnetic resonance line at $T > T_N$.

Figure 5 shows measurements of the resonance fields for various values of the frequency. The value of the resonance field is plotted along the x axis, and the frequency at which the measurement was performed is

plotted along the *y* axis ($H \perp b$, $T = 4.2$ K). It is evident in the figure that the field of each resonance depends linearly on the frequency, the slope angle corresponds to the *g* factor of 2, and the gap width Δ depends on the temperature ($\nu = \gamma H + \Delta$—solid lines in Fig. 5). Similar linear dependences were obtained for all samples in a series.

Figure 6 shows the dependence of the resonance field on the angle between *H* and *b*. Anisotropy was not observed in the *ac* plane ($T = 4.2$ K, $\nu = 54.2$ GHz).

4. DISCUSSION

Antiferromagnetic resonance (AFMR) was previously investigated in the submillimeter frequency range [10]. The results of the investigation were interpreted by the authors of this work on the basis of the model of a two-sublattice antiferromagnet with "easy axis" ($\| b$) magnetic anisotropy and canting of the magnetic sublattices due to the Dzyaloshinskiĭ–Moriya interaction. In the notations adopted in Turov's monographs [1], the values of the magnetic constants ($T \ll T_N$) obtained by the authors of this work from the AFMR spectrum are as follows: $H_e = 33.9$ T, $H_a = 5.3$ T, and $H_D = 0.2$ T. The strong uniaxial anisotropy gives rise to a large gap in the AFMR spectrum, signifying that in the frequency range 10–100 GHz and weak fields, as compared with the spin-flop field, $H \ll H_c \approx 20$ T, AFMR lines should not be expected to appear. The presence of a large energy gap in the magnetic excitation spectrum is also confirmed by neutron-scattering experiments [11].

In summary, the low-frequency absorption lines observed in the present work are probably not an antiferromagnetic resonance of $LaMnO_3$.

We note that a trace at 135 GHz is presented in [10]. Aside from absorption corresponding to an antiferromagnetic resonance, the trace contains a line whose position agrees well with the extrapolation of the frequency dependence obtained in the present work (Fig. 4). We also observed a low-frequency absorption line in ceramic $LaMnO_3$ samples synthesized by the standard solid-phase technique. Thus, the observed low-frequency absorption line is present in samples obtained by different methods.

The intensities of the absorption lines at $T < 15$ K does not depend on the temperature. This fact shows that the observed absorption lines are not related with the electron paramagnetic resonance of impurity magnetic ions.

The absorption lines observed in the present work could be associated with low-frequency excitations in a system of ferromagnetic drops, which was observed in [12]. Unfortunately, we know of no theoretical investigations of the magnetic excitation spectrum of a system of such drops in an antiferromagnetic matrix. It can be expected that the spectrum of magnetic excitations of such drops will be similar to the spectrum of a bulk ferromagnet. In magnetic fields much greater than the effective crystal anisotropy field, the ferromagnetic resonance frequency is proportional to *H* [1] with proportionality coefficient corresponding to the *g* factor of 2, which is observed in the present experiments. It can be expected that the nonuniform distribution of the magnetic moment over the volume of the sample will lead to an effective excitation of the nonuniform magnetic oscillations by a uniform microwave magnetic field. The absorption of microwave power in weak magnetic fields seems to be associated with the excitation of nonuniform oscillations (Figs. 2, 3). The presence of fine structure in the absorption line attests to the presence of periodicity in the distribution of the magnetic moment over the volume of the sample, and the gaps in the spectrum of each of the two sharp fine-structure lines (Fig. 5) are of an exchange nature.

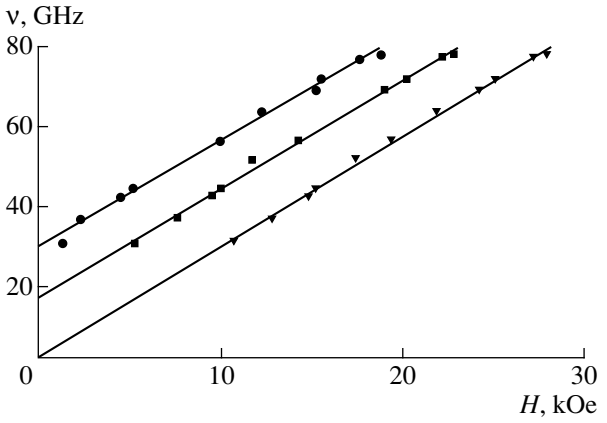

Fig. 5. Frequency dependences of the resonance fields obtained for samples closest to stoichiometry. $H \perp b$, $T = 4.2$ K.

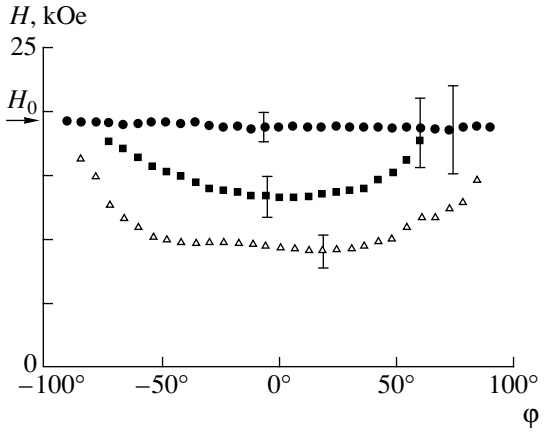

Fig. 6. Resonance fields versus the angle between *H* and *b*. $T = 4.2$ K, $\nu = 54.2$ GHz.

The model discussed is a working hypothesis. It cannot be asserted unequivocally on the basis of our experiments that the observed absorption lines are related with magnetic excitations in a system of ferro-

magnetic drops. It is possible that these absorption lines are associated with magnetic excitations from domain walls arising because of, specifically, the presence of twins in the crystal. The character of the magnetic anisotropy near a wall of a twin can differ substantially from the anisotropy in the volume of the crystal and, correspondingly, the gap in the excitation spectrum can be lower than in the bulk.

It is important to investigate the EPR spectrum in a $LaMnO_3$ single crystal with no twins. Obtaining such a single crystal is a complicated, but technically solvable problem.

ACKNOWLEDGMENTS

We thank L.A. Prozorova and A.I. Smirnov for helpful discussions.

REFERENCES

1. E. A. Turov, *Magnetic Properties of Magnetically Ordered Crystals* (Akad. Nauk SSSR, Moscow, 1963), p. 61.
2. G. H. Jonker and J. H. van Santen, Physica **16**, 337 (1950).
3. P.-G. de Jennes, Phys. Rev. **118**, 141 (1960).
4. C. Zener, Phys. Rev. **82**, 403 (1951).
5. S. Jin, T. H. Tiefel, M. McCormack, *et al.*, Science **264**, 413 (1994).
6. D. Goodenough, *Magnetism and the Chemical Bond* (Interscience, New York, 1963; Metallurgiya, Moscow, 1968), p. 182.
7. E. L. Nagaev, Usp. Fiz. Nauk **166**, 833 (1996) [Phys. Usp. **39**, 781 (1996)].
8. M. Yu. Kagan, D. Khomskiĭ, and M. Mostovoy, E-print archive, cond-mat/9804213 (1998).
9. G. Matsudo, J. Phys. Soc. Jpn. **29**, 606 (1970).
10. S. Mitsudo, K. Hirano, H. Nogiri, *et al.*, J. Magn. Magn. Mater. **177–181**, 877 (1998).
11. F. Moussa, M. Hennion, J. Rodríguez-Carvajal, and H. Moudden, Phys. Rev. B **54**, 15149 (1996).
12. M. Hennion, F. Moussa, G. Biotteau, *et al.*, Phys. Rev. Lett. **81**, 1957 (1998).
13. G. Allodi, R. De Renzi, G. Guidi, *et al.*, Phys. Rev. B **56**, 6036 (1997).
14. A. K. Bogush, V. T. Pavlov, and L. V. Balyko, Cryst. Res. Technol. **18**, 589 (1983).

Translation was provided by AIP

Journal of Experimental and Theoretical Physics, Vol. 90, No. 3, 2000, pp. 479–487.
Translated from Zhurnal Éksperimental'noĭ i Teoreticheskoĭ Fiziki, Vol. 117, No. 3, 2000, pp. 548–558.

SOLIDS
Structure

Long-Period Incommensurate Superstructures in Cu–Au Alloys: Relation with Short-Period Ordering

O. I. Velikokhatnyĭ[1], S. V. Eremeev[1], I. I. Naumov[1, *], and A. I. Potekaev[2]

[1]*Institute of Strength Physics and Materials Science, Siberian Division, Russian Academy of Sciences, Tomsk, 634021 Russia*

[2]*Siberian Physicotechnical Institute, Tomsk, 634050 Russia*

**e-mail: naumov@ispms.tsc.ru*

Received June 2, 1999

Abstract—The nature of the stability of incommensurate long-period structures in alloys of the system Cu–Au is investigated on the basis of first-principles calculations of the electronic structure. It is shown that many structural properties of such formations can be explained only if the latter are treated as superstructures with respect to ordinary superstructures ($L1_2$ or $L1_0$): the electron spectrum of the superstructure and not that of the initial disordered alloy must serve as the initial spectrum. The observed dependence of the long period N on the degree η of the "short" long-range order is explained. The reasons why two-dimensional long-period superstructures from in the alloy Au_3Cu are found. Arguments supporting the fact that among quasicrystalline substances long-period superstructures fall between incommensurate systems and quasicrystals are presented. © *2000 MAIK "Nauka/Interperiodica".*

1. INTRODUCTION

As is well known, very unusual ordered phases—one- or two-dimensional long-period superstructures—form in alloys based on the precious metals, CuAu, Cu_3Au, Au_3Cu, Cu_3Pd, Cu_3Pt, Au_3Mn, and others (see, for example, [1–7]). The periods of these superstructures are on the nanometer scale: up to 100 interplanar distances fit within their length. In contrast to the artificially produced metallic and semiconductor superlattices, long-period superstructures are thermodynamically equilibrium structures. In the phase diagram they correspond to a completely determined region.

The alloys Cu–Au are classic alloys for studying order–disorder phase transitions [1, 4, 7]. In these alloys, depending on the composition, both one-dimensional (Cu_3Au and CuAu) and two-dimensional ($CuAu_3$) incommensurate long-period superstructures are formed. They are characterized by a quasiperiodic arrangement of the antiphase boundaries—flat defects on which the sign of the phase of the long-range order parameter η, describing transitions from a disordered solid solution into ordinary (short-period) superstructures $L1_0$ or $L1_2$, changes sign. In one-dimensional long-period superstructures the antiphase boundaries are perpendicular to the [100] direction, and in the two-dimensional superstructures they are parallel to the [100] and [010] directions of the initial fcc lattice. Characteristically, the regions between the nearest antiphase boundaries are fragments of commensurate structures with a whole but random period: stochastic alternation of antiphase domains of different length occurs along the long quasiperiod. As the composition or temperature varies, the average (over a chaotic ensemble) half-period N varies continuously, assuming irrational values as well.

The first attempts to explain the formation of long-period superstructures were made back in the 1950s by Slater [8] and Nicolas [9]. They assumed that such superstructures are stabilized as a result of a decrease of the energy of the valence electrons because of the appearance of gaps in the electron spectrum near the Fermi level. This point of view goes back to the well-known idea of Mott and Jones [10] that phases are especially stable under conditions where the Fermi surface is in contact with the faces of the Brillouin zone. The works [8, 9] were experimentally confirmed in the classic works of Sato and Toth [11–13], who discovered a clear correlation between the average period N and the number of valence electrons per atom, e/a, in Cu–Au alloys doped with various elements. Significantly, in [8, 9, 11–13] no special attention was given to the deviation of the shape of the Fermi surface from a sphere; for example, in [11–13] the long half-period N of the system was estimated from the condition that the Fermi sphere touches new faces of the Brillouin zone (the fact that in reality the Fermi surface is nonspherical was taken into account only via the renormalization of the diameter $2k_F$ of the sphere by introducing a so-called correction factor).

Tachiki and Teramoto [14] were the first to advance the idea that flat sections of the Fermi surface in the [110] direction could be responsible for the appearance of long-period superstructures in the fcc alloys Cu–Au. Their calculations for an alloy with equiatomic compo-

sition CuAu showed that such sections lead to a displacement of the minima[1] in the electronic polarizability $\chi(\mathbf{q})$ (or the Fourier transform of the ordering potential $V(\mathbf{q})$) from the Lifshits point $X((2\pi/a)[001])$ into a point on the line X–W. Since $L1_0$ type ordering occurs along the star of the point X, while the displacement vector of the minimum $\Delta\mathbf{k} \parallel [100]$, this explained the appearance of the modulated superstructure of the type CuAuII with half-period $N \sim \pi/|\Delta\mathbf{k}|$ along [100] (we note that in [14] pure copper served as a prototype of the disordered alloy CuAu).

The idea of [14] that long-period superstructures appear because of the presence of flat sections of the Fermi surface was elaborated in [15–20]. As a result, by the mid-1980s, the idea developed that long-period superstructures are formed as a result of transitions similar to a Peierls transition [21] in one-dimensional metallic systems. The quasi-one-dimensionality of three-dimensional systems is due to the presence of flat sections of the Fermi surface in the [110] direction. When a long period arises, a gap opens up in the electron spectrum on the entire area of these sections, and the energy gain is sufficient to destabilize the initial short-period structure.

Despite the progress made, the problem of the stability of long-period superstructures in the alloys considered still contains a number of fundamental points that are unclear.

(1) The reasons why only one-dimensional superstructures form for some compositions (for example, CuAu and Cu_3Au) while two-dimensional long-period superstructures with substantially different periods $2N_1$ and $2N_2$ form for others (for example, Au_3Cu) are unclear.

(2) The reasons for the quite strong dependence of the long period $2N$ on the "short" order parameter η are not understood (in Au_3Cu and Cu_3Au, for example, N increases together with η [4]). According to existing ideas, the period $2N$ is fixed by the nesting vector $2\mathbf{k}_F$ of the disordered alloy, which is completely independent of η. The strong dependence of $2N$ on the alloy composition is likewise not understood [4, 7], since the number e/a of valence electrons per atom remains unchanged and the ratio $\mathbf{k}_F/\mathbf{G}$ ($\mathbf{G}$ is a reciprocal lattice vector), one would think, also should not change appreciably.

(3) The question of why long-period superstructures exist only in a narrow temperature range, while at sufficiently low temperatures the ordinary superstructures $L1_0$ or $L1_2$, which do not contain antiphase boundaries, become energetically favorable has not been answered.

The answers to these questions cannot be found on the basis of the standard approach [14–20], which derives the structure and properties of long-period superstructures from an initial electron spectrum $\varepsilon_\lambda(\mathbf{k})$ of the initial disordered state. This approach is based on the assumption that the renormalization of the initial spectrum as a result of the short-period ordering is small and can be neglected (see, for example, [18]). This assumption, however, is invalid already on the basis of the following simple considerations. In the first place, in the alloys under discussion the initial flat sections of the Fermi surface lie near the superstructure vectors of the type $(2\pi/a)[110]$, and for this reason they will inevitably be transformed in the process of short-period ordering. In the second case, long-period superstructures always coexist with a high degree of order η, arising as a result of sharp first-order transitions with a typical jump $|\Delta\eta| \sim 0.6$ [4]; such a jump and a further increase of η should lead to an appreciable change of the spectrum $\varepsilon_\lambda(\mathbf{k})$ of the disordered state.

In the present paper, we shall investigate the questions formulated above, proceeding from the fact that the structure of the long-period formations must be derived from the initial electronic spectrum $\varepsilon_\lambda(\mathbf{k})$ of the basic superstructures ($L1_2$, $L1_0$), corresponding to a given degree of short-range order η. Actually, we consider only two extreme situations, complete order and complete disorder, in order to estimate qualitatively the region between $\eta = 0$ and $\eta = 1$. The investigation is based on first-principle calculations of the electronic structure of the electron-energy spectrum $\varepsilon_\lambda(\mathbf{k})$, the generalized susceptibility $\chi(\mathbf{q})$, various sections of the Fermi surface of pure metals and ordered alloys. In Section 2 the required information about the basic superstructures and the details of numerical calculations are presented. Section 3 is devoted to a detailed discussion of the characteristic features of the Fermi surface in the pure Cu and Au metals as prototypes of the disordered alloys Cu–Au; the computational results for the polarizability $\chi(\mathbf{q})$ for Cu are compared with the above-mentioned results obtained by Tachiki and Teramoto [14]. In Section 4, the change in the geometric features of the Fermi surface accompanying a transition from disordered to ordered alloys is examined; the observed dependences $N(\eta)$ and the fact that N changes substantially from one alloy to another are explained. Section 5 is devoted to an analysis of the nature of two-dimensional long-period superstructures in Au_3Cu. Finally, in Section 6 the results are summarized and discussed in the light of the questions raised above; the question of the place of long-period superstructures among quasicrystalline substances is touched upon.

2. STRUCTURE OF SHORT-PERIOD PHASES. COMPUTATIONAL PROCEDURE

The ordering of an fcc solid solution according to types $L1_2$ (Cu_3AuI) and $L1_0$ (CuAuI) is done [22] on the basis of the star of the vector $\mathbf{k}_s = (2\pi/a)[001]$. The transition into the $L1_2$ phase proceed along a three-ray channel: all three vectors of a star, $(2\pi/a)[100]$, $(2\pi/a)[010]$,

[1] It should be noted that in [14] the polarizability was defined as a negative quantity. In what follows, we shall define it, as usual, as a positive quantity.

and $(2\pi/a)[001]$, contribute to the density function. As a result, the initial cubic symmetry is preserved, and the number of atoms in a unit cell increases from 1 to 4. The Brillouin zone of the $L1_2$ structure is identical to that in a simple cubic lattice and is obtained from the Brillouin zone of the fcc lattice by "folding" the latter along (100) type planes. The transition into the $L1_0$ phase proceeds only along one ray, $(2\pi/a)[001]$. Such ordering is accompanied by period doubling along [001] and the appearance of a tetragonal distortion c/a; for the alloy CuAuI c/a reaches the value 0.93.

In what follows, we shall use the following formal device to make it convenient to compare the electronic structure of fcc solutions and the superstructures $L1_2$ and $L1_0$. We shall assume that they all have four atoms per unit cell (just as $L1_2$). Then the Brillouin zone of the fcc lattice will be identical to that of the superstructure $L1_2$, and the Brillouin zone of the $L1_0$ phase will differ from it only by a weak tetragonal distortion (we note that the natural Brillouin zone of the $L1_0$ structure is also tetragonal, but it has twice the volume [23]).

The "full-potential" LMTO method based on the local electron density approximation was used in the calculation [24]. The Barth–Hedin exchange-correlation potential was used [25]. The integration over occupied states was performed by the tetrahedon method [26], using 120–165 reference points in the self-consistent calculation of the spectrum $\varepsilon_\lambda(\mathbf{k})$ and 1053 (Cu, Au) points, 1771 ($L1_2$ structure) and 4851 ($L1_0$ structure) points in the irreducible part of the Brillouin zone for calculating $\chi(\mathbf{q})$. To calculate the polarizability of the noninteracting electrons,

$$\chi(\mathbf{q}) = \frac{2\Omega}{(2\pi)^3}\int d\mathbf{k}\sum_{\lambda,\lambda'}\frac{f(\varepsilon_\lambda(\mathbf{k}))[1-f(\varepsilon_{\lambda'}(\mathbf{k}+\mathbf{q}))]}{\varepsilon_{\lambda'}(\mathbf{k}+\mathbf{q})-\varepsilon_\lambda(\mathbf{k})},$$

only the energy bands λ intersecting the Fermi level and determining the behavior of this quantity were taken into account: the sixth band in Cu and Au and 22nd–24th bands in Cu_3Au, CuAu, and Au_3Cu. The following lattice parameters were used (in a.u.): $a = 6.805$ (Cu), $a = 7.675$ (Au), $a = 7.079$ (Cu_3Au), $a = 7.467$ and $c = 6.956$ (CuAu) and $a = 7.476$ (Au_3Cu).

3. GEOMETRY OF THE FERMI SURFACE AND THE BEHAVIOR OF $\chi(\mathbf{q})$ IN Cu AND Au

In this section we shall be interested in the nesting features of the Fermi surface in pure Cu and Au metals as prototypes of disordered Cu–Au alloys. The assumption that the Fermi surface in the Cu–Au alloys is similar to that in pure metals is completely justified. Cu and Au are isoelectronic analogs, so that the electronic structure of their alloys is described well in the "average" crystal approximation [4, 15–17, 27].

We note first that the computed Fermi surfaces of Cu and Au agree very well with the experimental surfaces [28, 29]. For example, in Cu the theoretical smallest and largest radii of the necks of the Fermi surface are identical to the experimental values [28] (expressed in units of the radius of the Fermi sphere of free electrons, they are 0.16 and 0.21, respectively).

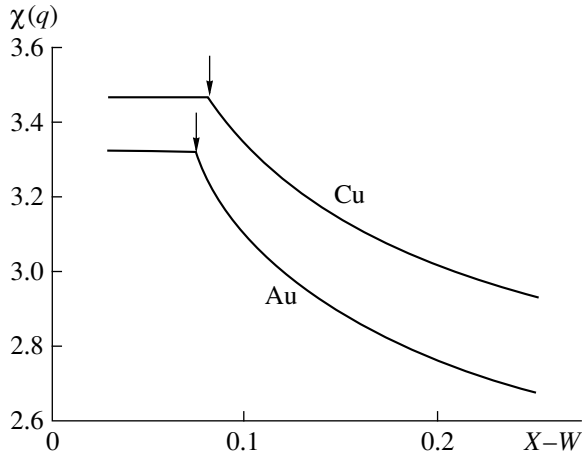

Fig. 1. Electronic polarizability $\chi(\mathbf{q})$, measured in electrons/(Ry cell), in Cu and Au in the X–W direction. The arrows correspond to the vectors $\mathbf{Q}$.

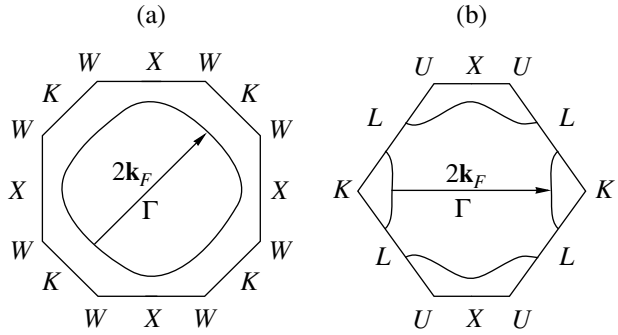

Fig. 2. Fragments of sections of the Fermi surface in copper in the planes (a) $z = 0$ and (b) $x + y = 2\pi/a$.

The electronic polarizabilities, calculated in the directions X–W, of the metals under discussion are shown in Fig. 1. Away from the point X they remain essentially unchanged, but then they decrease sharply, so that a characteristic kink forms on their curves. The coordinates $\mathbf{Q}$ of the kinks, evidently, can be represented as $\Delta\mathbf{k} + \mathbf{k}_s$, where $\mathbf{k}_s = (2\pi/a)[001]$ is a superstructural vector (or the point X of the Brillouin zone), while the vectors $\Delta\mathbf{k}$ are equal to $0.08(2\pi/a)[100]$ and $0.075(2\pi/a)[100]$, respectively, for Cu and Au. As the analysis showed, these coordinates are identical to the points $\mathbf{Q}$ of the Kohn anomalies, determined by the condition

$$\mathbf{Q} + \mathbf{G}_{111} = 2\mathbf{k}_F, \qquad (1)$$

where $\mathbf{G}_{111} = (2\pi/a)[111]$ is a reciprocal lattice vector, the vector $2\mathbf{k}_F$ connects the cylindrical sections of the Fermi surface in the [110] or Γ–K direction (Fig. 2). To

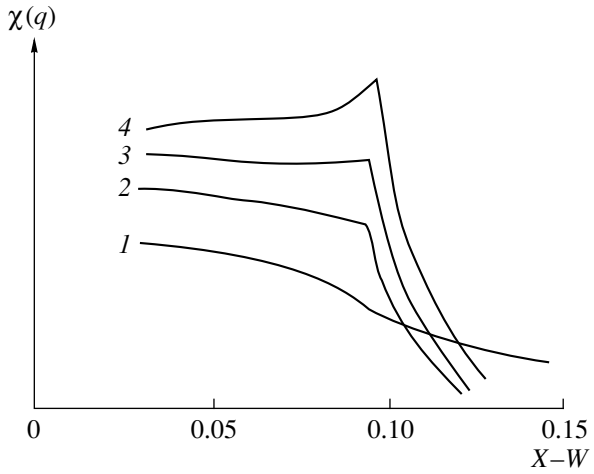

Fig. 3. Electronic polarizabilities $\chi(\mathbf{q})$ of a univalent fcc metal with different Fermi surfaces: (*1*) sphere with radius $2\mathbf{k}_F$; (*2*) with cylindrical sections along [110], characterized by radius $2\mathbf{k}_F$ and height $0.5(2\pi/a)$; (*3*, *4*) with cylindrical sections of large radius.

show more clearly the role of such sections in the formation of the features in the function $\chi(\mathbf{q})$, we performed calculations of this quantity with artificial Fermi surfaces, which were obtained from a sphere by replacing spherical segments on it in the [110] direction by cylindrical sections with different radii of curvature R but the same height $0.5(2\pi/a)$. Curve *1* in Fig. 3 shows the behavior of $\chi(\mathbf{q})$ for a spherical Fermi surface; it is characterized by a logarithmic singularity at $\mathbf{q} = \mathbf{Q}$, satisfying the condition (1) (the value of $2k_F$ was chosen to be $0.94 \cdot 2\pi/a$). The curve *2* corresponds to the introduction of cylindrical sections with radius of curvature R equal to k_F. Finally, the curves *3* and *4* correspond to the addition of cylindrical segments with even larger radii (the sections of the Fermi surface in the [110] direction become increasingly flatter). It is evident that for a sufficiently large radius R a step appears in the curve $\chi(\mathbf{q})$, just as in Fig. 1.

The form which we have obtained for $\chi(\mathbf{q})$, is substantially different from the form presented in [14]: the Kohn singularity appears not in the form of a sharp peak but rather only as a step. This difference in the results is explained by the low accuracy of the calculations performed in [14]. An investigation of the convergence of $\chi(\mathbf{q})$ as a function of the number of reference points in the irreducible part of the Brillouin zone leads to this conclusion. It turned out that for a small number of reference points ($\simeq$490) the susceptibility possesses a peak whose character is close to that of the peak presented in [14]. As the number of reference points increases, the peak gradually transforms into the step described above (the step remains practically unchanged when the number of points is increased to 1053).

We shall now determine the long period of hypothetical long-period superstructures, which would appear in the metals under consideration when a gap opens in the cylindrical sections of the Fermi surface. Using the formula $N = \pi/|\Delta\mathbf{k}|$, we obtain the values 6.25 and 6.67, respectively, for copper and gold (in units of the lattice parameter a). These values will be used below to estimate the quantity $N(\eta = 0)$ in the alloys Cu–Au.

For clarity in the exposition below, it is important to verify that the character of the features in $\chi(\mathbf{q})$ and the values of N found in pure metal remain the same as before, if their crystal structure is treated not as fcc but rather as $L1_2$ (four atoms per cell). On switching from an fcc lattice to the $L1_2$ phase the Brillouin zone transforms in a manner so that the X–W direction transforms into the Γ–X direction, and the flat sections of the Fermi surface along [110] are close to the points M. Comparing the curves $\chi(\mathbf{q})$ for copper along the directions X–W and Γ–X (Figs. 1, 4a), we verify that they both possess the same stepped form. The distances from the initial points (Γ, X) to the kinks in the curves are identical (they are equal to $0.08(2\pi/a)$). Whereas previously the kink was determined by 6–6 transitions (the diameter of the Fermi surface in the sixth band), now they are determined by all possible transitions with the participation of the 23rd and 24th bands: these are the bands into which the sixth band transforms on switching to a new representation of the structure.

4. GEOMETRY OF THE FERMI SURFACE AND BEHAVIOR OF $\chi(\mathbf{q})$ IN ORDERED ALLOYS. THE FUNCTION $N(\eta)$

Figure 4 shows the curves $\chi(\mathbf{q})$, calculated for the alloys Cu_3Au, CuAu and Au_3Cu in the direction Γ–X on its initial section. On the whole, they are similar to the corresponding curve for Cu (Fig. 4a), but they differ from it by the absence of an initial horizontal plateau and the appearance of additional kinks (in the case of CuAu and Au_3Cu). The kinks are much less pronounced than in pure metals.

To understand these results we shall examine how the spectrum $\varepsilon_\lambda(\mathbf{k})$ transforms on switching from an fcc lattice to the structures $L1_2$ and $L1_0$. It is evident from Fig. 5 that in pure copper (and disordered alloys) the electronic term is four-fold degenerate at the point M. Such a high degree of degeneracy is due, of course, to the artificial representation of the electronic spectrum of the fcc metal in the Brillouin zone of the structure $L1_2$. In true superstructures $L1_2$, the term under study splits, as should happen, into a doubly degenerate level M_5' and singlet levels M_1 and M_3. Significantly, the relative arrangement of the split levels can be arbitrary. This is easy to show, using the four-wave approximation of the pseudopotential method [27]. In this approximation the values of the terms M_5', M_1, and M_3 can be found explicitly; they are equal to $T - \Delta v_{110}$, $T + \Delta v_{110} + 2\Delta v_{100}$, and $T + \Delta v_{110} - 2\Delta v_{100}$, respectively, where T is the kinetic energy in the "empty" lattice, and Δv_{110} and Δv_{100} are the differences of the pseudopotentials of the

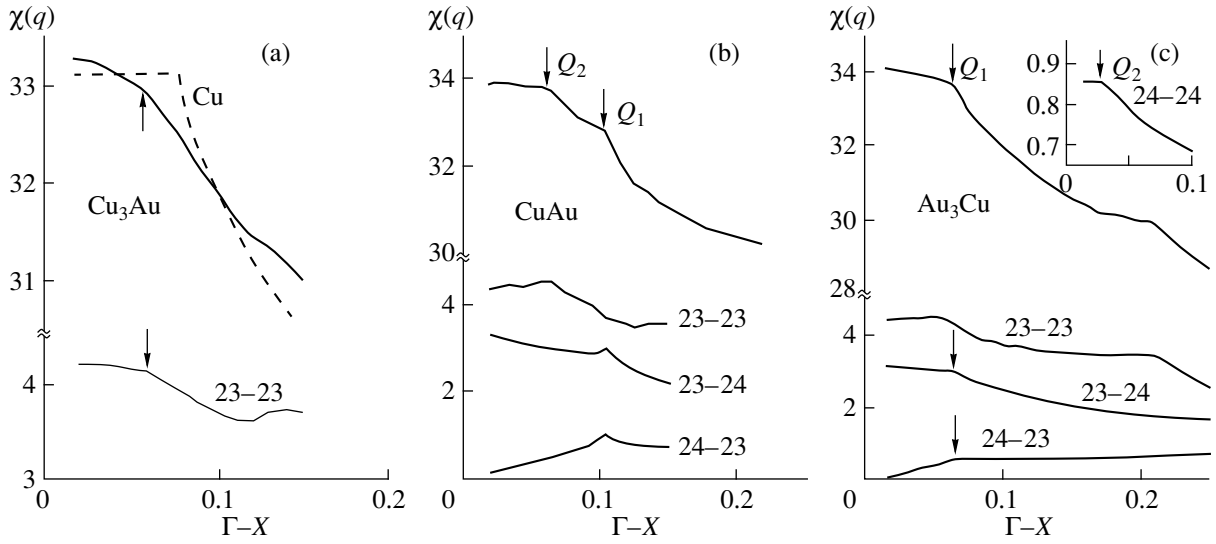

Fig. 4. Electronic polarizability $\chi(\mathbf{q})$ [electrons/(Ry · cell)] and its partial contributions to (a) Cu_3Au, (b) CuAu, and (c) Au_3Cu in the direction Γ–X($\langle 100 \rangle$). The dashed curve in Fig. 4a corresponds to pure copper.

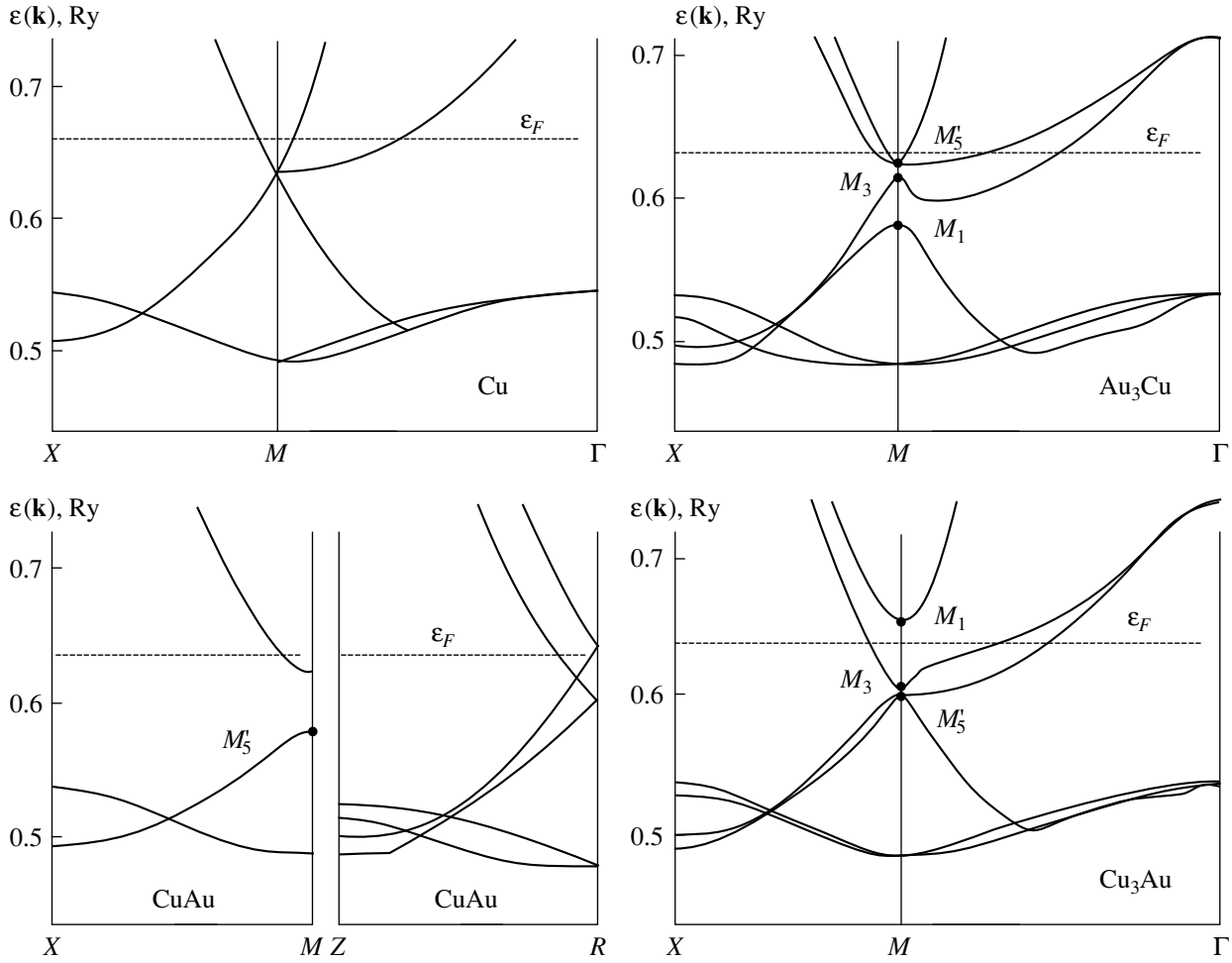

Fig. 5. Electron-energy spectrum $\varepsilon_\lambda(\mathbf{k})$ near the points M and R in Cu, Au_3Cu, CuAu, and Cu_3Au.

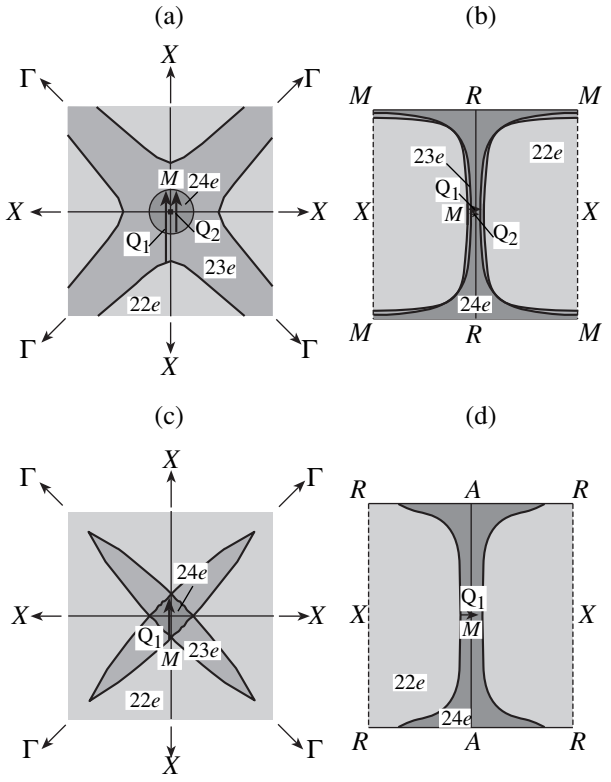

Fig. 6. Fragments of sections of the Fermi surface in (a, b) Au_3Cu and (c, d) CuAu in the planes $z = 0$ (a, c—on an enlarged scale) and $x = 0.5 \cdot 2\pi/a$ (b, d).

components at the superstructural sites of the reciprocal lattice $(2\pi/a)[110]$ and $(2\pi/a)[100]$. Since the signs and absolute values of the form factors Δv_{110} and Δv_{100} can be arbitrary, the relative arrangement of the levels is not completely determined. For example, the level M_5' in Au_3Cu lies above the other two levels, while in Cu_3Au it lies below them.

On switching from an fcc lattice to the superstructure $L1_0$ (with four atoms per unit cell), the flat sections of the Fermi surface are close to the points *M* and *R* of the new (tetragonal) Brillouin zone. The dispersion curves $\varepsilon_\lambda(\mathbf{k}) \approx \varepsilon_F$ near these points are presented in Fig. 5. It is evident from the figure that at each point the initial four-fold degenerate term (characteristic for an fcc solution) splits in a manner so that two doubly degenerate levels arise. Here, at the point *M*, in contrast to the case of the superstructure $L1_2$, the levels M_1 and M_3 are "stuck to one another": now the matrix elements Δv_{010} and Δv_{100} (but not Δv_{001}!) are zero, and the terms mentioned above M_5', M_1, and M_3 acquire the values $T - \Delta v_{110}$, $T + \Delta v_{110}$, and $T + \Delta v_{110}$, respectively.

In the alloy Cu_3Au, near the point *M*, there exists only one electronic section of the Fermi surface, corresponding to the 23rd band. The kink in the polarizability at $\mathbf{q} = \mathbf{Q} = 0.06(2\pi/a)[100]$ (it corresponds to the half-period $N = 8.3$) is associated with the diameter of this section or 23–23 transitions. In Au_3Cu, in contrast to Cu_3Au, two electronic sections (23rd and 24th bands) are realized near the point *M*, so that the total electronic polarizability of this alloy is determined by transitions occurring with the participation of these two bands. Only the interband transitions 23–24 and 24–23 are responsible for the kink in the function $\chi(\mathbf{q})$ at $\mathbf{q} = \mathbf{Q}_1 = 0.065(2\pi/a)[100]$ ($N_1 = 7.7$) (Fig. 4c). The kink is also seen in the partial contribution of 24–24 with a very small vector $\mathbf{Q}_2 = 0.0275(2\pi/a)[100]$ (see inset in Fig. 4c): this feature, which is essentially not manifested in the total electronic polarizability, will be discussed below.

In CuAu one kink in the curve $\chi(\mathbf{q})$ at $\mathbf{q} = \mathbf{Q}_1 = 0.105(2\pi/a)[100]$ is due to an interband nesting (transitions 23–24 and 24–23) near the point *M* (Figs. 6c, 6d); it corresponds to the long-period superstructure with $N_1 = 4.8$. The second kink at $\mathbf{q} = \mathbf{Q}_2 = 0.065(2\pi/a)[100]$ is due to the intraband transitions 23–23 near the points *M* and *R*; it corresponds to a superstructure with average half-period $N_2 = 7.7$. Thus, for an alloy with the equivalent composition the calculations predict two different possible values of *N*: 4.8 and 7.7. Only the first of these two possibilities is realized: the experimental values of *N* in this alloy are close to 5 [1, 4, 11–13]. In this connection, in what follows, to construct the qualitative dependences $N(\eta)$ in CuAu we shall proceed from the fact that $N(\eta = 1) = 4.8$.

Enough data has now be obtained to judge the dependence of the antiphase domain *N* on the degree of long-range order η. In completely ordered alloys ($\eta = 1$) we have $N = 8.3$ (Cu_3Au), $N = 4.8$ (CuAu), and $N = 7.7$ (Au_3Cu). In disordered alloys ($\eta = 0$) the quantity *N* can be easily estimated on the basis of the values found above for pure Cu (6.25) and Au (6.67) and using Vegard's law. Having the "reference points" $N(\eta = 1)$ and $N(\eta = 0)$ and assuming the functions $N(\eta)$ to be linear, we shall construct the latter for each alloy. It is evident from Fig. 7 that the theoretical curves $N(\eta)$ agree well with the experimental curves, not only qualitatively but also quantitatively. It is interesting that the theory in the case of CuAu predicts the "anomalous" behavior of $N(\eta)$—a decrease of the size *N* of the antiphase domain with increasing η. Unfortunately, we know of no experimental measurements of the function $N(\eta)$ in this alloy.

5. NATURE OF THE TWO-DIMENSIONAL LONG-PERIOD SUPERSTRUCTURE IN THE ALLOY Au_3Cu

In this alloy, as we have already mentioned, two-dimensional long-period superstructures with substantially different periods $2N_1$ and $2N_2$ along two mutually orthogonal directions ($N_1 = 7.2$ and $N_2 = 17$–19 [4]) are realized. In the discussion above we associated one of the periods with the feature in the susceptibility at $\mathbf{q} = \mathbf{Q}_1 = 0.065(2\pi/a)[100]$. The superperiod $N_1 = \pi/|\mathbf{Q}_1| \simeq 7.7$ cor-

responding to this feature correlates well with the experimental value $N_1 = 7.2$ [4]. The second period must be associated with the feature of the partial contribution of 24–24 at $\mathbf{q} = \mathbf{Q}_2 = 0.0275(2\pi/a)[100]$: $N_2 \sim \pi/|\mathbf{Q}_2| = 18$, which agrees very well with the second observed value $N_2 = 17$–19 [4]. We shall verify that the vectors $\mathbf{Q}_1$ and $\mathbf{Q}_2$ do indeed separate sections of the Fermi surface which have the same shape, i.e., they correspond to the positions of Kohn anomalies.

In Au_3Cu, as we have underscored (Figs. 6a, 6b), two electronic sections of the Fermi surface (23rd and 24th bands), genetically related with the splitting of the level M at a transition in the $\mathbf{k}$ point of the general position, arise near the point M_5'. In the section $z = 0$ (Fig. 6a) they have the shape of a cross and a circle of very small radius, respectively, and in the section $x = 0.5$ they have the shape of thin rectilinear strips, strongly elongated along the line M–R and centered on it (Fig. 6b); the latter fact is partially due to the circumstance that the level M_5' does not split on the line M–R itself. On the whole, the electronic section of the 24th band is a thin cylindrical rod, which coincides with itself under a translation by a small vector $\mathbf{Q}_2 = 0.0275(2\pi/a)[100]$ (Figs. 6a, 6b). This is why the electronic polarization (due only to 24–24 transitions) at the point $\mathbf{Q}_2$ undergoes a characteristic kink (see inset in Fig. 4c). The rod under study also fits well with the electronic section of the 23rd band when the rod is transported by the vector $\mathbf{Q}_1 = 0.065(2\pi/a)[100]$; this gives rise to a kink, studied above, in the dependence $\chi(\mathbf{q})$ at this wave vector.

The following simple mechanism leading to the formation of two-dimensional long-period superstructures follows from what we have said above. Each of the two systems of coinciding sections of the Fermi surface induces the formation of its superperiod along one of two mutually orthogonal directions. If, for example, the coinciding sections, separated by the vector $\mathbf{Q}_1$, induce a period along [100], then the sections corresponding to the vector $\mathbf{Q}_2$ induce a period along the orthogonal direction ([010] or [001]).

As shown in our recent work [30], these same arguments explain the formation of two-dimensional long-period superstructures in the alloy Cu_3Pd also.

6. DISCUSSION

As one can see from the preceding sections, "short" ordering results in splitting and deformations of the electronic states that determine nesting on the Fermi surface (and, therefore, the stability of the long-period superstructures). Significantly, such "renormalization" of the spectrum $\varepsilon_\lambda(\mathbf{k})$ is of a different character for the compositions Cu_3Au, CuAu, and Au_3Cu; this gives rise to the specific nature of the superstructures in each of these alloys.

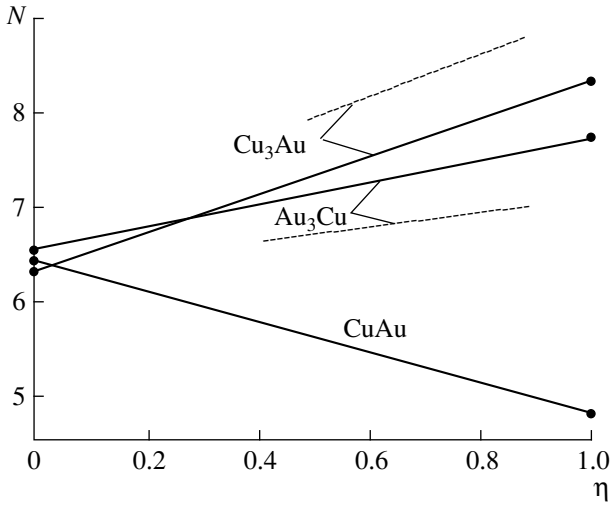

Fig. 7. Size N of an antiphase domain as a function of the degree η of long-range order in the alloys Cu–Au: theory (solid lines) and experiment [4] (dashed lines).

In the ordered alloy Cu_3Au, just as in a disordered state, only a single pair of coinciding sections, separated by the nesting vector $\mathbf{Q} \parallel [100]$, arises. A different situation occurs in the alloys CuAu and Au_3Cu, where two pairs of such sections, corresponding to the vectors $\mathbf{Q}_1$ and $\mathbf{Q}_2$, are realized in this direction. In Au_3Cu, the latter circumstance leads to a very nontrivial result: the formation of a two-dimensional long-period superstructure with substantially different periods N_1 and N_2 along perpendicular directions. It is interesting that in the experiments a two-dimensional superstructure is formed only with very prolonged annealing, which puts the system into complete thermodynamic equilibrium [4]. In the absence of complete equilibrium in Au_3Cu, just as in alloys with other compositions, a one-dimensional long-period superstructure arises.

In this case, only one of two pairs of coinciding sections, corresponding to a long period N_2, is "actuated" in Au_3Cu. Conversely, in CuAu only a pair corresponding to the smaller period N_1 is realized. This explains why the periods of the superstructures in these two alloys are substantially different. Hence there also follows the conclusion that in these alloys the dependence $N(\eta)$ should be inverse: the quantity N should increase with η in Au_3Cu and decrease in CuAu. Indeed, to the extent of the ordering, the splitting of the electronic spectrum at the point M of the Brillouin zone increases and the value of $N(\eta)$ should deviate increasingly from the initial value $N(\eta = 0)$ (Fig. 7).

The different character of the splitting of $\varepsilon_\lambda(\mathbf{k})$ near the point M on switching from one alloy to another also explains the quite strong dependence of the half-period N on the composition x. Let us assume that as the composition varies continuously, we move from the alloy CuAu to Au_3Cu. Then a transition should occur from

the "branch" with the shorter half-period (N_1) in CuAu to the "branch" with the long half-period (N_2) in Au_3Cu. It is obvious that such "boundary conditions" will give not only a strong dependence of N on x, but also, possibly, a nonlinear dependence.

On account of the splitting examined above and the deformation of the "critical" electronic states, the "quality" of nesting decreases when we switch from pure metals (disordered alloys) to the superstructures $L1_2$. It is evident from Figs. 1 and 4a that in pure metals and gold the polarizability has a more pronounced feature (step) than in ordered alloys. Hence follows the following unexpected conclusion: at a definite stage short-period ordering can begin to destabilize the long-period superstructure. This circumstance is fundamental for explaining why in the alloys studied long-period superstructures exist only in a small temperature range, becoming energetically unfavorable compared with ordinary superstructures ($L1_2$ and $L1_0$) at sufficiently low temperatures.

The behavior of the electronic polarizability in pure metals, Cu and Au (and disordered solutions Cu–Au), near the point X is different from that in the calculations in [14]: a step with an extended horizontal plateau arises instead of a peak. This means, essentially, that the appearance of the long-period superstructures cannot be explained on the basis of an analysis of the potential $V(\mathbf{q})$ or the Fourier transform of the pair potential $V_{AA}(\mathbf{r}) + V_{BB}(\mathbf{r}) - 2V_{AB}(\mathbf{r})$, calculated in second-order perturbation theory with respect to the electronion interaction. Indeed, such an explanation presupposes [14] that the minimum of the potential $V(\mathbf{q})$, proportional to the polarizability, shifts from the Lifshits point $\mathbf{k}_s$ precisely as a result of the peak in the dependence $\chi(\mathbf{q})$. In reality, however, there are no such peaks on the curve $\chi(\mathbf{q})$, and the reasons for the appearance of long-period superstructures must be sought outside the perturbation theory and pair interatomic interaction approximation.

This result agrees with the results of [17, 18], where a simple, exactly solvable model (Kronig–Penney type) was solved. It was shown there that stabilization of the long-period superstructures is possible not only in systems with flat or cylindrical sections of the Fermi surface but also with ellipsoidal sections, leading to a relatively weak (logarithmic) singularity in $\chi(\mathbf{q})$. Of course, flat, nearly cylidnrical, sections of the Fermi surface also promote the appearance of long-period superstructures in the alloys studied.

The cylindrical sections of the Fermi surface lead only to a square-root singularity in the dependence $\chi(\mathbf{q}) \propto \pm\sqrt{|\mathbf{q} - 2\mathbf{k}_F|}$, and therefore they cannot be a source of strong Kohn anomalies in the phonon spectrum. This is actually observed. Inelastic neutron scattering experiments [31, 32] in disordered alloys based on copper $Cu_{0.84}Al_{0.16}$ and $Cu_{0.715}Pd_{0.285}$ did not show any appreciable Kohn anomalies. Even in pure copper at low temperatures (i.e., under conditions when "alloy" and temperature broadening of the Fermi surface are absent) the Kohn anomalies at the phonon frequencies are very weak: only a change in slope and not a dip in the dispersion curves $\omega(\mathbf{k})$ is observed [28]. As far as strong "Kohn singularities" in diffuse scattering of x-rays, $I(\mathbf{q})$, by the disordered alloys Cu–Au, Cu–Al, Cu–Pd, and others [20, 33] are concerned, here, as Krivoglaz underscores in [20], a unique mechanism that intensifies the effect is realized. This mechanism consists of the following. In these alloys, an extremely nonuniform short-range order characterized by the presence of local regions (microdomains) 10–20 Å in size is formed. These sizes are close to the periods $N = \pi/|\Delta\mathbf{k}|$ of the future long-period superstructures and therefore they give rise to peaks in the intensity $I(\mathbf{q})$ on the surfaces of the reciprocal space, where $\mathbf{q}$ or $\mathbf{q} + \mathbf{G}$ coincide with the diameter $2\mathbf{k}_F$ in the [110] direction. The intensity $I(\mathbf{q})$ is especially high at the points of intersection of these surfaces, and this is what explains the appearance of the "cross" consisting of four Kohn spots near positions of the type $2\pi/a[110]$ (see [20, 33]).

In conclusion, we shall discuss the question of the place of long-period structures among other quasicrystalline substances. Having an incommensurate period, the superstructures studied above are undoubtedly similar in some respects to ordinary incommensurate crystals (systems with charge-density waves, helicoidal magnetic structures, and so on). Thus, as the concentration varies, they can undergo a transition into commensurate long-period superstructures, whose average period can be expressed as a rational fraction m/n (m and n are integers). For example, in the system Cu–Pd such a *lock-in* transition occurs as the Pd concentration increases (at the point 21.3 at %Pd) [5]. As the composition varies above this point, the values of m/n start to vary in a discrete manner [5]: a "devil's staircase" of commensurate transitions arises.

Despite their well-known similarity to ordinary incommensurate crystals [34–36], long-period superstructures still fit poorly within the standard picture of the behavior of incommensurate systems. In the first case, as we have already mentioned, they form as a result of sharp first-order transitions, immediately acquiring a domain (soliton) character and bypassing the initial stage, corresponding to their modulation by a single plane wave. As temperature decreases, the density of the domain walls changes very little; usually it increases slightly. On further cooling, long-period superstructures undergo a sharp first-order transition into Lifshits superstructures $L1_0$ or $L1_2$ [4, 7]. In ordinary incommensurate structures, however, as is well known [34, 35], a soliton lattice evolves differently: the density of solitons decreases rapidly with temperature and vanishes at point of the *lock-in* transition (a second-order or nearly second-order transition).

The fundamental difference between long-period superstructures and ordinary incommensurate systems

is that the average size $2N$ of domains in them cannot assume arbitrary values, but rather it is fixed by the diameters $2\mathbf{k}_F$ of the initial Fermi surface. But this relates them to quasicrystals, whose stability is based essentially on the same factors: the "interaction" of the Fermi surface with Bragg planes [37]. As is well known [38], quasicrystals can be represented as a quasiperiodic packing of two (or more) unit cells with different shapes. This packing is organized in a manner so that the Fermi surface is in contact with a Brillouin pseudozone, due to icosahedral symmetry of the quasicrystal [37]. It is easy to see that domains of different length in long-period superstructures and different unit cells in quasicrystals essentially play the same role: by their specific alternation they give the quasiperiod $N \sim \pi/|2\mathbf{k}_F|$ required to lower the electronic energy. Thus, the long-period superstructures studied here have a unique place among quasicrystalline substances: they fall between incommensurate systems and quasicrystals.

ACKNOWLEDGMENTS

We thank É.V. Kozlov for helpful discussions. This work was supported by the Ministry of General and Professional Education (grant no. 98-26-54-63).

REFERENCES

1. H. Sato, Sci. Rep. Res. Inst. Tohoku Univ., Ser. A **4**, 1 (1952); **4**, 169 (1952).
2. M. Guymont and D. Gratias, Phys. Status Solidi A **36**, 329 (1976).
3. D. Watanabe, in *Proceedings of the International Conference on Modulated Structures, Kailna Kona, Haw., 1979* (New York, 1979), p. 229.
4. N. M. Matveeva and É. V. Kozlov, *Ordered Phases in Metal Systems* (Nauka, Moscow, 1989).
5. D. Broddin, G. van Tendeloo, J. van Landuyt, *et al.*, Philos. Mag. **54**, 395 (1986).
6. D. Watanabe and O. Terasaki, in *Proceedings of the Phase Transformation Solids Symposium, Malemе-Chania, Crete, 1983* (New York, 1984), p. 231.
7. A. I. Potekaev, Izv. Vyssh. Uchebn. Zaved. Fiz., No. 6, 3 (1995).
8. J. C. Slater, Phys. Rev. **84**, 179 (1951).
9. J. E. Nicolas, J. Phys. Soc. (London) Sect. A **66**, 201 (1953).
10. N. F. Mott and H. Jones, *The Theory of the Properties of Metals and Alloys* (Oxford Univ. Press, London, 1936).
11. H. Sato and R. S. Toth, Phys. Rev. **124**, 1833 (1961).
12. H. Sato and R. S. Toth, Phys. Rev. **127**, 469 (1962).
13. R. S. Toth and H. Sato, J. Appl. Phys. **33**, 3250 (1962).
14. M. Tachiki and K. Teramoto, J. Phys. Chem. Solids **28**, 375 (1966).
15. V. M. Dement'ev and É. V. Kozlov, Izv. Vyssh. Uchebn. Zaved. Fiz., No. 6, 21 (1973).
16. V. M. Dement'ev and É. V. Kozlov, Izv. Vyssh. Uchebn. Zaved. Fiz., No. 6, 30 (1974).
17. D. A. Vul' and M. A. Krivoglaz, Fiz. Met. Metalloved. **51**, 231 (1981).
18. D. A. Vul' and M. A. Krivoglaz, Fiz. Met. Metalloved. **55**, 869 (1983).
19. M. A. Krivoglaz, Zh. Éksp. Teor. Fiz. **84**, 355 (1983) [Sov. Phys. JETP **57**, 205 (1983)].
20. M. A. Krivoglaz, *Diffuse Scattering of X-rays and Neutrons by Fluctuation Nonuniformities in Nonideal Crystals* (Naukova Dumka, Kiev, 1984).
21. R. E. Peierls, *Quantum Theory of Solids* (Oxford Univ. Press, London, 1955).
22. A. G. Khachaturyan, *The Theory of Phase Transformations and the Structure of Solids Solutions* (Nauka, Moscow, 1974).
23. É. V. Kozlov, V. M. Dement'ev, N. M. Kormin, *et al.*, *Structure and Stability of Ordered Phases* (Tomsk. Gos. Univ., Tomsk, 1994).
24. S. Yu. Savrasov and D. Yu. Savrasov, Phys. Rev. B **46**, 12181 (1992).
25. U. Barth and L. Hedin, J. Phys. C **5**, 1629 (1972).
26. J. Rath and A. J. Freeman, Phys. Rev. B **11**, 2109 (1975).
27. W. Heine, M. Cohen, and D. Weaire, *The Pseudopotential Concept; The Fitting of Pseudopotential to Experimental Data and Their Subsequent Application: Pseudopotential Theory of Cohesion and Structure* (McCraw-Hill, New York, 1970; Mir, Moscow, 1973).
28. G. Nilsson and S. Rolandson, Phys. Rev. B **9**, 3278 (1974).
29. M. R. Halse, Philos. Trans. R. Soc. London, Ser. A **265**, 507 (1969).
30. O. I. Velikokhatnyĭ, S. V. Eremeev, I. I. Naumov, *et al.*, Pis'ma Zh. Éksp. Teor. Fiz. **69**, 548 (1999) [JETP Lett. **69**, 589 (1999)].
31. H. Chou, S. M. Shapiro, S. C. Moss, *et al.*, Phys. Rev. B **42**, 500 (1990).
32. Y. Noda, D. Kumar, and K. I. Oschima, J. Phys.: Condens. Matter **5**, 1655 (1993).
33. V. I. Iveronova and A. A. Katsnel'son, *Short-Range Order in Solid Solutions* (Nauka, Moscow, 1977).
34. W. L. McMillan, Phys. Rev. B **14**, 1496 (1976).
35. W. L. McMillan, Phys. Rev. B **16**, 4655 (1977).
36. L. N. Bulaevskiĭ and D. I. Khomskiĭ, Zh. Éksp. Teor. Fiz. **74**, 1863 (1978) [Sov. Phys. JETP **47**, 971 (1978)].
37. J. Friedel and F. Denoyer, C. R. Acad. Sci., Ser. 2 **305**, 171 (1987).
38. J. E. S. Sokolar, T. C. Lubensky, and P. J. Steihardt, Phys. Rev. B **34**, 3345 (1986).

Translation was provided by AIP

Journal of Experimental and Theoretical Physics, Vol. 90, No. 3, 2000, pp. 488–490.
Translated from Zhurnal Éksperimental'noĭ i Teoreticheskoĭ Fiziki, Vol. 117, No. 3, 2000, pp. 559–561.

SOLIDS
Structure

Critical Dynamics of Models of the Antiferromagnet Cr_2O_3

A. K. Murtazaev, I. K. Kamilov*, Kh. K. Aliev, and V. A. Mutaĭlamov

Institute of Physics, Dagestan Scientific Center, Russian Academy of Sciences, Makhachkala, 367003 Russia
**e-mail: kamilov@datacom.ru*

Received June 10, 1999

Abstract—The critical dynamics of models of the real antiferromagnet Cr_2O_3 is investigated by the Monte Carlo method. The relaxation times of systems with $N = 256$, 500, 864, 2048, and 2916 spins are determined using the autocorrelation functions formalism. The values of the dynamic critical index z are calculated based on them. © *2000 MAIK "Nauka/Interperiodica".*

The investigation of the dynamic critical properties of spin systems is one of the important problems of statistical physics. In the last few years, substantial progress has been made in investigations and the understanding of static critical phenomena, whereas the study of the critical dynamics by conventional methods encounters great difficulties [1–4]. As a result, the critical dynamics is at the present time being investigated intensively by the methods of computational physics, specifically, Monte Carlo methods [5–10]. In the last few years, careful investigations of the critical dynamics of the Ising model [5] and the classical Heisenberg model [6] have been performed on a simple cubic lattice with calculation of the dynamical critical exponent z. The values obtained for the dynamic critical exponent z are close to 2 for both the Ising and Heisenberg models. For the Ising model this value agrees with the theoretically predicted values [1], but this cannot be said of the Heisenberg model, since for isotropic ferromagnets (J model [1]) the theory predicts the value $z = (d + 2 - \eta)/2 \approx 2.5$ (d is the dimension of the space, η is Fisher's exponent).

On this level, there is great interest in the investigation of the critical dynamics of antiferromagnets and the degree to which it is influenced by weak relativistic interactions (anisotropy) that perturb the initial behavior.

In the present work we have made the first investigation of the critical dynamics of models of a real Heisenberg antiferromagnet Cr_2O_3 with complicated rhombohedral structure. The Hamiltonian of Cr_2O_3 can be represented in the form [11–13]

$$H = -\frac{1}{2}\sum_{i,j} J_1(\mu_i\mu_j) - \frac{1}{2}\sum_{k,l} J_2(\mu_k\mu_l) - D_0\sum_i (\mu_i^z)^2, \quad |\mu_i| = 1, \tag{1}$$

where, according to the experimental data of [11], J_1 and J_2 are the parameters of the interaction of each spin with one nearest neighbor and three nearest neighbors, respectively ($J_2 = 0.45J_1$, $J_1 < 0$, $J_2 < 0$). The various relativistic interactions were fixed by the effective single-ion anisotropy $D_0 > 0$.

From our standpoint the following ratios between the anisotropy D_0 and exchange J_1 need to be considered:

$$\text{I. } D_0/|J_1| = 2.5 \times 10^{-4},$$

corresponding to real Cr_2O_3 samples, and

$$\text{II. } D_0/|J_1| = 2.5 \times 10^{-2},$$

characteristic for small magnetic systems with uniaxial anisotropy and dimensions of several tens of angstroms [14].

We call the first case model I and the second case II. All crystallographic, exchange, and other data employed for model I correspond to real Cr_2O_3 samples. In model II, a value characteristic for small magnetic systems (particles) is used for the anisotropy constant D_0, since, despite the presence of periodic boundary conditions, the systems modeled by the Monte Carlo method have finite linear dimensions ($L \ll \infty$, $L \propto N^{1/3}$), and as a result certain properties characteristic for small systems could be manifested.

The calculations were performed by the Monte Carlo method using the standard Metropolis algorithm, for which systems with periodic boundary conditions and $N = 256$, 500, 864, 2048, and 2916 spins, located and interacting in a strict correspondence with the crystallographic and exchange characteristics of real Cr_2O_3 crystals, were formed.

According to the dynamic finite-dimensional scaling [6, 15], the relaxation time τ in the critical region scales as

$$\tau(\xi, L, t) = L^z f(\xi/L, t/L^z), \tag{2}$$

where ξ is the correlation length, and $f(x, g)$ is the scaling function. At the critical point the characteristic correlation length is determined by the dimensions L of the

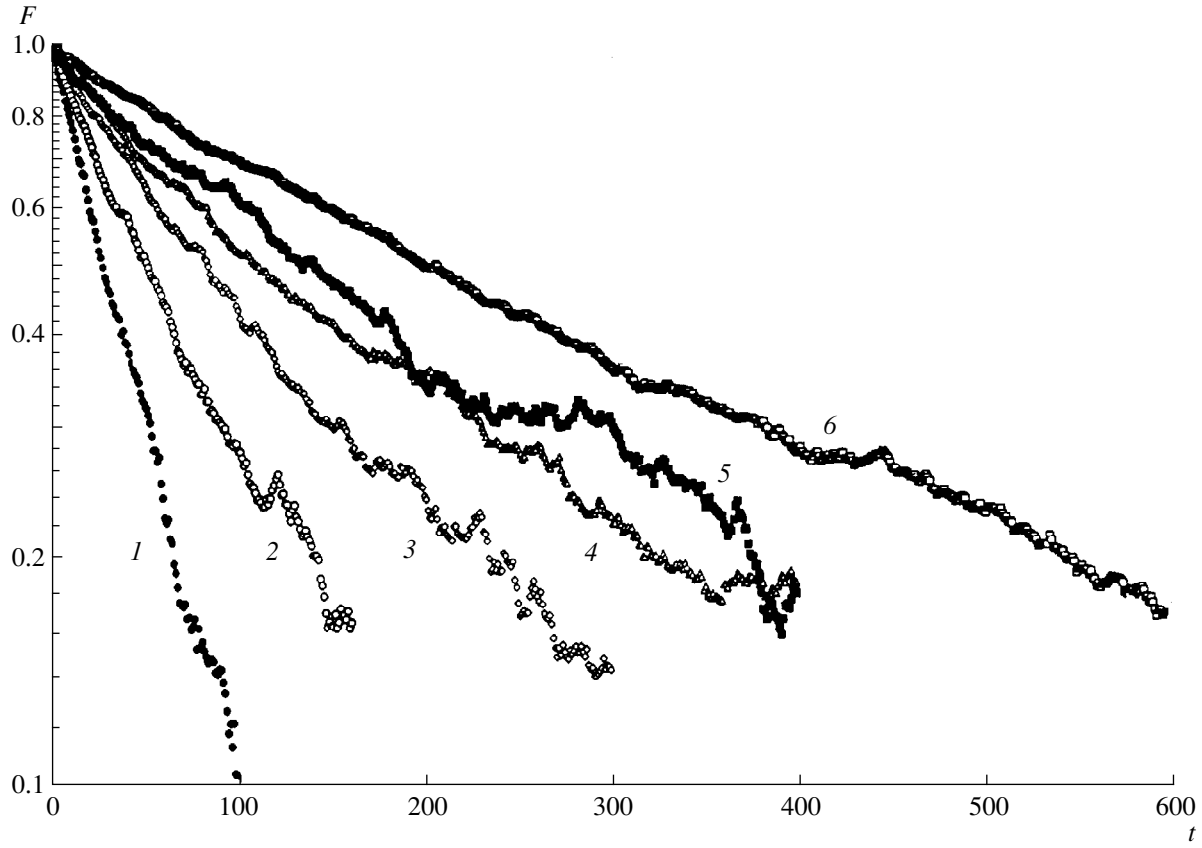

Fig. 1. Time dependences of the autocorrelation functions F for systems with different numbers of spins N (model II): N = (*1*) 256; (*2*) 500; (*3*) 864; (*4*) 1372; (*5*) 2048; (*6*) 2916. The time t is measured in Monte Carlo steps and is normalized per spin.

system, and therefore the relaxation time is determined as

$$\tau \propto L^z \tag{3}$$

for asymptotically large L. To determine z it is necessary to find the relaxation times of the system with different values of L. For this, we employed the apparatus of autocorrelation functions. The autocorrelation functions

$$F(t) = \frac{\langle \mathbf{M}(0)\mathbf{M}(t)\rangle - \langle \mathbf{M}(0)\rangle\langle \mathbf{M}(0)\rangle}{\langle \mathbf{M}(0)\mathbf{M}(0)\rangle - \langle \mathbf{M}(0)\rangle\langle \mathbf{M}(0)\rangle}, \tag{4}$$

where $\mathbf{M}(t)$ is the value of the order parameter at the time t, were calculated for the order parameter of the antiferromagnetism vector. The autocorrelation functions for each system were followed until the value of $F(t)$ decreased to 0.1. The values obtained for $F(t)$ were approximated by the exponential function $F(t) = A\exp(-t/\tau)$, from which the relaxation times τ were determined by a nonlinear leastsquares method.

After the equilibrium state was reached, a sequence of configurations, where one configuration was separated from another by a time greater than τ for each system, was generated in order to perform the averaging in the expression (4). Thus, manner, successive configurations were independent. For all systems, n = 30 000 averages were made for each system with a necessary minimum of 22 000. After the system reached equilibrium, an additional section of a Markov chain of length 5τ was cut off. A series of checking experiments with all control numbers increased by a factor of 2 was also performed. A substantial improvement in the results was not observed. Binder's cumulant method was used to determine the critical temperatures of the systems studied [16].

Figure 1 shows the characteristic dependences of the autocorrelation functions $F(t)$ for systems with different numbers of spins for model II. Similar dependences were also studied for model I. Using the values of τ determined using the scheme indicated above, double-logarithmic dependences of the relaxation times τ on the linear dimensions L were constructed. Figure 2 illustrates such a dependence for model I. In this figure the slope angle of the straight line determines the value of the index z. The values obtained in this manner for the dynamic critical index z are $z = 2.54 \pm 0.08$ for model I and $z = 2.33 \pm 0.08$ for model II. We note that the value $z = 2.54 \pm 0.08$ disagrees with the theoretical estimates for isotropic ($z = d/2$, G-model [1]) and anisotropic ($z \approx 2.0$ [4]) antiferromagnets, but agrees well

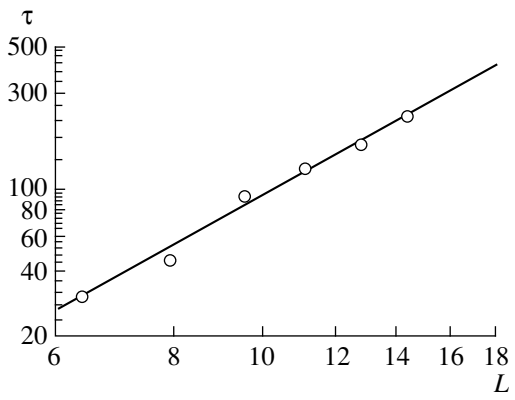

Fig. 2. Relaxation time τ [Monte Carlo step/spin] versus the linear size of the system L (model I, $z = 2.54 \pm 0.08$).

with the values predicted for isotropic ferromagnets ($z \approx 2.5$, J-model [1]). Similarly, the quantity $z = 2.33 \pm 0.08$ obtained for model II also differs substantially from the theoretical estimates for antiferromagnets and falls between the values predicted for isotropic ferromagnets ($z \approx 2.5$ [1]) and anisotropic magnets ($z \approx 2$, A-model [1]). It is obvious that such a change in z from model I to model II is due to a substantial intensification of the term describing the single-ion anisotropy.

REFERENCES

1. P. C. Hohenberg and B. C. Halperin, Rev. Mod. Phys. **49**, 435 (1977).
2. A. Z. Patashinskiĭ and V. A. Pokrovskiĭ, *Fluctuation Theory of Phase Transitions* (Pergamon Press, Oxford, 1979; Nauka, Moscow, 1982, 2nd ed.).
3. S. Ma, *Modern Theory of Critical Phenomena* (Benjamin, Reading, 1976; Mir, Moscow, 1980).
4. I. K. Kamilov and Kh. K. Aliev, Usp. Fiz. Nauk **168**, 953 (1998).
5. S. Wansleben and D. P. Landau, Phys. Rev. B **43**, 6006 (1991).
6. P. Peczak and D. P. Landau, Phys. Rev. B **47**, 14260 (1993).
7. R. Marz, D. Hunter, and N. Jan, J. Stat. Phys. **74**, 903 (1994).
8. A. N. Vakilov and V. V. Prudnikov, Pis'ma Zh. Éksp. Teor. Fiz. **55**, 709 (1992) [JETP Lett. **55**, 741 (1992)].
9. V. V. Prudnikov and A. N. Vakilov, Zh. Éksp. Teor. Fiz. **103**, 962 (1993) [JETP **76**, 469 (1993)].
10. O. N. Markov and V. V. Prudnikov, Fiz. Tverd. Tela (St. Petersburg) **37**, 1574 (1995) [Phys. Solid State **37**, 854 (1995)].
11. E. J. Samuelson, M. T. Hutchings, and G. Shirane, Physica **48**, 13 (1970).
12. A. K. Murtazaev, Kh. K. Aliev, I. K. Kamilov, and K. Sh. Khizriev, Fiz. Nizk. Temp. **24**, 462 (1998) [Low Temp. Phys. **24**, 349 (1998)].
13. A. K. Murtazaev, I. K. Kamilov, Kh. K. Aliev, and K. Sh. Khizraev, Fiz. Tverd. Tela (St. Petersburg) **40**, 1661 (1998) [Phys. Solid State **40**, 1511 (1998)].
14. P. K. Hendriksen, S. Linderoth, and P.-A. Lindgard, Phys. Rev. B **48**, 7259 (1993).
15. M. Suzuki, Prog. Theor. Phys. **58**, 1142 (1977).
16. K. Binder, Phys. Rev. Lett. **47**, 693 (1981).

Translation was provided by AIP

Journal of Experimental and Theoretical Physics, Vol. 90, No. 3, 2000, pp. 491–498.
Translated from Zhurnal Éksperimental'noĭ i Teoreticheskoĭ Fiziki, Vol. 117, No. 3, 2000, pp. 562–570.

SOLIDS
Structure

Structural Phase Transition in a Large Cluster

R. S. Berry[1] and B. M. Smirnov[2, *]

[1]*University of Chicago, Chicago, IL 60637 USA*

[2]*IVTAN Scientific Association (Institute of High-Temperatures), Russian Academy of Sciences, Moscow, 127412 Russia*

**e-mail: smirnov@orc.ru*

Received July 28, 1999

Abstract—The effect of a phase transition between structures in a large cluster with a pair interatomic interaction on the thermodynamic parameters of the cluster is analyzed. The statistical parameters of a cluster consisting of 923 atoms are determined for an icosahedron and a face-centered cubic (fcc) structure. The specific heat and entropy of this cluster are calculated in the case when the transition between the icosahedron and fcc structures has the greatest effect on these parameters, so that at zero temperature this cluster has the structure of an icosahedron, and as the temperature increases to the melting point it assumes an fcc structure. Even with this, the contribution of the excitations of the atomic configurations to the thermodynamic parameters of a cluster is small compared with the excitation of vibrations in the cluster. The contribution of a configurational excitation in the thermodynamic parameters of a cluster becomes substantial for the liquid state of clusters. © *2000 MAIK "Nauka/Interperiodica".*

1. INTRODUCTION

We are studying a phase transition between structures for a large cluster with a pair interatomic interaction, where the interaction between nearest neighbors, i.e., a short-range interaction, makes an appreciable contribution to the energy of the cluster. This transition influences the thermodynamic parameters of the cluster, specifically, its specific heat and entropy. Finding these parameters is the subject of the present paper. It would appear that the type of interaction under study, which pertains to systems of inert-gas atoms, is the simplest of the possible interactions. Nonetheless, it has its peculiarities. At zero temperature the macroscopic system of atoms under study forms a close-packed crystal lattice, where each inner atom has twelve nearest neighbors. The crystalline hexagonal and fcc lattices are close-packed structures. For a Lennard–Jones interatomic interaction potential a hexagonal lattice is more advantageous [1, 2], while all solid inert gases (except helium) have an fcc crystal lattice [2–4], though under special conditions the hexagonal structure of solid inert gases is observed in thin films [5–7]. Competition between these structures is possible in systems of coupled atoms with a pair interaction. Clusters, which are systems with a finite number of bound atoms, can also form an icosahedral structure [8], which is characterized by central symmetry and two types of distances between nearest neighbors, differing by 5%. This structure is preferable for small clusters and competes with the fcc structure right up to sizes of the order of a thousand atoms in a cluster [9–14]. Thus, despite its simplicity, the character of the interaction under study permits systems of bound atoms to exist in various forms.

We note that a cluster with a pair interaction between the atoms is a convenient object for computer simulation, which has shown that melting of clusters is fundamentally different from the melting of macroscopic systems of bound atoms [15–23]. In the first place, in a macroscopic system a phase transition between a solid and a liquid occurs at a certain temperature, while for a cluster there exists a temperature range where the solid and liquid phases coexist. In the second place, computer simulation of melting of clusters with closed shells makes it possible to identify several phase transitions corresponding to melting of individual shells [22, 23]. Thus, a cluster is a more complicated system than a macroscopic system of atoms, and the features indicated above must be taken into account when analyzing the properties of a cluster.

Evidently, a phase transition influences the thermodynamic properties of a cluster. This is investigated in the present paper. The greatest effect is observed when a cluster possesses one structure at zero temperature, while heating changes the structure, i.e., different structures correspond to zero and nonzero temperatures of a cluster. In what follows, we shall examine such a case for a cluster containing 923 atoms, so that the icosahedral structure of this cluster is characterized by closed shells, while the fcc structure is characterized by open shells. Let the ground state of this cluster correspond to the structure of an icosahedron and the excitation energy of the fcc structure be relatively small. The energy gap between the structures can be controlled by varying the parameter in the interatomic interaction potential, specifically, the Morse parameter for a Morse potential [24, 25]. The ground state for an fcc structure of a cluster is characterized by a large statistical weight, since the last shell of a cluster is unfilled. For this rea-

1063-7761/00/9003-0491$20.00

son, if the energy gap between the structures is small, heating the cluster makes the fcc structure thermodynamically favorable, i.e., heating changes the structure of the cluster. This affects the thermodynamic parameters of a cluster, and in what follows we shall calculate the specific heat and entropy of a solid cluster as a function of the temperature and energy gap between the icosahedral and fcc structures. These quantities correspond to a configurational excitation of a cluster. The role of transitions between structures in the thermodynamics of a cluster can be determined by comparing the values of these quantities with the corresponding values due to vibrational excitation of a cluster. This is the aim of the present paper.

2. STATISTICAL PARAMETERS OF AN EXCITED SOLID CLUSTER

To determine the statistical and thermodynamic parameters of a solid cluster consisting of atoms with a pair interaction, we shall divide the energy of a cluster into three parts [26]: the first part is determined by the interaction between nearest neighbors, the second part is determined by the interaction between atoms which are not nearest neighbors, and the third part refers to the stress energy. We shall consider the case where the interaction between the nearest neighbors makes an appreciable or the main contribution to the energy of a cluster. This is a common case, specifically, the popular Lennard–Jones interaction potential pertains to this case. Under these conditions, to a first approximation, we construct a cluster on the basis of a short-range interaction of atoms, so that the state of the cluster is characterized by the number of bonds between nearest neighbors. In the second approximation we include in the analysis the interaction of nonnearest neighbors and the stress energy in a cluster, which is related with the displacement of the equilibrium distances between nearest neighbors as a result of a long-range interaction. This scheme is convenient for analyzing the competition between fcc and icosahedral structures [24, 25]. In this scheme, the long-range interaction of atoms is important for the competition between structures, since the number of bonds between the nearest neighbors for these structures is close. Conversely, the long-range interaction is not important for the excitation of a cluster. Indeed, the excitations considered are related with a change in the positions of one or several atoms, so that the long-range interaction in a cluster changes little with such transitions, and the excitation can be characterized by the change in the number of bonds between the nearest neighbors.

Thus, in the present scheme the excitation of a cluster is characterized by the number of broken bonds between the nearest neighbors, i.e., the excitation energy, measured from the energy of the ground state of a cluster with a given structure, is expressed in units of the energy required to break one bond and is an integer. The statistical weight g_i of the excited state of a cluster with a given structure is equal to the number of configurations of atoms in the cluster that correspond to the number i of broken bonds with respect to the ground state of this structure. As one can see, in this case we assume that the vibrational and configurational excitations separate, since the configurational excitation is relatively weak.

We shall determine the statistical parameters of our cluster with an icosahedral structure. A cluster consisting of 923 atoms possesses filled shells. It is characterized by 2172 bonds between nearest neighbors, belonging to neighboring layers, and 2730 bonds between nearest neighbors in the same layer [15]. This cluster has 561 inner atoms, and the surface layer of this cluster includes 12 vertex atoms, 150 edge atoms, and 200 atoms inside surface triangles. Each vertex atom possesses six nearest neighbors, each edge atom possesses seven nearest neighbors, and each atom on the inner surface of a cluster possesses nine nearest neighbors. If a new atom is placed on the surface of this cluster in a cavity between the surface atoms, the atom will have three nearest neighbors. There are 720 such positions, which is equal to the number of triangles that can be formed from the surface atoms.

The excitation of the configurations of atoms in a cluster corresponds to transferring surface atoms into the centers of the surface triangles. In what follows, transitions with the participation of a small number of atoms, which determine the thermodynamic parameters of a cluster at low temperatures, will be considered. The minimum excitation energy of our cluster with an icosahedral structure is $\Delta\varepsilon = 3$ and corresponds to transferring a vertex atom to the surface of the cluster. The statistical weight for such an excitation is $g_3 = 12 \times 715 = 8580$ and is much greater than the statistical weight for the ground state $g_0 = 1$. We shall take account of the fact that five positions on the surface of a cluster lie next to the vertex atom undergoing a transition, and in what follows we shall neglect this compared with the total number of surface cavities. Further, the excitation energy $\Delta\varepsilon = 4$ of a cluster corresponds to a transition of one edge atom, and $\Delta\varepsilon = 6$ corresponds to the excitation of one surface atom or two vertex atoms. We have

$$g_4 = 150 \times 720 = 1.08 \times 10^5,$$

$$g_6 = \frac{12 \times 11}{1 \times 2} \times \frac{720^2}{2} + 200 \times 720 = 1.7 \times 10^7.$$

Thus, the partial statistical weight for the excitation of v atoms from vertices, e atoms from edges, and s atoms from the surface is

$$g_i = C_{12}^v C_{150}^e C_{200}^s C_{720}^k \approx C_{12}^v \frac{150^e}{e!} \frac{200^s}{s!} \frac{720^k}{k!}, \qquad (1)$$

where $k = v + e + s$ is the total number of excited atoms and the energy of this excitation is $\varepsilon_i = 3v + 4e + 6s$. This formula is valid for a small number k of excited

atoms. We shall neglect the following circumstances. First, the displaced atoms cannot occupy a vertex of a surface triangle in which one of the vertex atoms has been removed. Second, two displaced atoms cannot be placed at the center of neighboring triangles, since the distance between these centers is $a/\sqrt{3}$, where a is the distance between the nearest neighbors. Third, we neglect the possible bonds between the displaced atoms, since the number of such atoms is relatively small. Thus, the expression (1) is valid for weak excitations and makes it possible to determine the statistical properties of a cluster at low temperatures. The statistical weights of the first few excitations of our cluster are presented in Table 1.

We note that if the excitation corresponds to a transition of several atoms, the excitation of edge atoms makes the main contribution to the statistical weight of the cluster. For example, the statistical weight for the excitation $\Delta\varepsilon = 12$ is $g' = 3.5 \times 10^{13}$ for edge atoms, $g'' = 5.2 \times 10^9$ for surface atoms, and $g''' = 5.5 \times 10^{12}$ for vertex atoms.

The method for analyzing clusters with a Morse interatomic interaction potential [24, 25] makes it possible to determine the statistical weight of the lower states of a solid cluster consisting of 923 atoms and possessing an fcc structure. The optimal figure for a cluster with fcc structure is a regular truncated octahedron, whose surface includes eight hexagons and six squares [27]. We shall present the ground state of a cluster with an fcc structure consisting of 923 atoms. The basis for it is a cluster-octahedron with filled shells, which consists of 891 atoms and has 4620 bonds between nearest neighbors. Its surface consists of eight regular triangles, and each of the 12 edges contains 11 atoms (including vertex atoms). Cutting off six pyramids near each vertex, we obtain a truncated regular octahedron, containing 861 atoms with 4476 bonds between nearest neighbors [28]. Each of the removed pyramids contains five atoms and possesses edges consisting of two atoms. The surface of the cluster formed consists of eight irregular hexagons and six squares, containing nine atoms each. The long edge of the hexagon contains seven atoms (including vertex atoms). Using the standard designations [5], the squares have {100} directions, and the hexagons have {111} directions.

Growth of a given cluster occurs by filling of its faces with direction {111}. A new layer on one face contains 46 atoms and increases the number of bonds between the nearest neighbors by 252. To construct a cluster consisting of $n = 923$ atoms, we start with a cluster consisting of 926 atoms, which contains a new layer on one face, and the other face contains a regular hexagon consisting of 19 atoms. This configuration of the surface atoms is shown in Fig. 1. The addition of a hexagon consisting of 19 atoms increases the number of bonds between the nearest neighbors by 99. Thus, an fcc cluster consisting of 926 atoms possesses in the ground state 4827 bonds between nearest neighbors. To find the statistical weight of this state, we note that the faces which we are considering can be filled in $7 \times 8 = 56$ ways. Further, a regular hexagon can be placed on the surface of a face in 10 different ways, which gives a statistical weight $g = 560$ for the ground state of an fcc cluster containing 926 atoms.

Table 1. Statistical weight of the excited states of a cluster with 923 atoms and an icosahedral structure

ε_i	g_i	ε_i	g_i	ε_i	g_i
0	1	6	1.7×10^7	10	3.9×10^9
3	8.6×10^3	7	9.3×10^8	11	8.4×10^{12}
4	1.1×10^5	8	5.2×10^9	12	4.0×10^{13}

To convert this cluster into a cluster consisting of 923 atoms, three atoms must be removed from it. This operation can be performed with both filled and partially filled faces. As a result, 17 bonds between nearest neighbors will be lost, i.e., 4810 bonds correspond to the ground state of an fcc cluster containing 923 atoms. The statistical weight of this cluster is equal to the product of the number of operations required to form a cluster consisting of 926 atoms by the number of operations to remove three atoms from it:

$$g_0 = 8 \times 7 \times (3 \times 10 + 3 \times 10 + 3 \times 13) = 5544. \quad (2)$$

The first term in parentheses corresponds to the removal of three atoms from the filled face, the second term corresponds to the removal of the top edge or two bottom side edges of a regular hexagon of the face being filled, and the third term describes the removal of the bottom edge or two top side edges of a regular hexagon. As one can see, the statistical weight of an fcc cluster is much greater than for an icosahedral cluster with filled shells.

We shall now formulate the general properties of the our cluster on the basis of our approach. The total number of bonds between nearest neighbors in the case of

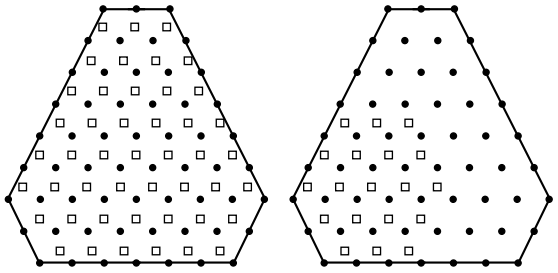

Fig. 1. Filling of the {111} faces of a cluster of an fcc structure, containing 926 atoms, in the ground state. The positions of the atoms on the filled layers are indicated by filled circles, and the positions of the atoms on the layers being filled are marked by open squares. The number of bonds between the nearest neighbors of a cluster is 4827 (for an icosahedral cluster with $n = 926$ the number of bonds is 4914).

Table 2. Statistical weights for the lower states of an fcc cluster with 923 atoms

i	g_i/g_0	i	g_i/g_0
1	100	5	9.3×10^5
2	500	6	1.4×10^7
3	8000	9	5.6×10^{10}
4	1600	12	4.1×10^{13}

an fcc structure is 4810, while for a cluster with icosahedral structure, where the distances between the nearest neighbors are suboptimal, it is 4902. As a result of the closeness of these quantities, the crossing of the energy levels for different structures is determined by the interaction of the non-nearest neighbors. Specifically, for a Morse interatomic interaction potential the energies of clusters for our structures are identical for the Morse parameter in the pair interaction potential $\alpha = 7.1$ [24, 25]. Thus, the cluster energy is determined mainly by the interaction between the nearest neighbors, but the competition between the structures and the parameters of the crossing of the energy levels are sensitive to the form of the interatomic interaction potential [10–15]. Specifically, the greater the contribution of the interaction of non-nearest neighbors to the cluster energy is, the larger the clusters for which crossing of energies occurs for fcc and icosahedral structures. However, in analyzing the lower excited states of a cluster, the interaction of non-nearest neighbors can be neglected, as was done above.

The statistical weight of the bottom excited states of an fcc cluster containing 923 atoms can be found by the same method as for the ground state. This method becomes more complicated as the excitation increases (Table 2 contains the values of the statistical weights of a cluster for $\varepsilon_i \le 6$). For subsequent excitation of a cluster, we obtain a statistical weight that is all the larger, the larger the number of atoms that move on its surface. Specifically, for $\varepsilon_i = 9$ the transfer of three vertex atoms on its surface, where there are 552 free positions, so that the statistical weight of this excitation is

$$g_9 \sim C_{24}^3 C_{552}^3 g_0 \sim 5.6 \times 10^{10} g_0,$$

makes the main contribution. Similarly, we find the statistical weight of the excitation when 12 bonds are broken. These results are included in Table 2, where the data make it possible to determine the thermodynamic parameters of fcc clusters up to temperatures $T = 0.3$–0.35.

The partial partition function Z_i for a given excitation energy ε_i and statistical weight g_i of this excitation and the total partition function Z can be calculated on the basis of the parameters obtained:

$$Z_i = g_i \exp\left(-\frac{\varepsilon_i}{T}\right), \quad Z = \sum_i Z_i. \tag{3}$$

Here and below we express the temperature T in energy units. Introducing the separate partition functions Z_{ico} and Z_{fcc} for the icosahedral structure and the fcc structure, we have $Z = Z_{ico} + Z_{fcc}$. Then the probability η of an icosahedral structure being realized follows from the formula

$$\eta = \frac{Z_{ico}}{Z_{ico} + Z_{fcc}}. \tag{4}$$

We note that the partition function can be divided into configurational and vibrational parts. Since we are dealing with weak excitations, the vibrational part of the partition function does not depend on the excitation of configurations and can be separated from it. Correspondingly, we shall analyze below only the configurational part of the partition function. The specific heat C and S of a cluster which correspond to the configurational excitations are

$$C = \frac{\partial E_{exc}}{\partial T} = \frac{\partial}{\partial T}\left(\frac{1}{Z}\sum_i \varepsilon_i Z_i\right) = \frac{1}{T^2}\left[\frac{1}{Z}\sum_i \varepsilon_i^2 Z_i - \left(\frac{1}{Z}\sum_i \varepsilon_i Z_i\right)^2\right] = \frac{\overline{E^2}}{T^2} - \left(\frac{\bar{E}}{T}\right)^2, \tag{5}$$

$$S = \ln Z + \frac{\bar{E}}{T} = \ln \sum_i Z_i + \frac{1}{TZ}\sum_i \varepsilon_i Z_i. \tag{6}$$

Here E_{exc} is the configurational excitation energy of a cluster, and $\bar{E}$ and $\overline{E^2}$ are the average and mean-square values of the excitation energy of a cluster. At low pressures the difference between the specific heats of a cluster at constant pressure and volume is relatively small, so that we shall assume that they are the same and denote them by C. The energies ε_i of the configurational excitation and temperature of a cluster can be expressed in reduced units, i.e., in terms of the energies required to break one bond.

3. STRUCTURAL TRANSITIONS AND THERMODYNAMIC PARAMETERS OF A SOLID CLUSTER

We shall use the general formulas presented above to determine the thermodynamic parameters of our cluster. The ground state of the cluster possesses an icosahedral structure and is separated from the ground state of the fcc structure by an energy gap, which we denote as Δ. The excited states contribute to the partition function, starting at the temperatures $T \approx 0.2$, and the statistical weights presented in Tables 1 and 2 make it possible to determine the thermodynamic parameters of a cluster up to $T \approx 0.3$–0.35, while the melting temperature is $T_m = 0.44$ [29] for a cluster containing $n = 923$ atoms. A phase transition between icosahedral

and fcc structures is possible if the cluster in the ground state possesses an icosahedral structure and the energy gap Δ is small. We note that the energy gap can be regulated by varying the parameter of the interatomic interaction potential, specifically, for the Morse potential the gap is zero for a cluster when the Morse parameter $\alpha = 7.1$ [24, 25].

We shall now determine the temperature T_{tr} of a transition between structures using the relation $Z_{ico}(T_{tr}) = Z_{fcc}(T_{tr})$, and for $\Delta \sim 1$, when a transition occurs at low temperatures, we have $T_{tr} = \Delta/\ln g_0 = 0.116\Delta$, where the statistical weight g_0 of the ground for the fcc structure is determined by equation (2). A structural transition leads to resonance in the specific heat of a cluster, and its maximum value is $C_{\max} = (\ln g_0/2)^2 \approx 19$. But this value is small compared with the specific heat of a cluster due to the vibrations of the atoms, specifically, according to the Dulong–Petit formula, the latter is $C = 3n \approx 3000$ (n is the number of atoms in a cluster). The relative width of a resonance in the temperature dependence of the specific heat of a cluster is small, and for small Δ it is

$$\Delta T = \frac{2T_{tr}^2}{\Delta} = \frac{2T_{tr}}{\ln g_0} = 0.23T_{tr}, \tag{7}$$

i.e., this resonance is not sharp.

For a structural transition it is convenient to separate in equation (5) the terms referring to the icosahedral and fcc structures. We have

$$C = \frac{Z_{ico}}{Z}C_{ico} + \frac{Z_{fcc}}{Z}C_{fcc} + \frac{1}{T^2}\frac{Z_{ico}Z_{fcc}}{Z^2}(\overline{\varepsilon_{ico}} - \overline{\varepsilon_{fcc}} - \Delta)^2. \tag{8}$$

Here Z_{ico} and Z_{fcc} are the partition functions for the corresponding structure of a cluster, $Z = Z_{ico} + Z_{fcc}$, C_{ico} and C_{fcc} are the specific heats for each structure of the cluster in the absence of the other structure, and $\overline{\varepsilon_{ico}}$ and $\overline{\varepsilon_{fcc}}$ are the average energies of the configurational excitation for a given structure, if zero energy corresponds to the ground state of this structure. Figure 2 shows the temperature dependence of the specific heat of a cluster for different values of the energy gap Δ between the ground states of the icosahedral and fcc structures. The resonance character of these curves is due to the effect of a structural phase transition on the specific heat of a cluster. Figure 3 displays the caloric curves for the states of the cluster under study. We note that a change in the energy gap shifts the energy of the fcc structure, and near the melting temperature of a cluster the contributions of the icosahedral and fcc structures to the excitation energy of a cluster from the ground state of the given structure are comparable.

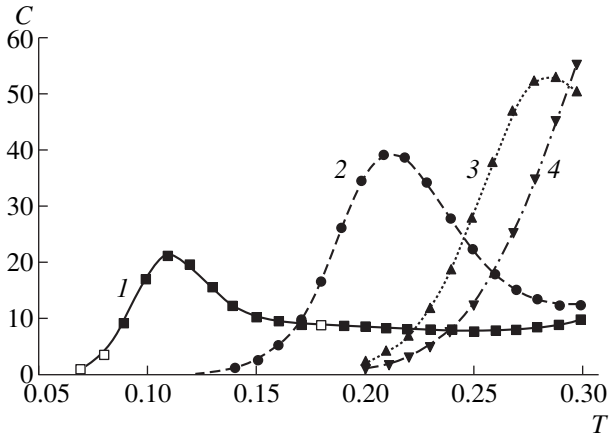

Fig. 2. Temperature dependences of the specific heat of a solid cluster consisting of $n = 923$ atoms, which is associated with the configurational excitation, for the following values of the energy gap width Δ between the ground states of the icosahedral and fcc cluster: $\Delta =$ (*1*) 1, (*2*) 2, (*3*) 3, and (*4*) 4.

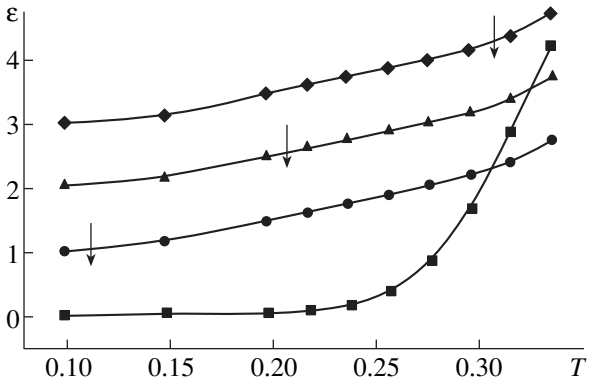

Fig. 3. Caloric curves for icosahedral and fcc structures of a cluster with 923 atoms. The arrows on the curves indicate the positions of a phase transition between the icosahedral and fcc structures.

The expression (8) shows the character of the resonance of the specific heat of a cluster that occurs when both structures make the same contribution to the specific heat. Indeed, let us take in this expression $\overline{\varepsilon_{ico}} \ll \Delta$ and $\overline{\varepsilon_{fcc}} \ll \Delta$, so that the maximum corresponds to $Z_{ico} = Z_{fcc} = Z/2$. This gives for the maximum specific heat

$$C_{\max} = \frac{1}{2}(C_{ico} + C_{fcc}) + \left(\frac{\Delta}{2T}\right)^2, \tag{9}$$

where T is the temperature of the structural phase transition. In the limit of small Δ, when $C_{ico} = C_{fcc} = 0$ and $T = T_{tr} = \Delta/\ln g_0$, we have $C_{\max} = (\ln g_0/2)^2$, as was obtained above.

Since the entropy, according to equation (6), is determined by the excited configurations of the atoms

Table 3. Entropy of a cluster in the limit of small and large widths of the energy gap between the icosahedral and fcc structures of a cluster

T	$\Delta \longrightarrow 0$	$\Delta \longrightarrow \infty$
0.2	11.3	0.05
0.25	12.8	0.88
0.3	14.0	5.85
0.35	16.5	15.6

in a cluster, it is zero at zero temperature, since the cluster is in the ground state of the filled structure of an icosahedron. A temperature increase and phase transition increase the entropy, which increases monotonically with increasing temperature and with decreasing energy gap Δ between the ground states of the structures studied. This can be demonstrated in the limit of small values of Δ, when the phase transition occurs at low temperature in accordance with equation (7). In this case, only the ground configurational states of atoms for these structures determine the parameters of a cluster Z and $\bar{E}$ near the phase-transition temperature, and the entropy in this temperature range is

$$S = \ln(1 + g_0 e^{-\Delta/T}) + \frac{\Delta}{T}\frac{g_0 e^{-\Delta/T}}{1 + g_0 e^{-\Delta/T}},$$
$$\frac{dS}{dT} = \frac{\Delta^2}{T^3}\frac{g_0 e^{-\Delta/T}}{(1 + g_0 e^{-\Delta/T})^2}. \qquad (10)$$

It follows from the last equation that $dS/dT > 0$, i.e., the entropy is a monotonic function of temperature. The derivative of the entropy itself has a maximum at the phase-transition point $T_{tr} = \Delta/\ln g_0$, where the derivative is

$$\frac{dS}{dT}(T_{tr}) = \frac{\Delta^2}{4T_{tr}^3} = \frac{\ln g_0^3}{4\Delta}. \qquad (11)$$

This gives for the entropy at the phase-transition points

$$S(T_{tr}) = \ln 2 + \frac{\Delta}{2T_{tr}} = \ln\sqrt{\frac{g_0}{2}} \approx 4.0. \qquad (12)$$

Far from a phase transition, where $g_0\exp(-\Delta/T) \gg 1$, the entropy is

$$S = \ln g_0 - \frac{\Delta}{2T}.$$

Thus, in the limit of small values of Δ and high temperatures, the entropy approaches the limit $S = \ln g_0 = 9.6$. This limit corresponds to the entropy of the ground state of the fcc structure.

It is possible to determine the dependence of the entropy of a cluster on the width Δ of the energy gap between the structures. Then, in the limit of small Δ the entropy is determined by the fcc structure of the cluster, while its statistical weight is relatively large, and in the limit of large Δ the entropy corresponds to the icosahedral structure. The values of the entropy at different temperatures for these limiting cases are given in Table 3.

Let us compare the contribution of excitations of the configurations of atoms in a cluster and excitations of vibrations of a cluster to the thermodynamic parameters of a solid cluster. The contribution of excitations of configurations to the entropy is relatively small. Specifically, in the classical limit the entropy of a cluster due to excitation of its vibrations is determined by the expression [30]

$$S_{vib} = 3n\left(\ln\frac{T}{\hbar\omega_D} - 1\right), \quad T \gg \hbar\omega_D, \qquad (13)$$

where ω_D is the Debye frequency and n is the number of atoms in a cluster. For the cluster under study, this formula gives $S_{vib} \sim 1000$, which is much greater than the entropy due to the configurational excitation of a cluster. For example, using the approximate method, described above, for determining the partition function for a cluster with an icosahedral structure, when only transitions of atoms from an edge of this figure are taken into account, we obtain for the configurational part of the entropy at the melting temperature of the cluster $T_m = 0.44$ [29] the partition function $Z = 165$, specific heat $C = 141$, and entropy $S = 32$. These values attest to a small contribution from configurational excitation to the parameters, under study, of the solid cluster.

This conclusion is incorrect for melting of a cluster, and we shall analyze it for condensed inert gases. The liquid state is characterized by the formation of voids inside the system [31], and condensed inert gases can be viewed as a macroscopic system of atoms with short-range interatomic interaction [32], i.e., when only nearest neighbors interact. This makes it possible to use the parameters presented above for condensed inert gases to analyze the melting in a system of bound atoms with a short-range interaction. Specifically, in the units employed, the melting energy per atom for condensed inert gases is $\Delta H_{fus} = 0.98$ [32], so that the change in entropy on melting of a cluster is

$$\Delta S = \frac{\Delta E}{T_m} = \frac{n\Delta H_{fus}}{T_m} = 2060. \qquad (14)$$

Here ΔE is the change in the internal energy of a cluster as a result of melting, T_m is the melting temperature, and $n = 923$ is the number of atoms in the cluster. It was assumed that the specific energy of melting is the same for a cluster and a macroscopic system. As one can see, the entropy jump on melting of a cluster is comparable to the entropy due to vibrations of atoms in a cluster. Thus, the configurational part of the entropy is substantial for the liquid state of a cluster and negligible for its solid state. We note that the melting temperature for condensed inert gases $T_m = 0.58$ [32] is greater than the melt-

ing temperature for our cluster $T_m = 0.44$ [29]. Therefore, we shall employ the overestimated values for the specific melting energy of a cluster. The estimates made and the conclusions drawn are nonetheless valid.

This conclusion also pertains to the specific heat of a cluster. Indeed, we shall employ the relation between the partition functions for liquid (Z_{liq}) and solid (Z_{sol}) states

$$\frac{Z_{liq}}{Z_{sol}} = \exp\left(-\frac{\Delta E}{T} + \Delta S\right). \quad (15)$$

Assuming the internal energy E_{vib} of a cluster due to excitation of the vibrations of the cluster to be a smooth function of the temperature, we represent the total internal energy of a cluster in the form

$$E = E_{vib} + \Delta E w_{liq},$$

where $w_{liq} = Z_{liq}/(Z_{sol} + Z_{liq})$ is the probability of finding a cluster in the liquid state. Hence we obtain for the specific heat $C = \partial E/\partial T$ of a cluster near a phase transition, by analogy to equation (8),

$$C = C_0 + \left(\frac{\Delta E}{2T_m}\right)^2 \exp[-\alpha(T - T_m)^2],$$
$$\alpha = \left(\frac{\Delta E}{2T_m^2}\right)^2, \quad (16)$$

where the specific heat C_0 is related with the vibrations of the cluster. For the cluster parameters employed, we obtain for the maximum specific heat $(C_V)_{\max} = 1.1 \times 10^6$ and $\alpha = 5.5 \times 10^6$ K^{-2}, i.e., the width ΔT of the transition region is $\sim 10^{-3}$ K. As one can see, in this region the specific heat due to the configurational excitation of a cluster is two orders of magnitude greater than the contribution due to vibrations in a cluster.

The fundamental difference between the excitation of the configurations of a cluster at a structural phase transition and accompanying melting lies in the character of this excitation. In the case of a structural phase transition, the configurational excitation corresponds to a change in the positions for one or several atoms, while all atoms participate in a vibrational excitation. On melting the number of voids formed is comparable to the number of atoms in a cluster, so that this transition is stronger and changes the thermodynamic parameters of the cluster.

4. CONCLUSIONS

The method used for clusters with a pair interatomic interaction, where the interaction between nearest neighbors makes an appreciable contribution to the energy of a cluster, makes it possible to determine the thermodynamic parameters of a cluster taking account of the phase transition between structures. The effect of a phase transition is strongest for a cluster with 923 atoms, in which the shells are filled for the icosahedral structure and unfilled for the fcc structure, for two reasons. First, the energy gap between the ground and first excited states is larger in an icosahedral cluster with filled shells than in an fcc cluster with an unfilled shell. Second, the statistical weights for the ground and first excited states of an fcc cluster are appreciably larger than for an icosahedral cluster. On account of this difference between the structures, the phase transition is reflected in the thermodynamic parameters of this cluster much more strongly than for clusters with other sizes. A phase transition between structures leads to a resonant temperature dependence of the specific heat of a cluster, and a phase transition between the solid and liquid has a much stronger effect on the properties of the cluster.

The contribution of a configurational excitation to the specific heat and entropy of a solid cluster is small compared with the contribution of the vibrations of the atoms in a cluster, even in the presence of a phase transition between the structures. For this reason, a configurational excitation has only a negligible effect on the thermodynamic parameters of a solid cluster. Conversely, the configurational part of the excitation in the liquid state of a cluster is has a large effect.

ACKNOWLEDGMENTS

We are grateful to the hospitality of the Institute of Nuclear Physics at the University of Washington, where this work was initiated. The work of one of us (B. M. S.) is partially supported by the Russian Foundation for Basic Research (project no. 99-02-16094).

REFERENCES

1. T. Kihara and S. Koba, J. Phys. Soc. Jpn. **7**, 348 (1952).
2. C. Kittel, *Introduction to Solid State Physics* (Wiley, New York, 1986).
3. G. Leibfried, *Gittertheory der Mechanischen und Termischen Eigenschaften den Kristallen* (Springer, Berlin, 1965), Vol. VII, Part 2.
4. C. Bunn, *Crystals* (Academic, New York, 1964).
5. N. M. Ashcroft and N. D. Mermin, *Solid State Physics* (Hort, Rinehart, and Wilson, New York, 1976).
6. O. Bostanjonglo and B. Kleinschmidt, Z. Phys. A **21**, 276 (1977).
7. E. Schuberth, M. Creuzburg, and W. Müller-Lierheim, Phys. Status Solidi B **76**, 301 (1976).
8. Y. Sonnenblick, E. Alexander, Z. H. Kalman, and I. T. Steinberger, Chem. Phys. Lett. **52**, 276 (1977).
9. A. L. Mackay, Acta Crystallogr. **15**, 916 (1962).
10. J. W. Lee and G. D. Stein, J. Phys. Chem. **91**, 2450 (1987).
11. J. A. Northby, J. Chem. Phys. **87**, 6166 (1987).
12. B. W. van de Waal, J. Chem. Phys. **90**, 3407 (1989).
13. J. A. Northby, J. Xie, D. L. Freeman, and P. Doll, Z. Phys. D **12**, 69 (1989).
14. J. Xie, J. A. Norhtby, D. L. Freeman, and P. Doll, J. Chem. Phys. **91**, 612 (1989).

15. B. M. Smirnov, Chem. Phys. Lett. **232**, 395 (1995).
16. R. S. Berry, J. Jellinek, and G. Natanson, Phys. Rev. A **30**, 919 (1984).
17. J. Jellinek, T. L. Beck, and R. S. Berry, J. Chem. Phys. **84**, 2783 (1986).
18. R. S. Berry, T. L. Beck, H. L. Davis, and J. Jellinek, Adv. Chem. Phys. **90**, 75 (1988).
19. D. J. Wales and R. S. Berry, J. Chem. Phys. **92**, 4283 (1990).
20. D. J. Wales, Chem. Phys. Lett. **166**, 419 (1990).
21. H. P. Cheng and R. S. Berry, Phys. Rev. A **45**, 7969 (1992).
22. R. E. Kunz and R. S. Berry, Phys. Rev. E **49**, 1895 (1994).
23. R. S. Berry, Nature **393**, 238 (1998).
24. R. S. Berry, B. M. Smirnov, and A. Yu. Strizhev, Zh. Éksp. Teor. Fiz. **112**, 1082 (1997) [JETP **85**, 588 (1997)].
25. B. M. Smirnov, A. Yu. Strizhev, and R. S. Berry, J. Chem. Phys. **110**, 7412 (1999).
26. J. P. K. Doye, D. J. Wales, and R. S. Berry, J. Chem. Phys. **103**, 4234 (1995).
27. S. W. Wang, L. M. Falikov, and A. W. Searcy, Surf. Sci. **143**, 609 (1984).
28. B. M. Smirnov, Phys. Scr. **52**, 710 (1995).
29. A. Rytkonen, S. Valkealahti, and M. Manninen, J. Chem. Phys. **106**, 1888 (1997).
30. L. D. Landau and E. M. Lifshitz, *Statistical Physics*, 3rd ed. (Nauka, Moscow, 1976, 3rd ed.; Pergamon Press, New York, 1980), Part 1.
31. H. Reiss, H. L. Frish, and J. L. Lebowitz, J. Chem. Phys. **31**, 369 (1959).
32. B. M. Smirnov, Usp. Fiz. Nauk **164**, 1165 (1994) [Phys. Usp. **37**, 1079 (1994)].

Translation was provided by AIP

Journal of Experimental and Theoretical Physics, Vol. 90, No. 3, 2000, pp. 499–507.
Translated from Zhurnal Éksperimental'noĭ i Teoreticheskoĭ Fiziki, Vol. 117, No. 3, 2000, pp. 571–581.

SOLIDS
Electron Properties

Modification of the Domain Wall Structure and Generation of Submicron Magnetic Formations by Local Optical Irradiation

A. S. Logginov*, A. V. Nikolaev, E. P. Nikolaeva, and V. N. Onishchuk

Moscow State University, Vorob'evy gory, Moscow, 119899 Russia
**e-mail: asl@osc.phys.msu.su*

Received August 9, 1999

Abstract—Experimental and theoretical investigations are made of the generation of vertical Bloch lines in a magnetic iron garnet film exposed to pulsed optical radiation. High-speed photography and anisotropic dark-field microscopy are used to study characteristic features of the generation of Bloch lines and domain structure relaxation processes after the local action of a laser pulse. Optimum optical irradiation parameters to ensure the controlled generation of Bloch lines are established. A theoretical model is developed which links the generation of Bloch lines to the migration of domain walls induced by local changes in the distribution of the degaussing fields caused by a reduction in magnetization with temperature at the optical radiation focusing point. The experimental results indicate that the controlled formation of magnetic structures smaller than or of the order of 0.1 μm by local optical irradiation is quite feasible. © *2000 MAIK "Nauka/Interperiodica".*

1. INTRODUCTION

The miniaturization of magnetic memory devices, reduction in "bit size", and increase in data storage density have created a need to search for new physical mechanisms and methods of writing and reading out information in a magnetic medium and require a detailed understanding of the magnetization behavior on scales of the order of tens and hundreds of nanometers [1]. Among the various approaches to the detection, modification, and study of the magnetic structure of matter on the submicron level, optical methods are of particular interest. This is because of the interest shown in fundamental aspects of the interaction of matter with electromagnetic radiation and because of the practical requirements for the development of new generations of devices with optical and thermomagnetic data recording.

In this context new physical effects described for the first time in [2], involving the generation and migration of vertical Bloch lines in the domain wall in an iron garnet film under the action of focused laser radiation are of particular interest. The Bloch lines are stable magnetic vortices separating sections of the domain wall of opposite polarity [3]. The characteristic sizes of these vertical Bloch lines are tenths and hundredths of micron.

The essence of these effects is that, as its energy increases, the action of a single laser pulse (having a duration of $\simeq$10 ns and focused to the center of a stripe domain in a region around 3–4 μm in diameter) induces (1) the displacement of vertical Bloch lines in the domain wall; (2) the generation of a pair of vertical Bloch lines at walls initially free from these lines; (3) an irreversible change in the shape of the domain wall and the overall domain structure.

Unlike conventional thermomagnetic recording technology (in which a magnetic domain is recorded and its size is generally determined by the effective diameter of the focused laser beam or an artificially created potential relief [4, 5]), the effects observed in [2] show that it is possible to create a stable structure inside the domain wall (having dimensions of $\lesssim$0.1 μm) as a result of the action of a laser beam focused in a region of a few micron.

The present paper is a further development of [2] and is devoted to determining the optical irradiation parameters and refining the physical mechanism responsible for the controlled formation of Bloch lines and also gives a more detailed description of the original experimental method developed for this purpose.

2. EXPERIMENTAL METHOD

We used a sample of iron garnet film grown on a ⟨111⟩-oriented substrate having the composition $(BiTm)_3(FeGa)_5O_{12}$. The sample had the following parameters: saturation magnetization $4\pi M_s$ = 173 G, collapse field H_{col} = 126 Oe, period of equilibrium stripe structure 8.5 μm, film thickness 7.5 μm, and quality factor Q = 3.8.

The experiment was carried out using a combination of high-speed photography and polarized anisotropic dark-field observation (PADO).

High-speed photography allows us to study the fast dynamic transformations of the domain structures in real time [6, 7]. In order to visualize the magnetization structure, at fixed times after the beginning of a partic-

1063-7761/00/9003-0499$20.00

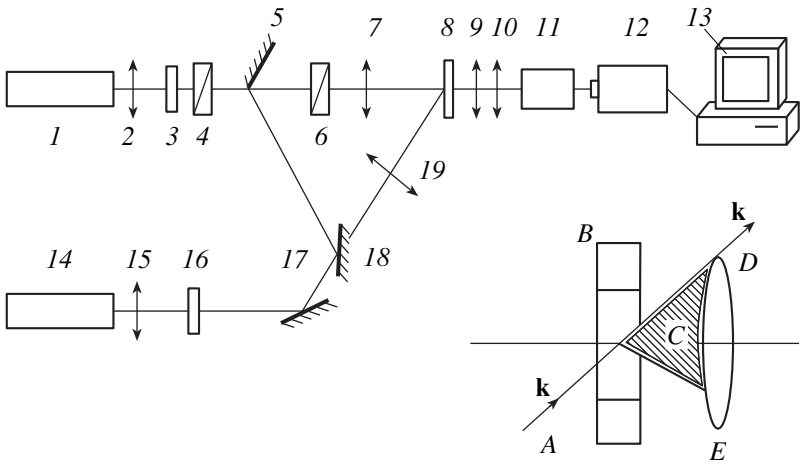

Fig. 1. Schematic of experimental apparatus for high-speed photography and anisotropic dark-field illumination: (*1*, *14*) LGI-21 pulsed nitrogen lasers; (*2*, *15*) quartz lenses; (*3*, *16*) quartz cells containing rhodamine and oxazine dyes, respectively; (*4*, *6*) crystal polarizers; (*5*, *17*, *18*) mirrors; (*7*, *19*) focusing objectives; (*8*) sample; (*9*, *10*) polarizing microscope; (*11*) image converter with image intensifier; (*12*) video camera with CCD matrix; (*13*) computer. The inset shows a schematic of one-sided dark-field illumination; (*A*) incident beam; (*B*) sample; (*C*) diffracted beam; (*D*) direct beam; (*E*) objective.

ular dynamic process initiated by some external action, the sample is illuminated by a short pulse of polarized light. The duration of the illuminating pulse is selected to be much shorter than the characteristic time of the process being studied. The magnetooptic image thus obtained is the "instantaneous" distribution of the magnetization perturbed by the external action. By varying the time delay between the beginning of the action and the illuminating pulse, we can study the evolution of this perturbation.

In order to monitor the internal structure of the domain wall and visualize the vertical Bloch lines whose size lies below the spatial resolution limit of standard "light-field" magnetooptic microscopy, we used anisotropic dark-field observation. In this method the illuminating beam in the microscope is incident on the sample at a certain angle and bypasses the objective, while the image is only formed by light scattered at the domain wall as a result of magnetooptic diffraction and carries information on small-scale inhomogeneities of the magnetization (see inset to Fig. 1) [8, 9]. The plane of incidence of the light is perpendicular to the plane of the domain wall. In this case the wall resembles a light band against a dark background and local changes in the brightness of the domain wall image are treated as sites where vertical Bloch lines are localized (see Fig. 2, the contrast of the image is inverted, and the Bloch lines are indicated by arrows).

The apparatus is shown schematically in Fig. 1. The source of optical radiation modifying the domain wall structure is an LGI-21 nitrogen laser (*1*) having the wavelength $\lambda \simeq 337$ nm and pulse duration $\tau \simeq 10$ ns. The laser radiation is focused by a quartz lens *2* into a cell *3* containing a rhodamine 6G solution and is reemitted at $\lambda \simeq 540$ nm. The instant of emission and its intensity are monitored by an avalanche photodiode. The dye radiation is passed through a system of polarizers *4*, *6* and focused by an objective *7* having a numerical aperture of 0.2 onto a sample *8*. The diameter of the focused beam is around 4 μm. The diameter of the focused beam can be reduced or increased by placing additional lenses ahead of the objective. The focused beam is positioned on the sample by means of the precision movement mechanisms of the objective. The light pulse reemitted by the dye and incident on the sample ("writing" pulse) has a maximum energy $W_{max} \sim 10^{-6}$ J (with an instability of around 15%). The amplitude (energy) of the light pulse is varied continuously by changing the relative angular position of the system of polarizers *4*, *6* (see Fig. 1).

In order to visualize the structural changes in the magnetization caused by the action of the writing laser pulse *1*, optical illumination is again used provided by a second LGI-21 pulsed laser (*14*) whose radiation (after wavelength conversion by the oxazine dye) is split into two channels by a semitransmitting mirror *18* (see Fig. 1). One channel is fed to the optic axis which coincides the with the axis of the first LGI-21 laser and is used for direct (light-field) illumination of the sample and to record the domain structure in the geometry of the magnetooptic Faraday effect. The radiation in the second channel is directed onto the sample at an angle in order to achieve one-sided dark-field illumination. This arrangement of the optical system means that both light-field and dark-field geometries can be used to observe the same section of the sample and to visualize magnetic structures on different spatial scales. By using high-speed photography and changing the time delay between the writing pulse and the illuminating pulse, we can study the dynamic processes in the domain structure and the change in the internal structure of the domain wall.

These domain structures are observed using a polarizing microscope *9*, *10* and recorded using an image converter *11* with an image intensifier and a video camera *12* with a CCD matrix connected to a computer *13*.

Before the beginning of the experiment the sample was demagnetized from the single-domain state in the presence of a static magnetic field (directed in the plane of the magnetic film) to produce an equilibrium array of stripe domains whose walls were free from vertical Bloch lines.

The experiments were carried out as follows. The video camera connected to the computer produced an initial image of the domain walls on the monitor screen obtained by one-sided dark-field illumination. A single writing laser pulse of given energy was then generated and the dynamic transformations in the domain structure or the internal structure of the domain wall were then identified by means of light-field or dark-field observations.

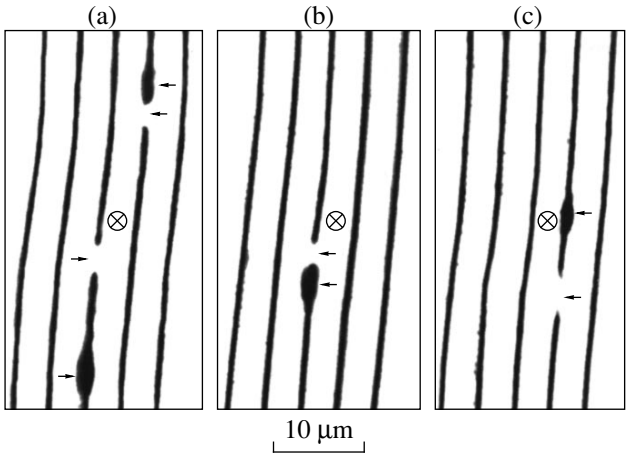

Fig. 2. Typical images of Bloch lines generated in domain walls after the action of a writing laser pulse. The ⊗ symbol indicates the beam focusing site and the vertical Bloch lines are indicated by arrows. The photographs were obtained in a one-sided dark field and the contrast is inverted.

3. EXPERIMENTAL RESULTS

3.1 Influence of Optical Radiation Parameters on the Generation of Bloch Lines

Under the experimental conditions [2] the generation of Bloch lines did not exhibit regular behavior. For constant irradiation parameters, not every laser pulse resulted in the formation of vertical Bloch lines. In the present study we establish some dependences which link the reproducibility of the results with the degree of focusing of the optical radiation, the relative position of the focusing region and the domain walls, and the energy of the focused radiation.

3.1.1. Influence of the degree of focusing of optical radiation localized at the center of a stripe domain on the probability of creating vertical Bloch lines. The action of a 4 μm diameter laser beam having a pulse energy $W \simeq 0.2W_{max}$ focused at the center of a domain induces the generation of a pair of vertical Bloch lines at walls initially free from these lines. Figure 2 shows typical dark-field images obtained after a single pulse (the beam focusing point is indicated by ⊗). We can see that regions of modified contrast corresponding to pairs of Bloch lines form at the walls. In terms of their form in the one-sided dark field and the dynamic response to the field pulses in the plane of the magnetic film and the bias field, these lines are identical to those generated in domain walls by the "traditional" method, as a result of the migration of the walls at above-critical velocity [3].

Convergence of the generated pairs (for example, using field pulses directed in the plane of the magnetic film along the wall) leads to their annihilation from which it follows that the pairs are untwisted [3]. After a single laser pulse a maximum of four vertical Bloch lines are generated (two pairs). Their number and position on the domain wall relative to the laser beam focusing point cannot be predicted.

The probability of pairs of vertical Bloch lines being created increases as the amplitude (energy) of the optical pulses increases, although above a certain level any further increase in energy results in the formation of magnetic film defects while the generation of lines remains irregular as before.

As the degree of focusing of the beam increases, or the spot size decreases to 2–2.5 μm, the energy range in which vertical Bloch lines are generated but irreversible structural changes do not yet occur [2], is significantly reduced. Defect formation is observed even at comparatively low optical pulse energies ($W < 0.2W_{max}$) and no reproducible generation of vertical Bloch lines can be achieved.

An increase in the diameter of the focused spot to 4.5–5 μm leads to changes in the generation of vertical Bloch lines. As the diameter increases, the light spot begins to cover the adjacent domain walls and as a result of the action of a single laser pulse Bloch lines form predominantly at adjacent walls rather than at the walls closest to the beam site (see Fig. 3d). In this geometry the generation of vertical Bloch lines is also irregular and takes place with a probability of less than one.

3.1.2. Influence of the position of the optical beam relative to the domain walls on the generation of vertical Bloch lines. Figure 4 shows a histogram of the probability of vertical Bloch lines being generated under the action of an optical pulse for various positions of the beam relative to the domain wall. The movement of the beam is perpendicular to the domain wall and the origin of the x axis on the figure corresponds to the center of the domain wall. In these experiments the diameter of the beam at the focus is around 3 μm and the pulse power $W = 0.2W_{max}$. We can see that Bloch lines are created when the center of the beam is

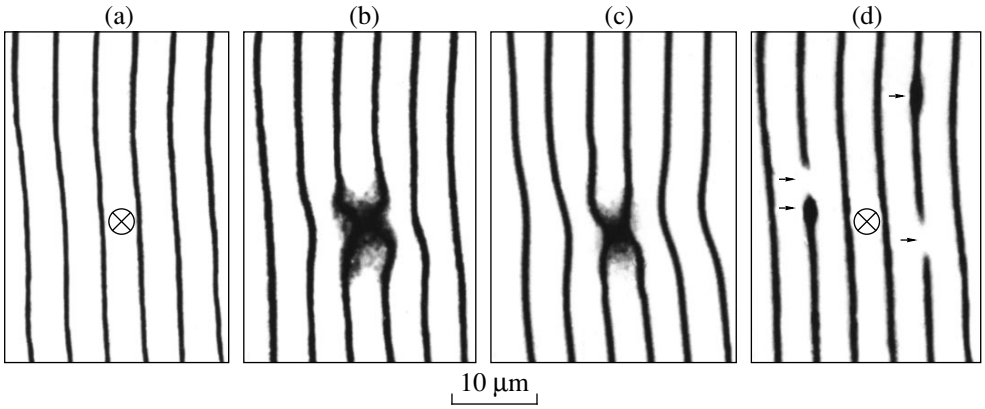

Fig. 3. Generation of Bloch lines as a result of the action of a laser beam focused in a region 4.5 μm in diameter. The photographs show: the initial image of the domain structure (a), instantaneous dynamic configurations of the domain structure 100 ns (b) and 300 ns (c) after the application of a writing laser pulse, and the resulting pairs of vertical Bloch lines (d). The symbol ⊗ indicates the laser beam focusing site. Photographs (a) and (d) were obtained in a one-sided dark field with inverted contrast.

displaced by 1.5–2 μm relative to the center of the domain wall and in a certain position the probability of generating vertical Bloch lines reaches one. This was determined over 50–75 realizations. Figure 5l shows typical photographs illustrating the relative position of the domain wall and the laser beam for the reliable generation of Bloch lines and also the resultant pair of these lines. Note that the laser beam is slightly displaced from the center of the domain toward the domain wall but does not cover it.

3.1.3. Influence of laser beam power on the generation of vertical Bloch lines. We considered the probability of generating Bloch lines as a function of the laser pulse power for a fixed position of the beam near the point at which vertical Bloch lines are reliably generated, which was determined above. At powers $W < 0.13W_{max}$ we observe no change in the internal structure of the wall. From $W \simeq 0.15W_{max}$ we observe some generation of Bloch lines and at $W > 0.16W_{max}$ the generation probability increases substantially (see histogram in Fig. 6). At the same time, Fig. 6 shows that the generation probability is only exactly one for a single value of W. This is because the line generation effect depends strongly on the position of the beam relative to the domain wall (Fig. 4 shows that systematic displacements of the beam center at intervals of approximately 0.15 μm initially causes the line generation probability to increase from 0.1 to 1 and then drop to 0.4). In these experiments, the only possible method of continuously varying the pulse energy involves changing the relative angular position of the polarizers (see Fig. 1). Even with the optical system carefully aligned, rotation of the polarizer leads to unavoidable displacement of the center of the focused beam on the sample and departure from the optimum conditions for the generation of vertical Bloch lines. For points on the histogram (Fig. 6) with $W > 0.16W_{max}$ and a probability of line generation less then one, systematic fine correction of the beam position using precision positioners allows us to observe the generation of a Bloch line pair with a probability of one.

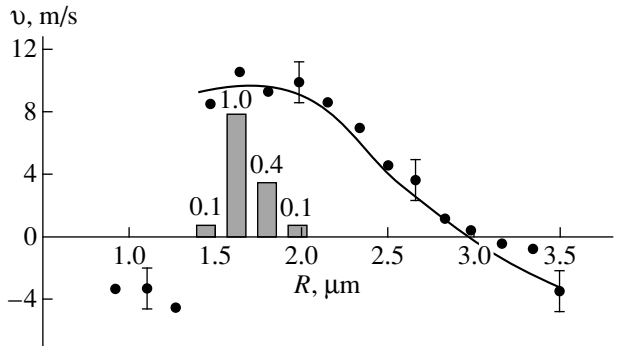

Fig. 4. Histogram showing the probability of Bloch line generation and the domain wall velocity v at the kink for various positions R of the center of the focused laser beam relative to the domain wall. Laser pulse energy $W = 0.2W_{max}$.

3.2. Dynamic Processes in the Domain Structure and the Domain Wall after a Laser Pulse

The high-speed photographic method used in the present study allows us to investigate in real time the characteristics of Bloch line generation and the dynamic processes taking place in the domain structure and the domain wall after the action of a laser pulse.

Figure 5 shows typical series of photographs demonstrating the processes in the domain wall and the generation of a pair of vertical Bloch lines at this wall as a result of the action of a laser pulse under conditions where these lines are generated with a probability of one (the focused beam is displaced toward one of the domain walls relative to the center of the domain, see Section 3.1.2). Figures 5a–5f show "instantaneous" domain structure configurations obtained using a direct

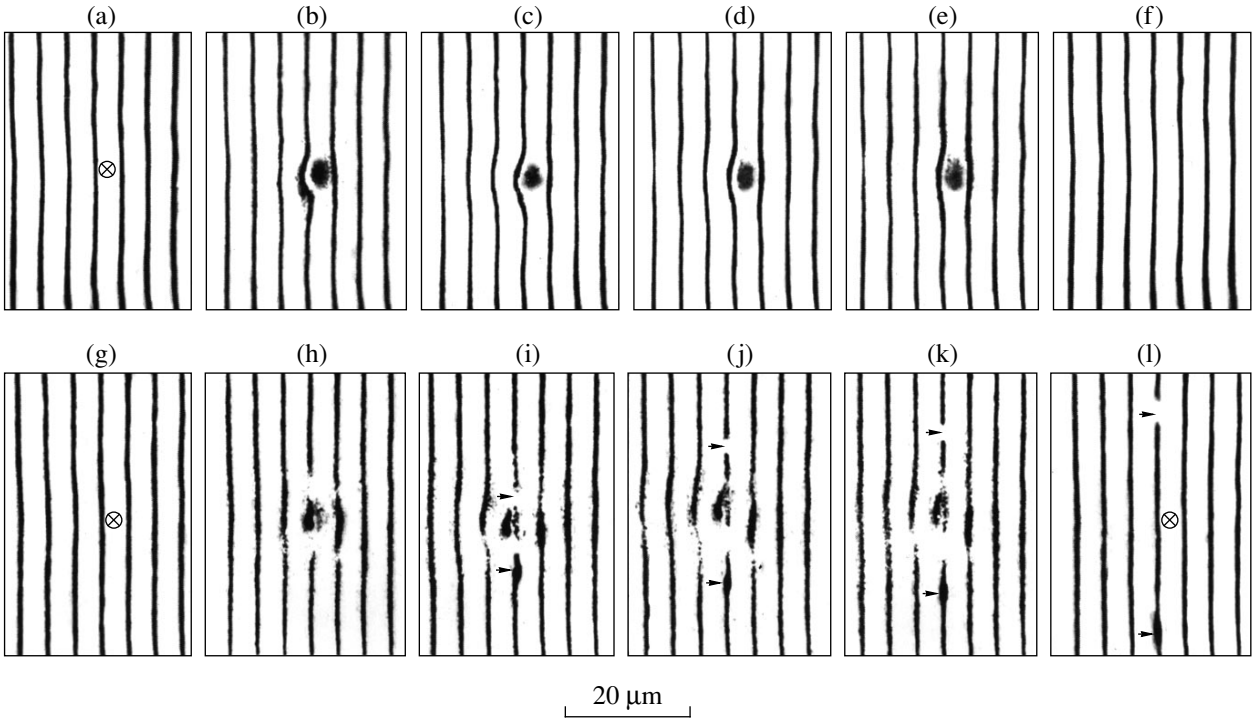

Fig. 5. Instantaneous dynamic configurations of the domain structure at various times after the application of a writing laser pulse. The symbol ⊗ shows the laser focusing point. The images were obtained: before the pulse (a, g), with delays of 100 ns (b, h), 300 ns (c, i), 700 ns (d, j), and 1000 ns (e, k) relative to the pulse application time, and after the end of the dynamic processes (f, l). The Bloch lines are indicated by arrows. Photographs (a–f) were obtained using a direct light-field illumination geometry with crossed polarizers while (g–l) were obtained using the dark field method (the image contrast is inverted).

light-field illumination geometry with crossed polarizers. The photographs show that at the focusing point of the optical pulse indicated by a cross, there is a dark region and the domain wall nearest to the beam is displaced, forming a kink. (When the beam is localized at the center of the domain, a similar pattern is observed with both walls deflected symmetrically, see [2].) The kink grows for the first 200 ns after the action of the laser pulse. It then relaxes slowly to the initial state over 1500–2000 ns and at the same time the dark region disappears. Photographs 5g–5l show the same section of the sample and the same process observed by the dark-field method which allows us to visualize the Bloch lines. In this case, the kink in the domain wall looks like a local change in the brightness of the wall image, which makes it difficult to observe the exact site and the instant at which a pair of Bloch lines is generated. However, Fig. 5 shows that the Bloch lines are displaced from their postulated generation site (in the immediate vicinity of the site of localization of the optical beam) toward a steady-state position. On the photographs the Bloch lines become noticeable at the edges of the domain-wall kink approximately 300 ns after the application of the laser pulse. The Bloch lines then continue to migrate at gradually decreasing velocity and reach their final position 1500–2000 ns after the action of the writing pulse. At the initial stages of their motion, the velocity of the Bloch lines is approximately 30 m/s.

By recording the kink in the domain wall at various times after the application of the laser pulse, we can construct a graph of the wall displacement as a function of time and determine its velocity. Typical time dependences of the domain wall displacement at the center of the kink are plotted in Fig. 7. The graphs correspond to beam focusing regimes at the center of the domain (*1*) and near the domain wall (*2*). The curves clearly show

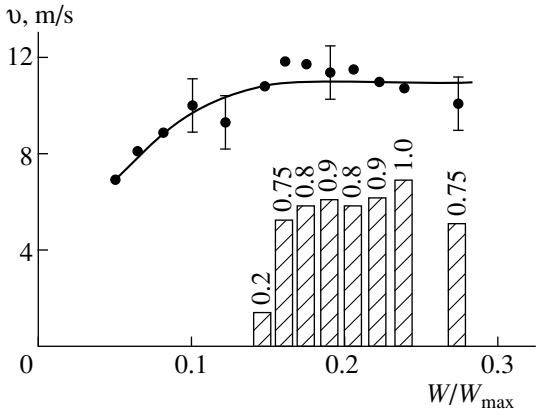

Fig. 6. Histogram showing the probability of Bloch line generation and the domain wall velocity v at the kink as a function of laser pulse energy W for a fixed position of the beam relative to the domain wall.

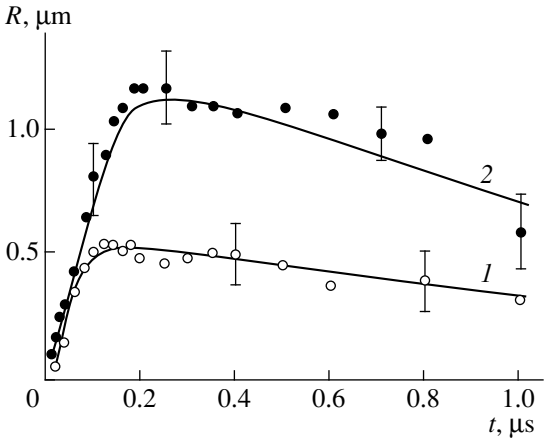

Fig. 7. Time dependence of the domain wall displacement at the center of the kink when the laser beam is focused at the center of the domain (*1*) and near the domain wall (*2*) at laser pulse energy $W = 0.2W_{max}$.

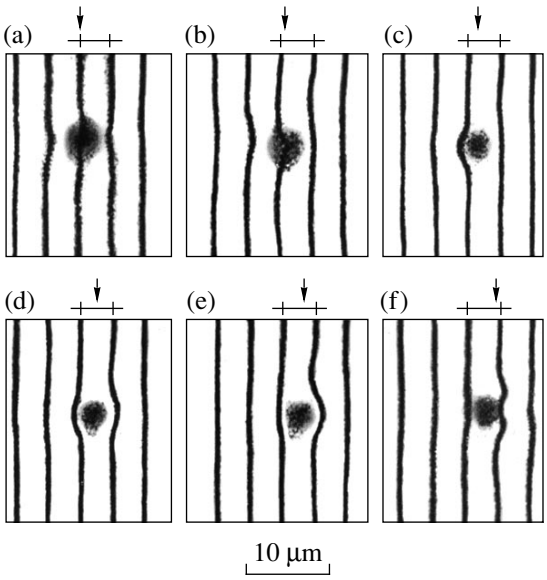

Fig. 8. Change in the domain wall propagation regime as the laser beam is gradually displaced perpendicular to the walls. The displacement of the beam is shown schematically in the insets above the photographs. Dynamic images of the walls were obtained by high-speed photography with an 80 ns delay after the laser pulse.

sections of initial linear displacement of the wall, a quasi-stable position, and finally slow relaxation to the initial position. On comparing curves *1* and *2*, we note that when the beam is focused near the domain wall, the wall migrates further (being displaced over a larger distance) whereas the overall character of the wall motion and its velocity at the initial stage are the same in both cases.

Time dependences of the domain wall displacement for various pulse energies were used to plot curves of its velocity as a function of energy *W*. The velocity was determined at the initial linear section of the movement. Figure 6 shows a typical dependence for the case where the beam is localized near the wall. (When the laser beam is positioned symmetrically relative to the domain wall, its velocity graph is the same as that shown in Fig. 6 to within measurement error). For a given energy *W* we determined the wall velocity as a function of the position of the focused spot relative to the wall (see Fig. 4). The histograms in Figs. 4 and 6 show the probabilities of the generation of vertical Bloch lines corresponding to the experimental points.

Figure 4 shows that depending on the localization of the beam center relative to the domain wall, its velocity has positive or negative values. This corresponds to different types of distortion of the particular wall after the application of the laser pulse and a change in the direction of motion depending on the coordinate of the focused beam. In this case the origin coincides with the static position of the wall. Motion of the domain wall to the left (with the beam positioned to the right of the wall) corresponds to a positive velocity while motion to the left corresponds to negative velocity. The solid curve in Fig. 4 obtained by a least-squares fit to an approximately Gaussian function reflects the fundamental trends of the wall velocity. Figure 8 shows typical dynamic configurations of domain walls which illustrate how their motion changes as the laser beam is gradually displaced perpendicular to the wall (the displacement of the beam is shown schematically in the insets above the photographs). Figure 8a shows the center of the focused beam positioned exactly at the domain wall which in this case is displaced negligibly. As the beam moves to the right so that its center is located in the domain and its edge covers the domain wall, the wall is displaced, being "drawn" into the overheated region (Fig. 8b). In this case, the velocity of the domain wall is low (Fig. 4, $R = 0.9$–1.3 μm). As soon as the left edge of the beam goes beyond the domain wall (Fig. 8c), the direction of displacement of the wall changes and the velocity reaches maximum values (Fig. 4, $R = 1.5$–2.0 μm). Figure 8d shows the shape of the kink in the domain walls when the laser beam is approximately equidistant from the walls. In this case, the domain wall velocity remains constant to within measurement error (Fig. 4, $R = 2.0$–2.2 μm). As the focused spot is shifted further, the displacement of the left wall decreases and changes sign (Figs. 8e and 8f). The corresponding change in the wall velocity and the reversal of its direction is shown in Fig. 4, $R = 2.5$–3.5 μm. Figure 8f shows a typical wave-shaped kink in the domain wall which corresponds to the regime when the edge of the laser beam only begins to cover the wall region.

A study of the domain wall dynamics after the application of a radiation pulse focused in regions of different diameter (see Section 3.1.1) shows that if the focusing region begins to cover the domain walls, these are drawn into the exposed region, as in Figs. 3b and 3c. Figure 3 shows the motion of the next pair of domain

walls toward the beam focusing region. As we have already noted, in this experimental geometry vertical Bloch lines may be generated not at the walls closest to the focused beam but at neighboring ones (see Fig. 3).

4. DISCUSSION OF THE RESULTS

The illustrations shows that the local action of optical radiation on an iron garnet film leads to some displacement of parts of the domain wall and (under certain conditions) results in the generation of Bloch lines at these walls. According to the hypothesis put forward in [2], the motion of the walls is caused by the local perturbation of the degaussing field of the sample. The dark area visible in Figs. 3b and 3c,. 5b–5f, and 8 occurs in a part of the sample with reduced Faraday rotation caused by a local reduction in the saturation magnetization of the film (and possibly a transition to the paramagnetic phase) as a result of the laser heating. A local change in the magnetization during heating and subsequent cooling significantly changes the distribution of the degaussing fields in this region, which induces displacement of the nearest domain wall. A graph of the domain wall displacement as a function of time (Fig. 7) confirms the thermal hypothesis on the nature of this motion: the initial stage of the motion corresponds to rapid heating of the magnetic film which is followed by cooling and spreading of the hot spot accompanied by slow relaxation of the domain wall to its initial position. Calculations of the domain wall configuration of a stripe domain in the presence of a cylindrical local nonmagnetic region showed good qualitative agreement with the proposed physical model and the experimental results (see below) [10].

The graphs plotted in Figs. 4 and 6 can be used to analyze characteristic features of Bloch line generation as a function of the nature of the domain wall motion and its velocity. It can be seen that in all optical irradiation regimes leading to the generation of Bloch lines, this generation is associated with motion of domain walls. In [2] Logginov *et al.* put forward the hypothesis that the domain wall velocity after optical irradiation may exceed the critical value at which, according to [3], loops of horizontal Bloch lines are generated and broken to form a pair of vertical Bloch lines. In our dynamic experiments, the domain wall velocity at which vertical Bloch lines are created is 10–12 m/s. Bearing in mind that the domain wall motion after laser irradiation takes place under variable temperature conditions, this value completely correlates with the critical wall velocity of approximately 30 m/s measured for a given sample during domain wall motion in a uniform pulsed bias field at 20°C. Note that the reproducible generation of Bloch lines not only requires domain wall motion at a certain critical velocity but the diameter of the focused laser beam and its position relative to the domain wall must also be optimized. This may be because in the hypothesis involving the breaking of horizontal Bloch lines to create vertical ones [3] the formation of a horizontal Bloch line and its migration from one surface of the magnetic film to the other occupies a finite time. The measurements showed (see Fig. 7) that when the beam is focused near the domain wall, the motion of the wall takes longer than when the beam is positioned symmetrically. This may well be responsible for better reproducibility in the breaking of horizontal Bloch lines and the generation of vertical ones. There is also the possibility that thermostatic stresses may be generated at the laser pulse irradiation site and the elastic wave may influence the generation and breaking of a horizontal Bloch line depending on the distance between the domain wall and the center of the laser focusing [11].

Observations of the generation of vertical Bloch lines (Fig. 5) showed that a pair of Bloch lines may migrate along the domain wall at a velocity of around 30 m/s (see Section 3.2) which is typical of the motion of vertical Bloch lines under the influence of a field applied in the plane of the sample [12]. The mechanism for the motion of the vertical Bloch lines shown in Fig. 5 may resemble ballistic aftermotion accompanied by dissipation of the energy stored in the horizontal Bloch line.

Figure 5 also reveals a change in the dark-field contrast of the domain wall near its kink. According to a model for the formation of the domain-wall image under conditions of anisotropic dark-field illumination [13], the change in the contrast of the wall may be caused by a change in the angle between the plane of the domain wall and the light incidence plane or by distortion of the wall profile over the sample thickness. In the first case, the brightness of the image decreases monotonically from a certain value I_0 to zero as the angle between the light incidence plane and the plane of the domain wall decreases from 90° to 0°, respectively. As a result of distortion of the vertical profile of the wall, the brightness of its image may be higher or lower than I_0 and changes substantially at short distances along the wall. The change in the contrast of the dark-field image of the domain wall in Fig. 5 indicates some complex deviation of its profile from the normal to the plane of the magnetic film near the laser focusing region. Further confirmation of this assumption is provided by the visible blurring of the wall at the kink which can be seen from the instantaneous dynamic photographs obtained by high-speed photography using a Faraday geometry with crossed polarizers.

The hypothesis on the thermal nature of the domain wall displacement after the action of a writing pulse [2] was checked by calculating the domain wall configuration in the presence of a nonmagnetic region [10].

In order to construct a model of the domain wall motion, for simplicity we confine ourselves to an isolated stripe domain stabilized by a bias field. We shall assume that under the action of an optical beam focused in a small region inside the domain, the domain is heated resulting in the formation of a nonmagnetic

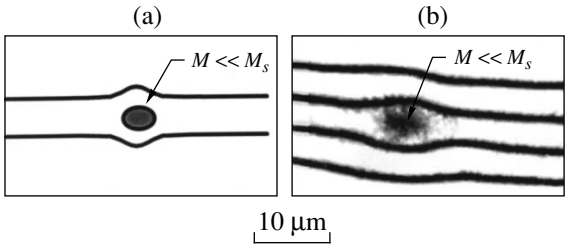

Fig. 9. Calculated configuration of domain wall profile in the presence of a local cylindrical nonmagnetic region (a) and instantaneous dynamic image of the stripe domain obtained experimentally 100 ns after application of the laser pulse (b).

cylindrical region. This region generates an additional magnetostatic field which distorts the domain walls. In order to calculate the quasi-equilibrium domain profile under conditions where a nonmagnetic region exists, we calculate the magnetostatic energy and then determine the domain configuration for which this energy will have a minimum.

The functional of the magnetostatic energy has a complex structure determined by the distribution of the magnetization vector in a self-consistent magnetic field which is a function of the magnetization distribution. The quasi-equilibrium distribution of the magnetization vector minimizes the functional of the total energy. This functional problem can only be solved approximately, for example, by using the method of Ritz trial functions. As a first approximation we take the magnetization distribution determined by varying the bias field consistent with the influence of a nonuniform field on the nonmagnetic cylindrical region at the center of the domain. In this case, the distortion of the domain wall shape of the stripe domain will be determined by the following transcendental equation:

$$\frac{H_0}{4\pi M_s} = \frac{2(r_0/h)^2}{[8(x/h)^2 + (w/h)^2]^{3/2}} + \frac{1}{\pi}\left\{2\arctan\frac{h}{w} - \frac{w}{h}\ln\left[1 + \left(\frac{h}{w}\right)^2\right]\right\}, \quad (1)$$

where H_0 is the bias field which stabilizes an isolated stripe domain, M_s is the saturation magnetization, h is the thickness of the magnetic film, w is the domain width at a certain point on the x axis directed along the stripe domain and having its origin at the center of the nonmagnetic cylindrical region, and r_0 is the radius of the nonmagnetic region. Formula (1) gives the implicit dependence of the stripe-domain width w on the x coordinate.

Figure 9a shows the profile of the stripe domain obtained in accordance with (1). Figure 9b illustrates the experimentally observed expansion of the stripe domain after the action of the laser radiation, which leads to the generation of Bloch lines. The central region in the figure can be identified as the nonmagnetic region formed as a result of the local laser heating. The figures reveal qualitative agreement between theory and experiment which indicates that the thermal mechanism for domain wall motion as a result of laser irradiation is valid.

Further confirmation of the key role played by the thermally induced change in the degaussing fields during the domain wall motion is provided by the experimentally observed change in the displacement behavior of the domain walls as a function of the relative position of the focused spot and the domain wall (see Fig. 8 and also Figs. 3 and 5). Quite clearly the configuration of the additional degaussing field changes substantially for different positions of the nonmagnetic region (Figs. 8a–8c), which leads to different types of domain wall displacement.

5. CONCLUSIONS

We have made an experimental investigation of the generation of Bloch lines by local optical irradiation which changes the magnetization state of an iron garnet magnetic film. We determined the influence of the optical radiation parameters (intensity, diameter of focused beam, and its position relative to the domain wall) on the generation of vertical Bloch lines. We established the optimum irradiation parameters to achieve the controlled generation of Bloch lines. Using a combination of high-speed photography and anisotropic dark-field observation, we studied the characteristics of Bloch line generation and the dynamic processes taking place in the domain structure and the domain wall after the action of the laser pulse. We observed that near the laser focusing zone the shape of the domain wall undergoes a reversible local distortion which depends on its position relative to the laser beam. Vertical Bloch lines are generated on the moving section of the domain wall when this is displaced at above-critical velocity. However, this condition is not sufficient for the reproducible generation of vertical Bloch lines. The diameter of the focused beam and its position relative to the domain wall must also be optimized.

We analyzed a theoretical model of Bloch line generation which relates the motion of the domain walls to the local heating of the magnetic film and a change in the distribution of the degaussing fields as the magnetization decreases at the laser focusing site. The actual mechanism for the generation of vertical Bloch lines is determined by the generation and breaking of loops of horizontal Bloch lines as the domain walls migrate at above-critical velocity. Calculations of the domain wall configuration in the presence of a local cylindrical nonmagnetic region give good qualitative agreement between theory and experiment.

The controlled generation of vertical Bloch lines by local optical irradiation can be considered as the basis

for a new approach to the recording of information in superdense magnetic memory devices with optical access. The approaches developed so far are based on reducing the wavelength of the recording laser radiation, using special high-aperture optics, and also various buffer structures and substrates which artificially limit the size of the recorded bit. Unlike these techniques, the effect of Bloch line generation described here demonstrates the fundamental possibility of achieved controlled and reproducible optical recording of a submicron magnetic information bit (in the form of vertical Bloch lines) using a laser beam focused in a substantially larger region. In this case, the bit size is determined by its physical nature as a low-dimension formation inside the domain wall and not by the characteristic scale of the recording instrument or the buffer structures.

ACKNOWLEDGMENTS

This work was supported under the program "Universities of Russia—Basic Research" and by the Russian Foundation for Basic Research (project no. 97-02-17788).

REFERENCES

1. E. Dan Dahlberg and Jian-Gang Zhu, Phys. Today **48**(4), 34 (1995).
2. A. S. Logginov, A. V. Nikolaev, V. N. Onishchuk, and P. A. Polyakov, Pis'ma Zh. Éksp. Teor. Fiz. **66**, 398 (1997) [JETP Lett. **66**, 426 (1997)].
3. A. P. Malozemoff and J. C. Slonczewski, *Magnetic Domain Walls in Bubble Materials* (Academic Press, New York, 1979; Mir, Moscow, 1982).
4. M. Marsuripur, *The Physical Principles of Magneto-Optical Recording* (Cambridge University Press, Cambridge, 1995).
5. Takao Suzuki, MRS Bull. **21**(9), 42 (1996).
6. G. J. Zimmer, T. M. Morris, and F. B. Humphrey, IEEE Trans. Magn. **10**, 651 (1974).
7. L. P. Ivanov, A. S. Logginov, and G. A. Nepokoĭchitskiĭ, Zh. Éksp. Teor. Fiz. **84**, 1006 (1983) [Sov. Phys. JETP **57**, 583 (1983)].
8. A. Thiaville, F. Boileau, J. Miltat, and L. Arnaud, J. Appl. Phys. **63**, 3153 (1988).
9. K. Patek, A. Thiaville, and J. Miltat, Phys. Rev. B **49**, 6678 (1994).
10. A. S. Logginov, A. V. Nikolaev, P. A. Polyakov, and Yu. V. Boltasova, in *Abstracts of the XVI International School-Seminar on New Magnetic Materials in Microelectronics, Moscow, 1998* (Mosk. Gos. Univ., Moscow, 1998), p. 488.
11. V. É. Gusev and A. A. Karabutov, *Laser Optoacoustics* (Nauka, Moscow, 1991).
12. A. S. Logginov, A. V. Nikolaev, and V. V. Dobrovitski, IEEE Trans. Magn. **29**, 2590 (1993).
13. A. Thiaville, J. Ben Youssef, Y. Nakatani, and J. Miltat, J. Appl. Phys. **69**, 6090 (1991).

Translation was provided by AIP

Journal of Experimental and Theoretical Physics, Vol. 90, No. 3, 2000, pp. 508–516.
Translated from Zhurnal Éksperimental'noĭ i Teoreticheskoĭ Fiziki, Vol. 117, No. 3, 2000, pp. 582–592.

SOLIDS
Electron Properties

Investigation of the Parametric Excitation and Relaxation of Phonons in Antiferromagnetic α-Fe_2O_3

A. V. Andrienko

Russian Research Centre Kurchatov Institute, pl. Kurchatova 1, Moscow, 123182 Russia
e-mail: andrienko@imp.kiae.ru

Received September 10, 1999

Abstract—Parametric excitation of magnetoelastic waves was investigated in the easy-plane antiferromagnet α-Fe_2O_3 by parallel and perpendicular microwave pumping over a wide range of frequencies, magnetic fields, and temperatures, and the parametric resonance thresholds were measured. The frequencies of the natural magnetoelastic vibrations of the sample were investigated as a function of the magnetic field and temperature. The results of the measurements were used to calculate the parameters of the magnetoelastic wave spectrum and the rate of relaxation of the excited quasi-phonons. Possible mechanisms for quasi-phonon damping were analyzed.

1. INTRODUCTION

One of the fundamental problems in the experimental physics of dielectrics is the study of the spectra and relaxation rate of elementary elastic and magnetic excitations, i.e., phonons and magnons. Phonons are usually excited and recorded using transducers attached to the sample, while the most powerful means of investigating the relaxation rate of electron and nuclear magnons is by their parametric excitation under microwave pumping (see the reviews [1–3]). As a result of the strong magnetoelastic interaction in easy-plane antiferromagnets, parametric phonons can also be excited by a microwave magnetic field. This method opens up the possibility of studying phonon relaxation in a sample which is not loaded acoustically with transducers.

Increasing the microwave magnetic field $h\cos\omega_p t$ above a threshold value h_c induces parametric instability in the sample involving the decay of a pump quantum into a pair of phonons having equal and oppositely directed wave vectors (k and $-k$) and the frequency sum ω_p. We shall only consider the case of degenerate pumping, when waves are generated in one branch of the spectrum at the half frequency ($\omega = \omega_p/2$). The main advantages of the parametric resonance method are that a narrow wave packet ($\Delta k \ll k$) is excited and the relaxation rates γ_k of the parametric waves can be determined from the threshold field h_c at which instability develops. For degenerate pumping we have

$$h_c = \min(\gamma_k/V). \quad (1)$$

Here $V = (\partial\omega/\partial H)/2$ is the coefficient of wave coupling with the microwave field which is determined by the effective magnetic moment of the excited wave. $\omega = \omega(k, H)$ is the dispersion law for the excited waves, and H is the static magnetic field.

2. PARAMETRIC PHONONS IN ANTIFERROMAGNETS

A distinguishing feature of easy-plane antiferromagnets is the existence of a low-activation, quasi-ferromagnetic (f), branch of the spin wave spectrum and the so-called exchange amplification of magnetoelastic interactions (see, for example, the review [4]). The magnetoelastic interaction leads to strong mixing of initially pure quasi-ferromagnetic and elastic modes as a result of which the vibrations of the new quasi-phonon branch acquire a magnetic moment and consequently a nonzero coupling coefficient with the microwave magnetic pump field V. The spectra of the coupled quasi-magnon and quasi-phonon branches of the vibrations have the form

$$\omega_{1k} = [g^2H(H + H_D) + g(H_{\Delta 2})^2 + v^2k^2]^{1/2}, \quad (2a)$$

$$\omega_{ph} = c[1 - (gH_{\Delta 1}/\omega_{fk})^2]^{1/2}k = \tilde{c}k. \quad (2b)$$

Here H_D is the Dzyaloshinskii field, g is the gyromagnetic constant, $H_{\Delta 1}$ is the magnetoelastic interaction constant, $gH_{\Delta 2}$ is the magnetostrictive gap in the spin wave spectrum, v is the spin wave velocity, and c is the nonrenormalized velocity of sound. Usually, in the frequency range studied by us, $\omega_{ph}/2\pi \sim 10^9$ Hz the term v^2k^2 in (2b) can be neglected, i.e., we can assume that the renormalized velocity of sound $\tilde{c} = \tilde{c}(H, k)$ does not depend on the wave vector. However, hematite is the highest-temperature antiferromagnet, with record values of the exchange field and the spin wave veloc-

ity. As a result the term v^2k^2 is already significant for $k \sim 10^4$ cm^{-1} which makes all the formulas and the treatment of the experimental results extremely complex.

The two methods of parametric excitation (two pump geometries) differ as a function of the relative orientation of the static **H** and microwave **h**(t) magnetic fields in the basal plane of the crystal: perpendicular pumping **H** $\perp$ **h** and parallel pumping **H** $\parallel$ **h**. These two methods differ fundamentally in terms of the mechanism for coupling the microwave field with the excited phonons. In the case of perpendicular pumping, the alternating field linearly excites uniform vibrations of the quasi-ferromagnetic branch of the spectrum at the line wing. As a result of the nonlinear magnetoelastic interaction, these vibrations generate phonons in a threshold process. In the case of parallel pumping the microwave field energy is transferred to the magnetic (and then to the elastic) subsystem both as a result of the linear excitation of uniform vibrations at the line wing of the antiferromagnetic branch and by modulating the spectrum of quasi-ferromagnons and quasi-phonons. In other words, the coupling coefficients $V_\perp$ and $V_\parallel$ are formed by different interactions of the pump field with the magnetic and magnetoelastic subsystems of the crystal. This is why it is interesting to study the parametric excitation of phonons for both perpendicular and parallel relative orientations of the magnetic fields.

Under conditions of perpendicular pumping parametric excitation of phonons in $CoCO_3$ (at frequency $\omega_p/2\pi$ = 50 GHz) was first observed by Borovik-Romanov, Zhotikov, and Kreines [5] and in $FeBO_3$ (at $\omega_p/2\pi$ = 10 GHz) by Wettling, Jantz, and Patton [6]. It was established that transverse phonons having the frequency $\omega_{ph} = \omega_p/2$ are excited by a threshold process in both antiferromagnets when **h** $\perp$ **H** (i.e., the case of degenerate pumping is achieved) although the dependences of the threshold field on the experimental parameters were not studied in detail by these authors. Later Kotyuzhanskiĭ and Prozorova [7] measured the temperature and field dependences for the threshold field $h_\perp$ in $FeBO_3$ at $\omega_p/2\pi$ = 35 GHz and estimated the relaxation rate of phonons excited parametrically by transverse pumping.

Parallel pumping of phonons in antiferromagnets has been observed in $FeBO_3$, $CoCO_3$, and α-Fe_2O_3 single crystals at frequencies $\omega_p/2\pi$ = (600–1400) MHz [8–11]. The most detailed study was made of iron borate in which transverse phonons at frequency $\omega_{ph} = \omega_p/2$ are excited by parallel pumping, detailed measurements were made of the threshold field h_c, and of the linear and nonlinear phonon relaxation rates, and the relationship between the amplitude of the threshold field and the phonon relaxation rate was determined experimentally.

The present paper is devoted to a detailed study of the parametric excitation processes and the rate of phonon relaxation in hematite single crystals over wide ranges of experimental parameters for various pumping geometries.

3. SAMPLES AND EXPERIMENTAL METHOD

Hematite crystals possess rhombohedral symmetry (D_{3d}^6) with the plane of easy magnetization and the growth plane coinciding with the basal plane of the crystal. The temperature of magnetic ordering in the easy-plane phase is T_N = 960 K. Dzyaloshinskiĭ–Moriya interaction leads to spin canting which results in the appearance of a weak ferromagnetic moment lying in the basal plane. When the temperature falls below the Morin point $T_M \approx 260$ K, the hematite undergoes an orientational phase transition to the easy-axis antiferromagnetic phase.

Measurements of the parametric phonon resonance threshold were made for two single crystals of antiferromagnetic α-FeO_3. The samples comprising 0.35 and 0.39 mm thick plates with clearly visible growth steps, were grown by V.N. Seleznev at Simferopol University. The linear dimensions of the samples in the basal plane were 2–6 mm.

The parametric phonon excitation was investigated using a decimeter-range spectrometer [3]. The resonant absorbing cell was an open copper resonator in the form of a cylindrical spiral 0.5 cm in diameter with loaded Q factor $Q \sim 500$. The sample was attached to a Teflon holder using a Teflon tape so that the resonator axis and therefore the field **h** lay in the plane of easy magnetization of the sample. The resonator together with the sample was placed in a copper container with a heating coil wound on it. The entire structure was placed in a cryostat filled with nitrogen gas. The electromagnet was rotated so that the static field **H** was always parallel to the plane of easy magnetization. In order to excite the natural vibration mode of the sample we used an additional coil consisting of several turns of copper wire wound coaxially with the resonator. The diameter of the modulation coil was 2 cm.

The measurements were made in static magnetic fields H = 0–2 kOe at temperatures T = 250–480 K in the range of pump frequencies $\omega_p/2\pi$ = 0.5–2 GHz.

The parametric phonon excitation was recorded in a pulsed microwave generation regime from the appearance of characteristic distortion of the pulse profile after passing through the resonator. We used pulses having durations of 50–300 μs at repetition frequency 50 Hz. The relative accuracy of the measurements of the threshold field h_c at fixed pump frequency was 5% and the absolute measurement accuracy was 25%.

4. EXPERIMENTAL RESULTS OF MEASUREMENTS OF THE PARAMETRIC INSTABILITY THRESHOLDS

Parametric phonon excitation was observed for any geometry of the static and magnetic microwave fields lying in the basal plane of the crystal. Figures 1 and 2

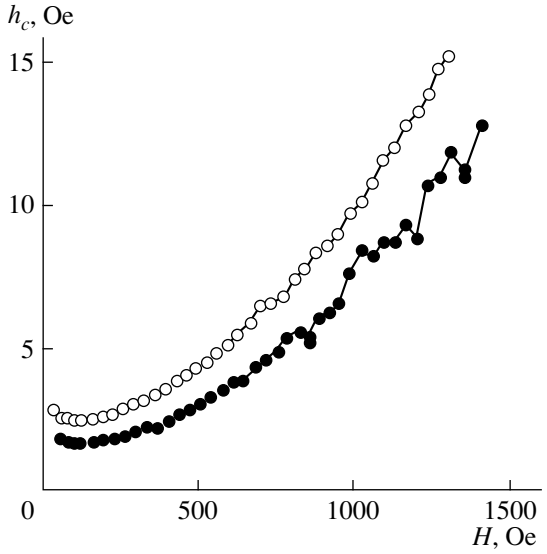

Fig. 1. Dependences of the threshold parallel (○) and perpendicular (●) pump fields on the magnetic field at T = 20°C, $\omega_p/2\pi$ = 1364 MHz.

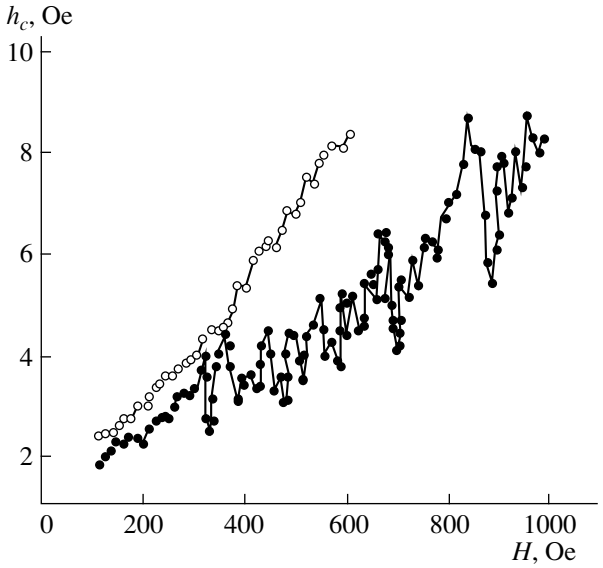

Fig. 2. Dependences of the threshold parallel (○) and perpendicular (●) pump fields on H at T = 197°C, $\omega_p/2\pi$ = 584 MHz.

show typical dependences of the threshold fields on the magnetic field for various frequencies, temperatures, and pump geometries. It is easy to see that these dependences are nonmonotonic: numerous dips are observed, these being particularly strong for $\mathbf{h} \perp \mathbf{H}$ and low pump frequencies. Similar threshold minima were observed earlier as a result of phonon pumping in iron borate [8, 10] and were attributed to the excitation of a standing magnetoelastic wave at frequency $\omega_p/2$ over the thickness of the plate. Under perpendicular pumping conditions these dips (resonances) were considerably greater because, in addition to parametric phonons at frequency $\omega_{ph} = \omega_p/2$, sound at frequency $\omega_{ph} = \omega_p$ is also excited linearly. It will be shown subsequently that as the frequency and temperature increase, and also as the amplitude of the static magnetic field decreases, the range of the parametric phonons decreases, with the result that the boundaries of the sample have a weaker influence on the parametric instability threshold and the dips on the threshold curve gradually disappear. We also note that in hematite the threshold fields $h_{c\perp}$ and $h_{c\parallel}$ have approximately the same dependence on the magnetic field unlike $FeBO_3$ and $CoCO_3$ for which the dependences $h_{c\perp}(H)$ and $h_{c\parallel}(H)$ differ substantially [10].

Figure 3 shows a typical dependence of the instability threshold on the magnetic field geometry. The perpendicular pumping condition corresponds to $\phi = 0°$. It can be seen that in hematite the highest threshold is obtained for parallel pumping whereas for $FeBO_3$ the converse is true, $h_{c\perp} > h_{c\parallel}$ [10].

Figure 4 shows the temperature behavior of $h_{c\perp}$ and $h_{c\parallel}$ for fixed values of the pump frequency and the magnetic field. Both fields have the same dependence on T: an almost linear increase in $h_c(T)$ is observed except for a narrow region of temperature near the Morin point where the pump threshold increases steeply. At temperatures below T_M no parametric phonon excitation was observed.

Figure 5 shows dependences of the thresholds on the microwave pump frequency. It is easy to see that the threshold fields $h_{c\perp}$ and $h_{c\parallel}$ have different frequency dependences and in the range $\omega_p/2\pi > 750$ MHz the field $h_{c\parallel}$ is almost proportional to frequency. At $\omega_p/2\pi \leq 750$ MHz the threshold fields $h_{c\perp}$ and $h_{c\parallel}$ are almost equal and then increase with decreasing frequency.

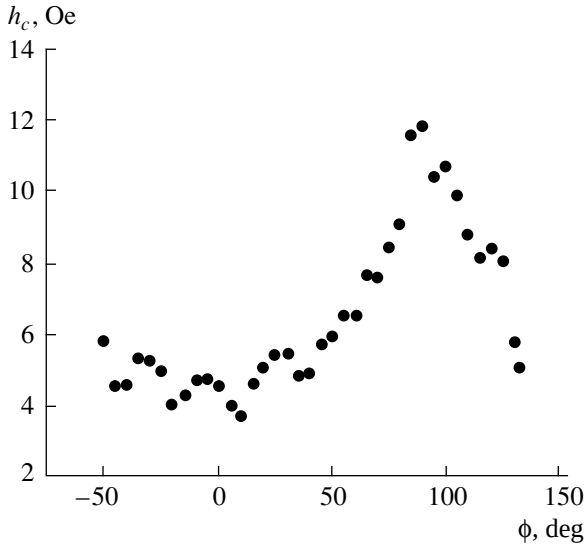

Fig. 3. Angular dependence of the parametric instability threshold at T = 172.5°C, H = 361 Oe, $\omega_p/2\pi$ = 1363 MHz; $\phi = 0$ corresponds to the perpendicular pumping condition.

Note that in $FeBO_3$ the threshold field $h_{c\|}$ did not depend on the pump frequency at all [9].

5. MEASUREMENT OF THE MAGNETOELASTIC PARAMETERS OF HEMATITE

In order to calculate the phonon relaxation rate from the threshold amplitude of the paramagnetic resonance, we need to know the magnetic, elastic, and magnetoelastic parameters of hematite. Numerous studies have been devoted to such measurements (see, for example, [4, 12–15]). Particular attention has been paid to studying the spin wave and antiferromagnetic resonance spectra, and also the velocity of sound which for convenience of analyzing the experimental results we write in the form

$$\tilde{c} = c[1 - \Delta_1/(H + H^2/H_D + \Delta_2 + K)]^{1/2}. \qquad (3)$$

Here the parameters $\Delta_1 = (H_{\Delta 1})^2/H_D$ and $\Delta_2 = (H_{\Delta 2})^2/H_D$ describe the magnetoelastic interaction, and the term $K = (vk)^2/g^2H_D$ gives the dependence of the velocity of sound on the wave vector (at low frequencies ω_{ph} this term can be neglected). The Dzyaloshinskiĭ field for hematite at room temperature is $H_D = 22$ kOe [13] and the spin wave velocity along the C_3 axis is $v = 24 \times 10^5$ cm/s [12]. Measurements of the velocity of sound and the antiferromagnetic resonance frequency show that the parameter $\Delta_1 \approx$ 400–500 Oe obtained by various authors for different hematite samples is the same within measurement error while the value of the constant Δ_2 varies from one sample to another and at room temperature is $\Delta_2 \simeq$ 500–1000 Oe. Since Δ_2 is caused by spontaneous magnetostriction, the value of $\Delta_2 \simeq 500$ Oe is evidently observed in samples having the fewest defects. The corresponding gap in the spin wave spectrum is 9.3 GHz.

Estimates of the parameter K show that in our experiments this is K = 15–500 Oe, i.e., in most cases this term cannot be neglected compared with H and Δ. From the formulas (2) we express K in terms of the parameters which can be measured experimentally:

$$K = \frac{(vk)^2}{g^2H_D} = \frac{1}{2}\left\{\Delta_1 - \Delta_2 - H + \frac{1}{H_D}\left(\frac{\omega_{ph}}{g}\right)^2\left(\frac{v}{c}\right)^2 + \left[\left(\Delta_1 - \Delta_2 - H + \frac{1}{H_D}\left(\frac{\omega_{ph}}{g}\right)^2\left(\frac{v}{c}\right)^2\right) + \frac{4}{H_D}\left(\frac{\omega_{ph}}{g}\right)^2\left(\frac{v}{c}\right)^2(H + \Delta_2)\right]^{0.5}\right\}. \qquad (4)$$

A fairly accurate method of measuring the magnetoelastic parameters involves measuring the frequency of the natural vibrations of the sample. Calculations [14] show that for an acoustic resonator in the form of a disk in which the field **H** is directed along the binary crystallographic axis X, the frequency of the natural vibrations of the α-Fe_2O_3 sample is given by

$$F = F_0\left[1 - \frac{\Delta_2 - \Delta_1}{H + H^2/H_D + \Delta_2 - \Delta_1}\right]^{1/2}. \qquad (5)$$

Results of measurements of F for fields $H > 100$ Oe are given in [14] and these are accurately described by formula (5). The value of $(\Delta_2 - \Delta_1) \approx 100$ Oe obtained in these measurements at T = 293 K agrees with the best values of Δ_2.

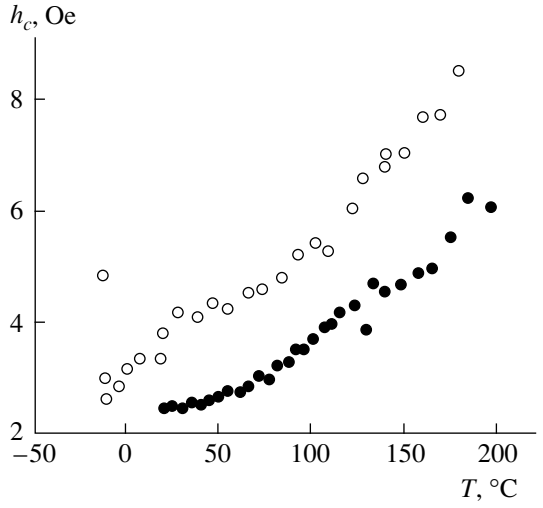

Fig. 4. Temperature dependences of the threshold parallel (○) and perpendicular (●) pump fields at H = 425 Oe, $\omega_p/2\pi$ = 1370 MHz.

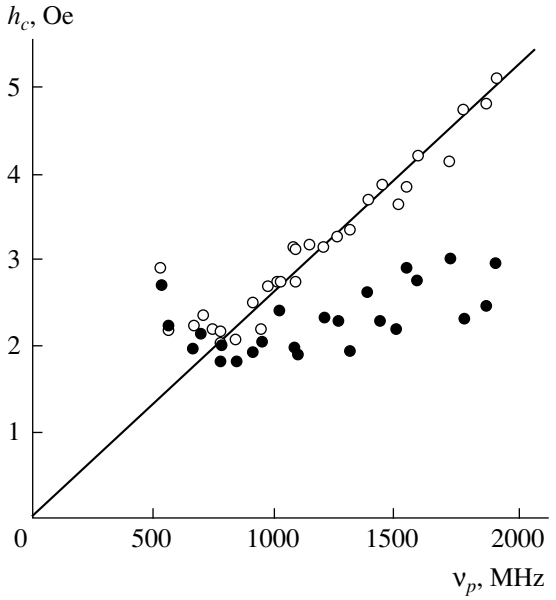

Fig. 5. Dependences of the threshold parallel (○) and perpendicular (●) pump fields on the frequency of the exciting microwave field at T = 20°C, H = 425 Oe.

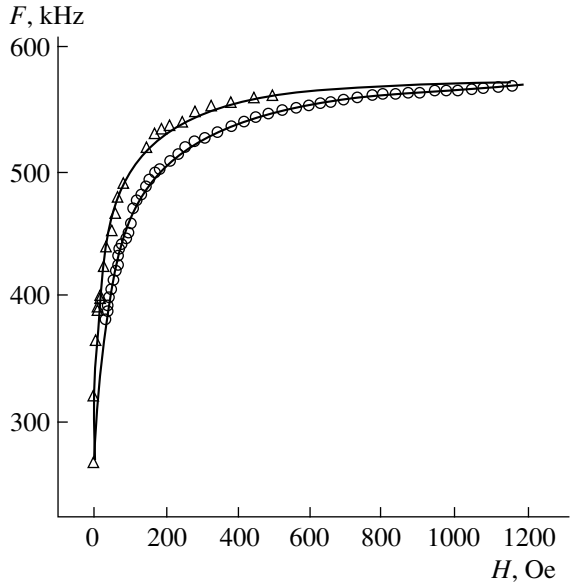

Fig. 6. Dependences of the frequency of the natural elastic vibrations of the sample on the magnetic field at $T = 20°C$ (○) and $T = 189°C$ (△). The solid curves give the calculations using formula (5) for the following values of the parameters: $F_0 = 590.32$ kHz, $\delta_1 = 85.75$ Oe, $\delta_2 = 110.29$ Oe at $T = 20°C$; $F_0 = 582.08$ kHz, $\delta_1 = 45.75$ Oe, $\delta_2 = 56.53$ Oe at $T = 189°C$.

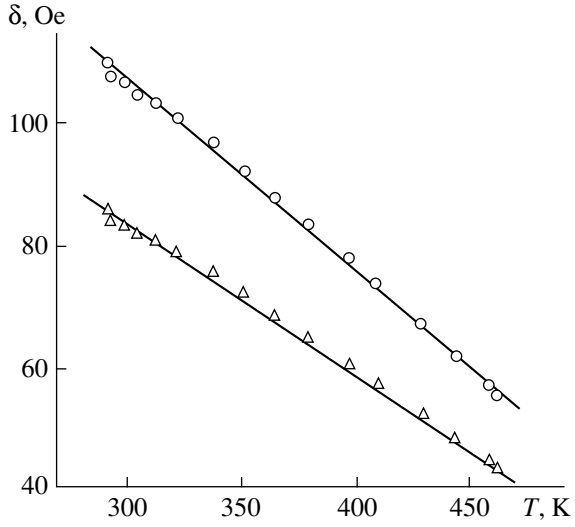

Fig. 7. Temperature dependences of the magnetoelastic parameters δ_1 (△) and δ_2 (○). The straight lines gives the calculations using the empirical formula (7).

Since the parameters of the phonon spectrum differ for different samples, in order to calculate the phonon relaxation rate we need to measure the values of the magnetoelastic parameters in the same crystal as that used to measure the pump thresholds. We measured these parameters using both the formulas (3) and (5) given above to some extent.

The first method used by us to measure the magnetoelastic parameters was based on the suppression of parametric phonon instability by low-frequency modulation of their spectrum [8]. When studying the influence of the field $H_m \cos\omega_m t$ on the pump thresholds, we observed that when the modulation frequency was equal to the natural vibration frequency of the sample, the dependence $h_c(\omega_m)$ had a sharp peak. This effect occurs because when the modulation frequency is the same as the frequency F of the natural elastic vibrations of the sample, these elastic vibrations are excited. The elastic vibrations of the crystal create an effective modulating magnetic field which actually intensifies the influence of the field H_m on the magnon and phonon spectrum and hence on the parametric instability threshold. By measuring the position of this peak as a function of the magnetic field, we obtained the field dependence of the natural vibration frequency of the sample. These measurements were made over a wide range of temperature. The results of measurements of F for two temperatures are plotted in Fig. 6. According to the calculations [14], these dependences for a disk should be described by expression (5). However, in our sample the frequency F was accurately described by the formula

$$F = F_0[1 - \delta_1/(H + H^2/H_D + \delta_2)]^{1/2}, \qquad (6)$$

which is similar to (5) but the values of $\delta_1 = 85.75$ Oe and $\delta_2 = 110.29$ Oe (at $T = 20°C$) differ, although they are close to the value of $(\Delta_2 - \Delta_1) \approx 100$ Oe obtained in [14]. The fact that $\delta_1 \neq \delta_2$ is clearly attributable to the irregular shape of our sample and to the random direction of the magnetic field relative to the second-order crystallographic axes.

Temperature dependences of the parameters δ_1 and δ_2 are plotted in Fig. 7. We can see that over the entire temperature range the parameters δ_1 and δ_2 are reasonably well described by linear functions of temperature and their ratio remains constant at $\delta_1/\delta_2 = 1.29 \pm 0.02$. The empirical expressions for the temperature dependences of δ_i have the form

$$\delta_i \approx \delta_{i0}[1 - (T - 293)/330]. \qquad (7)$$

Here T is the temperature and δ_{i0} is the value of the parameter at $T = 293$ K. Since δ_i are linear combinations of the magnetoelastic constants Δ_2 and Δ_1 and all these constants decrease smoothly with increasing T, we can postulate that the behavior of Δ_2 and Δ_1 will be described by the same function of temperature. We used formula (7) to calculate Δ_2 and Δ_1 in our calculations of the temperature dependence of the phonon relaxation rate.

The second method used by us to determine the magnetoelastic constants was based on observing the size effect of the parametric waves over the crystal thickness. If the magnetic field is varied at fixed phonon frequency, the velocity of sound and the magnetoelastic wavelength λ vary. For particular values of H the con-

dition $d = n(\lambda/2)$ is satisfied, i.e., an integer number of half-waves fall within the sample thickness (n is an integer). For these values of the field the pump threshold has minima. The spacing ΔH between these minima is determined by the field dependence of the velocity of sound (3). Using formulas (2) and (3) and assuming $n \gg 1$, we obtain the following expression:

$$\Delta H \approx 2\pi c(H + \Delta_2 + K)^{1/2} \times (H + \Delta_2 - \Delta_1 + K)^{3/2}/(\Delta_1 \omega_{ph} d). \quad (8)$$

In expression (8) the parameter K is a function of the magnetic field and the pump frequency. However, at the lower edge of our frequency range its value is small, $K \approx 20$ Oe, and in addition, in fields of $500 < H < 1100$ Oe the value of K only varies by 20% so that its field dependence at low frequencies can be neglected in (8). Unfortunately, at low frequencies the phonon wavelength increases so that the condition $n \gg 1$ is satisfied less accurately. Experimental results of detailed measurements of the spacing between the threshold minima for parallel pumping are plotted in Fig. 8. Since the number of experimental points is small, an analysis of these results by the least squares method with two independent parameters gives a large error. Thus, we used the result obtained previously $(\Delta_2 - \Delta_1) \approx 100$ Oe, retaining a single fitting parameter Δ_2 in formula (8). The solid curve in Fig. 8 was calculated by the least squares method using formula (8) into which we substituted the value $K = 25$ Oe averaged over the range of fields. The magnetoelastic constants for our sample are $\Delta_1 = 480$ Oe, $\Delta_2 = 580$ Oe, which agrees with the values obtained previously for higher-quality single crystals. The corresponding magnetostrictive gap in the spin wave spectrum is $gH_{\Delta 2}/2\pi \simeq 10$ GHz. This estimate is indirectly confirmed by our attempts to observe the antiferromagnetic resonance signal at 9.37 GHz. In weak fields intensive absorption of microwave power began to occur, but this did not reach a maximum even at $H = 0$, which indicates that the antiferromagnetic resonance frequency is close to 9.37 GHz at $H = 0$ although, quite obviously, the antiferromagnetic resonance frequency is slightly higher than the oscillator frequency, i.e., of the order of 10 GHz.

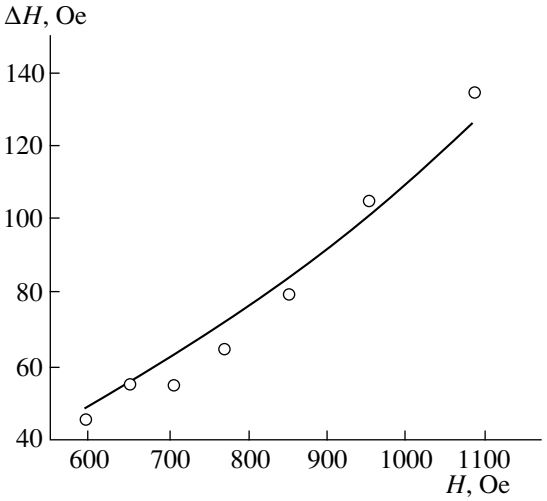

Fig. 8. Spacing between neighboring minima of the threshold field $h_{c\parallel}$ as a function of the static magnetic field H for $\omega_p/2\pi = 574.6$ MHz, $T = 20°$C. The solid curve gives the calculations using formula (8) for the following values of the parameters: $c = 4.1 \times 10^5$ cm/s [15], $\Delta_1 = 480$ Oe, $\Delta_2 = 580$ Oe, $d = 0.39$ mm, $K = 25$ Oe.

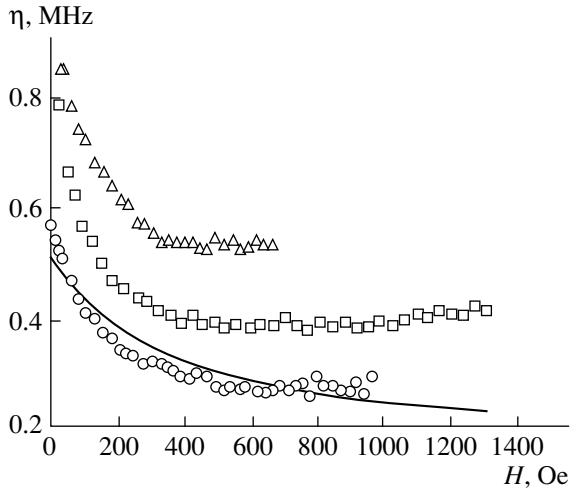

Fig. 9. Dependences of the phonon relaxation rate on the magnetic field at $T = 20°$C and various pump frequencies: (△) $\omega_p/2\pi = 1761$ MHz, (□) $\omega_p/2\pi = 1364$ MHz, (○) $\omega_p/2\pi = 1081$ MHz. The solid curve gives the calculations using formula (11).

6. CALCULATIONS OF PHONON RELAXATION. DISCUSSION OF RESULTS

Using formulas (1)–(3), we obtain the following expression for the phonon relaxation parameter $\eta = \gamma_k/2\pi$:

$$\eta = \frac{h_c \nu_p \Delta_1 \left(\frac{2H}{H_D} + 1\right)}{8\left(H + \frac{H^2}{H_D} + \Delta_2 + K\right)\left(H + \frac{H^2}{H_D} + \Delta_2 - \Delta_1 + K\right)}. \quad (9)$$

Here $\nu_p = \omega_p/2\pi$ is the microwave pump frequency and the parameter K is given by expression (4). Note that this formula is usually reduced to a simplified form, i.e., it is assumed that $\Delta_2 = \Delta_1$ and the terms H^2/H_D and K are neglected. Formula (9) was checked experimentally for the case $\mathbf{h} \parallel \mathbf{H}$ in [8] (the coefficient of phonon coupling with the threshold field was measured under parallel pumping conditions). No such investigations were made for the case of perpendicular pumping. In addition, under perpendicular pumping, before-threshold excitation of phonons occurs at frequency $\omega_{ph} = \omega_p$

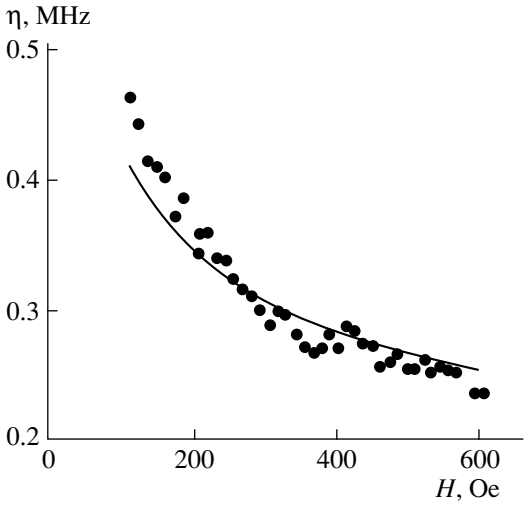

Fig. 10. Dependences of the phonon relaxation rate on the magnetic field at $T = 197°C$, $\omega_p/2\pi = 584$ MHz. The solid curve was obtained using formula (11).

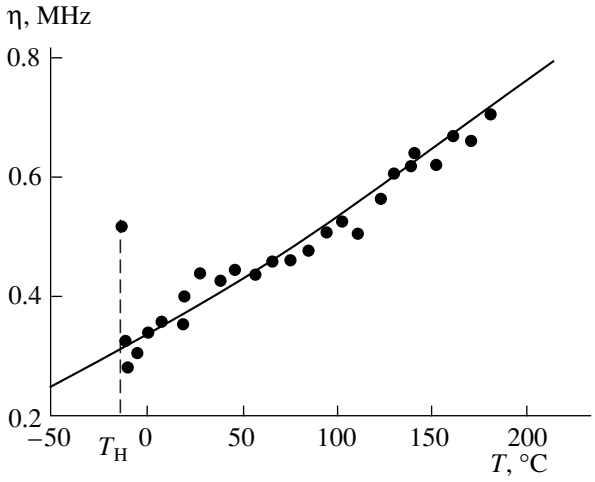

Fig. 11. Temperature dependence of the phonon relaxation rate at $H = 425$ Oe, $\omega_p/2\pi = 1370$ MHz. The solid curve gives the dependence $\eta \propto T^{3/2}$.

which may influence the parametric excitation threshold particularly when a standing wave of these phonons forms over the sample thickness. Thus, for our calculations of the phonon relaxation rate we only used the threshold value of the parallel pump field.

Figure 9 gives field dependences of the phonon relaxation rate at three pump frequencies. Quite clearly, these have approximately the same dependence on H: the relaxation rate increases with decreasing H in fields of less than 400 Oe and then tends toward a constant value with increasing field. It can be seen from Fig. 10 that a similar dependence is observed at high temperature.

Figure 11 shows the temperature dependence of the phonon relaxation rate. Over almost the entire range of temperature $\eta(T)$ is described by the function $\eta \propto T^{3/2}$. The only exception is a narrow range of temperature near the orientational phase transition temperature. The relaxation mechanisms making the major contribution to η will be discussed below.

Figure 12 gives the phonon relaxation parameter as a function of the pump frequency. For $\omega_p/2\pi > 750$ MHz a monotonic, almost linear increase in relaxation rate is observed. When $\omega_p/2\pi < 750$ MHz the phonon relaxation rate departs from this dependence and becomes almost constant at $\eta \approx 0.15$ MHz. The change in the phonon relaxation behavior at this point can be seen most clearly in Fig. 5 from the frequency dependence of the parallel pumping threshold. The value $\eta \approx 0.15$ MHz corresponds to the phonon mean free path $l \approx 1.6$ mm. This value is four times the sample thickness $d = 0.39$ mm. We can postulate that after several reflections from the crystal boundary, the parametric phonons cease to be coupled with the pump field, i.e., at low frequencies phonon scattering at the crystal boundaries begins to have a strong influence on the parametric instability threshold. This influence of the sample boundaries on the pump threshold can also be seen clearly from the large number of dips on the threshold curves at low frequencies (see, for example, Fig. 2). We recall that this jaggedness of the threshold curves diminishes as the pump frequency increases and the amplitude of the magnetic field decreases. This is clearly caused by an increase in the phonon relaxation rate and a decrease in the velocity of sound in weak fields, which has the result that many parametric phonons no longer reach the sample boundary and the influence of the finite dimensions of the sample on the threshold becomes weaker. It would be interesting to measure the threshold in larger samples for which the ten-

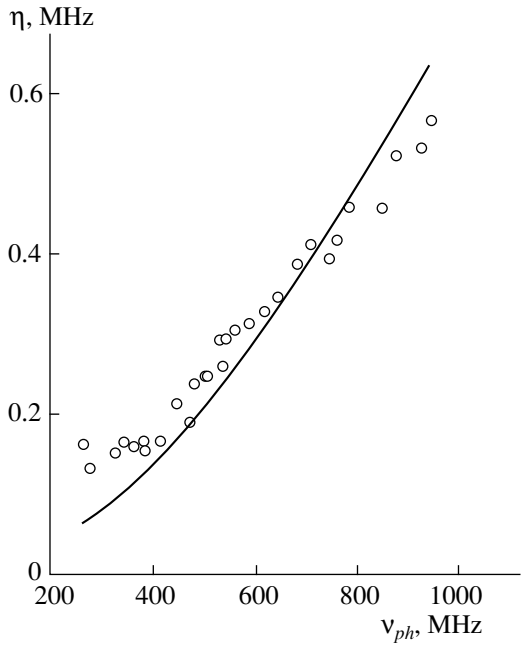

Fig. 12. Dependence of the phonon relaxation rate on frequency at $T = 20°C$, $H = 425$ Oe. The solid curve gives the calculations using formula (11).

dency of η to become constant would most likely not be observed at these frequencies. Unfortunately, no parametric excitation occurred at all in the large hematite crystals grown in other laboratories which were available to us. (The quality of these crystals was apparently poorer and the threshold pump amplitude was very high.) Hence, as yet we cannot categorically confirm that the kink on the experimental curve is attributable to the influence of the crystal boundaries.

It is interesting to note that although the frequency dependences of the pump thresholds in hematite and $FeBO_3$ (see [9]) differ substantially, this is not associated with differences in the phonon relaxation behavior but arises because the parameter K in the threshold formula (9) plays an important role for hematite, whereas it is negligible for iron borate. As a result, the frequency dependences of the phonon damping in these two materials were very similar: the phonon relaxation is approximately proportional to their frequency, i.e., the phonon Q factor is almost independent of frequency, except that in $FeBO_3$ it was twice as high.

An analysis of possible mechanisms for the damping of sound in hematite must take into account that the field and temperature dependence of the relaxation parameter are almost the same for all phonons in the frequency range $\omega_{ph}/2\pi > 380$–950 MHz. Assuming that several factors make major contributions to the relaxation, in this case all these contributions must have the same (similar) dependences on all the experimental parameters T, H, and ω_{ph}. This evidently implies that there is a single fundamental relaxation mechanism whose influence on the phonon scattering is significantly greater than all the other contributions to η. Consequently, the main contribution to the phonon relaxation in hematite is approximately proportional to ω_{ph}, increases with increasing temperature as $T^{3/2}$, increases rapidly with decreasing H in fields $H < 400$ Oe, and is almost independent of H in strong fields.

The most well-known mechanism for the relaxation of sound in high-quality nonmagnetic dielectric single crystals at high temperatures is the Akhiezer mechanism, involving the damping of sound at thermal phonons (see, for example, the review [16]). When $\omega_{ph}\tau \ll 1$, where τ is the thermal phonon lifetime, the elastic wave does not interact with an individual thermal phonon but with an overall ensemble of thermal phonons. This elastic wave may be considered as a field which modulates the frequency and therefore the distribution function of the thermal phonons. Redistribution of phonons over the spectrum is accompanied by phonon–phonon collisions which lead to relaxation of the elastic wave energy. This contribution to the relaxation of the elastic wave has the form [16]

$$\gamma_A \approx G^2 \sigma T \omega_{ph}^2 / \rho \tilde{c}^2 \bar{c}^2. \quad (10)$$

Here G is the Gruneisen constant, σ is the thermal conductivity, ρ is the density, and $\bar{c}$ is the mean velocity of the thermal phonons which, unlike $\tilde{c}$, is almost independent of the magnetic field. Having in mind that (a) the thermal conductivity of dielectrics at high temperature is approximately described by the dependence $\sigma \propto T^{-1}$, (b) the Gruneisen constant at $T \sim T_D$ is almost independent of temperature (the Debye temperature for hematite is $T_D \approx 400$ K [17]), and (c) the velocity of the sound excited by us depends on the magnetic field, frequency, and temperature in accordance with formulas (3) and (4), we obtain the following dependence for the Akhiezer mechanism in hematite

$$\gamma_A \propto f(T)\omega_{ph}^2/\tilde{c}^2(H, T, \omega_{ph}). \quad (11)$$

Here $f(T)$ is a weak function of temperature. The solid curves in Figs. 9, 10, and 12 give the dependences of the relaxation rate γ_A on the magnetic field and frequency corresponding to expression (11). Quite clearly, expression (11) describes the frequency and field functional dependences of the relaxation parameter reasonably well. However, the temperature dependence (11) differs significantly from the experimental one. As T increases, the value of $\tilde{c}$ increases slightly for a fixed field $H = 425$ Oe which should lead to an approximately 25% reduction in relaxation in the temperature range under study. However, an increase in relaxation by a factor of ~2.3 is observed experimentally which may be obtained by assuming that $f(T) \propto T^{3/2}$. In addition, an estimate of the absolute value of the phonon relaxation parameter in hematite using formula (10) gives $\eta_A \sim 10$ kHz at $\omega_{ph}/2\pi = 500$ MHz, $T = 300$ K whereas the experimental value of the relaxation under the same conditions is $\eta \approx 250$ kHz. Thus, both formula (10) and formula (11), which allows for the role of magnetoelastic interaction in the renormalization of the velocity of sound, describe by no means all the facets of the phonon damping behavior in hematite.

The influence of the magnon system on the sound damping efficiency in antiferromagnets with easy-plane anisotropy was examined in the greatest detail in [18]. It was shown that although the effective anharmonicity may exceed the elastic by two orders of magnitude in the long-wavelength part of the spectrum, it makes only a negligible contribution to the interaction of sound with thermal phonons, i.e., to the Akhiezer mechanism. On the other hand, a substantial increase is observed in the efficiency of the phonon–phonon interaction of sound with long-wavelength quasi-phonons having the wave vector $k \sim (\omega_{f0}/c)$, where ω_{f0} is the antiferromagnetic resonance frequency. The corresponding sound relaxation parameter has the form [18]

$$\gamma_{ph} = \frac{\beta}{2^5}\omega_{ph}\frac{\theta^6 T \theta_N}{\omega_{f0}^5 (mc^2)^3}, \quad (12)$$

where $\beta \sim 1$ is a numerical coefficient which depends on the direction and polarization of the acoustic wave, θ is the magnetoelastic interaction energy, θ_N is the Neel temperature, and m is the unit-cell mass. At first glance, this formula predicts an increase with temperature $\gamma_{ph} \propto T$ but taking into account the temperature

dependences of θ and ω_{f0} we find that as T increases from 260 to 470 K, the parameter γ_{ph} decreases by more than an order of magnitude. In addition, expression (12) does not give the required dependence of the relaxation rate on the frequency and magnetic field (in strong fields it follows from (12) that $\gamma_{ph} \propto H^{-5/2}$) whereas an estimate of the relaxation parameter at room temperature gives an absolute value $\eta_{ph} \sim$ 1–10 kHz, which does not exceed the contribution of the Akhiezer mechanism. Thus, the sound damping mechanisms considered in [18] intensified by magnetoelastic interactions also cannot explain our experimental results.

In [10] we suggested another phonon relaxation mechanism. The physical meaning of this mechanism is that [19] as a result of the interaction of coupled vibrations, not only do their frequencies change but also the relaxation parameters become renormalized. For instance, if one branch of these vibrations (magnons) was initially damped, as a result of interacting with it, a second branch of coupled vibrations receives an additional contribution to the relaxation. This influence of magnon relaxation on the damping time of vibrations coupled with them was first observed in studies of nuclear spin waves in antiferromagnetic $CsMnF_3$ [19]. A similar contribution of the magnon branch to the phonon damping has the form

$$\gamma_k^{(ph)} = (d\omega_{ph}/d\omega_{fk})\gamma_{fk}^{(m)}. \quad (13)$$

Using the experimental results on the relaxation of magnons in $FeBO_3$ we were able to describe the main contribution to phonon relaxation at high temperatures using a model in which the width of the magnon branch is "renormalized" to the coupled phonon branch. This conclusion from [8] was later confirmed in studies of the Q factor of the natural elastic vibrations of an $FeBO_3$ single crystal [20]. This mechanism may well be responsible for the phonon damping in hematite. In order to estimate this contribution to the phonon relaxation, we require experimental data on the relaxation of magnons coupled to them. Unfortunately, at present we do not have any such results on magnon relaxation in hematite. However, we can put forward the following reasoning.

Using expressions (2) and (13), we obtain for fixed H and T

$$\gamma_k^{(ph)} \propto \omega_{ph}\gamma_{fk}^{(m)}.$$

Under the same conditions, the experiment gives a dependence close to $\gamma_k \propto \omega_{ph}$. Thus, in order to describe the experimental results, we impose the constraint that at fixed magnon frequency, their rate of relaxation in hematite should not depend on the wave vector. This behavior of the damping parameter of magnons with $k \sim 10^4$ cm^{-1} at high temperatures is predicted by the theory of magnon–phonon relaxation [21] and has also been observed in various low-temperature antiferromagnets [3, 19] where it has usually been attributed to inhomogeneous broadening of the spin wave spectrum. By renormalizing these relaxation parameters to the phonon branch we obtain the dependence $\gamma_k \propto \omega_{ph}$.

ACKNOWLEDGMENTS

The author is grateful to S.V. Kapel'nitskiĭ, V.I. Ozhogin, V.L. Safonov, and A.Yu. Yakubovskiĭ for discussions of the results. This work was supported by the Russian Foundation for Basic Research (projects nos. 97-02-17586 and 96-15-96738).

REFERENCES

1. V. E. Zakharov, V. S. L'vov, and S. S. Starobinets, Usp. Fiz. Nauk **114**, 609 (1974) [Sov. Phys. Usp. **17**, 896 (1974)].
2. A. S. Borovik-Romanov, V. G. Zhotikov, N. M. Kreines, *et al.*, Phys. Rev. A **1**, 247 (1979).
3. A. V. Andrienko, V. I. Ozhogin, V. L. Safonov, and A. Yu. Yakubovskiĭ, Usp. Fiz. Nauk **161**, 1 (1991).
4. V. I. Ozhogin and V. L. Preobrazhenskiĭ, Usp. Fiz. Nauk **155**, 593 (1988) [Sov. Phys. Usp. **31**, 713 (1988)].
5. A. S. Borovik-Romanov, V. G. Zhotikov, and N. M. Kreines, in *Light Scattering in Solids*, Ed. by J. L. Birman, H. Z. Cummins, and K. K. Rebane (Plenum, New York, 1979), p. 175.
6. W. Wettling, W. Jantz, and C. E. Patton, J. Appl. Phys. **50**, 2030 (1979).
7. B. Ya. Kotyuzhanskiĭ and L. A. Prozorova, Zh. Éksp. Teor. Fiz. **83**, 1567 (1982) [Sov. Phys. JETP **56**, 903 (1982)].
8. A. V. Andrienko and L. V. Podd'yakov, Zh. Éksp. Teor. Fiz. **95**, 2117 (1989) [Sov. Phys. JETP **68**, 1224 (1989)].
9. A. V. Andrienko and L. V. Podd'yakov, Zh. Éksp. Teor. Fiz. **99**, 313 (1991) [Sov. Phys. JETP **72**, 176 (1991)].
10. A. V. Andrienko, L. V. Podd'yakov, and V. L. Safonov, Zh. Éksp. Teor. Fiz. **101**, 1083 (1992) [Sov. Phys. JETP **74**, 579 (1992)].
11. A. V. Andrienko and L. V. Podd'yakov, J. Magn. Magn. Mater. **123**, L27 (1993).
12. E. J. Samuelsen and G. Shirane, Phys. Status Solidi **42**, 241 (1970).
13. M. H. Seavey, Solid State Commun. **10**, 219 (1972).
14. E. A. Andrushchak, N. N. Evtikhiev, S. A. Pogozhev, *et al.*, Akust. Zh. **27**, 170 (1981) [Sov. Phys. Acoust. **27**, 93 (1981)].
15. A. Yu. Lebedev, B. S. Abdurakhmanov, and A. M. Balbashov, Zh. Tekh. Fiz. **59**, 165(2) (1989) [Sov. Phys. Tech. Phys. **34**, 231 (1989)].
16. V. V. Lemanov and G. A. Smolenskiĭ, Usp. Fiz. Nauk **108**, 465 (1972).
17. F. van der Woude, Phys. Status Solidi **17**, 417 (1966).
18. V. S. Lutovinov, V. L. Preobrazhenskiĭ, and S. P. Semin, Zh. Éksp. Teor. Fiz. **74**, 1159 (1978) [Sov. Phys. JETP **47**, 609 (1978)].
19. A. V. Andrienko, V. I. Ozhogin, V. L. Safonov, and A. Yu. Yakubovskiĭ, Zh. Éksp. Teor. Fiz. **89**, 1371 (1985) [Sov. Phys. JETP **62**, 794 (1985)].
20. V. L. Safonov, P. M. Loaiza, and L. E. Svistov, J. Magn. Magn. Mater. **173**, 43 (1997).
21. S. A. Breus, V. L. Sobolev, and B. I. Khudik, Fiz. Nizk. Temp. **4**, 1167 (1978) [Sov. J. Low Temp. Phys. **4**, 550 (1978)].

Translation was provided by AIP

Journal of Experimental and Theoretical Physics, Vol. 90, No. 3, 2000, pp. 517–526.
Translated from Zhurnal Éksperimental'noĭ i Teoreticheskoĭ Fiziki, Vol. 117, No. 3, 2000, pp. 593–603.

SOLIDS
Electron Properties

Electron Transport Across a Microconstriction in an Arbitrarily Oriented Homogeneous Magnetic Field

N. G. Galkin, V. A. Geyler*, and V. A. Margulis
Mordovian State University, Saransk, 430000 Russia
**e-mail: geyler@mrsu.ru*
Received July 14, 1999

Abstract—An analysis is made of ballistic electron transport in three-dimensional microconstrictions of elliptic cross section located in an arbitrarily oriented magnetic field. The model of a parabolic confinement potential is used to obtain and analyze the dependence of hybrid frequencies on the magnitude and direction of the magnetic field. An expansion of the conductance as a Fourier series is obtained and used to study Aharonov–Bohm and Shubnikov–de Haas oscillations as a function of the field and the stepped quantization structure of the conductance. A possible explanation is given for the experimentally observed effect of conductance quantization at fairly high temperatures. © *2000 MAIK "Nauka/Interperiodica".*

1. INTRODUCTION

Ballistic electron transport in three-dimensional microconstrictions (point contacts) has recently attracted growing interest [1–9] following the experimental observation of conductance quantization effects in these systems, even at room temperature. The properties of three-dimensional (3D) microconstrictions differ substantially from those of the two-dimensional (2D) microconstrictions [10, 11] in which conductance quantization was first observed. The character of the conductance quantization in 3D microconstrictions depends strongly on the profile of the cross-section and also on the length of the contact [7]. In particular, in a symmetric constriction (circular cross section) the height of the conductance quantization step measured in conductance quantum units $G_0 = 2e^2/h$, is proportional to the degree of degeneracy of the transverse energy levels [7]. An applied magnetic field **B** changes the transport regime of the constriction. This is because the field changes the electron confinement and may enhance (for an elliptic cross section) or induce (for a circular cross section) effective anisotropy of the constriction cross section. In [7] the generalized Buttiker–Landauer formula was used to study the conductance (mainly by numerical methods) of a 3D microconstriction for cases of longitudinal and transverse magnetic fields and also in the particular case of a tilted magnetic field [the field lies in the *yz* plane, i.e., $\mathbf{B} = (0, B_y, B_z)$. The numerical results show that changes in the cross-sectional profile, magnitude, and direction of the field **B** lead to changes in the electron transport regime. Graphs of the conductance *G* as a function of the field **B** plotted in [7] show that Aharonov–Bohm and Shubnikov–de Haas oscillations may occur in a longitudinal magnetic field. The nature of these oscillations depends strongly on the magnitude of the magnetic field. It was noted in [7] that the length of the microconstriction also strongly influences the transport regime. In particular, the results of a numerical analysis indicate that the conductance quantization effect (stepped structure) and the Aharonov–Bohm oscillations may disappear in short microconstrictions.

We note that a convenient model of the geometric confinement potential which can allow for the role of the microconstriction shape and the influence of the magnitude and direction of the magnetic field is the "soft wall" potential. This potential was used in [10, 11] for 2D constrictions and in [7] for 3D constrictions. This potential characterizes the cross-sectional profile of the constriction and its length. This factor is extremely important because in the ballistic regime the geometry of the microconstriction is a source of resistance.

Near the constriction bottleneck, the arbitrary smooth geometric-confinement potential in second order with respect to the coordinates (*x*, *y*, *z*) is expressed in the form

$$V(x, y, z) = V_0 + \frac{1}{2}m^*(\omega_x^2 x^2 + \omega_y^2 y^2 - \omega_z^2 z^2). \quad (1)$$

Here V_0 is the potential at the saddle point of the constriction, m^* is the effective electron mass, and *z* is the coordinate along the constriction axis. The frequency ω_z is determined by the microconstriction length *l*: $\omega_z = \hbar/m^* l^2$. The microconstriction cross section is approximated to within second-order terms by an ellipse having the semiaxes

$$a = \frac{1}{2}\sqrt{\frac{\hbar}{m^*\omega_x}}, \quad b = \frac{1}{2}\sqrt{\frac{\hbar}{m^*\omega_y}}.$$

1063-7761/00/9003-0517$20.00 © 2000 MAIK "Nauka/Interperiodica"

The Hamiltonian of the one-electron states in an applied static, uniform magnetic field $\mathbf{B} = (B_x, B_y, B_z)$ has the form

$$H = \frac{1}{2m^*}\left(\mathbf{p} - \frac{e}{c}\mathbf{A}\right)^2 + V(x, y, z), \qquad (2)$$

where $\mathbf{A}$ is the vector potential of the field $\mathbf{B}$. For $\mathbf{A}$ we select the following gauge:

$$\mathbf{A} = \left(\frac{1}{2}B_y z - B_z y\right)\mathbf{i} + \left(B_x y - \frac{1}{2}B_y x\right)\mathbf{k}. \qquad (3)$$

By rotating the axes in phase space, we can reduce the quadratic Hamiltonian (2) to the diagonal form. This Hamiltonian then has the same form as that in the absence of the magnetic field but with different frequencies of the effective potential:

$$H = \frac{1}{2m^*}\mathbf{P}^2 + \frac{m^*}{2}(\omega_1^2 Q_1^2 + \omega_2^2 Q_2^2 - \Omega^2 Q_3^2), \qquad (4)$$

where $\mathbf{P}$ and Q are the new phase variables. The new characteristic frequencies ω_1, ω_2, and Ω are functions of the magnitude and direction of the magnetic field $\mathbf{B}$.

The probability of propagating from a mode having the quantum numbers (m, n) to the (m', n') mode is determined by the generalized Buttiker formula [12] and has the form

$$T_{m, n; m', n'} = \delta_{mn'}\delta_{nn'}[1 + \exp(-2\pi\varepsilon_{mn})]^{-1}, \qquad (5)$$

where $\varepsilon_{mn} = (E - V_0 - E_{mn})/\hbar\Omega$, the quantum numbers of the oscillators are m and $n = 0, 1, 2, \ldots$, the energy of the electron motion in the plane Q_1Q_2 is $E_{mn} = \hbar\omega_1(m + 1/2) + \hbar\omega_2(n + 1/2)$, and E is the total electron energy.

Effects of electron tunneling through the effective potential

$$V_{\text{eff}}(z) = V_0 + E_{mn} - m^*\Omega^2 z^2/2$$

lead to smearing of the threshold energy $V_{\text{eff}}(0)$ which then has the result that the probability of propagating through channels with $E < V_{\text{eff}}(0)$ becomes nonzero [7]. A comparison between the factor in brackets in (5) and the Fermi distribution $f_0(E)$ shows that the value of $\hbar\Omega/2\pi$ plays the same role as the temperature in the Fermi distribution, i.e., smears the threshold electron energy.

The conductance of a 3D constriction for $T \neq 0$ is given by

$$G(T) = \int_0^\infty dE\left(-\frac{\partial f_0}{\partial E}\right)G(T = 0), \qquad (6)$$

where $G(T = 0)$ is given by the Landauer expression:

$$\frac{G(T = 0)}{G_0} = \sum_{m, n = 0}^{\infty} [1 + \exp(-2\pi\varepsilon_{mn})]^{-1}. \qquad (7)$$

On the basis of the above reasoning on the smearing of the threshold energy, the upper limit in the sums (7) over m and n is infinity.

Since (7) contains a double sum over the quantum numbers m, n and (6) has an integral over energy, it is difficult to use these expressions directly to analyze the conductance of a 3D constriction (unlike the case of a nanowire of constant cross section where no smearing of the threshold energy occurs in (7) and the sums are easily calculated). This is evidently why in [7] further investigation of the conductance using (6) and (7) was made by numerical methods. Moreover, the general case when $\mathbf{B} = (B_x, B_y, B_z)$ was not considered at all in [7].

We make another important observation. Formula (7) is similar to the magnetic response of a degenerate gas of two-dimensional oscillators having the temperature $T = \hbar\Omega/2\pi$ and the chemical potential $\mu = E - V_0$. The magnetic response of this type of gas was studied in [13] where the corresponding series were summed over a single index and (6) and (7) were reduced to a one-dimensional Fourier series.

The present article is constructed as follows. In Section 2, for the general case of an arbitrary magnetic field $\mathbf{B} = (B_x, B_y, B_z)$ we determine the frequencies ω_1, ω_2, and Ω in terms of the roots of a cubic equation and we construct the dependences of these frequencies on the magnitude and direction of the field. In Section 3 we obtain an expansion of the conductance of a 3D constriction as a one-dimensional Fourier series, by isolating the monotonic and oscillating components of the conductance, i.e., we obtain for the conductance an analog of the Landau formula for the magnetic response of a degenerate gas. In Section 4 we study the oscillating component of the conductance and demonstrate analytically that Aharonov–Bohm and Shubnikov–de Haas oscillations exist in a longitudinal field. In this section we also investigate the case of a transverse field and study the stepped structure of the conductance as a function of the orientation of the field.

2. DIAGONALIZATION OF THE HAMILTONIAN

We shall analyze the Hamiltonian (2) with the potential (1) and the magnetic field $\mathbf{B} = (B_x, B_y, B_z)$ arbitrarily oriented relative to the axes x, y, z, where the z axis is directed along the microconstriction, and the x and y axes are directed along the minor and major axes of the elliptic cross section of the constriction, respectively. In phase space (p_x, p_y, p_z, x, y, z) the Hamiltonian (2)

defines a quadratic form with the sixth-order symmetric matrix

$$M = \frac{1}{2m^*} \times \begin{Vmatrix} 1 & 0 & 0 & 0 & 2B_3 & -B_2 \\ 0 & 1 & 0 & 0 & 0 & 0 \\ 0 & 0 & 1 & B_2 & -2B_1 & 0 \\ 0 & 0 & B_2 & k_1^2 & -2B_1B_2 & 0 \\ 2B_3 & 0 & -2B_1 & -2B_1B_2 & k_2^2 & -2B_2B_3 \\ -B_2 & 0 & 0 & 0 & -B_2B_3 & k_3^2 \end{Vmatrix}. \quad (8)$$

Here the following notation is introduced

$$B_1 = \frac{e}{2c}B_x, \quad B_2 = \frac{e}{2c}B_y, \quad B_3 = \frac{e}{2c}B_z,$$
$$k_1^2 = m^{*2}\omega_x^2 + B_2^2,$$
$$k_2^2 = m^{*2}\omega_y^2 + 4B_1^2 + 4B_3^2, \quad (9)$$
$$k_3^2 = -m^{*2}\omega_z^2 + B_2^2.$$

The canonical form (4) of the Hamiltonian (2) is determined by the eignevalues of the matrix IM, where I is the symplectic unit [14]:

$$I = \begin{Vmatrix} 0 & -E \\ E & 0 \end{Vmatrix}, \quad E = \begin{Vmatrix} 1 & 0 & 0 \\ 0 & 1 & 0 \\ 0 & 0 & 1 \end{Vmatrix}. \quad (10)$$

The eignevalues λ of the matrix M are obtained from the following sixth-order equation

$$(\lambda^2 + \omega_x^2)(\lambda^2 + \omega_y^2)(\lambda^2 - \omega_z^2) + \lambda^2(\lambda^2 + \omega_x^2)\omega_{cx}^2 + \lambda^2(\lambda^2 + \omega_y^2)\omega_{cy}^2 + \lambda^2(\lambda^2 - \omega_z^2)\omega_{cz}^2 = 0, \quad (11)$$

where $\omega_{cj} = eB_j/m^*c$, $j = x, y, z$.

To be specific, we assume that $\omega_x \geq \omega_y$ and we investigate the cubic equation obtained for $\xi = \lambda^2$. We denote by $P(\xi)$ the third-degree polynomial of ξ on the right-hand side of (11). Then it is quite clear that

$$P(-\infty) = -\infty, \quad P(-\omega_x^2) > 0,$$
$$P(0) < 0, \quad P(\omega_z^2) > 0.$$

Thus the equation $P(\xi) = 0$ has three different roots:

$$\xi_1 \in (-\infty, -\omega_x^2), \quad \xi_2 \in (-\omega_x^2, 0), \quad \xi_3 \in (0, \omega_z^2).$$

Consequently by means of a symplectic transformation of phase space, the Hamiltonian (2) is reduced to the canonical form (4) in which $\omega_{1,2}^2 = -\xi_{1,2}$, $\Omega^2 = \xi_3$ [14]. Note that by making the substitution $\omega_z^2 \longrightarrow -\omega_z^2$ the equation $P(\xi) = 0$ yields a cubic equation for the effective frequencies of a particle in a three-dimensional parabolic quantum well in a magnetic field [15]. The hybrid frequencies ω_j and Ω were determined in [7] in the extremely specific case where the field **B** lies in one of the coordinate planes. Graphs of the hybrid frequencies ω_j as a function of the magnitude and direction of the field **B** (the direction is defined by the angles θ and φ of orientation of the field relative to the coordinates (x, y, z) related to the microconstriction) are plotted in Fig. 1 where one of the angles is fixed ($\varphi = \varphi_0$ or $\theta = \theta_0$). It can be seen that the frequencies ω_j depend on the magnitude and direction of the field so that the conductance of the microconstriction will also depend on these.

3. EXPANSION OF THE CONDUCTANCE AS A FOURIER SERIES

We shall first consider the conductance of a microconstriction at zero temperature. We shall use expression (7) and introduce the notation $\beta = 2\pi/\hbar\Omega$ and $E - V_0 = \varepsilon$. We then have

$$\frac{G(T=0)}{G_0} = \sum_{m,n=0}^{\infty} [1 + \exp(-\beta(\varepsilon - E_{mn}))]^{-1}. \quad (12)$$

As we show in the Appendix, the following formula holds

$$\frac{1}{1+e^x} = \frac{1}{2\pi i}\int_{\alpha - i\infty}^{\alpha + i\infty} \frac{\pi}{\sin \pi p} e^{-px} dp, \quad 0 < \alpha < 1. \quad (13)$$

Assuming in (13) $x = \beta(E_{mn} - \varepsilon)$, we obtain

$$\frac{G(T=0)}{G_0} = \frac{1}{2i} \times \int_{\alpha - i\infty}^{\alpha + i\infty} \frac{d\xi}{\sin \pi\xi} \sum_{m,n=0}^{\infty} \exp[-\xi(E_{mn} - \varepsilon)\beta]. \quad (14)$$

Using the relationship

$$\sum_{m,n=0}^{\infty} \exp\left\{-\zeta\left[\hbar\omega_1\left(m + \frac{1}{2}\right) + \hbar\omega_2\left(n + \frac{1}{2}\right)\right]\right\} = \left[4\sinh\left(\frac{\hbar\omega_1\zeta}{2}\right)\sinh\left(\frac{\hbar\omega_2\zeta}{2}\right)\right]^{-1} \quad (15)$$

and introducing $\zeta = \beta\xi$, we obtain from (14) and (15)

$$\frac{G(T=0)}{G_0} = \frac{1}{8i\beta} \times \int_{\alpha - i\infty}^{\alpha + i\infty} \frac{e^{\varepsilon\zeta} d\zeta}{\sin(\pi\zeta/\beta)\sinh(\hbar\omega_1\zeta/2)\sinh(\hbar\omega_2\zeta/2)}. \quad (16)$$

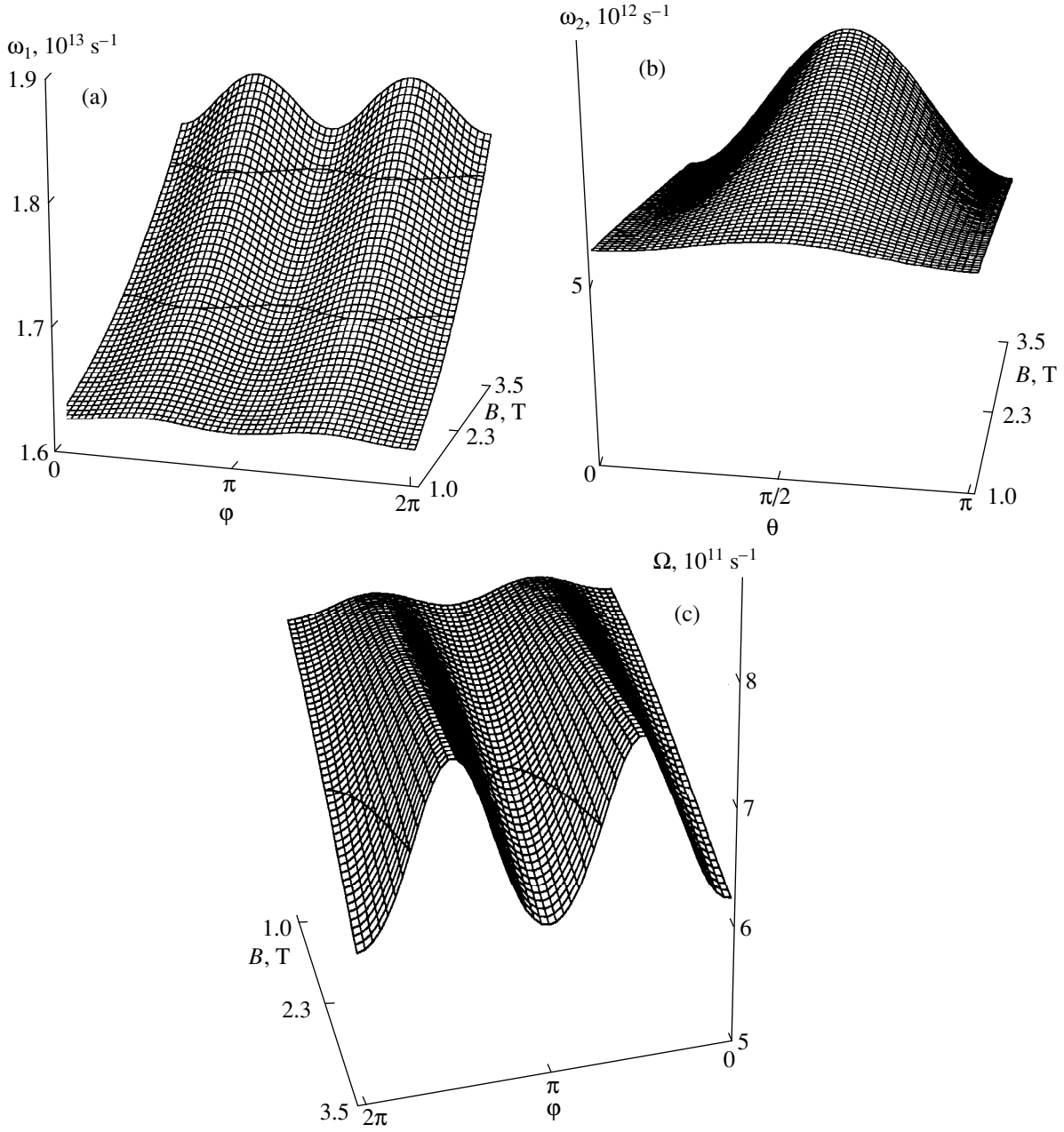

Fig. 1. Dependences of the frequencies ω_1, ω_2, and Ω on the magnitude B and direction (θ and φ) of the magnetic field: $\omega_x = 1.61 \times 10^{13}$ s^{-1}, $\omega_y = 0.61 \times 10^{13}$ s^{-1}, $\omega_x/\omega_z = 20$, φ_0, $\theta_0 = \pi/5.578$.

The integral in (16) can be calculated using the contour closed in the left half-plane. Summing the residues inside the contour, we obtain

$$\frac{G(T=0)}{G_0} = \frac{\pi}{4\beta} \times \sum_i \operatorname{res}\left[\frac{e^{\varepsilon z}}{\sin(\pi z/\beta)\sinh(\hbar\omega_1 z/2)\sinh(\hbar\omega_2 z/2)}, z_k\right]. \quad (17)$$

The function in the integrand in (16) has a third-order pole at zero and for incommensurable frequencies it has simple poles at the points $z_i = \{2\pi ni/\hbar\omega_1, 2\pi mi/\hbar\omega_2, k\beta\}$, $n, m = 0, \pm 1, \pm 2, \ldots, k = -1, -2, \ldots$.

After simple but fairly cumbersome calculations we find

$$\frac{G(T=0)}{G_0} = \frac{1}{6\omega_1\omega_2}\left[\frac{3(E-V_0)^2}{\hbar^2} + \frac{\Omega^2 - \omega_1^2 - \omega_2^2}{4}\right]$$

$$+\sum_{k=1}^{\infty}(-1)^k\frac{\exp[-2\pi k(E-V_0)/\hbar\Omega]}{4\sinh(\pi k\omega_1/\Omega)\sinh(\pi k\omega_2/\Omega)}$$
$$+\frac{\Omega}{2}\sum_{n=1}^{\infty}(-1)^{n+1}\left[\frac{1}{\omega_1}\frac{\cos[2\pi n(E-V_0)/\hbar\omega_1]}{\sin(\pi n\omega_2/\omega_1)\sinh(\pi n\Omega/\omega_1)}\right. \quad (18)$$
$$\left.+\frac{1}{\omega_2}\frac{\cos[2\pi n(E-V_0)/\hbar\omega_2]}{\sin(\pi n\omega_1/\omega_2)\sinh(\pi n\Omega/\omega_2)}\right].$$

Expression (18) becomes meaningless for commensurable values of the hybrid frequencies (in this case, some of the poles lying on the imaginary axis have a multiplicity greater than one). However, since a real number with a probability of one is irrational, we shall subsequently assume that the frequencies ω_1 and ω_2 are incommensurable. Note that even for incommensurable frequencies the question of the convergence of the Fourier series in (18) should be studied separately since the factors $\sin(\pi n\omega_2/\omega_1)$ and $\sin(\pi n\omega_1/\omega_2)$ in the denominator may be small. This problem is similar to the problem of small denominators in celestial mechanics [13].

Using an approach based on the Kolmogoroff–Arnol'd–Moser theory [13] we can show that the series in (18) converge uniformly if the Diophantine condition of incommensurability is satisfied for the frequencies (this condition is satisfied with a probability of one).

In order to find the temperature dependence of the microconstriction conductance we use formulas (6) and (18). After simple calculations we obtain

$$\frac{G(T)}{G_0} = G^{mon} + G^{osc}. \quad (19)$$

Here we have

$$G^{mon} = \frac{1}{6\omega_1\omega_2}\left[\left(\frac{\Omega^2-\omega_1^2-\omega_2^2}{4}+\frac{3V_0^2}{\hbar^2}\right)\right.$$
$$\left.\times\left[1+\exp\left(-\frac{\mu}{T}\right)\right]^{-1}-\frac{6V_0T}{\hbar^2}F_0\left(\frac{\mu}{T}\right)+\frac{6T^2}{\hbar^2}F_1\left(\frac{\mu}{T}\right)\right]$$
$$+\sum_{k=1}^{\infty}(-1)^k\frac{\exp[-2\pi k(\mu-V_0)/\hbar\Omega]}{4\sinh(\pi k\omega_1/\Omega)\sinh(\pi k\omega_2/\Omega)}$$
$$\times\left(1+\frac{2}{3}\frac{\pi^4k^2T^2}{\hbar^2\Omega^2}\right),$$

$$G^{osc} = \frac{\pi^2\Omega T}{\hbar\omega_1^2}\sum_{n=1}^{\infty}(-1)^{n+1}$$
$$\times\left[\frac{n\cos[2\pi n(\mu-V_0)/\hbar\omega_1]}{\sinh(2\pi^2nT/\hbar\omega_1)\sin(\pi n\omega_2/\omega_1)\sinh(\pi n\Omega/\omega_1)}\right.$$
$$\left.+\frac{\omega_1^2}{\omega_2^2}\frac{n\cos[2\pi n(\mu-V_0)/\hbar\omega_2]}{\sinh(2\pi^2nT/\hbar\omega_2)\sin(\pi n\omega_1/\omega_2)\sinh(\pi n\Omega/\omega_2)}\right],$$

where F_0 and F_1 are Fermi integrals.

Formula (19) gives an expansion of the constriction conductance as a Fourier series. The Fourier series in (19) gives the oscillating component of the conductance and the first term gives the monotonic component of the conductance. This formula is in a certain sense an analog of the Landau formula for the magnetic response of an electron gas, which describes the de Haas–van Alphen effect. Graphs constructed using formula (19) for various angles φ and θ are plotted in Figs. 2 and 3.

Unlike the starting formulas (6) and (7) used for the numerical analysis in [7], formula (19) is suitable for an analytic investigation of the conductance. In particular, it can be seen from this formula that the role of the effective length of the constriction in the magnetic field (defined in terms of the frequency Ω) is exactly the same as the role of temperature. As the effective length of the constriction decreases (with increasing Ω), the degrees of quantization become more strongly smeared and may ultimately disappear completely.

It follows from (19) that the oscillating component of the conductance G^{osc} has maxima at points where $\mu - V_0 = \hbar\omega_{1,2}(n + 1/2)$. These maxima are attributable to crossing of levels E_{mn} with the energy $\mu - V_0$ and are a manifestation of the analog of the Shubnikov–de Haas effect in the conductance.

4. ANALYTIC INVESTIGATION OF THE CONDUCTANCE CURVE

It follows from (18) and (19) that the monotonic component of the conductance G^{mon} has an almost parabolic profile (for $T \neq 0$). The oscillating component consists of almost three triangular peaks smoothed as a result of the temperature and the finite length of the constriction. Summation of these two curves gives the stepped structure of the curve $G(\mu)$. It is interesting to note that the smoothing of G^{osc} for $T \neq 0$ is determined by the product of two factors, $\sinh(2\pi^2nT/\hbar\omega_j)\sinh(\pi n\Omega/\omega_j)$, each influencing the profile of the oscillations. However, if the length of the constriction is fairly large, an increase in the first factor with temperature may be compensated by the smallness of the second factor to such an extent that quantization of the conductance may also be observed at fairly high temperatures. Thus, formula (19) can apparently explain why quantization of the conductance may well be observed in 3D constrictions even at fairly high temperatures, as was reported in [5, 6, 8].

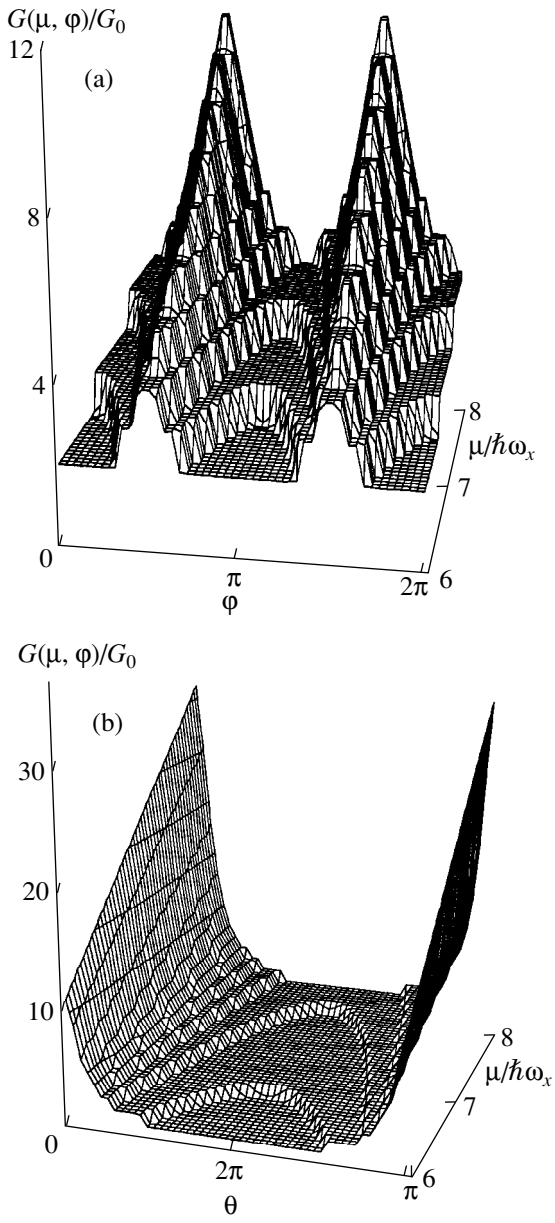

Fig. 2. Dependences of the conductance on the chemical potential $\mu = E$ and on the direction of the magnetic field defined by the polar φ and azimuthal θ angles: $\omega_x = 1.61 \times 10^{13}$ s^{-1}, $\omega_y = 0.61 \times 10^{13}$ s^{-1}, $\omega_x/\omega_z = 20$, $B = 25$ T, $V_0 = 0.6 \times 10^{-13}$ erg, φ_0, $\theta_0 = \pi/5.578$, $T = 0.5$ K.

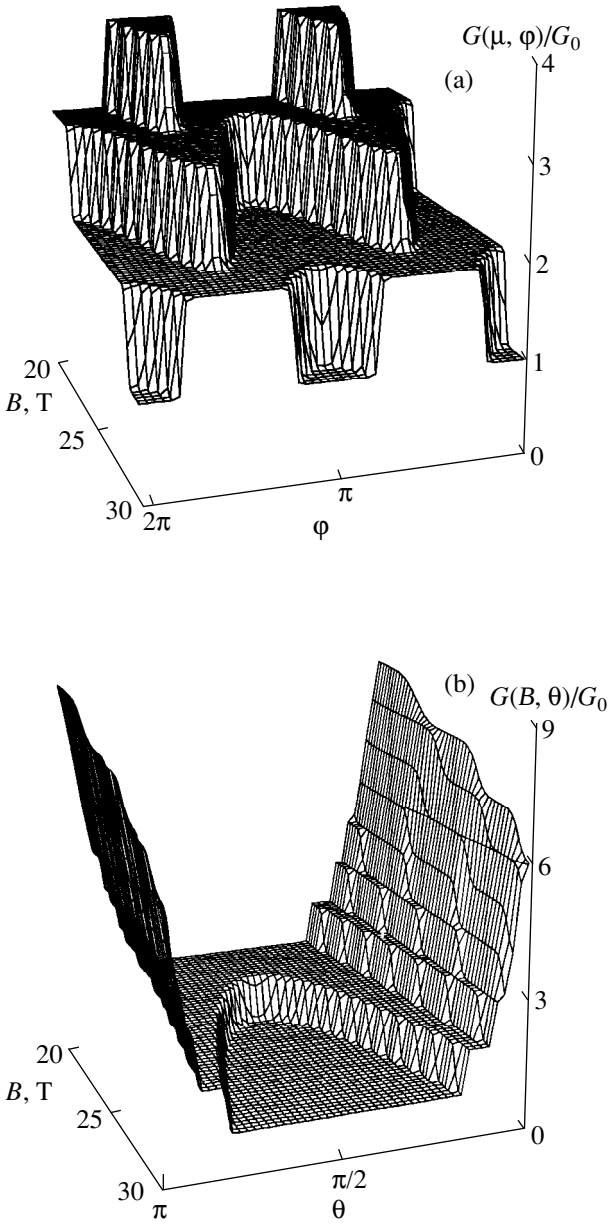

Fig. 3. Dependences of the conductance on the magnitude B and direction of the magnetic field defined by the polar φ and azimuthal θ angles: $\omega_x = 1.61 \times 10^{13}$ s^{-1}, $\omega_y = 1 \times 10^{13}$ s^{-1}, $\omega_x/\omega_z = 20$, $\mu = 1.05 \times 10^{-13}$ erg, $V_0 = 0.5 \times 10^{-13}$ erg, φ_0, $\theta_0 = \pi/5.578$, $T = 0.5$ K.

4.1. Longitudinal Field

In this case, the hybrid frequencies ω_j have the form [7]

$$\omega_{1,2} = \frac{1}{2}\left[\sqrt{\omega_c^2 + (\omega_x + \omega_y)^2} \pm \sqrt{\omega_c^2 + (\omega_x - \omega_y)^2}\right], \quad \Omega = \omega_z. \tag{20}$$

In the simplest case when the cross-section is symmetric and the magnetic field is weak, $\omega_c \ll \omega_x = \omega_y = \omega_0$, these frequencies can be represented to within terms of the order $O(\omega_c/\omega_0)$ in the form $\omega_{1,2} \sim \omega_0 \pm \omega_c/2$. We introduce the effective cross-section radius using the formula

$$\mu - V_0 = \frac{m^*\omega_1\omega_2 R_{\text{eff}}^2}{2}. \tag{21}$$

The magnetic field flux across a cross-section having this radius is given by $\Phi = \pi B R_{\text{eff}}^2$. In consequence we

find $\mu - V_0 = (\hbar\omega_1\omega_2/\omega_c)\Phi/\Phi_0$, where $\Phi_0 = 2\pi\hbar c/e$ is the magnetic flux quantum. Hence

$$\frac{\mu - V_0}{\hbar\omega_{1,2}} = \frac{m^*\omega_0 R_{eff}^2}{2\hbar} \mp \frac{\Phi}{2\Phi_0}. \tag{22}$$

Substituting (22) into (19) and discarding terms of higher order of smallness in ω_c/ω_0: (bearing in mind that $\omega_1/\omega_2 \simeq 1 + \omega_c/\omega_0$, $\omega_2/\omega_1 \simeq 1 - \omega_c/\omega_0$), we obtain the following expression for the oscillating component of the conductance of a 3D constriction

$$\frac{G^{osc}}{G_0} \simeq \frac{2\pi^2\Omega T}{\hbar\omega_0^2} \times \sum_{n=1}^{\infty} \frac{n\sin(m\omega_0 R_{eff}^2\pi n/\hbar)\sin(\pi n\Phi/\Phi_0)}{\sin(\pi n\omega_c/\omega_0)\sinh(2\pi^2 nT/\hbar\omega_0)\sinh(\pi n\Omega/\omega_0)}. \tag{23}$$

It can be seen from (23) that in this case, the conductance undergoes Aharonov–Bohm oscillations. Neglecting the weak dependence of the Fourier coefficients on the magnetic field (the oscillations are almost periodic), the period will be equal to two flux quanta (Fig. 4a).

For the case of a strong field ($\omega_c \gg \omega_0$) and a symmetric structure, (20) yields the estimate $\omega_1 \simeq \omega_c$, $\omega_2 = \omega_0^2/\omega_c \ll \omega_1$. In this case, the second term in the oscillating component (19) becomes appreciably smaller than the first because of the high value of $\sinh(2\pi^2 nT/\hbar\omega_2)$ and can be neglected. The main contribution to G^{osc} is then made by the first term with the numerator $\propto\cos[2\pi n(\mu - V_0)/\hbar\omega_c]$. This term gives Shubnikov–de Haas oscillations in the conductance at high frequency, periodic in terms of the inverse magnetic field $\Delta(1/B) = e\hbar/m^*c(\mu - V_0)$. In order to demonstrate the existence of Aharonov–Bohm oscillations in the region of strong ($\omega_c \gg \omega_0$) magnetic fields, we introduce the number of flux quanta $\eta = \Phi/\Phi_0$ in the formula for the oscillating component of the conductance (19). We then obtain

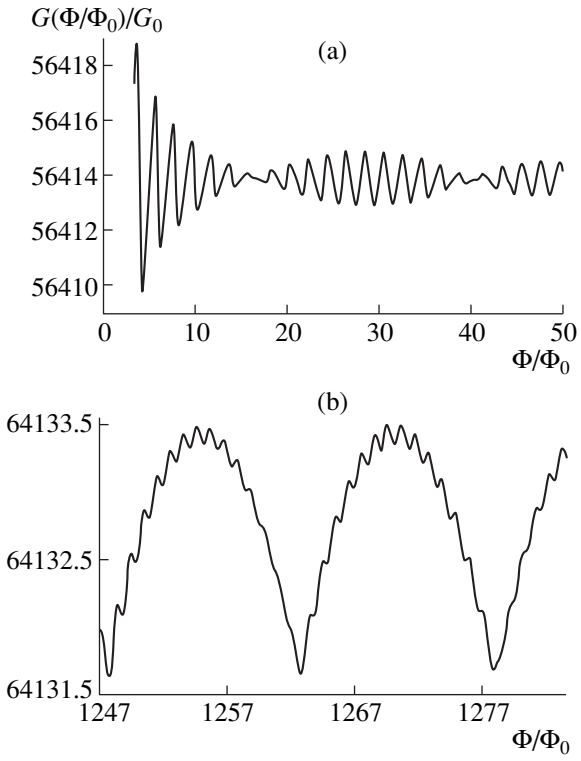

Fig. 4. Dependences of the conductance on the magnetic flux Φ/Φ_0 for (a) weak and (b) strong longitudinally oriented magnetic fields: $\omega_x = 0.161\times10^{13}$ s^{-1}, $\omega_y = 0.161\times10^{13}$ s^{-1}, $\omega_x/\omega_z = 20$, $\mu = 6.2\times10^{-13}$ erg, $V_0 = 0.5\times10^{-13}$ erg, $T = 0.6$ K.

$$\frac{G^{osc}}{G_0} = \frac{\pi^2\Omega T}{\hbar\omega_1^2}\sum_{n=1}^{\infty}(-1)^{n+1}n \times\left\{\frac{\cos(2\pi n\eta\omega_2/\omega_c)}{\sin(\pi n\omega_2/\omega_1)\sinh(2\pi^2 nT/\hbar\omega_1)\sinh(\pi n\Omega/\omega_1)} + \frac{\omega_1^2}{\omega_2^2}\frac{\cos(2\pi n\eta\omega_1/\omega_c)}{\sinh(\pi n\omega_1/\omega_2)\sinh(2\pi^2 nT/\hbar\omega_2)\sinh(\pi n\Omega/\omega_2)}\right\}. \tag{24}$$

The hyperbolic sines in the denominators in this formula only give broadening of the oscillation peaks, so we shall subsequently confine our analysis to the behavior of two functions:

$$f(\eta) = \frac{\cos(2\pi n\eta\omega_2/\omega_c)}{\sin(\pi n\omega_2/\omega_1)}, \qquad g(\eta) = \frac{\cos(2\pi n\eta\omega_1/\omega_c)}{\sin(\pi n\omega_1/\omega_2)}. \tag{25}$$

We shall subsequently show that these factors give oscillations of each term in the series in (24). We equate to zero the derivative of these factors with respect to the number of flux quanta η and find equations for the extremum points of the functions $f(\eta)$ and $g(\eta)$, bearing in mind that the frequencies are incommensurable, $\sin(\pi n\omega_1/\omega_2) \neq 0$ and $\sin(\pi n\omega_2/\omega_1) \neq 0$, and then

$$\begin{aligned}\sin(2\pi n\eta\omega_1/\omega_c)\sin(\pi n\omega_1/\omega_2) &= (-\omega_c/\eta\omega_2)\cos(2\pi n\eta\omega_2/\omega_c)\cos(\pi n\omega_2/\omega_1),\\ \sin(2\pi n\eta\omega_2/\omega_c)\sin(\pi n\omega_2/\omega_1) &= (-\omega_c/\eta\omega_1)\cos(2\pi n\eta\omega_1/\omega_c)\cos(\pi n\omega_1/\omega_2).\end{aligned} \tag{26}$$

We shall assume that $\omega_c/\eta\omega_1 = \hbar\omega_2/\mu - V_0$ and $\omega_c/\eta\omega_2 = \hbar\omega_1/\mu - V_0$, from which it follows that

$\sin(2\pi n\eta\omega_{1,2}/\omega_c) \ll 1$ in formula (26). We then have the estimate for the extremum points:

$$\sin(2\pi n\eta\omega_2/\omega_c) \approx 0,$$
$$\sin(2\pi n\eta + 2\pi n\eta\omega_2/\omega_c) \approx 0. \quad (27)$$

These relations (27) were derived assuming that $\omega_1 = \omega_2 + \omega_c$ and that the frequencies ω_1 and ω_2 are incommensurable. The first of the relations (27) gives at the extremum points

$$\frac{\mu - V_0}{\hbar\omega_1} = N, \quad N = 1, 2, \ldots \quad (28)$$

Since in regions of strong fields $\omega_1 \approx \omega_c$, these extrema correspond to Shubnikov–de Haas oscillations in the conductance. These oscillations are attributed to the second term in braces (24).

We shall analyze the second of the relations (27) near the extrema of the Shubnikov–de Haas oscillations, $\omega_2\eta/\omega_c = N$. From this it follows that for integer values of η extrema also exist, corresponding to oscillations of the small first term in the oscillating component (24). The distance between the neighboring maxima in this case is equal to the flux quantum ($\Delta\eta = 1$). These oscillations also occur far from the extrema of the Shubnikov–de Haas oscillations but their periodicity with respect to the flux is destroyed. Hence, the first series in (24) gives Aharonov–Bohm oscillations in the conductance. We note that, as follows from (24), the amplitude of these oscillations is ω_1^2/ω_2^2 times smaller than the amplitude of the Shubnikov–de Haas oscillations so that as the field increases, the amplitudes of the Aharonov–Bohm oscillations decreases as B^2 and for fairly strong fields these oscillations are completely smeared by temperature. The Aharonov–Bohm oscillations are thus superposed on the Shubnikov–de Haas oscillations and yield the fine structure of the maxima (Fig. 4b).

4.2. Transverse Field

For the case of a transverse field we find $\omega_2 = \omega_0$ so that the second series in the general expression (19) for the conductance gives no oscillations with respect to the magnetic field. If the magnetic field **B** is weak ($\omega_c \ll \omega_0$) then, as was shown in [7], the frequencies ω_1 and Ω satisfy the equalities

$$\omega_1 = \omega_0 + O\left(\frac{\omega_c^2}{\omega_0^2 + \omega_z^2}\right),$$
$$\Omega = \omega_z + O\left(\frac{\omega_c^2}{\omega_0^2 + \omega_z^2}\right). \quad (29)$$

Since $\omega_1 \approx \omega_0$, the oscillations with respect to the field of the first series in (19) are very small and are smeared by temperature. In a strong magnetic field we find $\omega_1 \simeq \omega_c$, $\Omega \simeq \omega_z\omega_0/\omega_c$ [7] so that no Aharonov–Bohm oscillations occur in this case and the Shubnikov–de Haas oscillations are weak (their amplitudes are ω_0^2/ω_c^2 times smaller than those in a longitudinal field) and are also smeared by temperature. Note that as the field increases, the value of Ω decreases and consequently the effective length $l_{eff} = \sqrt{\hbar/m^*\Omega}$ of the constriction is increased [7]. It follows from (19) that as the field increases, the factors $\sinh(\pi n\Omega/\omega_j)$, $j = 1, 2, \ldots$, decrease and consequently the smoothing of the oscillating component of the conductance in (19) caused by the finite length of the constriction also decreases. Thus, a strong transverse magnetic field improves the stepped structure of the conductance quantization curve $G(\mu)/G_0$.

Note that in a weak field the curve $G(\mu)/G_0$ is very similar to that in the absence of a field when the frequencies ω_x and ω_y are similar but different. This is because, as we noted in the Introduction, when $\omega_x = \omega_y = \omega_0$, the height of the conductance quantization steps is proportional to the degree of degeneracy of the levels but a weak magnetic field leads to some effective asymmetry of the constriction and removes this degeneracy (the step height becomes equal to the conductance quantum).

4.3. Effects Caused by a Change in the Direction of the Field

It can be seen from the graphs plotted in Fig. 1 that the frequencies ω_1, ω_2, and Ω depend on the orientation of the field **B** relative to the axes of symmetry of the microconstriction (the angles θ and φ). It is clear from the reasoning put forward above that when the angles θ and φ change (for constant $|\mathbf{B}|$), the nature of the electron transport regime in the constriction changes.

Figures 2 and 3 show the dependences $G(\varphi)/G_0$ and $G(\theta)/G_0$ which reveal the stepped structure of the conductance.

For weak magnetic fields ($\omega_c^2 \ll \omega_x^2, \omega_y^2, \omega_z^2$) the frequencies $\omega_{1,2}$ and Ω show a clear dependence on the angles θ and φ. For this, in equation (11) we set $\xi_{1,2} = -\omega_{x,y}^2 + \varepsilon_{1,2}$ and $\xi_3 = \omega_z^2 + \varepsilon_3$. Using the known relationship between the coefficients and the roots of the cubic equation and neglecting small terms of the order ε_j^2 and ε_j^3, we obtain a system of linear equations to find ε_j. Note that terms of the order ε_j^2 cannot be neglected if $\omega_x \approx \omega_y$.

The system of equations to find ε_j has the form

$$\begin{aligned}\varepsilon_1 + \varepsilon_2 + \varepsilon_3 &= \omega_c^2,\\ \varepsilon_1\omega_z^2\omega_y^2 + \varepsilon_2\omega_z^2\omega_x^2 - \varepsilon_3\omega_x^2\omega_y^2 &= 0,\\ (\omega_z^2 - \omega_y^2)\varepsilon_1 + (\omega_z^2 - \omega_x^2)\varepsilon_2 - (\omega_x^2 - \omega_y^2)\varepsilon_3 &= a,\end{aligned} \tag{30}$$

where $a = \omega_{cx}^2\omega_x^2 + \omega_{cy}^2\omega_y^2 - \omega_{cz}^2\omega_z^2$. The solution of this system is $\varepsilon = \Delta_j/\Delta$, $j = 1, 2, 3$, where

$$\begin{aligned}\Delta &= -(\omega_x^2 + \omega_y^2)\omega_z^4 - (\omega_x^2 + \omega_z^2)\omega_y^4 - (\omega_y^2 + \omega_z^2)\omega_x^4,\\ \Delta_1 &= -\omega_x^2(\omega_y^2 + \omega_z^2)(\omega_c^2\omega_x^2 + a),\\ \Delta_2 &= \omega_y^2(\omega_x^2 + \omega_z^2)(\omega_c^2\omega_y^2 + a),\\ \Delta_3 &= \omega_z^2(\omega_x^2 - \omega_y^2)(\omega_c^2\omega_z^2 + a).\end{aligned} \tag{31}$$

The above reasoning yields the estimate

$$\begin{aligned}\omega_1 &= \sqrt{\left|\omega_x^2 - \frac{\Delta_1}{2\Delta}\right|},\\ \omega_2 &= \sqrt{\left|\omega_y^2 - \frac{\Delta_2}{2\Delta}\right|},\\ \Omega &= \sqrt{\left|\omega_z^2 - \frac{\Delta_3}{2\Delta}\right|}.\end{aligned} \tag{32}$$

Note that Δ does not depend on the angles θ and φ but the dependence on the angles in Δ_j is determined by the value of a which depends on the angles according to the formula

$$\begin{aligned}a = (&\omega_x^2\cos^2\varphi\sin^2\theta\\ &+ \omega_y^2\sin^2\varphi\sin^2\theta - \omega_z^2\cos^2\theta)\omega_c^2.\end{aligned} \tag{33}$$

For a strong field ($\omega_x^2, \omega_y^2, \omega_z^2 \ll \omega_c^2$) equation (11) can be conveniently written in the form

$$\xi^3 + a\xi^2 + b\xi = \varepsilon, \tag{34}$$

where

$$\begin{aligned}a &= \omega_c^2 + \omega_x^2 + \omega_y^2 - \omega_z^2, \quad \varepsilon = \omega_x^2\omega_y^2\omega_z^2,\\ b &= \omega_x^2\omega_y^2 - \omega_y^2\omega_z^2 - \omega_x^2\omega_z^2\\ &\quad + \omega_{cx}^2\omega_x^2 + \omega_{cy}^2\omega_y^2 - \omega_{cz}^2\omega_z^2,\end{aligned} \tag{35}$$

and $a \gg b \gg \varepsilon$. A solution of equation (34) may be found by asymptotic methods using a Burman–Lagrange series. We then have

$$\begin{aligned}\omega_1 &= \sqrt{a - \frac{b}{a}} + O(\varepsilon), \quad \omega_2 = \sqrt{\frac{|b|}{a}} + O(\varepsilon),\\ \Omega &= \sqrt{\frac{\varepsilon}{|b|}} + O(\varepsilon^2).\end{aligned} \tag{36}$$

In formula (36) only b depends on the angles:

$$\begin{aligned}b = &\omega_x^2\omega_y^2 - \omega_x^2\omega_z^2 - \omega_y^2\omega_z^2 + (\omega_x^2\cos^2\varphi\sin^2\theta\\ &+ \omega_y^2\sin^2\varphi\sin^2\theta - \omega_z^2\cos^2\theta)\omega_c^2.\end{aligned} \tag{37}$$

Note that the numerical solutions of equation (11) show good agreement with (32) for weak fields and with (36) for strong fields.

5. CONCLUSIONS

An analytic investigation of the conductance of a microconstriction located in an arbitrarily directed magnetic field reported in the present paper has explained various transport regimes of the microconstriction. For any orientation of the field the dependence $G(\mu)$ has a stepped structure. The height of each step is equal to the conductance quantum. The temperature and finite length of the microconstriction lead to smearing of the step thresholds. In this case, as follows from (19) the value of $\hbar\Omega/2\pi$ plays exactly the same role as the temperature.

In fairly long constrictions (low frequency Ω) the factors characterizing the smearing of the step thresholds as a result of temperature and the finite length of the constriction may be compensated. This effect may give rise to a stepped structure of the conductance even at relatively high temperatures. The stepped structure of the conductance curve $G(\mu)$ is produced by the summation of the almost parabolic monotonic component $G^{mon}(\mu)$ and the oscillating component of the conductance $G^{osc}(\mu)$ consisting of almost triangular peaks.

In an arbitrarily oriented magnetic field the hybrid frequencies ω_1, ω_2, and Ω depend on the angles of orientation of the field **B** relative to the axes of symmetry of the system. The explicit form of these dependences is determined in Section 4 for cases of weak and strong fields. These dependences lead to a conductance quantization effect (Fig. 3).

For a longitudinal magnetic field the dependence of the conductance on the field exhibits oscillating behavior. In this case, the transport regimes for weak and strong magnetic fields differ. In a weak field Aharonov–Bohm oscillations occur with a period equal to two flux quanta. These oscillations are clearly manifested in long constrictions (Fig. 4a). Aharonov–Bohm oscillations also occur in a strong field but their period is equal to a single flux quantum. Shubnikov–de Haas oscillations are also observed in a strong field and are periodic in terms of the reciprocal field $\Delta(1/B) = e\hbar/m^*c(\mu - V_0)$. The Shubnikov–de Haas oscillations have an amplitude ω_1^2/ω_2^2 times larger than the Aharonov–Bohm oscillations. As the field increases, the amplitude of the Aharonov–Bohm oscillations decreases as B^2 and in fairly strong fields they are completely smeared by temperature. In strong fields the Aharonov–Bohm oscillations are superposed on the Shubnikov–de Haas oscillations and

produce a fine structure at the maxima of these oscillations (Fig. 4b).

In a weak transverse field, the oscillations over the magnetic field are very small and are easily smeared by temperature and scattering, which is determined by the effective length of the microconstriction. In a strong transverse field no Aharonov–Bohm oscillations occur and the Shubnikov–de Haas oscillations are weak since their amplitude is ω_1^2/ω_2^2 times smaller than that in a longitudinal field. In this case, as the field increases the effective length of the microconstriction increases and consequently the stepped structure of the curve $G(\mu)$ deteriorates.

ACKNOWLEDGMENTS

This work was supported by grants from the Russian Foundation for Basic Research and the Ministry of Education.

APPENDIX

We shall analyze the Fourier transform of the function $\varphi(t) = f(t)e^{xt}$:

$$\varphi(t) = \frac{1}{2\pi}\int_{-\infty}^{\infty} d\xi \int_{-\infty}^{\infty} \varphi(\eta) e^{i\xi(t-\eta)} d\eta. \qquad \text{(A.1)}$$

We substitute (A.1) in the form

$$f(t)e^{xt} = \frac{1}{2\pi}\int_{-\infty}^{\infty} d\xi e^{i\xi t} \int_{-\infty}^{\infty} f(\eta) e^{(x-i\xi)\eta} d\eta. \qquad \text{(A.2)}$$

We introduce $p = x - i\xi$ and then

$$f(t)e^{xt} = \frac{1}{2\pi}\int_{-\infty}^{\infty} d\xi^{i\xi t} \int_{-\infty}^{\infty} f(\eta) e^{p\eta} d\eta. \qquad \text{(A.3)}$$

We introduce the notation

$$\int_{-\infty}^{\infty} f(\eta) e^{p\eta} d\eta = F(p). \qquad \text{(A.4)}$$

We then have

$$\begin{aligned} f(t) &= \frac{1}{2\pi}\int_{-\infty}^{\infty} d\xi e^{-t(x-i\xi)} F(p) \\ &= \frac{1}{2\pi i}\int_{x-i\infty}^{x+i\infty} dp e^{-pt} F(p). \end{aligned} \qquad \text{(A.5)}$$

It follows from (A.5) that

$$f(t) = \frac{1}{2\pi i}\int_{x-i\infty}^{x+i\infty} e^{-pt} F(p) dp, \qquad \text{(A.6)}$$

where the function $F(p)$ is determined by formula (A.4). Expression (A.6) is an analog of the Mellin transformation. Using the relation [16]

$$\int_{-\infty}^{\infty} \frac{e^{px} dx}{1+e^x} = \frac{\pi}{\sin \pi p}, \quad 0 < \mathrm{Re}\, p < 1 \qquad \text{(A.7)}$$

and formulas (A.4) and (A.6), we obtain formula (13) from Section 3:

$$\frac{1}{1+e^x} = \frac{1}{2\pi i}\int_{\alpha-i\infty}^{\alpha+i\infty} \frac{\pi}{\sin \pi p} e^{-px} dp, \qquad \text{(A.8)}$$

where $\alpha = \mathrm{Re}\, p$.

REFERENCES

1. U. Landman, W. D. Luedtke, N. A. Burnham, and R. J. Colton, Science **248**, 454 (1990).
2. E. N. Bogachek, A. M. Zagoskin, and I. O. Kulik, Fiz. Nizk. Temp. **16**, 1404 (1990) [Sov. J. Low Temp. Phys. **16**, 796 (1990)].
3. J. A. Torres, J. I. Pascual, and J. J. Sáenz, Phys. Rev. B **49**, 16581 (1994).
4. E. N. Bogachek, M. Jonson, R. I. Shekhter, and T. Swahn, Phys. Rev. B **47**, 16635 (1993); 50, 18341 (1994).
5. J. I. Pascual, J. Méndez, J. Gómez-Herrero, *et al.*, Phys. Rev. Lett. **71**, 1852 (1993).
6. J. I. Pascual, J. Méndez, J. Gómez-Herrero, *et al.*, Science **267**, 1793 (1995); J. Vac. Sci. Technol. B **13**, 1280 (1995).
7. A. G. Scherbakov, E. N. Bogachek, and Uzi Landman, Phys. Rev. B **53**, 4054 (1996).
8. L. Olesen, E. Laegsgaard, I. Stensgaard, *et al.*, Phys. Rev. Lett. **72**, 2251 (1994).
9. N. Agrait, J. G. Rodrigo, and S. Vieira, Phys. Rev. B **47**, 12345 (1993).
10. M. Buttiker, Phys. Rev. B **41**, 7906 (1990).
11. M. Buttiker, Semicond. Semimet. **35**, 19 (1992).
12. L. D. Landau and E. M. Lifshits, *Quantum Mechanics: Non-Relativistic Theory* (Nauka, Moscow, 1989, 4th ed.; Pergamon Press, Oxford, 1977, 3rd ed.).
13. V. A. Geyler and V. A. Margulis, Phys. Rev. B **55**, 2543 (1997).
14. J. Williamson, Am. J. Math. **58**, 141 (1936).
15. Q. P. Li, K. Karai, S. K. Yip, *et al.*, Phys. Rev. B **43**, 5151 (1991).
16. A. P. Prudnikov, Yu. A. Brychkov, and O. I. Marichev, *Integrals and Series* (Nauka, Moscow, 1981–1986; Gordon and Breach, New York, 1986–1989), Vols. 1–3.

Translation was provided by AIP

Journal of Experimental and Theoretical Physics, Vol. 90, No. 3, 2000, pp. 527–534.
From Zhurnal Éksperimental'noĭ i Teoreticheskoĭ Fiziki, Vol. 117, No. 3, 2000, pp. 604–612.

SOLIDS
Electron Properties

Fermi Surface in the New Organic Quasi-Two-Dimensional Metal α-$(BETS)_2TlHg(SeCN)_4$¶

S. I. Pesotskiĭ[1, 2, 3, 4], R. B. Lyubovskiĭ[1, 2], V. I. Nizhankovskiĭ[2], W. Biberacher[3], M. V. Kartsovnik[3], K. Andres[3], J. A. A. J. Perenboom[4], N. D. Kushch[1], E. B. Yagubskiĭ[1], and H. Kobayashi[5]

[1] *Institute of Problems of Chemical Physics, Russian Academy of Sciences, Chernogolovka, Moscow oblast, 142432 Russia*
[2] *International Laboratory of High Magnetic Fields and Low Temperatures, 53-529, Wroclaw, Poland*
[3] *Walther-Meissner-Institute, D-85748, Garching, Germany*
[4] *High Field Magnetic Laboratory, Catholic University, NL 6525, ED Nijmegen, Netherlands*
[5] *Institute for Molecular Science, Okazaki 444, Japan*

Received September 10, 1999

Abstract—Quantum oscillations of de Haas–van Alphen and Shubnikov–de Haas and semiclassical angular oscillations of the magnetoresistance have been observed in the quasi-two-dimensional organic metal α-$(BETS)_2TlHg(SeCN)_4$. The quantum oscillations are connected with the cylindrical part of the Fermi surface. The angular oscillations are associated with the carrier motion on both the cylindrical part and quasi-planar sheets of the Fermi surface. The values of the Dingle temperature, $T_D \approx 2$–3 K, and the effective mass, $m^* \approx 1.03m_0$, have been defined. The possibility of the weakening of multibody interactions has been shown in this compound. © *2000 MAIK "Nauka/Interperiodica".*

1. INTRODUCTION

Charge-transfer salts with alpha-type crystal structure α-$(ET)_2MHg(XCN)_4$, where (ET) = (BEDT-TTF) (bis(ethyleneditio)-tetrathiofulvalene) and M = K, Tl, Rb, NH_4, X = S, Se, are among the most popular objects in the physics of organic conductors. Their studies have provided important results in the fermiology of low-dimensional metals. There are some reasons for this. The specific shape of the Fermi surface (FS) in these compounds was shown to include both a cylindrical part characteristic of quasi-two-dimensional electron systems and corrugated planar sheets characteristic of quasi-one-dimensional electron systems [1]. Alpha-metals with M = K, Tl, Rb and X = S undergo the Peierls-type phase transition at $T_p \leq 10$ K associated with the nesting of the one-dimensional part of the FS [2–4]. Such a transition leads to considerable reconstruction of FS [5]. The other known metals of this family retain their high-temperature structure down to the lowest temperatures [6, 7]. Only one of them, $(ET)_2NH_4Hg(SCN)_4$, undergoes a superconducting (SC) transition [8]. The reasons for the presence or absence of phase transformations in these isostructural alpha-type metals are not yet clear. All these compounds can be investigated by different techniques of fermiology, such as Shubnikov–de Haas (SdH) quantum oscillations of magnetoresistance, de Haas–van Alphen (dHvA) quantum oscillations of magnetization, and semiclassical angle-dependent magnetoresistance oscillations (AMRO) in high magnetic fields [1]. These effects are easily observed both in the alpha salts that undergo phase transitions and those that maintain their electron structures at low temperatures. Therefore, one can study in detail the effect of slight changes in the chemical compositions of organic conductors upon radical changes in their electron structure. Such investigations are a necessary condition for directed chemical syntheses.

It was shown earlier [6, 7] that the substitution of S atoms by Se ones in the anions of $(ET)_2TlHg(SCN)_4$ and $(ET)_2KHg(SCN)_4$ giving $(ET)_2TlHg(SeCN)_4$(hereinafter, ET-Tl-Se) and $(ET)_2KHg(SeCN)_4$ (hereinafter, ET-K-Se) results in the suppression of the phase transitions. The complex with Tl shows such an effect even upon substituting half of the sulphur atoms in the anion by selenium ones [9]. One observes an increase of the effective mass in selenium complexes as compared to sulphur analogs and a significant role of multibody interactions [7, 10].

Recently, the family of metallic alpha salts has been essentially widened by substituting the ET molecule by BETS, which includes four central selenium atoms instead of the four sulphur ones in ET [11]. In ET-metals, the overlapping of sulphur orbitals provides metallic conductivity in ET layers. Therefore, one could expect that the substitution of a portion of sulphur atoms would result in significant changes in conducting properties of metals synthesized on the base of BETS

¶This article was submitted by the authors in English.

as compared with ET analogs. Indeed, on cooling the new organic metals, α-$(BETS)_2KHg(SCN)_4$ (hereinafter, BETS-K-S) and α-$(BETS)_2NH_4Hg(SCN)_4$ (hereinafter, BETS-NH-S) do not demonstrate the phase transitions characteristic of the ET analogs [12]. Besides, the parameters of electronic structures of new metals change significantly as compared to the ET analogs; namely, the effective mass decreases, the width of the conductivity band increases, and the Coulomb repulsion becomes weaker [12].

The present paper reports the study of magnetic field properties of the new metallic alpha-phase compound, $(BETS)_2TlHg(SeCN)_4$ (hereinafter, BETS-Tl-Se), isostructural to α-$(ET)_2MHg(XCN)_4$ [13]. This compound was found to show quantum oscillations (dHvA and SdH) and semiclassical angle-dependent magnetoresistance oscillations. The studies enabled us to determine the shape and size of the FS, evaluate the parameters of the electronic structure, and analyze the low-temperature state in comparison with ET-Tl-Se and other alpha salts.

2. EXPERIMENTAL PROCEDURE

The BETS-Tl-Se samples grow as parallelepipeds with an average size of $1 \times 0.5 \times 0.05$ mm^3. The procedure of chemical synthesis of the samples and their crystal structure are described in detail in [13]. Conducting layers of BETS parallel to the *ac*-plane alternate along the **b** direction with the anion layers. The longest size of samples corresponds to the **a** direction and the shortest one corresponds to the **b*** direction. The averaged conductivity of the samples in the conducting plane amounts to $\approx 50\ \Omega^{-1}\ \mathrm{cm}^{-1}$ at room temperature.

DHvA oscillations were observed by a contilever torquemeter in magnetic fields up to 14.4 T [14]. The temperature could be lowered to 0.45 K. The magnetic field orientation was varied by rotating the sample with respect to the field direction in the *ab**-plane.

The magnetoresistance was measured by a standard four-probe technique using 330 Hz ac applied mainly perpendicularly to the plane of the highest conductivity *ac*. This direction provides the best conditions for the observation of AMRO [1]. The maximal magnetic field value was 14 T in AMRO experiments, and the minimal temperature was 1.45 K. The sample orientations were changed by using a two-axes-rotation insert with which the sample could be rotated with respect to the field direction in different planes perpendicular to the *ac*-plane. This portion of the SdH experiments was carried out using magnetic fields up to 20 T with the temperature reduced to 1.3 K, and at the current direction along **a**.

3. RESULTS

All the BETS-Tl-Se samples showed a metal-like dependence of resistance on temperature with no peculiarities. The residual resistance ratio at 1.4 K is about 200. In the magnetic field perpendicular to the conducting plane and at the current direction along **b***, the resistance grows almost without saturation and increases approximately five times at 14 T [13]. At the current direction along **a** (Fig. 1), the magnetoresistance is more than two times less and saturation is present.

In magnetic fields higher than 10 T, SdH and dHvA quantum oscillations are observed (Figs. 1, 2). At the field direction perpendicular to the conducting plane, quantum oscillations contain only the fundamental frequency $F \approx 640$ T. The angular dependence of this frequency from the dHvA experiment is depicted in Fig. 3 and is described by the relationship

$$F(\theta) \approx 640[\mathrm{T}]/\cos\theta, \tag{1}$$

where θ is the angle between **b*** and the field direction. In magnetic fields tilted from the **b*** direction, one observes the beat of the fundamental frequency (Figs. 1, 2). The beat is absent only at the angles close to $\theta = 0$ and $\theta = \pm 20°$. The angular dependence of the beat frequency in the rotation plane *ab** from the dHvA and SdH experiments is presented in Fig. 4. It can be described by the expression:

$$F_{beat} = \Delta F \approx 30[\mathrm{T}]/\cos\theta \tag{2}$$

(F_{beat} is the difference between frequencies on the FFT spectrum: see inserts in Figs. 1 and 2).

The angular dependence of the dHvA oscillation amplitude is presented in Fig. 5. At field directions corresponding to $\theta = \pm 45°$, the oscillation amplitude vanishes. Most probably, this vanishing is due to so-called "spin zeros" associated with the spin reduction factor R_S from the Lifshitz–Kosevich (LK) formula [15]

$$R_S = \cos(\pi r \mu g/2), \tag{3}$$

where $r = 1, 2, 3, \ldots$ is the harmonic index, $\mu = m^*/m_0$ is the relative effective mass (m_0 is the mass of the free electron), and g is the g-factor. Factor R_S vanishes under condition $\mu g = 2n + 1$, where $n = 0, 1, 2, \ldots$.

The effective mass of the samples under study (which does not always coincide with m^* from (3)) was estimated from the changes in the amplitudes of dHvA oscillations with temperature. Such changes are described by the temperature reduction factor R_T in the LK formula for the oscillation amplitude [10]:

$$R_T = \frac{\alpha r \mu T}{H} \frac{1}{\sinh(\alpha r \mu T/H)}, \tag{4}$$

where $\alpha = 2\pi^2 k_B m_0/eh \approx 14.7$ T/K. The dHvA results for the effective mass at different field directions are

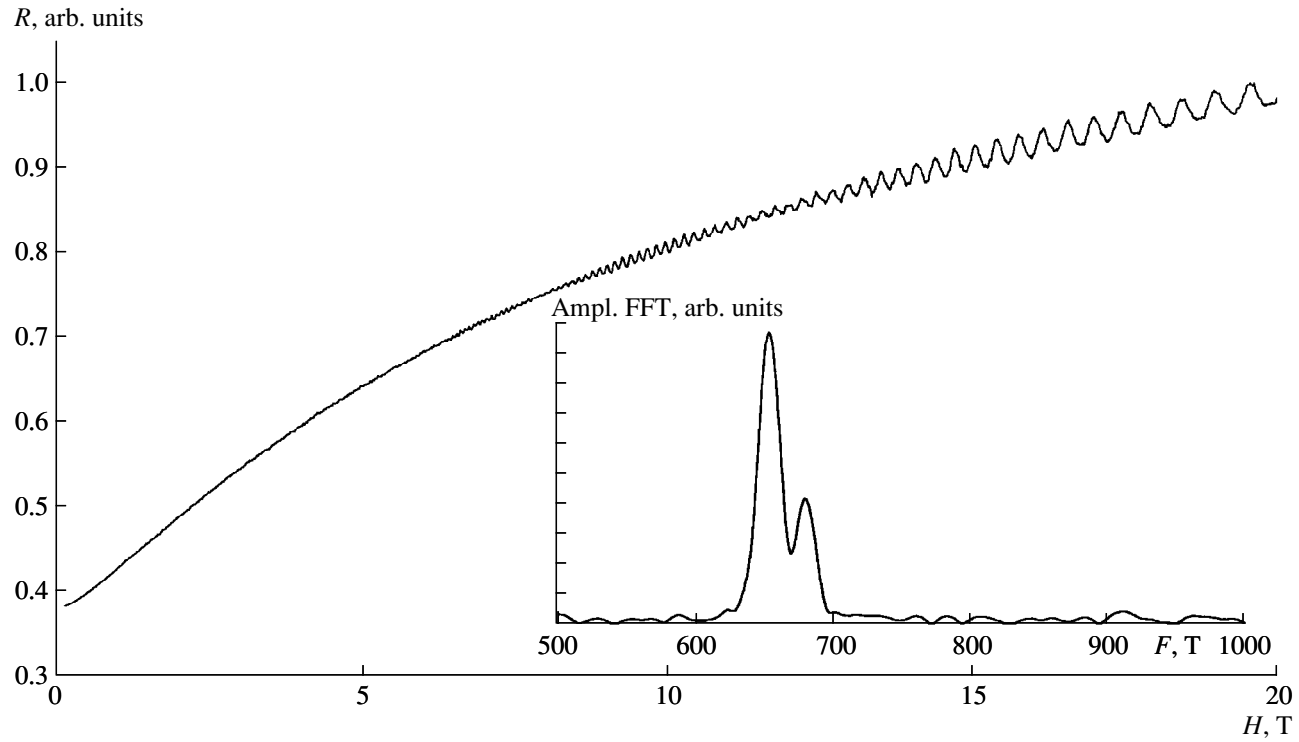

Fig. 1. Magnetoresistance showing Shubnikov–de Haas oscillations; $T = 13$ K, $\theta \approx 5°$, **I** || **a**. Insert: FFT of these oscillations.

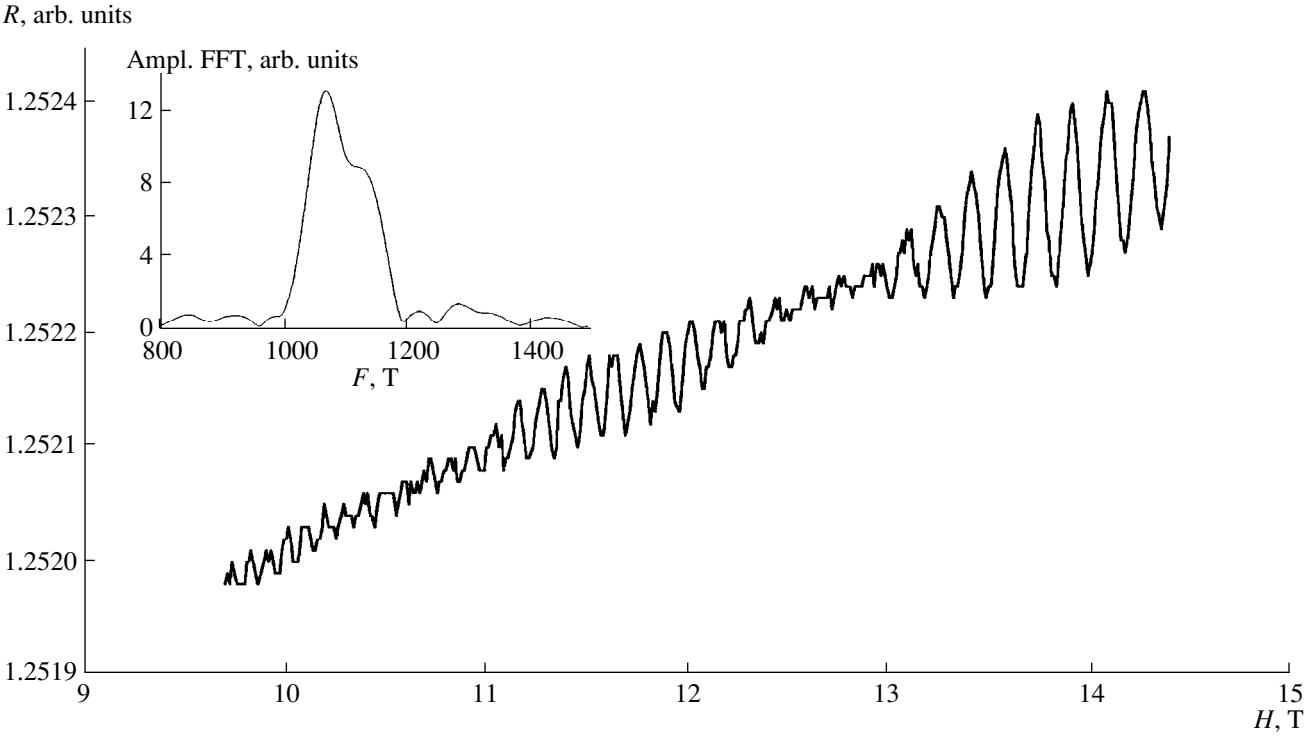

Fig. 2. Magnetization with de Haas–van Alphen oscillations; $T = 0.45$ K, $\theta = -50°$. Insert: FFT of these oscillations.

shown in Fig. 6. The angular dependence of the mass is quite well fitted by the expression:

$$m^* \approx 1.03 m_0 / \cos\theta, \qquad (5)$$

i.e., the value of the effective mass in the conducting plane constitutes $m^*(0) = 1.03 m_0$.

The Dingle temperature was evaluated from the field dependencies of the dHvA oscillation amplitude

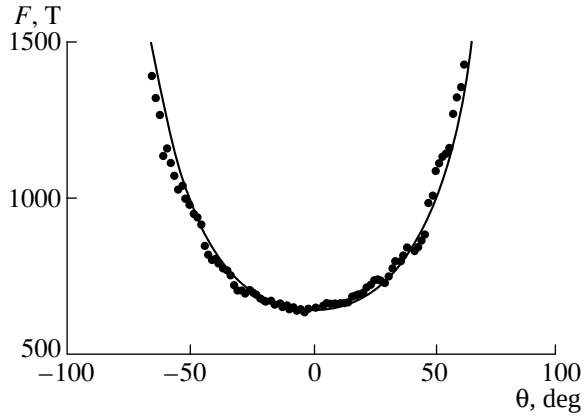

Fig. 3. Angular dependence of the fundamental frequency of dHvA oscillations. The solid line corresponds to (1).

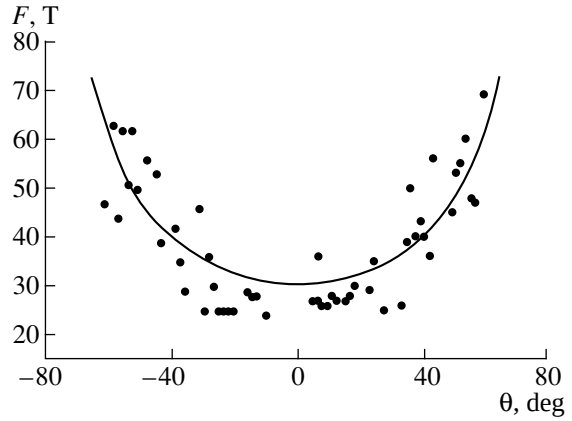

Fig. 4. Angular dependence of the beat frequency of dHvA and SdH oscillations. The solid line corresponds to (2).

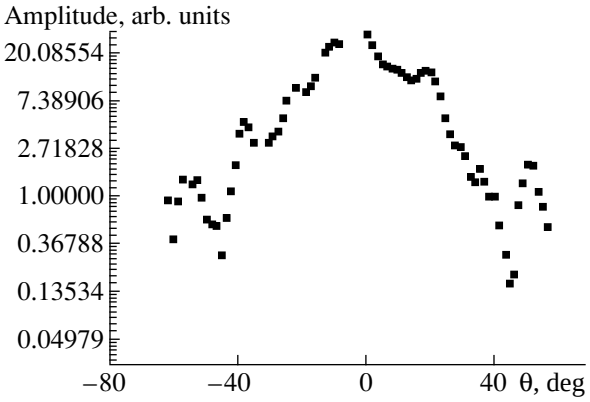

Fig. 5. Angular dependence of the dHvA oscillation amplitude.

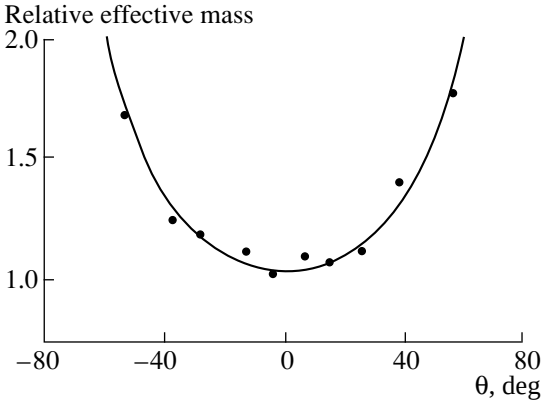

Fig. 6. Angular dependence of the effective mass. The solid line corresponds to (5).

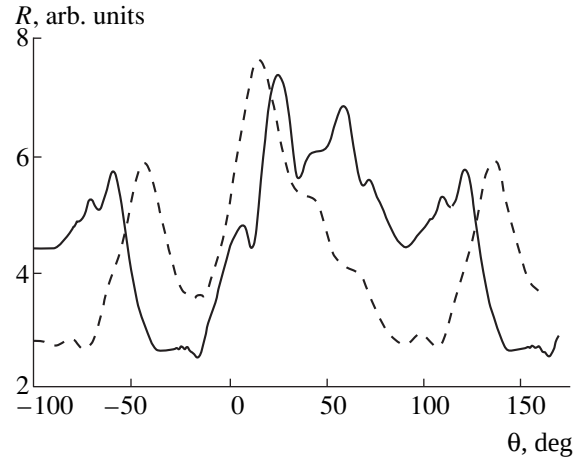

Fig. 7. Angular dependencies of the magnetoresistance; H = 14 T, T = 1.45 K, **I** ∥ **b***. The solid line corresponds to the rotation plane b^*c; the dashed line corresponds to the rotation plane close to b^*a.

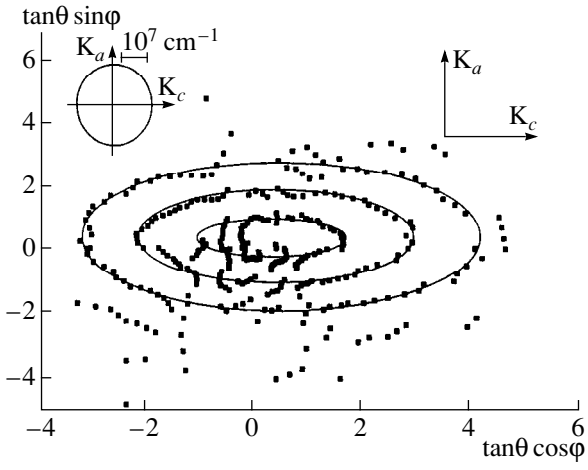

Fig. 8. AMRO maxima positions in the tanθ scale plotted in polar coordinates. The polar angle corresponds to the azimuthal angle in the *ac*-plane. Arrows show the directions of the reciprocal lattice. Insert: the FS cross section reconstructed from these data.

using the expression for the Dingle reduction factor R_D [15]:

$$R_D = \exp(-\alpha r \mu T_D/H).$$

To minimize the undesirable effect of the beat on the field dependence of the amplitude, the Dingle plots were made for θ = 0°, at which no beating was observed. Such an evaluation yields T ≈ 2–3 K.

The angular dependencies of the magnetoresistance were measured using the two-axes-rotation insert in the following way. At first, at the initial position of the sample rotator **b*** ⊥ **H**, a screw for manual φ-rotation (φ is an azimuthal angle lying in the *ac*-plane) around the **b*** axis was connected with the rotator, and a definite plane of θ-rotation was set. An angular coordinate θ of this rotation was measured from the c axis. After that, the screw was disconnected and the sample was rotated with a stepper motor around the axis perpendicular to the field direction. The angular coordinate of the recorded magnetoresistance corresponded to the angle θ between **H** and the **b*** axis. The measurements were done for a set of φ in the range 0°–180° with a 4° step. Examples of recorded dependencies for φ = 0° and φ = 88° are presented in Fig. 7. Angular magnetoresistance oscillations (AMRO) are well pronounced. The results of the AMRO observations at all rotations are summarized in Fig. 8 and Fig. 9 by plotting the minima and maxima of the magnetoresistance, respectively, in polar coordinates where the angle φ acts as a polar angle and the length of a radius-vector of every point corresponds to the tangent of angle θ, at which the extremum of AMRO was observed. Arrows indicate the directions corresponding to vectors of the reciprocal lattice. In Fig. 9, only positive values of tanθsinφ are taken in to account.

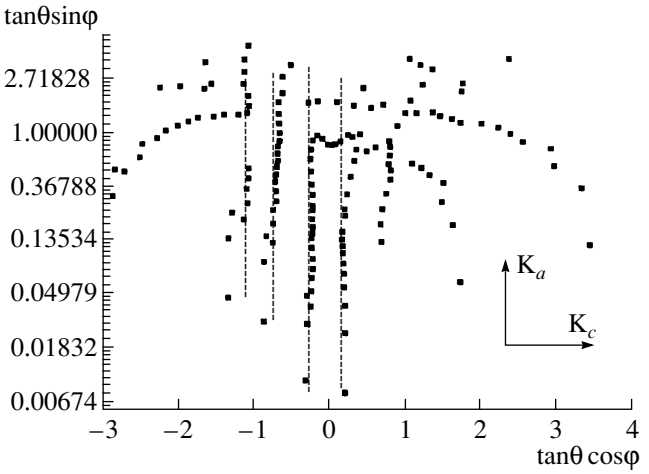

Fig. 9. AMRO minima positions in the tanθ scale plotted in polar coordinates. The polar angle corresponds to the azimuthal one in the *ac*-plane. Arrows show directions of the reciprocal lattice.

4. DISCUSSION

On decreasing the temperature from 295 K to 1.45 K, the resistance of the samples falls monotonically without any anomaly [13]. No sign of a SC transition, as observed in $(ET)_2NH_4Hg(SCN)_4$ [8], or of a Peierls-type transition, realized in a series of other alpha-salts [2–4], could be detected. The field dependence of the resistance in BETS-Tl-Se appears as a regular curve with almost no saturation [13]. Thus, both the new alpha-phase metal and its ET analog [10] have no phase transitions within the 1.45–295 K temperature range. The residual resistance ratio in BETS-Tl-Se, RRR ≈ 200, the value of the classical magnetoresistance at **H** ∥ **b*** and H = 14 T, is almost an order of magnitude higher than the same averaged values of the ET analog [6, 10]. Such a difference is unlikely caused by the increase of the relaxation time in the new metal, since the Dingle temperature is two to three times higher than in the ET salt. The amplitude of the SdH oscillations is significantly lower in the new metal than that in the ET salt and is in accordance with the higher values of the Dingle temperatures [10]. The large value of classical magnetoresistance seems to be most probably caused by an essentially higher contribution of carriers associated with the quasi-one-dimensional FS sheets in the BETS salt as compared with the ET one. The current direction along open Fermi sheets **I** ∥ **b*** provides the best conditions for the maximal value of this contribution. The weak saturation of the magnetoresistance, which is characteristic of open orbits, supports this supposition. Indeed, changing the current direction to **I** ∥ **a** decreases the value of the magetoresistance almost 2.5 times, and noticeable saturation can also be observed (Fig. 1).

Quantum oscillations SdH and dHvA demonstrate, in the samples under study, the only fundamental frequency $F \approx 640$ T at **H** ∥ **b***. This value is close to that found in the quantum oscillations of the ET analog [10]. As expected for quasi-two-dimensional metals, the behavior of the angular dependence of the fundamental frequency is described by the relationship (1) and corresponds to the cylindrical shape of FS with the axis along the **b*** direction.

AMRO presented in Fig. 7 are characteristic features of many low-dimensional organic metals [1]. They may be associated with carrier motion on the cylindrical part of FS if this cylinder is slightly corrugated along the **b*** axis [16]. In this case, the maxima of AMRO are periodic in tanθ and their positions are described by the relationship [17]:

$$\tan\theta_n(\varphi) = \frac{\pi(n - 1/4) \pm (\mathbf{k}_\parallel^{\max}(\varphi) \cdot \mathbf{u})}{k_H^{\max}(\varphi) d}, \qquad (6)$$

where $\mathbf{k}_{\|}^{\max}(\varphi)$ is the in-plane *ac* Fermi wave vector component whose projection $\mathbf{k}_H^{\max}$ to the field rotation plane defined by an angle φ is maximal; **u** is the in-plane *ac* component of the electron hopping vector; *d* is an interlayer distance; and $n = \pm 1, \pm 2, \ldots$ is an integer. The sign "±" corresponds to positive or negative values of the angle θ_n. Knowing the value of the period of AMRO $\Delta(\tan\theta_n)$, one could determine the value $\mathbf{k}_H^{\max}$ at a fixed azimuthal angle φ, and, knowing a set of $\mathbf{k}_H^{\max}$ at different angles φ, one could determine in detail the shape of the FS cross section in the conducting plane [17]. If all the values of $\tan\theta_n$ are drawn in the polar coordinate system with the azimuthal angle φ as a polar one, they form a set of concentric closed curves. At fixed angles φ, the distances between the curves are equidistant and equal to the period of AMRO in this rotation plane. Figure 8 shows the maxima of AMRO in polar coordinates. They form a set of closed curves. The period of AMRO varies from $\Delta \approx 0.9$ at the sample rotating in the *ab**-plane to $\Delta \approx 1.2$ at the sample rotating in the *cb**-plane. According to [17], the reconstruction of the FS yields the cross section of the cylindrical FS in the conducting plane as a figure resembling an ellipse with half-axes $k_{Fc} \approx 1.2 \times 10^7$ cm^{-1} and $k_{Fa} \approx 1.6 \times 10^7$ cm^{-1} (see insert in Fig. 8). The area of such an ellipse, $S \sim \pi k_{Fa} k_{Fc}$, is in a good agreement with the frequency of quantum oscillations.

The second possible mechanism for the appearance of AMRO in low-dimensional metals is the motion of carriers along the planar FS sheets characteristic of quasi-one-dimensional electron systems. In this case, the FS sheets must be corrugated in two directions [18]. Now the minima of magnetoresistance oscillations are periodic in $\tan\theta$ and follow the relationship [19]:

$$\tan\theta_n(\varphi)\cos\varphi = \cot\beta + nK_1/K_2\sin\beta, \qquad (7)$$

where φ is the azimuthal angle counted from the direction parallel to the FS plane; K_1 and K_2 are the lengths of the translation vectors of the reciprocal lattice that lie in the FS plane; β is the angle between them; and $n = 0, \pm 1, \pm 2, \ldots$ is an integer. In polar coordinates (where the angle φ acts as a polar angle), all values of $\tan\theta_n$ form a set of straight lines parallel to the one-dimensional axis of the crystal under study. The distance between these straight lines constitutes $K_1/K_2\sin\beta$. Figure 9 depicts the minima of AMRO in polar coordinates. A set of straight lines parallel to $\mathbf{K}_a$ is well pronounced. In this case, the vectors $\mathbf{K}_b$ and $\mathbf{K}_c$ of the reciprocal lattice act as vectors $\mathbf{K}_1$ and $\mathbf{K}_2$, respectively. The distance between the straight lines constitutes $0.45 \approx K_b/K_c\sin\beta$, which is in good agreement with the parameters of the crystal lattice [13]. Therefore, the results presented in Fig. 9 indicate open FS sheets perpendicular to the $\mathbf{K}_a$ direction.

It should be noted that these results appear as the first simultaneous observation of quasi-one-dimensional and quasi-two-dimensional AMRO in the alpha-type crystals. For example, only AMRO associated with the cylindrical FS sheet were observed in ET-Tl-Se [10]. The observation of quasi-one-dimensional AMRO in BETS-Tl-Se is most probably associated with a larger degree of corrugation of the open FS sheets along the c direction. In the isostructural BETS-K-S and BETS-NH-S salts, the increase of corrugation in this direction was predicted theoretically [20]; therefore, this assumption seems to be right. Such an enhancement of corrugation may be one of the reasons for the suppression of the Peierls-type transition in the alpha-BETS salts. (The simultaneous presence of AMRO associated with closed and open FS parts results in the appearance of "wrong" points in Figs. 8 and 9. For example, a minimum with no physical origin always exists between two maxima of magnetoresistance associated with the cylindrical FS.) Thus, it is shown experimentally that FS in BETS-Tl-Se consists of a quasi-one-dimensional part (two corrugated planes parallel to the K_cK_b-plane) and a quasi-two-dimensional part (corrugated cylinder with the axis along **b***).

The corrugation of the cylindrical part of the FS may be reflected in the beating behavior of the quantum oscillations, since the corrugated cylinder contains at least two close extremal cross sections. In this case, at the magnetic field direction approaching the directions described by (6), the frequency of the beat tends to zero [1] and the amplitude of oscillations with the fundamental frequency sharply increases [16, 17]. The BETS-Tl-Se samples show the beat of the fundamental frequency (Figs. 1, 2); however, its behavior differs from that described above. The observed beat disappear at field directions corresponding to $\theta = 0°$ and $\theta = \pm 20°$; however: (1) the angular dependence of magnetoresistance shows no AMRO with the maxima at these angles (see Fig. 7); and (2) at angles approaching $\theta = 0°$ and $\theta = \pm 20°$, the frequency of the beat remains almost unchanged (Fig. 4) and the oscillation amplitude in the nodes increases in such way that the nodes fully disappear at these angles. Therefore, the observed beat cannot be explained by the corrugation of the FS cylinder. Another explanation could be crystal imperfections (twinning, bicrystal), but the X-ray analysis of the crystal structure does not support this possibility. The magnetic interaction seems hardly to be the reason for the beat [15], since the amplitude and the dHvA oscillation frequency are rather small. Thus, the reason for the beat observed has not yet been clarified and requires further investigations.

The angular dependence of the effective mass follows (5) as expected for a cylindrical FS. The value of

the effective mass in the conducting plane $m^* = 1.03m_0$ is two times lower than that in the ET salt and is close to the value of the effective mass observed in BETS-K-S and BETS-NH-S [12]. The decrease of the effective mass seems to be characteristic of all alpha-phase metals with the BETS cation. The angular dependence of the dHvA oscillation amplitude exhibits "spin zeros" at $\theta \approx \pm 45°$. Using the condition for the "spin zeros" $\mu g = 2n + 1$ and the angular dependence of the effective mass as $\mu(\theta) = \mu(0)/\cos\theta$ and assuming $n = 1$, one could estimate the value of the spin-splitting factor [15]:

$$S = \frac{\mu g}{2} = \frac{g_S m_c(1+\alpha)}{2m_0(1+\alpha')} \approx 1.05, \quad (8)$$

where g_S is the g-factor taken from the ESR measurements and approximately equal to 2 for most organic metals [1], m_c is a band mass, α is a correction constant to the band mass which includes electron-electron coupling, and α' is a correction constant to the g-factor which includes electron–electron coupling. If electron-electron coupling is neglected, (8) yields: $m_c \approx 1.05m_0$. (Taking into account that only the "spin zero" at $\theta \approx \pm 45°$ is observed, the choice of the value n = 1 needs explanation. If we assume $n = 2$, then the value of the band mass $m_c \approx 0.6m_0$ is too small in comparison, for example, with the theoretically calculated band mass for BETS-K-S and $(BETS)_2TlHg(SeCN)_4$, $m_c \sim 0.6m_0$ [12]. If we assume $n = 2$, then the value of the band mass $m^* \approx 1.8m_0$ is too large in comparison with the effective mass $m^* \approx 1.03m_0$ mentioned above.) Thus, the band mass coincides with the effective mass determined from the temperature dependencies of the quantum oscillations amplitude. The band mass m_c is generally renormalized not only by the electron–electron but also by the electron–phonon coupling:

$$m^* = m_c(1+\alpha)(1+\lambda), \quad (9)$$

where λ is the electron–photon coupling correction constant. This would be in agreement with the experimental data if we suppose the full absence of multibody interactions ($\alpha = \alpha' = \lambda = 0$) in BETS-Tl-Se. This could explain the absence of any phase transitions in this compound. Considering that such transitions were observed neither in BETS-K-S nor in BETS-NH-S and that the value of the effective mass in these compounds is also close to m_0 [12], one could suggest the weakening of multibody interactions in these salts as well, and, therefore, the absence of the SC transition in BETS-NH-S is easily explained. In this case, one should suggest that all α-BETS metals are not promising for realization to the SC state.

However, the above conclusions have a few objections: (1) The band mass evaluated from theoretical calculations differs almost two times from the effective mass determined experimentally in BETS-K-S and BETS-NH-S [12], in contrast to the experimental results for BETS-Tl-Se; (2) The contribution of electron–electron coupling may be sufficiently large in organic low-dimensional metals due to a low carrier concentration [21]. Therefore, the problem of multibody interactions in α-BETS metals requires new, detailed experiments.

5. SUMMARY

The SdH and dHvA quantum oscillations and AMRO have been studied in the new organic metal $(BETS)_2TlHg(SeCN)_4$. The AMRO associated with the carrier motion both on cylindrical and quasi-planar parts of the FS were for the first time simultaneously observed in alpha-type metals. The detailed study of AMRO enabled us to determine the shape and size of the FS. The quantum oscillations show the only fundamental frequency, $F(0) \approx 640$ T, connected with the carrier motion on the cylindrical part of the FS. The beat of the fundamental frequency is observed. The beat behavior cannot be explained by effects which are presently known. The evaluation of the parameters of carriers associated with the cylindrical FS, namely, the Dingle temperature $T_D \approx 2$–3 K and the effective mass in the conducting plane $m^* \sim 1.03m_0$ was carried out. The angular dependence of the dHvA oscillation amplitude showed "spin zeros." The analysis of the positions of "spin zeros" considering the values of the effective mass allowed one to suggest the weakening of multibody interactions in the α-$(BETS)_2TlHg(SeCN)_4$.

ACKNOWLEDGMENTS

This work was supported by the Volkswagen-Stiftung grant 1/70 206, the Russian National Program "Physics of Quantum Wave Processes," and the NWO Grant.

REFERENCES

1. J. Wosnitza, *Fermi Surface of Low Dimensional Metals and Superconductors* (Springer-Verlag, Berlin, 1996).
2. T. Sasaki, Y. Toyota, M. Tokumoto, *et al.*, Solid State Commun. **75**, 93 (1990).
3. N. D. Kushch, L. I. Buravov, M. V. Kartsovnik, *et al.*, Synth. Met. **46**, 271 (1992).
4. N. Kinoshita, M. Tokumoto, and H. Anzai, J. Phys. Soc. Jpn. **60**, 2131 (1991).
5. M. V. Kartsovnik, A. E. Kovalev, and N. D. Kushch, J. Phys. I **3**, 1183 (1993).
6. L. I. Buravov, N. D. Kushch, V. N. Laukhin, *et al.*, J. Phys. I **4**, 441 (1994).
7. T. Sasaki, H. Orawa, H. Mori, *et al.*, J. Phys. Soc. Jpn. **65**, 231 (1995).
8. H. H. Wang, R. D. Carlson, U. Geiser, *et al.*, Physica C **166**, 57 (1990).
9. S. I. Pesotskiĭ, A. E. Kovalev, P. Boehm, *et al.*, Zh. Éksp. Teor. Fiz. **112**, 2178 (1997) [JETP **85**, 1192 (1997)].

10. A. E. Kovalev, M. V. Katsovnik, and N. D. Kushch, Solid State Commun. **72**, 859 (1993).
11. R. Kato, H. Kobayashi, and A. Kobayashi, Synth. Met. **41–43**, 2093 (1991).
12. S. A. Ivanov, C. H. Mielka, T. Coffey, *et al.*, Phys. Rev. B **55**, 4191 (1997).
13. N. D. Kushch, L. I. Buravov, S. I. Pesotskiĭ, *et al.*, J. Mater. Chem. **8**, 897 (1998).
14. P. Christ, W. Biberacher, H. Muller, and K. Andres, Solid State Commun. **91**, 451 (1994).
15. D. Shoenberg, *Magnetic Oscillations in Metals* (Cambridge University Press, Cambridge, 1984).
16. K. Yarnaji, J. Phys. Soc. Jpn. **58**, 1520 (1989).
17. M. V. Kartsovnik, V. N. Laukhin, S. I. Pesotskiĭ, *et al.*, J. Phys. I **2**, 89 (1992).
18. T. Osada, S. Kagoshima, and N. Miura, Phys. Rev. B **46**, 1812 (1992).
19. M. V. Kartsovnik and V. N. Laukhin, J. Phys. I **6**, 1753 (1996).
20. D.-K. Seo, M.-H. Wangbo, B. Fravel, and L. K. Montgomery, Solid State Commun. **100**, 191 (1996).
21. N. Toyota, E. W. Fenton, T. Sasaki, and M. Tachiki, Solid State Commun. **72**, 859 (1989).

Journal of Experimental and Theoretical Physics, Vol. 90, No. 3, 2000, pp. 535–543.
Translated from Zhurnal Éksperimental'noĭ i Teoreticheskoĭ Fiziki, Vol. 117, No. 3, 2000, pp. 613–623.

SOLIDS
Electron Properties

Superconductivity in a Simple Model of the Pseudogap State

E. Z. Kuchinskiĭ* and M. V. Sadovskiĭ**

Institute of Electrophysics, Ural Division, Russian Academy of Sciences, Yekaterinburg, 620049 Russia
**e-mail: kuchinsk@ief.uran.ru*
***e-mail: sadovski@ief.uran.ru*
Received September 20, 1999

Abstract—An analysis is made of characteristics of the superconducting state (*s*- and *d*-pairing) using a simple, exactly solvable model of the pseudogap state produced by fluctuations of the short-range order (such as antiferromagnetic) based on a Fermi surface model with "hot" sections. It is shown that the superconducting gap averaged over these fluctuations is nonzero at temperatures higher than the mean-field superconducting transition temperature T_c over the entire sample. At temperatures $T > T_c$ superconductivity evidently exists in isolated sections ("drops"). Studies are made of the spectral density and the density of states in which superconducting characteristics exist in the range $T > T_c$ however, in this sense the temperature $T = T_c$ itself is no different in any way. These anomalies show qualitative agreement with various experiments using underdoped high-temperature superconducting cuprates. © *2000 MAIK "Nauka/Interperiodica".*

1. INTRODUCTION

Among the numerous anomalies in the electronic properties of high-temperature superconductors particular interest is being directed toward the pseudogap state observed mainly at below-optimum carrier concentrations [1, 2]. These anomalies appear in many experiments such as optical conductivity measurements, NMR, inelastic neutron scattering, angle-resolved photoemission spectroscopy (ARPES), and so on (see the review [1]). Particularly clear evidence of the existence of this state is observed in ARPES experiments [1, 3] which demonstrate essentially anisotropic changes in the spectral density of the carriers over a wide range of temperature in the normal and superconducting phases of these systems. The maximum of these anomalies is observed near the point $(\pi, 0)$ in the Brillouin zone, while they are almost completely absent in the direction of the zone diagonal [near the point (π, π). Qualitatively these anomalies can be considered as the complete "destruction" of the Fermi surface near the point $(\pi, 0)$, with Fermi-liquid behavior conserved in the direction of the diagonal. In this sense it is usual to talk of the "*d*-symmetry" of the pseudogap matching the symmetry of the superconducting gap in these compounds [1–3]. However, the fact that pseudogap anomalies are observed up to temperatures $T \sim T^*$, appreciably higher than T_c, may indicate that the nature of these anomalies is completely different and is not directly related to superconducting pairing. This conclusion is also supported by the fact that the pseudogap state is mainly observed for nonoptimum compositions close to the antiferromagnetic phase of high-temperature superconducting cuprates.

In the theoretical context, attempts to construct models of the pseudogap state of high-temperature superconductors follow two main approaches. One is based on the very popular model of the formation of Cooper pairs above the superconducting transition temperature [2, 4–7]. The other assumes that the pseudogap state is caused by fluctuations of the antiferromagnetic short-range order (see, for example, [8–12]).

Most theoretical studies have been made of the pseudogap state in the normal phase a $T > T_c$. In a recent study [13] Posazhennikova and Sadovskii proposed a very simple, exactly solvable model of the pseudogap state, based on the concept that the Fermi surface has "hot" (planar) sections, and this model was used to construct a Ginzburg–Landau expansion for various types of Cooper pairing and to study the qualitative effects of the pseudogap (caused by fluctuations of the antiferromagnetic short-range order) on the fundamental properties of superconductors near T_c. The present paper is devoted to the further development of this simplified model and analyzes the characteristic features of the superconducting state over the entire temperature range $T < T_c$.

2. MODEL OF THE PSEUDOGAP STATE

We shall analyze an extremely simplified model of the pseudogap state [13] based on a pattern of well-developed fluctuations of the short-range antiferromagnetic order, similar to the model of "hot spots" on the Fermi surface [11].[1] We shall assume that the Fermi surface of a two-dimensional electron system has the form shown in Fig. 1. This type of Fermi surface has in fact been observed in ARPES experiments on high-

[1] We note that our analysis can essentially also be applied to the case of short-range order fluctuations of the charge density wave type and other similar models.

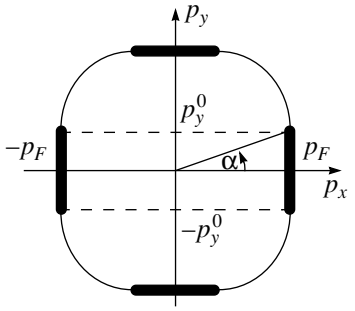

Fig. 1. Fermi surface of a two-dimensional system. The hot sections, of width $\sim\xi^{-1}$, are shown by the heavy lines.

temperature superconducting cuprates (see, for example, the very recent studies [14, 15]). We shall assume that the fluctuations of the short-range order are static and Gaussian, determining their correlation function in the following form (see [8]):

$$S(\mathbf{q}) = \frac{1}{\pi^2}\frac{\xi^{-1}}{(q_x - Q_x)^2 + \xi^{-2}}\frac{\xi^{-1}}{(q_y - Q_y)^2 + \xi^{-2}}, \quad (1)$$

where ξ is the correlation length of the fluctuations and the scattering vector is taken in the form $Q_x = \pm 2k_F$, $Q_y = 0$ or $Q_y = \pm 2k_F$, $Q_x = 0$. We postulate that only electrons from the planar ("hot") parts of the Fermi surface shown in Fig. 1 interact with these fluctuations and this scattering is in fact one-dimensional. The effective electron interaction with these fluctuations will be described by $(2\pi)^2 W^2 S(\mathbf{q})$ where the parameter W has the dimensions of energy and determines the energy scale (width) of the pseudogap.[2] The choice of scattering vector $\mathbf{Q} = (\pm 2k_F, 0)$ or $\mathbf{Q} = (0, \pm 2k_F)$ implies a pattern of incommensurate fluctuations (it is possible to generalize to the commensurate case [13] but we do not consider this here). In the limit $\xi \longrightarrow \infty$, this model can have an exact solution using methods proposed for the one-dimensional case in [16]. For finite ξ we can construct an "almost" exact solution [11, 12] using a generalization of the one-dimensional approach developed in [17, 18]. In the present study we only consider the simplest variant of the model with $\xi \longrightarrow \infty$, when the effective interaction with the fluctuations (1) has the very simple form:[3]

$$(2\pi)^2 W^2 \{\delta(q_x \pm 2p_F)\delta(q_y) + \delta(q_y \pm 2p_F)\delta(q_x)\}. \quad (2)$$

In this case we can easily sum all the perturbation theory series for an electron scattered at these fluctuations [16] and for the single-electron Green's function we obtain [13]

$$G(\epsilon_n, p) = \int_0^\infty dD\,\mathcal{P}(D)\frac{i\epsilon_n + \xi_p}{(i\epsilon_n)^2 - \xi_p^2 - D(\phi)^2}, \quad (3)$$

where $\xi_p = v_F(|\mathbf{p}| - p_F)$ (v_F is the velocity at the Fermi surface), $\epsilon_n = (2n + 1)\pi T$, and the fluctuating dielectric gap $D(\phi)$ is only nonzero in the hot sections:

$$D(\phi) = \begin{cases} D, & 0 \le \phi \le \alpha, \quad \dfrac{\pi}{2} - \alpha \le \phi \le \dfrac{\pi}{2}, \\ 0, & \alpha \le \phi \le \dfrac{\pi}{2} - \alpha, \end{cases} \quad (4)$$

where $\alpha = \arctan(p_y^0/p_F)$ and ϕ is the polar angle determining the direction of the vector $\mathbf{p}$ in the plane $p_x p_y$. For other values of ϕ the value of $D(\phi)$ is obviously determined by analogy with (4) from symmetry concepts.

The amplitude of the dielectric gap D is random and obeys a Rayleigh distribution [17] (its phase is then also random and uniformly distributed on the interval $(0, 2\pi)$):

$$\mathcal{P}(D) = \frac{2D}{W^2}\exp\left(-\frac{D^2}{W^2}\right). \quad (5)$$

Thus, at the hot sections the Green's function has the form of a "normal" Gor'kov Green's function averaged over the fluctuations of the dielectric gap D distributed in accordance with (5). The "anomalous" Gor'kov functions at these "dielectrified" sections are zero (because of the random phases of the dielectric gap D), which corresponds to the absence of any long-range order but their pair averages are nonzero and make some contribution to the two-particle Green's function [13, 16]. By varying the parameter α in (4) in the range $0 \le \alpha \le \pi/4$, we can change the size of the hot sections on the Fermi surface for which the nesting conditions $\xi_{p-Q} = -\xi_p$ is satisfied. In particular $\alpha = \pi/4$ corresponds to a square Fermi surface. Outside the hot sections [the second inequality in (4)] the Green's function (3) is simply the same as the Green's function of the free electrons.

Results of calculations of the electron density of states and the spectral density corresponding to (3) are presented in [13] and demonstrate the formation of a pseudogap (having the characteristic width $\sim 2W$) and non-Fermi-liquid behavior at the hot sections. In the model having a finite correlation length ξ the Green's function for these sections is represented as a continuous fraction [19] (see similar results in [11, 12, 17, 18]). In this case, the spectral density demonstrates increasingly smeared behavior (compared with the case $\xi \longrightarrow \infty$) with decreasing ξ, which was described in detail in [11, 12, 18]. In [19] this model was used to calculate the optical conductivity of a two-dimensional system in the pseudogap state.

[2] We can say that we are introducing the effective interaction "constant" with fluctuations of the type $W_{\mathbf{p}} = W[\theta(p_x^0 - p_x)\theta(p_x^0 + p_x) + \theta(p_y^0 - p_y)\theta(p_y^0 + p_y)]$.

[3] We stress that because of the Gaussian nature of the fluctuations the limit $\xi \longrightarrow 0$ does not imply the establishment of any long-range order.

3. SUPERCONDUCTIVITY IN THE PSEUDOGAP STATE

We shall now analyze superconductivity using this model. We shall assume that superconducting pairing is caused by an attractive potential which has the following very simple form [13]:

$$V(\mathbf{p}, \mathbf{p}') = V(\phi, \phi') = -Ve(\phi)e(\phi'). \quad (6)$$

Here ϕ is the angle which, as before, determines the direction of the electron momentum $\mathbf{p}$ in the plane and for $e(\phi)$ we take the simplest model dependence:

$$e(\phi) = \begin{cases} 1 & (s\text{-pairing}), \\ \sqrt{2}\cos(2\phi) & (d\text{-pairing}). \end{cases} \quad (7)$$

The attraction constant V is usually assumed to be nonzero in a certain layer of width $2\omega_c$ near the Fermi level (ω_c is the characteristic quantum frequency responsible for the attraction of electrons). In this case, the superconducting gap has the form

$$\Delta(\mathbf{p}) \equiv \Delta(\phi) = \Delta e(\phi). \quad (8)$$

We shall first consider superconductivity in a system in which there is a fixed dielectric gap D at the "hot" sections of the Fermi surface. The problem of superconductivity in a system with a partially dielectrified spectrum at various parts of the Fermi surface has been addressed in various studies (see, for example [20, 21]) and was analyzed by Bilbro and McMillan [22] using a model very close to our case, from which we can use some of the results directly or simply generalize them.

In particular, for s-pairing the equation for the superconducting gap Δ in this model has the form

$$1 = \lambda\int_0^{\omega_c} d\xi \left\{ \tilde{\alpha}\frac{\tanh\frac{\sqrt{\xi^2 + D^2 + \Delta^2(D)}}{2T}}{\sqrt{\xi^2 + D^2 + \Delta^2(D)}} + (1-\tilde{\alpha})\frac{\tanh\frac{\sqrt{\xi^2 + \Delta^2(D)}}{2T}}{\sqrt{\xi^2 + \Delta^2(D)}} \right\}, \quad (9)$$

where $\lambda = VN_0(0)$ is the dimensionless pair-interaction constant [$N_0(0)$ is the density of states of free electrons at the Fermi level] and the parameter $\tilde{\alpha} = 4\alpha/\pi$ determines the fraction of hot (planar) sections on the Fermi surface.

In equation (9) the first term on the right-hand side corresponds to the contribution of hot (dielectrified) sections for which the electron spectrum has the form [22] $E_p = \sqrt{\xi_p^2 + D^2 + \Delta^2}$ and the second term gives the contribution of the "cold" (metal) sections where the spectrum has the usual form in BCS theory: $E_p = \sqrt{\xi_p^2 + \Delta^2}$. Equation (9) determines the superconducting gap $\Delta(D)$ for a fixed dielectric gap D which is nonzero at the "hot" sections.

For d-pairing the similar equation has the form

$$1 = \lambda\frac{4}{\pi}\int_0^{\omega_c} d\xi \times \left\{ \int_0^{\alpha} d\phi e^2(\phi)\frac{\tanh\frac{\sqrt{\xi^2 + D^2 + \Delta^2(D)e^2(\phi)}}{2T}}{\sqrt{\xi^2 + D^2 + \Delta^2(D)e^2(\phi)}} + \int_{\alpha}^{\pi/4} d\phi e^2(\phi)\frac{\tanh\frac{\sqrt{\xi^2 + \Delta^2(D)e^2(\phi)}}{2T}}{\sqrt{\xi^2 + \Delta^2(D)e^2(\phi)}} \right\}. \quad (10)$$

It can be seen from these equations that $\Delta(D)$ decreases with increasing D and $\Delta(0)$ is the same as the usual gap Δ_0 in the absence of any dielectrification at the planar sections which appears at the temperature $T = T_{c0}$ determined by

$$1 = \lambda\int_0^{\omega_c}\frac{d\xi}{\xi}\tanh\frac{\xi}{2T_{c0}} \quad (11)$$

both for s- and d-pairing.

For $D \longrightarrow \infty$ the first terms in (9) and (10) vanish since the corresponding equations for $\Delta_\infty = \Delta(D \longrightarrow \infty)$ have the form

$$1 = \lambda\int_0^{\omega_c}\frac{d\xi(1-\tilde{\alpha})}{\sqrt{\xi^2 + \Delta_\infty^2}}\tanh\frac{\sqrt{\xi^2 + \Delta_\infty^2}}{2T} \quad (12)$$

(s-pairing),

$$1 = \lambda\frac{4}{\pi}\int_0^{\omega_c} d\xi \int_{\alpha}^{\pi/4}\frac{d\phi e^2(\phi)}{\sqrt{\xi^2 + \Delta_\infty^2 e^2(\phi)}}\tanh\frac{\sqrt{\xi^2 + \Delta_\infty^2 e^2(\phi)}}{2T} \quad (13)$$

(d-pairing).

Equation (12) agrees with the equation for the gap $D = 0$ with the renormalized coupling constant $\tilde{\lambda} = \lambda(1 - \tilde{\alpha})$ so that for s-pairing

$$\Delta_\infty = \Delta_0 \quad (\tilde{\lambda} = \lambda(1-\tilde{\alpha})) \quad (14)$$

and thus a nonzero gap for $D \longrightarrow \infty$ appears when $T < T_{c\infty}$,

$$T_{c\infty} = T_{c0} \quad (\tilde{\lambda} = \lambda(1-\tilde{\alpha})). \quad (15)$$

For the case of *d*-pairing we obtain from equation (13)

$$T_{c\infty} = T_{c0} \quad (\tilde{\lambda} = \lambda(1 - \alpha_d)), \tag{16}$$

where

$$\alpha_d = \tilde{\alpha} + \frac{\sin(\pi\tilde{\alpha})}{\pi} \tag{17}$$

is the effective fraction of planar sections for *d*-pairing. Hence, for $T < T_{c\infty}$ the gap is nonzero for any values of D and decreases from Δ_0 to Δ_∞ with increasing D. When $T_{c\infty} < T < T_{c0}$, the gap is only nonzero when $D < D_{\max}$. The corresponding dependences of Δ on D are easily obtained by solving equations (9) and (10) numerically.

In our model of the pseudogap state the dielectric gap D is not fixed but is a random quantity with a distribution given by (5). The equations obtained above must be averaged over all these fluctuations. Then we can directly calculate the exact superconducting gap $\langle\Delta\rangle$ averaged over the fluctuations of D:

$$\langle\Delta\rangle = \int_0^\infty dD\mathcal{P}(D)\Delta(D) = \frac{2}{W^2}\int_0^\infty dDD\exp\left(-\frac{D^2}{W^2}\right)\Delta(D). \tag{18}$$

The dependences $\Delta(D)$ described above have the result that the average gap (18) is nonzero as far as $T = T_{c0}$, i.e., as far as the superconducting transition temperature in the absence of pseudogap anomalies. However, the superconducting transition temperature T_c in a superconductor with a pseudogap is clearly lower than T_{c0} [13]. This paradoxical behavior of $\langle\Delta\rangle$ evidently implies that local regions with $\Delta \neq 0$ (superconducting drops) induced by fluctuations of D appear over the entire temperature range $T_c < T < T_{c0}$ and a superconducting state coherent over the entire sample is only established in the region $T < T_c$. Quite clearly, this qualitative picture can only be completely substantiated by analyzing a more realistic model where the fluctuations of the antiferromagnetic short-range order have a finite length ξ.[4] However, the simplicity of the $\xi \longrightarrow \infty$ model considered here means that an exact solution can be obtained immediately for $\langle\Delta\rangle$.

In order to determine the superconducting transition temperature T_c in the entire sample we shall use the standard procedure of the mean-field approximation (see, for example, a similar procedure applied to a superconductor with impurities [24]) which is under the assumption of self-averaging of the superconducting gap over the fluctuations of D (i.e., Δ is independent of the fluctuations of D). The equations for the mean-field gap Δ_{mf} then have the form

$$1 = \lambda\int_0^{\omega_c} d\xi\left\{\tilde{\alpha}\frac{2}{W^2}\int_0^\infty dDD\exp\left(-\frac{D^2}{W^2}\right) \times \frac{\tanh\frac{\sqrt{\xi^2 + D^2 + \Delta_{mf}^2}}{2T}}{\sqrt{\xi^2 + D^2 + \Delta_{mf}^2}} + (1 - \tilde{\alpha})\frac{\tanh\frac{\sqrt{\xi^2 + \Delta_{mf}^2}}{2T}}{\sqrt{\xi^2 + \Delta_{mf}^2}}\right\} \tag{19}$$

for *s*-pairing and

$$1 = \lambda\frac{4}{\pi}\int_0^{\omega_c} d\xi\left\{\int_0^\infty dDD\exp\left(-\frac{D^2}{W^2}\right) \times \int_0^\alpha d\phi e^2(\phi)\frac{\tanh\frac{\sqrt{\xi^2 + D^2 + \Delta_{mf}^2 e^2(\phi)}}{2T}}{\sqrt{\xi^2 + D^2 + \Delta_{mf}^2 e^2(\phi)}} + \int_\alpha^{\pi/4} d\phi e^2(\phi)\frac{\tanh\frac{\sqrt{\xi^2 + \Delta_{mf}^2 e^2(\phi)}}{2T}}{\sqrt{\xi^2 + \Delta_{mf}^2 e^2(\phi)}}\right\} \tag{20}$$

for *d*-pairing.

From equations (19) and (20) we can easily derive the corresponding equations for T_c. For example, for *s*-pairing we have

$$1 = \lambda\left\{\tilde{\alpha}\frac{2}{W^2}\int_0^\infty dDD\exp\left(-\frac{D^2}{W^2}\right) \times \int_0^{\omega_c}\frac{d\xi}{\sqrt{\xi^2 + D^2}}\tanh\frac{\sqrt{\xi^2 + D^2}}{2T_c} + (1 - \tilde{\alpha})\int_0^{\omega_c}\frac{d\xi}{\xi}\tanh\frac{\xi}{2T_c}\right\}. \tag{21}$$

For *d*-pairing $\tilde{\alpha}$ in (21) must be replaced by α_d from (17). These equations for T_c are the same as those obtained in the microscopic derivation of the Ginzburg–Landau expansion using this model in [13] where they were studied in detail. In general we always have $T_{c\infty} < T_c < T_{c0}$.

[4] The qualitative situation here resembles the formation of an inhomogeneous superconducting state induced by strong fluctuations of the local density of states near the Anderson metal–insulator transition [23, 24].

The temperature dependences of the average gap $\langle\Delta\rangle$ and the mean-field gap Δ_{mf} obtained by means of a numerical solution of the equations from our model for the case of *s*-pairing are plotted in Fig. 2.[5] The gap Δ_{mf} vanishes when $T = T_c < T_{c0}$, while $\langle\Delta\rangle$ is nonzero as far as $T = T_{c0}$, and the corresponding "tails" in the temperature dependence of $\langle\Delta\rangle$ in the range $T_c < T < T_{c0}$ are, in our view, consistent with the existence of superconducting "drops" in this region in the absence of superconductivity over the entire sample, as was described above. We note that the temperature dependences $\langle\Delta(T)\rangle$ presented in Fig. 2 are similar to those for the gap in underdoped high-temperature superconducting cuprates extracted from ARPES experiments [3, 25] and from measurements of the specific heat [26] assuming that the observed temperature T_c in these samples corresponds to our mean-field T_c whereas drops with $\langle\Delta\rangle \neq 0$ exist in the range $T > T_c$ as far as T_{c0} which is substantially higher than T_c. This interpretation of the data would imply that in the absence of a pseudogap the underdoped cuprates would have a significantly higher superconducting transition temperature.

Although, in our opinion, superconductivity is not present over the entire sample when $T_c < T < T_{c0}$, the existence of a nonzero average gap $\langle\Delta\rangle$ in this region leads to the appearance of various anomalies in the observable quantities, such as the tunneling density of states and the spectral density measured in ARPES experiments, as we shall see subsequently.

4. SPECTRAL DENSITY AND DENSITY OF STATES

The delayed electron Green's function near the hot section of the Fermi surface in the superconducting state has the form

$$G^R(E, \xi_p) = \int_0^\infty dD\mathcal{P}(D) \times \frac{E + \xi_p}{(E + i0)^2 - \xi_p^2 - D^2 - \Delta^2(D)e^2(\phi)}. \quad (22)$$

The corresponding spectral density is:

$$A(E, \xi_p) = -\frac{1}{\pi}\mathrm{Im}G^R(E, \xi_p) = \frac{2}{W^2}\int_0^\infty dDD\exp\left(-\frac{D^2}{W^2}\right)(E + \xi_p) \times \delta(\xi_p^2 + D^2 + \Delta^2(D)e^2(\phi) - E^2). \quad (23)$$

[5] For *d*-pairing the temperature dependences of $\langle\Delta\rangle$ and Δ_{mf} are qualitatively similar to the corresponding dependences for *s*-pairing.

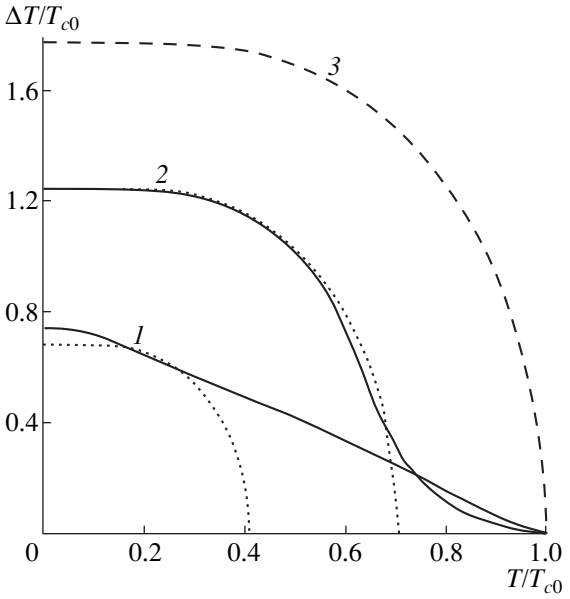

Fig. 2. Temperature dependences of the superconducting gaps Δ_{mf} (dotted curves), $\langle\Delta\rangle$ (solid curves), and Δ_0 (dashed curve) for *s*-pairing: (*1*) $\lambda = 0.4$, $\tilde{\alpha} = 2/3$, $\omega_c/W = 3$ ($T_c/T_{c0} = 0.42$), (*2*) $\lambda = 0.4$, $\tilde{\alpha} = 0.2$, $\omega_c/W = 1$ ($T_c/T_{c0} = 0.71$).

Using the mean-field procedure, in which we assume that $\Delta = \Delta_{mf}$ does not depend on D, we obtain

$$A_{mf}(E, \xi_p) = \frac{|E| + \xi_p \mathrm{sgn}E}{W^2} \times \exp\left(\frac{\xi_p^2 + \Delta_{mf}^2 e^2(\phi) - E^2}{W^2}\right) \times \theta(E^2 - \xi_p^2 - \Delta_{mf}^2 e^2(\phi)). \quad (24)$$

In this approximation a gap appears in the spectral density at the Fermi surface ($\xi_p = 0$) when $|E| < \Delta_{mf}$, and disappears when $T \longrightarrow T_c(\Delta_{mf} \longrightarrow 0)$. In fact we have seen that the gap Δ depends strongly on the dielectric gap D [see (9) and (10)] so that from (23) we have

$$A(E, \xi_p) = \sum_i \frac{|E| + \xi_p \mathrm{sgn}E}{W^2}\exp\left(-\frac{D_i^2}{W^2}\right) \times \left|1 + \frac{d\Delta^2(D)}{dD^2}\right|_{D = D_i} e^2(\phi)\Bigg|^{-1}, \quad (25)$$

where D_i are the positive roots of the equation $D^2 + \xi_p^2 + \Delta^2(D)e^2(\phi) - E^2 = 0$. The energy dependences of the spectral density for $\xi_p = 0$, i.e., for the electron momentum at the Fermi surface (we shall subsequently confine our analysis to this case) are plotted in Figs. 3 and 4 for *s*- and *d*-pairing respectively.

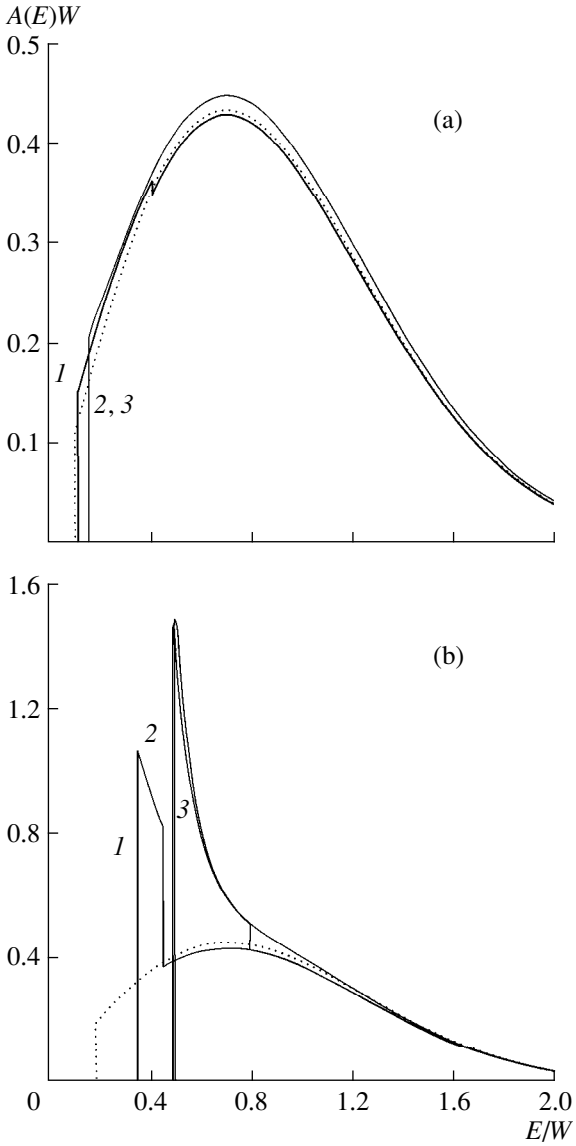

Fig. 3. Spectral density at the Fermi surface for *s*-pairing and T/T_{c0} = (*1*) 0.8, (*2*) 0.4, (*3*) 0.1: (a) $\lambda = 0.4$, $\tilde{\alpha} = 0.2$, $\omega_c/W = 1$ ($T_c/T_{c0} = 0.71$, $T/T_{c0} = 0.54$); dotted curve—mean-field spectral density $A_{mf}(E)$ for $T/T_{c0} = 0.4$; (b) $\lambda = 0.4$, $\tilde{\alpha} = 2/3$, $\omega_c/W = 3$ ($T_c/T_{c0} = 0.42$, $T_{c\infty}/T_{c0} = 7 \times 10^{-3}$); the dotted curve gives the mean-field spectral density $A_{mf}(E)$ for $T/T_{c0} = 0.1$.

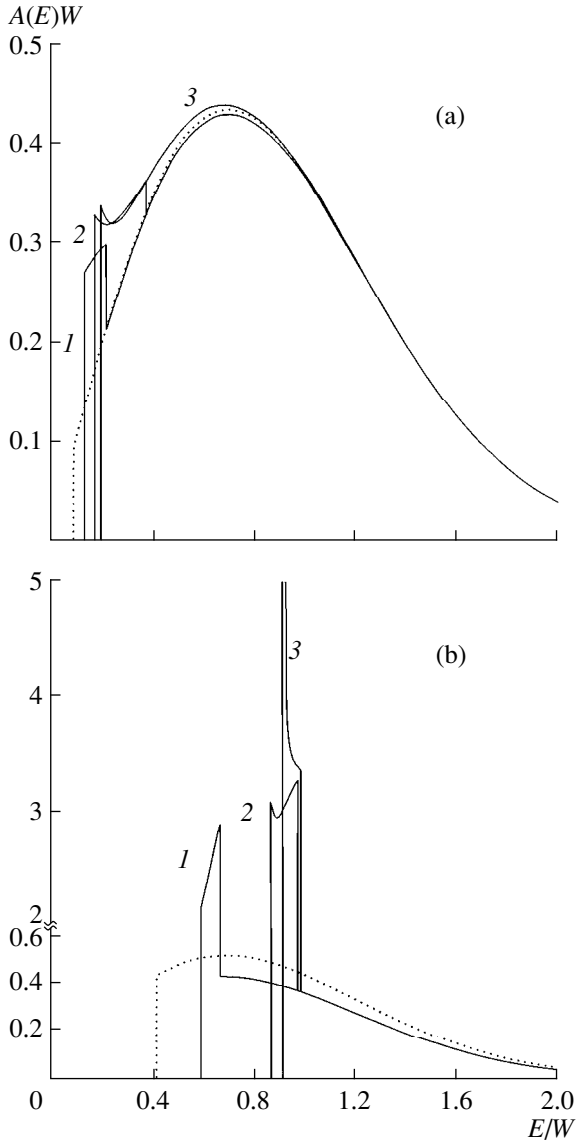

Fig. 4. Spectral density at the Fermi surface in the direction $\phi = 0$ for *d*-pairing when T/T_{c0} = (*1*) 0.8, (*2*) 0.6, (*3*) 0.1: (a) $\lambda = 0.4$, $\tilde{\alpha} = 0.2$, $\omega_c/W = 1$ ($T_c/T_{c0} = 0.42$, $T_{c\infty}/T_{c0} = 0.2$); (b) $\lambda = 0.4$, $\tilde{\alpha} = 2/3$, $\omega_c/W = 5$ ($T_c/T_{c0} = 0.48$, $T_{c\infty}/T_{c0} \sim 10^{-18}$). The dotted curves give the mean-field spectral density $A_{mf}(E)$ for $T/T_{c0} = 0.1$.

For $T_{c\infty} < T < T_{c0}$ a discontinuity is observed in the spectral density at $E = D_{\max}$ caused by a discontinuity in the derivative $d\Delta^2(D)/dD^2$ at $D = D_{\max}$ (i.e., the maximum value of D at which the gap $\Delta(D)$ is nonzero). Effects involving the finite correlation length ξ of the fluctuations inevitably smooth this discontinuity, although the characteristic dip after the principal spectral density peak is conserved. A similar dip was observed in the ARPES experiments [1, 3] although this has not yet been fully interpreted.

For the case of *s*-pairing the value of $D^2 + \Delta^2(D)$ increases with increasing D so that the equation $D^2 + \Delta^2(D) - E^2 = 0$ only has roots for $|E| > \Delta_0$. Thus, the gap in the spectral density is observed when $|E| < \Delta_0$ so that the width of this gap is determined by the value of Δ_0 and not Δ_{mf}. In addition, the gap in the spectral density appears when $T = T_{c0}$ and the behavior of the spectral density at the point $T = T_c$ does not exhibit qualitative changes.

For *d*-pairing when the pseudogap width W is fairly small and the fraction of planar sections α_d is small, the value of $D^2 + \Delta^2(D)e^2(\phi)$ also increases with increasing D and the width of the gap in the spectral density becomes equal to $\Delta_0 e(\phi)$ as in the case of *s*-pairing. However, as the pseudogap width W and the fraction of planar sections increase, $D^2 + \Delta^2(D)e^2(\phi)$ decreases with increasing D for fairly small D with the result that the width of the gap in the spectral density becomes smaller than Δ_0 and for $E = \Delta_0$ a discontinuity appears in the spectral density (the discontinuity at $E = D_{\max}$ is also retained).

We shall now analyze the tunneling density of states $N(E)$. For *s*-pairing we have

$$\frac{N(E)}{N_0(0)} = \frac{2}{W^2}\int_0^\infty dDD\exp\left(-\frac{D^2}{W^2}\right)$$

$$\times\left\{\tilde{\alpha}\frac{|E|}{\sqrt{E^2 - D^2 - \Delta^2(D)}}\theta(E^2 - D^2 - \Delta^2(D)) \right. \quad (26)$$

$$\left. + (1-\tilde{\alpha})\frac{|E|}{\sqrt{E^2 - \Delta^2(D)}}\theta(E^2 - \Delta^2(D))\right\}.$$

Under the assumption of self-averaging the gap Δ is equal to Δ_{mf} and does not depend on the fluctuations of D, and then

$$\frac{N_{mf}(E)}{N_0(0)} = \left\{\tilde{\alpha}\frac{2}{W^2}\int_0^{\sqrt{E^2-\Delta_{mf}^2}} dDD\exp\left(-\frac{D^2}{W^2}\right)\right.$$

$$\left.\times\frac{|E|}{\sqrt{E^2 - D^2 - \Delta_{mf}^2}} + (1-\tilde{\alpha})\frac{|E|}{\sqrt{E^2 - \Delta_{mf}^2}}\right\} \quad (27)$$

$$\times\theta(E^2 - \Delta_{mf}^2).$$

In this approximation when $|E| < \Delta_{mf}$ a gap appears in the density of states and disappears when $T \longrightarrow T_c(\Delta_{mf} \longrightarrow 0)$ but in this case a singularity remains (as discussed in [13]) in the form of a pseudogap caused by the antiferromagnetic fluctuations:

$$\frac{N(E)}{N_0(0)} = \tilde{\alpha}\frac{2}{W^2}\int_0^E dDD\exp\left(-\frac{D^2}{W^2}\right)$$

$$\times\frac{|E|}{\sqrt{E^2 - D^2}} + (1-\tilde{\alpha}). \quad (28)$$

In fact $\Delta(D)$ in (26) depends strongly on D in accordance with (9). It can be seen from (26) and the corresponding dependence $\Delta(D)$ that when $T < T_{c\infty}$ a gap is observed in the density of states for $E < \Delta_\infty$ but when $T > T_{c\infty}$, no gap is observed but some contribution to the pseudogap associated with the superconducting pairing still remains. For $T_c < T < T_{c0}$ the gap function $\Delta(D)$ is nonzero when $D < D_{max}$ so that differences from the pseudogap behavior caused only by antiferromagnetic fluctuations are observed in the density of states when $T_c < T < T_{c0}$ and the antiferromagnetic pseudogap (28) is only retained when $T > T_{c0}$.

Figure 5 shows the behavior of the density of states in the *s*-case at various temperatures. A kink on the density of states is observed at $|E| = \Delta_0$ and when $T > T_{c\infty}$ a second kink is observed for $|E| = \Delta_{\max} > \Delta_0$ although this kink is only appreciable at high temperatures $T \sim T_{c0}$. The density of states only undergoes qualitative changes at $T = T_{c0}$, and there are no particular features at the mean-field temperature T_c.

For *d*-pairing the expression for the density of states has the form

$$\frac{N(E)}{N_0(0)} = \frac{4}{\pi}\frac{2}{W^2}\int_0^\infty dDD\exp\left(-\frac{D^2}{W^2}\right)$$

$$\times\left\{\int_0^\alpha d\phi\frac{|E|}{\sqrt{E^2 - D^2 - \Delta^2(D)e^2(\phi)}}\right. \quad (29)$$

$$\times\theta(E^2 - \Delta^2(D)e^2(\phi) - D^2)$$

$$\left. + \int_\alpha^{\pi/4} d\phi\frac{|E|}{\sqrt{E^2 - \Delta^2(D)e^2(\phi)}}\theta(E^2 - \Delta^2(D)e^2(\phi))\right\}.$$

Under the assumption of self-averaging the gap Δ is equal to Δ_{mf} and does not depend on D. The width of the superconducting pseudogap in the density of states is then of the order Δ_{mf}, the corresponding contribution disappears when $T \longrightarrow T_c$, and only the pseudogap associated with the antiferromagnetic fluctuations (28) remains. In reality in (29) Δ depends on D and is determined by equation (10).

The behavior of the density of states in the *d* case is shown in Fig. 6. As in the case of *s*-pairing a substantial difference is observed between the exact density of states and that obtained in the mean-field approximation as a result of fluctuations of the superconducting gap (superconducting drops) caused by antiferromagnetic fluctuations of the short-range order. The exact density of states does not in fact sense the superconducting transition in the entire system which takes place at $T = T_c$. In this case, the characteristic width of the superconducting gap (pseudogap) in the density of states is of the order Δ_0 and not Δ_{mf} as follows from the mean-field approximation. The corresponding contributions become observable at $T = T_{c0} > T_c$.

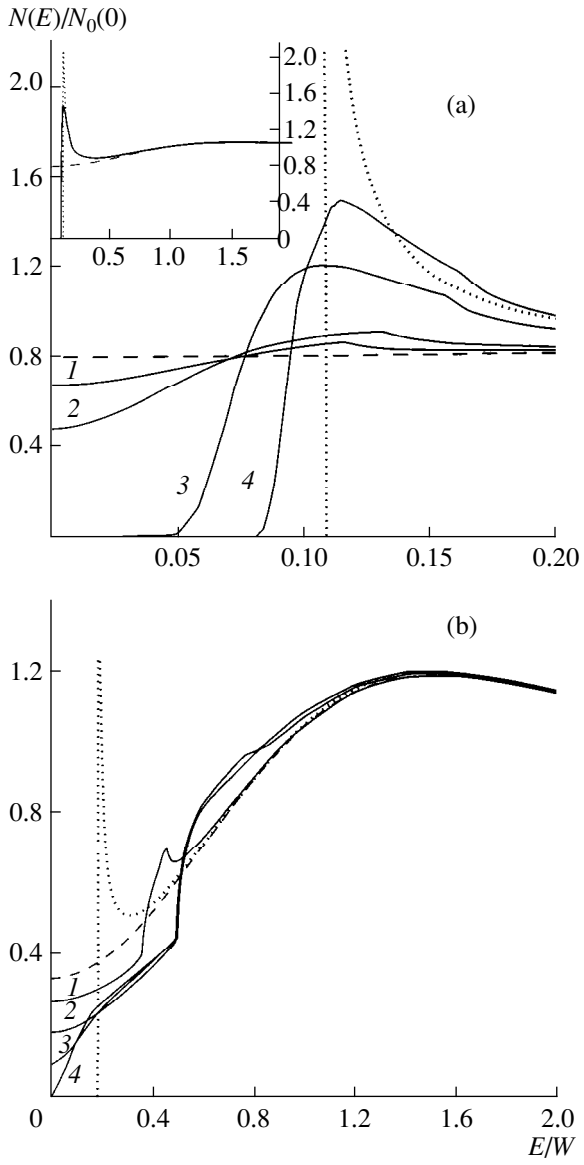

Fig. 5. Spectral density for *s*-pairing: (a) $\lambda = 0.4$, $\tilde{\alpha} = 0.2$, $\omega_c/W = 1$ ($T_c/T_{c0} = 0.71$, $T_c/T_{c0} = 0.54$), $T/T_{c0} = 0.8$ (*1*), 0.71 (*2*), 0.54 (*3*), 0.4 (*4*); dotted curve is mean-field density of states $N_{mf}(E)$ for $T_c/T_{c0} = 0.4$; inset shows density of states for $T_c/T_{c0} = 0.4$; (b) $\lambda = 0.4$, $\tilde{\alpha} = 2/3$, $\omega_c/W = 3$ ($T_c/T_{c0} = 0.42$, $T_{c\infty}/T_{c0} = 7 \times 10^{-3}$), $T/T_{c0} = 0.8$ (*1*), 0.42 (*2*), 0.2 (*3*), 0.05 (*4*); dotted curve is mean-field density of states $N_{mf}(E)$ for $T_c/T_{c0} = 0.2$, dashed curve displays pseudogap behavior of density of states for $T > T_{c0}$.

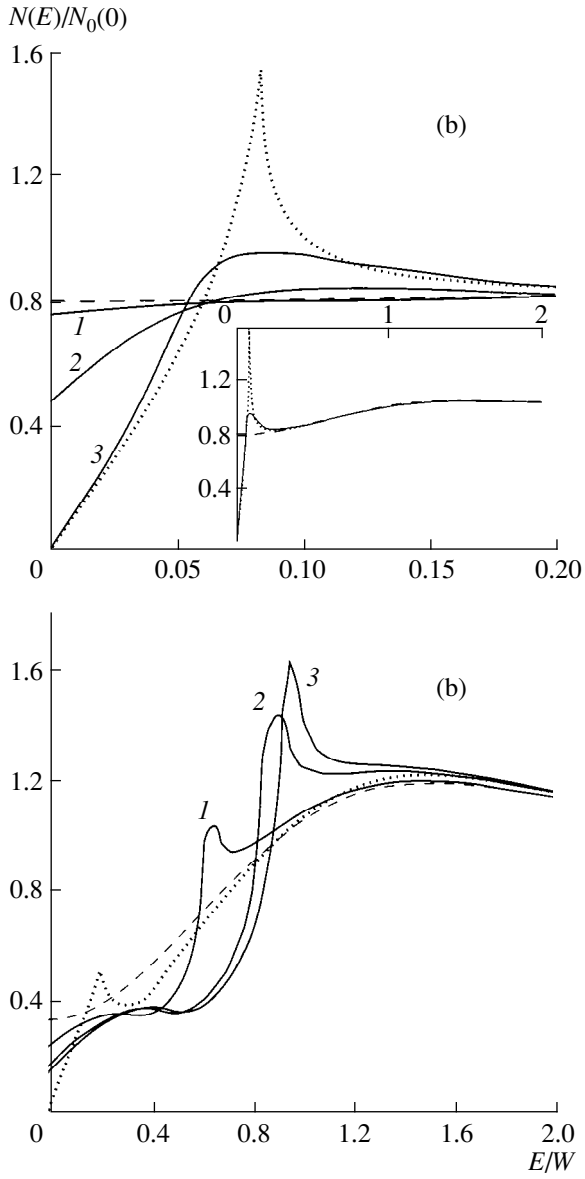

Fig. 6. Spectral density for *d*-pairing: (a) $\lambda = 0.4$, $\tilde{\alpha} = 0.2$, $\omega_c/W = 1$ ($T_c/T_{c0} = 042$, $T_c/T_{c0} = 0.2$), $T/T_{c0} = 0.8$ (*1*), 0.42 (*2*), 0.2 (*3*); dotted curve is mean-field density of states $N_{mf}(E)$ for $T/T_{c0} = 0.2$; inset shows density of states for $T/T_{c0} = 0.2$; (b) $\lambda = 0.4$, $\tilde{\alpha} = 2/3$, $\omega_c/W = 5$ ($T_c/T_{c0} = 0.48$, $T_{c\infty}/T_{c0} \sim 10^{-18}$), $T/T_{c0} = 0.8$ (*1*), 0.48 (*2*), 0.1 (*3*); dotted curve is mean-field density of states $N_{mf}(E)$ for $T/T_{c0} = 0.1$, dashed curve displays pseudogap behavior of density of states for $T > T_{c0}$.

5. CONCLUSIONS

In this study we have continued our investigation of characteristic features of the superconducting state using a highly simplified model of the pseudogap in a two-dimensional electron system which can have an exact solution [13]. The main simplifying assumption of our model (in addition to the condition of static fluctuations) involves using the limit $\xi \longrightarrow \infty$ for the correlation length of the antiferromagnetic fluctuations of the short-range order, which allows us to obtain fundamental equations in a fairly clear form. In particular, in this limit we can easily find an exact expression for the average superconducting gap (18). In principle, this model of a pseudogap state can be generalized to finite correlation lengths [11, 12, 19] although it is unclear how far an analysis of superconductivity outside the

scope of the mean-field approach can be carried out as part of this generalization, as we did above for the case $\xi \longrightarrow \infty$. It is qualitatively clear that finite ξ leads to some smearing of characteristics such as kinks and discontinuities, which were obtained in the $\xi \longrightarrow \infty$ model in the dependences of T_c and other characteristics of the superconducting state on ξ.

The results obtained above indicate that the pseudogap state induced by antiferromagnetic fluctuations of the short-range order (or similar fluctuations of charge density waves) not only leads to important characteristics of the normal state [11, 12, 19] but also gives fairly unusual properties of the superconducting state caused by the partial dielectrification of the electron spectrum (non-Fermi-liquid behavior) at the hot sections of the Fermi surface. These characteristics correlate with various anomalies observed in the superconducting state of underdoped high-temperature superconducting cuprates. Naturally a more serious comparison with the experiment can only be made using a more realistic approach which particularly allows for the effects of finite correlation length ξ which in real systems are relatively small. At low temperatures it is also important to allow for the fluctuation dynamics.

ACKNOWLEDGMENTS

This work was partly supported by the Russian Foundation for Basic Research (project no. 99-02-16285) and also by the State Programs "Statistical Physics" (project no. 020) and High-Temperature Superconductivity of the Russian Ministry of Science and Education (project no. 96-051).

REFERENCES

1. T. Timusk and B. Statt, Rep. Prog. Phys. **62**, 61 (1999).
2. M. Randeria, E-print archive, cond-mat/9710223 (1997).
3. M. Randeria and J. C. Campuzano, E-print archive, cond-mat/9709107 (1997).
4. V. B. Geshkenbein, L. B. Ioffe, and A. I. Larkin, Phys. Rev. B **55**, 3173 (1997).
5. V. Emery, S. A. Kivelson, and O. Zachar, Phys. Rev. B **56**, 6120 (1997).
6. J. Maly, B. Janko, and K. Levin, E-print archive, cond-mat/9710187 (1997); cond-mat/9805018 (1997).
7. V. P. Gusynin, V. M. Loktev, and S. G. Sharapov, Zh. Éksp. Teor. Fiz. **115**, 1243 (1999) [JETP **88**, 685 (1999)].
8. J. R. Kampf and A. P. Schrieffer, Phys. Rev. B **41**, 6399 (1990); **42**, 7967 (1990).
9. M. Langer, J. Schmalian, S. Grabowski, and K. H. Bennemann, Phys. Rev. Lett. **75**, 4508 (1995).
10. J. J. Deisz, D. W. Hess, and J. W. Serene, Phys. Rev. Lett. **76**, 1312 (1996).
11. J. Schmalian, D. Pines, and B. Stojkovic, Phys. Rev. Lett. **80**, 3839 (1998); Phys. Rev. B **60**, 667 (1999).
12. E. Z. Kuchinskiĭ and M. V. Sadovskiĭ, Zh. Éksp. Teor. Fiz. **115**, 1765 (1999) [JETP **88**, 968 (1999)]; E-print archive, cond-mat/9808321 (1998).
13. A. I. Posazhennikova and M. V. Sadovskiĭ, Zh. Éksp. Teor. Fiz. **115**, 632 (1999) [JETP **88**, 347 (1999)]; E-print archive, cond-mat/9806199 (1998).
14. R. Gatt, S. Christensen, B. Frazer, *et al.*, E-print archive, cond-mat/9906070 (1999).
15. D. L. Feng, W. J. Zheng, K. M. Shen, *et al.*, E-print archive, cond-mat/9908056 (1999).
16. M. V. Sadovskiĭ, Zh. Éksp. Teor. Fiz. **66**, 1720 (1974) [Sov. Phys. JETP **39**, 845 (1974)] ; Fiz. Tverd. Tela (Leningrad) **16**, 2504 (1974) [Sov. Phys. Solid State **16**, 1632 (1974)].
17. M. V. Sadovskiĭ, Zh. Éksp. Teor. Fiz. **77**, 2070 (1979) [Sov. Phys. JETP **50**, 989 (1979)].
18. M. V. Sadovskiĭ and A. A. Timofeev, Sverkhprovodimost': Fiz., Khim., Tekh. **4**, 11 (1991); J. Mosc. Phys. Soc. **1**, 391 (1991).
19. M. V. Sadovskiĭ, Pis'ma Zh. Éksp. Teor. Fiz. **69**, 447 (1999) [JETP Lett. **69**, 483 (1999)]; E-print archive, cond-mat/9902192 (1999).
20. Yu. V. Kopaev, Tr. Fiz. Inst. Akad. Nauk SSSR **86**, 3 (1975).
21. *Problems of High-Temperature Superconductivity*, Ed. by V. L. Ginzburg and D. A. Kirzhnits (Nauka, Moscow, 1977), Chap. 5.
22. G. Bilbro and W. L. McMillan, Phys. Rev. B **14**, 1887 (1976).
23. L. N. Bulaevskiĭ, S. V. Panyukov, and M. V. Sadovskiĭ, Zh. Éksp. Teor. Fiz. **92**, 672 (1987) [Sov. Phys. JETP **65**, 380 (1987)].
24. M. V. Sadovskiĭ, Sverkhprovodimost': Fiz., Khim., Tekh. **8**, 337 (1995); M. V. Sadovskiĭ, Phys. Rep. **282**, 225 (1997).
25. H. Ding, M. R. Norman, T. Yokoya, *et al.*, Phys. Rev. Lett. **78**, 2628 (1997).

Translation was provided by AIP

Journal of Experimental and Theoretical Physics, Vol. 90, No. 3, 2000, pp. 544–552.
Translated from Zhurnal Éksperimental'noĭ i Teoreticheskoĭ Fiziki, Vol. 117, No. 3, 2000, pp. 624–633.

SOLIDS
Electron Properties

Ground State of Fermi Systems with Strong Short-Range Order

Yu. B. Kudasov

Russian Federal Nuclear Center—VNIIEF, Sarov, Nizhniĭ Novgorod oblast, 607190 Russia
e-mail: kudasov@ntc.vniief.ru

Received May 21, 1999

Abstract—A new variational method is developed to calculate the ground-state energy of a fermion system with strong short-range order. As well as intrasite correlations, the Gutzwiller trial wave function explicitly contains nearest-neighbor correlations. The Kikuchi pseudo-ensemble method was used to calculate the total energy of the fermion system. The calculations were made for the paramagnetic and antiferromagnetic phases of the half-filled Hubbard model. It is shown that for two- and three-dimensional lattices the short-range order in the paramagnetic phase strongly influences the ground-state energy whereas in the antiferromagnetic phase it is insignificant. © *2000 MAIK "Nauka/Interperiodica".*

1. INTRODUCTION

Strong short-range order is one of the most important problems in the theory of strongly correlated fermions. The main difficulty encountered here involves constructing a ground state with strong short-range order and determining its energy. The fundamental aspects of the problem of short-range order may be studied using the base model of strongly correlated fermions, i.e., the Hubbard model [1–3]. The simplest variant of this model, where there is one nondegenerate band and spin 1/2 fermions can only hop to the nearest lattice site, can be formulated in the form of the following Hamiltonian:

$$H = t\sum_{\langle ij\rangle,\sigma}(a_{i\sigma}^{+}a_{j\sigma} + \text{h.c.}) + U\sum_{i} n_{i\uparrow}n_{i\downarrow}, \qquad (1)$$

where $a_{i\sigma}^{+}(a_{i\sigma})$ is the creation (annihilation) operator of a fermion of spin $\sigma = \uparrow, \downarrow$ at the ith lattice site. The angular brackets denote summation only over nearest neighbors, $n_{i\sigma} = a_{i\sigma}^{+}a_{i\sigma}$.

Several exact solutions of the Hamiltonian (1) are known: a homogeneous one-dimensional (1D) chain [4] and several special cases (see, for example [5, 6]). In the limit of an infinite-dimensional lattice ($D = \infty$) substantial simplifications of the problem are encountered and a Gutzwiller solution for the ground state of the system becomes almost exact [2, 7]. However, for lattices of intermediate dimensions, particularly 2D and 3D which are of important practical value, no exact solutions exist. Thus, numerous studies have been devoted to the analytic and numerical investigation of this problem [8–13]. In particular, the Gutzwiller trial wave function, which is exact for $D = \infty$ was used in a numerical variational Monte Carlo method [10, 11] and in an analytical procedure involving expansion in powers of $1/D + 1/D^2$ in dynamic mean-field theory [8, 12, 13]. In this latter case, it was necessary to make the typical assumption for perturbation theory methods that the structure of the wave function at finite-dimensional lattices does not differ significantly from the structure in the limit of an infinite-dimensional lattice, i.e., these solutions are in fact only valid for weak short-range order. For this reason they cannot be used in many cases of practical interest where the short-range order is known to be strong: Kondo systems, CuO_2 planes in high-temperature superconductors, and so on [8]. Hence, the main difficulty involved in studying finite-dimensional lattices is the need to allow for strong small-radius spatial correlations. In the phenomenological theory of an almost antiferromagnetic Fermi liquid, it was shown [14] that in many strongly correlated compounds the short-range order has a significant influence on the static and dynamic characteristics of the material. Thus, there is a need to develop a microscopic theory of systems with strong short-range order.

In the present paper a variational microscopic method is developed to calculate the ground-state energy of systems of fermions with strong short-range order and the ground state of the Hubbard Hamiltonian (1) is calculated for various lattices for a half-filled initial band in the paramagnetic and antiferromagnetic phases.

2. TRIAL WAVE FUNCTION

The Gutzwiller trial wave function can be expressed in the form [15]

$$|\psi\rangle = g_0^{\hat{X}}|\varphi_0\rangle, \qquad (2)$$

where $\hat{X} = \sum_i n_{i\uparrow}n_{i\downarrow}$, g_0 is a real parameter lying in the range [0, 1] for $U > 0$, $|\varphi_0\rangle$ is the initial N-particle

wave function of the uncorrelated electrons which can be constructed using Bloch functions

$$\prod_{\mathbf{k}<\mathbf{k}_{F\uparrow}} a^{+}_{\mathbf{k}\uparrow} \prod_{\mathbf{k}<\mathbf{k}_{F\downarrow}} a^{+}_{\mathbf{k}\downarrow}|0\rangle, \tag{3}$$

where $\mathbf{k}$ is the fermion wave vector and $\mathbf{k}_{F\sigma}$ is the Fermi wave vector for fermions of spin σ. It is assumed that the number of particles in the system is large but finite.

The meaning of the trial wave function (2) is that the amplitude of the fermion configurations decreases as a function of the number of doubly occupied sites in the configuration [2]. It should be noted that the N-particle trial function (2) remains antisymmetric. Moreover, since the operator on the right-hand side of expression (2) is translationally invariant, this trial wave function retains the translational symmetry of the initial wave function. In order to allow for small-radius spatial correlations in the trial wave function, we generalize the wave function (2) as [16]

$$|\psi\rangle = \prod_{\lambda} g_{\lambda}^{\hat{P}_{\lambda}}|\varphi_0\rangle, \tag{4}$$

where, in addition to the cofactor from expression (2), the product may contain a set of projection operators $\hat{P}_{\lambda}$ on all possible configurations of the state of the lattice site a the pair of neighboring sites. The real parameters g_i lie in the range $[0, \infty]$ which means that the amplitudes of the various configurations of the site pair can either decrease or increase.

We construct the trial wave function of the paramagnetic phase of the half-filled band. We have four projection operators isolating the particular state of the lattice sites:

$$\begin{aligned}
\hat{X}_1 &= \sum_i (1-n_{i\uparrow})(1-n_{i\downarrow}),\\
\hat{X}_2 &= \sum_i n_{i\uparrow}(1-n_{i\downarrow}),\\
\hat{X}_3 &= \sum_i (1-n_{i\uparrow})n_{i\downarrow},\\
\hat{X}_4 &= \sum_i n_{i\uparrow}n_{i\downarrow},
\end{aligned} \tag{5}$$

and ten projection operators on states of the pairs of nearest sites, for example

$$\begin{aligned}
\hat{Y}_1 &= \sum_{\langle ij\rangle} (1-n_{i\uparrow})(1-n_{i\downarrow})(1-n_{j\uparrow})(1-n_{j\downarrow}),\\
\hat{Y}_2 &= \sum_{\langle ij\rangle} n_{i\uparrow}n_{i\downarrow}n_{j\uparrow}n_{j\downarrow}
\end{aligned} \tag{6}$$

Table 1

Operator	Configuration		Degree of degeneracy
	site i	site j	
$\hat{Y}_1$			1
$\hat{Y}_2$	$\uparrow\downarrow$	$\uparrow\downarrow$	1
$\hat{Y}_3$	$\uparrow\downarrow$		2
$\hat{Y}_4$	$\uparrow$		2
$\hat{Y}_5$	$\downarrow$		2
$\hat{Y}_6$	$\uparrow$	$\uparrow$	1
$\hat{Y}_7$	$\uparrow$	$\downarrow$	2
$\hat{Y}_8$	$\uparrow\downarrow$	$\uparrow$	2
$\hat{Y}_9$	$\uparrow\downarrow$	$\downarrow$	2
$\hat{Y}_{10}$	$\downarrow$	$\downarrow$	1

and so on (see Table 1).

We shall subsequently confine our analysis to lattices for which the total number of pairs of nearest neighbors is $zL/2$, where z is the number of nearest neighbors of the site and L is the total number of lattice sites. We determine the normalized eigenvalues of the operators (5) and (6) as

$$\begin{aligned}
x_{\lambda}|\Phi\rangle &= L^{-1}\hat{X}_{\lambda}|\Phi\rangle,\\
y_{\lambda}|\Phi\rangle &= (zL/2)^{-1}\hat{Y}_{\lambda}|\Phi\rangle.
\end{aligned} \tag{7}$$

The eigenvalues are then coupled normalization conditions [17]

$$\sum_{\lambda} x_{\lambda} = 1, \quad \sum_{\lambda} \beta_{\lambda} y_{\lambda} = 1, \tag{8}$$

where β_{λ} is the degree of degeneracy, and self-consistency conditions [17]

$$\begin{aligned}
y_1 + y_3 + y_4 + y_5 &= x_1,\\
y_2 + y_3 + y_8 + y_9 &= x_4,\\
y_4 + y_6 + y_7 + y_8 &= x_2,\\
y_5 + y_7 + y_9 + y_{10} &= x_3.
\end{aligned} \tag{9}$$

Since the concentrations of fermions of each spin are assumed to be fixed, as in the Gutzwiller approximation there is only one independent parameter x_{λ}. Seven parameters y_{λ} are independent. For a half-filled band in the paramagnetic phase when the total spin of the system is zero, additional constraints appear:

$$y_1 = y_2, \quad y_6 = y_{10}, \quad y_4 = y_5 = y_8 = y_9, \tag{10}$$

and after introducing these, the number of independent parameters y_λ was reduced to three. We shall take $x = x_1 = x_4$, y_3, y_4, and y_7 as independent parameters. Then, taking into account the additional degeneracy formed as a result of the conditions (10), we obtain the final form of the trial wave function for the half-filled paramagnetic phase

$$|\psi\rangle = g_0^{\hat{X}} g_3^{\beta_3 \hat{Y}_3} g_4^{4\beta_4 \hat{Y}_4} g_7^{\beta_7 \hat{Y}_7} |\varphi_0\rangle = \hat{F}|\varphi_0\rangle. \quad (11)$$

We note the main properties of the trial wave function (11). The operator $\hat{F}$ is polynomial in $n_{i\sigma}$ so that the trial wave function is antisymmetric with respect to permutations. In addition, the operator $\hat{F}$ is invariant with respect to operations which transform the lattice into itself, translations, rotations, and reflections. Hence, all these symmetries are transferred from the initial wave function to the trial one. Finally, this trial wave function can control the structure of the short-range order.

3. GROUND STATE OF THE PARAMAGNETIC PHASE

We first need to calculate the norm of the trial wave function (11). Following [15, 18] we express this as

$$\langle\psi|\psi\rangle = \sum_{\{x, y_3, y_4, y_7\}} W_{\{x, y_3, y_4, y_7\}} g_0^{2Lx} g_3^{2zLy_3} g_4^{8zLy_4} g_7^{2zLy_7} = \sum_{\{x, y_3, y_4, y_7\}} R_{\{x, y_3, y_4, y_7\}}. \quad (12)$$

Here we have omitted the constant factor which is not important for the following calculations. Summation is performed over all sets $\{x, y_3, y_4, y_7\}$. The same set of independent variables can correspond to a certain number of configurations. The quantity $W_{\{x, y_3, y_4, y_7\}}$ is the number of configurations corresponding to the fixed set $\{x, y_3, y_4, y_7\}$ or the weight of this set. We shall calculate this using the Kikuchi pseudo-ensemble method [17, 19, 20]. Note that this method is exact for Bethe lattices [17]. For lattices having closed paths it only gives an approximate solution. According to the Kikuchi hypothesis, the weight of the set can be expressed in terms of the product:

$$W = \Gamma Q. \quad (13)$$

Here, for simplicity the subscripts are dropped. The quantity

$$Q = \frac{(zL/2)!}{\prod_\lambda [(zy_\lambda L/2)!]^{\beta_\lambda}} \quad (14)$$

is the number of permutations of ten elements corresponding to the pair configurations Y_λ along $zL/2$ bonds, and

$$\Gamma = \frac{L!\prod_\lambda (x_\lambda zL)!}{(zL)!\prod_\lambda (x_\lambda L)!} \quad (15)$$

is the fraction of regular permutations in the pseudo-ensemble. In expressions (14) and (15) the dependent parameters x_λ and y_λ should be expressed in terms of the independent ones as

$$x_2 = x_3 = 1/2 - x, \quad y_1 = y_2 = x - y_3 - 2y_4, \quad y_6 = y_{10} = 1/2 - x - y_7 - 2y_4. \quad (16)$$

In the thermodynamic limit $L \longrightarrow \infty$, as usual [2, 17–20], we can confine our summation to those terms of the series which are close to the maximum, i.e., for which the condition $\{x, y_3, y_4, y_7\} \longrightarrow \{x, y_3, y_4, y_7\}_{\max}$ is satisfied. The remaining terms are exponentially small. Since the function R is positive, it is convenient to seek the maximum of its logarithm instead of the function itself. We now transform all the factorials appearing in R using the asymptotic Stirling formula. We then take the logarithm of this expression and only retain the principal terms in L. It can be shown that this procedure is equivalent to the substitution $(zL/2)! \longrightarrow (L!)^{z/2}$ used in [17, 19, 20]. After direct calculations we obtain

$$L^{-1}\ln W = 2(z-1)[x\ln x + (1/2-x)\ln(1/2-x)] - z(y_2\ln y_2 + y_3\ln y_3 + 4y_4\ln y_4 + y_6\ln y_6 + y_7\ln y_7), \quad (17)$$

where y_2 and y_6 are expressed in terms of (16). The region of determination of the function $L^{-1}\ln R$ is bounded by conditions (8) and (9). For nonzero finite parameters g_i, its gradient at the boundaries is directed into this region so that the global maximum of the function $L^{-1}\ln R$ is its internal maximum. In this case, the necessary conditions for the maximum will be $\partial(\ln R)/\partial\eta_\lambda = 0$, where $\eta_\lambda = x, y_3, y_4, y_7$. Using these, we can express the parameters g_i in terms of x, y_3, y_4, y_7:

$$g_0 = \left(\frac{1/2-x}{x}\right)^{z-1}\left(\frac{x-y_3-2y_4}{1/2-x-y_7-2y_4}\right)^{z/2}, \quad g_3^2 = \frac{y_3}{x-y_3-2y_4}, \quad g_4^4 = \frac{4y_4^2}{(1/2-x-y_7-2y_4)(x-y_3-2y_4)}, \quad g_7^2 = \frac{y_7}{1/2-x-y_7-2y_4}. \quad (18)$$

Attention should be drawn to the fact that the function $L^{-1}\ln R$ is strictly upward convex in terms of the variables y_3, y_4, and y_7 for fixed x. This means that in practice we seek the maximum of the function of one implicitly defined variable rather than four variables.

In order to calculate the ground-state energy of the Hamiltonian (1), we need to calculate the first-order density matrix for the trial function obtained in Section 2:

$$\rho_1 = L^{-1}\frac{\langle\psi|\sum_{\langle ij\rangle,\sigma}(a^+_{i\sigma}a_{j\sigma} + \text{h.c.})|\psi\rangle}{\langle\psi|\psi\rangle}. \quad (19)$$

Here we encounter a significant complication compared with the Gutzwiller method because when a fermion hops from site i to site j, not only the configuration of the i–j pair changes but also that of the adjacent i–k and j–l pairs of lattice sites (Fig. 1). We take a certain lattice-fragment configuration consisting of an i–j bond and its adjacent bonds (Fig. 1) and we calculate the function W of the remaining lattice using expressions (13)–(15). Then, the fraction of the configurations containing the given fragment may be expressed in the form

$$\frac{W'}{W} = y_{(ij)}\prod_k\left(\frac{y_{(ki)}}{x_{(i)}}\right)\prod_l\left(\frac{y_{(jl)}}{x_{(j)}}\right), \quad (20)$$

where $y_{(\alpha\beta)}$ implies the value of y_λ corresponding to the bond configuration $\alpha\beta$. Now the contribution to the density matrix made by the transition from configuration 1 to configuration 2 will have the form

$$\frac{\prod_\alpha g_\alpha}{\prod_\beta g_\beta}\frac{W'(1)}{W}, \quad (21)$$

where the first cofactor is the ratio of the amplitude of configuration 1 to the amplitude of configuration 2, i.e., g_α corresponds to those bonds in configuration 2 which were absent in configuration 1 (or the converse for g_β). If configurations 1 and 2 differ by several like bonds, the parameters g_α and g_β are written in (21) in the appropriate powers. The procedure is broadly similar to the Gutzwiller method [2] where expression (21) only contained a single parameter g_0.

Using expressions (20) and (21), we can perform direct summation of all the configurations and calculate the density matrix (19):

$$\rho_1 = 4\left(2y_4(a_1a_2)^{z-1} + \frac{y_3g_7}{g_0g_3}a_1^{2(z-1)} + \frac{y_7g_0g_3}{g_7}a_2^{2z-1}\right), \quad (22)$$

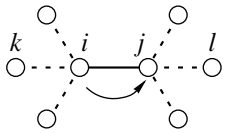

Fig. 1. Fragment of $z = 4$ lattice. When a fermion hops from site i to site j, the configurations of neighboring pairs also change.

where

$$a_1 = \frac{y_2g_4 + y_3g_4/g_3 + y_4(g_7+1)/g_4}{x},$$

$$a_2 = \frac{y_6g_4 + y_7g_4/g_7 + y_4(g_3+1)/g_4}{1/2 - x}.$$

Here and subsequently we use y_2 and y_6 instead of expressions (16) to shorten the notation. As in the Gutzwiller method, the density matrix has three terms, the first describing fermion motion in the Hubbard subband, the second and third describing transitions between the subbands. We eliminate the parameter g_i from formula (22) using (18) and after direct transformations we obtain

$$\rho_1 = 8(y_4 + \sqrt{y_3y_7})\times\left[\frac{y_4}{x(1/2-x)}(\sqrt{y_2}+\sqrt{y_3}+\sqrt{y_6}+\sqrt{y_7})^2\right]^{z-1}. \quad (23)$$

Finally, the complete energy of the fermion system can be conveniently represented in the Gutzwiller form [2]:

$$E = \frac{1}{L}\frac{\langle\psi|H|\psi\rangle}{\langle\psi|\psi\rangle} = q\varepsilon_0 + xU, \quad (24)$$

where $q = \rho_1/\rho_1^0$, ρ_1^0 is the density matrix of the uncorrelated electrons, i.e., for $U = 0$, and ε_0 is the average energy of the uncorrelated electrons. We now determine the ground-state energy by minimizing the function (24) in terms of the four variables: x, y_3, y_4, y_7. The search for the global minimum was performed numerically (using a refined Nelder–Mead simplex algorithm) and presented no difficulties because expression (24) is a smooth differentiable function without any singularities inside the region of determination.

Figure 2a gives results of calculations of the ground-state energy of the paramagnetic phase for a linear homogeneous chain ($z = 2$) with the dispersion law $\varepsilon_\mathbf{k} = -2\cos k_x$, Fig. 2b gives results for a planar square lattice ($z = 4$), $\varepsilon_\mathbf{k} = -2(\cos k_x + \cos k_y)$, and Fig. 2c gives results for a simple cubic lattice ($z = 6$), $\varepsilon_\mathbf{k} = -2(\cos k_x + \cos k_y + \cos k_z)$. Figure 3 shows the detailed structure of the ground state for a planar square lattice. Figure 4 gives

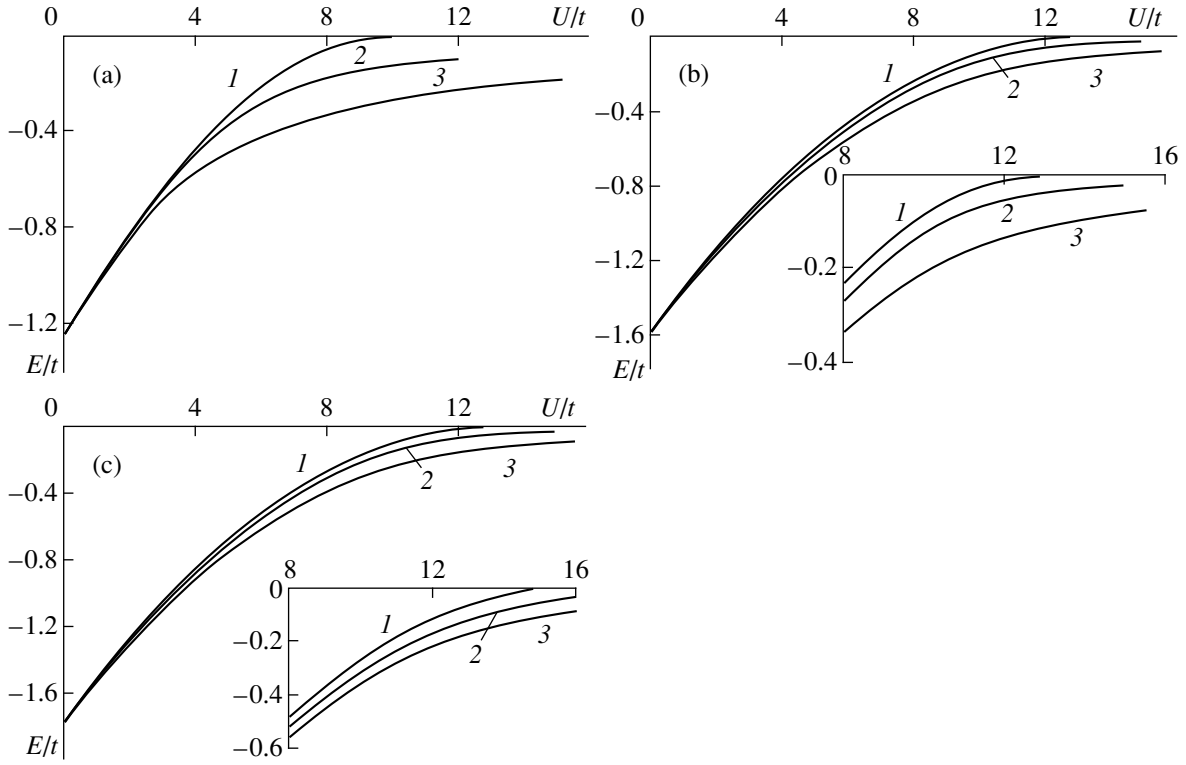

Fig. 2. Ground-state energies of fermions in the paramagnetic phases: (a) for a one-dimensional chain: Gutzwiller solution [2] (*1*), present study (*2*), exact solution [4] (*3*); and also for (b) planar square and (c) simple cubic lattices: Gutzwiller solution (*1*), VMC method [10] (*2*), present study (*3*). The inset shows an enlarged fragment of the graph near U_G.

the symmetric and antisymmetric correlation functions of a pair of nearest sites for various lattices:

$$\begin{aligned} G_s &= \langle n_\uparrow n_\uparrow\rangle' + \langle n_\downarrow n_\downarrow\rangle' = 2(y_2 + 2y_4 + y_6), \\ G_a &= \langle n_\uparrow n_\downarrow\rangle' + \langle n_\downarrow n_\uparrow\rangle' = 2(y_2 + 2y_4 + y_7). \end{aligned} \tag{25}$$

The prime in (25) denotes averaging over nearest neighbors.

In order to study the limit $D = \infty$ in the paramagnetic phase, we calculated the ground-state energy for hypercubic lattices $z = 50, 100, 200, 400, 1000$. As the dimensions of the lattice increased, the ground-state energy tended toward the Gutzwiller solution which is exact for $D = \infty$. For $z = 1000$, both solutions agreed to within 0.1% for U in the range $[0, U_C/2]$ and to within 1% in the range $[U_C/2, 2.8U_C]$, where $U_C = 8\varepsilon_0$ is the critical value of U in the Gutzwiller theory.

4. ANTIFERROMAGNETIC PHASE

In order to ensure that the trial wave function for the antiferromagnetic phase corresponded to the required translational properties, we need to select the initial wave function so that it possessed these properties. Thus, as usual [11, 21] we take the wave function $|\varphi_0^{AFM}\rangle$ of an antiferromagnetic metal (in Hubbard–Fock theory) [11, 21] as the initial wave function. The energy spectrum of the initial wave function and the magnetic moment of the sublattices then have the form [21]

$$\begin{aligned} \varepsilon_{\mathbf{k}}^{AFM} &= \frac{\varepsilon_{\mathbf{k}}}{\sqrt{1 + (\delta/\varepsilon_{\mathbf{k}})^2}}, \\ m &= \int \frac{\delta d\mathbf{k}}{\sqrt{\varepsilon_{\mathbf{k}}^2 + \delta^2}}, \end{aligned} \tag{26}$$

where $\varepsilon_{\mathbf{k}}$ is the energy spectrum of the uncorrelated fermions in the paramagnetic phase, δ is the antiferromagnetic order parameter, and integration is performed over the reduced Brillouin zone [21], $m = (\langle n_\uparrow\rangle_A + \langle n_\downarrow\rangle_B - \langle n_\downarrow\rangle_A - \langle n_\uparrow\rangle_B)/2$. In this last expression averaging is performed over sites in sublattices *A* and *B*.

In the antiferromagnetic phase the degeneracy of the operators $\hat{Y}_\lambda$ is partially lifted and their number increases (Table 2). The following expressions hold for the eigenvalues of the operators $\hat{X}_\lambda$:

$$\begin{aligned} x_2' &= x_2^A = x_3^B = 1/2 + m/2 - x, \\ x_3' &= x_3^A = x_2^B = 1/2 - m/2 - x. \end{aligned} \tag{27}$$

Then the normalization conditions (8) still hold. For a half-filled band we have additional constraints similar to (10):

$$\begin{aligned} y_1 &= y_2, \quad y_6 = y_{10}, \\ y_4 &= y_{4A} = y_{5B} = y_{8B} = y_{9A}, \\ y_5 &= y_{4B} = y_{5A} = y_{8A} = y_{9B}. \end{aligned} \tag{28}$$

The self-consistency conditions for the antiferromagnetic phase are written as

$$\begin{aligned} x_1 &= y_1 + y_3 + y_4 + y_5, \\ x_4 &= y_2 + y_3 + y_4 + y_5, \\ x_2' &= 2y_4 + y_5 + y_6, \\ x_3' &= 2y_5 + y_5 + y_6. \end{aligned} \tag{29}$$

We use expressions (28) and (29) to isolate the independent parameters in the antiferromagnetic phase of which there are six. We take the following as independent parameters: $x = x_1 = x_4$, y_3, y_4, y_5, y_6, and m and express the dependent parameters in terms of them:

$$\begin{aligned} y_2 &= x - y_3 - y_4 - y_5, \\ y_7 &= \frac{1}{2} + \frac{1}{2}m - x - y_6 - 2y_4, \\ y_{11} &= \frac{1}{2} - \frac{1}{2}m - x - y_6 - 2y_5. \end{aligned} \tag{30}$$

We now express the trial wave function of the antiferromagnetic phase in the form

$$|\psi^{AFM}\rangle = g_0^{\hat{X}} g_3^{\beta_3 \hat{Y}_3} g_4^{2\beta_4 \hat{Y}_4} g_5^{2\beta_5 \hat{Y}_5} g_7^{\beta_6 \hat{Y}_6} g_m^{\hat{M}} |\varphi_0^{AFM}\rangle, \tag{31}$$

where

$$\hat{M} = \frac{1}{2}\left[\sum_i^A (n_{i\uparrow} - n_{i\downarrow}) + \sum_i^B (n_{i\downarrow} - n_{i\uparrow})\right]$$

is an operator corresponding to the parameter m.

The calculations of the ground-state energy are similar to those for the paramagnetic phase. By calculating the function $L^{-1}\ln R$ we obtain the following expression for the weight of the set of independent variables:

$$\begin{aligned} L^{-1}\ln W &= (z-1)[2x\ln(x + x_2'\ln x_2' + x_3'\ln x_3')] \\ &- \frac{z}{2}(2y_2\ln y_2 + 2y_3\ln y_3 + 4y_4\ln y_4 + 4y_5\ln(y_5) \\ &+ 2y_6\ln y_6 + y_7\ln y_7 + y_{11}\ln y_{11}). \end{aligned} \tag{32}$$

Here and subsequently x_2', x_3', y_2, y_7, and y_{11} are used as abbreviated notation for expressions (27) and (30).

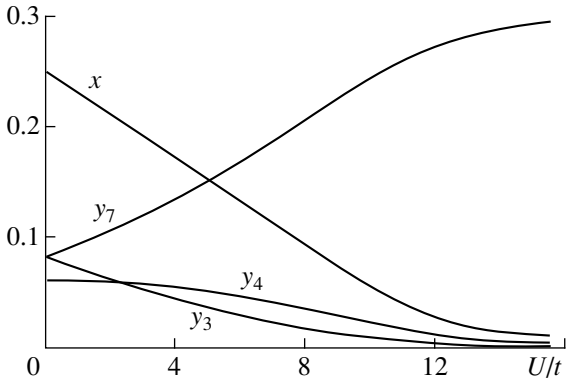

Fig. 3. Detailed structure of the ground state for a simple square lattice.

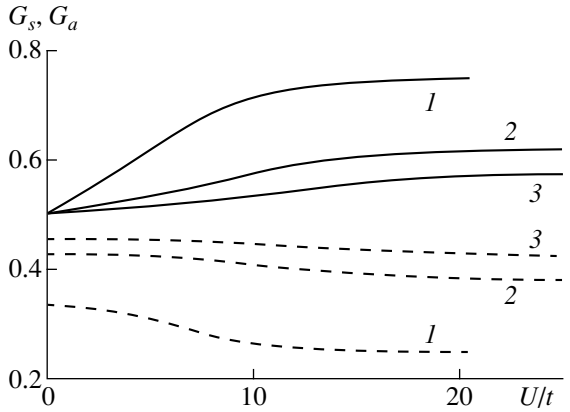

Fig. 4. Symmetric G_s (dashed curves) and antisymmetric G_a (solid curves) correlation functions (25) for a 1*D* chain (*1*), planar square (*2*) and simple cubic (*3*) lattices.

Differentiating the function $L^{-1}\ln R$ with respect to the independent parameters yields the conditions

$$\begin{aligned} g_0 &= \left(\frac{\sqrt{x_2'x_3'}}{x}\right)^{z-1}\left(\frac{y_2}{\sqrt{y_7 y_{11}}}\right)^{z/2}, \\ g_3^2 &= \frac{y_3}{y_2}, \quad g_4^2 = \frac{y_4}{y_7 y_2}, \\ g_5^2 &= \frac{y_5}{y_2 y_{11}}, \quad g_6^2 = \frac{y_6}{y_7 y_{11}}, \\ g_m^2 &= \left(\frac{x_3'}{x_2'}\right)^{(z-1)/2}\left(\frac{y_7}{y_{11}}\right)^{z/4}. \end{aligned} \tag{33}$$

We calculate the density matrix (19) for the antiferromagnetic trial wave function $|\psi^{AFN}\rangle$. We eliminate the parameters g_i using the substitution (33) and express the density matrix only in terms of independent parameters. Then, ρ_1 can be represented as a sum of two terms: $\rho_1 = \rho_{band} + \rho_{inter}$, where the first term is responsible for fermion motion in the Hubbard subbands and

Table 2

Operator	Configuration		Degree of degeneracy
	sublattice site A	sublattice site B	
$\hat{Y}_1$			1
$\hat{Y}_2$	↑↓	↑↓	1
$\hat{Y}_3$	↑↓		2
$\hat{Y}_{4A}$	↑		1
$\hat{Y}_{4B}$		↑	1
$\hat{Y}_{5A}$	↓		1
$\hat{Y}_{5B}$		↓	1
$\hat{Y}_6$	↑	↑	1
$\hat{Y}_{7A}$	↑	↓	1
$\hat{Y}_{7B}$	↓	↑	1
$\hat{Y}_{8A}$	↑↓	↑	1
$\hat{Y}_{8B}$	↑	↑↓	1
$\hat{Y}_{9A}$	↑↓	↓	1
$\hat{Y}_{9B}$	↓	↑↓	1
$\hat{Y}_{10}$	↓	↓	1

the second is responsible for transitions between subbands. After direct calculations similar to those for the paramagnetic phase we obtain

$$\rho_{band} = 4\frac{L_1 L_2 \sqrt{y_4 y_5}}{x^{z-1}}\left[\left(\frac{y_7}{y_{11}}\right)^{z/4}\frac{1}{(x_2')^{z-1} g_m^2} + \left(\frac{y_{11}}{y_7}\right)^{z/4}\frac{g_m^2}{(x_3')^{z-1}}\right],$$

$$\rho_{inter} = 2\frac{\sqrt{y_3}}{x^{z-1}} \times \left[\frac{y_7^{(2-z)/4} y_{11}^{z/4} L_1^2 g_m^2 + y_{11}^{(2-z)/4} y_7^{z/4} L_2^2 g_m^{-2}}{(x_2' x_3')^{(z-1)/2}} + \frac{y_7^{(z+2)/4} L_1^2}{y_{11}^{z/4} g_m^2}\left(\frac{x_3'}{(x_2')^3}\right)^{(z-1)/2} + \frac{y_{11}^{(z+2)/4} L_2^2 g_m^2}{y_7^{z/4}}\left(\frac{x_2'}{(x_3')^3}\right)^{(z-1)/2}\right], \quad (34)$$

where the following notation is introduced

$$L_1 = (\sqrt{y_2 y_4} + \sqrt{y_3 y_4} + \sqrt{y_5 y_6} + \sqrt{y_4 y_7})^{z-1},$$

$$L_2 = (\sqrt{y_2 y_5} + \sqrt{y_3 y_5} + \sqrt{y_4 y_6} + \sqrt{y_5 y_{11}})^{z-1}.$$

The total fermion energy in the antiferromagnetic phase can also be reduced to the Gutzwiller form:

$$E = \frac{1}{L}\frac{\langle \psi^{AFM}|H|\psi^{AFM}\rangle}{\langle \psi^{AFM}|\psi^{AFM}\rangle} = q\varepsilon_0^{AFM}(m) + xU. \quad (35)$$

The average energy of an uncorrelated fermion $\varepsilon_0^{AFM}(m)$ is calculated from the energy spectrum (26) and is a function of m. This dependence is implicitly given by the expressions (26). For this reason the value of the density matrix for the uncorrelated fermions $\rho_1^0(m)$ which appears in the band constriction factor $q = \rho_1/\rho_1^0(m)$ also depends on m and should be determined as the value of ρ_1 for $U = 0$ and some fixed m. The ground-state energy is calculated by minimizing the total energy (35) with respect to the variables x, y_3, y_4, y_5, y_6, and m. The function (35), despite being somewhat cumbersome, is a smooth differentiable function without any singularities inside the region of determination defined by expressions (27)–(30). Figure 5 gives results of calculations of the ground-state energy for a homogeneous chain. For planar and simple cubic lattices the ground-state energy almost agrees with the results of numerical calculations using the variational Monte Carlo (VMC) method.

5. DISCUSSIONS AND CONCLUSIONS

It is useful to compare the results of calculations of the ground-state energy made in the present study with the results obtained by the VMC method [10, 11] (see Figs. 2 and 5). In the VMC method the calculations are based on the Gutzwiller trial function (2), i.e., nonlocal correlations are virtually neglected. In the present study the ground-state energy is obtained for a trial function which explicitly includes nearest-neighbor correlations. The larger-radius correlations in our model obey the superpositional hypothesis [17]. Thus, the difference between the ground-state energies obtained by these two methods is attributed to the short-range correlations between the fermions in the ground state. For a one-dimensional chain (Fig. 2a) the difference in the ground-state energies is negligible and the results of the VMC method are not shown in the figure. For planar square and simple cubic lattices in the paramagnetic phase (Figs. 2b and 2c) it can be seen that near U_C the ground-state energy of the trial wave function (11) is substantially lower (two or three times) than that obtained by the VMC method, i.e., in the paramagnetic phase the short-range order substantially reduces the ground-state energy. The large difference between our results for the paramagnetic phase and the expansion

$1/D + 1/D^2$ [12, 13] also indicates that the nearest correlations for 2*D* and even for 3*D* lattices are fairly strong, i.e., perturbation theory methods are hardly suitable here. In the antiferromagnetic phase the influence of the short-range order is weak, and the ground-state energies obtained by the VMC method and the method described above are almost the same. The difference is within 1%. It can be said that the antiferromagnetic order impedes the establishment of short-range order.

We obtained the ground-state energy of the fermion system in analytic form and only used numerical calculations to minimize it. Consequently our proposed method possesses no indeterminacy, which is a characteristic of cluster methods such as Monte Carlo methods, on going to the limit of a large number of particles. It should also be noted that the Kikuchi pseudo-ensemble method can be used to study correlations, not only of a pair of sites, but also higher-order ones such as triple and so on [17, 20]. Closed paths on the lattice can then be included in the analysis [17, 20] and a real lattice can gradually be approached.

It can be seen from Fig. 4 that an exchange-correlation hole forms as U increases. For $U = 0$ no antisymmetric fermion spin correlations are observed ($G_a = 0.5$) but fermion correlations of the same spin do exist ($G_s < 0.5$), i.e., an exchange hole exists for the noninteracting fermions. It should be stressed that in this method an exchange hole at $U = 0$ occurs naturally when the energy is minimized with respect to the parameters y_λ. As the dimensions of the lattice increase the exchange-correlation hole around the electron gradually disappears and our solution tends to the Gutzwiller solution. Note that the correlation functions (25) do not uniquely describe the ground state of the Fermi system: this requires a complete set of independent parameters (see Fig. 3).

In the limit $|t|/U \ll 1$ the functions G_s and G_a tend to a certain constant value. This behavior occurs because for large U the half-filled Hubbard model is the same as the Heisenberg model for spin 1/2 which contains only one parameter $J(= 4t^2/U)$. If, before calculating the correlation functions the Heisenberg model is reduced to the dimensionless form ($H = \sum_{\langle ij \rangle} \mathbf{S}_i \mathbf{S}_j$), it becomes obvious that G_s and G_a must be constant when $|t|/U \ll 1$. We also note that unlike the well-known Hubbard III solution, the antiferromagnetic fermion correlations in this limit do not disappear, even in the absence of long-range order, which is consistent with the results of studying the ground state in the Heisenberg model [22].

A detailed analysis of the spectrum of elementary excitations and thermodynamic properties is outside the scope of the present study. Nevertheless, on the basis of the conclusions reached in [23], we can postulate that for the paramagnetic phase the effective electron mass will be renormalized by the factor q^{-1} and in the antiferromagnetic phase the quasiparticle spectrum will be renormalized by this factor and simultaneously deformed as the sublattice moment m increases as a result of a change in the initial spectrum (26).

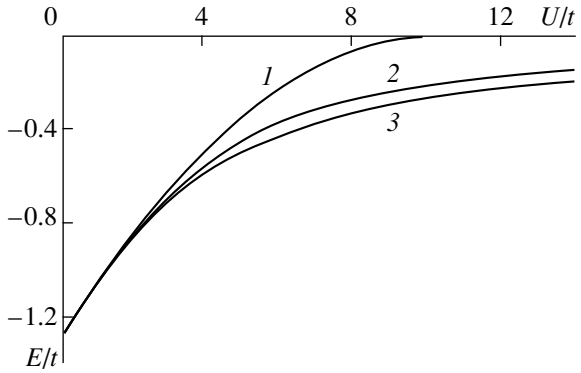

Fig. 5. Ground-state energy of fermions in the antiferromagnetic phase for a one-dimensional chain: (*1*) Gutzwiller solution [2], (*2*) present study, and (*3*) exact solution [4].

To conclude, we shall briefly discuss the behavior of the metal–insulator transition at $T = 0$ K. In the paramagnetic phase the ground-state energy as a function of U has no singularities whatsoever. As U increases, the quasiparticle band narrows continuously. Similar results were obtained in the dynamic mean-field theory [8, 12, 13] and by the VMC method [10, 11]. However, this scenario is at variance with the Hubbard III solutions where the ground-state energy has a singular point. Unfortunately, it is fairly difficult to study the change in the state of the paramagnetic phase experimentally, since for large U these changes are frequently masked by first-order paramagnetic metal–antiferromagnetic insulator transitions, as occurs in a $(V_{1-x}Ti_x)_2O_3$ solid solution at $T = 0$ K. It follows from the Lieb theorem on the ground state of the half-filled Hamiltonian (1) that a first-order transition is generally impossible at $T = 0$ K [24]. In other words, these transitions are not a property of the Hubbard model. Recently examples of strongly correlated compounds of *d*-metals have appeared where the quasiparticle band in the paramagnetic phase is extremely narrow (for example, LiV_2O_4 [25]). This supports the scenario proposed above. In real materials at finite temperatures a metal–insulator transition may take place in the paramagnetic phase as a result of the loss of coherence in the quasiparticle band. Thus, the quasiparticle lifetime should be $\tau \gg \hbar/q\varepsilon_0$. It can be seen that as the band becomes narrower, this condition becomes increasingly stringent.

In the calculations made in the present study, the energy of the antiferromagnetic phase was lower than the energy of the paramagnetic phase in all cases. However, in a narrow region $U < t$ the energy difference between the two phases is small and the numerical results are not completely reliable. Thus, it is desirable to make an analytic analysis of the ground-state energy

in the paramagnetic and antiferromagnetic phases near the point $U = 0$.

ACKNOWLEDGMENTS

The author is grateful to J. Brooks and W. Lewis for their interest in this work and invaluable support. The author thanks V.N. Zharkov for valuable discussions and P. Fulde for hospitality during his stay at the Max-Plank-Institut für Physik Komplexer Systeme (Dresden).

This work was carried out under project no. 829 of the International Science and Technology Center.

REFERENCES

1. J. Hubbard, Proc. R. Soc. London, Ser. A **276**, 238 (1963).
2. M. C. Gutzwiller, Phys. Rev. **137**, A1726 (1965).
3. J. Kanamory, Prog. Theor. Phys. **30**, 275 (1963).
4. H. Lieb and F. Wu, Phys. Rev. Lett. **20**, 1445 (1968).
5. E. B. Kolomeinski and J. P. Straley, Rev. Mod. Phys. **68**, 175 (1996).
6. U. Brandt and A. Giesekus, Phys. Rev. Lett. **68**, 2648 (1992).
7. W. Metzner and D. Vollhardt, Phys. Rev. Lett. **62**, 324 (1989).
8. A. Georges, G. Kotliar, W. Krauth, and M. J. Rozenberg, Rev. Mod. Phys. **68**, 13 (1996).
9. G. Senatore and N. H. March, Rev. Mod. Phys. **66**, 445 (1994).
10. H. Yokoyama and H. Shiba, J. Phys. Soc. Jpn. **56**, 1490 (1987).
11. H. Yokoyama and H. Shiba, J. Phys. Soc. Jpn. **56**, 3582 (1987).
12. W. Metzner and D. Vollhardt, Phys. Rev. Lett. **59**, 121 (1987).
13. F. Gebhard, Phys. Rev. B **41**, 9452 (1990).
14. D. Pines and B. Stojkovic, Phys. Rev. B **55**, 8576 (1997).
15. D. Vollhardt, Rev. Mod. Phys. **56**, 99 (1984).
16. Yu. B. Kudasov, Phys. Lett. A **245**, 153 (1998).
17. J. M. Ziman, *Models of Disorder; the Theoretical Physics of Homogeneously Disordered Systems* (Cambridge Univ. Press, Cambridge, 1979; Mir, Moscow, 1982).
18. T. Ogawa, K. Kanda, and T. Matsubara, Prog. Theor. Phys. **53**, 614 (1975).
19. R. Kikuchi, Phys. Rev. **81**, 988 (1951).
20. R. Kikuchi and S. G. Brush, J. Chem. Phys. **47**, 195 (1967).
21. P. J. des Cloizeaux, J. Phys. (Paris) **20**, 606 (1959).
22. E. Manousakis, Rev. Mod. Phys. **63**, 1 (1991).
23. W. F. Brinkman and T. M. Rice, Phys. Rev. B **2**, 4302 (1970).
24. A. Auerbach, *Interacting Electrons and Quantum Magnetism* (Springer, New York, 1994).
25. S. Kondo, D. S. Johnston, C. A. Swenson, *et al.*, Phys. Rev. Lett. **78**, 3729 (1997).

Translation was provided by AIP

Journal of Experimental and Theoretical Physics, Vol. 90, No. 3, 2000, pp. 553–561.
Translated from Zhurnal Éksperimental'noĭ i Teoreticheskoĭ Fiziki, Vol. 117, No. 3, 2000, pp. 634–643.

NONLINEAR PHYSICS

Self-Similar Solutions of Equations of the Nonlinear Schrödinger Type

V. G. Marikhin[1]*, A. B. Shabat[1], M. Boiti[2], and F. Pempinelli[2]**

[1]*Landau Institute of Theoretical Physics, Russian Academy of Sciences, Moscow, 117940 Russia*
[2]*Dipartimento di Fisica dell'Università and Sezione, Lecce, Italy*
**e-mail: mvg@itp.ac.ru*
***e-mail: Marco.Boiti@le.infn.it*
Received September 14, 1999

Abstract—A study is made of self-similar solutions of an entire family of one-dimensional integrable dynamic systems of the nonlinear Schrödinger equation type. This family is reduced to one of three canonical forms corresponding to a Toda chain, a Volterra chain, or to the Landau–Lifshitz model, which can also be reduced to three self-similar systems coupled by Miura transformations with the fourth Painleve equation. A commutative representation is constructed for this equation. A relationship is established between the poles of the rational solutions of the fourth Painleve equation and the steady-state distribution of the electric charges in a parabolic potential. A self-similar solution is constructed for the spin dynamics. An exact solution is obtained for the nonlinear Schrödinger equation with variable dispersion (optical soliton). © *2000 MAIK "Nauka/Interperiodica".*

1. INTRODUCTION

Self-similar solutions are useful for studying various physical applications of integrable systems. This derives from the fact that the asymptotic form of any solution is self-similar. Since integrable systems are being studied, self-similar solutions can be constructed merely by using their asymptotic form. This is a particular form of the Painleve test.

In the present study we establish a relationship between the self-similar solutions of a family of nonlinear Schrödinger equations and the fourth Painleve equation.

Despite being studied for many years (see, for example [1]), the problem of self-similar solutions is far from complete. In particular, the question of the necessary set of parameters has not yet been comprehensively studied. The aim of the present study is to construct equations for self-similar solutions of an entire family of nonlinear Schrödinger equations and also to obtain some interesting particular solutions.

We shall analyze integrable generalizations of the nonlinear Schrödinger equation written in the form of the Lagrange variational problem

$$\delta\iint(L_0 + V(p, q, q_x))dxdt = 0,$$
$$L_0 = iqp_t + p_xq_x. \tag{1}$$

We are mainly interested in the case (see [2])

$$V = \varepsilon p^2z^2 + \alpha pz^2 + \beta z^2 + \gamma p^2z + \delta p^2,$$
$$z = q_x, \tag{2}$$

when the potential $V(p, q, q_x)$ does not depend on q. In this case, the pair of equations for p, $z = q_x$ corresponding to (1)

$$ip_t = (V_z + p_x)_x, \quad iz_t = (V_p - z_x)_x, \tag{3}$$

has three zeroth-order conservation laws (see [3])

$$p_t + j_x = 0 \tag{4}$$

with densities ρ equal to p, z, and pz, respectively. This property is characteristic and isolates the system (3) among systems having the general form

$$iu_t - u_{xx} = F(u, v, u_x, v_x),$$
$$iv_t + v_{xx} = G(u, v, u_x, v_x). \tag{5}$$

This study is constructed as follows. In Section 2 we show that by means of translation and dilation transformations, any Lagrangian of the type (1) can be reduced to one of the canonical forms coupled by Miura transformations. Equations for the self-similar solutions will be obtained for each of these forms.

In Section 3 we consider various representations of the fourth Painleve equation and in particular a commutative representation of this equation.

We establish that if electrical charges are positioned at points in a complex plane corresponding to the position of the poles of any rational solution of the fourth Painleve equation, where the magnitude of these charges should be equal to the residue at this pole, this charge configuration is in equilibrium in a parabolic potential.

We also show that self-similar solutions of the nonlinear Schrödinger equation corresponding to the well-

known collapsing solution (see, for example [4]) exhibit $\mathbb{Z}_3$ symmetry like the solution of the fourth Painleve equation.

Section 4 is devoted to a study of the Landau–Lifshitz model. We construct a parametrization of the spin vector in terms of solutions of the auxiliary spectral problem and we obtain a polynomial solution for the spin dynamics in the self-similar regime.

We also obtain a particular self-similar solution for the nonlinear Schrödinger equation with variable dispersion, i.e., an optical soliton.

2. CANONICAL FORMS AND SELF-SIMILAR FORMULATION

Here we give the explicit form of the transformation of the Lagrangian (1) to one of the canonical forms.

2.1. Landau–Lifshitz Model $\epsilon \neq 0$.

By Using the Translations

$$P = p - \frac{\alpha}{2\epsilon}, \quad Q = q - \frac{\gamma}{2\epsilon}x - \frac{\alpha\delta}{\epsilon}t,$$
$$X = x + \frac{\alpha\gamma}{\epsilon}t$$

the Lagrangian (1) is reduced to the form

$$L = L_0 + \epsilon p^2 z^2 + \left(\delta - \frac{\gamma^2}{4\epsilon}\right)p^2 + \left(\beta - \frac{\alpha^2}{4\epsilon}\right)z^2. \quad (6)$$

Using the dilations $p \longrightarrow -p/\epsilon$ and $t \longrightarrow -t/\epsilon$ and changing the notation of the constants, we obtain

$$L_1 = L_0 - p^2 z^2 + \nu_1^2 p^2 + \nu_2^2 q_x^2. \quad (7)$$

Of particular interest is the isotropic Landau–Lifshitz model ($\beta = 0$, $\delta = 0$), i.e.,

$$L = L_0 - p^2 z^2. \quad (8)$$

2.2. Volterra Model ($\epsilon = 0$, $\alpha \neq 0$, $\gamma = 0$).

The Lagrangian (1) is Reduced to the Form

$$L_2 = L_0 + pz^2 + p^2 z \quad (9)$$

by means of the translations

$$P = p - \frac{\beta}{\alpha}, \quad Q = q - \frac{\delta}{\gamma}x - \frac{\delta^2\alpha}{\gamma^2}t - \frac{2\beta\delta}{\alpha}t, \quad (10)$$
$$X = x + 2\left(\frac{\alpha\delta}{\gamma} + \frac{\gamma\beta}{\alpha}\right)t$$

and the dilations

$$p \longrightarrow \frac{p}{\gamma}, \quad q \longrightarrow \frac{q}{\alpha}.$$

2.3. Toda Model ($\epsilon = 0$, $\alpha \neq 0$, $\gamma \neq 0$).

The Lagrangian (1) is Reduced to the Form

$$L_3 = L_0 + pz^2 + p^2 \quad (11)$$

by using the sequence of transformations

$$P = p - \frac{\beta}{\alpha}, \quad Q = q - 2\frac{\beta\delta}{\alpha}t \quad (12)$$

$$p \longrightarrow \frac{p}{\delta}, \quad q \longrightarrow \frac{q}{\alpha}. \quad (13)$$

We note that $p \longleftrightarrow q_x \rightleftharpoons \alpha \longleftrightarrow \gamma$. The other cases correspond to the linear problem.

In order to avoid confusion, we rewrite the equations (3) corresponding to the Lagrangians L_1, L_2, and L_3 using the notation

$$i\hat{p}_t = [2(\nu_2^2 - \hat{p}^2)\hat{z} + \hat{p}_x]_x,$$
$$i\hat{z}_t = [2(\nu_1^2 - \hat{z}^2)\hat{p} - \hat{z}_x]_x, \quad (14)$$

$$ia_t = [2ab + a^2 + 2\mu a + a_x]_x,$$
$$ib_t = [2ab + b^2 + 2\mu b - b_x]_x, \quad (15)$$

$$iz_t = (2p + z^2 - z_x)_x, \quad ip_t = (2zp + p_x)_x. \quad (16)$$

The coupling between these equations is given by the formulas

$$p = a_x + ab, \quad z = a + b + \mu, \quad (17)$$

$$a = \frac{\hat{p}_x}{\nu_2 + \hat{p}} + (\hat{p} - \nu_2)(\nu_1 - \hat{z}),$$
$$b = -(\hat{p} + \nu_2)(\hat{z} + \nu_1). \quad (18)$$

In particular, formula (18) couples the solutions of the equations (15) for $\mu = 2\nu_1\nu_2$ with the solutions (14). We also note that the right-hand side ρ of these transformation formulas is the density of the zeroth-order conservation law (4):

$$\rho = c_1 pz + c_2 p + c_3 z + c_4 + \partial_x \varphi(p, z),$$

whose form does not depend on the specific choice of equation (3).

The self-similar solutions of the system of equations (3) are determined by the simplest choice of self-similar formulation:

$$p = k^m(t)P'(\xi), \quad z = k^n(t)Q'(\xi),$$
$$\xi = xk(t), \quad k' = 2k^3, \quad (19)$$

where the primes denote differentiation with respect to the corresponding arguments. In this case, the condi-

tion of generalized homogeneity is imposed on the potential $V(p, z)$

$$V(k^m p, k^n z) = k^{m+n+1} V(p, z), \tag{20}$$

which allows separation of the variables ξ and t in the equations (3). For the self-similar solutions (3) we thus obtain the determining system of ordinary differential equations

$$\begin{aligned} 2i(m_1 P + c_1 + \xi P') - P'' &= V_z(P', Q'), \\ 2i(n_1 Q + c_2 + \xi Q') + Q'' &= V_p(P', Q'), \end{aligned} \tag{21}$$

where $m_1 = m - 1$, $n_1 = n - 1$, and c_1 and c_2 are integration constants. The choice of factors m and n in (21) is determined by the condition (20). These determining equations can lower the order and have the first integral

$$\begin{aligned} &2i[\xi P'Q' + (m + n - 1)R + c] \\ &= Q'P'' - P'Q'' + (zV_z + pV_p - V)(P', Q'), \end{aligned} \tag{22}$$

where $R' = P'Q'$. The existence of this integral is associated with the additional conservation law (4) having the density $\rho = pz$ and the right-hand side of (22) contains the corresponding flux j.

In particular, for the Lagrangian L_2 with $V = pz^2 + p^2 z$ condition (20) is satisfied for $m = n = 1$ and the determining system for the self-similar solutions is written in the following form:

$$\begin{aligned} 2i\xi a + c_1 - a' &= 2ab + a^2, \\ 2i\xi b + c_2 + b' &= 2ab + b^2, \end{aligned} \tag{23}$$

where $a = P'$ and $b = Q'$. It is easy to confirm that eliminating either of the unknown functions a or b yields the fourth Painleve equation (see [5]):

$$yy_{\eta\eta} = \frac{1}{2}y_\eta^2 + \frac{3}{2}y^4 + 4\eta y^3 + 2(\eta^2 - \alpha)y^2 + \beta. \tag{24}$$

In fact, if $y = y(\eta, \alpha, \beta)$ satisfies equation (24), a and b have the following form:

$$\begin{aligned} a &= \kappa y\left(\kappa\xi, -1 + i\left(\frac{c_2}{2} - c_1\right), \frac{1}{2}c_2^2\right), \\ b &= \kappa y\left(\kappa\xi, 1 + i\left(\frac{c_1}{2} - c_2\right), \frac{1}{2}c_1^2\right), \\ \kappa^2 &= -i. \end{aligned} \tag{25}$$

Quite clearly, the transformation formulas (17) and (18) and the scaling transformations allow us to express the self-similar solutions of the entire class of equations (3) and (2) in terms of the solutions (24) in some way or another. It is less obvious that any integrable generalization of the nonlinear Schrödinger equation (see [2]) reduces to these Lagrange equations.

3. FOURTH PAINLEVE EQUATION AND COULOMB GAS

The fourth Painleve transcendent is closely related to two auxiliary linear problems which may be expressed in the form

$$\Psi_{xx} = U(x, \lambda)\Psi. \tag{26}$$

Here the potential $U(x, \lambda)$ is a quadratic or linear function of the spectral parameter λ, respectively.

In the quadratic case the spectral dependence (58) reduces to (26) with the following parametrization $U(x, \lambda)$:

$$4U(x, \lambda) = (z - \lambda)^2 + 2z_x - 4p. \tag{27}$$

We show that the equations

$$\begin{aligned} &\psi_{xx} + (z - \lambda)\psi_x + p\psi, \\ &\lambda\psi_\lambda = (\lambda + x + z)\psi_x - p\psi \end{aligned} \tag{28}$$

form a Lax pair for the fourth Painleve equation. In fact, substituting

$$\begin{aligned} \psi_\lambda &= A\psi_x + B\psi \longrightarrow \psi_{x\lambda} \\ &= [A_x + B + (\lambda - z)A]\psi_x + [B_x - pA]\psi \end{aligned}$$

into

$$\psi_{xx\lambda} + (z - \lambda)\psi_{x\lambda} + p\psi_\lambda = \psi_x$$

yields the equations

$$\begin{aligned} -A_{xxx} + 4UA_x + 2U_x A &= \lambda - z, \\ 2B_x &= 1 + (zA - \lambda A - A_x)_x. \end{aligned} \tag{29}$$

The first of these equations for the case $\lambda A = \lambda + y(x)$ gives

$$\begin{aligned} 2yy_{xx} - y_x^2 &= 3y^4 - 4xy^3 + (x^2 + 2c_1)y^2 + c_2, \\ y &= z + x, \end{aligned} \tag{30}$$

which apart from trivial dilations of y and x is the same as equation (24) for the fourth Painleve equation.

Note that in this particular case $\lambda A = \lambda + y(x)$ the equations (29) may be rewritten in the form

$$\begin{aligned} z_x &= 2p + z^2 + zx + c_1, \\ (p_x + 2pz + px)_x + p &= 0 \end{aligned}$$

and z can be eliminated rather than p. This gives

$$\begin{aligned} Y_{xx}^2 + 4Y_x(Y_x^2 + \tilde{c}_1 Y_x + \tilde{c}_2) &= (Y - xY_x)^2, \\ Y_x &= p, \end{aligned} \tag{31}$$

where $\tilde{c}_1 = c_1 + 1$.

Formulas (61) and (28) clearly define the self-similar solutions (62).

In addition to equations (28) describing isomonodromic deformations coupled with the fourth Painleve

equation, an important role in the theory of this equation is played by the linear Schrödinger equation

$$\psi_{xx} = (u(x) - \lambda)\psi, \tag{32}$$

which corresponds to a linear potential $U(x, \lambda)$ with respect to λ in (26). The discrete symmetries (24) then correspond to Darboux transformations for the Schrödinger equation and the fourth Painleve equation itself is replaced by an equivalent system of first-order equations [6]

$$\begin{aligned} g_1' &= g_1(g_3 - g_2) + \alpha_1, \\ g_2' &= g_2(g_1 - g_3) + \alpha_2, \\ g_3' &= g_3(g_2 - g_1) + \alpha_3, \end{aligned} \tag{33}$$

with the additional first integral

$$g_1 + g_2 + g_3 = x\gamma, \quad \gamma = \alpha_1 + \alpha_2 + \alpha_3. \tag{34}$$

Taking into account the first integral, we can easily check [see (23)] that each function $g_j \equiv j$, $j = 1, 2, 3$ satisfies equation (24):

$$\begin{aligned} 2yy_{xx} - y_x^2 &= y^2(3y^2 - 4\gamma xy + \gamma^2 x^2 + 2c_j) - \alpha_j^2, \\ c_j &= \alpha_{j+2} - \alpha_{j+1}. \end{aligned} \tag{35}$$

Expressing g_2 in terms of g_1, we obtain one of the Backlund transformations for (24):

$$2\tilde{y} = \frac{\alpha_1 - y'}{y} - y + \gamma x.$$

The function $\tilde{y}$ satisfies equation (24) because of (35) but with modified parameters α, β.

One of the applications of (33) is an elegant formula which refines the relationship between equations (30) and (31). We introduce the notation

$$\begin{aligned} Y = g_1g_2g_3 + \alpha_1 g_2 - \alpha_2 g_1 &\longrightarrow Y' = \gamma h, \\ h &= g_1g_2. \end{aligned}$$

Using the first integral $x\gamma = g_1 + g_2 + g_3$ and the formulas

$$\begin{aligned} \frac{h'}{h} &= g_2\left(\frac{\alpha_1}{h} - 1\right) + g_1\left(\frac{\alpha_2}{h} + 1\right), \\ \frac{Y}{h} - x\gamma &= g_2\left(\frac{\alpha_1}{h} - 1\right) - g_1\left(\frac{\alpha_2}{h} + 1\right), \\ \gamma h &= Y', \end{aligned}$$

we can express g_1 and g_2 in terms of Y and its derivatives. As a result we obtain a second-order nonlinear ordinary differential equation

$$Y_{xx}^2 = \gamma^2(Y - xY_x)^2 + 4\gamma^{-1}Y_x(\alpha_1 - Y_x)(\alpha_2 + Y_x). \tag{36}$$

It is useful to note that in the limit $\gamma \longrightarrow 0$ the functions $h_i = g_ig_{i+1} + \mu_{i+1}$, $i \in \mathbb{Z}_3$ satisfy the equation for elliptic functions

$$\frac{1}{2}h'' + \frac{\partial}{\partial h}(h - \mu_1)(h - \mu_2)(h - \mu_3) = 0,$$

where $\alpha_n = \mu_n - \mu_{n+1}$. The obvious relationship between this equation and (36) is used in the theory of asymptotic integration of the fourth Painleve equation.

The representation (33) significantly simplifies the construction of known families of particular solutions of equation (24). In particular, the canonical reduction $g_3 = \alpha_3 = 0$ to lower the order of the system (33) yields a single-parameter family of solutions of (24) expressed in terms of Hermite functions. In fact, for $g_3 \equiv 0$ we find $g_1 = \gamma x - g_2$, and thus g_2 satisfies the Riccati equation

$$g_2' = \gamma x g_2 - g_2^2 + \alpha_2.$$

Substituting $g_2(x) = \lambda y'(\lambda x)/y(\lambda x)$ reduces the last equation to the Hermite equation

$$y'' - 2xy' - 2\frac{\alpha_2}{\gamma}y = 0. \tag{37}$$

Finally, as we can easily confirm by differentiating, the transformation

$$\begin{aligned} \hat{g}_1 &= g_1, \quad \hat{g}_2 = g_2 - \frac{\alpha_1}{g_1}, \\ \hat{g}_3 &= g_3 + \frac{\alpha_1}{g_1}; \quad \hat{\alpha}_1 = -\alpha_1, \\ \hat{\alpha}_2 &= \alpha_2 + \alpha_1, \quad \hat{\alpha}_3 = \alpha_3 + \alpha_1 \end{aligned} \tag{38}$$

converts the solution (33) back into a solution.

3.1. Rational Solutions

It is well-known [7] that equation (24) has rational solutions for special values of the parameters α, β. It is known [8] that for rational solutions (33) the following relations hold

$$\begin{aligned} \alpha_j &= \frac{\gamma}{3}\gamma_j, \quad \gamma_j \in \mathbb{Z}, \\ \gamma_1 + \gamma_2 + \gamma_3 &= 3, \quad \gamma_1 \equiv \gamma_2 \equiv \gamma_3 \pmod 3. \end{aligned} \tag{39}$$

Formulas (39) imply that $\boldsymbol{\alpha} = (\alpha_1, \alpha_2, \alpha_3)$ are positioned either at the center or at the vertices of the corresponding triangles. This corresponds to the case

$$\gamma_1 \equiv \gamma_2 \equiv \gamma_3 \equiv 0 \pmod 3,$$

and in particular, for $\alpha_3 = 0$ we find [see (37)]:

$$\begin{aligned} \boldsymbol{\alpha} = ((m+1)\gamma, -m\gamma, 0) &\longrightarrow g_1 = \gamma x - (\log P_m)_x, \\ g_2 &= (\log P_m)_x, \quad g_3 = 0, \end{aligned}$$

where P_m is an mth degree polynomial such that

$$P''_m = \gamma x P'_m - m\gamma P_m.$$

For the following it is important to have in mind the uniqueness [8] of the rational solution (33) for given $\boldsymbol{\alpha}$. In particular, from this uniqueness and the invariance of (33) relative to the involution $g_j(x) \mapsto -g_j(-x)$, it follows that the rational solutions correspond to odd functions $g_j(x)$.

For the general position, replacing g_j, $j \in \mathbb{Z}_3$ in (33) with Q_j, $j \in \mathbb{Z}_3$ using the formulas

$$g_j = \frac{1}{3}\gamma x + \partial_x \log(Q_{j+1}/Q_{j-1}),$$

we arrive at the following equations for the polynomials Q_j:

$$\begin{gathered}(Q''_j - xQ'_j + m_jQ_j)Q_{j+1} \\ + (Q''_{j+1} + xQ'_{j+1} - m_{j+1}Q_{j+1})Q_j = 2Q'_jQ'_{j+1}, \\ \gamma = 3.\end{gathered} \tag{40}$$

Here the normalization $\gamma = 3$ does not significantly restrict the generality and m_j denotes the degrees of the polynomials Q_j. On account of the periodic closure Q_j, $j \in \mathbb{Z}_3$ it follows from (40) that

$$\begin{gathered}Q''_1Q_2Q_3 + Q_1Q''_2Q_3 + Q_1Q_2Q''_3 \\ = Q'_1Q'_2Q_3 + Q'_2Q'_3Q_1 + Q'_3Q'_1Q_2,\end{gathered}$$

which then gives in the principal order with respect to x

$$\begin{gathered}(m_1 - m_2)^2 + (m_2 - m_3)^2 + (m_3 - m_1)^2 \\ = 2(m_1 + m_2 + m_3).\end{gathered} \tag{41}$$

Quite clearly, the equations (33) should follow from (40) and a comparison of the parameters of these equations yields

$$\begin{gathered}\alpha_j = \frac{\gamma}{3}(1 + m_{j+1} + m_{j-1} - 2m_j) \\ \longrightarrow \gamma_{j+1} - \gamma_j = 3(m_j - m_{j+1}).\end{gathered}$$

In particular, the relations (39) follow from this. The formulas given above together with (41) can be used to find m_1, m_2, and m_3 for given $\boldsymbol{\alpha} = (\alpha_1, \alpha_2, \alpha_3)$:

$$\begin{gathered}m_j = \frac{1}{3}(\gamma_j - 1)(\gamma_j - 2) + \frac{1}{9}(\gamma_j - \gamma_{j+1})(\gamma_{j-1} - \gamma_j), \\ \gamma_j = \frac{3}{\gamma}\alpha_j.\end{gathered} \tag{42}$$

We note another useful formula

$$m_1 + m_2 + m_3 = 1 - \frac{1}{3}(\gamma_1\gamma_2 + \gamma_2\gamma_3 + \gamma_3\gamma_1),$$

which is equivalent to (41).

The transform (39) with the mapping (42) generally goes beyond the set of nonnegative integers m_j. We can confirm that this contradiction is removed by the additional constraint

$$\gamma_1 \equiv \gamma_2 \equiv \gamma_3 \not\equiv 0 \pmod 3, \tag{43}$$

which isolates the centers of the triangles (39). This constraint evidently also guarantees that the coefficients of the polynomials Q_j determined from (40) are integers. We give several examples:

$$\begin{gathered}\boldsymbol{\alpha} = (-1, 2, 2), \quad \mathbf{Q} = (x, 1, 1), \\ \boldsymbol{\alpha} = (-1, 5, -1), \quad \mathbf{Q} = (x^2 - 1, 1, x^2 + 1), \\ \boldsymbol{\alpha} = (1, 4, -2), \quad \mathbf{Q} = (x, 1, x^2 + 1), \\ \boldsymbol{\alpha} = (5, -4, 2), \quad \mathbf{Q} = (x, x^4 + 2x^2 - 1, x^2 + 1).\end{gathered} \tag{44}$$

As we have already noted the rational solutions (33) correspond to odd functions g_j. The polynomials Q_j corresponding to these solutions are even functions of x if their degrees m_j are even and are odd functions in the opposite case. It can be shown that the polynomials Q_j determined from (40) and (43) cannot have common zeros.

We note that all possible solutions (40) for which one of $m_j = 0$ are given above. In this case, $Q_j = 1$ and the other two polynomials are Hermite polynomials on account of (40).

3.2. Coulomb Gas

The generally accepted definition of the fourth Painleve equation corresponds to the case $\gamma = -2$ in (30). We shall use the property of the fourth Painleve equation that any singularity of the solution in the finite part of the complex plane has the form

$$w \sim \frac{c}{\xi - \xi_0} - \xi_0, \quad c^2 = 1. \tag{45}$$

It is also well known that the asymptotic behavior of the functions g_i at infinity is defined as

$$g_i \longrightarrow -\frac{2}{3}\xi, \quad \xi \longrightarrow \infty, \tag{46}$$

or

$$g_1 \longrightarrow -2\xi, \quad g_2, g_3 \longrightarrow 0, \quad \xi \longrightarrow \infty. \tag{47}$$

We shall seek rational solutions of the fourth Painleve equation in the form

$$w = -\delta\xi + \sum_i \frac{c_i}{\xi - \xi_i}, \tag{48}$$

where $\delta = 2/3$ corresponds to the case of "centers" (46), (39) and $\delta = 0$ or $\delta = 2$ leads to the "angles" of a triangle. Substituting (48) into (45), we obtain

$$(\delta - 1)\xi_i = \sum_{j \neq i} \frac{c_j}{\xi_i - \xi_j}, \quad c_i = \pm 1. \tag{49}$$

Equation (49) describes an electron gas with Coulomb interaction with a parabolic potential and also the statistics of the eigenvalues of a random Hermitian matrix since (49) can be obtained by varying the following functional:

$$U = \sum_i \frac{1}{2}(1-\delta)c_i\xi_i^2 + \sum_{i \neq j} c_i c_j \log(\xi_i - \xi_j). \tag{50}$$

The particular case when all charges are $c_i = 1$ (or all $c_i = -1$) yields the well-known solution of the fourth Painleve equation

$$w = -2\xi + \frac{H_n'(\xi)}{H_n(\xi)}, \tag{51}$$

where $H_n(\xi)$ are Hermite polynomials (see [9]). Hence, the roots of the Hermite polynomials H_n describe the static distribution of like charges in the potential (50).

Interestingly, in the case of two unlike charges, no solution (48) exists, i.e., an electron is annihilated at a hole. At the same time the solution $\mathbf{Q}(1, 4, 2)$ [see (44)] determines three solutions of equation (49) for $\delta = 2/3$ of which two are trivial (they correspond to roots of the Hermite polynomials) and one corresponds to a system of two positive and one negative charges:

$$\xi_{1,2} \pm i, \quad \xi_3 = 0, \quad c_{1,2} = 1, \quad c_3 = -1. \tag{52}$$

In general we have three solutions of the system (49) where all positive charges are positioned at the roots of the polynomial Q_{j+1} and all negative charges are positioned at the roots of the polynomial Q_{j-1}; thus the number of charges is $N_\pm = \deg Q_{j\pm 1}$.

4. LANDAU–LIFSHITZ MODEL

In a certain sense, the most general of the integrable equations considered by us is the anisotropic Landau–Lifshitz model

$$\mathbf{S}_t = \mathbf{S} \times (\mathbf{S}_{xx} + \hat{J}\mathbf{S}), \quad S_1^2 + S_2^2 + S_3^2 = 1, \tag{53}$$

where $\hat{J}$ is a symmetric matrix. By parametrizing the vector $\mathbf{S}$

$$\begin{aligned} \mathbf{S} &= (S_1, S_2, S_3) \\ &= (p(q^2 - 1) + q, \quad ip(q^2 + 1) + iq, 2pq + 1) \end{aligned} \tag{54}$$

this vector equation is reduced to the Lagrange form (1):

$$\begin{aligned} L = {} & iqp_t + p_x q_x - q_x^2 p^2 - p^2 r(q) \\ & - \frac{1}{2} p r'(q) - \frac{1}{12} r''(q), \end{aligned} \tag{55}$$

where

$$4r(q) = -\left(\frac{\partial \mathbf{S}}{\partial p}\hat{J}\frac{\partial \mathbf{S}}{\partial p}\right). \tag{56}$$

For the case of a diagonal matrix $\hat{J}$ we have

$$\begin{aligned} 4r(q) = {} & (J_2 - J_1)q^4 \\ & + 2(J_1 + J_2 - 2J_3)q^2 + J_2 - J_1. \end{aligned} \tag{57}$$

It should be noted that having replaced the Lagrangian L_1 from (7) by (55), where $r(q)$ is an arbitrary fourth-degree polynomial with respect to the variable q, it could be confirmed that any integrable generalization of the nonlinear Schrödinger equation reduces to (1) or (55) (see, for example, [2, 3]).

In addition to (54), we can use other parametrizations of a complex sphere, such as the stereographic projection. The most interesting for us is the known relationship between the parametrization problem and the spectral problem

$$\psi_{xx} + (z(x) - \lambda)\psi_x + p(x)\psi = 0. \tag{58}$$

Specifically, if $\mathbf{S} = \mathbf{S}(x)$ is a curve on the sphere $(\mathbf{S}, \mathbf{S}) = S_1^2 + S_2^2 + S_3^2 = 1$, then

$$\begin{aligned} (\mathbf{S}, \mathbf{S}) = 1 \longrightarrow \mathbf{S}_x = k\mathbf{N}, \\ \mathbf{N}_x = -k\mathbf{S} + \chi\mathbf{B}, \quad \mathbf{B}_x = -\chi\mathbf{N}, \end{aligned} \tag{59}$$

where $\mathbf{B} = \mathbf{S} \times \mathbf{N}$ is the binormal. These Frenet equations are closely linked to (58) and having determined the coefficients p, z from the formulas

$$k^2 = 4p, \quad i\chi + z + (\log k)_x = \lambda, \tag{60}$$

we can confirm that the pair of solutions $\psi_j(x)$, $j = 1, 2$, of equation (58) can be used to reconstruct the curve $\mathbf{S}(x)$ for given curvature and twist:

$$\begin{aligned} w(x)S_3 = (\psi_1\psi_2)_x, \quad w(x)(S_1 + iS_2) = i(\psi_2^2)_x, \\ w(x)(S_1 - iS_2) = i(\psi_1^2)_x. \end{aligned} \tag{61}$$

Here $w = w(x)$ denotes the Vronskian

$$w = \psi_{1,x}\psi_2 - \psi_{2,x}\psi_1$$

of these solutions.

4.1. Case J = 0

We shall now show that the equations (16) define the temporal dynamics of curvature and twist for the isotropic Landau–Lifshitz model:

$$\mathbf{S}_t = \mathbf{S} \times \mathbf{S}_{xx}, \quad S_1^2 + S_2^2 + S_3^2 = 1. \tag{62}$$

In fact, by differentiating the Frenet equations (59) with respect to t, we obtain the following equations for the curvature k and twist χ:

$$k_t + 2k_x\chi + k\chi_x = 0, \quad x_t = \left(\frac{k_{xx}}{k^2} + \frac{1}{2}k^2 - \chi^2\right)_x.$$

Substituting (60) then converts these equations into (16):

$$\begin{gathered} i\psi_t = (z + \lambda)\psi_x - p\psi, \\ iw_t + w_{xx} + 2pw = 2\lambda w_x, \quad w_x = (\lambda - z)w. \end{gathered} \tag{63}$$

Using the Miura transformations (18) we can obtain an equation directly for the projection of the spin on the z axis for the model (62):

$$\begin{gathered} \left(\partial_\xi + \frac{w' + \gamma}{w}\right)S_3 = -(w + 2\xi), \\ \gamma = c_1 - c_2 + 2, \end{gathered} \tag{64}$$

where $w = w(\xi, \alpha, \beta)$ is an arbitrary solution of the fourth Painleve equation with the parameters

$$a = \frac{1}{2}(c_1 + c_2), \quad b = -\frac{1}{2}(c_1 - c_2 + 2)^2. \tag{65}$$

Equation (64) has the particular solution $\sigma = \pm 1$ if

$$\begin{gathered} w' + \gamma = \mp w(w + 2\xi) \longleftrightarrow w = -\xi \pm \frac{\psi_\nu'}{\psi_\nu}, \\ \psi'' + (2\nu + 1 - \xi^2)\psi = 0, \\ \mp(\gamma - 1) = 2\nu + 1, \end{gathered} \tag{66}$$

and if $\nu = 0, 1, 2, \ldots$, we again obtain a set of rational solutions of the fourth Painleve equation (51).

Since $\sigma = \pm 1 + C\psi e^{\pm\xi^2}$, the particular solution (64) has the form

$$S_3 = \pm 1 + CH_n(\xi). \tag{67}$$

Using the $\mathbb{Z}_3$ symmetry of the fourth Painleve equation, we can rewrite equation (64) in terms of the functions g_i [see (33)], immediately obtaining three self-similar solutions of the Landau–Lifshitz model (62)

$$(\partial_\xi + g_i - g_{i+1})S_3^i = g_i + g_{i+1}. \tag{68}$$

For the relationship between the Heisenberg model and the fourth Painleve equation see also [10].

5. NONLINEAR SCHRÖDINGER EQUATION MODEL

It is interesting to consider various (including nonintegrable ones) generalizations of the nonlinear Schrödinger equation. For instance, the nonlinear Schrödinger equation with time-dependent coefficients has the form

$$iq_t + f(t)q_{xx} + g(t)|q|^2 q = 0. \tag{69}$$

Changing the notation of the time

$$t \longrightarrow \int^t f(t')dt' \tag{70}$$

and the coupling constant $g(t)$

$$g(t) \longrightarrow \frac{g(t)}{f(t)}, \tag{71}$$

we rewrite the equation in the form

$$iq_x + q_{xx} + g(t)|q|^2 q = 0. \tag{72}$$

This can have a self-similar solution $g(t)$ of the type

$$g(t) = \alpha(4t)^{(m-1)/2}, \tag{73}$$

where $m \in R$ and the constant α can be set as ± 1 (the choice of sign is important). The self-similar solution (to within the scaling transformations and $t > 0$) has the form

$$\begin{gathered} q = |q|e^{i\Theta(\eta, t)}, \quad |q|^2 = 4k(t)^{m+1}Y'(\eta), \\ \eta = k(t)x, \quad k(t) = \frac{1}{2t^{1/2}}, \end{gathered} \tag{74}$$

where

$$\Theta(\eta, t) = \theta(\eta) + \theta_0 \log t, \quad \theta_0 \in R, \tag{75}$$

$$\theta(\eta) = \frac{\eta^2}{2} + m\int \frac{Y}{Y'}d\eta, \tag{76}$$

and Y satisfies the following equation:

$$\begin{gathered} 2Y'''Y' - Y''^2 + 4\eta^2 Y'^2 - 4m^2 Y^2 \\ + 16\alpha Y'^3 - 16\theta_0 Y'^2 = 0. \end{gathered} \tag{77}$$

The Painleve test for this equation yields the conclusion that the solutions (77) have no mobile singular points for $m^2 = 1$. In this case, equation (77) is integrated as far as a second-order equation [using the integrating factor Y''/Y', see (31)]

$$\begin{gathered} Y_{\eta\eta}^2 + 624(\eta Y_\eta - Y) \\ + 2\alpha Y_\eta(2Y_\eta - \alpha\theta_0)^2 + 2\alpha\mu^2 Y_\eta = 0, \end{gathered} \tag{78}$$

where μ^2 is the integration constant. A self-similar solution of the nonlinear Schrödinger was first obtained in [1] for the case $\theta_0 = 0$. In general, the properties of these

solutions of the nonlinear Schrödinger equation may be obtained as in [1]. The solution Y may be written in the form

$$-\alpha Y = \frac{1}{2}W(W-\eta)^2 + \frac{1}{8W}[W_\eta^2 - 2W_\eta - \mu^2 + 1] + \frac{1}{2}\theta_0(W-\eta), \tag{79}$$

where W satisfies the equation

$$WW_{\eta\eta} = \frac{1}{2}W_\eta^2 - 6W^4 + 8\eta W^3 - 2(\eta^2 - \theta_0)W^2 - \frac{1}{2}(\mu-1)^2, \tag{80}$$

which is the same as the fourth Painleve equation (apart from the change of variables). Equation (79) may be considered as an algebraic quadrature (78) which is quadratic with respect to $Y_{\eta\eta}$.

We note that

$$-2\alpha Y_\eta = (W-\eta)^2 + \frac{(W_\eta + \mu - 1)^2}{4W^2}. \tag{81}$$

Thus, for $\alpha = -1$ and real μ and W the condition $Y_\eta \geq 0$ is automatically satisfied. However, for $\alpha = 1$ and real μ and W we find that $Y_\eta \leq 0$, i.e., there are no self-similar solutions. We shall discuss the case $\alpha = -1$.

We can express W in terms of Y:

$$W = \frac{-\mu Y_{\eta\eta} + (2Y_\eta + \theta_0)(2Y + \eta\theta_0) + \eta\mu^2}{(2Y_\eta + \theta_0)^2 + \mu^2}. \tag{82}$$

On the basis of the Bureau derivation [11, p. 210] equation (78) can be solved by an algebraically different method, i.e., Y can be expressed in terms of a different function $\hat{W}$:

$$2Y = h\eta + \frac{\hat{W}_\eta^2}{2\hat{W}} - 2\hat{W}^3 - 4\eta\hat{W}^2 + 2(\eta^2 - a)\hat{W} + \frac{b}{4\hat{W}}, \tag{83}$$

where $\hat{W}$ satisfies the equation

$$\hat{W}\hat{W}_{\eta\eta} = \frac{1}{2}\hat{W}_\eta^2 - 6\hat{W}^4 + 8\eta\hat{W}^3 - 2(\eta^2 - a - \sigma^2)\hat{W}^2 + \frac{b}{4}, \tag{84}$$

where

$$\sigma^4 = -1,$$

and the constants a, b, and h are determined as follows:

$$4a^3 + 3(3\mu^2 - \theta_0^2)a + \theta_0(9\mu^2 + \theta_0^2) = 0, \tag{85}$$

$$3b = -2a^2 - 2(3\mu^2 - \theta_0^2), \tag{86}$$

$$h = \frac{2}{3}(a - 2\theta_0). \tag{87}$$

The roots of the algebraic equation at a have the form

$$a_1 = -\theta_0, \tag{88}$$

$$a_{2,3} = \frac{1}{2}\theta_0 \pm \frac{3}{2}i\mu. \tag{89}$$

Then

$$b_1 = -2\mu^2, \tag{90}$$

$$b_{2,3} = \frac{1}{2}(\theta_0 \mp i\mu)^2, \tag{91}$$

$$h_1 = -2\theta_0, \tag{92}$$

$$h_{2,3} = -\theta_0 \pm i\mu, \tag{93}$$

and thus the function $\hat{W}$ may be expressed in terms of Y.

For the case $a_1 = -\theta_0$ we obtain

$$\hat{W}_1 = \frac{1}{2}\eta - \frac{1}{2}\frac{Y}{Y_\eta} - \frac{\sigma^2}{4}\frac{Y_{\eta\eta}}{Y_\eta}, \tag{94}$$

and in the case $a_{2,3} = \theta_0/2 \pm 3i\mu/2$

$$\hat{W}_{2,3} = \frac{\eta Y_\eta - Y}{2Y_\eta + \theta_0 \pm i\mu} - \frac{\sigma^2}{2}\frac{Y_{\eta\eta}}{2Y_\eta + \theta_0 \pm i\mu}. \tag{95}$$

The values of $\hat{W}$ are related by

$$\frac{\zeta_2 W_2}{W_2 - W_1} = \frac{\zeta_3 W_3}{W_3 - W_1} = \frac{\zeta_3 W_3 - \zeta_2 W_2}{W_3 - W_2}, \tag{96}$$

where

$$\zeta_{2,3} = \frac{1}{2}(\theta_0 \pm i\mu). \tag{97}$$

The Backlund transformations for the nonlinear Schrödinger equation are reduced to the corresponding transformations for the self-similar solutions Y. We can obtain a new self-similar solution $\tilde{Y}$ which satisfies (78) for $\mu \longrightarrow 2 - \mu$ and has the form

$$\tilde{Y} = Y + \frac{1}{2}\frac{(\mu-1)[(2Y_\eta + \theta_0)^2 + \mu^2]}{[-\mu Y_{\eta\eta} + (2Y_\eta + \theta_0)(2Y + \eta\theta_0) + \eta\mu^2]}. \tag{98}$$

6. NONLINEAR SCHRÖDINGER EQUATION WITH VARIABLE DISPERSION. EXACT SOLUTION

We shall analyze the nonlinear Schrödinger equation with variable dispersion $d(z)$

$$i\psi_z + d(z)\psi_{xx} + g(\psi^*\psi)\psi = 0, \tag{99}$$

which can be obtained by varying the following Lagrangian:

$$L = \int dz \int dt \left[i\psi^*\psi_z - d(z)\psi_x^*\psi_x + \frac{g}{2}(\psi^*\psi)^2 \right]. \tag{100}$$

Using the canonical transformation $(\psi, \psi^*) \longrightarrow (\rho, \phi)$ (where $\psi = \rho^{1/2}e^{i\phi}$) the Lagrangian (100) becomes

$$L = \int dz \int dt \left[-\rho\phi_z - d\rho\phi_t^2 - d\frac{\rho_t^2}{4\rho} + \frac{g}{2}\rho^2 \right]. \tag{101}$$

The equation of continuity

$$p_z + 2d\partial_t\rho\phi_t = 0 \tag{102}$$

can be integrated, having selected the self-similar form ρ:

$$\begin{gathered} \rho = \lambda(z) f(\xi), \\ \phi = -\frac{\lambda'}{4d\lambda}t^2 + \phi_0(z), \quad \xi = \lambda t. \end{gathered} \tag{103}$$

The Lagrangian (101) with this choice of self-similar substitution is transformed to give

$$\begin{aligned} L = \int \frac{dz}{\lambda(z)} \int d\xi \Bigg[& -f\lambda\partial_z\phi_0(z) - \frac{d\lambda^3}{4}\frac{f_\xi^2}{f} + \frac{g}{2}\lambda^2 f^2 \\ & + \left\{ \frac{1}{\lambda}\left(\frac{\lambda'}{4d\lambda}\right)' - d\lambda\left(\frac{\lambda'}{2d\lambda}\right)^2 \right\} f\xi^2 \Bigg]. \end{aligned} \tag{104}$$

By varying the Lagrangian (104) with respect to f and ϕ_0, we can obtain equations for the self-similar solutions. If the following conditions are satisfied

$$\lambda d = \alpha, \quad (d')^2 = \epsilon d^2 + 4\alpha^3\gamma \tag{105}$$

the equation for the "density" f has the form

$$\frac{\alpha}{2}\left[\frac{f''}{f} - \frac{f''^2}{f^2} \right] + \gamma\xi^2 + gf = 0. \tag{106}$$

If $\alpha\gamma > 0$, we obtain a periodic solution for $d(z)$ but $f \longrightarrow \infty$ for $\xi \longrightarrow \infty$; if $\alpha\gamma < 0$, $\epsilon > 0$, (106) may be rewritten in the form

$$\begin{gathered} d = \sqrt{-\frac{4\alpha^3\gamma}{\epsilon}}\cosh(z\sqrt{\epsilon}), \\ y'' + \frac{\gamma}{\alpha}\xi^2 y + \frac{g}{\alpha}y^3 + Ey = 0, \quad y^2 = f. \end{gathered} \tag{107}$$

We shall say that in this case an exact self-similar solution of equation (99) is obtained since the solutions of equation (107) for y are finite for $\xi \longrightarrow \infty$, have no singular points, and possess known asymptotic forms (the Schrödinger oscillator equation with cubic nonlinearity). From this point of view, no exact solutions exist for the case of periodic dispersion. The periodic case is interesting because equation (99) describes the propagation of a signal in optical fibers consisting of extended sections of different dispersion. A variational solution of an equation of the type (99) was constructed in [12]. The conclusion that no exact solutions of (99) exist in the periodic case does not necessarily imply that no variational solutions exist, but may indicate that they are unstable.

The major part of this work has been devoted to the study of self-similar solutions of one-dimensional integrable dynamic systems. A general Lagrangian approach can nevertheless also be applied to nonintegrable systems. Quite clearly, various symmetries such as the Miura and Backlund transformations are absent. However, in this case equations for the self-similar solutions are easily derived by a dynamic method, i.e., with all possible parameters being conserved. It would be interesting to analyze self-similar solutions of dynamic systems in the two-dimensional case.

ACKNOWLEDGMENTS

This work was supported in part by the Russian Foundation for Basic Research (grant no. 98-01-01161) and the Program "Scientific Schools of the Russian Federation" (grant no. 96-15-96093).

REFERENCES

1. M. Boiti and F. Pempinelli, Nuovo Cimento B **59**, 40 (1980).
2. V. G. Marikhin and A. B. Shabat, Teor. Mat. Fiz. **118**, 217 (1999).
3. A. V. Mikhaĭlov and A. B. Shabat, Teor. Mat. Fiz. **62**, 163 (1985).
4. Yu. N. Ovchinnikov, Pis'ma Zh. Éksp. Teor. Fiz. **69**, 387 (1999) [JETP Lett. **69**, 418 (1999)].
5. V. I. Gromak, Diff. Eqns. **23**, 506 (1987).
6. A. P. Veselov and A. B. Shabat, Funct. Anal. Appl. **27**, 1 (1993).
7. N. A. Lukashevich, Diff. Eqns. **3**, 395 (1967).
8. V. E. Adler, Physica D **73**, 335 (1994).
9. P. Estévez and P. Clarkson, E-print archives, solv-int/9904002.
10. F. W. Nijhoff, G. R. W. Quispel, J. van der Linden, and H. W. Capel, Physica A **119**, 101 (1983); G. R. W. Quispel and H. W. Capel, Phys. Lett. A **88**, 371 (1982); Physica A **117**, 76 (1983).
11. F. J. Bureau, Annali di Matematica (IV) **91**, 163 (1972).
12. S. Turitsyn, Phys. Rev. E **58**, R1256 (1998).

Translation was provided by AIP

Journal of Experimental and Theoretical Physics, Vol. 90, No. 3, 2000, pp. 562–569.
From Zhurnal Éksperimental'noĭ i Teoreticheskoĭ Fiziki, Vol. 117, No. 3, 2000, pp. 644–652.

NONLINEAR PHYSICS

Adiabatic Invariance and Separatrix: Single Separatrix Crossing[¶]

B. V. Chirikov* and V. V. Vecheslavov**

Budker Institute of Nuclear Physics, Siberian Division, Russian Academy of Sciences, Novosibirsk, 630090 Russia
**e-mail: chirikov@inp.nsk.su*
***e-mail: vecheslavov@inp.nsk.su*

Submitted June 22, 1999

Abstract—Detailed numerical experiments on the dynamics and statistics of a single crossing of the separatrix of a nonlinear resonance with a time-varying amplitude are described. The results are compared with a simple approximate theory first developed by Timofeev and further improved and generalized by Tennyson and coworkers. The main attention is paid to a new, ballistic, regime of separatrix crossing in which the violation of adiabaticity is maximal. Some unsolved problems and open questions are also discussed. © *2000 MAIK "Nauka/Interperiodica".*

1. INTRODUCTION

Any conservation law, if only approximate, is of great importance in physics. One of those is the adiabatic invariance that is the conservation of the action variables (J) under a slow parametric perturbation. In the simplest case of a single arbitrarily large variation of the latter, the corresponding change in J is well known to be exponentially small in an appropriate adiabatic parameter ($\epsilon \longrightarrow 0$) provided the perturbation is an analytic function of time or of any other dynamical variable.

However, in the theory of dynamical systems, a much more interesting and important case is a stationary variation of the perturbation (e.g., periodic, quasiperiodic, or even chaotic). In this case, the adiabaticity is violated for sufficiently long length of time, no matter how slow the adiabatic perturbation is. Generic mechanism of such a nonadiabaticity are resonances, both driving and coupling ones, which always determine the long-term dynamics of Hamiltonian oscillator systems. This was first discovered and explained in 1928 by Andronov, Leontovich, and Mandelshtam [1]. Remarkably, it was sufficient, for this purpose, to carefully examine the well-known Mathieu equation and its solutions from the standpoint of physics. Indeed, the instability zones ("stop bands") exist for special but arbitrarily small values of the parameter ϵ, where the adiabaticity is completely destroyed in a sufficiently long length of time. This leads to an additional condition for the adiabatic invariance: the perturbation must be not only slow but also nonresonant.

At a separatrix, an asymptotic trajectory with infinite period of motion, both conditions are violated (see, e.g., [2, 3]). This is exactly the place where the dynamical chaos is born, the ultimate origin of chaos. In a Hamiltonian system, the separatrix is typically associated with nonlinear resonances. The violation of adiabaticity results in the formation of a narrow chaotic layer around the unperturbed separatrix. The set of all resonances is everywhere dense in phase space and forms the so-called "Arnold web." For the number of freedoms $N > 2$ (in a conservative system), a united chaotic component of motion is formed along which a chaotic (but nonergodic!) trajectory is covering the whole energy surface. This very intricate process was termed "Arnold diffusion," which is an universal instability of multidimensional nonlinear oscillations [3–5]. However, the rate of this diffusion, as well as the total measure of the web, is typically exponentially small in perturbation parameter ϵ. For large N or for a driving quasiperiodic perturbation with many frequencies, these nonadiabatic effects decay with ϵ as a power law but only within a finite range $\epsilon_{cr} \lesssim \epsilon \ll 1$ (the so-called fast Arnold diffusion [6]). Asymptotically, as $\epsilon \longrightarrow 0$, the decay is always exponential [7], the crossover value becoming smaller with larger numbers of unperturbed frequencies.

A more serious violation of adiabaticity was found for the crossing of the separatrix by a trajectory. In this case, the change of J is always a power law in ϵ, and, moreover, the measure of the chaotic component does not depend on ϵ at all and is always large. This is true for the slow resonance crossing [8, 9] as well as for the crossing of a single separatrix [9–13]. Interestingly, for the linear oscillator with the frequency value crossing zero, the change of J may be largely independent of ϵ [14].

In this paper, we present the results of numerical experiments for a single crossing of a single separatrix. The present work was stimulated by an interesting

[¶]This article was submitted by the authors in English.

study of the corresponding quantum adiabaticity [15]. We use the same classical model described in the next section.

2. MODEL

The model in [15] we use here is determined by the Hamiltonian

$$H(x, p, t) = \frac{p^2}{2} + A_0 \sin(\omega t)\cos x = \frac{p^2}{2} + \frac{A_0}{2}[\sin(x+\omega t) - \sin(x-\omega t)]. \quad (2.1)$$

The first expression describes a single nonlinear resonance in the pendulum approximation (see, e.g., [3, 5]) with a time-varying amplitude

$$A(t) = A_0 \sin(\omega t). \quad (2.2)$$

Alternatively, the model represents the interaction of two stationary resonances (the second expression in (2.1)) as suggested in [16, 17]. In the latter case, the formal resonance overlap parameter [5]

$$s = \frac{(\Delta p)_r}{\omega} \quad (2.3)$$

indefinitely increases as $\omega \longrightarrow 0$. Here, $(\Delta p)_r$ is the width of each resonance and 2ω is the distance between them. The adiabatic limit $\omega \longrightarrow 0$ corresponding to infinite resonance overlap was suggested in [17] as a new paradigm of "pure" chaos. However, this chaos is generally not ergodic.

Below, we keep to the first interpretation of the model as a single pulsating nonlinear resonance.

The dimensionless adiabaticity parameter is defined in the usual way as the ratio of perturbation/oscillation frequencies. Actually, we can introduce two such parameters:

$$\epsilon = \frac{\omega}{\sqrt{A_0}} \text{ and } \tilde{\epsilon} = \frac{\omega}{\sqrt{|A(t)|}}. \quad (2.4)$$

Here, $\sqrt{A_0}$ is a constant frequency of the small resonance oscillation for the maximal amplitude while $\sqrt{A(t)}$ is the current frequency, particularly at the instant of separatrix crossing. Correspondingly, we call ϵ the global parameter of adiabaticity, and $\tilde{\epsilon}$ the local one.

Two branches of the instant, or "frozen," separatrix at some t = const is defined by the relation

$$p_s(\tilde{x}; t) = \pm 2\sqrt{|A(t)|}\sin(\tilde{x}/2), \quad \tilde{x} = \begin{cases} x, & A(t) > 0, \\ x - \pi, & A(t) < 0. \end{cases} \quad (2.5)$$

Following previous studies of the separatrix crossing, we restrict ourselves to this frozen approximation in what follows. As we shall see, the latter provides quite good accuracy of rather simple theoretical relations.

In this approximation, the action variable is defined in the standard way as

$$J = \frac{1}{2\pi}\oint p(x)dx, \quad (2.6)$$

where the integral is taken over the whole period for x rotation (off the resonance) and over a half of that for x oscillation (inside the resonance). This distinction is necessary to avoid the discontinuity of J at the separatrix where the action is given by a simple expression

$$J = J_s(t) = \frac{4}{\pi}\sqrt{|A(t)|} \le J_{\max} = \frac{4}{\pi}\sqrt{A_0}. \quad (2.7)$$

At $\omega t = 0 \pmod{\pi}$, the action is $J = |p|$ and the conjugated phase is $\theta = x$. Note that, unlike p, the action $J \ge 0$ is never negative.

It is convenient to set $A_0 = 1$ and to introduce the dimensionless action by the transformation $J/J_{\max} \longrightarrow J$. The crossing region is then the unit interval, and J is simply related to the crossing time $t = t_{cr}$ by

$$|A(t_{cr})| = J^2, \quad 0 \le J \le 1, \quad (2.8)$$

while the adiabaticity parameters become

$$\epsilon = \omega \text{ and } \tilde{\epsilon} = \epsilon/J. \quad (2.9)$$

Numerical integration of the equations of motion for Hamiltonian (2.1) was performed in (x, p) variables using the so-called bilateral symplectic algorithm suggested in [18] and based on the symplectic fourth-order Runge–Kutta method in [19]. A typical number of iterations was ~100 per the minimal motion (oscillation) period 2π. This provides the conservation of the Hamiltonian in extended phase space [3] better than 10^{-6}.

As is well known, the variation of J under an adiabatic perturbation consists of one to two qualitatively different parts: (i) the average action, which is nearly constant between the crossings up to exponentially small corrections and which is of primary interest in our problem, and (ii) the rapid oscillations with the motion frequency (see, e.g., Fig. 7c in [20]). The ratio of the two time scales is $\sim\tilde{\epsilon} \ll 1$, which allows the efficient suppression of the second unimportant part of the J variation by simply averaging $J(t)$ over a long time interval $\sim 1/\epsilon$, the suppression factor being $\sim 1/\tilde{\epsilon} \gg 1$ (fairly large).

3. DYNAMICS OF SEPARATRIX CROSSING: DIFFUSIVE REGIME, $J \gtrsim \epsilon^{1/3}$

To the best of our knowledge, the first analytical estimates for the change in J due to separatrix crossing have been calculated in [11] followed shortly by a more accurate [12] and, later, by a more general [9] approxi-

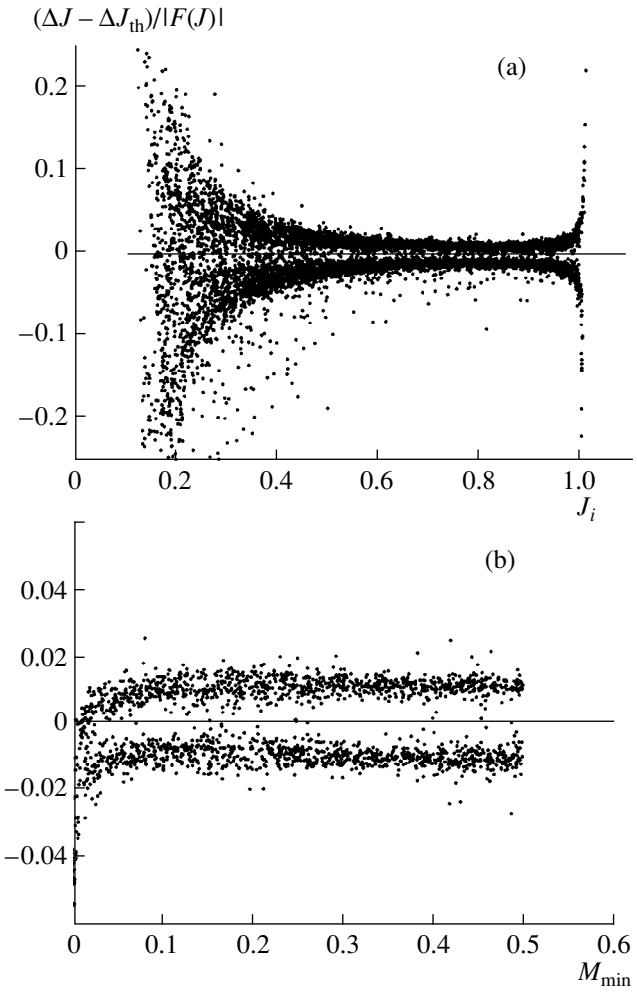

Fig. 1. Normalized deviation of numerical data for separatrix crossings from the simple theory (3.1) in model (2.1): 4 crossings ×2500 trajectories; $\epsilon = 0.001$. (a) Deviation dependence on J in the whole available interval: $0.2 \lesssim J < 1$ (see text). (b) Same data as a function of the crossing parameter M in the best described interval: $0.7 \lesssim J \lesssim 0.9$; accuracy (3.6) $\sigma \approx 0.01$.

mate (asymptotic in ϵ) theory. For model (2.1) under consideration here, these results (see also [21]) can be represented in the form

$$\Delta J(J, M, \epsilon) = F(J)\Phi(M). \tag{3.1}$$

Here, $\Delta J = J_f - J_i$ is the difference between the final and initial averaged values of J.

$$F(J) = -\frac{\epsilon}{2}\frac{\sqrt{1-J^4}}{J^2}\mathrm{sgn}(\dot{A}(t)) \tag{3.2}$$

is the dependence on the averaged action (usually, but not necessarily, the initial one), and

$$\Phi(M) = \ln|2\sin(\pi M)|, \tag{3.3}$$

where M is the "crossing parameter." It looks like a phase canonically conjugated to the action J [21], but it is not. A peculiarity of the separatrix crossing is that the conjugated phase θ cannot even be introduced on the frozen separatrix, because the motion frequency in this approximation is zero, and hence $\theta \equiv$ const. Instead, a different variable, the crossing parameter, is used in the theory [9, 12] determined by any of the following approximate relations:

$$M \approx w_x\frac{A_x^{3/2}}{2\dot{A}_x} \approx w_p\frac{A_p^{3/2}}{4\dot{A}_p} \approx \sin^2\left(\frac{\tilde{x}_s}{4}\right). \tag{3.4}$$

Here,

$$w_x = \frac{|\delta H(t_x)|}{A_x(t_x)}, \quad w_p = \frac{|\delta H(t_p)|}{A_p(t_p)} \tag{3.5}$$

are the closest dimensionless approaches of the trajectory to the unstable fixed point ($\tilde{x} = 0 \pmod{2\pi}$, $p = 0$) just before or after separatrix crossing at time t_x and t_p, respectively (for details, see [9, 12]). The absolute values are assumed for all quantities with subscripts. In the latter expression (3.4), the coordinate $\tilde{x}_s(t_{cr})$ is taken at the instant t_{cr} of separatrix crossing.

The physical meaning of seemingly complicated (3.4) is actually very simple: the main change in J occurs only at the closest approach to the unstable fixed point where the motion is very slow, allowing for the moving separatrix to considerably push or pull the trajectory along. The existing theory cannot distinguish between the three relations (3.4) with respect to their accuracy. However, our numerical experiments revealed that, taken by itself, the third relation ($M = M_3$) proved to be most accurate. On the other hand, if we make use of the first two and take the minimal one of them ($M = M_{\min} \le 0.5$), the accuracy further increases. In this case, it is important to take all the quantities at the corresponding instants t_x and t_p as indicated in (3.4) and (3.5), and not, e.g., at the crossing time t_{cr}. All quantities in (3.4) and (3.5) were computed using the linear interpolation over a single numerical iteration.

A comparison between the numerical results and the simple theory is presented in Fig. 1.

The empirical data (points) represent four separatrix crossings over one period of the adiabatic perturbation $A(t)$ in (2.1) for each of the 2500 trajectories with random initial conditions in the full interval of $\theta = x = (0, 2\pi)$ and of $J = \pi p/4 = (0, 1)$ at $t = 0$. The normalized deviation from the theory is presented as a function of initial $J = J_i$ (prior to a crossing) and of parameter M. In both cases, the optimal $M = M_{\min}$ is used. The best accuracy of the theory roughly corresponds to the interval $0.7 \lesssim J \lesssim 0.9$ (Fig. 1a). The latter is separately shown in Fig. 1b. Beyond this interval, the deviation increases at both sides.

For $J \longrightarrow 1$, the change in J becomes very small (3.1), which increases the theoretical errors. More interesting is the opposite limit ($J \longrightarrow 0$) where the theory becomes singular. It simply means that such a the-

ory is no longer applicable here. This new and interesting region of maximal nonadiabaticity will be considered in Section 4 below. Here we notice only that the absence of any points for $J \lesssim 0.2$ in Fig. 1a has a very simple explanation: using the best parameter, $M = M_{\min}$ becomes inapplicable in this region, because only one of the two close approaches remains here while the other one is never realized. If, instead, one uses a less accurate parameter $M = M_3$, which is always applicable, the deviations exceed 1, which means that the theory (3.1) has nothing to do with such a small J.

The highest accuracy achieved in our numerical experiments $\sigma \approx 0.01$ (see (3.6) and Fig. 1b) is comparable with the minimal theoretical errors $\sim \epsilon \ln \epsilon$ [9]. In a very narrow interval of $M_{\min} \approx 0$, the accuracy becomes somewhat worse but is still surprisingly good for such a simple theoretical relation as (3.1). A few points in this region are clearly seen also in Fig. 1a scattered over a wide interval in J.

The high numerical accuracy achieved reveals a complicated structure of the deviations from the theory. Besides irregular scattering of the points, there is a clear regular "splitting" symmetric with respect to zero deviation, which is determined by the sign of $A(t)$. It might be a result of insufficient J averaging (for discussion see [12]). These regular deviations could be excluded by the explicit computation of the first correction to the adiabatic invariant (2.6) as in [10]. However, it would hardly decrease appreciably the deviations, as they are already of the order of the terms omitted in the theory. In any event, we included this "splitting" in the definition of the accuracy of our numerical data in Fig. 1b for all of the four successive separatrix crossings:

$$\sigma^2 = \frac{\langle (\Delta J - \Delta J_{th})^2 \rangle}{F^2}. \tag{3.6}$$

Here, ΔJ is the empirical and ΔJ_{th} is the theoretical (3.1) value of the J change per crossing.

Another way to demonstrate agreement (or disagreement) of the existing theory with the empirical data is to look at the behavior of the transform

$$\Delta J \longrightarrow (\Delta J)^+ = -\Delta J \operatorname{sgn}(\dot{A}(t)). \tag{3.7}$$

As far as the relation (3.1) holds true, this new quantity has a strict upper bound

$$(\Delta J)^+ \le |F(J)| \Phi(1/2). \tag{3.8}$$

The results are shown in Fig. 2a.

The upper bound of points closely follows the theoretical dependence (3.8) down to $J_i \approx 0.2$ (cf. Fig. 1a). Remarkably, for small J_i, a clear upper bound also exists even though the unknown underlying dynamics is apparently completely different here. In particular, the upper bound in this region does not depend on J and forms a characteristic "plateau." The crossover between the two regions in Fig. 2a is at $J = J_{cro} \approx 0.1$ and scales as $J_{cro} \sim \epsilon^{1/3}$ (see (4.5) below). We shall call the well-understood behavior for $J \gtrsim J_{cro}$ the diffusive region and the other domain $J \lesssim J_{cro}$, to be considered in some detail below, the ballistic region, for reasons explained in the next section.

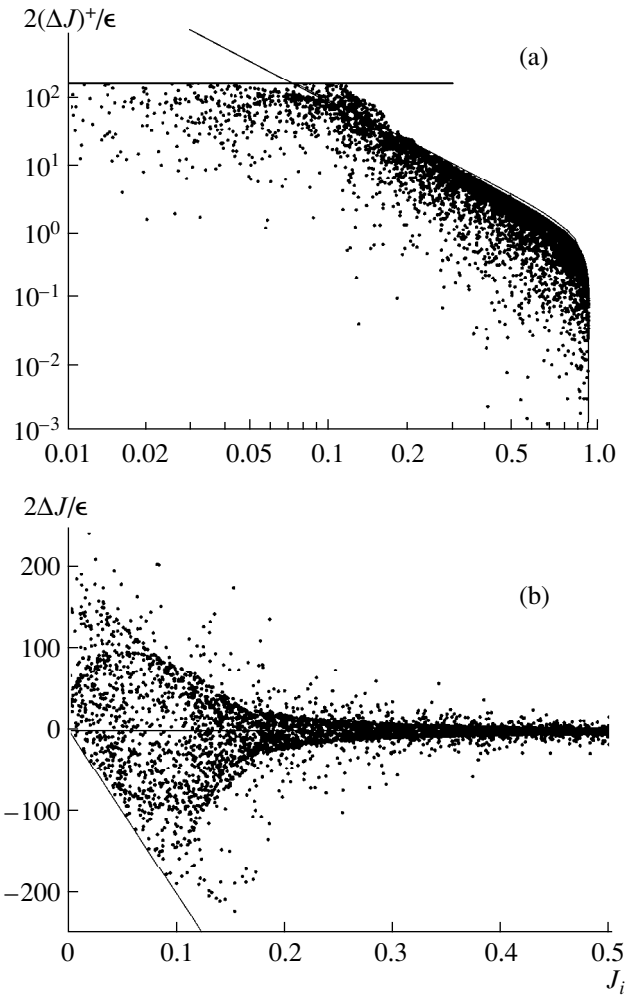

Fig. 2. The set of empirical ΔJ for the ensemble of trajectories as in Fig. 1 in the full range $J_i = (0, 1)$. (a) Transformed quantity $(\Delta J)^+$, (3.7); the solid curve is theory (3.8) shifted upwards by 20%; the horizontal line is empirical upper bound $2(\Delta J)^+/\epsilon \approx 150$ in the region where there is as yet no theory; crossover action $J_{cro} \approx 0.1$. (b) Actual ΔJ with correct signs: the oblique straight line is empirical lower bound $\Delta J \ge -J_i$ (see text).

4. STATISTICS OF SEPARATRIX CROSSING: BALLISTIC REGIME, $J \lesssim \epsilon^{1/3}$

For small $J \lesssim \epsilon^{1/3}$, not only is there the complete absence of any theory, but also constructing the empirical relations seems to us a hard task. Particularly, as is seen in Fig. 2b, the structure in this region is rather complicated.

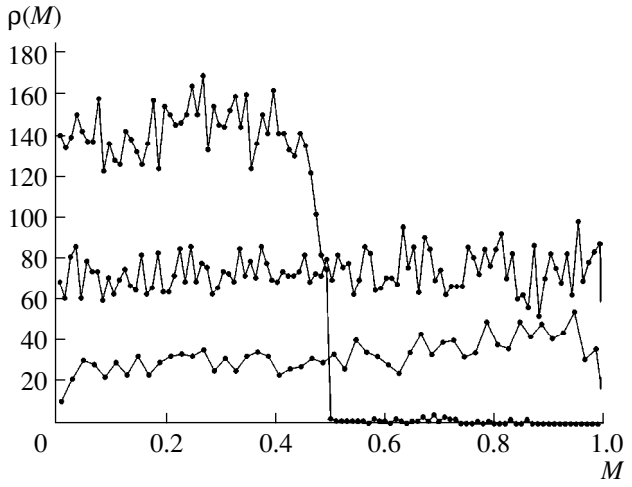

Fig. 3. Distribution $\rho(M)$ in number of crossings per bin: $\epsilon = 0.01$; $J_{cro} = 0.215$. Top to bottom: (i) $M = M_{\min}$, $J_i = (0.3, 1)$, the diffusive region, 6928 crossings, 100 bins; (ii) same for $M = M_3$, 7312 crossings; (iii) $M = M_3$, $J_i = (0, 0.2)$, the ballistic region, 1634 crossings, 50 bins.

Surprisingly, statistical properties here turned out to be fairly simple. To our knowledge, Mirbach was the first to study this problem numerically in 1998 [22].

Since, in this paper, the properties of the single separatrix crossings are considered, we need a statistical ensemble of trajectories before we turn to statistical numerical experiments. As the motion driven by separatrix crossing is known to be ergodic, or at least very close to that, within the crossing domain, it would be natural to make use of the ergodic ensemble. In this case, the distribution of the crossing parameter M in (3.1), which determines all the statistical properties of the single separatrix crossing, was shown to be homogeneous [9, 23]. Particularly, the two first moments of the M-distribution are

$$\mu_1 = \langle \Phi(M) \rangle = 0,$$
$$\mu_2 = \langle \Phi^2(M) \rangle = \frac{\pi^2}{12}. \tag{4.1}$$

Both numerical values hold in the diffusive region only. Moreover, it is insufficient to fix initial J_0 even for the full range of $\theta_0 = (0, 2\pi)$. For homogeneous M-distribution, the width of initial distribution $\Delta_0 J_0$ must exceed some critical value given by a simple approximate relation

$$\frac{\Delta_0 J_0}{J_0} > \epsilon \frac{\sqrt{1 - J_0^4}}{J_0^3} \ln\left(\frac{8}{\epsilon} \frac{J_0^3}{\sqrt{1 - J_0^4}} \right) \approx \frac{J_{cro}^3}{J_0^3} \ln\left(8 \frac{J_0^3}{J_{cro}^3} \right). \tag{4.2}$$

This relation is obtained from the condition that the initial strip $J_0 = (0, 1)$ is transformed in such a strip near an unstable fixed point (see (3.1)), which provides the full range of parameter $M = (0.1)$. In most of our statistical numerical experiments, we used the full range of $J_0 = (0, 1)$.

In Fig. 3, the M-distribution is shown for both definitions of this parameter.

Two upper distributions in the diffusive region are fairly homogeneous within statistical fluctuations. In contrast, the lower one in the ballistic region shows a clear slope, whose mechanism remains unclear.

The statistical properties we studied are characterized by the two first moments of the distribution function in ΔJ (see (3.1)) defined as follows:

$$(\Delta J)_2^2 \equiv \langle (\Delta J)^2 \rangle = F^2(J)\mu_2 = \frac{\epsilon^2}{4}\left(\frac{1}{J^4} - 1 \right)\mu_2,$$
$$(\Delta J)_1 \equiv \langle \Delta J \rangle = \frac{d}{dJ} \frac{\langle (\Delta J)^2 \rangle}{2} = -\frac{\mu_2 \epsilon^2}{2J^5}. \tag{4.3}$$

Both analytical expressions are valid in the diffusive region only. Moreover, the second one cannot be deduced from the existing first-order theory, as $\langle \Delta J \rangle \sim \epsilon^2$ is a second-order effect. Instead, one can use the well-known relation between the two moments (see, e.g., [3]), which generally holds true for a chaotic Hamiltonian system (for discussion, see [2]). This relation, as well as the second-order moment $\langle \Delta J \rangle$, which may seem to be negligible at first glance, are in fact very important for derivation of the correct diffusion equation

$$\frac{\partial f(J, \tau)}{\partial \tau} = \frac{\partial}{\partial J} \frac{D(J)}{2} \frac{\partial f}{\partial J}. \tag{4.4}$$

Particularly, this equation entails the relaxation to a homogeneous steady state $f(J, \tau) \longrightarrow f_s(J) = \text{const}$ as it should be for the ergodic system.

In (4.4), τ is the discrete time measured in the number of separatrix crossings and $D(J) = \langle (\Delta J)^2 \rangle$ denotes a "diffusion rate" [21, 23]. Actually, this is not the real diffusion rate which includes the correlation between successive crossings. This may be important in the problem under consideration according to numerical data in [21] (for further discussion, see Section 5 below).

The results of our numerical experiments on the statistical properties for a single separatrix crossing are presented in Fig. 4a. We used the same numerical data as in Fig. 2b, which upon ordering in J were averaged by the standard method of the moving window of width of 500 points, or $\Delta_w J \approx 0.05$. The transition from the diffusive to the ballistic regime is surprisingly sharp, especially for $(\Delta J)_1$ (lower curve). The crossover value

$$J = J_{cro} = \alpha \epsilon^{1/3}, \quad \alpha \approx 1.08, \tag{4.5}$$

where empirical factor α was found from the plateau (upper bound) for $(\Delta J)_2$ (upper curve). To this end, we substitute J_{cro} for J in (4.3) to obtain

$$(\Delta J)_2 \le \frac{\sqrt{\mu_2}}{2\alpha^2} \epsilon^{1/3}. \tag{4.6}$$

Remarkably, the empirical data follow with a reasonable accuracy the diffusive theory literally down to the very crossover. This allowed us to numerically discern the very small but important first moment and even to check its agreement with the theory.

Even though there is as yet no theory for the ballistic regime, the underlying physical mechanism of the transition is rather simple and comprehensible [22]. This transition is determined by the kinetics parameter

$$\kappa \sim \frac{(\Delta J)_2}{J} \sim \frac{\epsilon}{J^3} \ll 1, \tag{4.7}$$

which is a reduced dynamical scale in J. The latter strong inequality is a necessary condition for the diffusion approximation to the exact integro-differential kinetic equation to hold; hence, we get the term diffusive region for $J \gtrsim J_{cro} \sim \epsilon^{1/3}$. In the opposite limit ($\kappa \gtrsim 1$), the trajectory jumps over the whole region $\sim J$ in one separatrix crossing. This is usually called the ballistic regime.

Since the action $J \geq 0$ cannot be negative, the change ΔJ is necessarily restricted for any J. In the ballistic region, the restriction becomes very strong, as the strict lower bound in Fig. 2b demonstrates. It simply means that $J_f \geq 0$, as well as J_i. Also, there exists the strict upper bound $J \leq 1$, but it corresponds to a very big ΔJ unless $J \longrightarrow 1$ is close to the upper border of separatrix crossing. Near this border is also the second ballistic region, but its width is very small. Again, it is determined by the kinetics parameter (4.7), which now takes the form

$$\kappa \sim \frac{(\Delta J)_2}{J_1} \sim \frac{\epsilon}{\sqrt{J_1}}, \quad J_1 = 1 - J \tag{4.8}$$

whence a new crossover $J_1^{(cro)} \sim \epsilon^2$.

In the diffusive normalization used in Fig. 4a, the quantities $2(\Delta J)_{1,2}/\epsilon$ do not depend on ϵ in the diffusive region but do so in the ballistic domain. Instead, one may use a different, ballistic, normalization by introducing a new variable $\tilde{J} = J/\epsilon^{1/3}$. The result is presented in Fig. 4b for the two values of ϵ. Instead of (4.3), we now have the relations:

$$(\Delta \tilde{J})_2^2 = \frac{\mu_2}{4}\left(\frac{1}{\tilde{J}^4} - \epsilon^{4/3}\right), \quad (\Delta J)_1 = -\frac{\mu_2}{2\tilde{J}^5}. \tag{4.9}$$

The second one is independent of ϵ in the full range of J. Some difference between the two lower curves is apparently due to fluctuations, especially for the smaller ϵ. The first relation slightly depends on ϵ, but this is important near the upper border ($J \approx 1$) only. The diffusive theory (4.9) is shown in Fig. 4b for $\epsilon = 0.01$ (upper thin curve).

Even though there is as yet no theory for the ballistic region, some statistical properties can be predicted here from a general consideration. One of those is the survival probability $P(\tau)$ for a trajectory to stay in the ballistic region during a time $>\tau$. Namely, this probability is expected to decay exponentially

$$P(\tau) \approx \exp\left(-\frac{\tau}{\langle\tau\rangle}\right) \tag{4.10}$$

with some average survival time $\langle\tau\rangle \sim 1$. This is because, for large jumps of a trajectory across the whole ballistic region, there is a certain probability $w \sim 1$ for a trajectory to remain within this region after each separatrix crossing. Moreover, the successive probabilities are expected, for a chaotic motion, to be equal and

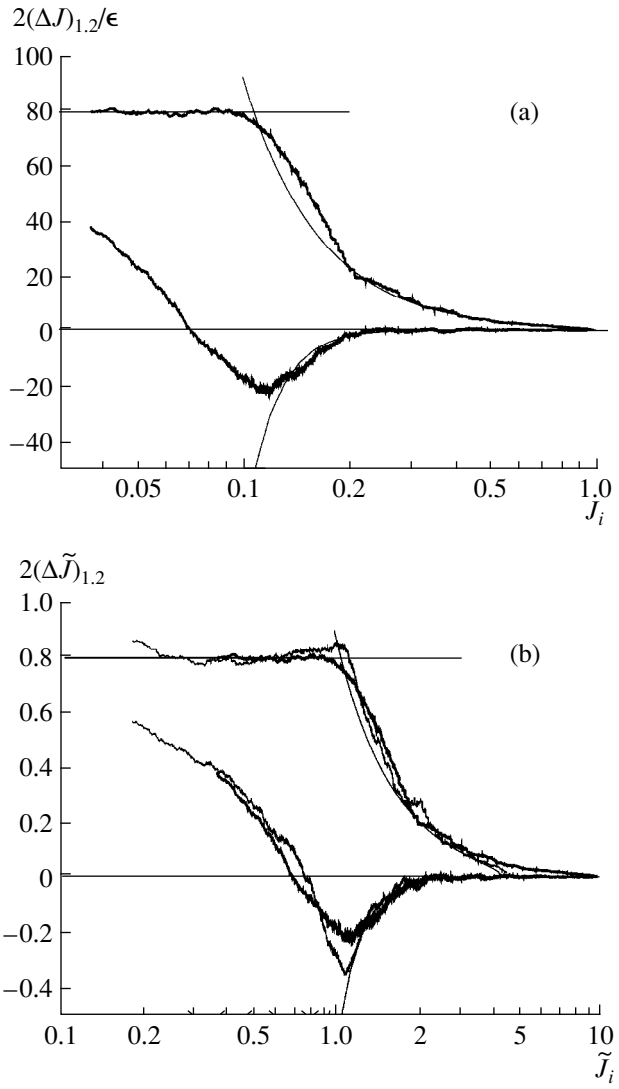

Fig. 4. Statistics of 10^4 separatrix crossings; window width $\Delta_w J \approx 0.05$. (a) $(\Delta J)_2$ (upper thick curve), and $(\Delta J)_1$ (lower curve) vs. J for $\epsilon = 0.001$; two thin solid curves represent the diffusive theory (4.3); the horizontal line is the empirical upper bound for $2(\Delta J)_2/\epsilon \approx 78$. (b) Same data for $\epsilon = 0.001$ and 0.01 in ballistic normalization: $\tilde{J} = J/\epsilon^{1/3}$; empirical upper bound $2(\Delta \tilde{J})_2 \approx 0.78$.

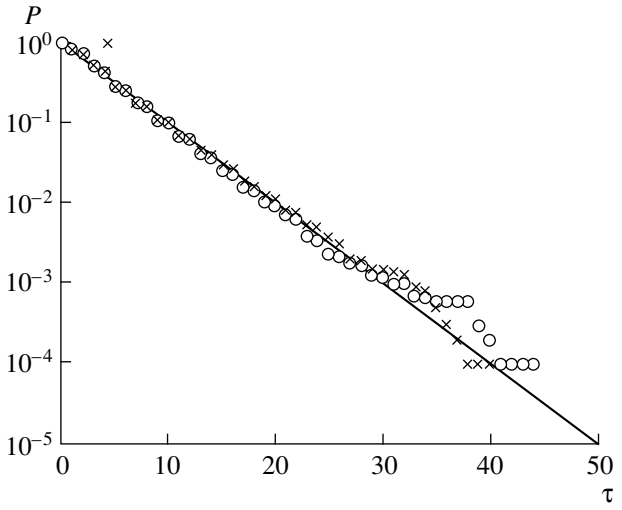

Fig. 5. Survival probability $P(\tau)$ in the ballistic region for $\epsilon = 0.001$ (circles) and $\epsilon = 0.01$ (crosses); 10^4 trajectories homogeneously distributed initially over the ballistic region; the straight line is the fit with $\langle\tau\rangle = 4.35$, $w = 0.79$.

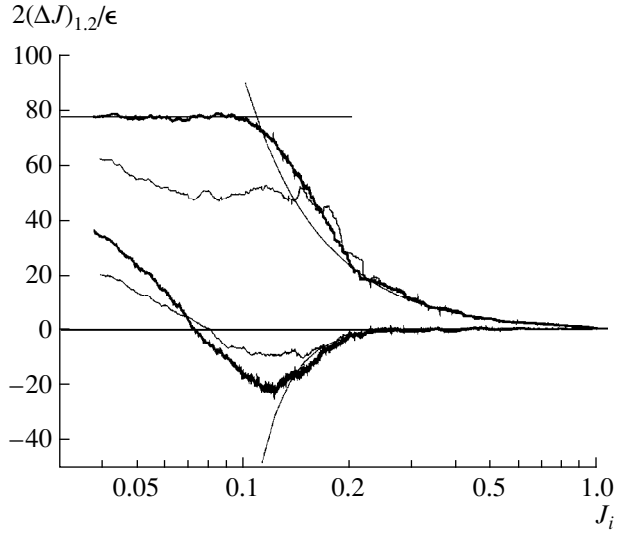

Fig. 6. The effect of correlation over four successive separatrix crossings. Two thick wiggly curves show statistics of the single crossing as in Fig. 4a. Thin wiggly curves represent the effect of fourfold crossings; both moments are normalized (see text).

statistically independent. This implies the exponential (4.10) with $\langle\tau\rangle = -1/\ln w$ independent of ϵ. The latter is especially clear in the ballistic normalization (4.9).

The results of numerical experiments are presented in Fig. 5.

Curiously, the diffusion equation (4.4) with constant $D \approx 0.16$ (in ballistic normalization, see Fig. 4b) also leads to the exponential decay (4.10) with the average survival time

$$\langle\tau\rangle \approx \frac{2}{Dk^2} \approx 5, \qquad (4.11)$$

where $k \approx \pi/2$ is the parameter of the first (main) eigenfunction of the diffusion equation: $f_1(\tilde{J}) \approx \cos(k\tilde{J})$. This is surprisingly close to the empirical value $\langle\tau\rangle \approx 4.4$ (Fig. 5) in spite of the formal inapplicability of the diffusion approximation in the ballistic region!

5. DISCUSSION

In the present paper, we reported the results of extensive numerical experiments aimed at the detailed study of the dynamics and statistics of separatrix crossing in the classical model (2.1). Our work was stimulated by an interesting investigation of the quantum behavior of this model [15].

First of all, we carefully checked the agreement of the empirical data with the existing fairly simple first-order theory [9, 12] and found it surprisingly good, close in fact to the formal limiting accuracy of the theory (Fig. 1). In addition, we were able to discern one second-order effect, the behavior of the first moment $\langle\Delta J\rangle(J)$, which is beyond the theory but very important for the diffusion equation. Our numerical results confirm the expected relation between the two moments (see (4.3) and (Fig. 4)).

On the other hand, we have found that such a nice agreement crudely breaks down in the ballistic region $J < J_{cro} \approx \epsilon^{1/3}$ (Fig. 4), which is qualitatively different from the complementary diffusive region $J > J_{cro}$. The new regime of separatrix crossing was first noticed and partly explained in [22]. It is a peculiarity of model (2.1) in which a pulsating separatrix crosses zero. In many other models studied numerically (see, e.g., [10, 11, 20, 21]), the authors tended to avoid the theoretical singularity at $J \longrightarrow 0$ (3.2). This is more simple, of course, but less interesting. Particularly, the largest violation of adiabaticity ($\Delta J \sim \epsilon^{1/3}$) is reached only in the ballistic region (Figs. 2 and 4).

Even though the dynamical theory in this region seems to be a hard task and has not yet developed the statistical properties of the motion, here it looks rather simple. Surprisingly, even a simplified diffusion equation, which may not hold in the ballistic region, still allows for some reasonably accurate estimates (Fig. 5).

In the present paper, we consider the dynamics and statistics of a single separatrix crossing only. Of course, this is insufficient for the full-scale statistical description of the separatrix crossing. As is well known (see, e.g., [20, 21]), the correlations in multiple crossings are generally very essential. In conclusion of our discussion, we present in Fig. 6 the commutative effect of four successive crossings over one period of the perturbation.

Both moments are normalized as follows: $(\Delta J)_1 \longrightarrow (\Delta J)_1/\tau$; $(\Delta J)_2^2 \longrightarrow (\Delta J)_2^2/\tau \equiv D(\tau)$ where discrete time

$\tau = 4$ is the crossing multiplicity in this case (see (4.3)). In the diffusive region 2, both curves coincide within fluctuations, which means that the correlations, if any, are small over four crossings. This is in agreement with the results in [21] (for a different model). Whether they will rise with τ and why is an interesting and open question. According to [21], they do so, but it may depend on the method of measuring the diffusion rate. In the ballistic region, the correlation effect is strong from the beginning, especially for the second moment. This is also in agreement with numerical data in [22]. According to data in Fig. 6, the normalized second moment (the "diffusion rate") decreases as $D(\tau) \propto 1/\sqrt{\tau}$. What is even more important, the size of the ballistic region grows: $J_{cro}(\tau) \propto \tau^{1/8}$. An intriguing question is whether this trend will continue and, if so, for how long.

ACKNOWLEDGMENTS

We are grateful to Bruno Mirbach, who kindly provided for us his numerical results prior to publication. We appreciate many interesting and stimulating discussions with him and Giulio Casati. This work was partially supported by the Russian Foundation for Fundamental Research, project no. 97-01-00865.

REFERENCES

1. L. I. Mandelshtam, *Complete Works* (Akad. Nauk SSSR, Moscow, 1948), Vol. 1, p. 297.
2. B. V. Chirikov, *Reviews of Plasma Physics*, Ed. by B. B. Kadomtsev (Énergoatomizdat, Moscow, 1984; Consultants Bureau, New York, 1987), Vol. 13.
3. A. Lichtenberg and M. Lieberman, *Regular and Chaotic Dynamics* (Springer, New York, 1992).
4. V. I. Arnold, Dokl. Akad. Nauk SSSR **156**, 9 (1961).
5. B. V. Chirikov, Phys. Rep. **52**, 263 (1979).
6. B. V. Chirikov and V. V. Vecheslavov, J. Stat. Phys. **71**, 243 (1993); Zh. Éksp. Teor. Fiz. **112**, 1132 (1997) [JETP **85**, 616 (1997)].
7. N. N. Nekhoroshev, Usp. Mat. Nauk **32** (6), 5 (1977); P. Lochak, Phys. Lett. A **143**, 39 (1990); Usp. Mat. Nauk **47** (6), 59 (1992); P. Lochak and A. Neishtadt, Chaos **2**, 495 (1992).
8. B. V. Chirikov, Dokl. Akad. Nauk SSSR **125**, 1015 (1959) [Sov. Phys. Dokl. **4**, 390 (1959)]; B. V. Chirikov and D. L. Shepelyanskiĭ, Zh. Tekh. Fiz. **52**, 238 (1982) [Sov. Phys. Tech. Phys. **27**, 156 (1982)].
9. J. Tennyson *et al.*, Phys. Rev. Lett. **56**, 2117 (1986); Phys. Rev. A **34**, 4256 (1986).
10. R. Best, Physica **40**, 182 (1968).
11. R. Aamodt and E. Jaeger, Phys. Fluids **17**, 1386 (1974).
12. A. V. Timofeev, Zh. Éksp. Teor. Fiz. **48**, 1303 (1978) [Sov. Phys. JETP **48**, 656 (1978)].
13. V. Ya. Davydovskiĭ and A. I. Matveev, Zh. Tekh. Fiz. **53**, 2125 (1983) [Sov. Phys. Tech. Phys. **28**, 1302 (1983)]; A. I. Neishtadt, Fiz. Plazmy **12**, 992 (1986) [Sov. J. Plasma Phys. **12**, 568 (1986)].
14. C. Eckart, Phys. Rev. **35**, 1303 (1930); A. S. Bakav and Yu. P. Stepanovsky, *Adiabatic Invariants* (Naukova Dumka, Kiev, 1981).
15. B. Mirbach and G. Casati, Phys. Rev. Lett. **83**, 1327 (1999).
16. C. Menyuk, Phys. Rev. A **31**, 3282 (1985).
17. Y. Elskens and F. Escande, Physica D **62**, 66 (1993).
18. L. Casetti, Phys. Scr. **51**, 29 (1995).
19. E. Forest and R. Ruth, Physica D **43**, 105 (1990).
20. J. Cary and R. Skodje, Physica D **36**, 287 (1989).
21. D. Bruhwiler and J. Cary, Physica D **40**, 265 (1989).
22. B. Mirbach, private communication.
23. J. Cary, F. Escande, and J. Tennyson, Report No. IFSR-155 (Institute for Fusion Studies Report, 1984).